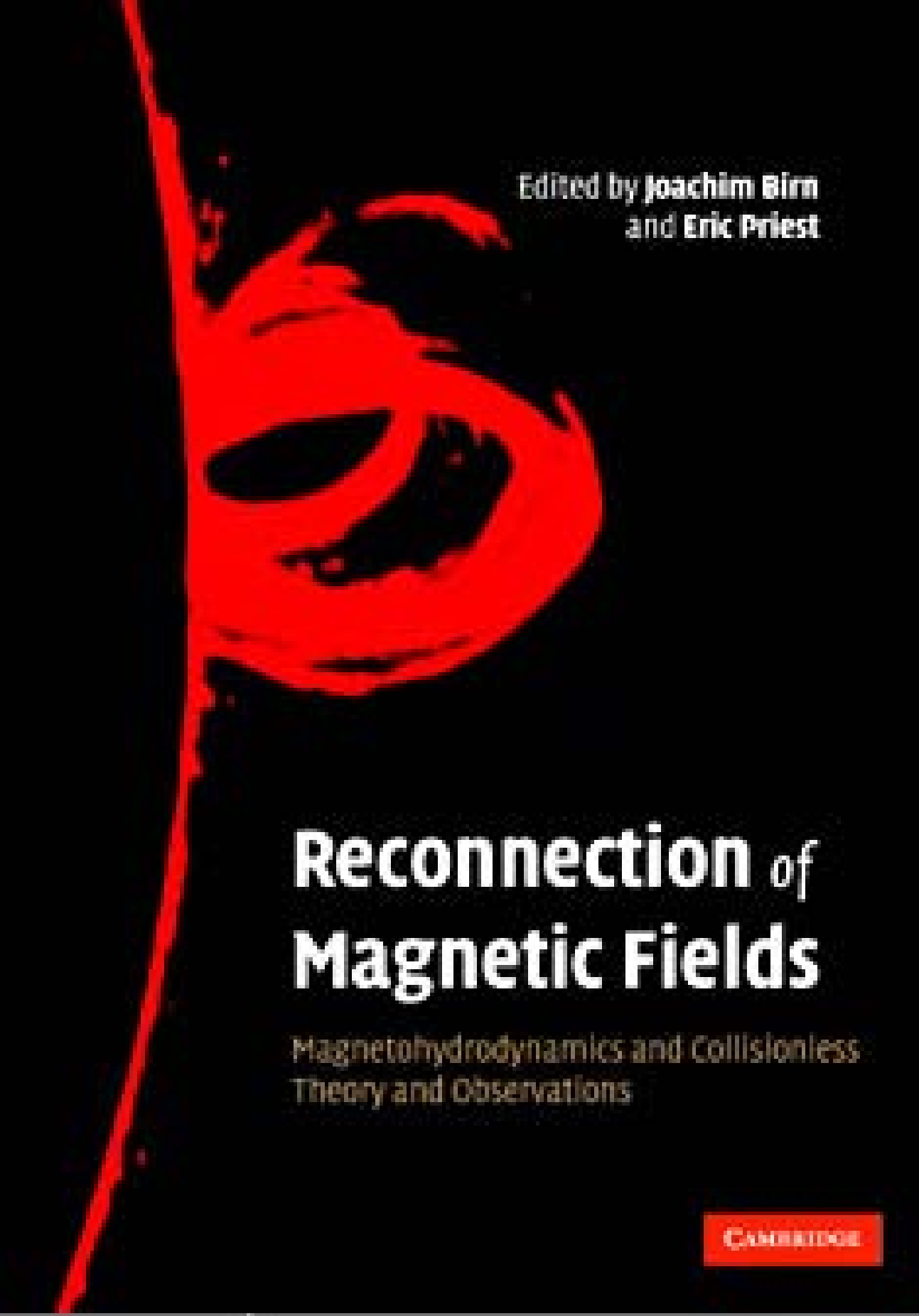

Edited by Joachim Birn and Eric Priest

Reconnection of Magnetic Fields

Magnetohydrodynamics and Collisionless Theory and Observations

CAMBRIDGE

CAMBRIDGE www.cambridge.org/9780521854207

This page intentionally left blank

RECONNECTION OF MAGNETIC FIELDS

Magnetohydrodynamics and Collisionless Theory and Observations

The reconnection of magnetic fields is one of the most fascinating processes in plasma physics, responsible for phenomena such as solar flares and magnetospheric substorms. The concept of reconnection has developed through recent advances in exploring the environments of the Sun and Earth through theory, computer simulations, and spacecraft observations. The great challenge in understanding it stems from balancing the large volumes of plasma and magnetic fields involved in energy release with the physical mechanism which relies on the strongly localized behavior of charged particles. This book, edited by and with contributions from leading scientists in the field, provides a comprehensive overview of recent theoretical and observational findings concerning the physics of reconnection and the complex structures that may give rise to, or develop from, reconnection. It is intended for researchers and graduate students interested in the dynamics of plasmas.

Joachim Birn is a staff member in the Space Science and Applications Group at Los Alamos National Laboratory. He was elected a Fellow of the American Geophysical Union in 2000.

Eric Priest is the James Gregory Professor of Mathematics at St. Andrews University and was elected a Fellow of the Royal Society in 2002.

RECONNECTION OF MAGNETIC FIELDS

Magnetohydrodynamics and Collisionless Theory and Observations

Edited by

J. BIRN

Los Alamos National Laboratory

and

E. R. PRIEST

University of St. Andrews

CAMBRIDGE
UNIVERSITY PRESS

cambridge university press
Cambridge, New York, Melbourne, Madrid, Cape Town, Singapore, São Paulo

Cambridge University Press
The Edinburgh Building, Cambridge cb2 2ru, UK

Published in the United States of America by Cambridge University Press, New York

www.cambridge.org
Information on this title: www.cambridge.org/9780521854207

First published in print format 2006

isbn-13 978-0-511-26004-9 eBook (EBL)
isbn-10 0-511-26004-0 eBook (EBL)

isbn-13 978-0-521-85420-7 hardback
isbn-10 0-521-85420-2 hardback

Contents

Contributors

Professor Wolfgang Baumjohann
Austrian Academy of Sciences
Space Research Institute
Schmiedlstrasse 6
Graz, 8042
Austria

Professor Amitava Bhattacharjee
EOS Space Science Center
University of New Hampshire
39 College Rd
Durham, NH 03824
USA

Dr. Joachim Birn
MS D466
Los Alamos National Laboratory
Los Alamos, NM 87545
USA

Professor Joerg Büchner
Max Planck Institute for Solar System Research
Max Planck Strasse 2
Katlenburg-Lindau, 37191
Germany

Dr. Gareth Chisham
British Antarctic Survey
High Cross
Madingley Rd
Cambridge, CB3 OET
United Kingdom

Dr. Iain J. Coleman
British Antarctic Survey
High Cross
Madingley Rd
Cambridge, CB3 OET
United Kingdom

Dr. William S. Daughton
University of Iowa
Department of Physics and Astronomy
Iowa City, IA 52242
USA

Dr. John C. Dorelli
EOS Space Science Center
University of New Hampshire
39 College Rd
Durham, NH 03824
USA

Professor James F. Drake
University of Maryland
Institute for Research in Electronics and Applied Physics
College Park, MD 20742
USA

Dr. Lyndsay Fletcher
University of Glasgow
Astronomy and Astrophysics Group
Department of Physics and Astronomy
Glasgow, G12 8QQ
United Kingdom

Dr. Terry G. Forbes
EOS Space Science Center
University of New Hampshire
39 College Rd
Durham, NH 03824-3525
USA

Dr. Mervyn P. Freeman
British Antarctic Survey
High Cross
Madingley Rd
Cambridge, CB3 OET
United Kingdom

Dr. Stephen Fuselier
Lockheed Martin
3251 Hanover St L9-42 B255
Palo Alto, CA 94304-1191
USA

Dr. K. Galsgaard
Niels Bohr Institute for Astronomy,
Physics and Geophysics
Blegdamsvej 17,
DK-2100
Copenhagen Ø,
Denmark

Dr. Paulo Giuliani
University of St Andrews
School of Mathematics and Statistics
St Andrews, KY16 9SS
United Kingdom

Dr. Michael Hesse
NASA Goddard Space Flight Center
Code 696
Greenbelt, MD 20771
USA

Dr. Gunnar Hornig
Dundee University
Division of Mathematics
23 Perth Rd
Dundee, DD1 4HN
United Kingdom

Dr. Masahiro Hoshino
University of Tokyo
Department of Earth and Planetary
Physics
7-3-1 Hongo, Bunkyo-ku
Tokyo, 113 0033
Japan

Dr. Kanya Kusano
Hiroshima University
ADSM
Kagamiyama 1-3-1
Higashi Hiroshima, 739-8530
Japan

Dr. Mark G. Linton
Naval Research Laboratory
Code 7675L
4555 Overlook Ave SW
Washington, DC 20375-5352
USA

Dr. Dana W. Longcope
Montana State University
Physics Department
Bozeman, MT 59717-0350
USA

Dr. Rumi Nakamura
Austrian Academy of Sciences
Space Research Institute

Schmiedlstrasse 6
Graz, 8042
Austria

Dr. Thomas Neukirch
University of St Andrews
School of Mathematics and Statistics
St Andrews, KY16 9SS
United Kingdom

Dr. Steven M. Petrinec
Lockheed Martin
3251 Hanover St L9-42 B255
Palo Alto, CA 94304-1191
USA

Dr. David I. Pontin
Dundee University
Division of Mathematics
23 Perth Rd
Dundee, DD1 4HN
United Kingdom

Professor Eric R. Priest
University of St Andrews
Mathematics Department
St Andrews, KY16 9SS
United Kingdom

Dr. Philip L. Pritchett
UCLA
Department of Physics
405 Hilgard Ave
Los Angeles, CA 90095-1547
USA

Prof. T. Sakurai
National Astronomical Observatory
2-21-1 Osawa, Mitaka
Tokyo 181-8588, Japan
e-mail: sakurai@solar.mtk.nao.ac.jp

Professor Karl Schindler
Ruhr-University Bochum
Faculty of Physics and Astronomy
Institute for Theoretical Physics IV
Bochum, D-44780
Germany

Professor Michael Shay
Department of Physics and Astronomy
223 Sharp Laboratory
Newark, DE 19716
USA

Dr Viacheslav S. Titov
SAIC Corp Headquarters
10210 Campus Point Drive
San Diego, CA 92121
USA

Dr. Karlheinz J. Trattner
Lockheed Martin
3251 Hanover St L9-42 B255
Palo Alto, CA 94304-1191
USA

Dr. Paul D. Wood
University of St Andrews
School of Mathematics and Statistics
St Andrews, KY16 9SS
United Kingdom

Preface

This book grew out of a month-long workshop on Magnetic Reconnection Theory held in 2004 at the Isaac Newton Institute, Cambridge, UK, organized by E. R. Priest, T. G. Forbes, and J. Birn. The focus of this workshop was on the most recent advances in understanding reconnection, particularly its three-dimensional aspects and the physics of collisionless reconnection. These are the two areas where the most rapid development beyond the classical theory of reconnection has taken place in recent years. In addition, it was found desirable to include new observational aspects from the two areas that have initiated the concept of reconnection as well as provided new, unprecedented details in remote and *in situ* observations, the Sun and the Earth's magnetosphere.

This book highlights recent progress and thus it is not a comprehensive overview. Rather it is complementary to recent reviews by Priest and Forbes (2000) and Biskamp (2000), which cover more of the traditional approaches to reconnection. Due to the focus on new results, rather than the classical concepts, about one-third of the citations in this book are from the new millenium, years 2001 to 2005. This makes it plausible that the latest developments have not led to a settled, unified, well-accepted picture, and that some topics are still controversial, even between different authors contributing to this book. We did not try to hide those controversies. Also, we did not try to consolidate various discussions of related topics into single sections or subsections. We found that, at this stage of the research development, different views of the same topic by different authors might actually be helpful to the reader to gain deeper insights.

Acknowledgments

The editors and the section authors gratefully acknowledge the hospitality of the Isaac Newton Institute, Cambridge, UK and its Director, Sir John Kingman, and the financial support provided by the Institute. Editors and authors also acknowledge support by the Institute of Geophysics and Planetary Physics at Los Alamos National Laboratory, which hosted a week-long follow-up workshop in Santa Fe, New Mexico, in 2005, during which the successful open discussion and collaboration was continued.

In addition, editors and authors acknowledge financial support by the following institutions: the US National Aeronautics and Space Administration (NASA), through its Sun-Earth Connection Theory, Living With a Star, and Supporting Research & Technology programs, the US Department of Energy through its Office of Basic Energy Sciences, the US Department of Defense, the US Office of Naval Research, the US National Science Foundation, and the UK Particle Physics and Astronomy Research Council.

Furthermore, the authors benefited greatly from discussions and collaborations with the following colleagues: Spiro Antiochos, Russell Dahlburg, Jean Heyvaerts, Joe Huba, Homa Karimabadi, Dietmar Krauss-Varban, Antonius Otto, Clare Parnell, and Grigory Vekstein, apart from discussions with each other.

1

Introduction

The Sun and the Earth's magnetosphere (hereafter simply called the magnetosphere) play particular roles in the history of reconnection, frequently also referred to as magnetic merging, as well as in the most recent advances in understanding the spatial structure and the physics of reconnection sites. The concept of reconnection (although not the term) was first suggested by Giovanelli (1946) as a mechanism for particle acceleration in solar flares. This proposed mechanism was extremely modern, as it considered not only electric fields along magnetic neutral lines (as in standard two-dimensional (2D) models; Section 2.1) but also electric fields with a local component along the magnetic field, which is the basic concept of *general three-dimensional* (3D) *magnetic reconnection* (Sections 2.2 and 2.3).

Investigations of reconnection in the magnetosphere have stimulated the development of the concept of 3D reconnection in the absence of magnetic nulls (Hesse and Schindler, 1988; Schindler *et al.*, 1988) and considerations of the interaction between a dipole (magnetosphere) and the surrounding (interplanetary) magnetic field have stimulated investigations of the topology of the magnetic field and topological changes associated with reconnection (Dungey, 1961, 1963). They have also motivated the first investigations into the 3D magnetic structure of magnetic null points (Greene, 1988; Lau and Finn, 1990). More recently, the complex structures of the coronal magnetic field, inferred from astonishing X-ray and EUV pictures, have motivated the further detailed exploration of the 3D topology of magnetic fields and its role in reconnection (Chapters 2 and 5).

Magnetospheric spacecraft observations on the other hand provide the most detailed *in-situ* information on particle populations and the structure of fields in the vicinity of potential and actual reconnection sites and have thereby motivated (and vice versa, are being motivated by) the most detailed computer simulations of reconnection in the collisionless regime (Chapters 3 and 4).

To understand the physical role that magnetic reconnection plays in solar and magnetospheric activity it seems essential to investigate not only the reconnection process itself but also the conditions that prevail before reconnection starts. In typical scenarios, the preonset phase starts with a slow evolution in response to external forces. During that phase, energy is supplied to the system, largely in the form of magnetic energy. After the onset of reconnection the system shows a fast evolution, which may involve a change of magnetic topology, associated with a conversion of magnetic to kinetic energy. This scheme applies to most models of solar eruptions

such as flares (Priest, 1981; Tandberg-Hanssen and Emslie, 1988), erupting prominences (Tandberg-Hanssen, 1994) or coronal mass ejections (Webb, 2000), and of magnetospheric substorms (McPherron *et al.*, 1973; Baker *et al.*, 1985).

A basic task is to understand what conditions the preonset evolution has to satisfy to initiate reconnection. Magnetospheric observations have provided strong evidence for the formation of a thin current sheet or several sheets, which seem to play a crucial role in magnetotail dynamics (Kaufmann, 1987; McPherron *et al.*, 1987; Baker and McPherron, 1990; Mitchell *et al.*, 1990; Sergeev *et al.*, 1990; Schindler and Birn, 1993). Thin current sheets are also believed to be important elements of solar activity (Priest, 1981; Parker, 1994). *Current sheets* in the solar context usually denote infinitely thin sheets, or sheets whose thickness is negligibly small compared with the structures considered, equivalent to tangential discontinuities in the framework of magnetohydrodynamics (MHD). In the magnetospheric context, thin current sheets are observed to have a finite thickness; this thickness is typically comparable to or even smaller than typical ion gyroradii or ion inertia lengths (Chapters 3 and 4); and they may also have a small but finite magnetic field component across the sheet. These small deviations actually play an important role when the stability of thin current sheets is considered (Sections 3.3 and 4.3).

In the simplest scenario, a quasi-steady evolution, driven by external forces, leads to the formation of a thin current sheet. If the current sheet has become sufficiently pronounced or if it experiences loss of equilibrium (Birn and Schindler, 2002), reconnection may start. However, the formation of a thin current sheet (or of multiple current sheets) may also be preceded, or followed, by a dynamic phase that does not involve reconnection, prior to the onset of reconnection.

In the solar atmosphere a thin current sheet might form following the sudden rise of a magnetic island or flux rope (Forbes, 2000) or as a consequence of a kink instability of a flux rope equilibrium (Kliem *et al.*, 2004). In the magnetotail the MHD ballooning mode, driven by pressure gradients in the direction of strong field line curvature in the center of the plasma sheet, has been considered as a possible candidate for substorm initiation (Roux *et al.*, 1991), although it is not clear yet how it might lead to reconnection.

Alternatively, current intensification might initiate a current-driven microinstability that by nonlinear coupling could lead to reconnection. Another possibility is a scenario in which *lower-hybrid drift instability* in the boundary regions of a current sheet might change the particle and current distribution within the sheet and thereby initiate, or accelerate, reconnection. Such scenarios are discussed in Section 3.5.

3D reconnection, collisionless reconnection, and reconnection at the Sun and in the magnetosphere are the particular focuses of this book. There are still many open problems and even controversies concerning the occurrence, operation, evolution, and consequences of reconnection. They include fundamental questions such as:

What is reconnection? What is the role of magnetic topology; how does it affect the physics of reconnection? The extension of 2D to 3D models is not straightforward, it may involve the full complexity of magnetic field structure (Chapter 2). On the particle level, collisionless reconnection involves not only ion scales but even electron scales (Chapter 3).

How and where is reconnection initiated? What is the dominant mechanism: increased current density or low magnetic field strength? What are the differences between reconnection in low-beta and high-beta plasmas? What is the role of flow fields?

What determines the rate of reconnection? (One, apparently simple, question has no full answer yet: How is the reconnection rate defined and measured in generalized configurations, locally, remotely, and globally?) Is it dominated by an external driving mechanism, by the local dissipation mechanism, or by the dynamics in the vicinity of the reconnection site? Recent investigations of reconnection through widely different simulation codes (Section 3.1) have provided strong evidence that, in a collisionless medium, Hall electric fields are essential in establishing the reconnection rate, regardless of the dissipation mechanism. However, this result need not be valid in all scenarios.

A plausible view of the role of external driving is that it leads to a build-up of the current density until a current-driven dissipation mechanism sets in which leads to an electric field that matches the driving electric field. But this picture is convincing only in simplified 2D models where the plasma cannot escape to the third dimension. Furthermore, it appears that the plasma response to external driving depends not only on the boundary conditions but also on the background or initial state (stable vs. unstable; small vs. large; 1D vs. 2D, 3D).

What is the role of reconnection in particle acceleration at thermal and suprathermal energies? Particle orbit studies in reconnecting fields (Sections 3.6, 4.4, 5.6) indicate that it is necessary to consider the 3D time-dependent structure of the electric and magnetic fields to fully identify acceleration mechanisms and to distinguish local acceleration near the reconnection site from quasi-adiabatic effects in the dynamically changing fields.

In the following two sections we give a brief overview of the solar and magnetospheric contexts of reconnection. These provide a background for fundamental investigations of the 3D aspects and the physics of collisionless reconnection discussed in Chapters 2 and 3. In the subsequent Chapters 4 and 5 we return to the applications of reconnection to the magnetospheric and solar environment.

1.1 The Sun

E. R. Priest

Magnetic reconnection is a fundamental process in the Sun, both in the interior (where it is essential in dynamo generation of magnetic fields) and in the atmosphere (where it lies at the core of a solar flare and is probably responsible for heating the corona). Here we give a brief background and overview of its role in the atmosphere as a prelude to the more detailed sections that follow.

The solar atmosphere, as classically understood, consists of three parts, namely, the *photosphere, chromosphere*, and *corona*. The photosphere is the thin surface layer of the Sun having a density and temperature of $10^{23}\,\mathrm{m}^{-3}$ and 6000 K, respectively, and from which most of the visible light is radiated into space. It represents the top of the turbulent convection zone which occupies the outer 30% of the solar interior. The photosphere is covered with small convection cells, called *granules*, typically 1 Mm across by comparison with the solar radius of 700 Mm, and having lifetimes of

5 min. In addition, there are large-scale *supergranules* which are 15 Mm in diameter and last for 1 or 2 days.

In two bands, north and south of the equator, dark regions called *sunspots* come and go and exhibit an 11-year cycle in their number. Sunspots have very strong magnetic fields (a few thousand gauss) and occur either singly or in groups. The region of enhanced magnetic field around a sunspot group is known as an *active region*. Outside active regions in the so-called *quiet Sun*, the photospheric magnetic field is highly fragmentary and located mainly around the boundaries and at the junctions of supergranules. This magnetic field is typically born as a small bipolar *ephemeral region*, the poles of which fragment and migrate rapidly to the supergranule boundaries. The lifetime of this magnetic flux is only typically 15 hours and the magnetic field emanating from it into the corona is known as the *magnetic carpet* (Schrijver *et al.*, 1998; Hagenaar *et al.*, 2003).

The *chromosphere* is warmer than the photosphere (about 10 000 K) and rarer (about $10^{17}\,\mathrm{m}^{-3}$) and above it lies the much hotter *corona*, with a temperature of about a million degrees and a density of $10^{14}\,\mathrm{m}^{-3}$. In classical models the corona was thought to be separated from the chromosphere by a narrow *transition region*. However, it is now known that the chromosphere, transition region, and corona represent the plasma that happens to be at typically 10^4 K, 10^5 K and 10^6 K, respectively, that is moving or arching along magnetic field lines and is highly dynamic and time-dependent, either heating up or cooling down.

During a solar eclipse (Fig. 1.1a) the corona can be seen for a few minutes as a beautiful pearly white glow, about as bright as the full Moon. All its structure is created by the magnetic field. It reveals large-scale bright closed regions, known as *helmet streamers*, and also large magnetically open regions along which the fast solar wind is escaping, known as *coronal holes*.

With soft X-ray telescopes on space satellites the corona can be viewed directly (Fig. 1.1b), where the magnetically closed and open regions show up as bright *coronal loops* and dark *coronal holes*, respectively. A third component of the corona is also visible, however, namely several hundred tiny bright spots known as *X-ray bright points*.

Large magnetic flux tubes containing thin vertical sheets called *prominences* or *filaments* are also present up at coronal levels but they are very much cooler and denser than the corona, having temperatures of only 7000 K. These prominences lie above large-scale polarity inversion lines in the component of the photospheric magnetic field that is normal to the solar surface. When existing inside or on the edge of an active region they tend to be small, but outside active regions they can be much larger. The main importance of prominences is that they represent regions of the solar atmosphere where the magnetic field is highly sheared and twisted, so that large quantities of magnetic energy are stored in excess of potential. For a given normal magnetic field distribution at the solar surface, the coronal magnetic field that has the minimum magnetic energy is the unique potential field based on that distribution of surface normal field.

1.1.1 Solar flares

Solar flares and *coronal mass ejections* are thought to occur when stored magnetic energy in excess of the potential field energy becomes so large that an

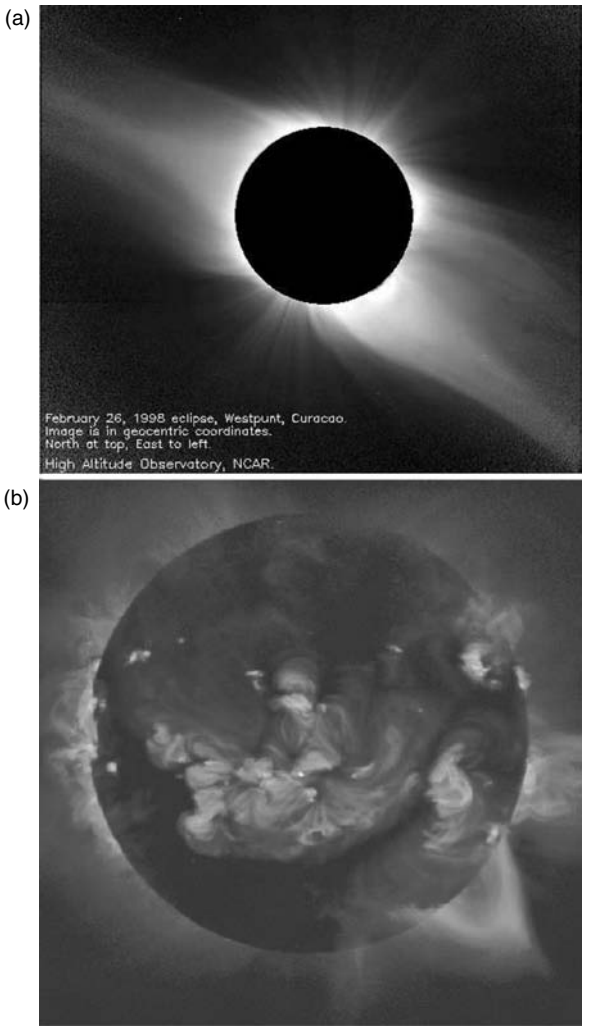

Fig. 1.1. The solar corona viewed (a) during a solar eclipse (courtesy High Altitude Observatory) and (b) by the Yohkoh satellite in soft X-rays (courtesy Yohkoh team).

eruptive instability or loss of equilibrium takes place. When a prominence and its overlying coronal arcade erupts, it gives rise to a *coronal mass ejection* (CME) (Fig. 1.2). Prominences may erupt from either outside or inside active regions. When they do so from within an active region, where the magnetic field and resulting magnetic force and electric field are very much larger than outside, a large *two-ribbon solar flare* occurs, in which two separating chromospheric ribbons are seen at the footpoints of a rising arcade of hot coronal loops.

Several ideas have been proposed to explain the eruption (Priest and Forbes, 2000). For example, one model (Priest and Forbes, 1990; Forbes and Priest, 1995) suggests that before the eruption there is a coronal arcade containing a largely horizontal magnetic flux tube supporting a prominence. At the initiation of eruption

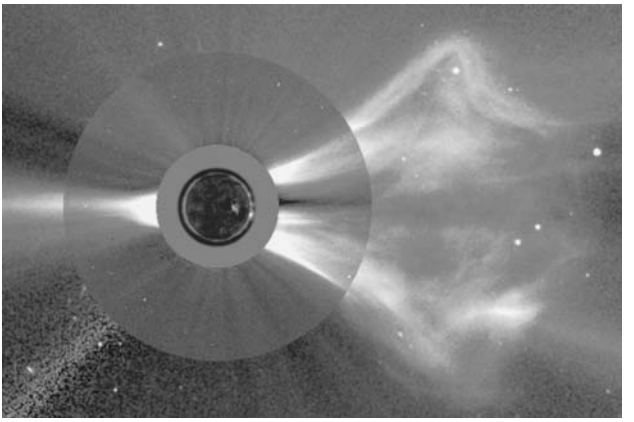

Fig. 1.2. A composite of three images of a large CME from the Extreme-ultraviolet Imaging Telescope (EIT) (the Sun shown by the small circle in the center) and the Large Angle and Spectrometric Coronagraph Experiment (LASCO) C2/C3 instruments (courtesy Solar and Heliospheric Observatory (SOHO), which is a project of international cooperation between ESA and NASA).

the magnetic configuration reaches a point of *magnetic nonequilibrium* or *catastrophe*, such that the configuration is no longer in equilibrium and the imbalance in forces drives an eruption (Fig. 1.3). The eruption is thought to drive reconnection below the rising flux tube. Priest and Forbes (1990) developed a $2\frac{1}{2}$-dimensional model of this process (neglecting variations in one spatial direction but including the field components in that dimension), whereas Amari *et al.* (2000) conducted a three-dimensional numerical experiment with similar quantitative features. A related *magnetic breakout* model was proposed by Antiochos *et al.* (1999).

Regardless of the proposed cause of the eruption, the nature of the reconnection process is similar in most models (Fig. 1.4). The energy released by the reconnection heats an arcade of very hot loops, which are filled by evaporation with hot plasma from the chromosphere and at the feet of which are located the bright chromospheric ribbons. As reconnection continues, the reconnection location rises and new hot loops are powered at a higher altitude; meanwhile, the underlying loops cool by radiation and conduction and their plasma drains back down to the solar surface.

One of the key effects of reconnection is to accelerate particles extremely rapidly (within a few seconds) to extremely high energies (Sections 5.6 and 5.7). A variety of mechanisms has been proposed for the way in which such particles may be accelerated by reconnection (Section 5.6), including: *DC acceleration* by the reconnection electric field; *stochastic acceleration* by the turbulence associated with reconnection; *shock acceleration* by either the slow-mode shocks associated with fast reconnection or the fast-mode shock that slows down the reconnection jet flowing down from the reconnection site towards the underlying closed coronal arcade; and finally by *betatron* and *Fermi acceleration* in the reconnection field lines below the reconnection point as they rapidly close down. Furthermore, recent observations from space satellites such as SOHO, TRACE, and RHESSI are giving important clues about the nature of the particle acceleration process (Section 5.7).

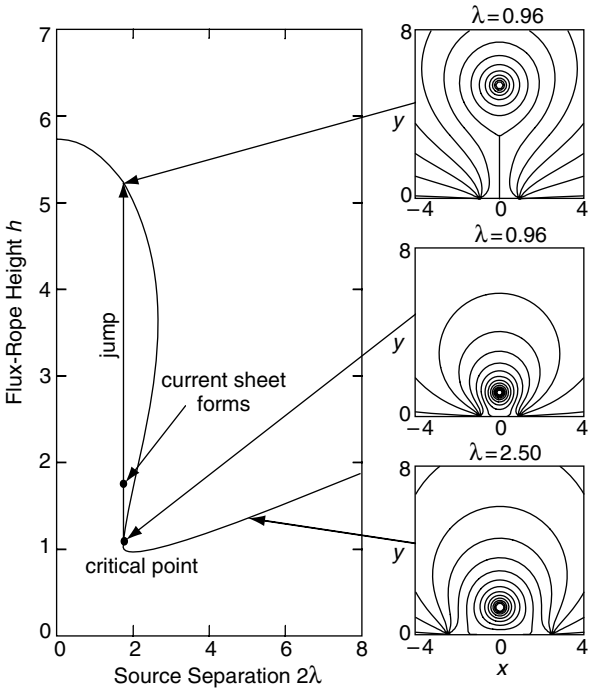

Fig. 1.3. Model for eruption by magnetic catastrophe. After Forbes and Priest (1995).

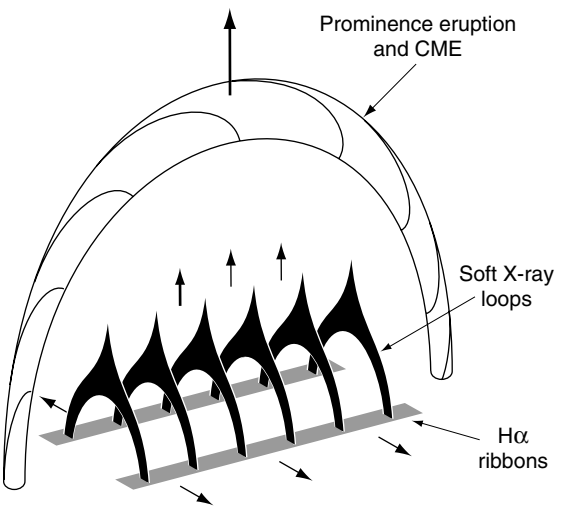

Fig. 1.4. Magnetic reconnection scenario in a two-ribbon flare.

1.1.2 Coronal heating

One of the biggest mysteries in solar physics is the nature of the mechanism that is heating the corona to a few million degrees. Reconnection now seems to be a likely candidate and can work in a variety of ways, as reviewed in Section 5.1. In the corona the magnetic field is by far the largest source of energy and it dominates the structures that we see. Furthermore, the Poynting flux of energy upwards from the photosphere is certainly sufficient to provide the energy required to heat the corona, but how does it do so?

Several mechanisms involving reconnection have been proposed. First of all, X-ray bright points are likely to be heated directly by reconnection driven by footpoint motions, as described in the *converging flux model* (Priest *et al.*, 1994; Parnell and Priest, 1995). This is because two-thirds of the X-ray bright points appear to be associated with the cancellation of the magnetic flux in the photosphere as opposite-polarity photospheric fragments come together and cancel. The remaining third are instead associated with emerging flux, as new flux emerges through the photosphere and reconnects with the overlying coronal magnetic field, as described by the *emerging flux model* (Heyvaerts *et al.*, 1977).

Coronal loops, on the other hand, may be heated by reconnection in other ways. The classical model for such heating was proposed by Parker (1972) and developed by Parker (1994) in terms of the formation and dissipation of current sheets by *braiding* of the footpoints of an essentially uniform magnetic field. This basic scenario has now been developed by Priest *et al.* (2002), who propose a *coronal tectonics model* that attempts to take account of the effect of the magnetic carpet on coronal heating. It suggests that myriads of current sheets are continually forming and dissipating at the separatrices and separators that form at the boundaries between the flux domains that originate at the multitude of photospheric magnetic fragments. Indeed, a recent estimate of the time for all the magnetic fields in the quiet corona to reconnect gives the extremely short value of only 1.5 hours (Close *et al.*, 2004b) so that an amazing amount of reconnection is continually taking place in the coronal magnetic field. Various ways of how reconnection might play a role in coronal heating are discussed in Chapter 5.

1.2 Earth's magnetosphere

J. Birn

The Earth's magnetosphere is the region above the ionosphere that is governed by the geomagnetic field and shaped by its interaction with the surrounding interplanetary plasma and field, the *solar wind*. The major regions within and around the magnetosphere are illustrated in Fig. 1.5. Its outer boundary is the *magnetopause*, a current layer that, to lowest order, separates the geomagnetic field from the solar wind. However, the interconnection between the two regions across the magnetopause is a crucial consequence of solar wind–magnetosphere interaction involving reconnection, discussed in Sections 4.1 and 4.2. Since the solar wind expands at speeds exceeding the fast magnetosonic speed, a *bow shock* is generated surrounding the magnetosphere. The shocked solar wind flowing around the magnetosphere outside the magnetopause forms the *magnetosheath*. The funnel-shaped regions that contain field lines approaching the vicinity of the magnetopause are the *cusps*. Through the

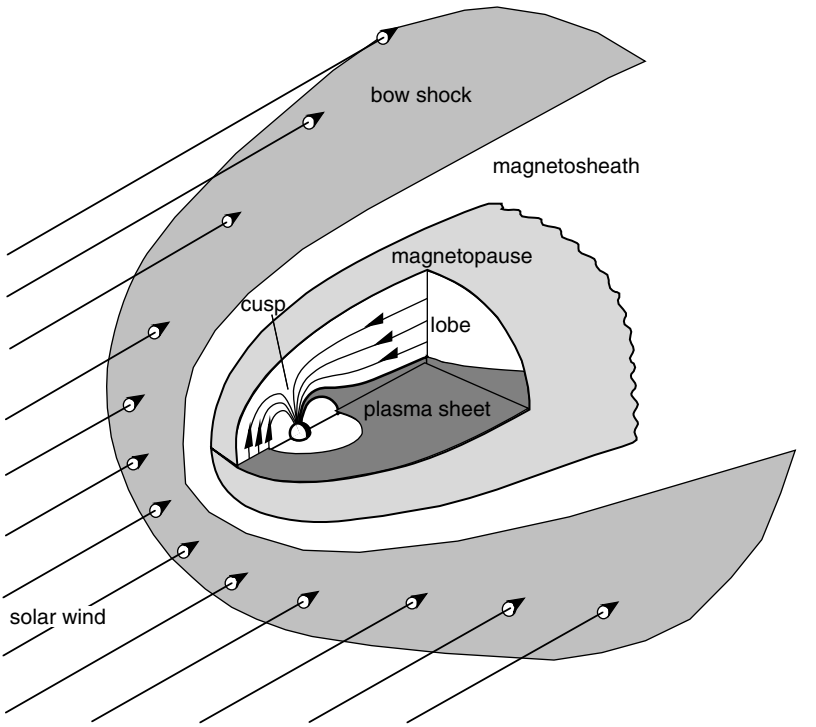

Fig. 1.5. Characteristic regions of the Earth's magnetosphere and the surrounding solar wind.

impact of the solar wind, the dayside magnetosphere is compressed, while the nightside is expanded, forming the long magnetotail, several hundreds of Earth radii (R_E) in length. The stretched, nearly antiparallel magnetic fields in the tail *lobes* enclose a current sheet containing hot plasma ($T_i \sim 2$–$20\,\mathrm{keV}$, $T_e \sim 0.4$–$4\,\mathrm{keV}$) with typical densities of ~ 0.1–$1\,\mathrm{cm}^{-3}$. This *plasma sheet* consists mainly of closed field lines, connected with the Earth at both ends, whereas the lobe field lines are open, that is, connected with the Earth only at one end (within the polar caps).

The occurrence of magnetic reconnection in the magnetosphere is closely related (although by no means exclusively) to magnetospheric *substorms*. We will therefore discuss the main reconnection sites in this context. While substorms were originally defined in terms of ground observations, particularly magnetic perturbations and auroral features (e.g., Akasofu, 1968), we focus here on magnetospheric features that are widely believed to be related to reconnection. The reconnection scenario of substorms (commonly called the *near-Earth neutral line model* or the *neutral line model*; Baker *et al.*, 1996) is shown schematically in Fig. 1.6. This schematic, which depicts magnetic field changes in the noon–midnight meridional plane was first published in a similar form by Hones (1977), although its major elements had been developed earlier (e.g., Atkinson, 1966; Schindler, 1972; McPherron *et al.*, 1973). It involves three basic reconnection sites.

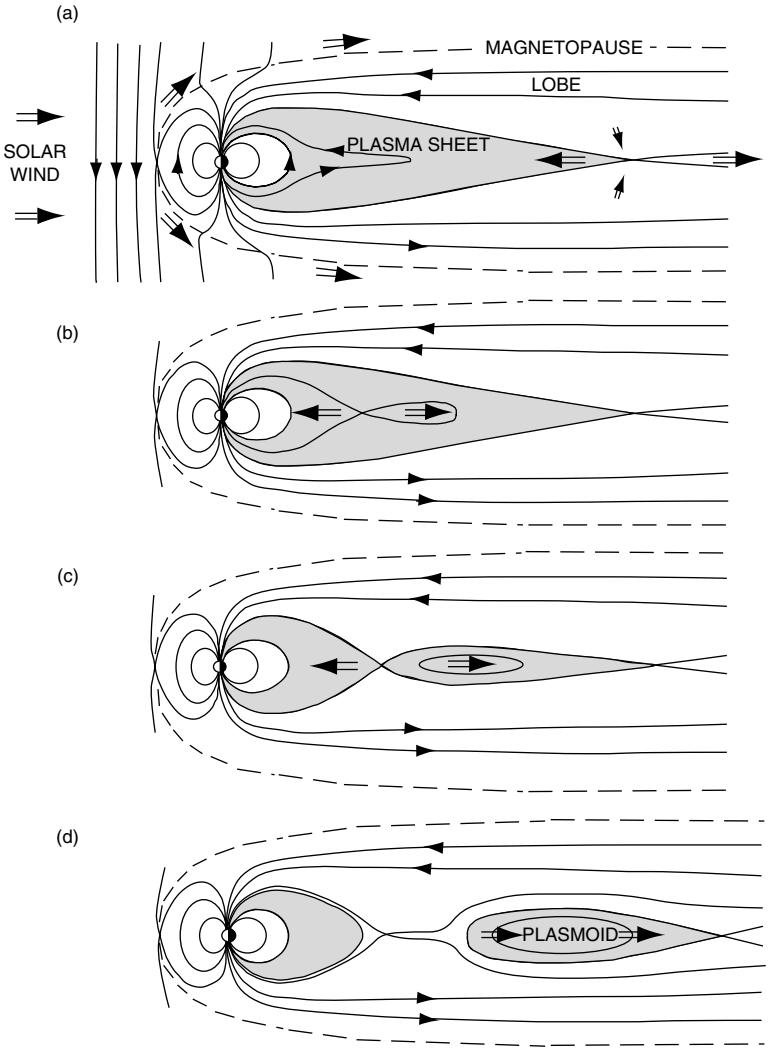

Fig. 1.6. Schematic of the topological changes of the magnetosphere in the noon–midnight meridional plane during a substorm, indicating major reconnection sites. This sequence was first depicted in a similar form by Hones (1977).

The first site is the frontside magnetopause. When the interplanetary magnetic field (IMF) is southward, or has a southward component, reconnection at the frontside leads to a transfer of magnetic flux and energy into the magnetosphere, which become transported into the tail. If reconnection at the dayside is not balanced by reconnection at the nightside, this leads to an increase of energy and magnetic flux in the tail lobes (Caan *et al.*, 1973; Holzer and Slavin, 1979), associated with an increased *flaring angle* of the tail boundary (Fairfield, 1985) and a stretching and intensification of the magnetic field in the inner tail (e.g., Baker *et al.*, 1981), causing the *substorm growth phase* (McPherron, 1970).

A second reconnection site is located in the distant magnetotail. Its role is the conversion of open (that is, lobe) magnetic field lines to closed (that is, plasma sheet field lines). The location of this site might vary, from several tens of R_E to hundreds of R_E (e.g., Baker *et al.*, 1984; Slavin *et al.*, 1985; Schindler *et al.*, 1989; Nishida *et al.*, 1995), and it need not be a single site as depicted in Fig. 1.6a. The basic magnetic topology with the two reconnection sites shown in Fig. 1.6a, involving the transport of field lines from the dayside through the nightside lobes into the plasma sheet, was first depicted by Dungey (1961) (Fig. 4.1, Section 4.1).

In principle, if magnetic reconnection at the distant site balances frontside reconnection, the configuration in Fig. 1.6a could represent a steady-state model of convection in the magnetosphere. This obviously requires that closed magnetic field lines are returned from the nightside to the dayside, involving transport in the direction out of the plane shown in Fig. 1.6. Although this steady-state convection picture still guides our general view of transport through the magnetosphere, it has been found to be inconsistent with the actual behavior and the typical magnetospheric structure. Erickson and Wolf (1980) found that adiabatic, that is mass and entropy conserving, transport of closed magnetic flux tubes from the distant to the near tail should lead to a pressure build-up that is inconsistent with force balance in the near tail. To avoid this force imbalance, a substantial fraction of mass and/or energy must be lost from the closed flux tubes as they convect earthward. Since losses into the ionosphere are sufficient only during episodes of very slow convection (Kivelson and Spence, 1988) and large-scale diffusive processes are unlikely in the highly conducting tail plasma sheet, the most obvious way of loss is the severance of a portion of the plasma sheet by new reconnection that occurs earthward from the distant site and leads to the formation and ejection of a *plasmoid* (Fig. 1.6b–d). The detection of plasmoid signatures in the distant tail (Hones, 1984) has been an important confirmation of the phenomenological neutral line model. Plasmoid encounters need not involve a crossing through the interior of a plasmoid; on the outside they are characterized by a typical north-then south deflection and a compression of the magnetic field (*traveling compression regions*, Slavin *et al.*, 1984).

The onset of reconnection in the near tail is enabled by the formation of a thin current sheet, forming within the near-Earth plasma sheet during the late substorm growth phase (e.g., McPherron and Manka, 1985; McPherron *et al.*, 1987; Kaufmann, 1987; Baker and McPherron, 1990; Mitchell *et al.*, 1990; Sergeev *et al.*, 1990; Pulkkinen *et al.*, 1994; Sanny *et al.*, 1994). As discussed above, the onset need not be a direct consequence of the current sheet formation but may involve other dynamic processes as intermediate steps (Sections 3.5 and 4.3). Stability properties of thin current sheets and the particular role of the magnetic field component perpendicular to the current sheet are discussed in Sections 3.3, 3.5 and 4.3.

A major feature of substorm-related magnetic field changes in the tail is a redistribution of currents providing a connection between the tail and the ionosphere through field-aligned currents that close through the ionosphere. This scenario, commonly denoted as the *substorm current wedge* (McPherron *et al.*, 1973), is depicted in Fig. 1.7. Within a central portion of the near-Earth tail the cross-tail current becomes disrupted or reduced, which is manifested by the *dipolarization* of the magnetic field inside the current wedge, that is, a return toward a more

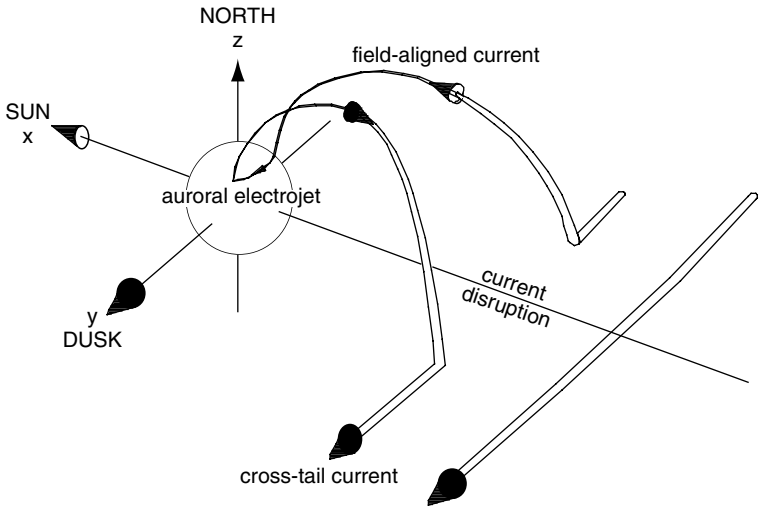

Fig. 1.7. Schematic of the substorm current wedge. After McPherron *et al.* (1973).

dipolar field from the stretched field associated with the substorm growth phase. The reduction of the cross-tail current is associated with a diversion of currents on the outside of the disruption region, leading to field-aligned currents connecting the tail with the ionosphere. On the ground, the ionospheric closure of the current wedge through the *auroral electrojet* causes characteristic north–south perturbations of the geomagnetic field. A combination of such magnetic perturbations from a number of auroral stations is used to form the *Auroral Electrojet (AE) index*, a commonly used indicator of substorms. Of course, this picture is highly simplified and there are many, more detailed, ionospheric and auroral features, which are by no means understood.

Figure 1.7 also introduces the coordinate system that is commonly used for magnetospheric applications, with the x axis pointing sunward, y pointing from dawn to dusk and z pointing northward. Observationally, one makes a distinction between the *Geocentric Solar Ecliptic (GSE)* system, in which the z axis is perpendicular to the ecliptic plane and the *Geocentric Solar Magnetospheric (GSM)* system, in which the z axis lies in the plane formed by the Earth's dipole axis and the Earth–Sun line. In either case, the y direction follows from completing the right-handed rectangular coordinate system.

The basic scenario illustrated in Fig. 1.6 is well established through observations in the tail (Section 4.5) and consistent with large-scale simulations of tail dynamics (Section 4.4). However, open problems and controversial views concern particularly the relationship between the onset of substorm activity and the onset of reconnection and the connection between tail dynamics and auroral activity. While in the simplest form of the scenario depicted in Fig. 1.6 the onset of reconnnection in the tail leads to further activity, an alternative scenario, usually called the *current disruption model* (Lui, 1996), assumes that a substorm is triggered locally in the inner magnetotail, presumably by an instability that involves a cross-tail wave vector component.

Potential mechanisms are cross-field current-driven instabilities (e.g., Lui *et al.*, 1991) or interchange/ballooning modes (e.g., Roux *et al.*, 1991; Hurricane *et al.*, 1997; Pu *et al.*, 1997; Bhattacharjee *et al.*, 1998; Cheng and Lui, 1998) (see also Sections 3.3, 3.5, and 4.3). In this scenario, dipolarization might result from a slippage of field lines without the necessity of neutral line formation. Reconnection as depicted in Fig. 1.6 might be a later consequence of the dynamic evolution.

We should note, however, that the current disruption model is not necessarily completely distinct from magnetic reconnection. Similar to magnetic reconnection, current disruption is assumed to be related to a breakdown of ideal MHD with its frozen-in field condition through increased current densities and decreasing gradient length scales. In contrast to standard reconnection models, the current disruption model does not assume or require a topological change in the magnetic field and the violation of ideal MHD is envisioned as a turbulent process not confined to the vicinity of a neutral line or separator (Lui, 1996). However, the lack of a topological change can also be a property of generalized magnetic reconnection in the absence of magnetic nulls (Section 2.3), so that the current disruption model might also be consistent with turbulent generalized magnetic reconnection.

On the other hand, the reconnection process, as depicted in the neutral line model, is not necessarily a large-scale, many R_E, phenomenon. In fact, high-speed plasma flows in the plasma sheet, which are usually interpreted as consequences of reconnection, tend to be localized with a width of only a few R_E and occur in an intermittent, bursty fashion (Baumjohann *et al.*, 1990; Nakamura *et al.*, 2004a; Section 4.5), leading to the name *bursty bulk flow* (BBF) events (Angelopoulos *et al.*, 1992). Such flow bursts are shown to have local features and auroral consequences consistent with a small current wedge (Fig. 1.7; Nakamura *et al.*, 2001a,b) but need not be associated with a full substorm.

Although substorm (and other) magnetospheric activity is clearly enhanced during times of southward IMF, when the magnetosphere couples more strongly to the solar wind, activity, as well as magnetic reconnection, is not restricted to such times. During times of northward IMF, reconnection might occur at higher latitudes (Dungey, 1963; Sections 4.1 and 4.2). This is illustrated in Fig. 1.8. Note that high-latitude reconnection takes place between interplanetary field lines (without connection to the Earth) and lobe field lines, which connect to the Earth at one side. After reconnection, the newly connected field lines have the same topology, so that there is no net flux transfer between the two regions (Reiff and Burch, 1985). Later, however, the newly connected lobe field lines are dragged toward the tail and may again reconnect, with another lobe field line. This process, sometimes named *re-reconnection*, is illustrated at the bottom of Fig. 1.8. It creates a newly closed field line and a fully disconnected field line and thereby transports magnetic flux from the lobes into the closed region. Figure 1.8 depicts the scenario for the case when the IMF has an anti-sunward component in addition to the northward component. In this case high-latitude reconnection should take place first in the northern hemisphere, followed by re-reconnection in the southern hemisphere. In the absence of a sunward IMF component, the two processes might operate simultaneously; this is the scenario originally depicted by Dungey (1963), shown in the bottom panel of Fig. 4.1.

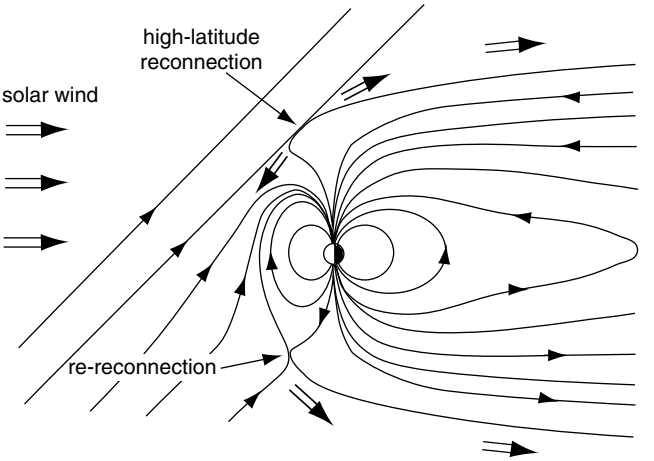

Fig. 1.8. Schematic of high-latitude reconnection when the interplanetary magnetic field has a northward component.

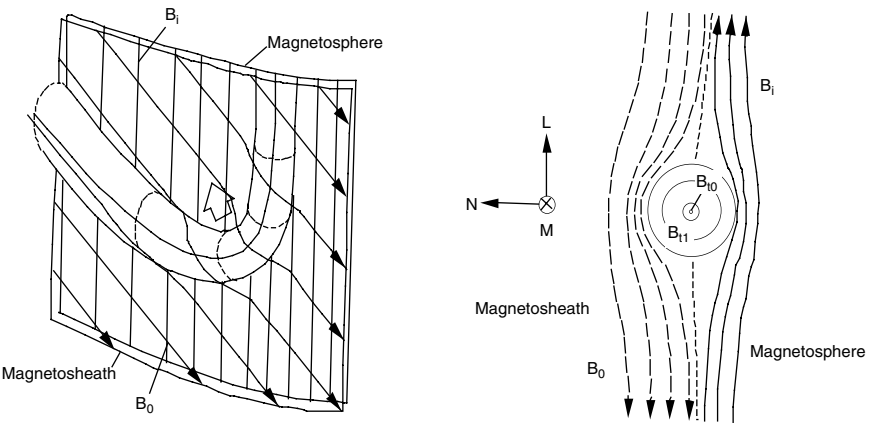

Fig. 1.9. Schematic of flux transfer event at the magnetopause, interpreted as spatially and temporally localized reconnection that leads to an interconnected flux rope. After Russell and Elphic (1978); Elphic (1995).

Magnetopause reconnection need not be quasi-stationary, as indicated in Fig. 1.6 but apparently also occurs in a localized, temporally limited fashion. The main evidence for the latter is bipolar signatures of the magnetic field component normal to the magnetopause surface, which are observed in its vicinity, both inside and outside. This signature indicates the passage of a flux rope, connecting magnetospheric with magnetosheath plasma (Thomsen *et al.*, 1987). Such encounters are termed *flux transfer events* (FTEs)(Russell and Elphic, 1978; Elphic, 1995; Fig. 1.9).

As discussed further in Chapter 4, the reconnection scenarios at the magnetopause and in the magnetotail current sheets differ particularly in the role of the magnetic

field components present in addition to the field associated with the main current. At the magnetopause, a field component in the direction of the current (*guide field*) presumably influences where and how reconnection occurs (Sections 4.1 and 4.2), whereas in the magnetotail the field component perpendicular to the current sheet critically controls its stability (Sections 3.3 and 4.3).

2

Basic theory of MHD reconnection

2.1 Classical theory of two-dimensional reconnection

T. G. Forbes

The term *magnetic reconnection* was introduced by Dungey (1953) who was interested in the problem of particle acceleration in the Earth's magnetosphere. Earlier studies (Giovanelli, 1946; Hoyle, 1949) had considered the acceleration of particles at magnetic neutral points in the presence of an electric field produced by plasma convection, but these studies did not include the magnetic field that is produced by the current associated with the motion of the particles. Using the framework of magnetohydrodynamics (MHD), Dungey argued that this current would take the form of a thin sheet in which the diffusion of the magnetic field would necessarily dominate. Furthermore, this diffusion would cause field lines passing through the current sheet to change their connectivity to one another. This process was described as field line *disconnection* followed by *reconnection*. The importance of thin current sheets as a site for plasma heating and particle acceleration in solar flares was also recognized by Cowling (1953) at about the same time.

In this section we outline basic, two-dimensional approaches to magnetic reconnection, based on resistive MHD theory. More detailed information can be found in the original papers and recent books by Biskamp (2000) and Priest and Forbes (2000). For future reference and the introduction of relevant quantities we here list the basic MHD equations as used in this book, based on standard international MKS units and standard notations:

$$\mathrm{d}\rho/\mathrm{d}t \equiv \partial\rho/\partial t + \mathbf{v}\cdot\nabla\rho = -\rho\nabla\cdot\mathbf{v}, \tag{2.1}$$

$$\rho\,\mathrm{d}\mathbf{v}/\mathrm{d}t = -\nabla p + \mathbf{j}\times\mathbf{B}, \tag{2.2}$$

$$\mathrm{d}p/\mathrm{d}t = -\gamma p\,\nabla\cdot\mathbf{v} + (\gamma-1)\eta j^2, \tag{2.3}$$

$$\partial\mathbf{B}/\partial t = -\nabla\times\mathbf{E}, \tag{2.4}$$

$$\nabla\times\mathbf{B} = \mu_0\mathbf{j}, \tag{2.5}$$

$$\mathbf{E} + \mathbf{v}\times\mathbf{B} = \eta\mathbf{j}. \tag{2.6}$$

Here $\mathrm{d}/\mathrm{d}t$ denotes the convective time derivative, i.e., the time derivative in a frame that moves with the plasma, ρ and $\mathbf{v}$ denote the plasma mass density and flow velocity, respectively, and p is the plasma pressure, assumed to be isotropic. $\mathbf{E}$ denotes the electric field, $\mathbf{B}$ is the magnetic induction, and $\mathbf{j}$ the electric current density. In

space, solar, and astrophysical applications, **B** is related to the magnetic field simply by the constant factor μ_0, the permeability of free space. Therefore, **B** is frequently, but not quite accurately, denoted as the "magnetic field." The quantity η denotes electric resistivity, assumed to be scalar, but not necessarily constant in space. Typically, in space and solar coronal plasma, η is very small, so that the resistive term $\eta\mathbf{j}$ in (2.6) can be neglected. This is the basis of the *ideal MHD* approximation, further discussed in Section 2.2. The local breakdown of this approximation, however, is a necessary feature of magnetic reconnection. The assumption of a resistive Ohm's law (2.6) to permit this local breakdown forms the basis of the traditional approaches to reconnection described in this section. However, a simple Ohm's law, as given by (2.6), is generally not satisfied in collisionless, or nearly collisionless, space and solar coronal plasmas, or the resistive term is so small that it becomes irrelevant. Chapter 3 hence is devoted to the physical mechanisms that govern dissipation and enable reconnection in collisionless plasma environments.

The quantity γ represents the ratio of specific heats; for isotropic plasmas, usually $\gamma = 5/3$. For vanishing electrical resistivity, $\eta = 0$, Eq. (2.3) with $\gamma = 5/3$ describes adiabatic, i.e., entropy-conserving, transport, $\mathrm{d}(p/\rho^\gamma)/\mathrm{d}t = 0$. This approximation neglects heat flux and radiative transport, which may play a significant role in the solar corona but not in the magnetosphere. Frequently, other values of γ are used to account for effects not included explicitly in Eqs. (2.1)–(2.6). For instances, $\gamma = 1$ for isothermal changes, and $\gamma = 1.1$ is frequently used to summarily include the effects of heat conduction and radiative transport in the solar corona. The limit of $\gamma \to \infty$ formally corresponds to the assumption of incompressibility, $\nabla \cdot \mathbf{v} = 0$ or $\mathrm{d}\rho/\mathrm{d}t = 0$.

2.1.1 Steady-state reconnection

A few years after Dungey's introduction of the concept of reconnection, Sweet (1958a) and Parker (1957) developed the first quantitative model. In order to make the analysis as analytically tractable as possible, they focused on the problem of two-dimensional, steady-state reconnection in an incompressible plasma. They assumed that reconnection occurs in a current sheet whose length is set by the global scale, L_e, of the field as shown in Fig. 2.1. Under these conditions they determined that the speed of the plasma flowing into the current sheet is approximately

$$v_\mathrm{e} = v_\mathrm{Ae} S^{-1/2}, \tag{2.7}$$

where $S = \mu_0 L_\mathrm{e} v_\mathrm{Ae}/\eta$ is the *Lundquist number*, representing the ratio between the time scales of resistive diffusion and typical Alfvén waves, L_e is the global scale length, and $v_\mathrm{Ae} = B_\mathrm{e}/\sqrt{\mu_0 \rho_\mathrm{e}}$ is the Alfvén speed in the inflow region. Often S is referred to as the *magnetic Reynolds number* (R_m), although in other definitions the latter term refers to a similar number based on a typical flow speed, rather than the Alfvén speed (Huba, 2004). The outflow speed of the plasma from the current sheet is v_Ae, and it does not depend on the value of S. The *reconnection rate* in two dimensions is measured by the electric field at the reconnection site. This electric field is perpendicular to the plane of Fig. 2.1, and it prescribes the rate at which magnetic flux is transported from one topological domain to another (Vasyliūnas, 1975).

The configurations of Figs. 2.1 and 2.2 can be generalized to include a magnetic field component perpendicular to the plane of the figures, but maintaining the invariance in that direction. In that case the embedded X-type magnetic neutral point

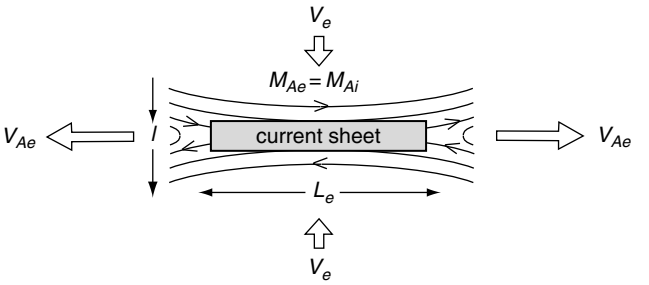

Fig. 2.1. The Sweet–Parker field configuration. Plasma flows into the upper and lower sides of a current sheet of length L_e, but must exit through the narrow tips of the sheet of width l. Because the field is assumed to be uniform in the inflow region, the external *Alfvén Mach number*, $M_\mathrm{Ae} = v_\mathrm{e}/v_\mathrm{Ae}$, at large distance is the same as the internal Alfvén Mach number, M_Ai, at the midpoint edge of the current sheet.

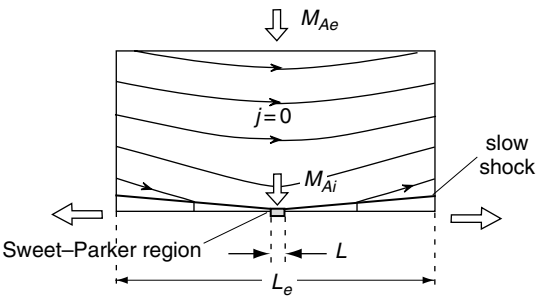

Fig. 2.2. Petschek's field configuration. Here the length, L, of the Sweet–Parker current sheet is much shorter than the global scale length, L_e, and the magnetic field in the inflow is nonuniform. Two pairs of standing slow-mode shocks extend outwards from the central current sheet. Petschek's model assumes that the current density in the inflow region is zero and that there are no external sources of field at large distance.

becomes a magnetic field line, denoted the magnetic *separator*, representing the intersection of *separatrix* surfaces between topologically distinct regions. Accordingly, the presence of an electric field along the separator has been used to define magnetic reconnection (Sonnerup *et al.*, 1984) in such a configuration, commonly described as *2.5-dimensional* (2.5D or $2\frac{1}{2}$D).

In two-dimensional (and 2.5-dimensional) steady-state models the electric field E in the invariant direction is uniform in space. Therefore, the Alfvén Mach number, $M_\mathrm{Ae} = v_\mathrm{e}/v_\mathrm{Ae} = E/(v_\mathrm{Ae}B_\mathrm{e})$, provides a quantitative measure of the reconnection rate, normalized by the characteristic electric field $v_\mathrm{Ae}B_\mathrm{e}$. In terms of this number, the Sweet–Parker reconnection rate is just $M_\mathrm{Ae} = S^{-1/2}$.

In astrophysical and space plasmas S is very large ($S \gg 10^6$), so Sweet–Parker reconnection is usually too slow to account for phenomena such as geomagnetic substorms or solar flares. Petschek (1964) proposed a model with an increased rate of reconnection associated with a greatly reduced length of the current sheet in the Sweet–Parker model. He did this by encasing their current sheet in an exterior field

with global scale length L_e. He also introduced two pairs of standing slow-mode shocks radiating outwards from the tip of the current sheet as shown in Fig. 2.2. In Petschek's solution most of the energy conversion comes from these shocks which accelerate and heat the plasma to form two hot outflow jets.

Petschek also assumed that the magnetic field in the inflow region is current free and that there are no sources of field at large distances. These assumptions, together with the trapezoidal shape of the inflow region created by the slow shocks, lead to a logarithmic decrease of the magnetic field as the inflowing plasma approaches the Sweet–Parker current sheet. This variation of the field leads in turn to Petschek's formula for the maximum reconnection rate, namely

$$M_{\mathrm{Ae[Max]}} = \pi/(8 \ln S), \tag{2.8}$$

where S and v_{Ae} are now the Lundquist number and Alfvén speed in the region far upstream of the current sheet as shown in Fig. 2.2. Because of its logarithmic dependence on S, the Petschek reconnection rate is many orders of magnitude greater than the Sweet–Parker rate, and for most space and laboratory applications Petschek's formula predicts that $M_{\mathrm{Ae}} \approx 10^{-1}$ to 10^{-2}.

Petschek's model uses the Sweet–Parker model to describe the flow of plasma and fields in the diffusion region. Because the Sweet–Parker model only gives average properties for this region, such as its length and thickness, no detailed matching is possible between the flows in the diffusion region and the flows in the external region outside. This lack of detailed matching is sometimes misunderstood to mean that there is no matching at all (e.g., Biskamp, 2000), but in fact the average properties of the diffusion region are rigorously matched to the external region to the extent that the Sweet–Parker model allows (see Vasyliūnas, 1975).

It is not always appreciated that Petschek's reconnection model is a particular solution of the MHD equations which applies only when special conditions are met. Firstly, it requires that the flows into the reconnection region be set up spontaneously without external forcing (Forbes, 2001). In general, driving the plasma externally creates a significant current density in the inflow region which violates Petschek's assumption that the inflow field is approximately potential. Secondly, Petschek's solution also requires that there be no external source of field in the inflow region. In other words, the field must be just the field produced by the currents in the diffusion region and the slow shocks. In many applications of interest neither of these conditions is met.

An alternate approach to reconnection in current sheets was pioneered by Green (1965) and Syrovatskii (1971), who considered what happens when a weak flow impinges on an X-line in a strongly magnetized plasma as indicated in Fig. 2.3. The imposed flow creates a current sheet which achieves a steady state when the rate of field line diffusion through the sheet matches the speed of the flow. A quantitative model of this process has been published by Somov (1992).

For a steady-state MHD model the variation of the field in the inflow region is the key quantity which determines how the reconnection rate scales with the Lundquist number, S. For any such model the electric field is uniform and perpendicular to the plane of the field. Thus, outside the diffusion region $E_{\mathrm{o}} = -v_y B_x$ where E_{o} is a constant, v_y is the inflow along the axis of symmetry (y axis in Fig. 2.3), and

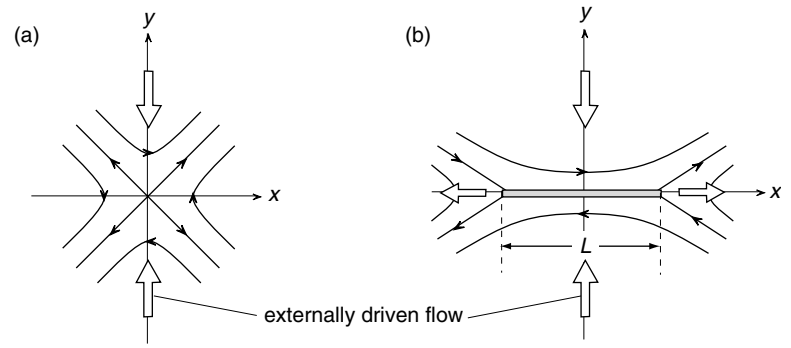

Fig. 2.3. Green's and Syrovatskii's field configuration. Unlike Petschek's configuration, this one has external sources which produce an X-type configuration even when local sources of current are absent (a). The application of external driving (b) creates a current sheet whose length, L, depends on the temporal history of the driving and the rate at which reconnection operates (Somov, 1992). The fastest reconnection rate occurs when L is equal to the external scale length, $L_{\rm e}$.

B_x is the corresponding field. Thus the inflow Alfvén Mach number, $M_{\rm Ae}$, at large distances can be expressed as

$$M_{\rm Ae} = M_{\rm Ai} B_{\rm i}^2 / B_{\rm e}^2, \tag{2.9}$$

where $M_{\rm Ai}$ is the Alfvén Mach number at the current sheet, $B_{\rm i}$ is the magnetic field at the edge of the current sheet, and $B_{\rm e}$ is the magnetic field at large distance.

In Syrovatskii's model the field along the inflow axis of symmetry varies as

$$B_x = B_{\rm i}(1 + y^2/L^2)^{1/2}, \tag{2.10}$$

where $B_{\rm i}$ is the field at the current sheet, y is the coordinate along the inflow axis, and L is the length of the current sheet. Combining (2.10) with (2.9) yields

$$M_{\rm Ae} = M_{\rm Ai}/(1 + L_{\rm e}^2/L^2), \tag{2.11}$$

which has its maximum value when $L = L_{\rm e}$. Thus the maximum reconnection rate in Syrovatskii's model scales as $S^{-1/2}$, the same as for the Sweet–Parker model.

By comparison, the field in Petschek's model along this axis varies approximately as

$$B_x = B_{\rm i} \frac{1 - (4/\pi) M_{\rm Ae} \ln(L_{\rm e}/y)}{1 - (4/\pi) M_{\rm Ae} \ln(L_{\rm e}/l)}, \tag{2.12}$$

where l is the current sheet thickness. (This expression for the field is only a rough estimate since the actual variation in the region $y < L$ is more complex; see Vasyliūnas, 1975; Priest and Forbes, 2000.) Evaluating this at $y = L_{\rm e}$ and substituting the result into Eq. (2.9) gives

$$M_{\rm Ai} = M_{\rm Ae}[1 - (4/\pi) M_{\rm Ae} \ln(L_{\rm e}/l)]^{-2}. \tag{2.13}$$

The Sweet–Parker theory can be used to eliminate $L_{\rm e}/l$, so as to obtain an expression for $M_{\rm Ae}$ as a function of S. This expression has a maximum value as given by Eq. (2.8).

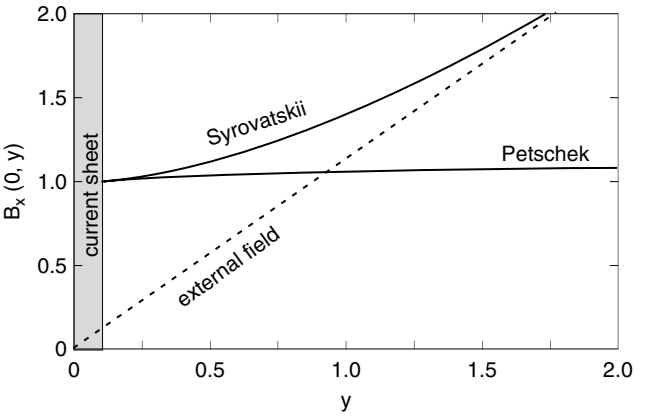

Fig. 2.4. The variation of the magnetic field in the inflow region of Petschek's and Syrovatskii's models along the axis of symmetry (y axis). At large distance the variation in Syrovatskii's model is determined by external field sources at infinity. The magnetic fields are normalized to their values at the edge of the current sheet, and the distance y is normalized to the length L of the current sheet. For the Petschek curve, $M_{\rm Ae} = 0.02$, $l = 0.1\ L$, and $L_{\rm e} = 2L$.

The variation of the field in the inflow region for the Syrovatskii and Petschek models is compared in Fig. 2.4. Although both fields increase with distance away from the current sheet, the rate at which they increase is markedly different. At large distance the rate of increase in the Syrovatskii model is dominated by the external field whose variation is fixed and independent of the reconnection rate. By contrast, the variation in the Petschek model is closely coupled to the reconnection rate, disappearing altogether when the rate goes to zero. This is one of the main reasons that the two models give such different predictions for the reconnection rate. It also explains why the numerical simulation by Biskamp (1986) of the evolution shown in Fig. 2.3 produces a Sweet–Parker-type scaling rather than a Petschek-type scaling.

More recently, Kulsrud (2001) has argued that the short current sheet in Petschek's solution is not consistent with the requirements for the transport of magnetic flux through the current sheet. However, the external field he uses is that of Syrovatskii's model, which is quite different from the external field appropriate for the Petschek model. Thus, it is not so surprising that he finds a mismatch in such circumstances. When the external field appropriate for Petschek's solution is used, no such mismatch occurs because the magnetic flux flowing into and out of the diffusion region is rigorously matched to the external field. This is true even though the detailed variation of the fields and flow within the diffusion region is not prescribed by the Sweet–Parker model. In the more formal treatments of the Petschek model (e.g., Soward and Priest, 1977; Priest and Forbes, 1986) the external field is obtained by solving Laplace's equation for the inflow region. Given a function which prescribes the variation of the normal field in the diffusion region one can always find a corresponding external solution. To first order in the expansion parameter $M_{\rm Ae}$ this solution is independent of the prescribed form of the function as long as the current sheet is short

($L \ll L_e$). Consequently, statements to the effect that Petschek's solution is generally invalid because of improper or inexact matching between the diffusion region and the external region are not correct. The main reason Petschek's solution is not generally valid is that it makes specific assumptions about the nature of the external field which are not appropriate in many situations.

Even in circumstances where Petschek's model would be expected to apply it sometimes does not. Several numerical simulations (e.g., Biskamp, 1986; Scholer, 1989) have been carried out in an attempt to verify the steady-state solution found by Petschek (1964), but none of these simulations has been able to replicate the scaling results predicted by Petschek's solution as long as the resistivity is kept uniform and constant. Only when a nonuniform, localized resistivity model (e.g., Ugai, 1988; Yan *et al.*, 1992) is used does the Petschek configuration appear. The fact that the resistivity apparently needs to be nonuniform does not contradict Petschek's model because it makes no assumption about whether the resistivity is uniform or not. It is equally valid for both cases because it assumes only that the region where resistivity is important is localized. Nevertheless, the question remains as to why a nonuniform resistivity appears to be necessary.

Although Petschek assumed that the current density, j, in the inflow region is zero to first order, it is not actually necessary to make such an assumption in order to obtain a solution. More generally, j can be nonzero to first order in the expansion of the inflow equations, so that the inflow magnetic field is no longer determined by solving Laplace's equation ($\nabla^2 A = 0$) for the vector potential, A, but by solving Poisson's equation ($\nabla^2 A = -\mu_0 j$) instead (Priest and Forbes, 1986). The relaxation of the assumption that j is zero introduces an additional degree of freedom so that there is now a whole family of solutions (Fig. 2.5). These solutions can be summarized in terms of the relation between the internal Alfvén Mach number, M_{Ai}, at the entrance to the diffusion region, and M_{Ae}, the Alfvén Mach number at the exterior inflow boundary (Fig. 2.2). The relation is

$$\frac{{M_{Ae}}^{1/2}}{{M_{Ai}}^{1/2}} = 1 - \frac{4}{\pi} M_{Ae}(1-b)\left[0.834 - \ln\tan\left(\frac{\pi}{4} S^{-1} M_{Ae}^{-1/2} M_{Ai}^{-3/2}\right)\right], \qquad (2.14)$$

where b is a parameter that corresponds to different assumptions about the inflow boundary conditions at $y = L_e$. The relation is plotted in Fig. 2.5 for $S = 100$ for various values of b. When $b = 0$, Petschek's solution is obtained, and when $b = 1$, a solution equivalent to that of Sonnerup (1970) is obtained. When $b < 1$, the solution somewhat resembles Syrovatskii's solution in that the magnetic field increases markedly with distance away from the current sheet. For these solutions the maximum reconnection rate is the same as for the Sweet–Parker model. As b increases beyond unity, a flux pile-up regime occurs where the magnetic field increases as the diffusion region current sheet is approached (Fig. 2.6). For very strong flux pile-up with $b \gg 1$, the flow approaches the MHD stagnation-point flow solution found by Parker (1973a) and Sonnerup and Priest (1975). The stagnation-point flow appears to be very fast since formally there is no limit to the value of M_{Ae}. However, large values of M_{Ae} require large variations in the gas pressure, which are not possible unless the plasma β is very much greater than unity. For low-β plasmas the amount of pile-up is limited, and when this limitation is taken into consideration the reconnection rate

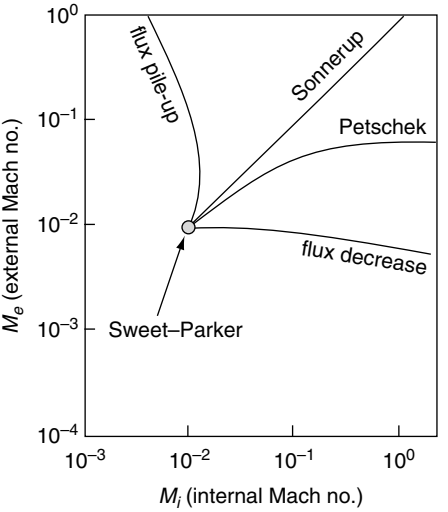

Fig. 2.5. External Alfvén Mach number, M_{Ae}, vs. the internal Alfvén Mach number, M_{Ai}, for the family of solutions obtained by Priest and Forbes (1986). These solutions are obtained by an expansion in terms of the inflow Alfvén Mach number for small variations of the field around the uniform inflow field assumed in the Sweet–Parker model. Solutions with the labeled characteristics are obtained for different choices of the parameters describing the boundary conditions at large distances.

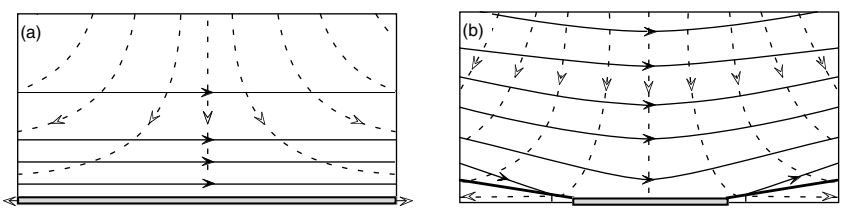

Fig. 2.6. The stagnation-point flow solution (a) obtained by Parker (1973a) for magnetic field annihilation at a current sheet, and the closely related flux pile-up solution (b) obtained by Priest and Forbes (1986).

is found to scale at the relatively slow Sweet–Parker rate (Litvinenko *et al.*, 1996; Priest, 1996; Litvinenko and Craig, 1999). For a low-β plasma the fastest rate occurs for $b = 0$, which is Petschek's solution.

Vasyliūnas (1975) was the first to point out that the differences between reconnection solutions are often related to the behavior of the gas and magnetic pressures in the inflow region. The inflow can be characterized as undergoing a compression or an expansion depending on whether the gas pressure increases or decreases as the plasma flows in towards the X-point. These compressions or expansions can further be characterized as being of the fast-mode type or the slow-mode type, depending on whether the magnetic pressure changes in the same sense as the gas pressure (fast-mode type) or in the opposite sense (slow-mode type). For the family of solutions

above one finds that in Petschek's solution ($b = 0$) the gas pressure is uniform to second order in the expansion parameter $M_{\rm Ae}$, so that to this order, the plasma is neither compressed nor rarefied as it flows towards the X-point. For the solutions with $b < 0$, the plasma undergoes a slow-mode compression, while for the solutions with $b > 1$ it undergoes a slow-mode expansion. Between $b = 0$ and $b = 1$ the solutions have a hybrid character with slow-mode and fast-mode expansions existing in different regions of the inflow. Although it does not happen in the above family of solutions, it is also possible to have hybrid solutions in which slow-mode expansions and slow-mode compressions co-exist in different regions of the inflow (e.g., Strachan and Priest, 1994).

2.1.2 Time-dependent reconnection

So far we have only considered the development of steady-state models of reconnection. However, many phenomena involving reconnection occur on such short time scales that a steady or quasi-steady state does not exist. For example, in high-speed coronal mass ejections (>1000 km/s) the current sheet created by the ejection grows in length at a speed which is on the order of, or in excess of, the ambient Alfvén wave speed (Lin and Forbes, 2000).

Time-dependent reconnection was first considered by Dungey (1958) who noted that, in a strongly magnetized plasma, motions in the vicinity of an X-line can lead to the very rapid formation of a current sheet. The first explicit solution demonstrating this possibility was published by Imshennik and Syrovatskii (1967). They found that if the gas pressure is negligible and the resistivity is small, then during the initial formation of the sheet, the electric field, E, at the X-line grows at a rate which is proportional to $(t_{\rm c} - t)^{4/3}$ where $t_{\rm c} = (\pi/2)^{3/2}$ times the Alfvén scale time of the system. At the time $t_{\rm c}$ the electric field becomes infinite, but the assumptions underlying the solution break down before this time is reached. Although several analyses and extensions of this solution have been done (see Chapter 7 of Priest and Forbes, 2000, for a list of published papers), little effort has been made to apply this theory to highly dynamic phenomena such as flares.

Most of the theoretical effort on time-dependent reconnection has concentrated on the *tearing instability* (Furth *et al.*, 1963), illustrated in Fig. 2.7. This is a nonideal instability in which the magnetic reconnection of field lines plays a central role. Tearing has been invoked in some flare models as a mechanism for releasing magnetic energy (e.g., Heyvaerts *et al.*, 1977), but, as a flare mechanism, it suffers from the fact that resistive tearing is relatively slow (Steinolfson and Van Hoven, 1984). The onset of most flares occurs over a time period on the order of the Alfvén time scale in the corona, but the time scale of the tearing mode is much slower being a combination of the Alfvén time scale and the much slower resistive time scale. The actual growth rate depends on the wavelength of the perturbation. For a simple current sheet the growth rate is zero if the wave number k is such that $kl > 1$ where l is the width of the sheet. This means that a current sheet which is shorter than 2π times its width is stable to tearing. For $S^{1/4}kl < 1$, small perturbations grow exponentially at a rate given by

$$\tau_{\rm tm} = (kl)^{2/5} S^{3/5}, \tag{2.15}$$

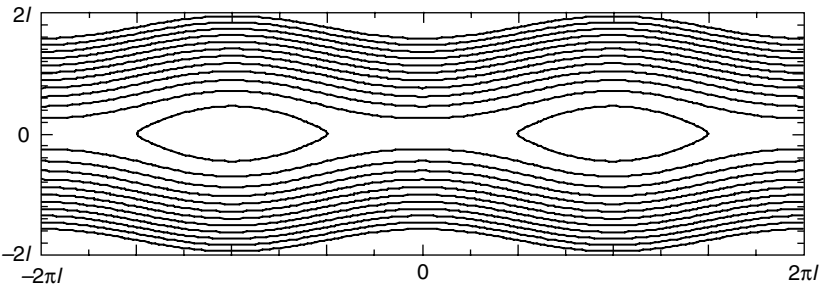

Fig. 2.7. Typical magnetic island structure resulting from tearing instability of a plane current sheet.

where $\tau_{\rm tm}$ is the growth period of the tearing mode and S is the Lundquist number based on the current sheet thickness and the external Alfvén speed. The fastest growing mode occurs when $kl \approx S^{-1/4}$ and the corresponding growth rate scales with $S^{-1/2}$. For values of kl less than this value, the above expression is not valid.

The threshold condition $kl < 1$ for tearing is a consequence of the fact that the field lines of the initial current sheet resist being bent. An initial perturbation which has a relatively short wavelength tends to straighten out before significant reconnection can occur, but as the wavelength of the perturbation increases, there is more time for diffusion to act. This diffusion occurs in a thin layer in the center of the sheet which has a thickness on the order of $S^{-2/5}l$ for the shortest wavelength mode and $S^{-1/4}l$ for the fastest growing mode.

The growth and stability of the tearing mode can be affected by many factors such as the geometry of the sheet, line-tying, the presence of a guide field (a magnetic field component in the direction of the current), externally driven flows, the mechanisms of magnetic diffusivity, and so on. A discussion of such effects can be found in Galeev (1979), Priest and Forbes (2000), and Wesson (1987).

Although a large body of literature devoted to two-dimensional reconnection exists, there are still some fundamental questions that remain unanswered. For example, what is the rate of reconnection in a rapidly driven system where the current sheet grows at a rate on the order of the ambient Alfvén speed? This situation is expected to occur in large coronal mass ejections whose speeds typically exceed the local Alfvén wave speed. Also, the effects of strong radiation, thermal conduction, and partial ionization have only been partially explored.

2.2 Fundamental concepts

G. Hornig

The concept of reconnection has been largely developed on the basis of two-dimensional models, as described in Section 2.1. However, many notions (and definitions) of reconnection based on such two-dimensional models do not transfer to three-dimensional configurations without inherent symmetry. Moreover, while in two dimensions reconnection can occur only at hyperbolic null points, so called X-points of the magnetic field, three dimensions may allow for reconnection both at magnetic null points and at places of nonvanishing field strength. With respect to the change

of the magnetic structure under reconnection these two cases differ essentially. Therefore Sections 2.3 and 2.4 deal with each case separately.

This section focuses on the change of the magnetic structure due to reconnection in general 3D configurations. It is important to know how reconnection changes the magnetic topology in order to determine the energy that is set free in the process. Often the magnetic energy dissipated in the reconnection process itself is small compared with the release of energy of the subsequent relaxation enabled by the change of magnetic topology. That is, a comparatively small event can trigger a huge energy release in a situation where much energy has been stored in the magnetic field structure. This is for instance the typical situation in solar flares and magnetospheric substorms.

Magnetic reconnection typically represents a sudden, drastic change of the magnetic structure in an environment which is otherwise an ideal plasma and hence conserves the magnetic topology. How to resolve this apparent contradiction between the properties of the plasma and the occurrence of reconnection is an important and in parts still open question. We start by investigating the most general conditions for magnetic flux and connectivity conservation, in order to give some insight into the way constraints of an almost ideal plasma can be broken.

This first section is also meant to broaden our view of reconnection. Firstly, reconnection might not always have the signature which we expect. Secondly, processes similar to reconnection can occur in different physical systems and the exchange of knowledge about related processes in other fields can be of mutual benefit.

Regarding the first point, we have to remind ourselves that our notion of magnetic reconnection was formed historically by a mixture of observations and simple theoretical models. Both sources, observations and models, had severe limitations. For instance we associate reconnection with a very fast, almost explosive process of energy release. However, a change of the magnetic structure might also occur with a lower energy output or on a slower time scale. These events may be equally important for the magnetic structure and can easily escape our observations, either because they are very different from standard reconnection and we do not recognize their signature, or they are just too small to be detected with current observational resolution.

With respect to the second point, we should be aware of the fact that processes analogous to reconnection are also known in other fields of physics. For instance, a process very similar to magnetic reconnection is known in hydrodynamics as reconnection of vortices, sometimes also called *cross-linking* or *cut and connect* (Kida and Takaoka, 1994). Vortices can also reconnect in superfluids, but here they are quantized string-like objects (Koplik and Levine, 1993). Similar processes are known for cosmic strings (Shellard, 1987) and liquid crystals (Chuang *et al.*, 1991). A remote similarity exists also to what is known in knot theory as surgery of framed knots (Kauffman, 1991), while in enzymology a process exists where topoisomerase reconnects strands of the DNA (Sumners, 1990).

2.2.1 Topological conservation laws

This section is intended to provide a background for understanding magnetic flux conservation, field line conservation, helicity conservation and their mutual

relation. In the following we assume that we have a fluid in a domain $D \subset I\!R^3$ with a velocity field $\mathbf{v}(\mathbf{x},t)$ satisfying for simplicity $\mathbf{v}\cdot\mathbf{n}|_{\partial D} = 0$. More general boundary conditions can be considered as well but yield no further insights for our purposes. We also assume that the velocity field is at least $\mathcal{C}^1$, that is continuously differentiable. Under these conditions the flow $\mathbf{F}(\mathbf{x},t)$ of $\mathbf{v}$, defined by

$$\frac{\partial \mathbf{F}(\mathbf{x},t)}{\partial t} = \mathbf{v}(\mathbf{F}(\mathbf{x},t),t) \quad \text{with} \quad \mathbf{F}(\mathbf{x},0) = \mathbf{x}, \tag{2.16}$$

exists for all $t \in [-\infty,\infty]$ and is a diffeomorphism of D. This means that for any given t $\mathbf{F}$ maps D onto itself, that this mapping is differentiable, and that its inverse $\mathbf{F}^{-1}(\mathbf{x},t) = \mathbf{F}(\mathbf{x},-t)$ is also differentiable (see e.g., Abraham *et al.*, 1983, p. 245).

$\mathbf{F}$ allows us to follow any geometrical object, like a line or surface, advected by the flow field. For instance a point $\mathcal{P}(0)$ advected by the flow is found a time t later in $\mathcal{P}(t) = \mathbf{F}(\mathcal{P}(0),t)$. Similarly a line $\mathcal{L}(0)$ at $t = 0$ is transported to $\mathcal{L}(t) = \mathbf{F}(\mathcal{L}(0),t)$. Note that due to the differentiability of the flow the topology of the advected objects is preserved: that is, a line remains a line, i.e. it cannot be cut or shrunk to a point. If the line were closed it would remain closed and if it were knotted the type of knottedness would be preserved as well. These objects advected by the flow are refered to as *comoving*.

The transport of geometrical objects by the flow can be used to define a transport of fields in D. In the simplest case we have a scalar field $\alpha(\mathbf{x})$ at time $t = 0$ and define the field to be constant for any comoving point, that is

$$\alpha(\mathbf{F}(\mathbf{x},t),t) := \alpha(\mathbf{x}) \quad \Leftrightarrow \quad \alpha(\mathbf{x},t) := \alpha(\mathbf{F}(\mathbf{x},-t)). \tag{2.17}$$

This implies an equation of evolution for the field,

$$\frac{\partial}{\partial t}\,\alpha + \mathbf{v}\cdot\nabla\alpha = 0 \quad \Rightarrow \quad \alpha(\mathbf{F}(\mathbf{x},t),t) = \text{const.} \tag{2.18}$$

The field α is said to be a *passive scalar* or to be *frozen-in*.

The transport of vector fields can now be derived from the transport of a passive scalar by representing the vector field in terms of scalar fields. In $I\!R^3$ there are two basic methods by which a vector field may be represented in terms of scalar fields. First we can represent any vector field by a set of six scalar fields in $I\!R^3$,

$$\mathbf{A}(\mathbf{x}) = \sum_{i=1}^{3} \alpha_i(\mathbf{x})\nabla\beta_i(\mathbf{x}). \tag{2.19}$$

Often the β_i can be considered as (general curvilinear) coordinates and $\nabla\beta_i$ are the corresponding unit vectors (not necessarily normalized), while the α_i are the components of $\mathbf{A}$ with respect to the coordinate system β_i. (Note, however, that a proper coordinate system requires $\nabla\beta_1\cdot\nabla\beta_2\times\nabla\beta_3 \neq 0$, which is not required here.) Transporting the six fields $\alpha^i(\mathbf{x})$ and $\beta^i(\mathbf{x})$, $i = 1\ldots3$ according to (2.18) yields an evolution equation for the vector field $\mathbf{A}$,

$$\frac{\partial}{\partial t}\mathbf{A} + \nabla(\mathbf{v}\cdot\mathbf{A}) - \mathbf{v}\times\nabla\times\mathbf{A} = 0 \quad \Rightarrow \quad \int_{C^1(t)} \mathbf{A}\cdot\mathrm{d}\mathbf{l} = \text{const.} \tag{2.20}$$

The last implication states that the integral over any comoving line or one-dimensional manifold, $C^1(t)$, is constant in time. The evolution equation and its integral form are the analogue of (2.18) for a vector field represented as (2.19).

The other basic representation of a vector field in $I\!R^3$ is given by

$$\mathbf{B}(\mathbf{x}) = \sum_{i=1}^{3} \nabla\alpha_i(\mathbf{x}) \times \nabla\beta_i(\mathbf{x}). \tag{2.21}$$

Again transportation of $\alpha^i(\mathbf{x})$ and $\beta^i(\mathbf{x})$ yields an evolution equation and a corresponding conserved integral of the form

$$\frac{\partial}{\partial t}\mathbf{B} + \mathbf{v}\cdot\nabla\mathbf{B} - \mathbf{B}\cdot\nabla\mathbf{v} + \mathbf{B}\ \nabla\cdot\mathbf{v} = 0 \quad \Rightarrow \quad \int_{C^2(t)} \mathbf{B}\cdot \mathrm{d}\mathbf{a} = \text{const.} \tag{2.22}$$

The conserved integral here is an integral over any comoving two-dimensional surface. We note that for a divergence-free field the evolution equation can be rewritten as

$$\frac{\partial}{\partial t}\mathbf{B} - \nabla\times\mathbf{v}\times\mathbf{B} = 0 \quad \text{for} \quad \nabla\cdot\mathbf{B} = 0. \tag{2.23}$$

In this form we recognize the induction equation (2.4) of ideal magnetohydrodynamics. A similar equation can be deduced for the evolution of vorticity in hydrodynamics in the limit of large Reynolds numbers and isentropic flow with $p = p(\rho)$.

To complete our list of *frozen-in* fields we have to mention another representation of a scalar field, namely

$$\rho(\mathbf{x}) = [\nabla\alpha(\mathbf{x}) \times \nabla\beta(\mathbf{x})]\cdot\nabla\gamma(\mathbf{x}). \tag{2.24}$$

Transporting $\alpha(\mathbf{x})$, $\beta(\mathbf{x})$, and $\gamma(\mathbf{x})$, the corresponding transport equation for ρ reads:

$$\frac{\partial}{\partial t}\rho + \nabla\cdot(\mathbf{v}\ \rho) = 0 \quad \Rightarrow \quad \int_{C^3(t)} \rho\ \mathrm{d}^3x = \text{const.} \tag{2.25}$$

An example of this kind of transport is the continuity equation for the mass density in fluid dynamics.

For the mathematically interested reader, we note that the frozen-in fields α, $\mathbf{A}$, $\mathbf{B}$, and ρ correspond to differential forms ω^k of grade $k = 0, 1, 2$, and 3. The evolution of the fields in time is given by so-called *pull-back* under the mapping $\mathbf{F}$, and the evolution equation is conveniently written with the help of the Lie derivative:

$$\frac{\partial}{\partial t}\omega^k + L_{\mathbf{v}}\omega^k = 0 \quad \Rightarrow \quad \int_{\mathbf{F}(C^k,t)} \omega^k = \text{const.} \tag{2.26}$$

The conservation of the corresponding integral over a k-dimensional domain is given by the Lie-derivative theorem (see e.g., Abraham *et al.*, 1983).

In addition to the representation with the help of scalar fields, a vector field can be represented also as the derivative of a flow, as defined in (2.16),

$$\mathbf{B}(\mathbf{F}_B(\mathbf{x}, s), s) := \frac{\partial \mathbf{F}_B(\mathbf{x}, s)}{\partial s}. \tag{2.27}$$

Here s is a parameter along the field line. Note that $\mathbf{F}_B(\mathbf{x}, s)$ is not a unique representation of the field lines. Any positive monotonic function $s'(s)$ can be used to rescale the parametrization, $\mathbf{F}_B(\mathbf{x}, s'(s))$. In this case (2.27) yields $\mathbf{B}\partial s'/\partial s$ for the

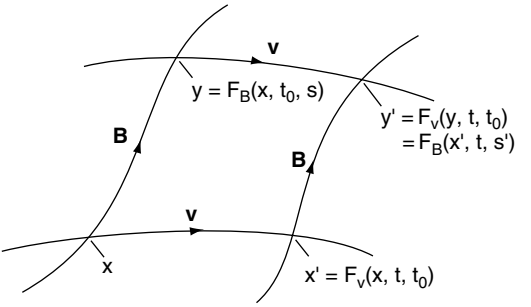

Fig. 2.8. Transport of the flow of $\mathbf{B}$ by the flow of $\mathbf{v}$.

corresponding vector field, which is proportional to $\mathbf{B}$ and therefore has the same field lines.

Now we can transport the field lines of $\mathbf{F}_B$ by the flow $\mathbf{F}$. The condition for this kind of transport (Hornig and Schindler, 1996) is

$$\mathbf{F}_B(\mathbf{F}(\mathbf{x},t),t,s'(s,t)) = \mathbf{F}(\mathbf{F}_B(\mathbf{x},t,s),t), \tag{2.28}$$

and it is illustrated in Fig. 2.8. Here we have used on the left-hand side $s'(s,t)$ instead of s, since a field line is independent of a scaling of this parameter, and so the scaling could change in time. Differentiating with respect to t and s leads to a differential equation for the evolution of field lines,

$$\frac{\partial}{\partial t}\mathbf{B} + \mathbf{v}(\mathbf{x})\cdot\nabla\mathbf{B}(\mathbf{x}) - \mathbf{B}(\mathbf{x})\cdot\nabla\mathbf{v}(\mathbf{x}) = \lambda\mathbf{B}. \tag{2.29}$$

Here the function λ is free and allows for changes of the field strength, which do not affect the field lines. It is easy to check that an evolution according to (2.29) preserves field lines together with properties such as linkage, knottedness, or ergodicity of field lines. It is also easy to prove that the number of isolated null points is preserved. It is less trivial to see that the local structure of null points, in particular the ratio of eigenvectors of the linearization of $\mathbf{B}$ at the null, is conserved as well (see Hornig and Schindler, 1996).

Relations between conservation laws

There are a number of relations between the five different conservation laws (2.18), (2.20), (2.22), (2.25), and (2.29). In the following we will mention only those relations which are relevant for magnetic reconnection. The full set of relations can be deduced most conveniently from a formulation in terms of differential forms. Here the application of the Lie derivative on the exterior product, as well as the commutation of the Lie derivative with the exterior derivative and the interior product, yields a large number of relations between different conservation laws (see e.g., Frankel, 1997).

Regarding the relations relevant for magnetic reconnection we first note that a conservation of a line density $\mathbf{A}$ as given by (2.20) implies the conservation of the

$\mathbf{B} = \nabla \times \mathbf{A}$ in the form of (2.22). The reverse implication does not hold, but we can make the following weaker statement: A flux-conserving, divergence-free field $\mathbf{B}$ possesses a vector potential $\mathbf{A}$ which is frozen-in according to (2.20). The proof (Hornig, 1997) uses the gauge freedom in order to find a vector potential which is frozen-in.

$$\begin{aligned} \frac{\partial}{\partial t}\mathbf{B} - \nabla \times \mathbf{v} \times \mathbf{B} = 0 \quad &\Rightarrow \quad \frac{\partial}{\partial t}\mathbf{A} - \mathbf{v} \times \nabla \times \mathbf{A} = -\nabla\Phi \\ \mathbf{A} \to \tilde{\mathbf{A}} = \mathbf{A} + \nabla\Psi \quad &\text{with} \quad \frac{\mathrm{d}\Psi}{\mathrm{d}t} = \Phi - \mathbf{v} \cdot (\mathbf{A} + \nabla\Psi) \\ &\Rightarrow \quad \frac{\partial}{\partial t}\tilde{\mathbf{A}} + \nabla(\mathbf{v} \cdot \tilde{\mathbf{A}}) - \mathbf{v} \times \nabla \times \tilde{\mathbf{A}} = 0. \end{aligned} \tag{2.30}$$

This in turn implies that the product $h = \mathbf{A} \cdot \mathbf{B}$, the helicity density, is frozen-in as a scalar density in the form of (2.25),

$$\frac{\partial}{\partial t}\mathbf{A} \cdot \mathbf{B} + \nabla \cdot (\mathbf{v}\ \mathbf{A} \cdot \mathbf{B}) = 0. \tag{2.31}$$

The helicity density becomes well defined, i.e. a gauge invariant quantity, if it is integrated over a simply connected volume V with vanishing normal magnetic field on the boundary ∂V, (Moffatt, 1978).

$$H(\mathbf{B}) := \int_V \mathbf{A} \cdot \mathbf{B}\ \mathrm{d}^3x \quad \text{for} \quad \mathbf{B} \cdot \mathbf{n}|_{\partial V} = 0. \tag{2.32}$$

It is a measure of the linkage of magnetic flux in the volume and therefore a topological measure of the magnetic field in V. The homogeneous Maxwell's equations yield a balance equation for the helicity density:

$$\frac{\partial}{\partial t} \underbrace{\mathbf{A} \cdot \mathbf{B}}_{\text{hel. density}} + \nabla \cdot (\underbrace{\Phi\mathbf{B} + \mathbf{E} \times \mathbf{A}}_{\text{hel. current}}) = \underbrace{-2\,\mathbf{E} \cdot \mathbf{B}}_{\text{hel. source}} \tag{2.33}$$

Here Φ is the electric potential, i.e., $\mathbf{E} = -\nabla\Phi - \partial\mathbf{A}/\partial t$. For an ideal Ohm's law, $\mathbf{E} + \mathbf{v} \times \mathbf{B} = 0$, the helicity source term vanishes and the helicity current becomes

$$\mathbf{h} = \mathbf{v}\mathbf{A} \cdot \mathbf{B} + (\Phi - \mathbf{v} \cdot \mathbf{A})\,\mathbf{B}.$$

The second term is not physically relevant and can be made to vanish for a certain gauge of the vector potential as used in (2.30). This leads in turn to (2.31).

Another important relation is that for a field $\mathbf{B}$ the conservation of flux $\int \mathbf{B} \cdot \mathrm{d}\mathbf{a}$ according to (2.22) implies a conservation of field lines (2.29). This is easy to prove, since we can choose the free function λ in (2.29) as $\lambda = \nabla \cdot \mathbf{v}$. Thus a flux-conserving evolution is also field line conserving. The reverse implication however does not hold in general.

Preparation for reconnection: detachment of a drop

Magnetic reconnection can be characterized as a localized breakdown of flux conservation in the form of (2.22). However, this breakdown occurs in a subtle way, such that the system is still flux conserving in many respects. This distinguishes

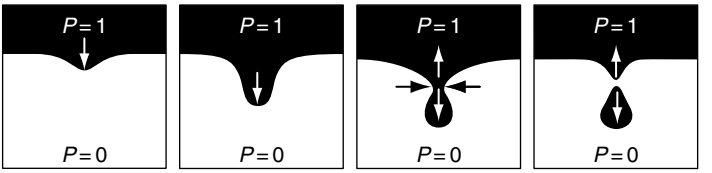

Fig. 2.9. The detachment of a drop as an example of reconnection of a scalar quantity.

reconnection from other dissipative processes which also violate the conservation law (2.22). In the following simple example, reconnection of a scalar quantity is used to demonstrate some basic properties of reconnection, before we turn to the more complicated reconnection of the vector quantity **B**.

Consider the simple example of "reconnection" of a scalar quantity as sketched in Fig. 2.9. The figure shows the detachment of a drop in a system characterized by a scalar quantity P which distinguishes the black ($P = 1$) and white ($P = 0$) phases. Although not explicitly shown in the figure we assume that there is a smooth transition between $P = 1$ and $P = 0$, so that P is a continuous quantity. The quantity P could be, for instance, a parameter characterizing the composition of a fluid where the black phase is heavier than the white phase. The unstable situation of the heavier fluid on top of the lighter fluid can then lead to a process as sketched in the figure. The physical system shown can be mathematically described by an equation determining the evolution of the velocity of the fluid, e.g., a Navier–Stokes equation, and an equation for the transport of the scalar quantity P by the flow. Since P is just a local property of the fluid it is natural to assume that the latter equation reads

$$\frac{\partial}{\partial t} P(\mathbf{x}, t) + \mathbf{v} \cdot \nabla P(\mathbf{x}, t) = 0. \tag{2.34}$$

The same equation would hold if P were the mass density of an incompressible fluid.

We now assume that we have solved the Navier–Stokes equation and are left with a physical, i.e., smooth, velocity field $\mathbf{v}$. The arrows in Fig. 2.9 indicate the direction of the flow in the various time steps. At the critical time when the detachment of the drop occurs the velocity field will show a stagnation flow. Surprisingly however, the determination of the evolution of P from (2.34) can never show a detachment of a drop. The reason for this is that for any smooth velocity field it takes an infinitely long time to transport a fluid element to the stagnation point, which is necessary for detachment. In order to see this we choose a coordinate system such that the inflow direction is, let us say, the x axis and the stagnation point is located at the origin. Then the velocity v_x along the x axis can be expanded at the stagnation point as a series in x: $v_x = -k^2 x + \mathcal{O}(x^2)$. The time it takes the flow to transport a fluid element over the last ϵ distance to the origin is

$$T_\epsilon = \int_{t(\epsilon)}^{t(0)} \mathrm{d}t = \int_{x=\epsilon}^{x=0} \frac{1}{v_x}\, \mathrm{d}x > \frac{1}{k^2} \left(-\ln(0) + \ln(\epsilon)\right) = \infty. \tag{2.35}$$

Thus any smooth flow will lead only to an increasing thinning of the neck of the drop but never to detachment in any finite time.

However, since it is an observational fact that drops can detach, the underlying equation (2.34) must be incorrect. That is, a term has to be added in the equation, which becomes relevant if length scales in the system become sufficiently small. It is obvious this has to occur at some point. Certainly by the time the width of the structure reaches the order of the distance between molecules, advection with the fluid velocity $\mathbf{v}$ becomes meaningless, and the equation has to be modified in some way. This can be accounted for by introducing a term $r(\mathbf{x},t)$ on the right-hand side of Eq. (2.34),

$$\frac{\partial}{\partial t}P(\mathbf{x},t)+\mathbf{v}\cdot\nabla P(\mathbf{x},t)=r(\mathbf{x},t). \tag{2.36}$$

We do not know much about the nature of this term, except that it has to be negligible when compared with $\mathbf{v}\cdot\nabla P(\mathbf{x},t)$, excluding those points where the latter vanishes. The value and profile of $r(\mathbf{x},t)$ turn out to be almost irrelevant for detachment to occur. It must only be of the right sign, or if it is a fluctuating quantity, have a time average of the right sign. The reason for this is that the width of the structure decreases exponentially with time, a result of the stagnation flow, and so the term on the right-hand side will, sooner or later, be sufficient to trigger detachment.

This is an important property of the system under consideration. The nonideal term on the right-hand side is essential for "reconnection" to occur, but its value and profile are not important since the process adjusts for this. In magnetic reconnection we find a very similar situation. The analogue to (2.36) is Ohm's law and the resistive term $\eta\mathbf{j}$, for instance, can play the role of the nonideal term $r(\mathbf{x},t)$.

Another important property of this example is that despite the nonideal term $r(\mathbf{x},t)$ the process is still ideal in many respects. In particular we can rewrite Eq. (2.36) as

$$\frac{\partial}{\partial t}P(\mathbf{x},t)+\mathbf{w}\cdot\nabla P(\mathbf{x},t)=0 \tag{2.37}$$

if we express $r=-\delta\mathbf{v}\cdot\nabla P$ and define $\mathbf{w}=\mathbf{v}+\delta\mathbf{v}$. Of course the new velocity $\mathbf{w}$ is not smooth, since ∇P vanishes at the point of detachment where $r\neq 0$. This requires a singularity in $\delta\mathbf{v}$, and consequently in $\mathbf{w}$, of the type $|\delta\mathbf{v}|\sim 1/|\nabla P|$. Contrary to the case of a smooth transport velocity (Fig. 2.10), this singular transport velocity $\mathbf{w}$ does

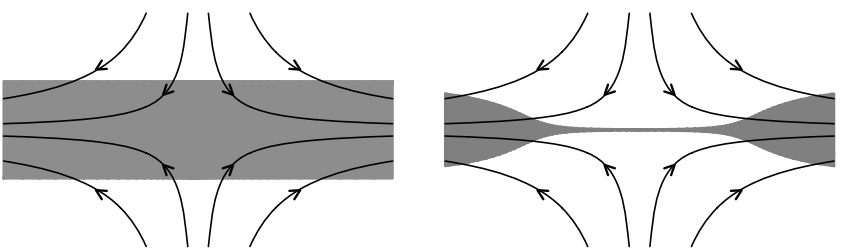

Fig. 2.10. No detachment in a finite time for a smooth $\mathbf{v}(\mathbf{x})\sim(-x,y,0)$!

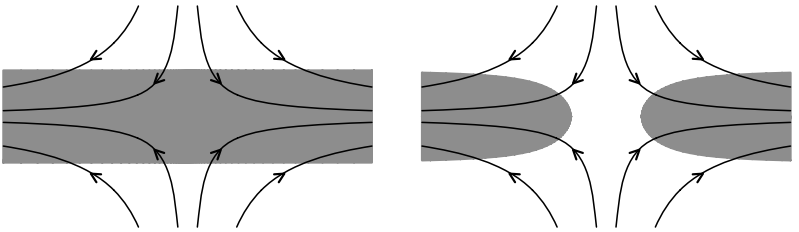

Fig. 2.11. Detachment is possible for a singular flow $\mathbf{w} \sim \left(-\frac{x}{x^2+y^2}, \frac{y}{x^2+y^2}, 0\right)$.

indeed lead to a detachment as Fig. 2.11 shows. In particular for a generic saddle point of the form $P \sim a - bx^2 + cy^2$ this implies a singularity like $w_x \sim -1/x$ along the inflow direction. A calculation analogous to (2.35) shows that the time it takes to transport a level line of P onto the stagnation point is now finite,

$$T_\epsilon = \int_{t(\epsilon)}^{t(0)} \mathrm{d}t = \int_{x=\epsilon}^{x=0} \frac{1}{w_x}\, \mathrm{d}x = \epsilon^2/2. \tag{2.38}$$

2.2.2 Conditions for magnetic reconnection to occur

From Section 2.1 we have already a good idea of the two-dimensional, i.e., standard, notion of magnetic reconnection. Reconnection in three dimensions comes in more variants than in two dimensions, some of which are far from fully explored yet. Because of this, and since we want to maintain the highest level of generality, we will start by defining reconnection in as broad terms as possible. We first infer properties from this definition before specializing to certain configurations.

Within the broadest possible definition of magnetic reconnection, i.e., in the spirit of the theory of general magnetic reconnection (Schindler *et al.*, 1988; Hesse and Schindler, 1988), magnetic reconnection requires only a change in the magnetic connectivity of plasma elements. An ideal plasma evolution, governed by

$$\mathbf{E} + \mathbf{v} \times \mathbf{B} = 0 \quad \Rightarrow \quad \frac{\partial}{\partial t}\mathbf{B} - \nabla \times \mathbf{v} \times \mathbf{B} = 0, \tag{2.39}$$

implies the conservation of magnetic flux (2.23), as well as field lines (2.29), and hence the connectivity of plasma elements cannot be changed. Therefore any form of reconnection requires a *nonideal* term $\mathbf{N}$, which we add here to the right-hand side of Ohm's law

$$\mathbf{E} + \mathbf{v} \times \mathbf{B} = \mathbf{N}. \tag{2.40}$$

Within the framework of resistive magnetohydrodynamics $\mathbf{N}$ would represent $\eta\mathbf{j}$, the resistive term in Ohm's law. However, depending on the parameter regime, other terms, such as the electron inertia term (Chapter 3), or the electron pressure tensor (see in particular Sections 3.1 and 3.2), are also thought to be responsible for reconnection. In order to keep the most general formulation we will not refer to any particular choice of $\mathbf{N}$, but rather investigate the properties which $\mathbf{N}$ has to have for reconnection to occur.

First we note that if $\mathbf{N}$ can be represented as

$$\mathbf{N} = \nabla\Phi + \mathbf{u}\times\mathbf{B} \tag{2.41}$$

we can rewrite (2.40) as

$$\mathbf{E} + (\mathbf{v}-\mathbf{u})\times\mathbf{B} = \nabla\Phi \tag{2.42}$$

$$\Leftrightarrow \quad \frac{\partial}{\partial t}\mathbf{B} - \nabla\times\mathbf{w}\times\mathbf{B} = 0 \quad \text{for} \quad \mathbf{w} = \mathbf{v}-\mathbf{u}. \tag{2.43}$$

Hence, while the connection of plasma elements might change because the field lines move with a velocity different from the plasma elements ($\mathbf{v}$), the topology of field lines remains the same since there exists a velocity $\mathbf{w}$ with respect to which the field is frozen-in (Hornig and Schindler, 1996), sometimes called a *flux transporting flow*. This implies also that there is no release of magnetic energy beyond that of an ideal relaxation of the field. A topological change of the magnetic structure on the other hand can release huge amounts of energy stored in the magnetic field. Thus this weak form of disconnection of plasma elements where $\mathbf{w}$, or $\mathbf{u}$, exists but does not coincide with the plasma velocity, is often not considered as reconnection and referred to instead as *slippage*, with $\mathbf{u}$ being the slippage velocity. For an illustration see Fig. 2.12.

Here a remark concerning the difference between conservation of magnetic flux (2.23) and conservation of field lines (2.29) is indicated. Since we began with the definition of magnetic reconnection as a change of connectivity of plasma elements, we could have based our analysis on the more general equation of field line preservation (2.29), rather than flux conservation. We have already noted that conservation of magnetic flux implies conservation of field lines. The reverse, however, does not hold. A simple example, which is line conserving but not flux conserving, is the resistive dissipation of a line current. The magnetic field consists of circular field lines enclosing the current and these field lines are preserved if the current distribution decays and broadens under a resistive dissipation of the current. The magnetic flux per unit length however decreases and hence the system is not flux conserving. Another set of fields with this property are linear force-free fields ($\nabla\times\mathbf{B} = \alpha\mathbf{B}$, $\alpha = \text{const.}$), which also dissipate magnetic flux without changing the topology

Fig. 2.12. Example of a flux tube crossing a nonideal region (gray) where the transport velocity of the magnetic flux $\mathbf{w}$ differs from the plasma velocity $\mathbf{v}$ while outside the nonideal region the plasma is ideal ($\mathbf{v} = \mathbf{w}$). The black and gray cross-sections are moving with the plasma velocity. The black cross-sections always remain in the ideal domain while the gray cross-section passes the nonideal region and is therefore later detached from the flux tube.

of field lines. The most general form of $\mathbf{N}$ which preserves the topology of field lines is

$$\mathbf{N} = \mathbf{A}_{\tilde{\lambda}B} + \mathbf{u} \times \mathbf{B} \quad \nabla \times \mathbf{A}_{\tilde{\lambda}B} = \tilde{\lambda}\mathbf{B}. \tag{2.44}$$

Note that this representation of $\mathbf{N}$ includes the form (2.41) for $\tilde{\lambda} \equiv 0$. In the following we will, however, always refer to magnetic flux conservation and correspondingly to (2.12), rather than to field line conservation, since magnetic reconnection is a process which is fast compared to the dissipative time scale, and hence we can ignore the difference between the two in this respect.

For certain forms of Ohm's law we can directly deduce that $\mathbf{N}$ is of the form (2.41) without referring to a particular process or magnetic field. Aside from the ideal Ohm's law, which trivially satisfies (2.41), important examples are the inclusion of a density-dependent pressure term (2.45) and/or a Hall term (2.46) in Ohm's law. In the latter case the transport velocity $\mathbf{w}$ turns out to be the electron bulk velocity,

$$\mathbf{E} + \mathbf{v} \times \mathbf{B} = -\frac{1}{en}\nabla P_{\mathrm{e}}(n) \quad \Rightarrow \mathbf{w} = \mathbf{v}, \tag{2.45}$$

$$\mathbf{E} + \mathbf{v} \times \mathbf{B} = \frac{1}{en}\mathbf{j} \times \mathbf{B} \quad \Rightarrow \mathbf{w} = \mathbf{v}_{\mathrm{e}} = \mathbf{v} - \frac{1}{en}\mathbf{j}. \tag{2.46}$$

Solutions for nonvanishing $\mathbf{B}$

Note that (2.41) is a nonlocal criterion. Nonlocal here means that for any $\mathbf{B}$ which does not vanish at a certain point, we can always find a solution $(\Phi, \mathbf{u})$ of (2.41) in the neighborhood of the point. The crucial question is whether this solution exists in the whole domain. Solutions $(\Phi, \mathbf{u})$ of (2.41) for given $\mathbf{N}$ and $\mathbf{B}$ can be found as follows. We split (2.41) into equations parallel and perpendicular to $\mathbf{B}$,

$$\mathbf{N}_{|} = \nabla_{|}\Phi, \tag{2.47}$$

$$\mathbf{N}_{\perp} = \nabla_{\perp}\Phi + \mathbf{u} \times \mathbf{B}. \tag{2.48}$$

We can now solve (2.47) by integrating the potential Φ along magnetic field lines and then use this solution to determine $\mathbf{u}$ from (2.48). The solution of (2.47), starting from a surface transversal to the magnetic field with $\Phi(\mathbf{x}(s=0)) = 0$, is

$$\Phi(\mathbf{x}(s)) = \int_{s'=0}^{s} \mathbf{N}(\mathbf{x}(s')) \cdot \frac{\mathbf{B}(\mathbf{x}(s'))}{|\mathbf{B}(\mathbf{x}(s'))|}\, \mathrm{d}s' \qquad \frac{\mathrm{d}\mathbf{x}(s)}{\mathrm{d}s} = \frac{\mathbf{B}(\mathbf{x}(s'))}{|\mathbf{B}(\mathbf{x}(s'))|}. \tag{2.49}$$

The corresponding solution for $\mathbf{u}$ is

$$\mathbf{u} = \frac{\mathbf{B} \times (\mathbf{N} - \nabla\Phi)}{B^2}. \tag{2.50}$$

The integration of Φ, however, may fail if the magnetic field lines are closed. For closed field lines the integral in (2.49) has to vanish, which is a nontrivial condition on $\mathbf{N}$. This argument also applies to ergodic field lines. If the magnetic field extends beyond the domain under consideration, i.e., if magnetic field lines cross the boundary, corresponding boundary conditions for Φ have to take into account the existence of an external field. For instance, a frozen-in external magnetic field would require $\Phi(\mathbf{x}_0) = \Phi(\mathbf{x}_1)$ for any pair of points $(\mathbf{x}_0, \mathbf{x}_1)$ connected by a field line in the external domain. If in addition the external field is static a possible solution for

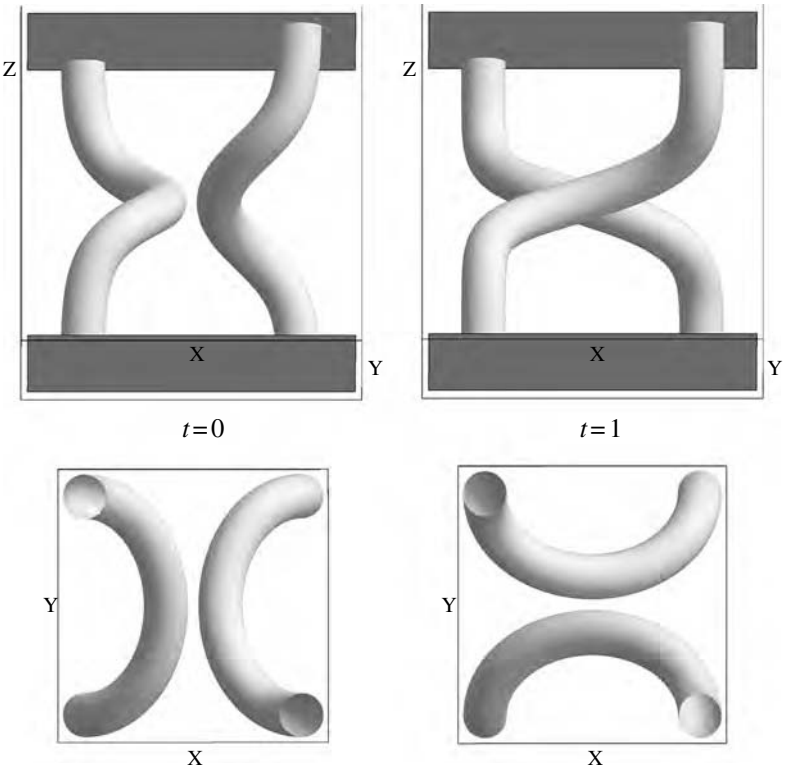

Fig. 2.13. Two flux tubes of a field of nonvanishing **B** in a bounded domain. The flux tubes undergo a nonideal evolution and are shown before ($t = 0$) and after ($t = 1$) the process. Bottom row: The view from above shows a behavior reminiscent of reconnection.

the external potential would be $\Phi = 0$, which implies $\mathbf{u} = 0$ on the boundaries. An example of the relevance of the boundary conditions is shown in Figs. 2.13 and 2.14.

Solutions at null points of **B**

Aside from boundary conditions there is another impediment to finding a solution to $(\Phi, \mathbf{u})$ from (2.41). This arises, for instance, if **B** vanishes in the nonideal region. Such points, which are generically isolated, are called null points. Since the direction of **B** at a null point is undefined the splitting into (2.47) and (2.48) breaks down at the null itself. A careful analysis of flows **u** in the vicinity of the null point shows that certain **N**, which generate changes in the ratio of eigenvalues of the linearization of **B** at the null, require diverging derivatives of **u** at the null (Hornig and Schindler, 1996). While it is debatable whether such a change of eigenvalues is already a change of the topology, a bifurcation of null points is definitely a change of topology and requires an infinite velocity **u** at the time of the bifurcation. Therefore magnetic null points are locations where the topology of the magnetic field can change such that no solution of (2.41) exists. While for $\mathbf{B} \neq 0$ the nonexistence of a solution $(\Phi, \mathbf{u})$ is always due to the lack of a global solution matching given boundary

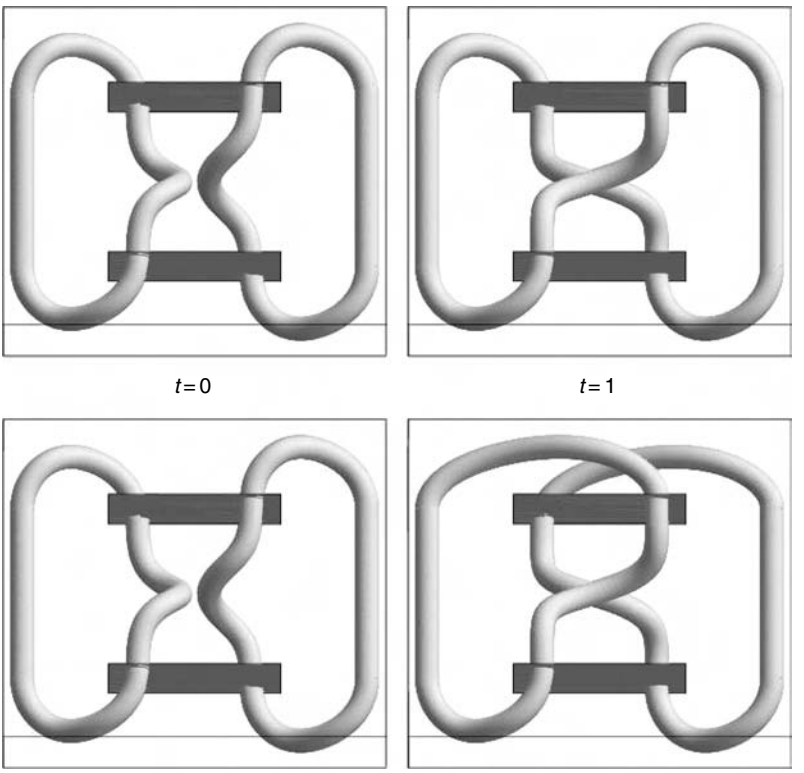

Fig. 2.14. Two possible evolutions of the external field for the process sketched in Fig. 2.13. Top row: The external field is static and therefore the evolution of the internal field causes a change of the topology (reconnection). No slippage solution exists in this case. Bottom row: The external field follows the motion of the flux tubes at the upper boundary, which allows for a slippage solution. Here the topology of the field does not change.

conditions, at null points the nonexistence can be the result either of the lack of a local solution (a result of a bifurcation, or a change of eigenvalues of the null), or due to a lack of a global solution. Examples for the latter case can be found in Section 2.4.

Solutions for $\mathbf{E}\cdot\mathbf{B}=0$

Another particular case occurs if $N_{\|}$ vanishes. Since $\mathbf{N}\cdot\mathbf{B}=\mathbf{E}\cdot\mathbf{B}\equiv 0$ this translates to a condition on the electromagnetic field. Note that the quantity $\mathbf{E}\cdot\mathbf{B}$ is a topological invariant of the electromagnetic field and is therefore conserved under ideal dynamics. In this case Φ has to be constant along field lines and it is solely determined by boundary conditions on all flux connected to the boundaries. In particular for boundary conditions $\Phi|_{\partial V}=0$ we have the trivial solution $\Phi\equiv 0$ and the solution for $\mathbf{u}$ reads

$$\mathbf{u}=\frac{\mathbf{B}\times\mathbf{N}}{B^2}. \tag{2.51}$$

Thus there always exists a solution for $\mathbf{u}$ unless $\mathbf{B}$ has null points and $\mathbf{N}$ is nonvanishing, or not sufficiently fast vanishing toward those null points. The assumption $\mathbf{N}_{\parallel} \equiv 0$ requires that, for generic three-dimensional magnetic null points, $\mathbf{N}$ has a null point at the same location as $\mathbf{B}$, since the field lines close to a generic three-dimensional isolated null point take on all possible directions. Thus any nonvanishing $\mathbf{N}$ in the vicinity of the null would violate the condition $\mathbf{N}_{\parallel} \equiv 0$. The condition $\mathbf{N} = 0$ where $\mathbf{B} = 0$ is very unlikely to be satisfied in a real plasma. However, in the two-dimensional case, for a long time the standard situation in which magnetic reconnection has been discussed, $\mathbf{N} \cdot \mathbf{B} \equiv 0$ is a typical case. In particular for $\mathbf{N} = \eta \mathbf{j}$, we have $\mathbf{N} \cdot \mathbf{B} \equiv 0$ since the current is perpendicular to the magnetic field. In two dimensions the generic null points of $\mathbf{B}$ are either elliptic (O-points) or hyperbolic (X-points). If $\mathbf{N}$ does not vanish at these points, singularities in $\mathbf{u}$ occur, which are indicative of either reconnection or a destruction/generation of magnetic flux as described below. $\mathbf{E} \cdot \mathbf{B} \equiv 0$ is therefore the natural generalization of the two-dimensional case to three dimensions.

Since (2.41) is the most general form of a nonideal term leading to an ideal induction equation for arbitrary transport velocities $\mathbf{w}$, we may conclude that any other form of $\mathbf{N}$ has to induce a change in the topological structure of the magnetic field. That is, $\mathbf{N}$ allows for a change of the topology if and only if

$$\mathbf{N} \neq \nabla \Phi + \mathbf{u} \times \mathbf{B}. \tag{2.52}$$

Above we identified situations where this condition is satisfied, or, in other words, where no solution $(\Phi, \mathbf{u})$ representing $\mathbf{N}$ exists. This is certainly a necessary condition for reconnection, but it is questionable whether all processes which change field line connectivity should be called reconnection. At least for the two-dimensional case we can clearly distinguish reconnection from a process where magnetic flux is lost or generated, as demonstrated below.

2.2.3 Two-dimensional reconnection

Let us assume we have a purely two-dimensional magnetic field, $\mathbf{B}(\mathbf{x}, t) = B_x(x, y, t)\mathbf{e}_x + B_y(x, y, t)\,\mathbf{e}_y$ in Cartesian coordinates, that is, the component perpendicular to the x, y plane, $\mathbf{B}_{\mathrm{n}}$, vanishes. The electric field can be decomposed into a component normal to the plane and a component tangent to the plane, $\mathbf{E}_{\mathrm{t}}(\mathbf{x}, t) = E_x(x, y, t)\mathbf{e}_x + E_y(x, y, t)\mathbf{e}_y$. Since $\nabla \times \mathbf{E}_{\mathrm{t}} = -\partial \mathbf{B}_{\mathrm{n}}/\partial t = 0$ the tangential component of the electric field has to be a gradient of a scalar potential. It can therefore not induce any change in connectivity of the magnetic field and we can without loss of generality assume $\mathbf{E}_{\mathrm{t}} = 0$. This implies $(\nabla \Phi)_{\mathrm{t}} = 0$ and hence $\nabla \Phi$ is at most a constant vector normal to the plane, $\nabla \Phi = \mathbf{N}_{\mathrm{c}}$. Moreover, we have $\mathbf{E} \cdot \mathbf{B} = \mathbf{N} \cdot \mathbf{B} = 0$. Under these conditions we can always define a flux conserving flow,

$$\mathbf{w} := \mathbf{v} - \mathbf{u} = \mathbf{v} - \frac{\mathbf{B} \times (\mathbf{N} - \mathbf{N}_{\mathrm{c}})}{B^2}. \tag{2.53}$$

We first note that the flow $\mathbf{w}$ is smooth with the exception of points where $\mathbf{B} = 0$ and $\mathbf{N} \neq 0$. Any nonideal evolution therefore manifests itself at the null points of the configuration.

The constant field $\mathbf{N}_c$ reflects the possibility of a constant electrostatic field normal to the plane. Many situations require $\mathbf{N}_c = 0$, e.g., an ideal plasma flow on the boundary ($\mathbf{N} = 0,\ \mathbf{u} = 0$). Therefore we will in the following assume that $\mathbf{N}_c = 0$. Whenever this assumption is not satisfied the formulas can easily be generalized by subtracting $\mathbf{N}_c$ from either $\mathbf{N}$ or $\mathbf{E}$.

The generic null points of a two-dimensional magnetic field are hyperbolic (X-points) and elliptic (O-points) null points. If $\mathbf{N}$ does not vanish at the null point, the flow $\mathbf{w}$ will have a singularity since $|\mathbf{w}| \sim 1/B$. For a generic null, the modulus $|\mathbf{B}|$ is locally, that is in lowest order near the null, proportional to the distance (x) from the null. Thus the singularity is of type $1/x$. The topology of the magnetic field near the null point determines the structure of the $\mathbf{w}$-flow. At an O-point, for instance, $\mathbf{w}$ is either converging onto or diverging away from the null point (Fig. 2.15), depending on the direction of $\mathbf{N}$ relative to the orientation of magnetic field or the current, respectively.

Consider first the converging case. Any point advected by this flow moves towards the null point and indeed reaches the null point in a finite time

$$T = \int_0^T \mathrm{d}t = \int_{x_0}^0 \mathrm{d}t/\mathrm{d}x\ \mathrm{d}x = \int_{x_0}^0 1/w_x \mathrm{d}x \sim x_0^2/2. \tag{2.54}$$

If we extend the two-dimensional magnetic field in the third dimension (z-direction) with a translational invariance, the O-point becomes a null line. Any cross-section of the magnetic field is advected in a finite time onto this null line, and "vanishes" there together with the magnetic flux threading it. We can determine a rate of loss of magnetic flux at the O-point (here r, ϕ, z are cylindrical coordinates at the null point), by integrating the magnetic flux over a comoving surface spanned by the invariant and the radial direction (see Fig. 2.16). If the normal of the surface is chosen along the magnetic field the rate of annihilation of magnetic flux is negative,

$$\frac{\mathrm{d}\Phi}{\mathrm{d}t} = \frac{\mathrm{d}}{\mathrm{d}t}\int_C \mathbf{B}\cdot\mathbf{n}\ \mathrm{d}a = -\oint \mathbf{E}\cdot\mathrm{d}\mathbf{l} = -\int_{\text{O-line}} E_\parallel\ \mathrm{d}l. \tag{2.55}$$

Note that in the loop integral over the electric field only the part along the O-line contributes, while the part along the outer edge of the surface vanishes since this line is comoving and hence the electric field vanishes there. For the diverging case the flow is reversed and we have a production of magnetic flux at the O-point, or,

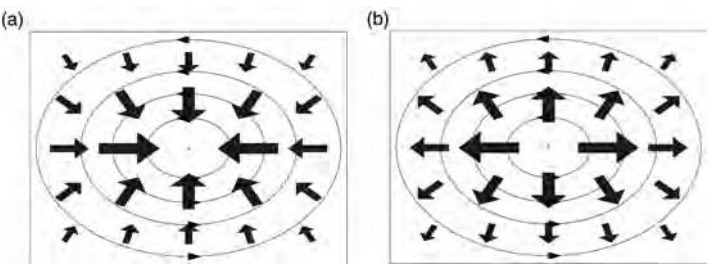

Fig. 2.15. Manifestation of loss (a) or creation (b) of flux at an O-point.

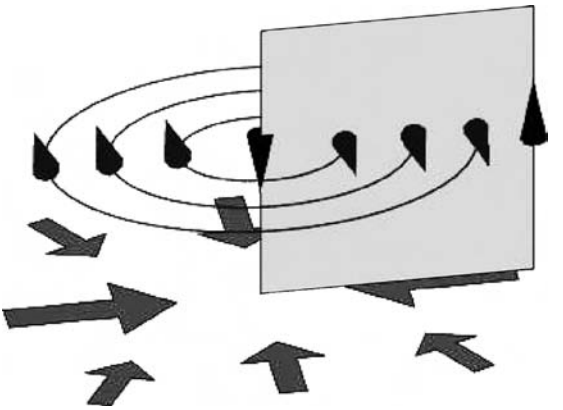

Fig. 2.16. Orientation of the surface (gray square) with respect to which the rate of loss/generation of flux is measured. The direction of the magnetic field lines (circles) determines the direction of the normal vector of the surface.

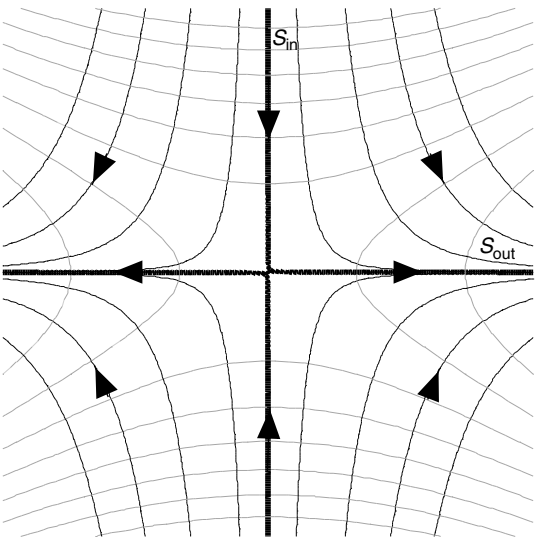

Fig. 2.17. Two-dimensional reconnection, the orientation of the flow depends on the orientation of **N** with respect to the orientation of the X-type magnetic field.

to be more precise, the system evolves as if there is a production of magnetic flux at the O-point. In this case (2.55) yields a positive rate.

For a hyperbolic null the structure of **w** at the null point is shown in Fig. 2.17. The singularity at the X-point scales in the same way ($\sim 1/x$) as for the O-point, but the structure now resembles that of a stagnation flow, that is, there is an inflow and an outflow direction. Correspondingly a point advected by this flow along the inflow separatrix (S_{in} in Fig. 2.17) is transported in a finite time onto the null point. Here it is not lost in the singularity, but rather re-emerges along the outflow separatrix (S_{out} in Fig. 2.17), since the transport away from the null also takes only a finite time.

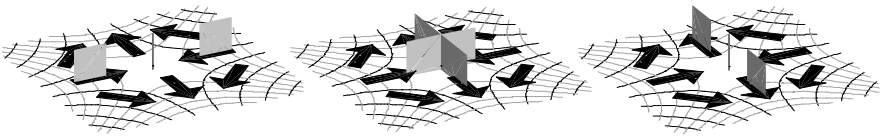

Fig. 2.18. Transport of cross-sections in the singular flow of a two-dimensional reconnection process.

If we consider the translational extension of the two-dimensional configuration in the third (invariant) direction, a surface in the inflow plane (i.e., the plane spanned by the inflow separatrix $S_{\rm in}$ and the invariant direction) follows the same evolution. This is demonstrated in Fig. 2.18. In close analogy to (2.55) we find the rate at which the magnetic flux is reconnected, either by considering the rate at which magnetic flux is transported onto the null line along the inflow separatrix, or at which the flux emerges from the null line along the outflow separatrix. In both cases the result is the same namely the electric field along the null line. We only have to be careful with choosing the sign of the reconnection rate. If we choose the same convention as in Fig. 2.16, i.e., a surface in the inflow direction with an orientation parallel to the magnetic field, we can define:

$$\frac{\mathrm{d}\Phi_{rec}}{\mathrm{d}t} = -\frac{\mathrm{d}}{\mathrm{d}t}\int \mathbf{B}\cdot\mathbf{n}\ \mathrm{d}a = \int_{\text{x-line}} E_{\parallel}\ \mathrm{d}l. \tag{2.56}$$

In this way the reconnection rate is always positive.

Note that the type of singularity in $\mathbf{w}$ and the structure of the flow are here the same as discussed in the example of the detachment of a drop.

Since X-points and O-points are the only generic null points in two dimensions this case is exceptionally easy to analyze. Reconnection can occur only at X-points and will arise whenever $\mathbf{N}-\mathbf{N}_{\rm c}$ does not vanish at the X-point, independent of the physical mechanism which is responsible for the nonideal behavior. Annihilation or dissipation of magnetic flux, as well as the reverse process of generation of magnetic flux, manifests itself at O-points and can be clearly distinguished from reconnection. Note that reconnection, even if it is driven by a dissipative term like $\eta\mathbf{j}$, does not require the dissipation of magnetic flux. Dissipation of magnetic energy and dissipation of magnetic flux must be clearly distinguished.

2.2.4 Three-dimensional reconnection: $\mathbf{E}\cdot\mathbf{B}=0$

The crucial condition we have used to determine $\mathbf{w}$ in the two-dimensional case was $\mathbf{E}\cdot\mathbf{B}=0$. This suggests that we can try to replace two-dimensionality by the more general condition $\mathbf{E}\cdot\mathbf{B}=0$. Indeed this implies $\mathbf{N}\cdot\mathbf{B}=0$ which in turn allows for a representation of $\mathbf{N}$ as $\mathbf{u}\times\mathbf{B}$ and (2.53) holds just as in the two-dimensional case. Again singularities in $\mathbf{w}$ can occur only at points with $\mathbf{B}=0$.

$\mathbf{E}\cdot\mathbf{B}=0$ is much less restrictive than two-dimensionality for the magnetic field. In fact the condition does not restrict the topology of the magnetic field, but only its dynamics. Thus in principle every magnetic field, even if it has ergodic field lines, can satisfy this condition provided the dynamics, i.e., the electric field, allow for it. Since singularities in $\mathbf{w}$ can occur only at null points of $\mathbf{B}$ it seems as if we could obtain

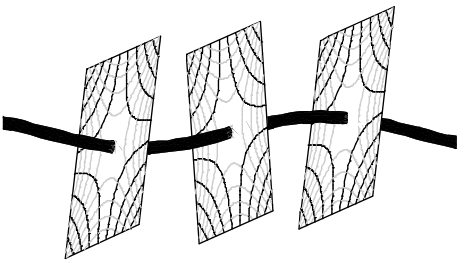

Fig. 2.19. Locally two-dimensional reconnection along a null line of an otherwise three-dimensional magnetic field ($\mathbf{E}\cdot\mathbf{B}=0$).

reconnection at isolated three-dimensional null points as well. However, reconnection under $\mathbf{E}\cdot\mathbf{B}=0$ can occur only at null lines and not at isolated three-dimensional null points. This can be easily proved by noting that in the vicinity of a three-dimensional null point $\mathbf{B}$ takes on every direction, so that $\mathbf{N}\cdot\mathbf{B}=0$ requires $\mathbf{N}=0$. Thus $\mathbf{N}\cdot\mathbf{B}=0$ together with $\mathbf{N}\neq 0$ indeed requires a locally two-dimensional configuration, i.e., in the vicinity of the null point the magnetic field is tangent to a plane perpendicular to $\mathbf{N}$ (see Fig. 2.19), and therefore the magnetic null point has to be part of a magnetic null line.

Summarizing the results, we say that when $\mathbf{E}\cdot\mathbf{B}=0$ reconnection occurs at X-type null lines of the magnetic field provided we have a nonvanishing component $\mathbf{N}\neq\nabla\Phi$ along the null line. The rate of reconnected flux is given by the generalization of (2.56) to a curved geometry,

$$\frac{\mathrm{d}\Phi_{\mathrm{rec}}}{\mathrm{d}t}=\int E_{\parallel}\,\mathrm{d}l. \tag{2.57}$$

Here $\parallel$ denotes the component parallel to the null line. If $\mathbf{N}$ is localized in the vicinity of the X-type null line (hyperbolic null line) the process does not involve any loss or generation of magnetic flux, as this can occur at an O-type null line only. This process does not involve any change of the total magnetic helicity of a configuration because the source term $\mathbf{E}\cdot\mathbf{B}$ vanishes.

2.2.5 Three-dimensional reconnection: $\mathbf{E}\cdot\mathbf{B}\neq 0$

Although the generalization discussed in the previous section covers a much wider class of configurations than the pure two-dimensional cases, the condition $\mathbf{E}\cdot\mathbf{B}=0$, or $\mathbf{N}\cdot\mathbf{B}=0$, respectively, is still very restrictive. In general we will have $\mathbf{N}\cdot\mathbf{B}\neq 0$ maybe except for very symmetric field configurations in, e.g., laboratory plasmas. In particular the different terms of a generalized Ohm's law responsible for $\mathbf{N}\neq 0$, such as the resistive term, the electron inertia, or the pressure tensor, do not imply $\mathbf{N}\cdot\mathbf{B}=0$. Moreover null lines of the magnetic field are topologically unstable, i.e., an arbitrarily small component of the magnetic field parallel to the null line can turn them into regular field lines and violate $\mathbf{E}\cdot\mathbf{B}=0$. This was recognized by Schindler *et al.* (1988) and led to the development of a theory of *general magnetic reconnection* (Hesse and Schindler, 1988; Hesse and Birn, 1993). Within this theory only a localized nonideal region with a nonvanishing integrated electric

field component parallel to the magnetic field is required for reconnection to occur. This corresponds to a nonvanishing reconnection rate as given by (2.57) where $\parallel$ now denotes the component parallel to an arbitrary field line.

The criterion $\int E_\parallel \, \mathrm{d}l \neq 0$ coincides with the criterion (2.52) under the assumptions that $\mathbf{B} \neq 0$ and $\mathbf{N}$ is localized. This can be proved as follows. First we note that localized means that there exists an environment with $\mathbf{N} = 0$ outside a finite domain D where $\mathbf{N} \neq 0$. This is sketched in Fig. 2.20. We now integrate $\mathbf{E}$ along a closed loop consisting of a magnetic field line crossing D and a material (i.e., comoving) line L in the external ideal region. L lies in the ideal region and therefore the electric field in the comoving frame vanishes, $\mathbf{E}' = \mathbf{E} + \mathbf{v} \times \mathbf{B} = 0$. Thus the integral over L does not contribute to the loop integral; the change of magnetic flux enclosed by this loop is given by the integral over the magnetic field line only, and is therefore nonvanishing. This contradicts the generalized flux conservation (2.43) and hence $\mathbf{N} \neq \nabla\Phi + \mathbf{u} \times \mathbf{B}$. Therefore

$$\frac{\mathrm{d}\Phi}{\mathrm{d}t} = \frac{\mathrm{d}}{\mathrm{d}t} \int \mathbf{B} \cdot \mathbf{n} \, \mathrm{d}a = \oint E_\parallel \, \mathrm{d}l \neq 0. \tag{2.58}$$

The conditions (2.52), or alternatively $\int E_\parallel \, \mathrm{d}s \neq 0$, are very general, and if used as a definition for magnetic reconnection many nonideal processes would qualify as reconnection. However, a more precise definition, similar to the one given in the $\mathbf{E} \cdot \mathbf{B} = 0$ case, is hard to find since, in the general three-dimensional geometry, there seems to be no clear distinction between a loss/generation of magnetic flux and reconnection. The analysis of the model of a three-dimensional reconnection process in the following section illustrates this property. This model shows among other things that for this type of reconnection the three properties, nonvanishing of the helicity source term, nonexistence of a flux-transport velocity and flipping of field lines, are closely related. The flipping of field lines is demonstrated in Fig. 2.21 and it is the result of following field lines being anchored in the ideal plasma surrounding the reconnection region. Since the field lines, threading the nonideal region, are frozen-in on both sides of the nonideal region, there is no unique velocity within the nonideal region, but two different field line motions. This creates the impression of splitting of field lines as they enter the nonideal region. This effect is well known from 2.5D models (see, for example, Priest and Forbes, 1992). An important and unsolved problem is the question about whether or not the corresponding flux tubes, of a

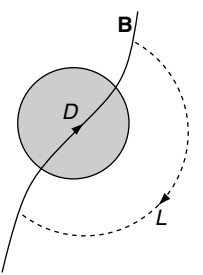

Fig. 2.20. Setup to prove that a nonvanishing $\int E_\parallel \, \mathrm{d}s$ along a magnetic field line due to a localized nonideal region D contradicts flux conservation.

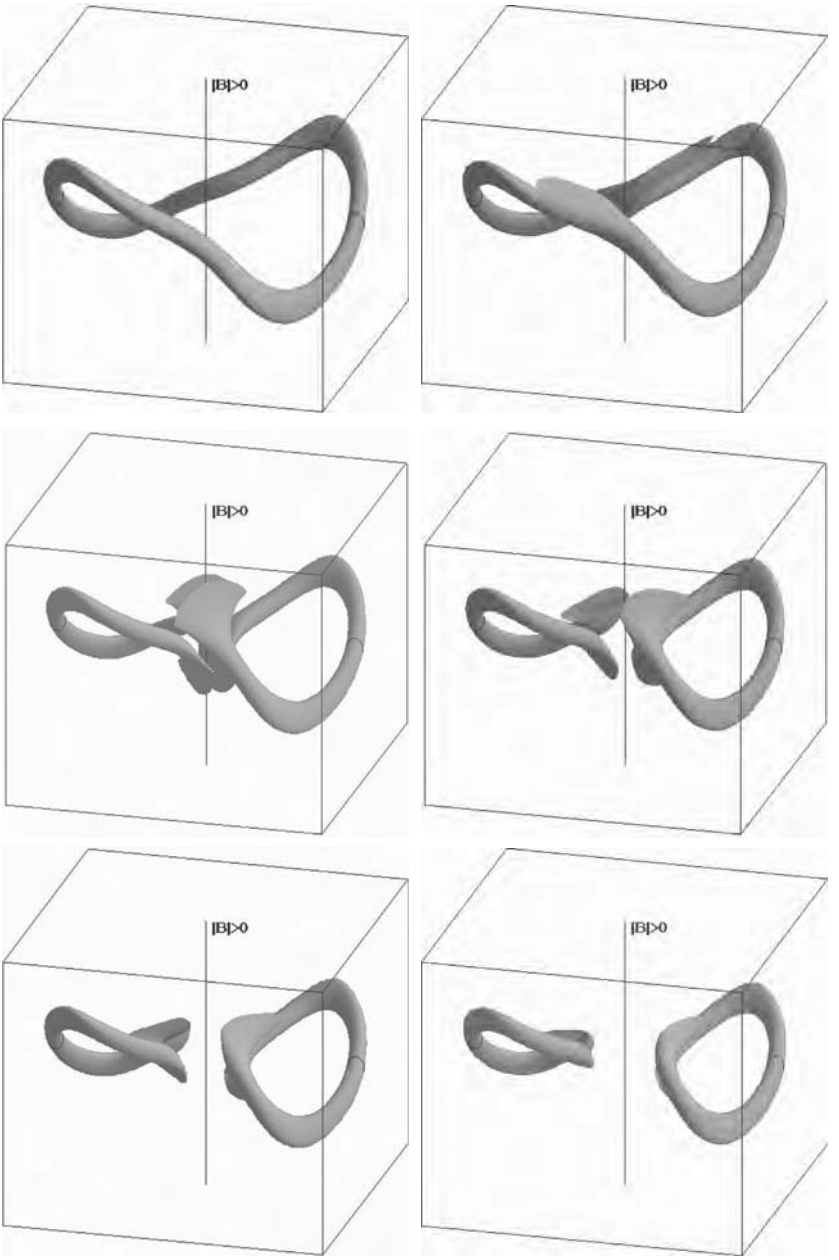

Fig. 2.21. Splitting and flipping of magnetic flux in the process of reconnection in a region of nonvanishing magnetic field. Reprinted with permission from G. Hornig, *Physics of Plasmas*, **10**, 2712. Copyright 2003, American Institute of Physics.

process as shown in Fig. 2.21, join again perfectly when they leave the nonideal region. As we will see in the discussion of the model in Section 2.3 the answer is that there is in general no perfectly reconnecting counterpart for an arbitrary flux tube undergoing reconnection. However, for reconnection processes limited in time there

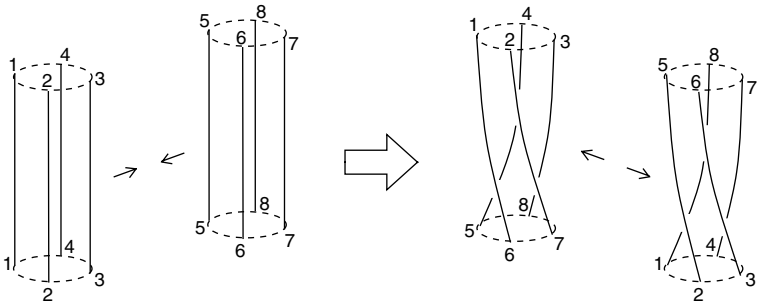

Fig. 2.22. Sketch of $\mathbf{E} \cdot \mathbf{B} \neq 0$ reconnection for two initially untwisted flux tubes. It is assumed that the process is bounded in time. The cross-sections shown are the particular cross-sections which are mapped onto each other during the process (perfectly reconnecting cross-sections). There are no pairwise reconnecting field lines, but the reconnecting flux tubes get twisted under reconnection. The resulting twist is consistent with the helicity production. Reprinted with permission from D. Pontin, G.Hornig and E. R. Priest, *Geophysical and Astrophysical Fluid Dynamics*, **98**, 407. Copyright 2004, Taylor and Francis.

exist distinguished closed flux surfaces, i.e., flux tubes, which are mapped onto each other. This effect is closely related to the helicity production in the process. While one can argue that due to the small size of the reconnection region compared to the volume of the magnetic flux undergoing reconnection, the production of helicity in the nonideal region will in general be small compared to the helicity of magnetic flux of the configuration, the helicity production has a non-negligible effect for the connectivity of field lines. The effect is sketched in Fig. 2.22 for two flux tubes undergoing reconnection. This rotation also shows that there cannot be a one-to-one reconnection of field lines. This among other things will be demonstrated with the example in the following Section 2.3.

2.3 Three-dimensional reconnection in the absence of magnetic null points

G. Hornig

In this section we will demonstrate fundamental properties of three-dimensional magnetic reconnection in the absence of null points of the magnetic field. We have to distinguish here two principally different reconnection scenarios. In plasmas of fusion devices, where the field closes upon itself after much less than a mean free path of the electrons, any nonideal process starting on a certain field line will quickly propagate along that field line and spread out along the whole torus. Thus the way field lines map the reconnection region upon itself is important for this type of reconnection and the nonideal domain is in the simplest case a toroidal domain. In astrophysical plasmas, however, length scales along the magnetic field are most often larger than the mean free path and the field lines are not necessarily closed, such that the localization of the reconnection region along the magnetic field is crucial. This is the generic type of reconnection in astrophysical plasmas and it is this scenario, where

the nonideal region (diffusion region) is bounded in all three dimensions, on which our model is based.

The analysis of three-dimensional magnetic reconnection in the absence of null points is hampered by several facts. Firstly, there is in general no distinguishable magnetic field line which, in analogy with the null line in the two-dimensional case, defines where the reconnection occurs. Field lines are locally either hyperbolic or elliptic, i.e., in the plane perpendicular to the magnetic field vector, the field shows an X-type or an O-type structure. This property, however, does not distinguish an individual field line but only certain domains, since with every hyperbolic (elliptic) field line there exists a neighborhood of other hyperbolic (elliptic) field lines. Where reconnection occurs will therefore not be determined by the local field topology, as in the two-dimensional case, but by the dynamics prior to the onset of reconnection, e.g., by the location where current sheets form. This location can, but does not necessarily need to, be determined by global topological features. Such features are for instance particular field lines, called separators, which connect two null points. Separators are the intersections of the two fan planes of the nulls and hence they are located at the intersection of four different flux domains. So the field lines in the vicinity of the separator are very sensitive to flows crossing the boundaries of the flux domains, which in turn indicates that currents will build up easily along these field lines (Section 5.2). Critical current densities which subsequently lead to reconnection can, however, also build up in the absence of any topological distinguished field lines. An appropriate measure to detect the sensitivity of a configuration to respond with current sheets to an ideal deformation is the squashing factor (see Section 5.3). It can be used to identify so-called quasi-separatrix layers where the field line connectivity varies strongly and which are therefore preferred locations for the formation of current sheets (Section 5.3).

Secondly, the clear distinction between reconnection and dissipation/generation of magnetic flux, which we find in two dimensions, is not present in three dimensions any more. Here, as we will see, both processes are closely related. The lack of a clear distinction between reconnection and dissipation/generation of flux is due to the absence of a general transport velocity for the magnetic flux. While in two dimensions such a velocity always exists (Section 2.2.3), no analogue is present in the general three-dimensional case, i.e., if $\mathbf{E}\cdot\mathbf{B}\neq 0$ (Hornig, 2001; Priest *et al.*, 2003a). Unfortunately this is the relevant case for reconnection in three dimensions.

Nevertheless, we can investigate the evolution of magnetic flux for $B\neq 0$ reconnection, provided the nonideal region is limited to a finite region (D) which does not contain any closed flux. Under these conditions all the flux in the nonideal region (D) is connected to the ideal environment. Then we can follow the evolution of magnetic flux inside D by following the magnetic flux frozen in the ideal external region. There is no flux-conserving velocity which satisfies $\mathbf{w}=\mathbf{v}_\perp$ on the whole boundary of D, but we can define a flux-conserving velocity $\mathbf{w}$ inside D which satisfies $\mathbf{w}=\mathbf{v}$ on either the part of the boundary where flux enters D or where it leaves D. We can call them, say, $\mathbf{w}^{\mathrm{in}}$ and $\mathbf{w}^{\mathrm{out}}$. However, contrary to the two-dimensional case, for the general three-dimensional case $\mathbf{w}^{\mathrm{in}}$ and $\mathbf{w}^{\mathrm{out}}$ will not coincide inside D. This is the nonexistence of a single flux-transporting velocity as stated above. The construction is shown in Fig. 2.23.

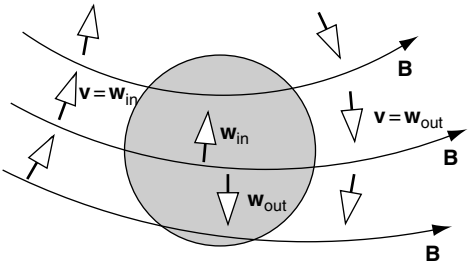

Fig. 2.23. The construction of the pair of flux-transporting velocities $\mathbf{w}_{\rm in}$ and $\mathbf{w}_{\rm out}$ in the nonideal region D.

Comparing the two velocities $\mathbf{w}_{\rm in}$ and $\mathbf{w}_{\rm out}$ at any cross-section within D shows how the nonidealness acts on the connectivity of plasma elements across D. We will use this method to investigate a simple model of three-dimensional reconnection as described by Hornig and Priest (2003).

2.3.1 The model

The model consists of an incompressible ($\nabla\cdot\mathbf{v}=0$) kinematic solution of the stationary resistive MHD equations:

$$\mathbf{E}+\mathbf{v}\times\mathbf{B}=\eta\mathbf{j}, \tag{2.59}$$

$$\nabla\times\mathbf{E}=0, \tag{2.60}$$

$$\nabla\cdot\mathbf{B}=0, \tag{2.61}$$

$$\nabla\times\mathbf{B}=\mu_0\,\mathbf{j}, \tag{2.62}$$

with a localized nonideal term $\eta\mathbf{j}$. It satifies the stationary continuity equation,

$$\nabla\cdot(\rho\ \mathbf{v})=0, \tag{2.63}$$

for instance with a uniform plasma density ($\rho=$ const.). The model can be easily modified to include the Hall term, $\mathbf{j}\times\mathbf{B}/(ne)$, in addition to the convective term $\mathbf{v}\times\mathbf{B}$ on the left-hand side of Ohm's law (2.59). This results in a term $\mathbf{v_e}\times\mathbf{B}$ up to terms of order $m_{\rm e}/m_{\rm i}$. Thus the plasma velocity is replaced by the electron velocity and *idealness* now refers to the magnetic field being frozen in the electron flow instead of the plasma flow, but this substitution does not affect the main results.

We start by prescribing the configuration of the magnetic field as a simple superposition of an X-type linear field in the x–y plane with a homogeneous field in the z direction,

$$\mathbf{B}=B_0\,(y/L\,\mathbf{e}_x+k^2x/L\,\mathbf{e}_y+\mathbf{e}_z). \tag{2.64}$$

Here k determines the magnitude of the electric current

$$\mathbf{j}=(k^2-1)B_0/(L\,\mu_0)\,\mathbf{e}_z. \tag{2.65}$$

The advantage of this model is that we can integrate the field lines analytically from

$$\frac{\partial\mathbf{X}(s)}{\partial s}=\mathbf{B}\,(\mathbf{X}(s)) \tag{2.66}$$

and so obtain the equations $\mathbf{X}(\mathbf{x}_0, s)$ of the field line that passes through an initial point $\mathbf{x}_0$. The components of $\mathbf{X}(\mathbf{x}_0, s)$ and of the corresponding inverse mapping $\mathbf{X}_0(\mathbf{x}, s)$ are:

$$X = x_0 \cosh(B_0 ks/L) + y_0/k \sinh(B_0 ks/L), \tag{2.67}$$

$$Y = y_0 \cosh(B_0 ks/L) + x_0 k \sinh(B_0 ks/L), \tag{2.68}$$

$$Z = z_0 + B_0 s, \tag{2.69}$$

$$X_0 = x \cosh(B_0 ks/L) - y/k \sinh(B_0 ks/L), \tag{2.70}$$

$$Y_0 = y \cosh(B_0 ks/L) - xk \sinh(B_0 ks/L), \tag{2.71}$$

$$Z_0 = z - B_0 s. \tag{2.72}$$

Note that the parameter s, which parametrizes the magnetic field line, is not the distance λ along the field line, but is related to it by

$$\mathrm{d}s = \mathrm{d}\lambda/B, \tag{2.73}$$

where $B = |\mathbf{B}|$.

If we set $Z_0 = 0$ and solve Eq. (2.72) for s

$$s = z/B_0, \tag{2.74}$$

we can replace s in Eqs. (2.70) and (2.71). The corresponding expressions $X_0(x, y, z)$ and $Y_0(x, y, z)$ are Euler potentials for the magnetic field, i.e.,

$$\mathbf{B} = \nabla(\sqrt{B_0} X_0) \times \nabla(\sqrt{B_0} Y_0). \tag{2.75}$$

This property is important for comparison of our results with the theory of "general magnetic reconnection" developed by Schindler *et al.* (1988) and Hesse and Schindler (1988).

Equation (2.60) implies that the electric field is the gradient of a scalar function ϕ. Inserting this in Eq. (2.59) yields

$$-\nabla\phi + \mathbf{v} \times \mathbf{B} = \eta\, \mathbf{j}. \tag{2.76}$$

In order to have a localized nonideal term $\eta\mathbf{j}$ we have to localize the resistivity, since $\mathbf{j}$ is constant. Note that if we prescribe η we can always calculate ϕ from the component of Eq. (2.76) parallel to $\mathbf{B}$, $(\nabla\phi)_\parallel = -\eta \mathbf{j}_\parallel$, by integrating along the field lines:

$$\phi = -\int \eta\, \mathbf{j}_\parallel \,\mathrm{d}l + \phi_0 = -\int \eta\, \mathbf{j} \cdot \mathbf{B}\, \mathrm{d}s + \phi_0. \tag{2.77}$$

To obtain an analytical solution for ϕ we prescribe η as the following function of the coordinates x_0, y_0 of field lines in the plane $z = 0$ and the parameter s along the field lines:

$$\eta(x_0, y_0, s) = \eta_0 \exp(-(B_0^2 s^2 + x_0^2 + y_0^2)/l^2). \tag{2.78}$$

Substituting Eqs. (2.70), (2.71), and (2.74) in the expression for η yields $\eta(x, y, z)$. This function is positive, has a maximum η_0 at the origin, and is exponentially decreasing with distance from the origin, such that at a distance of $2l$ its value is less than 2% of the maximum. We call this region inside the surface $\eta = 0.02\eta_{\max}$ the nonideal region D. The shape of this domain is a sphere distorted towards a tetrahedron by the hyperbolic structure of the magnetic field (see Fig. 2.24).

The above method of prescribing the functional form of η is used for the sake of simplicity and to easily demonstrate the qualitative evolution of magnetic flux. Since, as we will see, ϕ is the relevant quantity for our main results, only the localization of the product $\eta \mathbf{j}_\parallel$ matters. In particular, it is not important whether this localization is obtained by a localization of η or of $\mathbf{j}_\parallel$ or, which is the physically most plausible case, a combination of both. Moreover, given a more general Ohm's law, it does not matter whether the nonidealness results from a resistive, inertia, or pressure term in Ohm's law. Important here is only the existence of a component parallel to $\mathbf{B}$, which is localized and is not the gradient of a scalar.

Now we can integrate ϕ from Eq. (2.77) starting with $\phi = \phi_0(x_0, y_0)$ in the plane $z = 0$:

$$\phi(x_0, y_0, s) = -\frac{\sqrt{\pi}\, B_0\, \eta_0\, l\, (k^2 - 1)\, \mathrm{erf}(B_0\, s/l)}{2\, L\, \mu_0\, \exp\left[(x_0^2 + y_0^2)/l^2\right]} + \phi_0(x_0, y_0). \tag{2.79}$$

Again we can use Eqs. (2.70), (2.71), and (2.74) to replace (x_0, y_0, s) by (x, y, z) in the expression for ϕ. This allows us to calculate $\nabla\phi(x, y, z)$ and to deduce the perpendicular component of the plasma velocity

$$\mathbf{v}_\perp = (-\nabla\phi - \eta\mathbf{j}) \times \mathbf{B}/B^2. \tag{2.80}$$

The resulting analytical expression is too long to be presented here explicitly but can be calculated by any computer algebra system immediately. Instead we use our

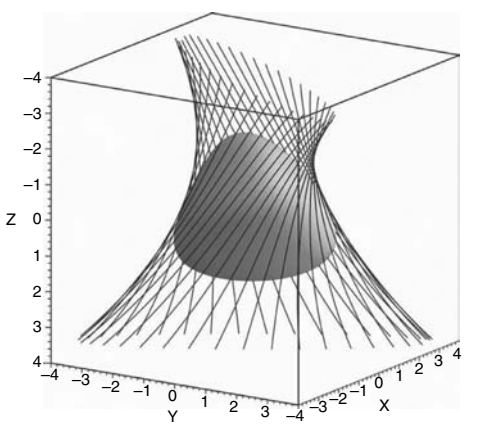

Fig. 2.24. The nonideal region D at 2% of the maximum value of η together with the hyperbolic flux tube enclosing D (parameters: $k = 2,\ L = 10,\ l = 1$). Figures 2.24, 2.25, and 2.27–2.33 are reprinted with permission from G. Hornig, *Physics of Plasmas*, **10**, 2712. Copyright 2003, American Institute of Physics.

freedom to add a component parallel to $\mathbf{B}$ to set the z component of the plasma velocity to zero,

$$\mathbf{v} = \mathbf{v}_\perp - (\mathbf{v}_\perp)_z \mathbf{B}/B_0. \tag{2.81}$$

This is convenient to show plots of the vector field in $z = \text{const.}$ planes, without suppressing any information, since now the velocity has only x and y components.

The freedom to choose $\phi_0(x_0, y_0)$ results from the fact that, for a given magnetic field, Ohm's law (2.76) can be decomposed into an ideal and a nonideal part,

$$-\nabla\phi_{\text{non-id.}} + \mathbf{v}_{\text{non-id.}} \times \mathbf{B} = \eta\,\mathbf{j}, \tag{2.82}$$

$$-\nabla\phi_{\text{id}} + \mathbf{v}_{\text{id}} \times \mathbf{B} = 0. \tag{2.83}$$

Identifying ϕ_0 with ϕ_{id}, we see that this is the source of an ideal plasma flow which can be superimposed on any reconnection solution. In particular, we choose

$$\phi_0(x_0, y_0) = \varphi_0\, x_0\, y_0 / l^2. \tag{2.84}$$

This choice is motivated by the following consideration. The use of Eqs. (2.70), (2.71), and (2.74) yields the corresponding expression in terms of (x, y, z) for (2.84). This choice of ϕ_0 corresponds to $\mathbf{v}_{\text{id}}$ being a stagnation flow. In particular, in the $z = 0$ plane it yields

$$\mathbf{v}_{\text{id}}(z{=}0) = \phi_0/(B_0\, l^2)\,(-x\,\mathbf{e}_x + y\,\mathbf{e}_y). \tag{2.85}$$

Thus, in the $z = 0$ plane the flow structure of the ideal flow is analogous to the structure of flow in classical two-dimensional reconnection. Contrary to the two-dimensional case, $\mathbf{v}_{\text{id}}$ is not singular at the origin, since ideal flows can cross the quasi-separatrix surfaces ($y = \pm kx$) when the z component of $\mathbf{B}$ is nonvanishing. It is only when $\mathbf{B} = 0$ that this results in a singularity in $\mathbf{v}_{\text{id}}$.

Before we come to explicit examples two comments may help to clarify the physical nature of the solutions. Firstly, as mentioned above, the velocity is divergence-free, which can be derived from the fact that the z component of curl Eq. (2.76) reduces to $B_0 \nabla \cdot \mathbf{v} = 0$ due to the constant B_z and the vanishing v_z. Therefore the solutions satisfy the continuity equation for a uniform density ρ.

Secondly, our choice of $\mathbf{B}$ leads to $\nabla \times (\mathbf{j} \times \mathbf{B}) = 0$. Thus we can find a plasma pressure p, such that

$$-\nabla p + \mathbf{j} \times \mathbf{B} = 0, \tag{2.86}$$

i.e., the solutions satisfy the momentum balance in the limit of slow flows (much smaller than the sound and Alfvén speeds). Moreover, in Section 2.3.4 we will use velocity fields which have a stagnation point in close similarity to the flows which are known to exist for the two-dimensional problem (see, for example, Priest and Forbes, 2000) and for which solutions to the full momentum balance exist. Note that the nonvanishing B_z component does not alter the momentum balance compared to the two-dimensional case, since here $\mathbf{j}$ has only a z component. Thus our kinematic solutions are in a certain limit solutions to the full MHD equations.

2.3.2 Purely rotational solutions

We start by analyzing the situation when $\phi_0 \equiv 0$. For this case the solution for $\mathbf{v}$ vanishes in the $z = 0$ plane and shows counter-rotating flows above and below the nonideal region, as shown in Fig. 2.25. The rotational flows are distorted by the hyperbolic structure of the magnetic field. Close to the $z = 0$ plane they are almost circular. For large values of z they become highly squashed. This effect grows with the ratio l/L.

Outside the nonideal domain D, nonzero flow is limited to regions where ϕ is nonzero. Since ϕ is constant along field lines in the ideal domain, this region consists of all field lines which are threading D. This domain is itself a flux tube, called a hyperbolic flux tube (see Titov *et al.*, 2002, for an exact definition of this term), as shown in Fig. 2.24.

The existence of rotational flows outside D (as shown in Fig. 2.25) can be proved for very general conditions as follows. Consider the electric field along the central field line, $x = y = 0$,

$$\mathbf{E}(0,0,z) = B_0\eta_0(k^2-1)\ \exp\left(-z^2/l^2\right)/(L\mu_0)\mathbf{e}_z. \tag{2.87}$$

It leads to a potential difference along the central field line above and below D given by

$$\phi(0,0,\pm\infty) = \mp\frac{\sqrt{\pi}\,B_0\ \eta_0\,l\,(k^2-1)}{2\,L\,\mu_0}. \tag{2.88}$$

Note that these limiting values are already reached to high accuracy at distances of $z/l > 2$. With the same accuracy any field line forming the envelope in Fig. 2.24 has a vanishing potential ϕ. The same holds for all other field lines outside this hyperbolic flux tube. The central field line (L_0), a field line of the envelope (L_1), and two radial lines connecting them above and below D (R_1, R_2) form a closed loop

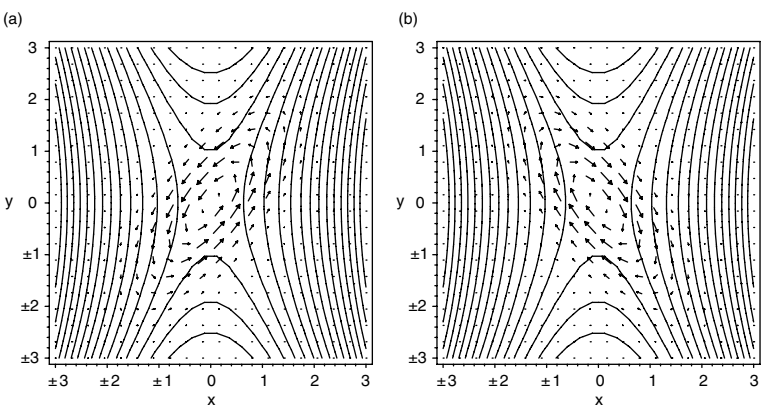

Fig. 2.25. Counter-rotating plasma flows for the purely rotational solution together with magnetic field lines (solid lines): (a) above ($z = 2$) and (b) below ($z = -2$) the reconnection region and for parameters: $k = 2,\ L = 10,\ l = 1$.

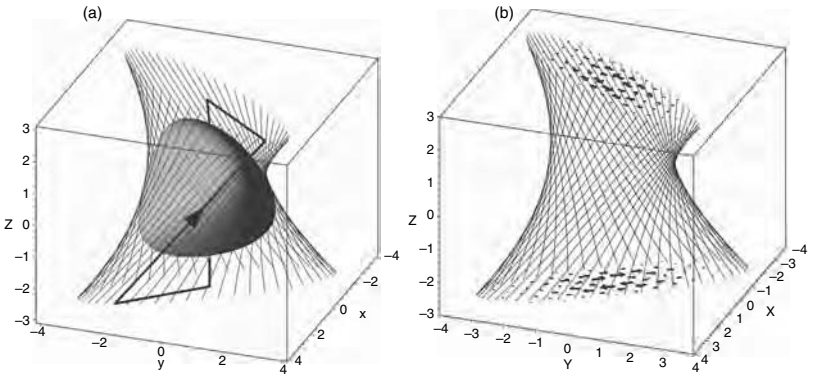

Fig. 2.26. (a) A closed loop consisting of the central field line and a field line of the envelope together with two radial connections. For the stationary case the vanishing of the integral over the electric field along such loops implies rotational flows above and below the reconnection region (b).

(L_0, R_1, L_1, R_2). Along this loop the integral over the parallel electric field has to vanish (see Fig. 2.26), since $\nabla \times \mathbf{E} = 0$, and so

$$\begin{aligned} 0 &= \oint \mathbf{E} \cdot \mathrm{d}\mathbf{l} \\ &= \int_{L_0} \mathbf{E} \cdot \mathrm{d}\mathbf{l} + \int_{R_1} \mathbf{E} \cdot \mathrm{d}\mathbf{l} + \int_{L_1} \mathbf{E} \cdot \mathrm{d}\mathbf{l} + \int_{R_2} \mathbf{E} \cdot \mathrm{d}\mathbf{l} \\ &= \Delta_{L_0}\phi + \Delta_{R_1}\phi + 0 + \Delta_{R_2}\phi \\ &= 2\,\phi(0,0,-\infty) + 2\,\Delta_R\phi. \end{aligned}$$

Here we have used the symmetry $z \leftrightarrow -z$ in the last equality. Therefore, the voltage drop along each of the radial parts of the loop equals $-\phi(0,0,-\infty)$. However, since the loop integral requires a direction of integration which is opposite for R_1 compared to R_2, the electric fields along R_1 and R_2 are oppositely directed. These electric fields induce a plasma flow perpendicular to the radial lines in planes of constant z, which is oppositely directed above and below D. This completes the proof of the existence of counter-rotating flows.

2.3.3 Reconnected flux

The rate of reconnected flux is given in general by the integral of the parallel electric field along the reconnection line (Schindler *et al.*, 1988; Hornig, 2001),

$$\frac{\mathrm{d}\Phi_{\mathrm{mag}}}{\mathrm{d}t} = \int \mathbf{E}_{\parallel} \mathrm{d}l. \tag{2.89}$$

In two-dimensional models the reconnection line is the extension of the hyperbolic null point along the invariant direction. Adding a constant component of $\mathbf{B}$ in the invariant direction turns the null line into a field line of maximal $\Delta\phi$ across D. For our example the rate of reconnected flux is given by $2\phi(0,0,-\infty)$.

The interpretation of a rate of reconnection of magnetic flux in this case, however, is different from what we are used to in two dimensions. In three dimensions no

unique line exists at which the flux is split and reconnected: instead, we have a whole flux tube (the hyperbolic flux tube enclosing D), within which every field line constantly changes its connection. To envisage the rate of reconnection in this case we use the method of constructing $\mathbf{w}^{\rm in}$ and $\mathbf{w}^{\rm out}$ as described in the introduction. These are the velocities of the field lines in D anchored in the ideal region either above (outflow region) or below (inflow region) D. To find these velocities we have to solve

$$-\nabla\phi^{\rm in/out} + \mathbf{w}^{\rm in/out} \times \mathbf{B} = 0 \tag{2.90}$$

$$\Rightarrow \quad \mathbf{w}_\perp^{\rm in/out} = (-\nabla\phi^{\rm in/out}) \times \mathbf{B}/B^2. \tag{2.91}$$

Since $\mathbf{w}^{\rm in}$ and $\mathbf{w}^{\rm out}$ coincide with $\mathbf{v}$ outside D we can use for the corresponding $\phi^{\rm in/out}$ just the asymptotic values of ϕ in Eq. (2.79) for large s, i.e., we replace the error function by its asymptotic values 1 and -1

$$\phi^{\rm in/out} = \pm \frac{\sqrt{\pi}\, B_0\ \eta_0\, l\, (k^2-1)}{2\, L\, \mu_0\, \exp\left[(x_0^2+y_0^2)/l^2\right]}. \tag{2.92}$$

Of course for an explicit calculation we have to replace x_0, y_0 with the help of Eqs. (2.70), (2.71), and (2.74) and insert the result in Eq. (2.91). If necessary we can also add a flow parallel to $\mathbf{B}$ to set the z component of $\mathbf{w}$ equal to zero, as we did for $\mathbf{v}$.

The rate of "mismatching" of flux is now given by the difference of $\mathbf{w}^{\rm in}$ and $\mathbf{w}^{\rm out}$ in D. For convenience we choose the plane $z = 0$, where the relative motion of the two flux tubes anchored in the outflow and inflow regions is given by

$$\begin{aligned} \Delta\mathbf{w}_\perp &= -\nabla(\phi^{\rm out} - \phi^{\rm in}) \times \mathbf{B}/B^2 \\ &= -2\,\nabla\phi^{\rm out} \times \mathbf{B}/B^2. \end{aligned} \tag{2.93}$$

Figure 2.27 shows the contours of $\phi^{\rm out} - \phi^{\rm in}$ and the corresponding velocity vector field. The rate at which flux crosses any radial line between the origin and the boundary of D is given by the potential difference along this line, i.e.,

$$\Delta\phi_{\Delta w} = 2\,\phi^{\rm out} = \Delta_{L_0}\phi = 2\,\phi(0,0,-\infty). \tag{2.94}$$

Note that we now have the same potential difference along a radial line as along the z axis (L_0), while for the previous integrals along R_1 and R_2 we had only half of this value.

Another important property is the fact that, as in the two-dimensional case, the diameter of the nonideal region, i.e., its extent in the x, y plane, does not affect the reconnection rate. To prove this we can use different scales, say l_{xy} and l, with respect to the (x_0, y_0)- and s-dependence in the expression (2.78) for the resistivity. It then turns out that in $\phi(0,0,\pm\infty)$ and hence in the reconnection rate l_{xy} does not appear. This property is essential for the onset of reconnection under realistic conditions, when the collapse of a current sheet may lead to small scales in the plane perpendicular to the current.

A simple pedagogical example gives further insight into the relation between this potential difference and a reconnection rate. Consider for simplicity a homogeneous

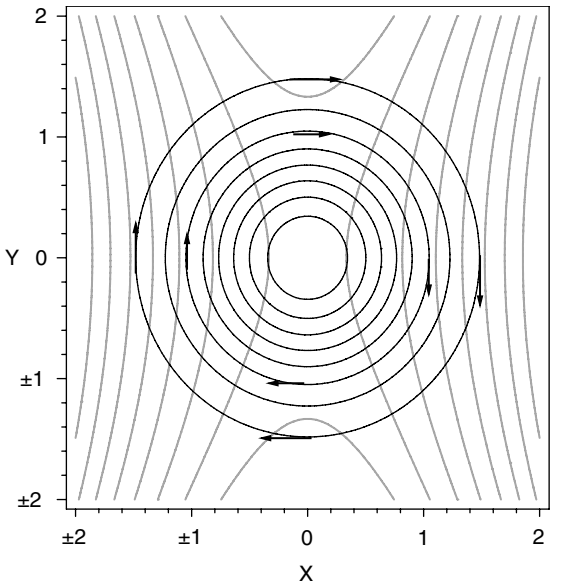

Fig. 2.27. Contours of $\phi^{\text{out}} - \phi^{\text{in}}$ (black) and difference velocity vectors (arrows) between flux anchored in the region above and below D and the projection of magnetic field lines (gray) in the plane $z = 0$ (parameters: $L = 10,\ l = 1,\ k = 2$).

magnetic field $\mathbf{B} = B_0 \mathbf{e}_z$ and assume that the difference velocity is a rigid rotation, with a constant angular velocity $\omega = 2\pi/T$. Integrating along a radial line the reconnection rate is then given by

$$\begin{aligned} \frac{\mathrm{d}\Phi_{\text{rec}}}{\mathrm{d}t} &= \int (\Delta\mathbf{w} \times \mathbf{B}) \cdot \mathrm{d}\mathbf{r} \\ &= 1/T \int 2\,\pi r B_0 \ \mathrm{d}r = \Phi_{\text{mag}}/T. \end{aligned} \tag{2.95}$$

Thus it takes a full turn for the reconnected flux to be equal to the total magnetic flux of the flux tube Φ_{mag}, although even after the first instant all field lines of the flux tube (with the exception of the central one) have changed their connections. Note that here the line crossed by $\Delta\mathbf{w}$ is a radius, while in the classical two-dimensional reconnection it is the X line.

Up to this point the hyperbolic structure of the magnetic field in the x, y plane was not relevant for the results, that is for an elliptic field in the x, y plane (O-point) the results would have been qualitatively the same. The reason is that the existence of counter-rotating flows is a topological property which can be proved without referring to any particular geometry of field lines and even for arbitrary time dependence. This has been done by Schindler (1995) building on the above mentioned Euler representation of the magnetic field (see also Schindler *et al.*, 1988; Hesse and Schindler, 1988). In particular, the plane for which $\mathbf{w}^{\text{in}}, \mathbf{w}^{\text{out}}$, and $\Delta\mathbf{w}$ is calculated is arbitrary as long as it is transversal to $\mathbf{B}$. The hyperbolic structure is, however, relevant for

the physical background of the reconnection process as discussed above and it will be found to be relevant in Section 2.3.4 when we consider more realistic reconnection solutions.

2.3.4 Composite solutions

The reconnection process in the foregoing example affects only the hyperbolic flux tube bounding the region D and even within this flux tube there is a certain order in which the field lines reconnect. To see this note that the level surfaces of ϕ^{in} are also level surfaces of ϕ^{out} (although for different values) and in addition they are flux surfaces for $\mathbf{B}$ and $\Delta\mathbf{w}$, since they satisfy the ideal equation Eq. (2.90). Thus, the reconnection changes the connection only within each level surface of $\phi^{\text{in/out}}$. There is no reconnection between field lines of different $\phi^{\text{in/out}}$ values. This can be changed by adding to the pure solution a solution of the ideal equation (2.83). Out of all possible ideal flows, however, those with a stagnation flow are of particular interest for two reasons.

Firstly, stagnation flows can create thin current sheets in a self-amplifying way, as shown in several 2.5-dimensional solutions (see Priest and Forbes, 2000, for references). In an astrophysical plasma we expect that the main reason for the localization of the nonideal term is the localization of the current, which then in turn might trigger a local anomalous resistivity due to turbulent effects on small scales. Thus stagnation flows are often an important prerequisite for having a localized nonideal term.

Secondly, the pure solution of the previous section affects only the hyperbolic flux tube enclosing D and hence is very restricted in its effect on the overall magnetic field. This can be changed if we have a flow which transports flux from the external region into the hyperbolic flux tube, lets it reconnect, and subsequently removes the reconnected flux from this region, thereby extending the effect of the nonideal region to a much larger domain. Such a process can be accomplished by a stagnation flow.

These are the motivations to use Eq. (2.84), which creates a stagnation-point flow in the plane $z = 0$, as a basic example for the effects of adding an ideal flow to the pure solution. To be more precise, the resulting flow is a stagnation flow outside the hyperbolic flux tube where the pure solution is negligible, but whether the pure solution dominates or not within the hyperbolic flux tube depends on the strength of the ideal flow compared to that of the pure reconnection solution. The parameter which determines the strength of the ideal flow is φ_0 in Eq. (2.84) and the critical value φ_{crit} is the value of φ_0 where the flow in D turns from O-point to X-point.

The critical φ_0 at which the nature of the flow changes can be determined analytically for our example (see Hornig and Priest, 2003):

$$\varphi_{\text{crit}} = \sqrt{\pi} B_0 \eta_0 l |k^2 - 1| / (L \mu_0). \tag{2.96}$$

The same critical value holds for $\mathbf{w}^{\text{in}}$ and $\mathbf{w}^{\text{out}}$. For $\varphi_0 > \varphi_{\text{crit}}$, $\mathbf{w}^{\text{in}}$, $\mathbf{w}^{\text{out}}$, and $\mathbf{v}$ have a stagnation point at $x = y = 0$ for every z. For $\varphi_0 < \varphi_{\text{crit}}$, $\mathbf{w}^{\text{in}}$ and $\mathbf{w}^{\text{out}}$ show an elliptic flow at $x = y = 0$ for every z. The same is true for $\mathbf{v}$ outside D. Inside D there is a critical distance from $z = 0$ at which $\mathbf{v}$ shows a transition from a hyperbolic to an elliptic point in $\mathbf{v}$.

Evolution of the magnetic flux

The effect of the additional flow on the reconnection process can be visualized best by the flows $\mathbf{w}^{\rm in}$ and $\mathbf{w}^{\rm out}$ in the $z = 0$ plane, or even more simply by plotting contour levels of $\phi^{\rm in}$ and $\phi^{\rm out}$ at $z = 0$, which coincide with flow lines $\mathbf{w}^{\rm in}$ and $\mathbf{w}^{\rm out}$, respectively. In Fig. 2.28 we show these lines for a case where $\varphi_0 > \varphi_{\rm crit}$, that is, we have stagnation flows in both $\mathbf{w}^{\rm in}$ and $\mathbf{w}^{\rm out}$.

The effect of reconnection on the magnetic flux can now be demonstrated by superimposing the two flow-line images so that the deviations from ideal flow become

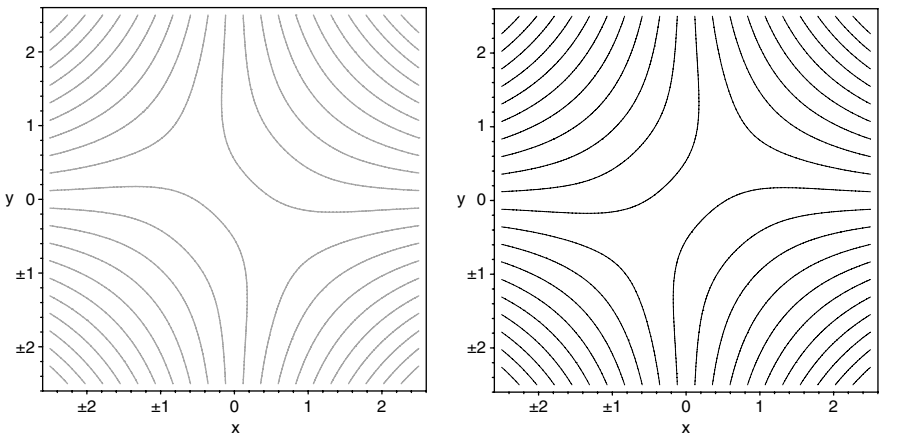

Fig. 2.28. The flow lines of $\mathbf{w}^{\rm in}$ (left) and $\mathbf{w}^{\rm out}$ (right) in the $z = 0$ plane for parameters $k = 2,\ \eta_0 = 0.001,\ L = 2,\ l = 1,\ B_0 = 3,\ \varphi_0 = 0.01 > \varphi_{\rm crit}$.

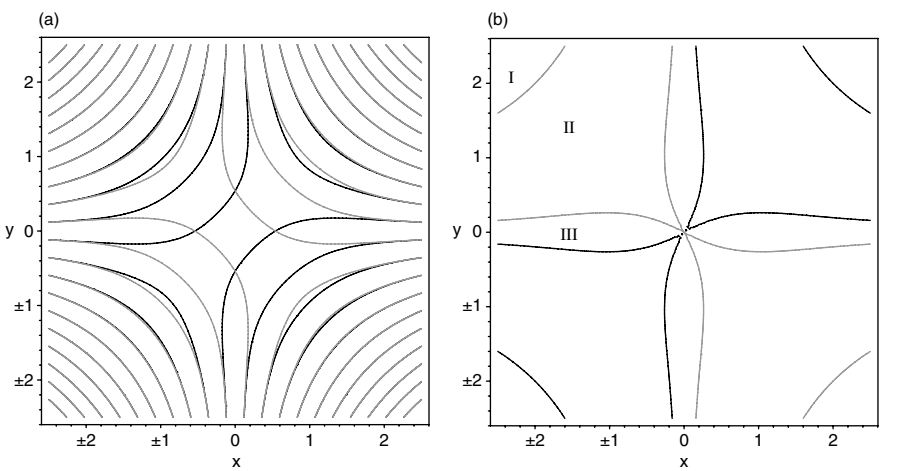

Fig. 2.29. (a) The superposition of the two flows in Fig. 2.28 shows regions of different reconnective behavior, depending on whether the flow lines of $\mathbf{w}^{\rm in}$ and $\mathbf{w}^{\rm out}$ coincide or separate. (b) The separatrices of $\mathbf{w}^{\rm in}$ and $\mathbf{w}^{\rm out}$ distinguish the regions which show almost classical reconnection (III), from the ideal region (I) together with the transition region (II).

apparent. This is shown in Fig. 2.29a, which may be read in the following way. Any point in the diagram represents a given field line. Starting with a given point (field line) there are always two flow lines of $\mathbf{w}^{\rm in}$ and $\mathbf{w}^{\rm out}$ intersecting at this point. They trace the path of the initial point (field line) frozen to $\mathbf{w}^{\rm in}$ (left) and $\mathbf{w}^{\rm out}$ (right), respectively. Whenever the flow lines cross at a given point a field line starting in this field will split into two if we follow both motions.

There are three types of matching or mismatching of magnetic field lines related to three types of regions in this diagram, as shown in Fig. 2.29b.

Firstly, for all flow lines which remain outside D (which is limited by $r \sim 2$ and indicated as type I in Fig. 2.29b) the two flow lines coincide perfectly. Moreover, the values of $\mathbf{w}^{\rm in}$ (left) and $\mathbf{w}^{\rm out}$ coincide, so that any field line of $\mathbf{B}$ threading the $z = 0$ plane at such flow lines is frozen-in ($\mathbf{w}^{\rm in} = \mathbf{w}^{\rm out} = \mathbf{v}$).

Secondly, there are cases where the flow lines of $\mathbf{w}^{\rm in}$ and $\mathbf{w}^{\rm out}$ separate only for a small part inside D and join again as they leave D (region of type II in Fig. 2.29b). A magnetic field line transported by this flow towards D will show a splitting into two of a field line entering D, and this splitting can remain even after both field lines have left D, since it might take both field lines different times to leave D. However, since the flow lines join again, the separation in time of the split field lines remains constant once they have left D.

Thirdly, there are cases where the flow lines separate within D and join with flow lines of opposite regions leaving D (regions of type III). A magnetic field line transported by this flow towards D will show a splitting in D, and will merge with field lines of a different region on leaving D. In particular, the distance in space or time of its initial partner grows even after both have left D. This distinguishes them from the previous case. The region of initial points which show this behavior is bounded by the separatrices of the two flows shown in Fig. 2.29b. This case is very similar to the "classical" two-dimensional reconnection in that field lines of very distant regions become newly connected.

However, there is in general no unique counterpart to a given field line. This is demonstrated in Fig. 2.30 for a single set of flow lines from region III. Starting with a fluid element (a) at an initial time we can find a counterpart (b) such that they coincide once they have left D in the negative y direction ($\mathrm{a}' = \mathrm{b}'$) but they will in general not match at the opposite side, i.e. $\mathrm{a}'' \neq \mathrm{b}''$. (For symmetry reasons the x axis in our example is exceptional in that here we can find perfect counterparts.) A field line, let us call it (a'''), which joins with (b'') lies on the same flow line as (a) but is shifted by a certain interval in time. If we iterate the process of finding the reconnecting counterparts, i.e., using (a''') as a new (a) and so on, we always obtain points which lie on the four trajectories shown in Fig. 2.30. So the counterparts of this reconnection process are not two field lines but the two flux surfaces given by the field lines crossing the inflow trajectories.

This implies that in general any flux tube will not have a counterpart with which it can reconnect perfectly in this stationary example. Note that by this process we always remain on the same level of $\phi^{\rm in}$ or $\phi^{\rm out}$ since we switch between $\phi^{\rm in}$ and $\phi^{\rm out}$ only outside D where they coincide. The regions of type III for which the field lines show genuine reconnection grow with η_0 until φ_0 reaches the critical value.

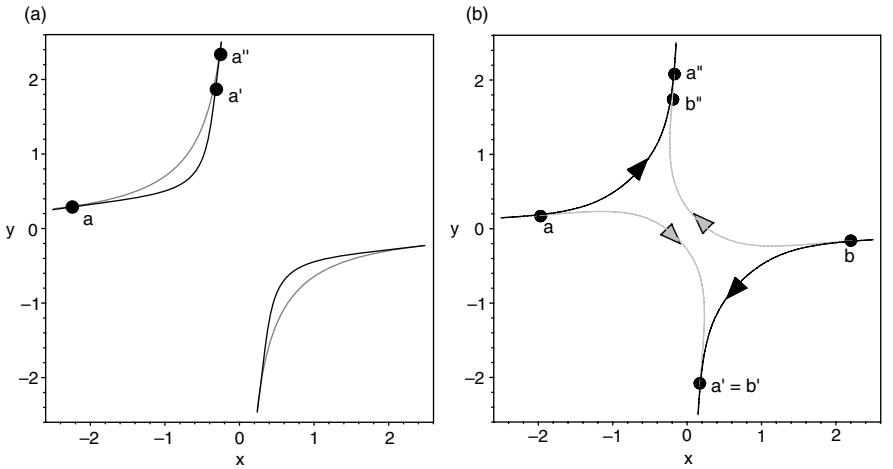

Fig. 2.30. The transport of fluid elements in the reconnecting flows of regions II (a) and III (b). For region II, plasma on a field line initially at point a is found after a transition through the nonideal region on field lines a′ and a″. For region III, two field lines at starting points a and b were chosen such that they join at $\mathrm{a}' = \mathrm{b}'$ but they will in general not match on the other side.

The example shown in Fig. 2.29 was based on the choice $\phi_0 \sim x_0 y_0$ (Eq. (2.84)) for the ideal flow. This choice generates a symmetric flow with respect to inflow and outflow. Since most reconnection simulations show an acceleration of plasma along the outflow direction we can account for this by choosing a potential which is nonsymmetric with respect to x_0 and y_0, for instance $\phi_0 \sim \tanh(x_0/l_x)\tanh(y_0/l_y)$. This potential yields a stagnation flow the characteristic width of which is limited in the inflow and outflow region to l_x and l_y, respectively. Choosing $l_x \neq l_y$ there is a net acceleration of plasma, i.e., the plasma in the outflow region at large distances from the reconnection site has a different kinetic energy than the plasma in the inflow region. Figure 2.31 shows the corresponding streamlines and separatrices in the $z = 0$ plane. Note that all the plasma in the inflow channels between the two separatrices eventually has to leave along the two outflow channels bounded by the same separatrices. Since in our example the flow is divergence-free and has no z component, the continuity equation requires a simple scaling of the size of inflow and outflow speed $v_{\mathrm{in}} l_x = v_{\mathrm{out}} l_y$.

Increasing η_0 in the example of Fig. 2.29 changes the flow pattern drastically. This is shown in Fig. 2.32 for the two flows separately and in Fig. 2.33a for the superposition. Figure 2.33b shows the different types of regions. Apart from regions I–III which are known from the previous example, there are now two new regions IV and V which result from the existence of the elliptic null in the center. Note that both regions are strictly within the hyperbolic flux tube and have no effect on the reconnective behavior of the hyperbolic flux tube with its environment. Only the sizes of regions I–III are important for the interaction with the environment. Region V in particular shows dynamics similar to the pure reconnection solution. An initial field line splits under the influence of counter-rotating flows, but

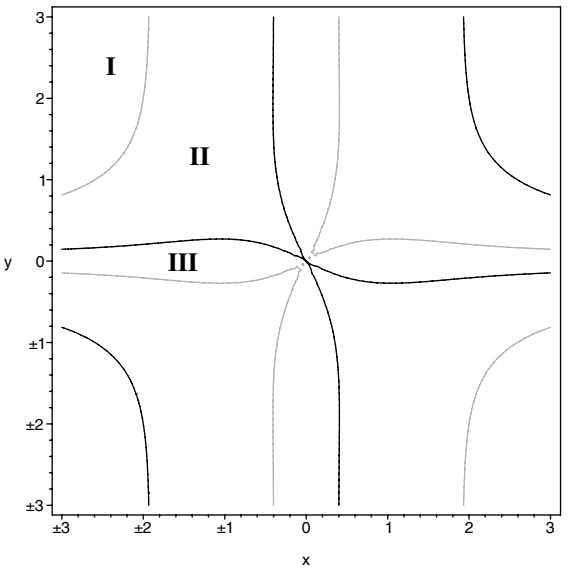

Fig. 2.31. An example of reconnecting flows which show an acceleration of plasma. The example uses $\phi_0 \sim \tanh(x_0/l_x)\tanh(y_0/l_y)$ with $l_x = 4,\ l_y = 1$. Note that the width of the outflow channel is significantly smaller than the width of the inflow channel, which implies an acceleration of plasma.

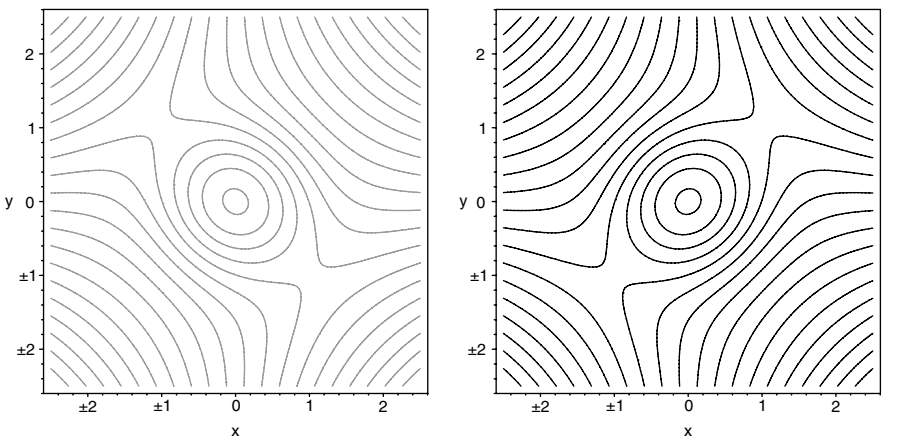

Fig. 2.32. The flow lines of $\mathbf{w}^{\text{in}}$ (left) and $\mathbf{w}^{\text{out}}$ (right) in the $z = 0$ plane for parameters $k = 2,\ \eta_0 = 0.01,\ L = 2,\ l = 1,\ B_0 = 3$ and $\varphi_0 = 0.01 < \varphi_{\text{crit}}$.

both parts rejoin after some time. Here the counter-rotating flows are dominant. Region IV is a kind of transition region between III and V. Here an initial field line splits, one part remains within the hyperbolic flux tube while the other leaves this domain.

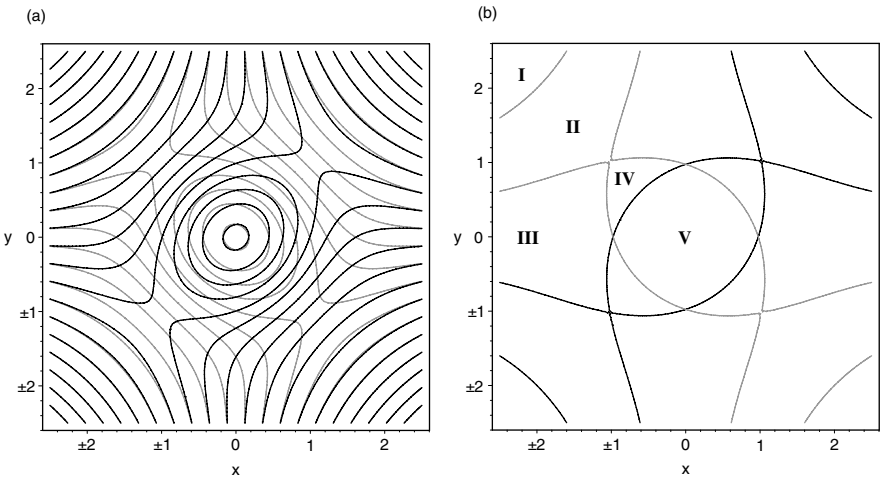

Fig. 2.33. (a) The superposition of the two flows for $\varphi_0 < \varphi_{\rm crit}$ (from Fig. 2.32) shows regions of different reconnective behavior. (b) The corresponding separatrix structure. Regions of type I–III are the same as in the previous example. Regions of type IV and V result from the existence of an elliptic null point in the flows for $\varphi < \varphi_{\rm crit}$.

Reconnection rate

The consideration concerning the reconnected flux in Section 2.3.3 still holds for the composite solution. In particular we can construct the flows $\mathbf{w}^{\rm in}$ and $\mathbf{w}^{\rm out}$ and their difference $\Delta\mathbf{w}$. Note that while $\mathbf{w}^{\rm in}$ and $\mathbf{w}^{\rm out}$ depend on the ideal flow induced by $\phi_0, \Delta\mathbf{w}$ does not and hence it is just the same as for the pure solution and so is the interpretation of $\Delta\mathbf{w}$ as the reconnecting engine. However, for the composite solutions the reconnection rate summarizes the effect of two ($\varphi_0 > \varphi_{\rm crit}$) or four ($\varphi_0 < \varphi_{\rm crit}$) quite different kinds of reconnective behavior: the almost classical type of reconnection of region III, the more slippage-like behavior of region II, and additionally the rotational reconnection of region V together with the transitional form of region IV for $\varphi_0 < \varphi_{\rm crit}$.

Note that the superposition of the ideal stagnation flow, although nonreconnective in itself, plays an important role in the process. It transports flux to D, where the reconnection occurs, and subsequently removes the reconnected flux. It is only due to the stagnation flow that a separation of the reconnected flux over larger distances occurs, as has been mentioned already by Schindler *et al.* (1988).

The reconnected flux is transported towards and away from the reconnection region via the channels bounded by the separatrices (region III in Figs. 2.29 and 2.33). The separatrices are streamlines of the ideal flow above and below the nonideal region and therefore the electric potential along these lines is constant. In the example of Fig. 2.29 they pass the point $x = y = 0$ at z values above and below the nonideal region. Therefore the difference of their electric potentials corresponds to the integrated parallel electric field along the field line $x = y = 0$ across the nonideal region, i.e., to the rate of reconnected flux. Outside the nonideal region the potential of the separatrices above and below the nonideal region is mapped along the field lines, so

that the separatrices of the $\mathbf{w}^{\text{in/out}}$ in the $z = 0$ plane, shown in Fig. 2.29, also have the potential difference of the reconnection rate. Thus the rate of magnetic flux transported into the reconnection region via the inflow channel, and the corresponding flux removed from the region through the outflow channel coincide and equal the total rate of reconnected flux. This property relies on the fact that the separatrices pass through $x = y = 0$, which is always the case if $\varphi_0 > \varphi_{\text{crit}}$. For $\varphi_0 < \varphi_{\text{crit}}$, as shown in Fig. 2.33, this is not true. The separatrices do not pass through $x = y = 0$ and hence their potentials differ by less than the reconnection rate. In particular in the example of Fig. 2.33 the potentials differ only by about 38 percent of the total reconnection rate. This suggests we define an *external reconnection rate*, which measures the flux transported towards and away from the reconnection region via the inflow and outflow channels. An *internal reconnection rate*, which describes the rate at which flux in regions V and IV, i.e., within the hyperbolic flux tube bounding the nonideal region, changes its connectivity. The internal reconnection rate is the difference between the total reconnection rate and the external reconnection rate,

$$\frac{\mathrm{d}\Phi_{\text{rec}}}{\mathrm{d}t} = \frac{\mathrm{d}\Phi_{\text{rec}}^{\text{external}}}{\mathrm{d}t} + \frac{\mathrm{d}\Phi_{\text{rec}}^{\text{internal}}}{\mathrm{d}t}. \tag{2.97}$$

Both extreme cases are conceivable: vanishing external reconnection rate or vanishing internal reconnection rate. The external reconnection rate vanishes if the ideal stagnation flow vanishes. This is the case of the *pure* solution discussed in Section 2.3.2. The effect of reconnection is confined to the hyperbolic flux tube bounding the nonideal region. On the other hand, the internal reconnection rate vanishes for $\varphi_0 > \varphi_{\text{crit}}$, i.e., if region V vanishes, and the total reconnection rate equals the external reconnection rate.

2.3.5 The two-dimensional limit

Since the results for three-dimensional reconnection are in many respects quite different from what is known of the two-dimensional case, it is natural to ask what the limit of vanishing guide field, i.e., $B_z \to 0$, yields. In this limit we should recover the classical two-dimensional reconnection pattern. It turns out that this limit is difficult to approach, since the construction we have used for calculating the electric potential along the magnetic field lines fails in this limit. This in turn is due to the choice of the $z = 0$ plane as a plane for fixing the initial condition for the integration of the electric potential. This plane is transversal to all field lines as long as $\mathbf{B}_z \neq 0$. However, in the limit $\mathbf{B}_z = 0$ the corresponding transversal surfaces should be $x = 0$ and $y = 0$. Obviously there is no smooth transition between the two. Therefore, instead of going through all the technical difficulties needed to properly take this limit, we demonstrate here only qualitatively how this limit works. We first restrict ourselves to the pure solution of Section 2.3.2. This solution shows rotational flows above and below the reconnection region. For $B_z \to 0$ the shape of these stream lines becomes distorted towards highly squashed ellipses, the major axes of which are aligned with the separatrices of the magnetic field in the $z = 0$ plane (see Fig. 2.34a). Since for reconnection the component of the flow parallel to $\mathbf{B}$ is not relevant, we have plotted in Fig. 2.34b only the perpendicular component of the flow. This perpendicular component has the same signature with regard to the

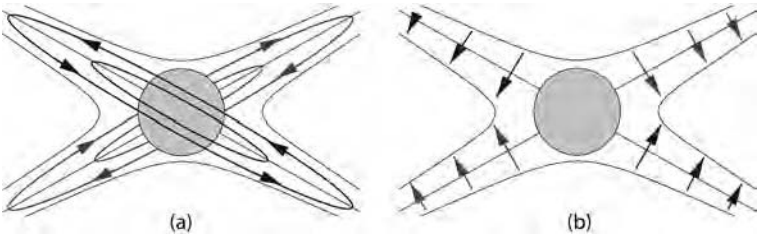

Fig. 2.34. (a) The rotational flow above and below the nonideal region takes on the shape of highly elongated ellipses as the guide field (B_z) tends to zero. (b) The component perpendicular to **B** of the counter-rotating flows transforms into an X-type flow in the 2D limit.

separatrices as the stagnation flow of the classical two-dimensional reconnection. In order to recover the proper two-dimensional stagnation flow in the whole domain, it has to be complemented by a corresponding ideal flow. Only carefully chosen combinations of *pure* and ideal flows have a proper smooth two-dimensional limit. Each component itself has singularities in the limit. This is not surprising since the *pure* solution does not exist in two dimensions and also there are no ideal stagnation flows crossing the separatrices of the magnetic field in this limit.

2.3.6 Conclusions

The process of three-dimensional magnetic reconnection at a localized nonideal region of a nonvanishing magnetic field shows features which are not present in two- (or 2.5-) dimensional models. The localization implies the existence of rotational flows above and below the nonideal region (with respect to the direction of the magnetic field). The process can be understood as a superposition of a nonideal process generating rotational flows within the flux tube enclosing the nonideal region together with an ideal flow transporting magnetic flux towards and away from the reconnection region. The total reconnection rate can also be split into a reconnection rate measuring only the reconnection with respect to the region outside the enclosing flux tube and a rate measuring the reconnection within the flux tube. Moreover, stationary reconnection is imperfect for most of the field lines in the sense that there is no cross-connection between pairs of field lines, i.e. the strict one-to-one correspondence of reconnecting field lines known from two-dimensional reconnection is broken in the three-dimensional case.

2.4 Three-dimensional reconnection at magnetic null points

D. I. Pontin

In many areas of plasma physics, magnetic reconnection can be associated with a restructuring of the magnetic field (**B**). Our ideas on how this restructuring occurs come mostly from the well-studied case of reconnection at two-dimensional hyperbolic null points (X-points, see Section 2.1). In three dimensions, reconnection can occur either at a null point or in the absence of a null point (Schindler *et al.*, 1988). The nature of reconnection at a three-dimensional null point is of particular interest since it is the three-dimensional generalization of a 2D X-point. Three-dimensional null points are also of crucial importance in the topology and interaction of complex

fields on the Sun. They are found in abundance in the corona (see e.g., Brown and Priest, 2001; Longcope *et al.*, 2003), where their associated separatrices and separators are thought to be likely candidates for sites of coronal heating (Longcope, 1996; Antiochos *et al.*, 2002; Priest *et al.*, 2002, and Section 5.1). There is also evidence that 3D null point reconnection may act as a trigger for at least some solar flares (Fletcher *et al.*, 2001).

Magnetic nulls are points in space at which the magnetic field strength falls to zero. The *skeleton* of the null point is made up of a pair of field lines which converge on (or diverge from) the null from opposite directions, which define the *spine* (Priest and Titov, 1996), and a family of field lines which radiate out of (or into) the null lying in a surface, known as the *fan* plane (Priest and Titov, 1996), see Fig. 2.35. The orientation of these structures is defined by the eigenvectors of the matrix $\nabla \mathbf{B}$ of partial derivatives, evaluated at the null (by considering a Taylor expansion of $\mathbf{B}$ about the null). When the magnetic field in the fan plane is directed into the null, then the null is termed *negative* (or A-type), while if it is directed out of the null, then the null is *positive* (or B-type).

The local structure of the magnetic field around a generic three-dimensional null point is shown in Fig. 2.35b (see also e.g., Greene, 1988; Lau and Finn, 1990). By *local* in this sense we mean that all of the magnetic components change linearly with position from the null, and that we are close enough to the null that these linear variations are much larger than quadratic variations that would appear in a Taylor expansion about the null. By *generic* we mean that the null is structurally or topologically stable in the sense that the structure of the null would be unchanged by a small perturbation in the magnetic field. Often for simplicity linear nulls are considered in which all of the fan field lines are straight (resulting from the fan eigenvalues being equal, see Fig. 2.35a), but this is a nongeneric situation, since in general when the fan eigenvalues are unequal, most of the field lines will touch one of the axes, as shown in Fig. 2.35b.

A general mathematical formalism for the structure of nulls is given by Parnell *et al.* (1996), who classify them depending, amongst other things, on the magnitude of the current density, $\mathbf{j}$, and the orientation of the current density vector with respect

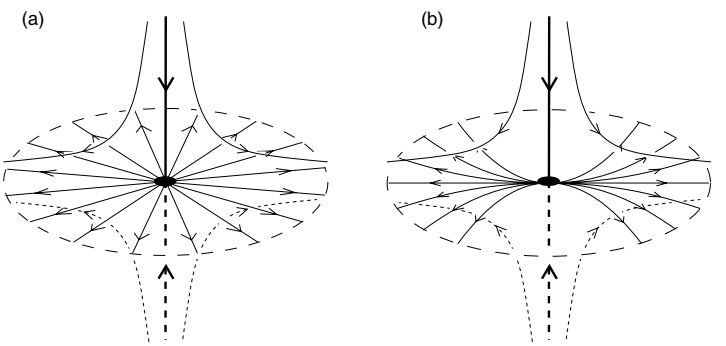

Fig. 2.35. The basic structure of a positive (or B-type) 3D null point when (a) the fan eigenvalues are equal and (b) they are unequal. The thick line is the spine field line, while the fan surface is marked out by the dashed circle.

to the spine and fan. If the current is zero then the null point is known as *potential*. In this case the null appears as in Fig. 2.35b; the spine and fan are perpendicular, and in general most of the field lines are tangent to one of the eigenvectors. However, when there is a current present directed parallel to the spine, the field lines in the fan form a spiral, while the fan and spine remain perpendicular. In contrast, if the current is parallel to the fan, then the spine and fan will no longer be orthogonal. In general, when the current has components in both directions, both of these effects will be present, as well as further characteristics, depending on the relative magnitudes of the spine-aligned and fan-aligned current components (see Parnell *et al.*, 1996, 1997, for a full description).

Priest *et al.* (2003a) have shown that three-dimensional reconnection is fundamentally different in a number of important ways from the familiar 2D case. These details have been illustrated by a kinematic solution for reconnection in the absence of a magnetic null point (Section 2.3; Hornig and Priest, 2003). Here we follow the same procedure for reconnection at 3D nulls. In Section 2.4.1 the differences between 2D and 3D reconnection are outlined. In Sections 2.4.2 and 2.4.3 the nature of reconnection is described at null points with spine- and fan-aligned currents. Finally, a summary is given in Section 2.4.4.

It should also be noted that a number of particular exact solutions to the steady-state incompressible MHD equations for so-called *reconnective annihilation* at 3D null points exist. These solutions describe current sheets of infinite extent, which are localized to either the fan (Craig *et al.*, 1995) or spine (Craig and Fabling, 1996) of the null. In each case, the current is aligned parallel to the fan, and field lines diffuse through the current sheet, and are reconnected with field lines advected across the other separatrix.

2.4.1 Properties of 3D reconnection

In order to investigate the evolution of magnetic flux in two dimensions, it is useful to define a flux-transporting velocity $\mathbf{w}$ (Hornig and Schindler, 1996; Hornig and Priest, 2003) which satisfies

$$\mathbf{E} + \mathbf{w} \times \mathbf{B} = \mathbf{0}, \tag{2.98}$$

which is possible in two dimensions since the electric field $\mathbf{E}$ is always perpendicular to the magnetic field $\mathbf{B}$. By comparison with an ideal Ohm's law, we can consider $\mathbf{w}$ to be a flow within which the magnetic flux is frozen. The component of $\mathbf{w}$ perpendicular to $\mathbf{B}$ can be found from

$$\mathbf{w}_\perp = \frac{\mathbf{E} \times \mathbf{B}}{B^2}. \tag{2.99}$$

However, in three dimensions this is not always possible. In general 3D reconnection $\mathbf{E} \cdot \mathbf{B}$ is nonzero within a finite diffusion region D (Schindler *et al.*, 1988; Hesse and Schindler, 1988), with the result that in general no unique flux-conserving velocity exists, or in other words there is no unique magnetic flux velocity $\mathbf{w}$ for flux which threads D (Section 2.2). We consider a finite region D as the generic situation for astrophysical plasmas, since in general the magnetic Reynolds number is extemely high, and dissipation is likely to be enhanced only in well-localized regions, for example when the presence of strong electric currents may drive microinstabilities.

Although no unique magnetic flux velocity exists, it is nonetheless possible to study the evolution of magnetic flux and field lines under certain circumstances. If no closed magnetic field lines exist within a localized nonideal region D then we can still follow the motion of individual field lines from certain chosen footpoints, since we know that in the ideal region on either side of D they must remain attached to the same plasma elements for all time. Suppose the surface of D is split into two parts, through one of which magnetic flux enters D, and through the other of which it leaves. Since each field line is anchored twice in the ideal environment, once on either side of the nonideal region, one can follow the motion of the field lines by tracing them through space from footpoints in either of these ideal regions. Consequently, it is possible to define a velocity with which the field lines passing *into* D move, say $\mathbf{w}_{\rm in}$, and another velocity $\mathbf{w}_{\rm out}$ at which the field lines passing *out of* D move. In the stationary case ($\partial/\partial t \equiv 0$), these two velocities can be calculated throughout space by mapping the electric potential (Φ, where $\mathbf{E} = -\nabla\Phi$) from each set of footpoints along the field lines. This leads us to the mathematical expressions

$$\mathbf{w}_{\rm in/out} = \frac{-\nabla\Phi_{\rm in/out} \times \mathbf{B}}{B^2}. \tag{2.100}$$

These two (pseudo-)magnetic flux velocities must each be identical to the plasma velocity $\mathbf{v}_\perp$ on the relevant section of the surface of D, but in contrast to the 2D case, they are not identical to each other inside D. This is a manifestation of the nonexistence of a unique magnetic flux velocity $\mathbf{w}$, as stated above. The result is that following any given field line from two footpoints moving on either side of the nonideal region D, that field line seems to split as soon as it is transported into D. Furthermore, the connectivity of field lines which thread D changes throughout the reconnection process.

The new properties of kinematic 3D reconnection described by Priest *et al.* (2003a) are, briefly,

- The mapping of field line footpoints is in general continuous during reconnection, the exception being at null point separatrices.
- A unique magnetic flux velocity does not in general exist, so that in order to describe the evolution of the magnetic flux during reconnection it is necessary to use *two* magnetic flux velocities (as described above).
- Hence, field lines change their connections *continually* and *continuously* throughout the nonideal region.
- Another way to look at this is to say that a field line traced through and beyond the nonideal region moves beyond the nonideal region in a virtual flow which is not the plasma velocity.
- There is no one-to-one reconnection of field lines; that is, for any given field line which is going to take part in the reconnection process, there is in general no *unique counterpart* field line on the opposite side of D with which its footpoints will become pairwise connected after the reconnection process.

2.4.2 Spine-aligned current

The model

It is instructive to seek insight into the structure of the highly complex process of 3D reconnection by considering solutions to a reduced set of the MHD

equations. We follow the method of Hornig and Priest (2003) and adopt the kinematic approximation (see Section 2.3), by solving the induction equation and Maxwell's equations, though not solving the equation of motion.

We seek a solution of the kinematic, steady, resistive MHD equations given by

$$\mathbf{E}+\mathbf{v}\times\mathbf{B}=\eta\mathbf{j}, \tag{2.101}$$

$$\nabla\times\mathbf{E}=\mathbf{0}, \tag{2.102}$$

$$\nabla\cdot\mathbf{B}=\mathbf{0}, \tag{2.103}$$

$$\nabla\times\mathbf{B}=\mu_0\mathbf{j}. \tag{2.104}$$

The nonideal term on the right-hand side of Eq. (2.101) is assumed to be localized. We consider here two separate, complementary cases. In this section we investigate reconnection at a null point with current parallel to the spine, while in the next section we consider the case where the current is parallel to the fan. In general the field in the vicinity of a spiral null point, the most simple null with spine-aligned current, can be written (Parnell *et al.*, 1996) in cylindrical polar coordinates as

$$\mathbf{B}=B_0\left(R, JR/2, -2z\right), \tag{2.105}$$

where B_0 and J are constants such that $\mathbf{j}=(B_0J/\mu_0)\hat{\mathbf{z}}$ is oriented in the z direction, parallel with the spine. Since the current is constant, it is necessary in this model to localize the resistivity in order to obtain a localized nonideal region. We take

$$\eta=\eta_0\begin{cases}\left((R/a)^6-1\right)^2\left((z/b)^6-1\right)^2 & R<a,\ z^2<b^2\\ 0 & \text{otherwise,}\end{cases} \tag{2.106}$$

where η_0, a, and b are constant and η_0 is the value of the resistivity (η) at the null point. The null point and diffusion region are shown in Fig. 2.36a.

From Eq. (2.102), $\mathbf{E}$ can be written as the gradient of some scalar, Φ say, so that Eq. (2.101) becomes

$$-\nabla\Phi+\mathbf{v}\times\mathbf{B}=\eta\mathbf{j}. \tag{2.107}$$

The component of this equation parallel to $\mathbf{B}$ may be integrated along field lines to give

$$\begin{aligned}\Phi&=-\int\eta\mathbf{j}_\parallel\,\mathrm{d}l+\Phi_0\\ &=-\int\eta\mathbf{j}\cdot\mathbf{B}\,\mathrm{d}s+\Phi_0(\mathbf{X_0}),\end{aligned} \tag{2.108}$$

where s is a parameter along the field lines, and $\mathbf{X_0}$ are the field line footpoint positions from which the integration is begun. We choose to integrate Φ by setting $s=0$ on surfaces $z=\pm z_0$, above and below D, and integrating in towards the $z=0$ plane. Note that solutions found by setting $s=0$ on other suitable surfaces (those which cut every field line once and only once) are equivalent when considered with respect to some given boundary conditions. The electric field $\mathbf{E}$ and the component of the plasma velocity $\mathbf{v}_\perp$ perpendicular to $\mathbf{B}$ can be found from

$$\mathbf{E}=-\nabla\Phi \tag{2.109}$$

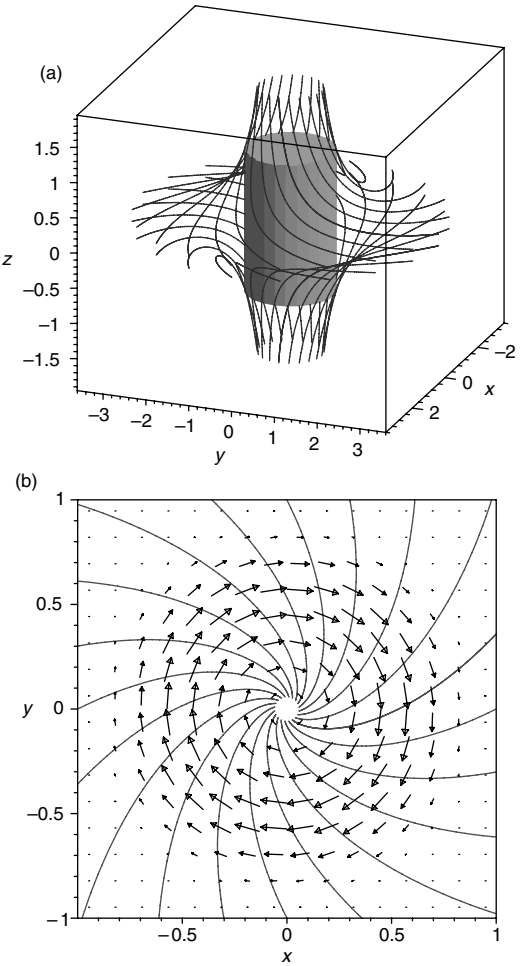

Fig. 2.36. (a) Field lines on the boundary of the envelope enclosing the diffusion region (cylinder), showing the region of influence of the local solution (for $a = b = J = 1$). (b) Vectors of the plasma flow $\mathbf{v}$, along with a projection of the magnetic field lines, in the plane $z = 0.4$, for the parameters $B_0 = a = b = \eta_0 = 1,\ J = 2$.

and

$$\mathbf{v}_\perp = (\mathbf{E} - \eta\mathbf{j}) \times \mathbf{B}/B^2. \tag{2.110}$$

When Φ_0 is zero, an "elementary" or "internal" solution is found, upon which an ideal flow may be superimposed by choosing Φ_0 nonzero. This is possible since, for a given magnetic field, Ohm's law (2.107) may be decomposed into a nonideal component (2.111) and an ideal component (2.112) as follows

$$-\nabla\Phi_{\text{nonid}} + \mathbf{v}_{\text{nonid}} \times \mathbf{B} = \eta\mathbf{j}, \tag{2.111}$$

$$-\nabla\Phi_{\text{id}} + \mathbf{v}_{\text{id}} \times \mathbf{B} = \mathbf{0}. \tag{2.112}$$

We have the freedom to add an ideal flow to the nonideal solution since we do not solve the momentum balance equation here, which would otherwise determine the ideal part of the flow.

The mathematical expressions for Φ, $\mathbf{E}$ and $\mathbf{v}_\perp$ are too lengthy to show here, but can be calculated in a straightforward way using a symbolic computation package. The full method of solution, as well as an in-depth analysis of the results, is described in Pontin *et al.* (2004).

The solution

We examine first the nature of the solution with $\Phi_{\rm id} = \Phi_0 = 0$, i.e., just the local behavior of the flux envelope enclosing the nonideal region D with no extra ideal flow. Choosing to integrate Eq. (2.108) from $z = z_0$ we automatically start with Φ constant for $z > b$. Hence the electric field and plasma velocity are zero for $z > b$. The velocity for $z < b$ is a rotation within the flux envelope.

For the purposes of illustration of the results, it is convenient to add a component of $\mathbf{v}$ parallel to $\mathbf{B}$ such that $v_z = 0$. This is achieved by defining

$$\mathbf{v} = \mathbf{v}_\perp - \frac{v_{\perp z}}{B_z}\mathbf{B}. \tag{2.113}$$

Our freedom to do this comes from the fact that Eq. (2.110) determines only the component $\mathbf{v}_\perp$ of $\mathbf{v}$ perpendicular $\mathbf{B}$. It is this perpendicular component which affects the transport of the magnetic flux, so for our purposes the parallel component is arbitrary. The plasma flow which we obtain is shown in a typical plane of constant z in Fig. 2.36b. The radial component (as well as the z component, due to (2.113)) of $\mathbf{v}$ is zero, so we have purely rotational flow.

We can show that these rotational flows are a general property for such a null point. They are not a result only of our particular choice of setup, for example the choice of η profile, but are in fact a consequence simply of the structure of $\mathbf{B}$ (and hence $\mathbf{j}$), and the presence of a localized nonideal region. Consider the potential drop along sections of the closed loop illustrated in Fig. 2.37a. The loop is made up of four sections; L1 and L3 are radial lines in planes $z \geq b$ and $z < b$, respectively, while L2 is a field line on the boundary of the envelope of flux threading D, and L4 lies along the spine of the null. The potential drop around any closed loop must be zero. The potential drop along lines L1 and L2 must be zero as they lie wholly outside D; L1 lies at $z \geq b$ and L2 lies on the boundary of the envelope, and so $\Phi = \Phi_0$ along their entire lengths. Thus

$$\Delta\Phi_{\rm L3} = \Delta\Phi_{\rm L4} = 0,$$

or

$$\Delta\Phi_{\rm L3} = -(\Phi_{34} - \Phi_0) \neq 0, \tag{2.114}$$

where Φ_{34} is the value of Φ at the vertex of L3 and L4, which must be different from Φ_0 since $\mathbf{E}$ is nonzero along the spine ($\mathbf{E}\cdot\mathbf{B} = \eta\mathbf{j}\cdot\mathbf{B} \neq 0$ on spine). Since there is a potential drop along L3 there must also be a nonzero electric field along it. This electric field, along with the nonzero B_z component, induces a plasma flow perpendicular to such a radial line, and since the choice of L3 is arbitrary, this gives a rotational flow. It is found that this rotation has the same sense for $z > 0$ and

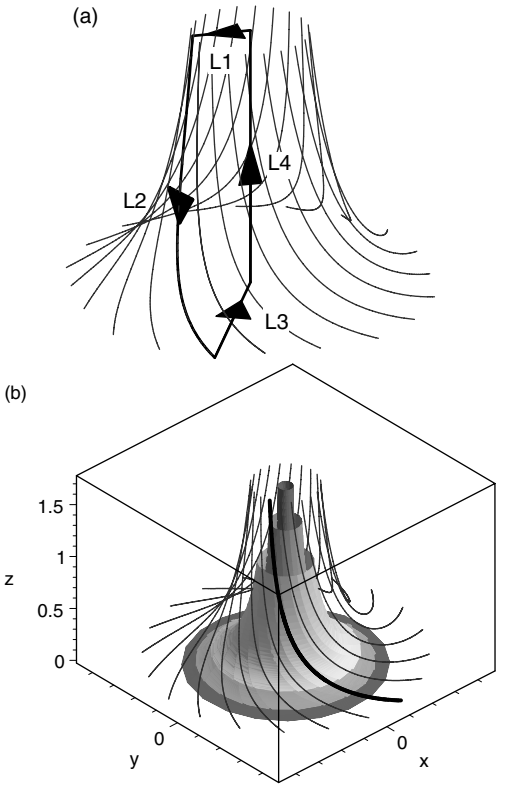

Fig. 2.37. (a) Closed loop made up of line sections. (b) Flux surfaces within which field lines periodically reconnect exactly with themselves.

$z < 0$, and has maximum magnitude in the $z = 0$ plane. Note that this argument is completely independent of the particular profile of η.

Since the plasma velocity is rotational, the motion of field lines during the reconnection process is rotational as well. Field lines are continually reconnected in "shells" within the flux envelope enclosing D (see Fig. 2.37b). This means that within any arbitrary period of time, every field line within the flux envelope changes its connectivity (except the spine, due to symmetry). An initial field line which splits into two will be periodically exactly reconnected with itself, every time the footpoint embedded in the flow at $R = a$ performs a full rotation of 2π radians. Note, however, that this rotation period is different for each shell, since it is not a rigid rotation. For this reason, if we consider a flux tube within the envelope with a finite radial extent, there will be no periodic return to the initial state.

As discussed in the previous section, we may superimpose any ideal flow upon the "elementary" or "internal" solution described above. We would like to choose an ideal flow which shows the global effect of the local rotational slippage behavior by transporting magnetic flux into and out of the local flux envelope. For this reason we choose to impose a stagnation-type ideal flow. Stagnation flows are also physically relevant flows to choose as they may perform the localization of the physical quantities, and

are common in reconnection solutions (Priest and Forbes, 2000; Hornig and Priest, 2003). On $z = \pm z_0$ we choose to set

$$\Phi_{\rm id}\,(x_0, y_0) = \varphi_0\, x_0\, y_0, \tag{2.115}$$

where φ_0 is a constant. The ideal plasma flow ($\mathbf{v}_{\rm id}$) takes the form of a stagnation point, which is distorted due to the spiralling of the field lines.

The full plasma flow in this "composite solution" is a competition between the rotational and stagnation flows. A number of different regions of flow exist, in each of which the rotational reconnection flow splits the field lines which are transported through the diffusion region. Two main types of behavior are seen. In the first, flux tubes traced from either end seem to "slip" apart relative to each other, but are carried away from the nonideal region in the same direction. In another region of space however, a more classical type of reconnective behavior is present, and initially joined flux tubes are split by the reconnection and are carried away in opposite directions, with the crucial characteristic being that the separation of the two initial sets of footpoints continues to increase in time (see Fig. 2.38). For a more detailed description of the process, see Pontin *et al.* (2004).

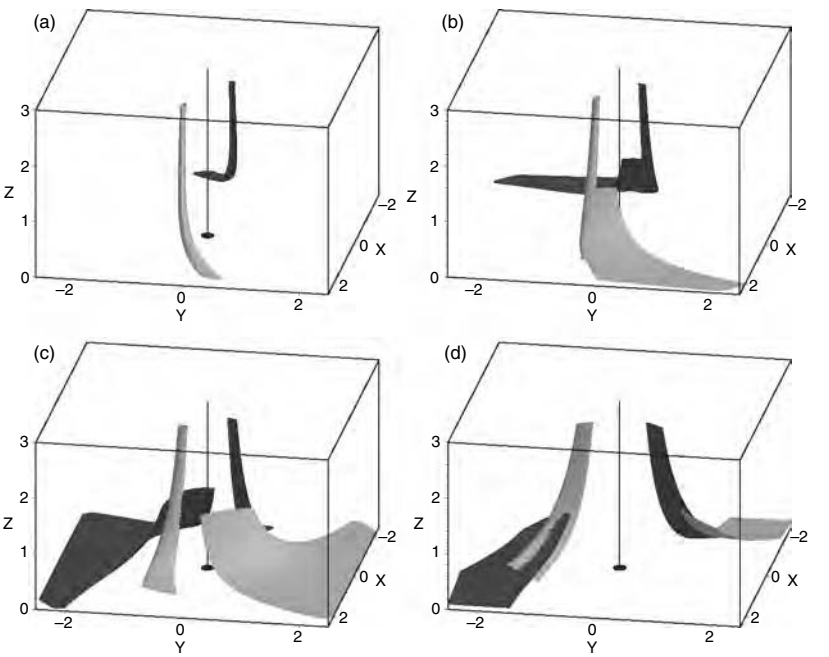

Fig. 2.38. Evolution of a pair of flux tubes, each traced from cross-sections at either end which move in the ideal flow. As the tubes enter the diffusion region they split, with the two parts of each of the initial two tubes flipping around the spine in opposite directions. Notice in (d) that after leaving D the four new tubes do not rejoin to form two unique flux tubes.

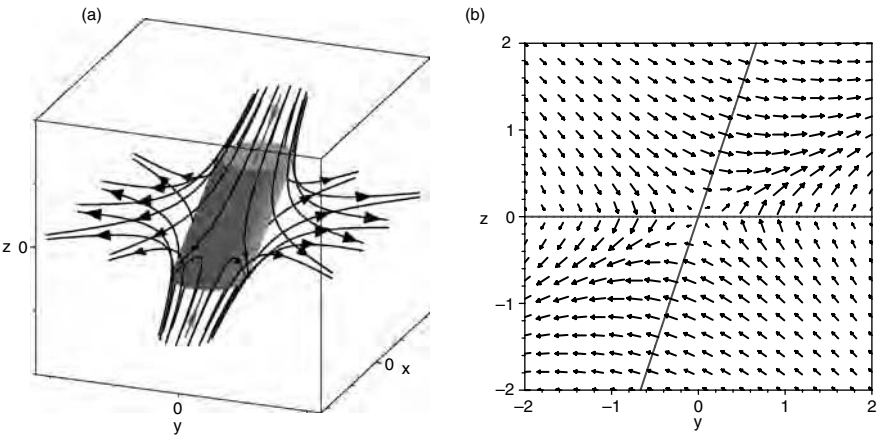

Fig. 2.39. (a) 3D null point with fan-aligned current. The shaded cylinder shows the diffusion region. (b) The structure of the plasma flow, along with the fan and spine (black lines) in a typical plane of constant x, for parameters $\eta_0 = B_0 = J = a = b = 1$.

2.4.3 Fan-aligned current

In this section we model reconnection at a null point with fan-aligned current, in exactly the same way as described above. This time we choose

$$\mathbf{B} = B_0\,(x,\, y - Jz,\, -2z)\,, \tag{2.116}$$

such that, without loss of generality, the current lies in the x direction parallel to the fan plane, and is given by $\mathbf{j} = (B_0 J/\mu_0)\hat{\mathbf{x}}$. The fan of this null point is coincident with the plane $z = 0$, while the spine is not perpendicular to this, but rather lies along $x = 0,\ y = Jz/3$ (see Fig. 2.39a). We now prescribe a resistivity of the form

$$\eta = \eta_0 \begin{cases} \left((R_1/a)^2 - 1\right)^2 \left((z/b)^2 - 1\right)^2 & R_1 < a, z^2 < b^2 \\ 0 & \text{otherwise,} \end{cases} \tag{2.117}$$

where $R_1^2 = x^2 + (y - Jz/3)^2$ and $\eta_0,\ a$, and b are constants. η_0 is the value of η at the null point, and the diffusion region is a tilted cylinder of radius a centered on the spine, extending to $z = \pm b$.

We now proceed as before, again setting $s = 0$ on $z = \pm z_0$ in order to perform the integration of Eq. (2.108). Setting $s = 0$ on $z = +z_0$, (2.108) gives an expression for $\Phi(\mathbf{X}_0, s)$ for $z > 0$, and setting $s = 0$ on $z = -z_0$ we obtain $\Phi(\mathbf{X}_0, s)$ for $z < 0$. In order for Φ to be physically acceptable, i.e., smooth and continuous at the fan plane such that $\mathbf{E}$ and $\mathbf{v}$ are finite there, we must set Φ at $z = \pm z_0$ (namely, Φ_0) to

$$\Phi_0 = \frac{32}{21}\,\eta_0 B_0\, J\, x_0. \tag{2.118}$$

$\Phi(\mathbf{X})$, $\mathbf{E}$ and $\mathbf{v}_\perp$ can now be obtained as before. The nature of the rearrangement of magnetic flux in the reconnection process can once again be studied by considering the motion of the plasma perpendicular to $\mathbf{B}$. The nature of the plasma flow in

a typical plane of constant x is shown in Fig. 2.39b. Note that the flow in the x direction vanishes at the spine, and is negligible for the reconnection process.

The plasma flow is nonzero across both the spine and the fan, and has a stagnation point structure in the y, z plane, centered on the null point. The result of the plasma flows across the spine and fan is that the nature of the field line behavior under the reconnection is qualitatively the same as described by Priest and Titov (1996) in the ideal analysis. Consider tracing field lines from footpoints in the ideal region situated in the spine-crossing flow. As these footpoints are advected across the top/bottom of the nonideal region (D), the field lines flip around the spine in the fan plane as they pass through D. The behavior is analogous to the *fan reconnection* of Priest and Titov (1996) (see Fig. 2.40). By contrast, considering footpoints anchored in the fan-crossing flow, the field lines are advected towards the fan until they lie in the fan plane, at which point they flip down the spine, and then move away from the null on the opposite side of the fan (as in *spine reconnection*).

Although a continuous stream of field lines is reconnected through the spine, no finite amount of flux is reconnected at it, since it is a single line. A finite amount of flux *is*, however, transported across the fan plane in an arbitrary time. This can be very important, since if we consider our null point to be surrounded by a global magnetic field, then the fan plane is a separatrix surface of this field, separating distinct regions of magnetic topology, and so the topology of this field changes when flux is transported across it. As described previously, in the solar atmosphere separatrices are thought to be very important locations for coronal heating (see Section 5.1).

The nature of the plasma flow across the fan plane is a major difference between this solution and the one described in the previous section. It can be shown once again that the fundamental nature of the reconnection is simply a consequence of the structure of $\mathbf{B}$ and the presence of a localized nonideal region, as follows. Consider the structure of $\mathbf{B}$ and $\mathbf{j}$ in the fan plane. $\mathbf{j}\cdot\mathbf{B}$ has opposite sign for $x > 0$ and $x < 0$, since $\mathbf{B}$ is radial and $\mathbf{j}$ is unidirectional. Hence, $\Phi = -\int \eta \mathbf{j}\cdot\mathbf{B}\, \mathrm{d}s$ has opposite sign for $x > 0$ and $x < 0$. As a result, in the fan plane close to the null, $\mathbf{E} \approx E_x$ is unidirectional across the spine, as shown in Fig. 2.41. Since $\mathbf{E}\times\mathbf{B}$ is nonzero in the fan plane, we obtain a plasma flow across the fan, in the z direction. Note that v_z must have different signs for $y > 0$ and $y < 0$ due to the different handedness of the vector product of $\mathbf{E}$ and $\mathbf{B}$ in these two regions (see Fig. 2.41). Note further that this argument is completely independent of the profile of η, and relies only upon the structure of $\mathbf{B}$ (and thus $\mathbf{j}$) and the fact that the nonideal region is localized. For a full description of the model and results described in this section, see Pontin *et al.* (2005b).

2.4.4 Summary

Two models for kinematic reconnection at 3D magnetic null points with different current orientations have been described. The behavior of the magnetic flux in each reconnection process shows many properties which are very different from the familiar 2D null point reconnection. The fact that no unique field line velocity exists results in a continual and continuous reconnection of field lines throughout the nonideal region. It can be demonstrated that these new properties are still present in 3D reconnection when the full set of MHD equations is solved (Pontin *et al.*, 2005a).

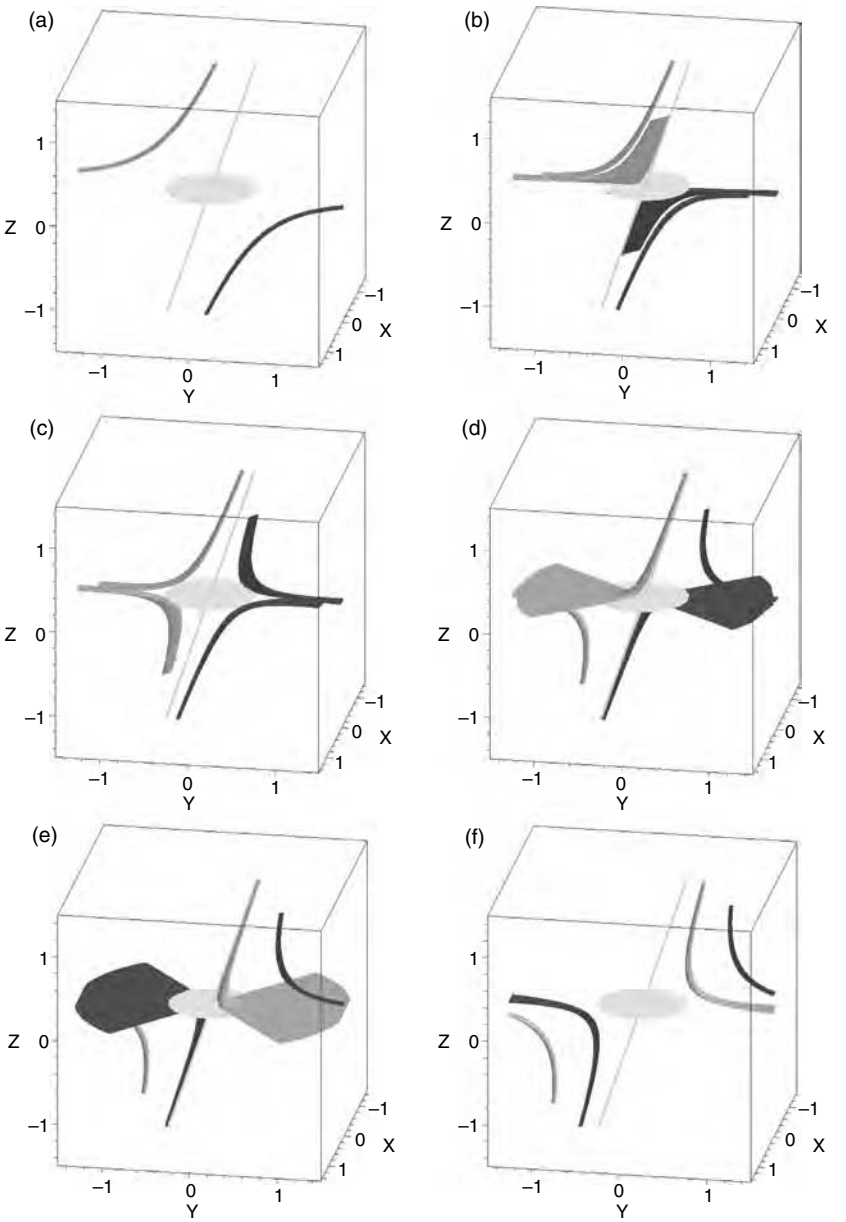

Fig. 2.40. Sequence of snapshots showing the reconnection of two flux tubes, initially chosen to be symmetric about the null. Field lines traced from footpoints anchored in the fan-crossing flow flip up the spine through the fan plane (b,c). Field lines traced from the top/bottom of the box (anchored in the spine-crossing flow) flip around the spine in the fan plane (d–f). The gray line represents the spine and the gray disk the fan.

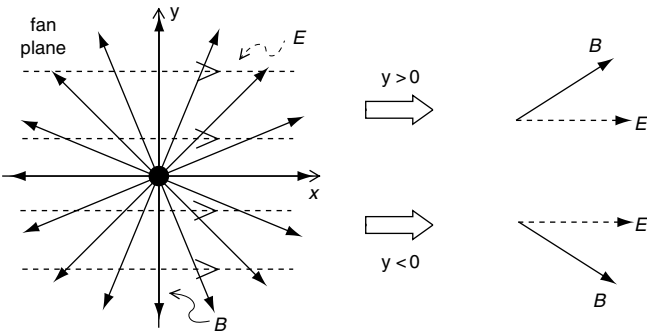

Fig. 2.41. The schematic structure of the magnetic field (**B**) and electric field (**E**) in the fan plane. The nonzero vector product of the two implies a flow across the fan, in opposite directions for $y > 0$ and $y < 0$.

A key point is that the orientation of the electric current is crucial in determining the nature of the reconnection. When the current is parallel to the spine of the null point, a rotational type of reconnection results, within a flux envelope enclosing the diffusion region. However, when the current is parallel to the fan, magnetic flux is advected through both the spine and the fan of the null point. The fan-crossing flow is of particular importance in a global magnetic field such as the solar corona, where the fan surfaces of nulls separate regions of different magnetic topology.

2.5 Three-dimensional flux tube reconnection

M. G. Linton

Three-dimensional reconnection is a complex subject, as is displayed by the variety of reconnection configurations presented in the preceding sections. Here we focus on a subset of these 3D configurations: the pair-wise collision and reconnection of isolated magnetic flux tubes. The flux tubes are initially surrounded by field-free plasma, and so do not fall easily into the topology classifications presented above, as the entire space outside the flux tubes has a null magnetic field. However, as soon as the flux tubes are pushed together and collide, they form a classical reconnection region at the collision interface between them. If the tubes are perfectly anti-aligned so that their fields exactly cancel at this interface, then they undergo null reconnection. However, in general 3D configurations the tubes will collide with imperfectly aligned fields, and so there will be a guide field, and the tubes will undergo non-null reconnection, if they reconnect at all. By focusing on these relatively simple configurations, we aim to simplify the 3D reconnection dynamics so that we can better understand the basics of such reconnection without getting lost in a truly complex interaction. From this study, we hope to build the tools necessary to understand more general 3D interactions, such as occur in the solar corona.

2.5.1 Untwisted flux tube reconnection

As a starting point for this discussion, we study the collision of untwisted flux tubes. This should be the most basic type of flux tube reconnection: if the fields each occupied half of the simulation domain instead of an isolated cylindrical tube,

their interaction would match that of 2.5D simulations. But as the fields are instead finite in extent and will only collide over a limited region, they will undergo a truly 3D interaction. The tubes simulated here have a magnetic field aligned along their axis of the form

$$B_{\text{axial}}(r) = B_0(1+\cos(\pi r/R))/2, \tag{2.119}$$

in cylindrical coordinates, for $r \le R$. The tube radius is $R = 3\pi/16$, in units where the periodic box extends from $-\pi$ to π in each direction. We align these tubes perpendicular to each other, as shown in the isosurface inset in Fig. 2.42a, with one aligned parallel to the y axis at $x = x_0 = \pi/4$, and the other aligned parallel to the z axis at $x = -x_0$. The tubes are pushed together at the center of the box ($x = y = z = 0$) by a stagnation-point flow of the form

$$\mathbf{v}(x,y,z) = v_0[-\sin x(\cos y + \cos z)\hat{\mathbf{x}} + \cos x(\sin y\ \hat{\mathbf{y}} + \sin z\ \hat{\mathbf{z}})]/2, \tag{2.120}$$

with a peak velocity amplitude of $v_0 = v_{\text{A}}/30$, where v_{A} is the initial Alfvén speed at the tube axis. This flow is initialized at the start of the simulation, and then evolves dynamically. These interactions are simulated with a 3D visco-resistive pseudo-spectral MHD code, discussed in detail in Dahlburg and Antiochos (1995). The viscous and resistive Reynolds (or Lundquist) numbers are, respectively, $Re = L_\nu = v_{\text{A}}R/(\pi\nu) = 560$ and $S = L_\eta = \mu_0 v_{\text{A}}R/(\pi\eta) = 5600$, in terms of the coefficients of kinematic viscosity (ν) and magnetic resistivity (η).

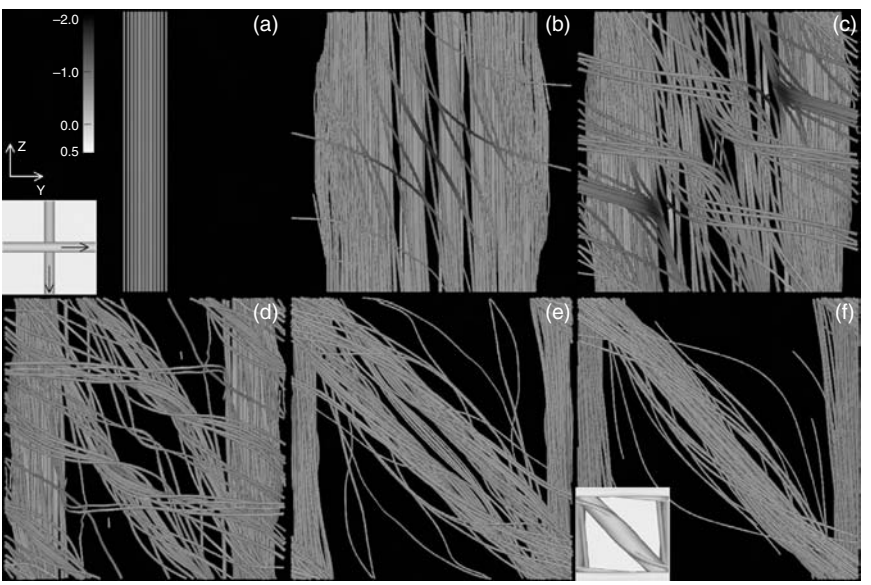

Fig. 2.42. Untwisted flux tube reconnection in a stagnation-point flow. Only field lines connecting to the vertical boundaries are traced. The field lines are shaded in proportion to the parallel electric current. The insets in panels (a) and (f) show isosurfaces of constant magnetic field strength. Adapted from Linton and Priest (2003).

The evolution of the field lines in this simulation is shown in Fig. 2.42 (from Linton and Priest, 2003). These are traced from particles entrained in the flow, subject to the momentum equation. Only the field lines connecting to the trace particles initially in the vertical tube are shown: this allows the interface between the tubes to be seen. The strength of the parallel electric currents along the field lines, a signature of 3D reconnection (Schindler *et al.*, 1988), is shown here by the grayscale shading (see the shade bar). These vertical field lines are initially well confined into a cylindrical volume in Fig. 2.42a. But the field is strongly influenced by the component of the flow perpendicular to the tube axis, and so quickly spreads out into a thin sheet of magnetic flux by Fig. 2.42b. The field starts to reconnect soon after it forms into this sheet. The field lines in Fig. 2.42b which pass near the center of the collision region change their connections so that they bend from the vertical to the horizontal flux tube and show large negative parallel currents as they pass through this central region. These reconnected field lines then spring away from the reconnection site due to the magnetic tension force. This central reconnection does not last undisturbed for long: by Fig. 2.42c it is broken up by the tearing instability (Furth *et al.*, 1963) into three separate reconnection regions: the original region plus a new one on either side of it. Each of these regions can again be identified by the strong parallel electric currents in them, and by the field lines curving away from them on either side, loosely forming an X shape. Upon reconnection, the field in between these three reconnection regions is trapped into two flux tubes. The part of the reconnected flux lying outside these reconnection points escapes to the upper right and lower left corners of the simulation box in Figs. 2.42d–f. At the same time, the flux trapped between the two flux tubes is pulled together by other reconnected flux wrapping around the tubes so that it coalesces into a single flux tube by Fig. 2.42f. Note that only about a third of the total flux reconnects in this simulation: the remaining flux is simply pushed to the sides of the simulation box by the flow, and can be seen as the purely vertical field lines in Fig. 2.42f.

For comparison with this reconnection, we now present a simulation in which the flux tubes approximately keep their cylindrical shape as they collide. To accomplish this, we impose a solid body motion on the flux tubes, accompanied by the back reaction of the displaced fluid outside the tubes. This fluid motion is taken from the classical solution for the motion of a cylinder through an incompressible fluid (e.g., Landau and Lifshitz, 1987). For the vertical tube at $x = -x_0$ and $y = 0$, it is, for $r > R$,

$$\mathbf{v} = v_0 \frac{R^2}{r^2} \left[\left(\frac{2(x+x_0)^2}{r^2} - 1 \right) \hat{\mathbf{x}} + 2 \frac{(x+x_0)y}{r^2} \hat{\mathbf{y}} \right], \tag{2.121}$$

while the flow for $r < R$ is simply $\mathbf{v} = v_0 \hat{\mathbf{x}}$. Figure 2.43 shows that this flow allows the tubes to collide in a more coherent manner. Reconnection progresses in much the same way as in the stagnation-point flow, but the initial, single reconnection region lasts for significantly longer, and as a result the topology of the reconnection at this stage is more clearly visible. Figures 2.43b and 2.43c show how the reconnected field lines fold over each other in a left-handed sense as they are traced from the vertical to the horizontal tube. The creation of this half turn of negative twist is a general result for such a reconnection event, as we will discuss below, and agrees with the

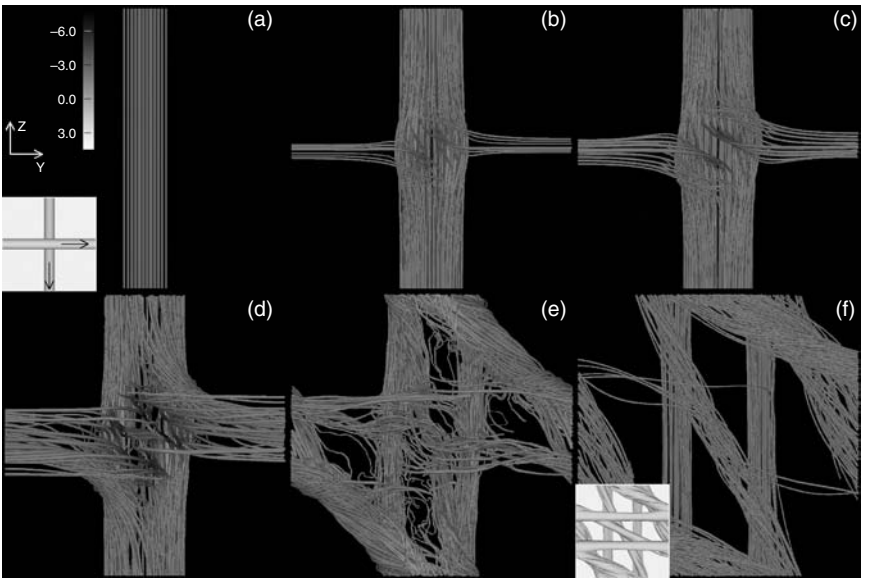

Fig. 2.43. Reconnection of untwisted flux tubes in the "solid body cylinder" flow given by Eq. (2.121).

negative sign of the parallel reconnection currents. By Fig. 2.43d, the tearing mode is again excited, though in this case only two reconnection regions are generated instead of three, because the length of the current sheet is shorter here than in the stagnation-point flow. These two reconnection regions again start to create a reconnected flux tube between them, in Figs. 2.43d and 2.43e. But this is only a very loosely coherent flux tube: it is really just the intersection of two sets of reconnected field lines, from the two reconnection regions, bending around each other. These two sets of reconnected field lines then reconnect with each other between Figs. 2.43d and 2.43f so that they nearly return to their initial vertical and horizontal alignments. As this second reconnection occurs at a slightly different point along the field lines than the first reconnection, the vertical reconnected field lines retain a small piece of the horizontal field lines, and vice versa. The result is shown by the field lines in Fig. 2.43f: here there are two singly reconnected, diagonal flux tubes at the top right and bottom left corners of the simulation, plus two completely vertical, unreconnected flux tubes near the center. But there is a fifth flux tube, slanting through the center of the simulation box, which is mostly vertical, with a small horizontal component. This flux tube is the result of the double reconnection. The inset in this panel shows the isosurfaces of these flux tubes. It also shows the corresponding horizontal flux tubes whose field lines are not plotted in the main figure: the two unreconnected horizontal tubes and the doubly reconnected tube which is mostly horizontal but has a small (negative) vertical component.

As the final simulation in our investigation of untwisted flux tube reconnection, we look at the case where the tubes are slightly twisted, but at such a low level that they are effectively untwisted on the scale of the reconnection region. We choose flux

tubes with a Gold–Hoyle profile (Gold and Hoyle, 1960) of the form

$$B_{\text{axial}}(r) = \frac{B_0}{1+\mathcal{T}^2 r^2}, \tag{2.122}$$

$$B_{\text{azimuthal}}(r) = \mathcal{T} r B_{\text{axial}}(r), \tag{2.123}$$

out to a radius of $R = 11\pi/48$, with zero field outside, as before. In contrast to the untwisted profile of Eq. (2.119), where the current goes smoothly to zero at $r = R$, this profile induces a strong current sheet at $r = R$ where the Gold–Hoyle field is abruptly cut off. The twist $\mathcal{T}$ for this simulation is one, meaning that the field makes one turn around the tube axis as it traverses the length of the simulation box. We again collide the tubes at right angles, in a stagnation-point flow. The simulation, shown in Fig. 2.44, clearly demonstrates the effect of the twist on the tubes: the stagnation-point flow has essentially no spreading effect on the flux tubes because the tension force of the twist counteracts it. Upon colliding, the tubes reconnect much as in the purely untwisted case with the cylindrical flow, though they never exhibit the tearing mode instability. A second major effect of the twist is that it keeps the tubes coherent throughout the reconnection so that all of the flux reconnects. In contrast to both untwisted simulations, none of the flux breaks away from the colliding flux tubes to bounce, unreconnected, away from the reconnection site. Thus the twist, even though its scale length is much longer than the length of the reconnection region, has a profound effect on the reconnection dynamics. Note that the reconnected tubes in Fig. 2.44 have about half a turn of right-handed twist each. This is again due to the fact that half a turn of left-handed twist is added to the field lines reconnecting at this collision angle.

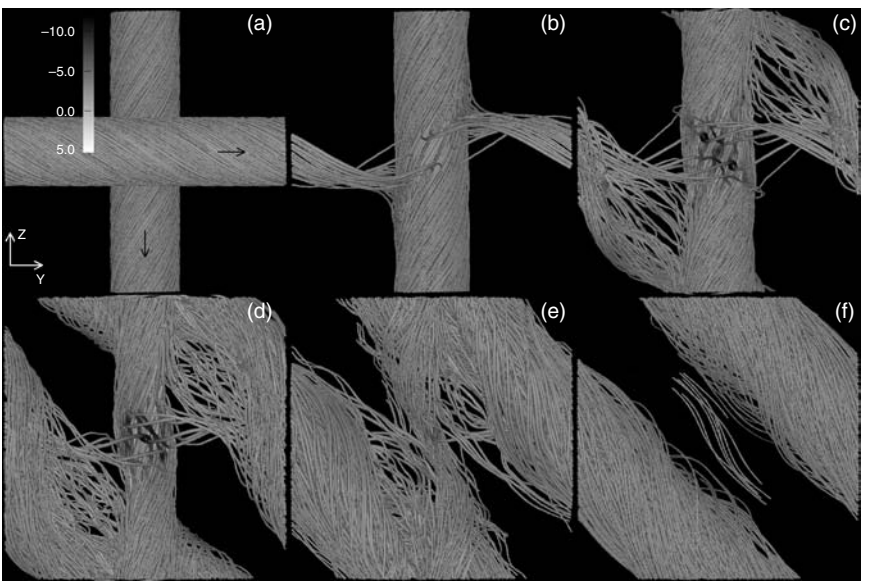

Fig. 2.44. Reconnection of slightly twisted ($\mathcal{T} = 1$) flux tubes. From Linton and Antiochos (2005).

2.5.2 Twisted flux tube reconnection

As evidenced by the low twist flux tube reconnection simulation of Fig. 2.44, twist can have a significant effect on the dynamics of reconnecting flux tubes. To study the effects of twist in more detail, we simulate the extreme case where the tubes have a twist of $\mathcal{T} = 10$. Here the scale of the twist is comparable to the tube radius, and therefore to the scale of the collision/reconnection region. We find that the relative signs of twist in the two flux tubes and the angle at which they collide have dramatic effects on the reconnection. Therefore we perform a complete simulation survey of both like-twisted and oppositely twisted flux tube interactions for collisions at all angles $\theta = N\pi/4$, where $N = 0$ to 7. The angle θ is measured in the left-handed sense about the x axis from the axis of the reference tube, which is aligned along the z axis, to the axis of the second tube. Each simulation is labeled according to the sign of twist of the tubes, R or L for right- or left-handed twist, and according to the angle N. Thus the $\mathcal{T} = 1$ collision shown in Fig. 2.44 is an RR6 collision. By mirror symmetry, an LL interaction at an angle θ is the same as an RR interaction at $2\pi - \theta$, so we only study the RR and RL collisions. These simulations are carried out at a somewhat higher resistivity than those of the previous section, with $L_\eta = 916$.

Four different interactions occur for these collisions, which again are induced by the stagnation-point flow of Eq. (2.120). The tubes can simply bounce, with no appreciable reconnection. They can reconnect in the classical manner presented in the previous section, which we will refer to as slingshot reconnection. They can tunnel through each other, as Dahlburg *et al.* (1997) discovered. Finally, they can merge together into a single flux tube. Firstly, we will discuss the energetics of the slingshot interactions in these simulations. Then we will discuss the merge interaction and the tunnel interaction.

For these high twist flux tubes, we found that the slingshot interaction occurs only for oppositely twisted flux tubes, though as Fig. 2.44 clearly shows, the slingshot does occur at low twist. The energetics of these oppositely twisted (RL) flux tube interactions are presented in Fig. 2.45a. The radial coordinate here is energy, while the azimuthal coordinate is the flux tube angle θ. The solid line shows twice the peak kinetic energy during the simulation while the dashed line shows the magnetic energy left in the tubes at the end ($tv_A/R = 150$) of the simulation. Both curves are normalized by the initial magnetic energy. A significant amount of energy is lost simply to magnetic diffusion, so that all simulations lose at least 70% of their energy, even if no reconnection occurs. Thus the energy scale, shown by the labeled circles, goes from 0% to 30% of the initial magnetic energy. Each simulation (radial spoke) on this plot is labeled with the angle N and with the type of interaction which occurred. This shows that the slingshot occurs at all angles in the range $\pi/2 \leq \theta \leq 3\pi/2$. At $\theta = \pi$, where the tubes are exactly antiparallel and all components of the field can reconnect completely, almost all of the magnetic energy is released. The slingshot interactions at other angles do not annihilate the flux tubes, but are still very energetic, releasing more than half of their magnetic energy via the reconnection (not counting what is lost to diffusion independent of reconnection). These obviously present prime energy release mechanisms for flux tube reconnections. On the other hand, for angles close to parallel, essentially no extra energy is released because the tubes bounce with little reconnection.

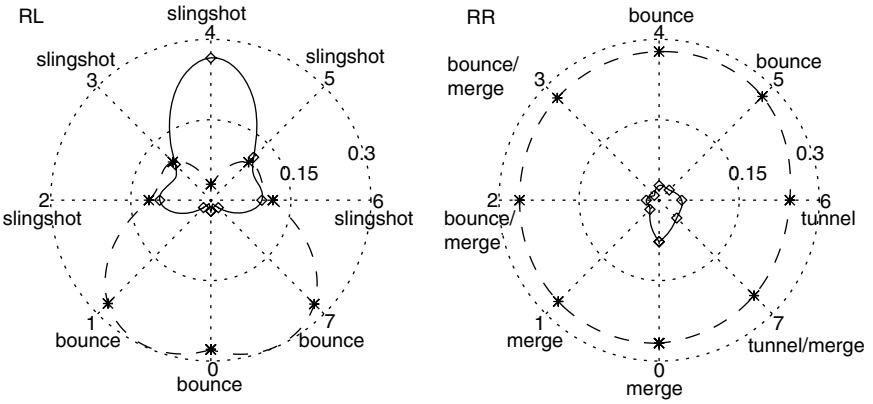

Fig. 2.45. Energy plot, in polar coordinates, for oppositely twisted (RL) and like-twisted (RR) $\mathcal{T} = 10$ flux tubes. The radial coordinate is the energy while the azimuthal coordinate is the collision angle θ. Twice the peak kinetic energy is plotted as the solid line, while the magnetic energy remaining at the end of the simulations is plotted as the dashed line. From Linton *et al.* (2001).

In general, the magnetic energy release in slingshot interactions, such as those of Figs. 2.42 to 2.44, is due to the shortening of the axial field lines as the flux tubes shorten. In addition, for the slingshot of oppositely twisted tubes such as those simulated by Linton *et al.* (2001) and by Ozaki and Sato (1997), there can be significant energy release from twist cancellation because the slingshot reconnection splices tubes with opposite twists together. The unbalanced torsion force generated by these unmatched twists sends torsional Alfvén waves along the tube until the twists cancel each other out. If both colliding tubes have the same amount, but opposite sign, of twist, then they can release their whole twist energy via this reconnection. This is a significant source of the magnetic energy release shown in Fig. 2.45a.

For comparison, Fig. 2.45b shows the same energy plot for the like-twisted (RR) flux tube interactions. This presents a very different picture, with much less energy released by reconnection at all angles than is released in the oppositely twisted slingshot reconnections. This is due mainly to the fact that these flux tubes cannot release their twist energy by cancellation. For this same reason, none of the flux tubes slingshot at this twist either. As they cannot cancel their twist, the main energy release from the slingshot would be from shortening the axial field lines. But this would compress the twist and, because the twist is so large, result in a net increase in the magnetic energy. Thus there is no energetic advantage to undergoing a slingshot reconnection at this level of twist. The source of energy release for these high twist tubes is the merge interaction, which occurs primarily at the angles of $N = 0$ and 1, and the tunnel interaction, which occurs at $N = 6$ and $N = 7$.

The merge interaction occurs in like-twisted flux tubes when the tube axes are closely aligned so that the azimuthal field is oppositely directed where the tubes collide. This azimuthal field then reconnects while the axial field largely does not. Such merge reconnections have been seen in interactions of perfectly parallel, like-twisted flux tubes by Lau and Finn (1996), Kondrashov *et al.* (1999), and Linton *et al.* (2001) in MHD simulations, and by Yamada *et al.* (1990) in a laboratory

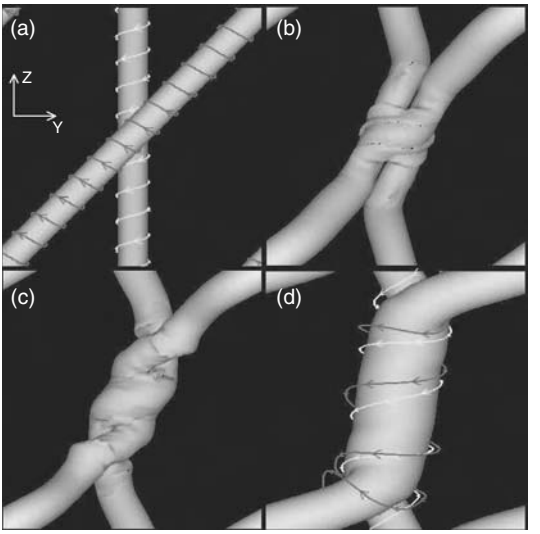

Fig. 2.46. Reconnection of highly twisted ($\mathcal{T} = 10$) flux tubes at an angle of $\theta = \pi/4$ (RR1). The azimuthal flux reconnects, pulling the tubes together so that they merge into a single tube. From Linton *et al.* (2001).

experiment. An example of the merge interaction for a nonparallel collision, the RR1 interaction, is shown in Fig. 2.46 (from Linton *et al.*, 2001). The field lines reconnect such that they wind about both flux tubes, bringing the axes into closer alignment by Fig. 2.46b, and thereby increasing the contact region and enhancing the reconnection. The reconnection progresses through Fig. 2.46c until the tubes are brought as close together as the boundary conditions will allow, and then the reconnection stops. While it is the periodic boundary conditions which keep the footpoints from merging together here, for coronal flux tubes the line-tying boundary conditions at the photosphere would serve the same purpose. The result, in Fig. 2.46d, is that the tubes are merged into a single tube along most of their length and then split to their respective footpoints as they approach the boundaries. The flux tubes release magnetic energy by merging because it decreases the twist in the tubes. The pitch of the field, i.e., the axial distance it covers when it travels a unit azimuthal distance, is conserved in the reconnection. As it has to wind around twice as much flux after the tubes merge, it therefore only winds half as many times per unit length. As a result the twist is reduced by a factor of two, and this reduces the energy. Note that this result can also be derived from helicity conservation. The helicity of a twisted flux tube is $\Phi^2\mathcal{T}$ (Berger and Field, 1984), where Φ is the axial flux of the tube. Thus the initial twist helicity of the two tubes is $2\Phi^2\mathcal{T}$, while the final twist helicity of the merged tube is $(2\Phi)^2\mathcal{T}_{\rm merge}$. For these two to be equal, the merged twist must be half the initial twist.

The second means by which energy is released for like-twisted flux tubes at high twist is via the tunnel. In a tunnel interaction, as shown in Fig. 2.47 for a $\mathcal{T} = 5.5$ simulation, tubes reconnect with each other such that they pass entirely through each other. This requires a pair of reconnections, as shown by Dahlburg *et al.* (1997). The

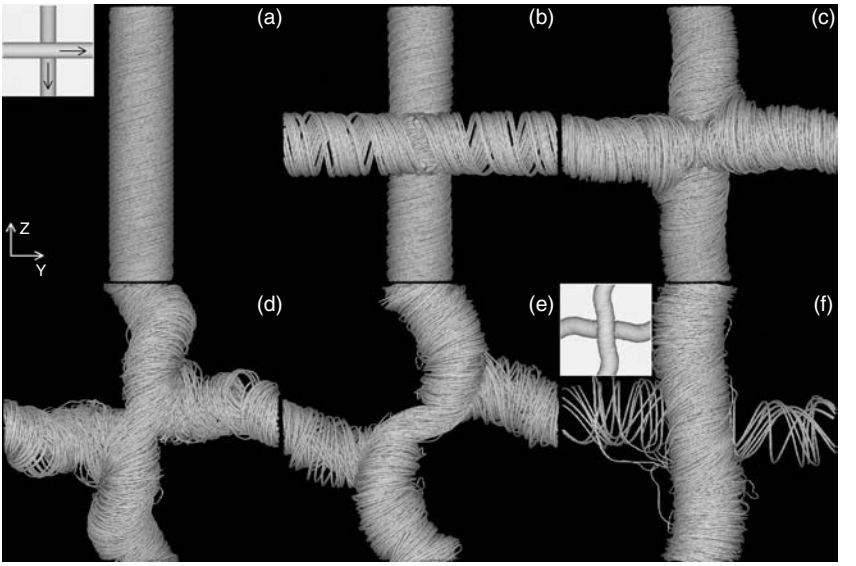

Fig. 2.47. Tunnel interaction of RR6 flux tubes at a twist of $\mathcal{T} = 5.5$. From Linton and Antiochos (2005).

reconnection occurs first as the tubes slingshot from Figs. 2.47b–d, and then a second time when the tubes rebound from the slingshot to collide again, in Figs. 2.47e,f. The energetics summary in Fig. 2.45b shows that this tunnel only occurs for our survey of $\mathcal{T} = 10$ interactions at angles $N = 6$ and 7, and that it does not occur in the inverse direction (angles $N = 2$ or 3). Why does this happen, and why is it not reversible? We will address this question in the next section.

2.5.3 Helicity conservation and energy release: tunnel vs. slingshot

When flux tubes cross each other, even if they have no twist, there is a magnetic helicity $\mathcal{H}$ associated with them. In a configuration where the flux penetrates the boundary, the helicity is poorly defined, but a useful form of helicity can be calculated either via the relative helicity (Berger and Field, 1984), or by mapping the volume to a toroidal volume (Linton and Antiochos, 2005). The toroidal mapping is the easier to calculate in this configuration, and so we shall adopt it here. In this formalism a pair of flux tubes crossing at $\theta = 6\pi/4$ as in Fig. 2.42 has a linking helicity of $\mathcal{H}_{\rm link}/\Phi^2 = \mathcal{L} = 0$. If these tubes reconnect in a slingshot to form a pair of parallel flux tubes crossing the domain on a diagonal, they will have a linking helicity of $\mathcal{L} = 1$. Finally, if these tubes tunnel through each other so that they cross at $\theta = 2\pi/4$, they will have a linking helicity of $\mathcal{L} = 2$. Including the ever twist helicity $\mathcal{T}$ discussed above, the total helicity for a pair of equally twisted flux tubes is $\mathcal{H}/\Phi^2 = 2\mathcal{T} + \mathcal{L}$ (Berger, 1986). If the resistivity is very low everywhere in the simulation except at the reconnection site itself, essentially no helicity will be lost in the simulation, and so the helicity after reconnection must equal the initial helicity. But the slingshot and tunnel reconnections shown here change the linking helicity from 0 to 1 and 2, respectively, so the twist helicity must change to compensate. The result is that

each flux tube must lose a half turn of positive twist in a slingshot reconnection, and must lose a full turn of positive twist in a tunnel reconnection. We have already seen this result for the slingshot simulations in Figs. 2.42 through 2.44. In particular, Figs. 2.43b,c show this negative half turn of twist being generated by the reconnection. This result has profound implications for the tunnel reconnection: if a pair of positively twisted flux tubes tunnel through each other from an RR6 configuration to an RR2 configuration, as in Fig. 2.47, then the loss of one turn of positive twist per tube means a net reduction in twist, and therefore a reduction in the magnetic energy. This explains, firstly, why the tunnel occurs at all and, secondly, why the inverse of the tunnel does not occur: a tunnel from RR2 to RR6 would increase the twist and therefore the magnetic energy.

We can use this prediction to estimate the final energy state of slingshot and tunnel reconnection tubes. If we assume that the tubes conserve helicity as above, and in addition that they conserve flux and mass, and evolve to a new equilibrium which is homologous with their original state, we find that the final energy state after slingshot is (from Linton and Antiochos, 2002)

$$ME_{\rm s} = \frac{L_{\rm s}^2}{L^2} E_{{\rm a}x} + \frac{L}{L_{\rm s}} \frac{1}{\mathcal{T}^2} \left(\mathcal{T} - \frac{1}{2} \right)^2 E_{{\rm a}z}, \tag{2.124}$$

where L is the initial tube length and $L_{\rm s}$ is the slingshot tube length. This is to be compared to an initial energy of $ME_0 = E_{{\rm a}x} + E_{{\rm a}z}$, where $E_{{\rm a}x}$ and $E_{{\rm a}z}$ are the initial axial and azimuthal energy, respectively. A tunnel interaction under the same assumptions will have a final energy of

$$ME_{\rm t} = E_{{\rm a}x} + \frac{(\mathcal{T}-1)^2}{\mathcal{T}^2} E_{{\rm a}z}. \tag{2.125}$$

These equations show how the decrease $(L_{\rm s}/L)$ in length decreases the axial magnetic energy but increases the azimuthal magnetic energy for the slingshot, and how the loss of twist due to reconnection decreases the azimuthal energy for both the tunnel and the slingshot. Figure 2.48 shows the post-reconnection equilibrium energies

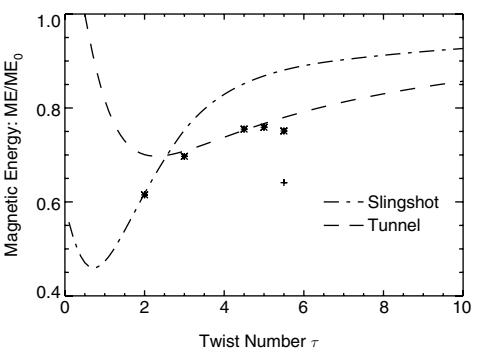

Fig. 2.48. Predicted equilibrium energy of RR6 flux tubes after a slingshot (dash-dotted) or tunnel (dashed) reconnection, from Eqs. (2.124) and (2.125). The estimated simulation values are shown by the asterisks for the slingshot and by the plus sign for the tunnel. From Linton and Antiochos (2005).

predicted by these equations. The slingshot energy is shown as the dash-dotted curve while the tunnel energy is shown as the dashed curve. The tunnel loses more energy at high twist, where the twist energy is dominant, but the slingshot loses more energy below a twist of 2.56, at which point the axial magnetic energy is the more important. This leads to the interesting prediction that the tunnel should occur at large twists but the slingshot at low twists. We will test this now. As helicity is easily lost at high levels of diffusion, the resistivity must be as low as numerically possible for this test, as it relies on helicity conservation for its predictions. At low resistivity, however, intense dynamics can make the code numerically unstable. We therefore need to keep the resistivity relatively high in the reconnection region where the intense dynamics occur. To accomplish this, we use a spatially nonuniform resistivity which peaks in a ball at the center of the simulation, where the tubes collide:

$$\eta = \eta_0(1 + 99\mathrm{e}^{-\lambda^2/(4R^2)}), \tag{2.126}$$

where λ is the radial distance from the center of the box in spherical coordinates. The decay scale length $2R$ is chosen so that most of the reconnection/collision site will be within the high resistivity region. For the RR6 simulations presented here in Figs. 2.47 and 2.49, we used a peak Lundquist number of 91 600 which decreases to 916 at the center of the simulation. The result is that the code remains stable, yet only 3% of the helicity is lost. These simulations show that the tunnel occurs down to a twist of $\mathcal{T} = 5.5$, shown in Fig. 2.47, while the slingshot occurs at and below twists of $\mathcal{T} = 5$, shown in Fig. 2.49. Thus the transition from tunnel to slingshot occurs at twists about two times higher than predicted by Fig. 2.48. The differences between these two simulations hint at why the transition occurs at such a high twist.

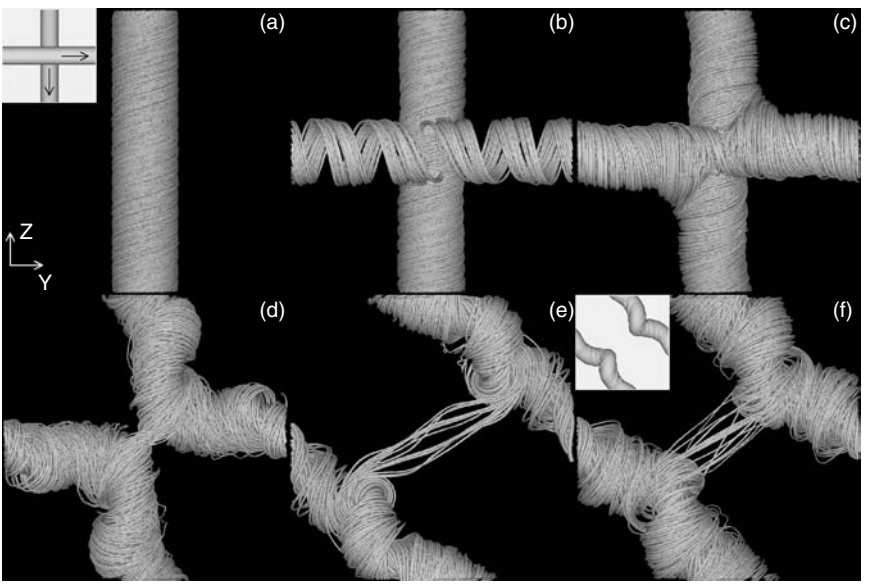

Fig. 2.49. Slingshot interaction of RR6 flux tubes at a twist of $\mathcal{T} = 5$. From Linton and Antiochos (2005).

Whereas in the tunnel at $\mathcal{T} = 5.5$, the tubes first slingshot and then come into contact again to reconnect a second time, at a slightly lower twist of $\mathcal{T} = 5$, the tubes never come into contact again. Thus the dynamics prevents the tubes from reconnecting a second time and tunneling to the lower energy state. The actual energy release from these tubes is estimated by measuring the magnetic energy of the tubes at the time where the reconnection in the field line plots appears to be complete. The result is shown in Fig. 2.48 as the asterisks and as the plus sign, for the slingshot and tunnel reconnections respectively. This shows that the energy release is about a factor of two larger than predicted. We argue that this is principally due to the reconnection-independent resistive losses, as the resistivity has a significantly larger effect on magnetic energy than on magnetic helicity (see, e.g., Berger, 1984). However, in the very low resistivity solar corona essentially no magnetic energy will diffuse in the absence of reconnection, and so these predictions should agree more accurately with the true energy release.

The theory above indicates that the tunnel should also occur at collision angles of $N = 5$ and 7, as both configurations will also lose a turn of twist upon tunneling (see Linton and Antiochos, 2002). We do indeed find the tunnel occurs for these collisions for a nonuniform Lundquist number of $S_\eta = 18\,300$ to 183 (see Linton and Antiochos, 2005). The RR7 tubes actually undergo three consecutive reconnections: first they slingshot, then they tunnel to form an RR1 configuration, and finally, just as in Fig. 2.46, they merge into a single flux tube. Thus the label tunnel/merge at N = 7 on the energy plot in Fig. 2.45b. The RR5 tubes, interestingly, bounce when $S_\eta = 91\,600$ to 916, as they do for a uniform Lundquist number of $S_\eta = 916$ (see N = 5 in Fig. 2.45b). Apparently, the reconnection they can undergo is too slow to take effect before they bounce away. But at the lower nonuniform Lundquist number of 18 300 to 183, they tunnel reasonably well, just as predicted. For both of these interactions, the transition from tunnel to slingshot also occurs at a higher level than predicted by the theory. The RR7 transitions at $\mathcal{T} = 3.5$ to 4 versus a prediction of 1.41, whereas the RR5 transition occurs at $\mathcal{T} = 7$ to 7.5 versus a prediction of 2.62. Again, looking at the simulations it becomes obvious that this is due to the extreme nature of the slingshot at and below the transition twist: this slingshot brings the tubes so far away from each other that they cannot reconnect again, and cannot tunnel to the lower energy state.

2.5.4 Summary

Three-dimensional flux tube reconnection can be a powerful tool for understanding complex reconnection configurations. Here we have presented a collection of flux tube interactions which display a wealth of information about the possibilities available in 3D reconnection. For untwisted flux tubes, we showed how the tearing mode instability can play an important role in the reconnection, channeling the reconnected flux into a collection of twisted flux tubes. We also showed that it is difficult to have all of the flux reconnect if the tubes are not continually forced into the reconnection region: usually a significant portion of the flux bounces away unreconnected. Yet even a small amount of twist can change this dramatically: the twist keeps the flux tubes coherent during reconnection and ensures that all of the flux reconnects. The presence of twist also adds significant complexity to flux tube

interactions: whereas untwisted flux tubes can only undergo a simple (yet powerful) slingshot reconnection, twisted flux tubes undergo merging and tunneling as well as the slingshot. In addition, helicity conservation plays an important role in reconnection. It adds (or subtracts) half a turn of twist per flux tube reconnection, depending on the configuration. This is what makes the tunnel reconnection possible at large twists: the double reconnection necessary for the tunnel takes away a turn of twist per flux tube, and therefore decreases the total magnetic energy. From simple assumptions about the final state of reconnected flux tubes, and about the conservation of helicity and flux, we can estimate the final energy state of slingshot and tunnel reconnections. This allows us to estimate which of these two interactions a flux tube pair will undergo, and to estimate how much energy they will release. We have tested these predictions and found they correctly predict which interactions can occur for a given tube configuration. However, we also found that they underestimate the lowest value of twist at which the tunnel interaction can occur, because the reconnection dynamics plays an important role in determining this critical twist. Finally, the energy release predicted by these estimates agrees to within a factor of two with that of the simulations, which is reasonable given the high rate of reconnection-independent diffusion in these simulations. If the agreement improves with decreasing resistivity, as is expected, this method should prove very useful in predicting energy release for flux tube reconnections in the very low resistivity solar corona.

3

Basic theory of collisionless reconnection

3.1 Fundamentals of collisionless reconnection

J. F. Drake and M. A. Shay

There are a number of well-documented deficiencies of the present resistive MHD models of magnetic reconnection (Section 2.1) that have motivated the exploration of reconnection models based on either a two-fluid or a kinetic description: the long energy release time, the absence of a well-defined mechanism for breaking the frozen-in condition, the onset problem, and the particle heating problem. As discussed in Section 2.1, the Sweet–Parker model of reconnection yields an inflow velocity of plasma into the dissipation region given by

$$v_{\rm in} \sim (\delta/\Delta) v_{\rm A}, \tag{3.1}$$

where $v_{\rm A}$ is the Alfvén speed just upstream of the dissipation region and the width of the current layer, $\delta \sim \eta^{1/2}$, is small compared with its length Δ. In the Sweet–Parker model Δ is given by the macroscopic system size L. As a consequence, the rate of reconnection given in Eq. (3.1) is small. In contrast, in Petschek's model (Section 2.1), the outflow region from the X-line opens up as a fan, leaving a relatively short dissipation region Δ in Eq. (3.1), and therefore boosting the reconnection rate dramatically. However, computations revealed that the open Petschek outflow geometry cannot be sustained in a model with a simple uniform resistivity (Biskamp, 1986). A model resistivity that increases sharply in regions with high current density, such as might be expected from current-driven turbulence, facilitates a Petschek-like reconnection configuration (Sato and Hayashi, 1979). However, the establishment and role of such *anomalous resistivity* during reconnection is not yet well understood (Papadopoulos, 1977; Galeev and Sagdeev, 1984; Drake *et al.*, 2003; see also Section 3.5) in spite of the wide use of anomalous resistivity models in MHD computations. New insight into processes driving the macroscale Sweet–Parker current layer has been recently developed. This current layer reflects an underlying singularity in the post-reconnection MHD state (Waelbroeck, 1989; Jemella *et al.*, 2003, 2004). Mechanisms that suppress this tendency toward singularity must compete with the ideal MHD processes that create the singularity.

Changing the topology of magnetic field lines, which is necessary for releasing energy during magnetic reconnection, requires some form of dissipation to break the frozen-in condition. The dissipation mechanisms, which have been identified largely on the basis of computer simulations, will be discussed in greater detail in Sections 3.2

and 3.5. Section 3.2 focuses on mechanisms that operate even in the absence of modes that vary in the main current direction, while Section 3.5 discusses potential effects of such modes. In planetary magnetospheres such as that of the Earth, where the plasma density is only a few particles per cubic centimeter or less, the collisional mean free path is large enough that classical collisions are negligible. In the absence of collisions the finite mass of electrons limits their response to a parallel electric field and allows magnetic field lines to reconnect. In a generalized fluid model these finite mass effects take the form of electron inertia and a nondiagonal pressure tensor (Section 3.2). In the intense current layers that define the dissipation region, instabilities generated by the relative streaming of electrons and ions may drive turbulence sufficient to produce anomalous resistivity (Section 3.5). In the solar corona, where the plasma is much less tenuous, collisions may play a role in facilitating reconnection, especially during the early stages of reconnection. However, the fast release of magnetic energy observed in the corona produces inductive electric fields that typically exceed the Dreicer runaway field (Miller *et al.*, 1997). For typical reconnection electric fields corresponding to reconnection inflow velocities of $0.1v_{\mathrm{A}}$, with v_{A} the Alfvén speed, the runaway criterion becomes

$$v_{\mathrm{A}} > 10 v_{\mathrm{te}} \frac{\nu_{\mathrm{ei}}}{\Omega_{\mathrm{e}}}, \tag{3.2}$$

where v_{te} and Ω_{e} denote the electron thermal velocity and cyclotron frequency, respectively, and ν_{ei} is the electron–ion collision rate. When the runaway condition is satisfied, the local dynamics becomes effectively collisionless. Thus, understanding collisionless reconnection remains critical to modeling the dynamics of both solar and magnetospheric systems.

An essentially universal feature of magnetized plasma systems is the storage-release cycle (Chapter 1). Magnetic energy slowly builds up due to input from external drivers, remains essentially quiescent, possibly for long periods (hundreds to thousands of Alfvén times), and then abruptly releases through topological changes in the magnetic configuration facilitated by reconnection. In all systems in which magnetic reconnection can be studied in detail, including disruptions in laboratory fusion experiments, substorms in the Earth's magnetosphere, and solar and stellar flares, a similar cycle is observed yet the underlying reasons for this universal behavior remain unclear. Is there a common mechanism underlying the sudden onsets of magnetic reconnection in this variety of systems or is the commmonality of the observations merely accidental? Is the absence of progress on the reconnection onset problem because the MHD modeling of such systems is missing key physics?

There is strong evidence that a significant fraction of the magnetic energy released during magnetic reconnection is channeled into energetic electrons and ions. Solar observations in particular have suggested that at least 50% of the energy released during flares is in the form of energetic electrons (Lin and Hudson, 1971; Miller *et al.*, 1997). Energetic electrons and ions have been measured in the Earth's magnetosphere (Terasawa and Nishida, 1976; Baker and Stone, 1976) and in disruptions in laboratory fusion experiments (Savrukhin, 2001). Since MHD is a single fluid model, it cannot describe the energy branching ratio between electrons and ions nor can it describe the production of energetic particles, causing high-energy tails of the

particle distributions (Section 3.6) that have been observed, for instance, in recent magnetotail satellite data (Øieroset *et al.*, 2002). Such heating processes can only be treated with kinetic models. The focus of this section is to introduce some of the non-MHD concepts that have emerged as dominant players in the dynamics of reconnection, including relevant spatial scales, to provide the basis for more detailed discussions in subsequent sections.

3.1.1 Basic kinetic processes and scales

The dynamics of magnetic reconnection is controlled by the dissipation region, the narrow boundary layer where dissipative processes allow the magnetic field to change topology. Understanding and modeling this layer has been challenging because collisions are typically weak and collisionless kinetic processes dominate. The intense currents driven by local electric fields can drive turbulence and nonlinear structures such as electron holes, solitary waves, and double-layers. In spite of these challenges significant progress has been made in identifying the dissipative mechanisms that break the frozen-in condition and the processes that control the structure of this layer (Section 3.2).

As outlined in Section 2.1, the aspect ratio of the dissipation region, the ratio of its width δ to its length Δ, controls the rate of reconnection based on the inflow–outflow condition in Eq. (3.1). In the MHD model δ is controlled by resistivity while Δ is linked to the macroscopic system scale length L, independent of the dissipation processes. A fundamental question is what physical processes control these scale lengths in a kinetic model. Specifically, what dissipative process controls the width of the dissipation region and what is the physics that determines the length of the dissipation region. If the length of the dissipation region remains macroscopic as in the MHD model, it is unlikely that even large values of the kinetic dissipation will be sufficient to raise the rate of reconnection to levels that can explain the observations.

An important yet perhaps unexpected result of the efforts to understand kinetic reconnection was the discovery that the motions of the electrons and ions, because of their very different masses, decouple at the small spatial scales defining the dissipation region (Sonnerup and Ledley, 1979; Mandt *et al.*, 1994; Horiuchi and Sato, 1994). This behavior can be understood from the electron equation of motion,

$$m_{\mathrm{e}}\frac{\mathrm{d}\mathbf{v}_{\mathrm{e}}}{\mathrm{d}t} = -e\mathbf{E} - e\mathbf{v}_{\mathrm{e}}\times\mathbf{B} - \frac{1}{n}\nabla\cdot\mathbf{P}_{\mathrm{e}} - m_{\mathrm{e}}\nu_{\mathrm{ei}}(\mathbf{v}_{\mathrm{e}}-\mathbf{v}), \tag{3.3}$$

where $\mathbf{v}$ is the bulk ion velocity, $\mathbf{P}_{\mathrm{e}}$ is the electron pressure tensor (in the electron rest frame), and $\mathrm{d}/\mathrm{d}t \equiv \partial/\partial t + \mathbf{v}_{\mathrm{e}}\cdot\nabla$ is the time derivative in the electron rest frame. This equation appears like an Ohm's law if $\mathbf{v}_{\mathrm{e}}$ is replaced with $\mathbf{v}_{\mathrm{e}} = \mathbf{v} - \mathbf{j}/ne$ and terms of order $m_{\mathrm{e}}/m_{\mathrm{i}}$ are neglected,[1]

$$\frac{m_{\mathrm{e}}}{ne^2}\left[\frac{\partial\mathbf{j}}{\partial\mathbf{t}} + \nabla\cdot\left(\mathbf{jv}+\mathbf{vj}-\frac{\mathbf{jj}}{ne}\right)\right] = \mathbf{E}+\mathbf{v}\times\mathbf{B} - \frac{\mathbf{j}\times\mathbf{B}}{ne} + \frac{\mathbf{1}}{ne}\nabla\cdot\mathbf{P}_{\mathrm{e}} - \eta\mathbf{j}. \tag{3.4}$$

[1] The $\mathbf{jj}$ term on the left-hand side of (3.4) can be combined with the electron pressure term to yield the electron pressure tensor in the plasma rest frame, $\mathbf{P}_{\mathrm{e}}^{\mathrm{CM}}$, which leads to

$$\frac{m_{\mathrm{e}}}{ne^2}\left[\frac{\partial\mathbf{j}}{\partial\mathbf{t}} + \nabla\cdot(\mathbf{jv}+\mathbf{vj})\right] = \mathbf{E}+\mathbf{v}\times\mathbf{B} - \frac{\mathbf{1}}{ne}\mathbf{j}\times\mathbf{B} + \frac{\mathbf{1}}{ne}\nabla\cdot\mathbf{P}_{\mathrm{e}}^{\mathbf{CM}} - \eta\mathbf{j}.$$

This is the form discussed by Vasyliūnas (1975).

The *generalized* Ohm's law (3.4) contains three terms that are not present in the resistive MHD limit, the electron inertia term on the left of (3.4), and the terms proportional to $\mathbf{j}\times\mathbf{B}$ (*Hall term*) and $\nabla\cdot\mathbf{P}_e$. The Hall term brings whistler dynamics into the system while the electron pressure term brings in kinetic Alfvén wave dynamics and unmagnetized electron dynamics when the pressure tensor is nongyrotropic.

At large spatial scales Eq. (3.4) reduces to $\mathbf{E}+\mathbf{v}\times\mathbf{B}=0$, the ideal MHD "Ohm's" law. From this relation it is easily shown that the magnetic field is frozen-in to the ion fluid (Section 2.2). The ideal MHD equations are scale invariant, meaning that they do not define a spatial scale. The other terms in Ohm's law are associated with specific spatial scales and are important when those spatial scales are reached. The electron inertial term is associated with the electron skin depth $d_e \equiv c/\omega_{pe}$, which can be derived by comparing the convective portion of the inertia term with the $\mathbf{j}\times\mathbf{B}$ term. At the spatial scales where electron inertia is important typically $v_e \gg v$ so that the $\nabla\cdot(\mathbf{jj}/ne)$ portion of the inertia dominates. The scale where the $\mathbf{j}\times\mathbf{B}$ (Hall) term becomes important is calculated by comparing it with the $\mathbf{v}\times\mathbf{B}$ term,

$$|\mathbf{v}\times\mathbf{B}|\sim v_A\mathbf{B} < \frac{|\mathbf{j}\times\mathbf{B}|}{ne}\sim\frac{\mathbf{1}}{\mu_0 ne}\frac{B^2}{\Delta} \tag{3.5}$$

or

$$\Delta < d_i \equiv c/\omega_{pi}. \tag{3.6}$$

If Δ is smaller than the ion inertial length d_i, j/ne exceeds v so that v_e exceeds v, which implies that electrons and ions no longer move together, unlike in the MHD regime, where $\mathbf{v}_e\sim\mathbf{v}$. The isotropic pressure term brings in the effective ion Larmor scale $\rho_s = (T_e/m_i)^{1/2}/\Omega_i$ (based on the *ion–sound speed*, $v_s = (T_e/m_i)^{1/2}$ for the limit where $T_e \gg T_i$). Since this scale does not follow from Ohm's law alone, we discuss this scale later.

The decoupling of electron and ion motion at small spatial scales implies that the Alfvén wave no longer controls the collective behavior of the plasma motion below these scales. In particular, the Alfvén wave no longer drives the acceleration of the plasma away from the X-line, allowing the bent, newly reconnected field lines to release their stored magnetic energy. Close to the X-line this role is taken over by either the whistler or kinetic Alfvén wave.

The issue of what breaks the frozen-in condition is of fundamental importance for the understanding of collisionless reconnection. The details of this mechanism will be discussed in Section 3.2. Very close to the X-line the convective portion of the inertial term can be neglected because the local velocity is nearly zero (from symmetry considerations) so only the nongyrotropic pressure can balance the reconnection electric field (Vasyliūnas, 1975). This result is true both with and without a guide magnetic field (the field component in the direction of the main current), which implies that the current layer driven by the reconnection electric field must scale with the electron Larmor radius even when the guide field becomes very large (Hesse *et al.*, 2002, 2004). Away from the X-line the convective portion of the inertia can be important, especially for the case with a guide field, where large parallel electric fields map the magnetic separatrices, extending outward far from the X-line (Pritchett and Coroniti, 2004; Drake *et al.*, 2005b).

A final question is how strongly the rate of reconnection depends on the dissipation mechanism. An important result of the *GEM Reconnection Challenge* (Birn *et al.*, 2001) and some earlier papers (Shay and Drake, 1998; Hesse *et al.*, 1999) is that the rate of late-time reconnection is insensitive to dissipation when whistler and kinetic Alfvén waves drive the outflow from the X-line. For simplicity, we break the more detailed discussion of these various issues into the case of antiparallel and guide-field (component) reconnection.

Reconnection with antiparallel magnetic fields

The case of antiparallel reconnection has been extensively explored because of its relevance to collisionless reconnection in the Earth's magnetotail and because the current layers that develop in the vicinity of the X-line are relatively broad in comparison with the case of a guide field and therefore computationally less challenging to model. In Fig. 3.1 is a schematic of the basic structure of the X-line region, including the field structure and electron and ion flows. At distances greater than d_i upstream from the X-line the electrons and ions flow together. At a distance around d_i upstream the electron and ion motion decouples and the ions are diverted into the outflow direction, forming an outflow jet and current layer of width around d_i. Inside of this region the ions are essentially demagnetized and respond mostly to electric rather than magnetic fields. The electrons remain frozen-in to the magnetic field and continue to move toward the X-line. The electrons decouple from the magnetic field when they approach within d_e of the X-line and are accelerated in the outflow direction in an outflow channel of width d_e. The peak outflow velocity of the electrons

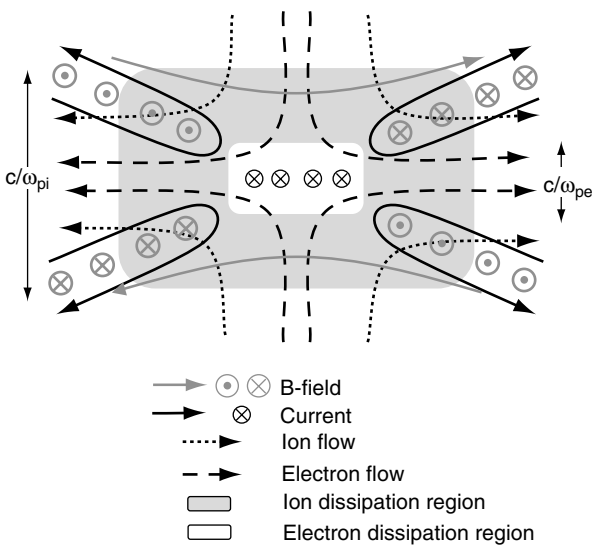

Fig. 3.1. Schematic of the multiscale structure of the dissipation region during antiparallel reconnection. Electron (ion) dissipation region in white (gray) with scale size c/ω_pe (c/ω_pi). Electron (ion) flows in long (short) dashed lines. In-plane currents marked with solid dark lines and associated out-of-plane magnetic quadrupole field in gray.

reaches the electron Alfvén speed $v_{\rm Ae} = B/\sqrt{\mu_0 m_{\rm e} n}$ and then drops sharply to match the ion outflow speed $v_{\rm A}$. The different trajectories of the electrons and ions in the reconnection plane produce closed current loops that generate a self-consistent out-of-plane magnetic field B_y. This field is the signature of the standing whistler wave that drives the electron outflow from the X-line.

For consistency with the remainder of this chapter, and the predominant applications to the Earth's magnetotail (Chapter 4), we adopt a cartesian coordinate system, where x is the coordinate in the direction of the main magnetic field, which reverses sign across the current sheet, y is the direction of the main current (the ignorable coordinate in 2D models), and z is the direction perpendicular to the current sheet. We note that these coordinates may differ from those in the original papers cited.

Shown in Fig. 3.2 are data from a 2D simulation of antiparallel reconnection with a particle-in-cell (PIC) code (Zeiler *et al.*, 2002). The data are consistent with the schematic shown in Fig. 3.1. A key discovery that is manifest in all models that include the Hall term in Ohm's law is that the dissipation region (broadly defined to include all of the regions where either the ions or electrons decouple from the magnetic field) remains spatially localized in the outflow direction – that is, unlike the Sweet–Parker model, the dissipation region is determined by the kinetic scales ($\Delta \sim 10 d_{\rm i}$) rather than the macroscale L. It is this scaling for Δ that facilitates fast reconnection ($v_{\rm in} \sim 0.1\, v_{{\rm A}x}$) from Eq. (3.1) even in large systems (Shay *et al.*, 1999, 2004; Huba and Rudakov, 2004). The reason for the different scaling of the Hall versus the MHD reconnection is linked to the dispersive character of the whistler wave (Rogers *et al.*, 2001). The insensitivity of the rate of reconnection to dissipation is also linked to the dispersive property (Birn *et al.*, 2001). Thus, how reconnection couples to the whistler wave is a crucial scientific issue.

Coupling to whistler waves The coupling of dispersive waves to reconnection is complicated by the 2D structure of the dissipation region and there has to date been no rigorous analytical model to describe the essential physics. A good qualitative understanding can be gleaned from a simple 1D picture as illustrated in Fig. 3.3, showing the magnetic field of a standing wave that is periodic in the z direction along a uniform magnetic field in the y and z directions. As suggested by the magnetic field line segments shaded dark, a segment of the field line can be treated as a newly reconnected field line formed as a result of reconnection and the resulting flow in the x direction treated as a proxy for the outflow generated during reconnection. In the case of the MHD model the solution of this standing Alfvén wave is

$$\tilde{B}_x = \tilde{B}_0 \sin(kz)\cos(kv_{\rm p}t), \tag{3.7}$$

$$\tilde{v}_x = v_{\rm p}\frac{\tilde{B}_0}{B_z}\cos(kz)\sin(kv_{\rm p}t), \tag{3.8}$$

$$v_p = v_{{\rm A}z}, \tag{3.9}$$

with $v_{\rm p}$ the wave phase speed. The amplitude of the x component of the velocity, $\tilde{B}_0/\sqrt{\mu_0 m_{\rm i} n}$, is simply the upstream Alfvén velocity, the usual outflow condition for magnetic reconnection. A similar calculation carried out with $B_y = 0$ at

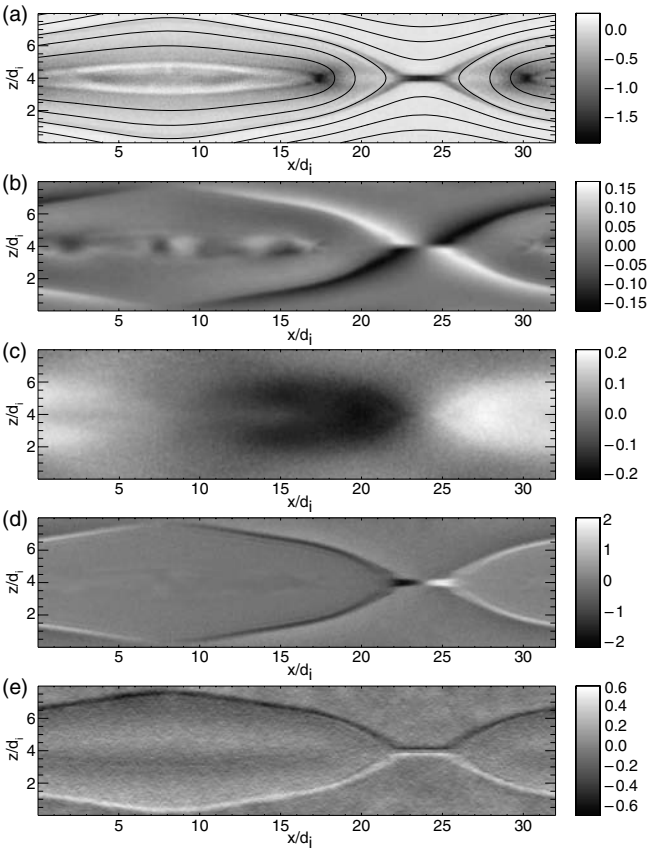

Fig. 3.2. Data from a PIC simulation of antiparallel reconnection with $m_\mathrm{i}/m_\mathrm{e} = 100$, $T_\mathrm{i}/T_\mathrm{e} = 12.0$, and $c = 20.0$ showing: (a) the current J_z and in-plane magnetic field lines; (b) the self-generated out-of-plane field B_z; (c) the ion outflow velocity v_x; (d) the electron outflow velocity v_{xe}; and (e) the Hall electric field E_y. Noticeable are the distinct spatial scales of the electron and ion motions, the substantial value of B_z which is the signature of the standing whistler, and the strong Hall electric field, E_y, which maps the magnetic separatrix. The overall reconnection geometry reflects the open outflow model of Petschek rather than the elongated current layers of Sweet–Parker.

scales below d_i yields the fields for the whistler wave and the electron outflow velocity,

$$\tilde{B}_y = \tilde{B}_0 \sin(kz)\cos(kv_\mathrm{p}t), \tag{3.10}$$

$$v_\mathrm{p} = kd_\mathrm{e}v_{\mathrm{A}ez}, \tag{3.11}$$

where $\tilde{B}_x$ and $\tilde{v}_x$ are the same as in Eqs. (3.7) and (3.8) with the whistler phase speed replacing that of the Alfvén wave. The whistler wave generates a magnetic field $\tilde{B}_y$ as the electron flow $\tilde{v}_{ye}$ drags the field $\tilde{B}_x$ out of the reconnection plane (Terasawa, 1983; Hassam, 1984). Associated with $\tilde{B}_y$ is the electron outflow $\tilde{v}_x$, which drives the electrons away from the X-line. Thus, the whistler wave replaces the Alfvén wave in

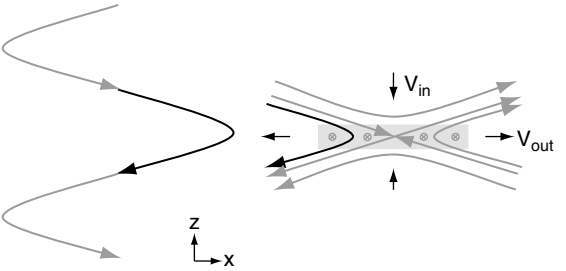

Fig. 3.3. Schematic showing how a newly reconnected field line can be represented as a segment of a simple 1D wave. The horizontal velocity v_x generated as the wave evolves corresponds to the outflow velocity from the reconnection site. The ratio of the peak horizontal velocity v_x to the horizontal magnetic field perturbation B_x is a constant in the case of the Alfvén wave but depends on the wave vector k_z in the case of whistler and kinetic Alfvén waves and is related to the dispersive property of these waves.

driving reconnection (Mandt *et al.*, 1994) and the characteristic outflow speed is the whistler phase speed based on the upstream magnetic field $\tilde{B}_0$.

Importantly, for a given value of $\tilde{B}_0$ the outflow velocity increases with k (see Eqs. (3.8) and (3.11)) or inversely with the width of the dissipation region δ. This is very different from reconnection driven by the Alfvén wave. A consequence is that the total flux of electrons from the dissipation region $n\tilde{v}_x$ is insensitive to δ and therefore the mechanism that breaks the frozen-in condition. The implication of this result is that the rate of reconnection should also not depend on the mechanism that breaks the frozen-in condition. Computer simulations of reconnection support this hypothesis (Shay and Drake, 1998; Hesse *et al.*, 1999; Birn *et al.*, 2001). In Fig. 3.4 we show results from the GEM Reconnection Challenge project (Birn *et al.*, 2001), in which the reconnected flux is shown as a function of time for a series of simulations with an MHD model, a Hall MHD model (including the $\mathbf{j}\times\mathbf{B}$ and $\nabla\cdot\mathbf{P}_\mathrm{e}$ terms in Ohm's law), a hybrid model (massless, fluid electrons and particle ions), and a PIC model. All of the models but MHD include the dynamics of whistlers and the runs were carried out with identical Harris equilibria with finite initial field perturbations. The rate of reconnection is the slope of the curve of reconnected flux. All models but MHD have indistinguishable rates of reconnection, which greatly exceed the MHD rate (obtained with uniform resistivity corresponding to a Lundquist number of 200). Since the mechanism that breaks the frozen-in condition in the various models differs (finite electron mass in the case of the PIC simulation and a hyper-resistivity in the other non-MHD models) these simulations confirm the insensitivity of the rate of reconnection to the dissipation mechanism if dispersive whistlers are included in the dynamics.

The GEM challenge did not address the question how the thin current sheet and the initial island were formed. Therefore, another collaborative study was performed to address this question (Birn *et al.*, 2005). This study grew out of a workshop on Magnetic Reconnection Theory, held in 2004 at the Isaac Newton Institute, Cambridge, UK, and was therefore dubbed the *Newton Challenge*. The simulations started from a current sheet that was four times thicker, in relation to the ion inertia

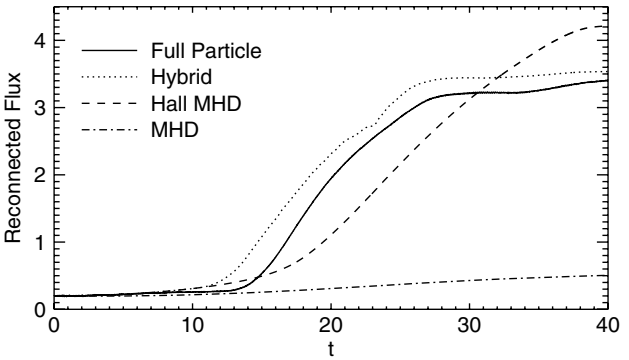

Fig. 3.4. Reconnected magnetic flux as function of time for various simulations of the GEM Reconnection Challenge project (Birn *et al.*, 2001), including an MHD model, a PIC model, a hybrid model, and a Hall MHD model, using the same initial conditions and parameters. The slope of the curves is the reconnection rate and is essentially the same for all models that include the Hall term (whistler dynamics).

length, than that in the GEM challenge, and current sheet thinning and the onset of fast reconnection was initiated by temporally limited, spatially varying inflow of magnetic flux. The simulations showed again fast reconnection, independent of the dissipation mechanism, when the Hall/whistler dynamics was included, consistent with the GEM study. Further evidence comes from PIC simulations where it has also been shown that the rate of reconnection is insensitive to the value of the electron mass (Shay and Drake, 1998; Hesse *et al.*, 1999; Pritchett, 2001b; Ricci *et al.*, 2002).

Thus, the dispersive property of the whistler, which controls the outflow of electrons from the dissipation region in antiparallel reconnection, renders reconnection insensitive to the mechanism that breaks the frozen-in condition. This result has the desirable consequence that the details of a kinetic model might not be required to model reconnection in large systems.

Structure of the electron dissipation region In the case of reconnection with no initial guide field the electron dissipation region is the narrow region around the reversal region where the electrons become demagnetized and decouple from the magnetic field. The width δ_e of this demagnetized electron region can be obtained using the conservation of canonical momentum, $p_y = m_\mathrm{e} v_y - eB'_x z^2/2c$, and energy, where $B'_x = \mathrm{d}B_x/\mathrm{d}z$. For a typical particle with the thermal velocity v_te,

$$\delta_\mathrm{e} = \sqrt{\frac{2v_\mathrm{te}}{\Omega'_{\mathrm{e}x}}}, \tag{3.12}$$

which is a hybrid of the electron Larmor radius based on the asymptotic magnetic field and the magnetic scale length $L_B = B_x/B'_x$ (Laval *et al.*, 1966). This expression, however, does not pin down the characteristic scale of the dissipation region because both the magnetic scale length and possibly the thermal velocity have to be determined self-consistently. For example, even if the inflowing electrons are very cold, the dissipation region is still expected to have a finite scale. The self-consistent

scaling can be determined by requiring that the electrons bouncing in the unmagnetized region balance the magnetic pressure and at the same time requiring that the current carried by the electrons within the dissipation region generate the jump in magnetic field across the layer. These two conditions, $B_x^2/2\mu_0 = m_e n v_b^2/2$ and $\delta_e v_b = d_e v_{Aex}$, yield the width of the current layer δ_e and the electron bounce velocity v_b in the dissipation region,

$$\delta_e = d_e, \tag{3.13}$$

$$v_b = v_{Aex}, \tag{3.14}$$

where the electron Alfvén velocity v_{Aex} should be evaluated just upstream of the electron current layer. This width is consistent with the data shown in Fig. 3.2. Note that the width of the electron current layer is independent of the magnetic field jump across the layer. If the electron thermal velocity of the inflowing plasma exceeds the electron Alfvén speed, the layer will be broader than in Eq. (3.13) so d_e is the minimum value of the width of the electron dissipation region. Simulations reveal that the minimum width is actually around $2d_e$ (Zeiler *et al.*, 2002).

How the electrons trapped in the unmagnetized region reach velocities as high as the electron Alfvén speed is not obvious. The inflow velocity associated with reconnection is a small fraction of v_{Aex} and is therefore not the driver. This inner electron region develops a substantial electric field E_z due to excess electrons at the turning points of their bounce motion in the unmagnetized region. This field points outward from the neutral line and accelerates the electrons into the unmagnetized region, producing the counterstreaming electron beams that make up distribution function at the X-line (Zeiler *et al.*, 2002; Swisdak *et al.*, 2005). Thermal spreading blurs the fine-scale structure of this layer when the electron thermal velocity approaches the electron Alfvén speed.

With the width of the dissipation region given in Eq. (3.13), an estimate of the electron outflow velocity from the electron dissipation region can be obtained. Equations (3.8) and (3.11) yield $k \sim 1/d_e$ so that

$$\tilde{v}_{ex} \sim v_{Aex}. \tag{3.15}$$

The scaling of the electron outflow velocity with the electron Alfvén speed was demonstrated in 2D hybrid simulations by varying the electron mass (Shay *et al.*, 2001). Outflow velocities consistent with this scaling have also been measured in full particle simulations (Hoshino *et al.*, 2001a).

Reconnection with a guide field

The introduction of an ambient magnetic field in the out-of-plane direction (the *guide field*), along the current direction, substantially changes the structure of the dissipation region even at rather low values of the guide field. With this additional magnetic field the out-of-plane inductive electric field that drives reconnection has a component parallel to the magnetic field and the resulting parallel acceleration of electrons produces strong out-of-plane currents, in contrast to the cross-field currents that dominate the antiparallel reconnection dynamics. The in-plane components of the parallel electron flows along newly reconnected field lines drive a pronounced

density asymmetry across the reconnection layer that couples reconnection to a kinetic Alfvén wave (Aydemir, 1992; Kleva *et al.*, 1995; Cafaro *et al.*, 1998). Thus, it is the kinetic Alfvén wave that drives the electron outflow from the X-line rather than the whistler. The guide field also suppresses the unmagnetized bounce motion of electrons that defines the width of the electron current layer in the antiparallel reconnection case. The result is that the electron current layer narrows substantially and surprisingly has a width that scales with the electron Larmor radius (Hesse *et al.*, 2002, 2004). A consequence is that the nongyrotropic behavior of electrons survives even when the guide field is large (see Section 3.2).

Coupling to kinetic Alfvén waves In Fig. 3.5 we show the out-of-plane current density j_y, the electron density n_e, and the parallel electric field from a simulation with an ambient guide field equal to the reversed field. Clearly seen in the plot of the density is the depletion of the density along two of the separatrices and enhancements along the remaining separatrices (Tanaka, 1996; Pritchett and Coroniti, 2004; Drake *et al.*, 2005). This density asymmetry is the signature of the kinetic Alfvén wave. A diagram showing the essential physics appears in Fig. 3.6 (Kleva *et al.*, 1995). A parallel electric field on newly reconnected field lines drives a parallel electron flow across the current layer, depleting the electron density on one side of the current layer and enhancing it on the other. The resulting electric field causes the ions to polarization drift across the current layer to charge neutralize the electrons. A surprise is the magnitude of the electron density depletion, which yields cavity densities as low as a few percent of the ambient background. The separatrix with the enhanced density in Fig. 3.5 carries most of the current and the result is a distinct twist of the current layer that is in contrast with the distinctly symmetric layer in the case of zero guide field. The perturbations of the kinetic Alfvén wave can be calculated as in the case of no guide field,

$$\tilde{B}_y = \sqrt{\mu_0 nT}\frac{\tilde{B}_0}{B_y}\sin(kz)\sin(kv_p t), \tag{3.16}$$

$$v_p = kd_e\frac{B_z}{B}c_{se}, \tag{3.17}$$

$$\tilde{n}T = -B_y\tilde{B}_y, \tag{3.18}$$

where $c_{se} = \sqrt{T/m_e}$ is the electron sound speed. As in the case of the whistler and Alfvén waves the outflow velocity $\tilde{v}_x$ is given in Eq. (3.8) but with the phase speed given in Eq. (3.17). In the case of a strong guide field the flow speeds are below the magnetosonic speed so the density and out-of-plane magnetic field perturbations are in pressure balance as given in Eq. (3.18). As in the case of the whistler wave, the kinetic Alfvén wave speed increases as the layer width decreases for a fixed value of the upstream magnetic field $\tilde{B}_0$. While there have been no reported scaling studies of the electron outflow velocity in the case of guide-field reconnection, the phase speed of the wave in Eq. (3.17) suggests that the outflow speed should scale with the electron sound speed.

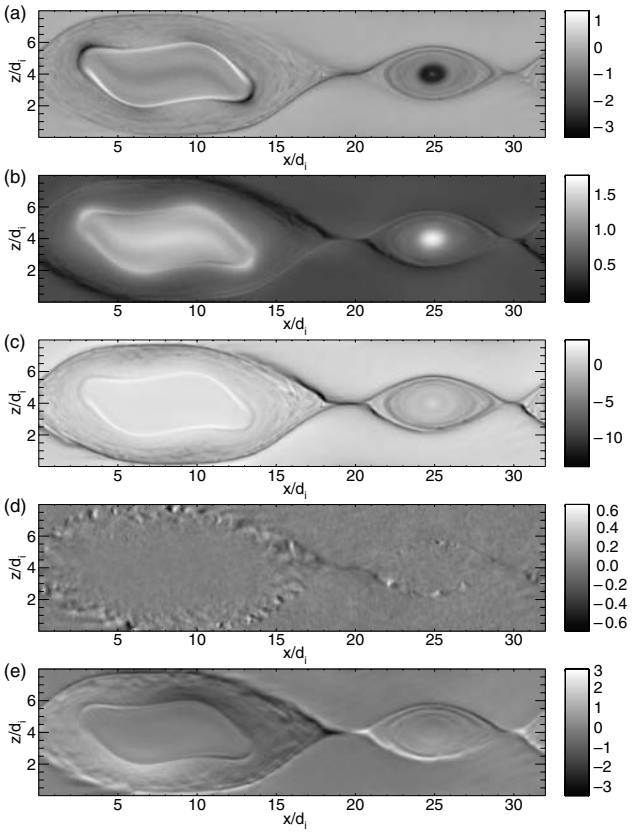

Fig. 3.5. Data from a PIC simulation of reconnection with a guide field (initially uniform) equal in magnitude to the reversed field. Other parameters are $m_\mathrm{i}/m_\mathrm{e} = 100$, $T_\mathrm{i}/T_\mathrm{e} = 12.0$, and $c = 20.0$. Shown are: (a) the current density j_y; (b) the electron density; (c) the electron parallel velocity $v_{\|\mathrm{e}}$; (d) the parallel electric field $E_\|$; and (e) the Hall electric field E_z. Noticeable are the canting and narrowing of the current layer at the X-line compared with the antiparallel case in Fig. 3.2, the density cavities that map two of the four separatrices connected to the X-line, the localization and structuring of the parallel electric field in the low-density cavities, the large parallel electron velocities that are a conseqence of acceleration by the parallel electric field in the low-density cavities, and the strong transverse Hall electric fields that maintain charge neutrality in the density cavities. The density asymmetry across the dissipation region reflects the coupling to the kinetic Alfvén wave. The development of the secondary magnetic island is typical during reconnection with a guide field.

Based on the simple 1D wave model, the values of the guide field and plasma β where the dispersive whistler and kinetic Alfvén waves dominate the dynamics of the inner dissipation region or where there are no dispersive waves have been identified (Rogers *et al.*, 2001). A detailed computational exploration remains to be completed.

An important remaining question is how large the guide field has to be in order to magnetize the electrons in the dissipation region and therefore impact the dynamics

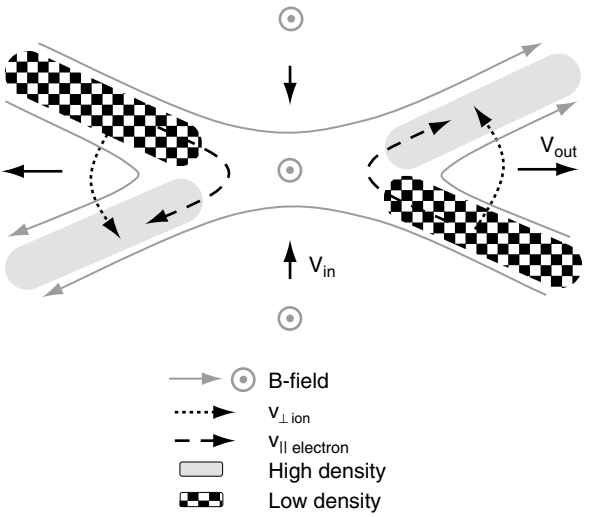

Fig. 3.6. Schematic of the structure of the dissipation region during reconnection with a guide field. Compression of parallel electron flows on newly reconnected field lines leads to a density asymmetry across the dissipation region in contrast to the symmetric system with no guide field. Ions polarization drift across the magnetic field to charge neutralize the electrons.

from that in an ideal system with no guide field. The dynamics of the antiparallel system should significantly change if the ambient guide field is sufficient to magnetize electrons injected into the reversal region. The inflow velocity of electrons is around $0.1v_{\mathrm{A}ex}$ – that is, around 0.1 of the outflow velocity of the electrons. The effective Larmor radius ρ_{g} of electrons with this velocity in the guide field is $\rho_{\mathrm{g}} = 0.1v_{\mathrm{A}ex}/\Omega_{ey}$, where $\Omega_{ey} = eB_y/m_{\mathrm{e}}$ is the cyclotron frequency in the guide field. The condition $\rho_{\mathrm{g}} < d_{\mathrm{e}}$ yields

$$B_y > 0.1B_x \tag{3.19}$$

as the condition for which the guide field can no longer be neglected in *antiparallel* reconnection (Swisdak *et al.*, 2005). Thus, only very small guide fields are required to alter the electron dynamics. We emphasize that much larger guide fields are required to alter the dynamics of ions.

Structure of the parallel electric field and the electron dissipation region In the absence of a guide field the electron dissipation region has a width that is comparable to the electron skin depth. A guide field can prevent the bounce motion of electrons across the current layer that controls the dynamics in the antiparallel field case, resulting in even narrower current layers. The electron dissipation region in the case of a guide field is controlled by the parallel electron current and therefore the parallel electric field. This parallel field is given approximately by

$$E_{\parallel} = -\partial A_y/\partial t - \nabla_{\parallel}\Phi, \tag{3.20}$$

where A_y is the y component of the vector potential that defines the in-plane magnetic field $\nabla A_y \times \hat{y}$, and $\nabla_\parallel \Phi$ is the parallel component of the electrostatic field. The latter is generated due to the parallel bunching of electrons. At a location where the in-plane magnetic field reverses, the parallel electrostatic field vanishes ($\nabla_\parallel \Phi = 0$) and reconnection generates a finite parallel electric field. The structure of Φ controls the spatial localization of $E_\parallel$. If the charge perturbation associated with electron parallel bunching can be balanced by the cross-field motion of either the electrons or ions, the parallel electric field can remain nonzero. Otherwise the electrostatic field cancels the inductive field and the electrons short out the parallel reconnection electric field (Drake and Lee, 1977). The electrons satisfy a kinetic equation based on drift orbits given by

$$\frac{\partial \tilde{f}}{\partial t} + v_\parallel \nabla_\parallel \tilde{f} + \frac{f_0}{B\Omega_\mathrm{e}} \frac{\mathrm{d}}{\mathrm{d}t} \nabla_\perp^2 \Phi + \frac{e}{m_\mathrm{e}} E_\parallel \frac{\partial f_0}{\partial v_\parallel} = 0, \tag{3.21}$$

where $f(\mathbf{x}, v_\perp, v_\parallel) = f_0 + \tilde{f}$ is the distribution function and the third term arises from the polarization drift. Because the electron layer is typically much smaller than an ion Larmor radius, the ion response to the potential must include the full ion orbital dynamics. Only the motion perpendicular to the magnetic field must be included. The ion density perturbation, $\tilde{n}_\mathrm{i}$, is given by

$$\tilde{n}_\mathrm{i} = [\Gamma_0(b) - 1] \frac{e\Phi}{T_\mathrm{i}} n_0, \tag{3.22}$$

$$\Gamma_0(b) = I_0(b) e^{-b}, \qquad b = -\rho_\mathrm{i}^2 \partial^2 / \partial z^2, \tag{3.23}$$

where $\rho_\mathrm{i} = \sqrt{T_\mathrm{i}/m_\mathrm{i}}/\Omega_\mathrm{i}$ is the ion Larmor radius and I_0 is the modified Bessel function. Equating this density perturbation with that of the electrons by solving Eq. (3.21), we find an equation for the potential as follows:

$$\nabla_\parallel H \Phi = -\frac{T_\mathrm{i}}{T_\mathrm{e} + T_\mathrm{i}} E_\parallel(0) + \frac{T_0}{n_0 e} \int \mathrm{d}v_\parallel \nabla_\parallel \tilde{h}, \tag{3.24}$$

$$\left(\frac{\partial}{\partial t} + v_\parallel \nabla_\parallel \right) \tilde{h} = \frac{e}{T_\mathrm{e}} f_0 \dot{E}_\parallel, \tag{3.25}$$

where

$$\nabla_\parallel \tilde{h} \equiv \nabla_\parallel \tilde{f} + \frac{e f_0}{T_\mathrm{e}} \left(E_\parallel + \rho_\mathrm{e}^2 \nabla_\parallel \frac{\partial^2 \Phi}{\partial z^2} \right), \tag{3.26}$$

$$H = \Gamma_0 \frac{T_0}{T_\mathrm{i}} - 1 + \rho_{\mathrm{e}0}^2 \frac{\partial^2}{\partial z^2}, \tag{3.27}$$

$$T_0 = \frac{T_\mathrm{e} T_\mathrm{i}}{T_\mathrm{e} + T_\mathrm{i}}, \qquad \rho_{\mathrm{e}0}^2 = T_0 \rho_\mathrm{e}^2 / T_\mathrm{e}, \tag{3.28}$$

and $\rho_{\mathrm{e}0}$ is the effective electron Larmor radius based on the hybrid temperature T_0. The operator H in Eq. (3.27) controls the response of the potential Φ to the parallel inductive electric field. The spatial structure of the parallel electric field therefore is controlled by this operator and the basic scales involved can be deduced from its zeros. Taking $\partial/\partial z \sim 1/\delta$ the zeros of H yield two distinct scales δ: the effective

electron Larmor radius ρ_{e0} based on the hybrid temperature T_0; and the effective ion Larmor radius $\rho_s = \sqrt{T_e}/m_i$. Earlier models of reconnection with a guide field had suggested that the transverse scale of $E_\parallel$ was the ion scale ρ_s, which is inconsistent with recent simulations (Hesse *et al.*, 2002, 2004; Swisdak *et al.*, 2005) that suggest that the parallel electric field is much more localized with a transverse scale given by the electron Larmor radius.

The structure of $E_\parallel$ can be deduced from Eqs. (3.24) and (3.25). For simplicity we consider simple linear tearing perturbations for which $\nabla_\parallel = ik_x z B_x'/B_y$. At $z = 0$ the $\tilde{h}$ term in Eq. (3.25) balances the inductive drive term but for $z \gtrsim \rho_{e0}$, $\tilde{h} \to 0$ and $\rho_{e0}^2 \partial^2/\partial z^2 \ll 1$. Since $\Gamma_0 \sim 0$ at scales below the ion Larmor radius, we find that $\nabla_\parallel \Phi \sim eq - (T_i/(T_i + T_e))\dot{A}_y/c$ or

$$E_\parallel = E_\parallel(0)\frac{T_e}{T_i + T_e}. \tag{3.29}$$

For $T_i \gg T_e$ the parallel electric field has dropped to a small fraction of its value at $z = 0$. $E_\parallel$ remains approximately constant at this level until $z \gtrsim \rho_s$ when $\Gamma_0 \sim 1$ and $\nabla_\parallel \phi \sim eqE_\parallel(0)$ so that $E_\parallel \sim eq0$. Earlier theories in which $E_\parallel$ remained constant out to ρ_s were valid only in the limit of zero ion temperature. In most space physics applications $T_i \gg T_e$ so the tranverse scale of $E_\parallel$ is effectively ρ_{e0}.

This analysis of the transverse structure of $E_\parallel$ does not provide information about the structure of $E_\parallel$ along the magnetic field. For example, after reconnection has approached quasi-steady conditions in a large system, what is the spatial extent of the region where $E_\parallel = 0$? Is this region localized to the X-line or does it extend large distances along the magnetic separatrices? The spatial extent of this region impacts the number of electrons that can be accelerated by the parallel electric field during magnetic reconnection and therefore the fraction of energy transferred from the magnetic field into electrons, a broadly important issue in essentially all reconnection applications.

The spatial extent of $E_\parallel$ is controlled by the dynamics of the standing kinetic Alfvén wave that is driven in the vicinity of the X-line. The deep density cavities produced along two of the four separatrices emanating from the X-line shown in Fig. 3.5 are regions where the reconnection electric field can maintain a finite $E_\parallel$ that extends a significant distance from the X-line (Pritchett and Coroniti, 2004). This is because the very low density of these cavities makes it more difficult for electrons to bunch and short out the parallel electric field. The spatial extent of $E_\parallel$ is therefore linked to the spatial extent of the density cavities. The cavities are formed as electrons approach the separatrix and are accelerated toward the X-line by the parallel electric field. The high parallel mobility of these low-mass particles allows the electric field to nearly evacuate the separatrix. The limit on the length of these density cavities has been linked to the upper limit on the in-plane current that results from the flow of electrons toward the X-line – that is, longer cavities require more current for their formation (Drake *et al.*, 2005). The in-plane current produces a self-consistent field $\tilde{B}_y$ whose pressure must be balanced by depressions in the local pressure and in-plane magnetic field. The result is an upper limit on the

length L_c of the cavities and a corresponding upper limit on the electron velocity $v_{\|}$ that results from parallel acceleration in these cavities,

$$L_c = 5d_i(1+\beta_x)B_x/B_y, \tag{3.30}$$

$$v_{\|} = \alpha\frac{(1+\alpha^2/4c^2)^{1/2}}{1+\alpha^2/2c^2}, \tag{3.31}$$

$$\alpha \equiv v_{Aex}(1+\beta_x)^{1/2}, \quad \beta_x = n(T_e+T_i)/B_x^2. \tag{3.32}$$

The energetic beams that are produced in these acceleration cavities are injected into the X-line so that the total current driven at the X-line during reconnection with a guide field is not just a result of local acceleration but is a more complex nonlocal process. The high-velocity beams produced in these acceleration cavities can also generate fluctuations over a broad range of frequencies (Cattell *et al.*, 2005). The impact of these fluctuations on the electron beams and reconnection remains an ongoing research topic. Can, for example, the electron-ion drag induced by these fluctuations compete with the nongyrotropic pressure in balancing the reconnection electric field at the X-line during steady reconnection?

3.1.2 Scaling of kinetic reconnection to macroscale systems

A second important result of the kinetic modeling concerns the scaling of the dissipation region with the system size. As discussed earlier, the reconnection rate is strongly dependent on the aspect ratio of the dissipation region, δ/Δ as defined in Eq. (3.1). In the Sweet–Parker model the dissipation region has a length that scales with the macroscopic system length L (Section (2.1)) and the small aspect ratio, δ/Δ leads to slow reconnection. In contrast, in Petschek's model, slow shocks bound the plasma flowing away from the X-line and are responsible for the outflow acceleration. Since in this model most of the outflowing plasma does not need to pass through the dissipation region, the length of the dissipation region Δ can be small compared with the system size, and according to Eq. (3.1) this allows for an enormous increase in the reconnection rate. Flux conservation through the slow shocks yields $v_{in} \sim v_{out}\tan\theta \sim v_{Ax}\theta$, where θ is the angle that the slow shocks make with the x axis. Comparing this relation with Eq. (3.1), we find that the opening angle of the outflow is directly related to the aspect ratio of the dissipation region.

While this open geometry does not appear in uniform-resistivity MHD models (Biskamp, 1986), it does appear in all of the models that couple to dispersive waves in the dissipation region (Shay *et al.*, 1999; Rogers *et al.*, 2001; Shay *et al.*, 2004). Why does wave dispersion allow the outflow region to open up as proposed by Petschek? The opening process is shown in Fig. 3.7 in a time sequence of the out-of-plane current from a numerical simulation of the transition from Sweet–Parker to Hall reconnection. The out-of-plane current is directly linked to the ion acceleration away from the X-line (via $\mathbf{j}\times\mathbf{B}$ force) and provides a good visualization tool for the reconnection geometry. In this simulation a system with steady Sweet–Parker reconnection was taken as an initial condition. The resistivity was reduced so that the width of the Sweet–Parker dissipation region fell below d_i. The transition was then triggered as the outflow jet opened sharply and the corresponding rate of reconnection increased.

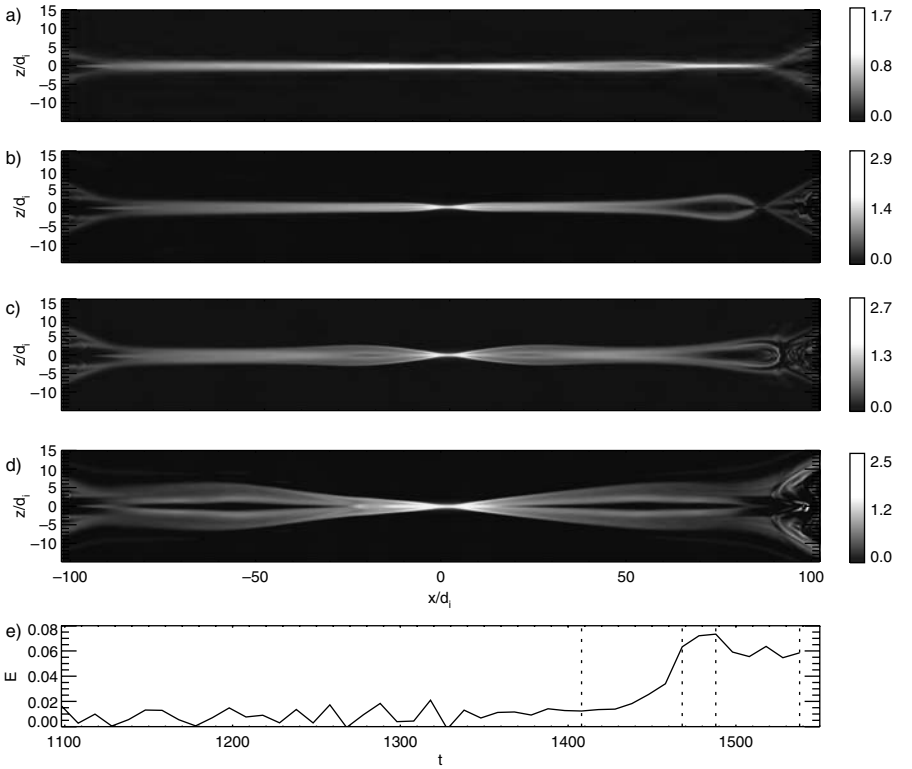

Fig. 3.7. Transition from Sweet–Parker to Hall reconnection. From a double current sheet simulation with system size $409.6c/\omega_{\rm pi} \times 204.8c/\omega_{\rm pi}$. Initially the system has a resistivity, or inverse Lundquist number, of $\eta = 0.015$ (based on a normalization using the length scale $c/\omega_{\rm pi}$ and the time scale $1/\Omega_{\rm ci}$). At $t = 1098$, the resistivity is lowered to 0.007. In (a)–(d) the total current along y as time progresses and in (e) the reconnection electric field versus time. The time of each figure in (a)–(d) is denoted by a dashed vertical line in (e). Figure provided by Paul Cassak.

Again, a rigorous theory of the connection between the X-line and the Petschek outflow solution has not been carried out but the essential physics of this transition can be understood from arguments similar to those used to analyze the outflow from the 1D waves. Instead of a simple 1D system depending only on z, we consider an initial condition with slow variation in the x direction corresponding to an open outflow geometry. Taking x to be the distance downstream of the X-line, $B_z \sim x$, $\tilde{B}_0 \sim x$ and the width of the outflow region $\delta \sim x$ so that $k \sim x^{-1}$. Through the incompressibility condition $\nabla \cdot \mathbf{v} = 0$ the x variation of the outflow velocity $\tilde{v}_x$ with distance from the X-line controls the contraction or expansion of the outflow jet in the z direction. If $\tilde{v}_x$ increases with x, then $\partial \tilde{v}_z / \partial z < 0$ and the outflow jet will constrict, reducing the rate of reconnection. On the other hand, if $\tilde{v}_x$ decreases with x, the outflow jet will expand into the Petschek open outflow configuration. Along the symmetry line $z = 0$ the outflow velocity scales like $v_{\rm p} \sin(k v_{\rm p} t)$ so the variation

of the phase speed $v_{\rm p}$ with distance x controls the structure of the outflow jet. In the MHD case $v_{\rm p} \sim x$ so that

$$\partial \tilde{v}_z / \partial z < 0 \tag{3.33}$$

and the outflow jet contracts in the z direction as was seen in earlier MHD simulations (Uzdensky and Kulsrud, 2000). In the case of whistler driven outflow $v_{\rm p}$ is a constant and $\tilde{v}_x$ decreases with x so that

$$\partial \tilde{v}_{ze} / \partial z > 0. \tag{3.34}$$

In this case the outflow jet expands in the z direction as shown in Fig. 3.7 and leads to the open outflow configuration of Petschek and fast reconnection.

Thus, in the case of the whistler the increase of the width of the outflow jet and the increase of the magnetic field with distance downstream counterbalance so that the whistler phase speed is nearly constant, allowing the outflow jet to remain open. This behavior is, of course, linked to the dispersive property of the whistler.

The simulations performed showing this open outflow geometry via Hall physics are quite small compared to the actual physical systems which exhibit reconnection such as the solar corona and the Earth's magnetosphere. It is therefore important to show that the length of the dissipation region Δ is independent of system size L. Even a weak dependence can cause an extreme slowdown of reconnection when extrapolated to real systems. For the antiparallel case, a study using hybrid simulations of the double tearing mode yielded reconnection inflow velocities of $0.1 v_{\rm A}$ with no dependence on system size (Shay *et al.*, 1999). Recently, this result has been confirmed with two-fluid simulations of a system with open boundary conditions (Huba and Rudakov, 2004). The independence of the rate of reconnection from system size can be visualized in Figs. 3.7c and d. In these figures, the angle θ that the open current wedge makes with the x axis is established locally around the X-line and then propagates outwards. By the time of Fig. 3.7d, this wedge of current has propagated about 1/2 of the total system size, with no appreciable change in the angle θ. The angle θ, therefore, is set up locally at the X-line, independent of system size.

Reconnection rates on the order of $0.1 v_{\rm A}$ yield time scales for global energy release and magnetic reconfiguration that are consistent with those seen in solar flares and magnetospheric substorms. In a typical X-class flare, reconnection drives a global energy release, in the form of hard and soft X-ray emissions that last around 100 seconds. With rough estimates of the magnetic field and density in the solar corona ($B \approx 100\,{\rm G}$ and $n \approx 10^{10}\,{\rm cm}^{-3}$), the reconnection inflow velocity is around $2 \cdot 10^7\,{\rm cm/s}$. A typical magnetic flux tube involved in a flare has an area of $10^{18}\,{\rm cm}^2$ and a length of $10^9\,{\rm cm}$, giving a time of 50 s to reconnect much of the magnetic field in the flux tube, which is consistent with the duration of typical flares (Miller *et al.*, 1997). During a substorm, a significant fraction of magnetotail lobe flux is reconnected causing a massive dipolarization of the magnetotail. Typical values of lobe properties ($B \approx 15\,{\rm nT}$ and $n \approx 0.05\,{\rm cm}^{-3}$) yield a reconnection inflow speed of 150 km/s. In around 10 minutes, a typical time scale for the expansion phase of a substorm, about 15 $R_{\rm E}$ of magnetic flux in the lobes can reconnect.

The results that the reconnection rate is insensitive to system size and electron dissipation are not without controversy. The above results have been questioned

in studies of forced reconnection and double tearing mode reconnection, where it has been found that either the reconnection rate or the time scales of reconnection have a dependence on electron dissipation and system size (d_i/L and ρ_s/L) (Grasso *et al.*, 1999; Wang *et al.*, 2001; Porcelli *et al.*, 2002; Fitzpatrick, 2004; Bhattacharjee *et al.*, 2005). An example will be discussed in Section 3.4. Some of the disparities may arise from differences in the definition of the reconnection time – whether or not to include the initiation phase when the island width $w \sim d_\mathrm{i}, \rho_\mathrm{s}$ – or from the difficulty in identifying weak dependencies, such as a 1/6-th power electron mass dependence discussed in Section 3.4. It is also not clear to what extent simulations with contrasting results cover identical regimes of the evolution. More studies with $w \gg d_\mathrm{i}, \rho_\mathrm{s}$ will be necessary to settle this question.

3.1.3 Transitions from slow to fast reconnection

The structure and rate of reconnection in the collisional MHD model differ drastically from that of the Hall reconnection model. An important question is how systems with finite resistivity undergoing reconnection transition between the two states. Do the rates of reconnection change continuously between the two regimes or is there a sharp transition? Is the transition related to the observed onset of reconnection, e.g., in the onset of solar flares or of sawtooth events in laboratory tokamak experiments? In the environment of the Earth's magnetosphere this issue is probably of less importance because of the absence of resistivity.

For a given plasma resistivity, rather general arguments suggest that there are two stable solutions (fast and slow) to the reconnection problem for a given value of the plasma resistivity (Cassak *et al.*, 2005). The Sweet–Parker solution, governing slow reconnection, is valid provided the half-width of the current layer δ exceeds the relevant kinetic scale lengths,

$$\frac{\delta}{L} = \sqrt{\frac{\eta}{\mu_0 v_\mathrm{A} L}} > \frac{d_\mathrm{i}}{L}, \frac{\rho_\mathrm{s}}{L}, \tag{3.35}$$

where the magnetic field is to be evaluated immediately upstream of the current layer. For the antiparallel reconnection case, this reduces to

$$\frac{\eta_\mathrm{sf}}{\mu_0} \sim \frac{v_\mathrm{A} d_\mathrm{i}^2}{L}, \tag{3.36}$$

so Sweet–Parker reconnection is valid for $\eta > \eta_\mathrm{sf}$. For example, in the solar corona, $n \sim 10^{16}\,\mathrm{m}^{-3}$, $L \sim 10^7\,\mathrm{m}$ and $B \sim 10^{-2}\,\mathrm{T}$ (Miller *et al.*, 1997), so $\eta_\mathrm{sf} \sim 10^{-6}\,\mathrm{ohm/m}$ in MKS units, corresponding to a temperature of $10^2\,\mathrm{eV} \sim 10^6\,\mathrm{K}$.

The converse condition, that resistivity be sufficiently small to not impact the whistler or kinetic Alfvén dynamics that drive kinetic reconnection, yields a distinct condition. As in the Sweet–Parker analysis, we balance resistive diffusion with convection at the electron inertial scale d_e,

$$\frac{\eta_\mathrm{fs}}{\mu_0 d_\mathrm{e}^2} \sim \frac{v_\mathrm{in,e}}{d_\mathrm{e}} \sim 0.1 \frac{v_\mathrm{Ae}}{d_\mathrm{e}},$$

or

$$\frac{\eta_{\rm fs}}{\mu_0} \sim 0.1 v_{\rm A} d_{\rm i}, \tag{3.37}$$

with $v_{\rm A}$ evaluated upstream of the electron current layer. The fast reconnection solution is valid if $\eta < \eta_{\rm fs}$. The value of $\eta_{\rm fs}$ is independent of system size and is enormous for most physical systems. Equation (3.37) suggests that once fast reconnection onsets, resistive effects are unlikely to influence the dynamics.

In typical systems of interest the ratio of $\eta_{\rm sf}$ to $\eta_{\rm fs}$ is very small,

$$\frac{\eta_{\rm sf}}{\eta_{\rm fs}} \sim 10 \frac{d_{\rm i}}{L} \ll 1, \tag{3.38}$$

because $d_{\rm i} \ll L$ for most systems of physical interest. For example, the ratio in Eq. (3.38) is 10^{-6} for the data from the solar corona presented earlier. Thus, transitions from fast to slow reconnection occur at much higher resistivities than the reverse, so for a large range of resistivity $\eta_{\rm sf} < \eta < \eta_{\rm fs}$ there are two stable solutions to the reconnection problem.

These theoretical predictions were tested with numerical simulations using a two-fluid code (Cassak *et al.*, 2005). The electron to ion mass ratio was $m_{\rm e}/m_{\rm i} = 1/25$. For a $409.6 d_{\rm i} \times 204.8 d_{\rm i}$ computational domain, the critical resistivities are $\eta'_{\rm sf} \sim 0.01$ and $\eta'_{\rm fs} \sim 0.03$, where $\eta' = \eta/\mu_0 v_{\rm A} d_{\rm i}$ is the normalized resistivity. Larger systems would produce greater separations of $\eta_{\rm sf}$ and $\eta_{\rm fs}$. Shown in Fig. 3.8 are plots of the out-of-plane plasma current from two quasi-steady reconnection simulations of the two-fluid equations. The upper (lower) simulation has a normalized reconnection rate $E' = E/(v_{\rm A} B) = 0.055$ (0.014), corresponding to the fast (slow) reconnection solution. At the time shown both of these simulations have identical parameters: $\eta' = 0.015$. The separate solutions were obtained through differing initial conditions: the slow solution being initialized with resistive initial conditions (adding the Hall terms after

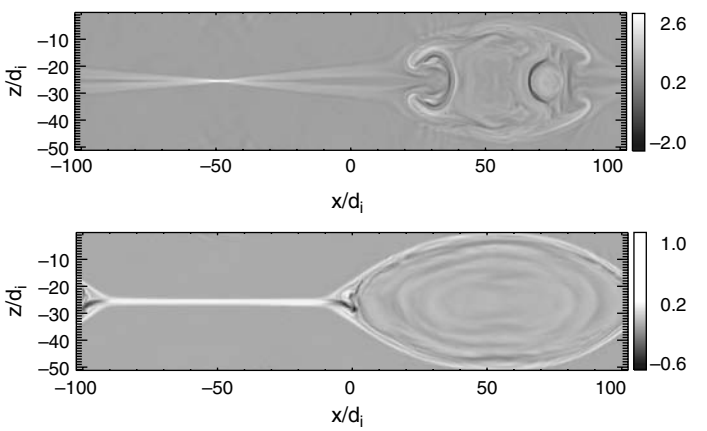

Fig. 3.8. Current density j_y for fast (upper panel) and slow (lower panel) reconnection solutions for a resistivity $\eta' = 0.015$. The parameters of the two runs are identical and each solution remains stable until all of the available flux has reconnected.

a transient initial period); and the fast solution being initialized as collisionless (no resistivity but subsequently including it). The range of resistivity over which there are dual reconnection solutions is apparent in Fig. 3.9, where the reconnection rates and current layer widths are shown versus plasma resistivity. The solid (open) circles correspond to the resistive (collisionless) initial conditions. The range of dual solutions matches well the theoretical estimates. The important result is that the slow solution disappears when the width of the Sweet–Parker current layer falls below d_i and at this point the rate of reconnection abruptly increases. Since the Sweet–Parker reconnection rate decreases with the system size L but the fast rate is independent of L, the jump in the rate of reconnection will be enormous for large-scale systems such as the solar corona. From the condition for the disappearance of the Sweet–Parker solution in Eq. (3.35), a reduction of the local resistivity or an increase in the local Alfvén velocity can trigger the transition. The upstream Alfvén velocity typically increases with time as large magnetic fields convect into the X-line during reconnection so this model yields a clear mechanism for the transition from slow to fast reconnection. Possible applications of such an onset model are the solar corona and disruptions in tokamak fusion experiments. Because of the absence of collisional resistivity in the Earth's magnetosphere, this model cannot explain onset in this system.

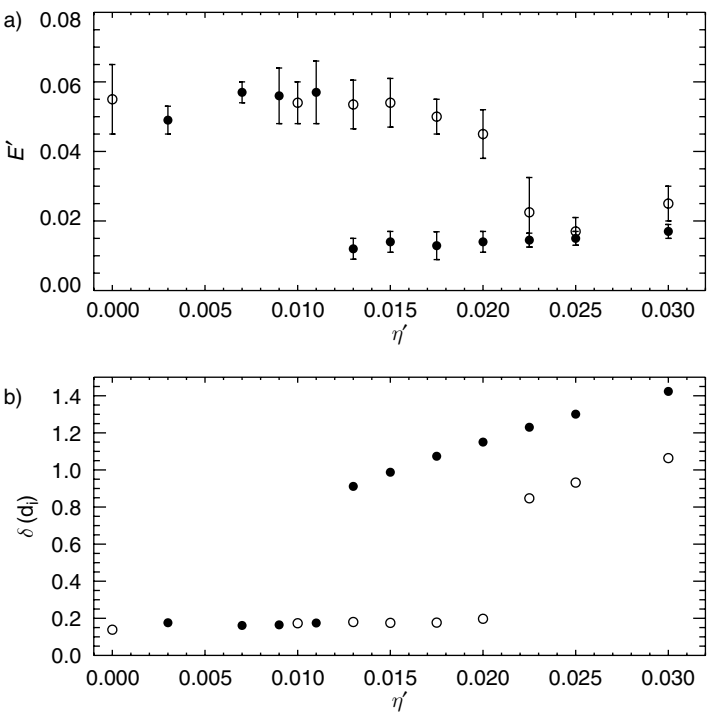

Fig. 3.9. (a) Normalized reconnection rate, $E' = E/Bv_\mathrm{A}$ and (b) current sheet width, δ, as a function of normalized resistivity, $\eta' = \eta/\mu_0 v_\mathrm{A} d_\mathrm{i}$, for runs analogous to those in Fig. 3.8.

3.2 Diffusion region physics

M. Hesse

As discussed in Sections 2.1 and 3.1, in standard resistive MHD models the structure of the reconnection site is characterized by a resistive diffusion region, where dissipation is governed by the Ohmic term ηj^2, embedded in a wide, essentially dissipation-free, region governed by ideal MHD. In the collisonless regime the structure and the dissipation mechanism become more complicated, as illustrated schematically in Fig. 3.1. This is most easily demonstrated by the generalized Ohm's law, derived from the equation of motion of the electron fluid (3.3)

$$\mathbf{E} = -\mathbf{v}_\mathrm{e} \times \mathbf{B} - \frac{1}{ne} \nabla \cdot \mathbf{P}_\mathrm{e} - \frac{m_\mathrm{e}}{e} \left(\frac{\partial \mathbf{v}_\mathrm{e}}{\partial t} + \mathbf{v}_\mathrm{e} \cdot \nabla \mathbf{v}_\mathrm{e} \right), \tag{3.39}$$

where now the ion–electron collision term is neglected. Again, the pressure tensor is defined in the rest frame of the electrons. Joule dissipation is generally defined by $\mathbf{j} \cdot \mathbf{E}'$, where $\mathbf{E}' = \mathbf{E} + \mathbf{v} \times \mathbf{B}$ is the electric field in the plasma rest frame. Since the first term on the right-hand side (RHS) of (3.39) can also be expressed approximately by $-\mathbf{v} \times \mathbf{B} + \mathbf{j} \times \mathbf{B}/ne$ (assuming one singly charged ion species, for simplicity), and the Hall term, $\mathbf{j} \times \mathbf{B}$, does not contribute to the dissipation, it is obvious that the dissipation mechanism must rely on either thermal, i.e., pressure-based (second term on the RHS of Eq. 3.39), or inertial effects (last term on the RHS of Eq. 3.39). Of these, the pressure-based dissipation might rely on current-aligned pressure gradients, or, in regions of sufficiently small magnetic field, on nongyrotropies of the distribution function (Vasyliūnas, 1975; Lyons and Pridmore-Brown, 1990; Hesse and Winske, 1993).

We should note that equations equivalent to (3.39) hold self-consistently for all plasma species, so that, in principle, dissipation could also be derived from the ion pressure and inertia terms. However, these terms are approximately balanced by the Lorentz force $\mathbf{j} \times \mathbf{B}$, so that the net dissipation is given by very small differences between large ion terms, which are in fact related to electron effects. Therefore it is much better to discuss the dissipation directly on the basis of the electron terms.

Owing to its very small size and to a lack of sufficiently fast plasma measurements, the properties of the electron diffusion region have not been clearly identified in spacecraft observations. Thus the physics of the dissipation region remained a mystery until very recently when highly sophisticated computer simulations of collisionless plasmas permitted the study of electron effects. In this section we present an overview of our present understanding of how particles become demagnetized in the diffusion region of the reconnection process. The emphasis of the discussion will be on electrons; however, many results apply equally to ions, after a suitable change of charge and mass. The section focuses primarily on the thermal- or bulk-inertia-based dissipation processes that have been validated in a large number of numerical models.

The structure of this section follows the historical evolution of theoretical research of the diffusion region. Following an introduction of the base model for most simulations in Section 3.2.1, we discuss antiparallel magnetic reconnection in Section 3.2.2. Section 3.2.3 presents an analysis of our present knowledge of guide-field magnetic reconnection, which is arguably the more generic of the two cases. Both sections include summaries of translationally invariant and fully three-dimensional models.

3.2.1 The model and initial configuration

Most of the results presented in this overview are based on the application of particle-in-cell codes. The system studied by many researchers is similar to that selected in the GEM reconnection challenge (Birn *et al.*, 2001). This system is described in the following.

In most of our analysis we employ dimensionless quantities. For this purpose, we normalize densities by a typical density n_0 in the current sheet, and the magnetic field by the asymptotic value of the reconnection magnetic field B_0. Ions are assumed to be protons (mass m_p) throughout, and length scales are normalized by the ion inertial length c/ω_pi, where the ion plasma frequency $\omega_\mathrm{pi} = \sqrt{e^2 n_0/\varepsilon_0 m_\mathrm{p}}$ is evaluated for the reference density. Velocities are measured in units of the ion Alfvén velocity $v_\mathrm{A} = B_0/\sqrt{\mu_0 m_\mathrm{p} n_0}$, based on the reference magnitudes of magnetic field and density. The electric field is measured in units of $E_0 = v_\mathrm{A} B_0$, the pressure in units of $p_0 = B_0^2/\mu_0$, and the current density is normalized to $j_0 = \omega_\mathrm{pi} B_0/c\mu_0$.

The magnetic field represents a modified Harris sheet (Harris, 1962) of the following form:

$$B_x = \tanh(2z) + a_0 \pi/L_z \cos(2\pi x/L_x) \sin(\pi z/L_z), \tag{3.40}$$

$$B_z = -a_0 2\pi/L_z \sin(2\pi x/L_x) \cos(\pi z/L_z). \tag{3.41}$$

The perturbation amplitude $\mathrm{a}_0 = 0.1$ leads to an initial value of the normal magnetic field of about 3% of B_0. The system size matches that of the GEM reconnection challenge by $\mathrm{L}_x = 25.6$ and $\mathrm{L}_z = 12.8$. In addition, we here employ a constant magnetic field component directed along the main current flow,

$$B_y = B_{y0}, \tag{3.42}$$

where B_{y0} is the initial value of the guide field magnitude. The choice of ion–electron mass ratio varies for different studies; it ranges from $m_\mathrm{i}/m_\mathrm{e} = 25$ in the original GEM challenge problem to $m_\mathrm{i}/m_\mathrm{e} = 1836$ in some recent implicit particle-in-cell calculations (Ricci *et al.*, 2002).

The system evolution is modeled by particle-in-cell codes similar to the one used by Hesse *et al.* (1999). Particle orbits are calculated in the electromagnetic fields, and the electromagnetic fields are integrated on a two- or three-dimensional grid.

3.2.2 Antiparallel reconnection

Previous analyses of time-dependent magnetic reconnection (Hewett *et al.*, 1988; Horiuchi and Sato, 1994, 1997; Pritchett, 1994; Hesse *et al.*, 1995; Tanaka, 1995b,a; Cai and Lee, 1997; Hesse and Winske, 1998; Kuznetsova *et al.*, 1998; Shay and Drake, 1998; Hesse *et al.*, 1999; Shay *et al.*, 1999; Hoshino *et al.*, 2001a,b) have begun to shed light on the electron behavior in different parameter regimes, primarily in the regions of low magnetic field. It was found that, for antiparallel magnetic reconnection, deviations from gyrotropy in the electron distribution function can give rise to reconnection electric fields via nongyrotropic electron pressure terms

$$E_y = -\frac{1}{n_e e}\left(\frac{\partial P_{xy}}{\partial x} + \frac{\partial P_{yz}}{\partial z}\right). \tag{3.43}$$

This process can be understood as an inertial effect of thermal electrons which bounce in the field reversal region. It is therefore equivalent to a *thermal inertia* effect, i.e., a mechanism by which particle thermal motion rather than bulk fluid inertia balances the reconnection electric field. This bounce motion was first described by Horiuchi and Sato (1994). Hesse and Winske (1998) performed a particle-in-cell simulation of collisionless reconnection in the GEM geometry. Their analysis showed indeed the presence of electron pressure nongyrotropies near the X-point. The magnitude of these tensor components proved to be sufficient to provide the reconnection electric field via the expression (3.39).

These studies were taken a step further by Hesse *et al.* (1999), who investigated the effect of different electron masses on the collisionless dissipation process in the reconnection region. The target of the investigation was to study whether different physics in the diffusion region might lead to different dissipation, thereby influencing and potentially changing the larger scale behavior of the system under investigation. In order to test the dependence of the reconnection process on the assumed electron mass, Hesse *et al.* (1999) performed a set of simulations with varying ion/electron mass ratio, ranging from $m_i/m_e = 9$ to $m_i/m_e = 100$. Figure 3.10 shows the magnetic field evolution for the run with $m_i/m_e = 25$ with the current density in gray scale. The figure shows that magnetic reconnection, initiated by the initial perturbation, causes large changes of the magnetic field and current density distribution. Figure 3.10 demonstrates two features: The current sheet thickness in the reconnection region is, at all times, somewhat larger than the electron skin depth, and the current density exhibits a saddle-point at the location of the reconnection region. The latter feature becomes most prominent at later times. Similar features were also found in hybrid and particle simulations of a similar system.

The relevant off-diagonal components of the pressure tensor are shown in Fig. 3.11, for a PIC simulation using an ion–electron mass ratio of $m_i/m_e = 256$ (M. Hesse, unpublished). This figure demonstrates that electron pressure nongyrotropies are found even for large mass ratios. Similar results were also found by Pritchett (2001b).

It is apparent from the discussion above that the processes responsible for these electron pressures rely on the inertia of individual electrons, which contributes to all of the fluid terms on the RHS of Eq. (3.39). Heavier electrons should spend more time in the region of low magnetic field, leading to more acceleration and thus stronger reconnection electric fields. Intuitively, one might expect that the electron mass should have a significant impact on the evolution of the system. Figure 3.12 proves that this expectation is essentially incorrect. Figure 3.12 shows, for each of the runs described above, the time evolution of the reconnected magnetic flux, defined by

$$F_{rec} = \int_{X-O} B_z \mathrm{d}x, \tag{3.44}$$

where the integral is taken between the major X- and O-points, if there are more than one of each. Each graph consists of an initial slow growth, typically for the first seven to eight ion cyclotron times, followed by a rapid time evolution. After

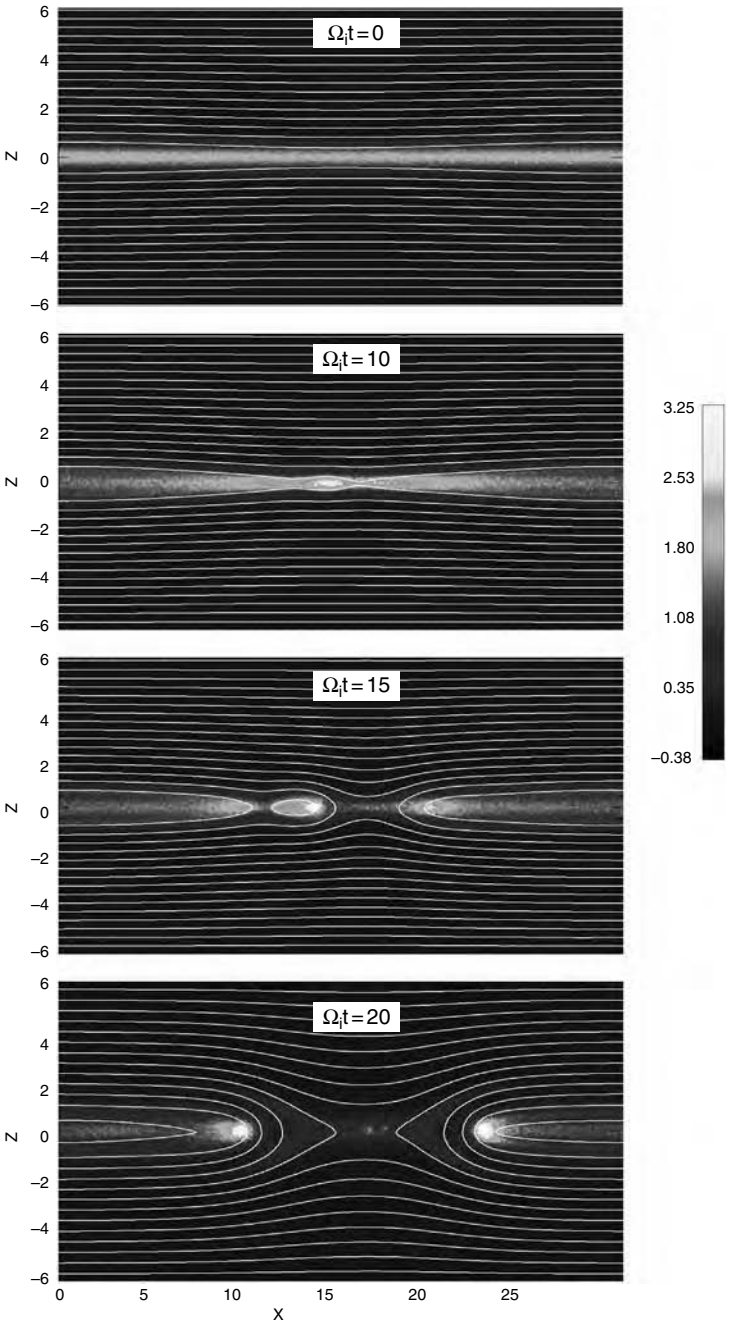

Fig. 3.10. Evolution of the magnetic field and current density (shown in gray scale) in the x, z plane for a simulation with $m_\mathrm{i}/m_\mathrm{e} = 25$, in the absence of a magnetic guide field. After Hesse *et al.* (1999).

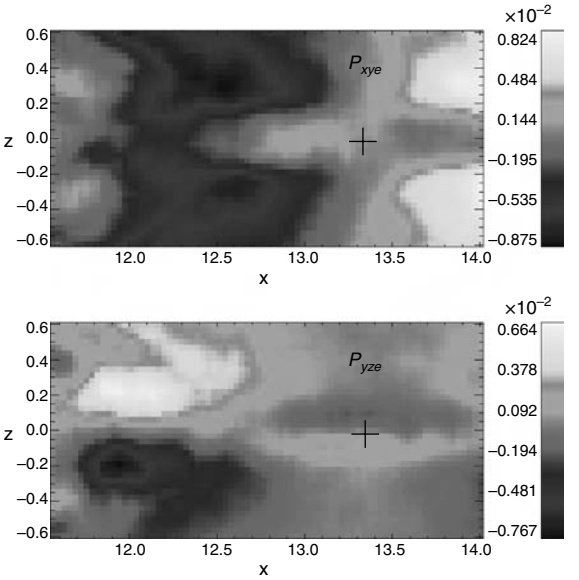

Fig. 3.11. Electron pressure tensor components at the central reconnection site (indicated by the cross-shaped symbol). The tensor components are taken from a calculation with $m_\mathrm{i}/m_\mathrm{e} = 256$. (M. Hesse, unpublished). See also color plate.

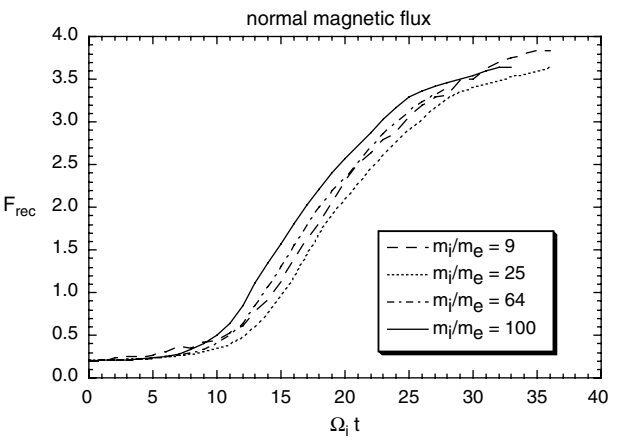

Fig. 3.12. Evolution of the reconnected magnetic flux for different ion–electron mass ratios. After Hesse *et al.* (1999).

that time, the evolution slows down considerably. This is due to a depletion of the magnetic flux in the source regions adjacent to the current sheet which reduces the energy available to power the reconnection process, and a build-up of plasma and magnetic pressure in the magnetic island, which reduces the "pulling" of plasma away from the reconnection region.

A comparison between the different graphs reveals a surprising result: With the exception of a small difference in the duration of the slow evolution, all graphs look essentially alike. This result showed that the electron mass appears to be of little importance to the large-scale evolution, as has been suggested on the basis of hybrid simulations with electron inertia (Shay and Drake, 1998; Shay *et al.*, 1999). In fact, a comparison of other parameters such as velocities and current densities shows striking similarities also (Hesse *et al.*, 1999).

Figure 3.12 shows that the large-scale evolution is apparently controlled by the inertia of the ions and might therefore occur on similar time scales independent of the local electron physics. Hesse *et al.* (1999) used this result to derive an approximate scaling equation for the electric field in the diffusion region. They began with the realization that the electron orbit excursion in a field reversal, and thus the scale of the electron diffusion region, is given by Eq. (3.12) (Biskamp and Schindler, 1971)

$$\delta_{\mathrm{e}} = \left[\frac{2v_{\mathrm{te}}}{\Omega'_{\mathrm{ex}}}\right]^{1/2} = \left[\frac{2m_{\mathrm{e}}T_{\mathrm{e}}}{e^2B'^2_x}\right]^{1/4}, \tag{3.45}$$

where $\Omega'_{\mathrm{ex}} = eB'_x/m_{\mathrm{e}}$ and B'_x denotes the derivative of B_x with respect to the z direction normal to the current sheet. The corresponding bounce orbit is sketched in Fig. 3.13. This result, combined with the corresponding scale length in the x direction can be used for an estimate of the electric field from (3.43):

$$E_y = -\frac{1}{n_{\mathrm{e}}e}\left(\frac{\partial P_{xye}}{\partial x} + \frac{\partial P_{yze}}{\partial z}\right) \approx \frac{1}{n_{\mathrm{e}}e}\left(\frac{P_{xye}}{\delta_{\mathrm{e}}} + \frac{P_{yze}}{\delta_{\mathrm{e}}}\right). \tag{3.46}$$

Here the values of the pressure tensors are to be taken at the edges of the current sheet, where electrons begin to become magnetized. In these regions, the pressure tensor components can be approximated by (Kuznetsova *et al.*, 1998)

$$P_{xye} \approx \frac{p_{\mathrm{e}}}{2\Omega_{\mathrm{e}z}}\frac{\partial v_{\mathrm{e}x}}{\partial x} \tag{3.47}$$

and

$$P_{yze} \approx -\frac{p_{\mathrm{e}}}{2\Omega_{\mathrm{e}x}}\frac{\partial v_{\mathrm{e}z}}{\partial z}. \tag{3.48}$$

Here the cyclotron frequencies $\Omega_{\mathrm{e}} = eB/m_{\mathrm{e}}$ are evaluated in the z and x components of the magnetic field, at the diffusion region boundary in the x and z directions,

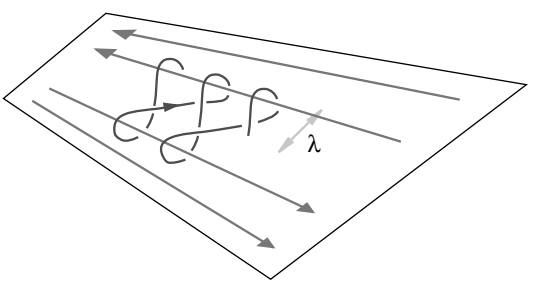

Fig. 3.13. Schematic of the electron meandering orbits in a magnetic field reversal.

respectively. The two velocity derivates are related via an approximate, incompressible, equation of continuity. By relating, e.g., $B_x = B'_x \delta_\mathrm{e}$, a small amount of algebra leads to

$$E_y \approx \frac{1}{e} \frac{\partial v_{\mathrm{e}x}}{\partial x} \sqrt{2 m_\mathrm{e} T_\mathrm{e}} \tag{3.49}$$

for the electric field in the electron diffusion region. This electric field is essentially constant throughout the electron demagnetization region (Hesse *et al.*, 1999).

Since our simulations indicate that the reconnection electric field appears to be independent of the electron mass, (3.49) indicates that the gradient of the electron flow velocity needs to scale like the inverse square root of the electron mass, assuming no substantial changes in the electron temperature. Similarly, by combining (3.49) and (3.45) one finds that the peak electron outflow velocity scales with the inverse fourth root of the electron mass. For an Alfvénic ion outflow velocity, the peak electron outflow will therefore be of the order of $v_\mathrm{e} \sim 6.5\, v_\mathrm{A}$.

The importance of this bounce motion-based dissipation mechanism was verified in a number of further investigations. Comprising one element of the GEM challenge studies, Pritchett (2001b) found electron pressure tensor components of the necessary magnitudes in translationally invariant particle-in-cell models. Similar results were also found by Hesse *et al.* (2001a) and Kuznetsova *et al.* (2001). Pressure tensor-based dissipation was also seen in implicit particle-in-cell simulation with realistic ion–electron mass ratios (Ricci *et al.*, 2002).

The next step consisted of extending the modeled domain to three spatial dimensions. Pritchett (2001a) performed a set of three-dimensional simulations of open and closed magnetic field configurations. Although Pritchett did not investigate electron anisotropies explicitly, he noted that the structure of the reconnection diffusion region is essentially identical to the one found in translationally invariant models. Tanaka (2001) found similar results: reconnection regions that start as two-dimensional structures remain so even in a fully three-dimensional simulation. In addition, Hesse *et al.* (2001b) found that reconnection, when forming out of noise, tends to self-organize into quasi-two-dimensional channels. The prominent dissipation mechanism appeared to be electron nongyrotropy, unchanged from translationally invariant models. Finally, Zeiler *et al.* (2002) found in a high mass ratio simulation that lower-hybrid drift modes do not destroy the quasi-two-dimensional nature of the electron current layer.

Thus, the diffusion region in antiparallel reconnection appears fairly well understood. Nevertheless, there are other modes and instabilities that may change the reconnecting system substantially, without necessarily changing the bounce motion-based dissipation process. These modes and their effects are discussed in Section 3.5.

3.2.3 Guide field reconnection

In principle it is to be expected that the presence of a guide magnetic field, aligned with the current direction, may destroy the bounce motion of the electrons (and ions) in the inner dissipation region. Electron orbits become strongly modified once the thermal electron Larmor radius $r_\mathrm{L} = v_\mathrm{te}/\Omega_\mathrm{e}$ is smaller than or equal to the

bounce width in the reconnecting magnetic field component, given by (3.45). After a small amount of algebra, one finds that this condition is equivalent to

$$B_y \geq B'_x \delta_e. \tag{3.50}$$

Equation (3.50) states that electron bounce orbits in the field reversal region become affected by the presence of a finite guide magnetic field once the magnitude of the latter is as big as that of the reconnecting magnetic field at the location of the farthest excursion of an electron bounce motion.

The question of how kinetic dissipation operates if the guide field exceeds the condition (3.50) remains a subject of much debate today. Similar to the antiparallel reconnection case, a set of theory and modeling analyses have been performed, however, without a final conclusion. While some early calculations (e.g, Hesse *et al.*, 1999, 2002; Pritchett, 2001b) indicate that thermal inertial effects may again be the main contributor to the dissipation process, there are many indications that processes that involve variations in the current direction may play a role, too (e.g., Pritchett and Coroniti, 2004; Swisdak *et al.*, 2003). In this section, we provide some detail on the present understanding of the mechanism supporting electron thermal dissipation. However, we will also discuss the present understanding of alternate dissipation processes.

In a situation where B_y exceeds the threshold (3.50), electron nongyrotropies need to be based on perturbations of the dominant Larmor motion about the guide magnetic field. In the wake of earlier results pertaining to electron thermal dissipation (Hesse *et al.*, 1999, 2002; Pritchett, 2001b), Hesse *et al.* (2004) generated a high-resolution numerical calculation of the GEM challenge system for $m_i/m_e = 256$, and a guide magnetic field of 80% of the reconnection magnetic field component. An overview of the evolution of this system, shown in Fig. 3.14, demonstrates the

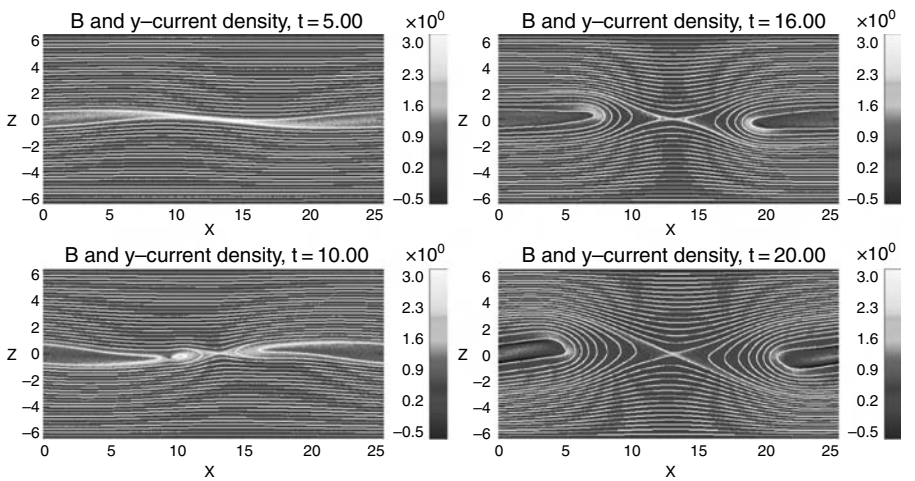

Fig. 3.14. Evolution of the magnetic field and current density for a guide field of 80% and an ion–electron mass ratio of $m_i/m_e = 256$. After Hesse *et al.* (2004). See also color plate.

similarity of the reconnecting system to that found in calculations without guide field components. The initial, X-type perturbation leads to a reconfiguration. The most prominent difference to antiparallel merging is the inclination of the reconnecting current sheet with respect to the x axis. The figure also indicates the presence of a very thin current sheet in the central reconnection region, which is likely associated with electron demagnetization.

The panels of Fig. 3.15 show a blow-up of the inner reconnection region, taken at $t = 16$. The top panel shows magnetic field lines and the total current density in the x, z plane, as well as electron flow velocities. The center panel shows that strong electron flows are associated with strong gradients of the magnetic guide field component B_y. The plot demonstrates the presence of a quadrupole-like magnetic perturbation, albeit strongly distorted and on top of the underlying guide field magnitude of

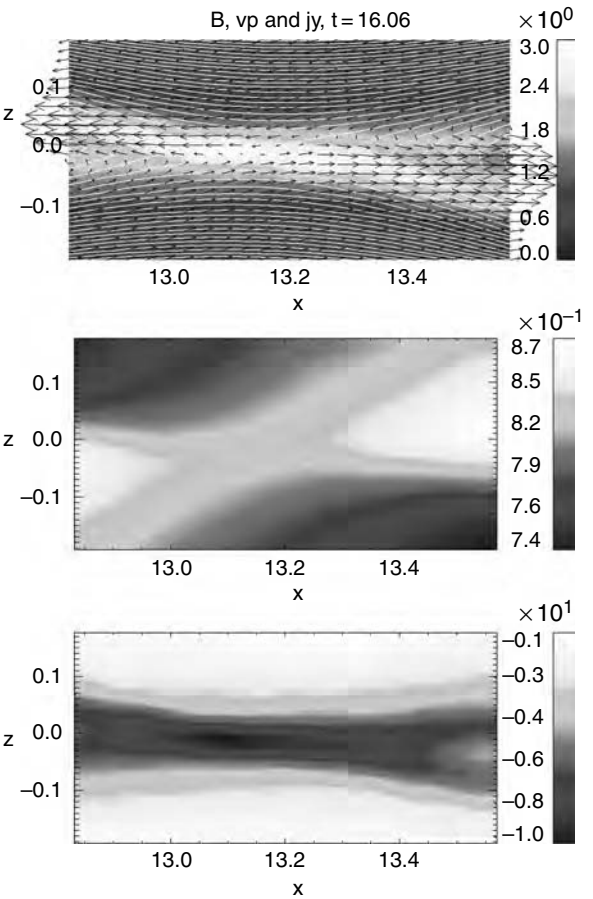

Fig. 3.15. Detailed analysis of the reconnection region in the guide field case. Shown are: Magnetic field and electron flow velocity in the x, z plane with the y component of the current density (top panel); out-of-plane magnetic field B_y and electron flow velocity v_{ey} (center and bottom panels, respectively). After Hesse *et al.* (2004). See also color plate.

$B_{y0} = 0.8$. Finally, the lower panel of Fig. 3.15 displays the electron flow speed in the y direction. While flow velocity magnitudes are similar to those found in simulations of antiparallel merging, the layer is strongly concentrated on a scale substantially smaller than the ion inertial length. We point out that the relative drift between ions and electrons in the present calculation is, for the temperatures encountered in the simulation, close to but not larger than the marginally Buneman-unstable threshold.

The relevant pressure tensor components, P_{xye} and P_{yze}, are shown in the top two panels of Fig. 3.16. The top panels indicate that, despite the magnetizing effect of the guide magnetic field, strong gradients exist particularly in P_{yze}, which provide

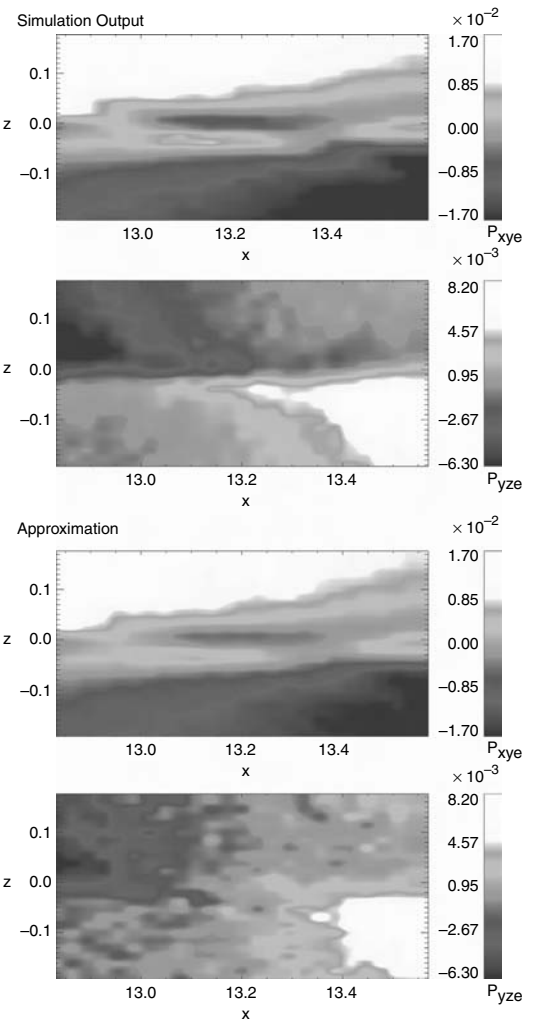

Fig. 3.16. Electron pressure tensor components, derived directly from the particle information (top panels), or from the approximation (3.52) (bottom panels). While the xy components match very well, the yz components show a noticeable difference near $z = 0$ and $x = 13.15$. After Hesse *et al.* (2004). See also color plate.

a sufficiently large reconnection electric field by virtue of (3.46), with an adjacent additional contribution from the electron inertia term (Hesse *et al.*, 2004).

The bottom two panels display the results of the approximation (Hesse *et al.*, 2002)

$$P_{xye} \approx -\frac{P_{zze}}{\Omega_e}\frac{\partial v_{ey}}{\partial z} + (P_{yye} - P_{zze})\frac{B_x}{B_y}, \tag{3.51}$$

$$P_{yze} \approx \frac{P_{xxe}}{\Omega_e}\frac{\partial v_{ey}}{\partial x} + (P_{yye} - P_{xxe})\frac{B_z}{B_y}. \tag{3.52}$$

The panels of Fig. 3.16 show a reasonable agreement between the direct simulation output and the approximation based on (3.51) and (3.52). However, a closer inspection of Fig. 3.16 reveals an important difference: While the particle data-derived value of P_{yze} features a clear gradient in the z direction at the reconnection location, at approximately $x = 13.15$, this is not the case in the approximation. This deficiency leads to a substantially reduced value of the reconnection electric field, if calculated based on (3.52). While P_{xye} appears to be remarkably well represented by its (3.51), we thus find that (3.52) does not represent the entire, dominant components of the pressure tensor component P_{yze}.

Investigating this discrepancy further, Hesse *et al.* (2004) found that heat flux tensor effects had to be added into (3.52), with the result

$$P_{yze} \approx \frac{P_{xxe}}{\Omega_e}\frac{\partial v_{ey}}{\partial x} + (P_{yye} - P_{xxe})\frac{B_z}{B_y} + \frac{1}{\Omega_e}\left(\frac{\partial Q_{xxye}}{\partial x} + \frac{\partial Q_{xyze}}{\partial z}\right), \tag{3.53}$$

where Q_{xxy} and Q_{xyz} are components of the heat flux tensor defined below in (3.55).

The second heat flux-related term in (3.53) is dominant in the immediate vicinity of the reconnection region. Therefore, (3.53) can be simplified

$$P_{yze} \approx \frac{P_{xxe}}{\Omega_e}\frac{\partial v_{ey}}{\partial x} + (P_{yye} - P_{xxe})\frac{B_z}{B_y} + \frac{1}{\Omega_e}\frac{\partial Q_{xyze}}{\partial z}. \tag{3.54}$$

The result of this approximation, depicted in Fig. 3.17, shows an excellent match with the direct determination of P_{yze} from the particle data. Thus, an appropriate approximation of the pressure nongyrotropy in the immediate vicinity of the neutral

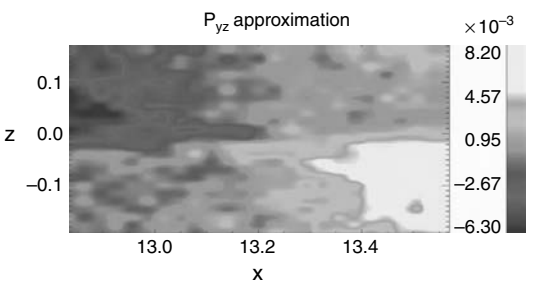

Fig. 3.17. Approximation of the pressure tensor component P_{yze} that includes heat flux contributions. This approximation shows an excellent match with Fig. 3.16. After Hesse *et al.* (2004). See also color plate.

point of the magnetic field in the x, z plane cannot be found without inclusion of a heat flux tensor component.

Derivation of a scaling law of the reconnection process therefore requires an analytic expression of an evolution equation for the entire heat flux tensor. Hesse *et al.* (2004) developed this expression for collisionless systems. The heat flux tensor is defined in the electron center-of-mass system as

$$\mathbf{Q} = m_s \int \mathrm{d}^3u(\mathbf{u}-\mathbf{v})(\mathbf{u}-\mathbf{v})(\mathbf{u}-\mathbf{v})f_s. \tag{3.55}$$

Here, f_s and m_s denote the distribution function and mass of plasma species s, $\mathbf{u}$ the phase space velocity, and $\mathbf{v}$ the bulk flow speed. An evolution equation for $\mathbf{Q}$ is obtained by multiplying the Vlasov equation by $\mathbf{uuu}$ and integrating over phase space. The result needs to be transformed into the center-of-mass frame of species s in order to derive an evolution equation for $\mathbf{Q}$. After a considerable amount of algebra, one finds for the components of the heat flux tensor (index e omitted for simplicity)

$$\begin{aligned}
&\tfrac{\partial}{\partial t}Q_{ijk} \\
&+\sum_l \tfrac{\partial}{\partial x_l}(\Gamma_{ijkl} + P_{kl}v_iv_j + P_{il}v_jv_k + P_{jl}v_iv_k + Q_{ijk}v_l) \\
&+\sum_l Q_{lij}\tfrac{\partial}{\partial x_l}v_k + \sum_l Q_{ljk}\tfrac{\partial}{\partial x_l}v_i + \sum_l Q_{lik}\tfrac{\partial}{\partial x_l}v_j \\
&+\tfrac{e_s}{m_s}\sum_{r>s}\begin{bmatrix} [Q_{ijs}B_r - Q_{ijr}B_s]\varepsilon_{rsk} \\ +[Q_{iks}B_r - Q_{ikr}B_s]\varepsilon_{rsj} \\ +[Q_{jks}B_r - Q_{jkr}B_s]\varepsilon_{rsi} \end{bmatrix} = 0.
\end{aligned} \tag{3.56}$$

Here e_s denotes the charge of species s, and ε_{ijk} is the usual, totally antisymmetric tensor. Equation (3.56) relates the time evolution of Q_{ijk} to lower order moments such as pressure and velocities, as well as to the fourth order tensor Γ_{ijkl}. The last term in (3.56) represents the effects of particle cyclotron motion on the heat flux tensor. Clearly, (3.56) is invariant under change of order of indices, leading to a totally symmetric heat flux tensor.

Further progress toward a simple scaling relation requires simplifying assumptions. Neglecting time dependence and the 4-tensor, an expression for Q_{xyz} can be obtained from the x, y, x component of (3.56)

$$\begin{aligned}
&\sum_l \tfrac{\partial}{\partial x_l}(2P_{xl}v_xv_y + P_{yl}v_xv_x + Q_{xyx}v_l) \\
&+\sum_l Q_{lxy}\tfrac{\partial}{\partial x_l}v_x + \sum_l Q_{lyx}\tfrac{\partial}{\partial x_l}v_x + \sum_l Q_{lxx}\tfrac{\partial}{\partial x_l}v_y \\
&-\tfrac{e}{m_e}(2Q_{xyy}B_z - 2Q_{xyz}B_y + Q_{xxx}B_z - Q_{xxz}B_x) = 0.
\end{aligned} \tag{3.57}$$

Neglecting magnetic field components other than B_y, the convection term $\sum_l \frac{\partial}{\partial x_l}(Q_{xyx}v_l)$, and assuming $Q_{rst} \text{¡} P_{rs}v_t$ (a reasonable assumption for a nearly gyrotropic plasma) near the reconnection region, reduces (3.57) to the simple expression

$$Q_{xyz} \approx -\frac{1}{\Omega_y}\left[\frac{\partial}{\partial x}\left(P_{xx}v_xv_y + 0.5P_{xy}v_x^2\right) + \frac{\partial}{\partial z}\left(P_{xz}v_xv_y + 0.5P_{yz}v_x^2\right)\right]. \tag{3.58}$$

The leading order terms in (3.58) are

$$Q_{xyz} \approx -\frac{1}{\Omega_y}\frac{\partial}{\partial x}(P_{xx}v_x v_y) \approx -\frac{P_{xx}v_y}{\Omega_y}\frac{\partial v_x}{\partial x} \tag{3.59}$$

for the relevant component of the electron heat flux tensor. This approximation was found to be adequate in the electron current sheet.

The reconnection region now has two transitions, the first, where the convection electric field becomes equal to the inertial electric field, at a scale L_1, and a second, L_2, where the inertial electric field is matched to the pressure tensor-derived electric field. L_1 is readily determined by the expansion (e.g., Vasyliūnas, 1975)

$$\begin{aligned} |E_{\text{inertial}}| &\sim \frac{m_\text{e}}{e}v_{\text{e}z}\frac{\partial v_{ey}}{\partial z} \sim \frac{1}{L_1^2}\frac{B_0 v_{\text{e}z}}{\mu_0}\frac{m_\text{e}}{e^2 n_\text{e}} \\ &= B_0 v_{\text{e}z}\frac{c^2}{\omega_{\text{pe}}^2}\frac{1}{L_1^2} = |E_{\text{convection}}|\frac{c^2}{\omega_{\text{pe}}^2}\frac{1}{L_1^2}. \end{aligned} \tag{3.60}$$

The pressure electric field is derived from the first term of (3.45). With the addition of (3.61), the pressure tensor y, z component (3.57) becomes

$$P_{yze} \approx \frac{P_{xxe}}{\Omega_{ey}}\frac{\partial v_{ey}}{\partial x} + (P_{yye} - P_{xxe})\frac{B_z}{B_y} - \frac{1}{\Omega_{\text{e}y}}\frac{\partial}{\partial z}\left(\frac{P_{xxe}v_{ey}}{\Omega_{ey}}\frac{\partial v_{ex}}{\partial x}\right), \tag{3.61}$$

where the last term dominates the reconnection electric field near the zero of the magnetic field in the x, z plane. Ignoring lower order terms, and assuming a divergence-free electron velocity, the pressure electric field can be scaled

$$\begin{aligned} |E_{\text{pressure}}| &\sim \frac{1}{n_\text{e}e}\frac{1}{\Omega_{ey}}\frac{\partial^2}{\partial z^2}\left(\frac{P_{xxy}v_{ey}}{\Omega_{ey}}\frac{\partial v_{ex}}{\partial x}\right) \\ &\sim \frac{1}{n_\text{e}e}\frac{1}{\Omega_{ey}}\frac{\partial^2}{\partial z^2}\left(\frac{P_{xxe}v_{ey}}{\Omega_{ey}}\frac{\partial v_{ez}}{\partial z}\right) \\ &\sim |E_{\text{inertial}}|\frac{1}{L_2^2}\frac{P_{xxe}}{\Omega_{ey}^2}\frac{1}{n_\text{e}m_\text{e}} = |E_{\text{inertial}}|\frac{r_\text{L}^2}{L_2^2}. \end{aligned} \tag{3.62}$$

Equation (3.62) states that the transition from inertia-based to pressure-based dissipation occurs at a scale length equal to the electron Larmor radius in the guide magnetic field component.

Thus we find that there may be two scale lengths associated with collisionless magnetic reconnection in the presence of moderate guide fields. The first, well-known scale is reached when the inertial electric field equates the magnitude of the convection electric field. This scale length is the collisionless skin depth. For values of the electron $\beta = \mu_0 p_{\text{e}\perp}/B^2$ of less than unity, the second transition occurs at a scale length of an electron Larmor radius in the guide magnetic field. The very small scales associated with the electron Larmor radius permit the heat flux to take on an unprecedented role in the electron dissipation process.

Physically, electron scattering can occur if the Larmor radius in the guide field is comparable to the gradient scale length in the reconnecting electric field. The situation is sketched in Fig. 3.18. Electron scattering occurs due to the interaction of field-aligned and gyromotions with the ambient reconnecting electric field components.

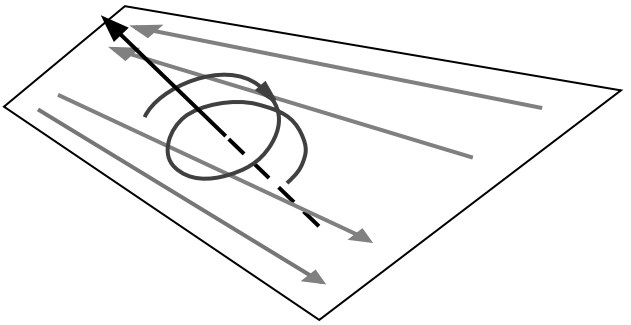

Fig. 3.18. Schematic of the interaction of the electron Larmor motion about the guide field with the reconnection magnetic field component.

It should be noted that the electron-based electric field expression

$$E_y \approx \frac{1}{en_\mathrm{e}} \frac{1}{\Omega_{\mathrm{e}y}} \frac{\partial}{\partial z} \left(\frac{P_{xx\mathrm{e}} v_{\mathrm{e}y}}{\Omega_{\mathrm{e}y}} \frac{\partial v_{\mathrm{e}x}}{\partial x} \right) \sim \frac{1}{e} \frac{\partial v_{\mathrm{e}x}}{\partial x} T_\mathrm{e} \frac{1}{\Omega_{\mathrm{e}y}^2} \frac{\partial^2 v_{\mathrm{e}y}}{\partial z^2} \tag{3.63}$$

may equally well be expressed through the ions, which exhibit similar dynamics, albeit on the larger scale of an ion Larmor radius. The result is the same as (3.63), but with an index change, and a sign change.

While this analysis presents a consistent solution to the reconnection dissipation problem in the presence of a guide field, the question remains whether the additional freedom of a fully three-dimensional evolution might enable other dissipative processes such as discussed in Section 3.5. While Silin and Büchner (2003b) find that lower-hybrid drift, kink, and sausage modes appear suppressed in the presence of a guide field, and Scholer *et al.* (2003) saw the formation of essentially two-dimensional reconnection channels, a candidate process is based on the formation of electrostatic, solitary structures associated with the nonlinear evolution of the Buneman instability (Drake *et al.*, 2003). Drake *et al.* argue that correlations of electron density fluctuations that are associated with these *electron holes* provide a mechanism for anomalous resistivity. The modeled electrostatic solitons are well matched by observations of the magnetopause current layer (Cattell *et al.*, 2002a), which reveal the presence of electrostatic solitary waves that propagate rapidly along the current direction. Although the overall morphology and reconnection rates of Drake *et al.*'s (2003) three-dimensional simulations are very similar to translationally invariant calculations, and Pritchett and Coroniti (2004) advocate inertial processes, the Buneman mode-based dissipation process deserves further studies to clarify its viability in guide-field magnetic reconnection.

3.3 Onset of magnetic reconnection

P. L. Pritchett

As discussed in Chapter 1 and in Section 3.1, many scenarios of the occurrence of reconnection involve a sudden transition from a quiescent, slowly evolving state to a rapid energy release. A critical problem hence is not only to explain fast reconnection rates, responsible for the energy release, but also to identify the mechanism for

this transition, that is, the mechanism for the onset of reconnection, or the onset of fast reconnection. This holds particularly for the onset of reconnection in the terrestrial magnetotail, which appears to be closely related to the onset of magnetospheric substorms (Section 1.2). To lowest order, the magnetotail current sheet configuration resembles the classical Harris (1962) neutral sheet. It was proposed very early in the space era (Coppi *et al.*, 1966) that collisionless reconnection could occur in the Earth's magnetotail as a result of an electron tearing mode driven by the electron Landau interaction. It was hypothesized that this tearing instability could serve as the triggering mechanism that powers the sudden onset of magnetic reconnection associated with the expansion phase of substorms in the terrestrial magnetotail.

This simple one-dimensional picture of the magnetotail must fail, however, inasmuch as the field lines must connect to the intrinsic dipolar magnetic field of the planet. For the Earth there is a small northward component of the magnetic field in the region of the current sheet whose magnitude is typically a few nanoteslas, which is about 10% of the asymptotic (lobe) field strength (e.g., Fairfield and Ness, 1970). As we shall discuss, the presence of this *normal* magnetic field component has profound implications for the possibility of magnetic reconnection in a planetary magnetotail; the investigation of these consequences is generally referred to as the *onset* problem for magnetic reconnection. On the most fundamental level, the resulting cyclotron motion of electrons in even a very weak normal field removes the electron Landau resonance (Galeev and Zelenyi, 1976), thus ruling out the possibility of an electron tearing mode.

More general consequences of a two-dimensional (2D) isotropic equilibrium configuration were deduced by Schindler (1972) and Birn *et al.* (1975). Let $z = a(x) > 0$ be the location of the magnetopause (assumed to be a field line). There are then two possible situations depending on the sign of $\mathrm{d}a/\mathrm{d}x$ (assuming that x increases in the tailward direction): (1) $\mathrm{d}a/\mathrm{d}x > 0$ (i.e., the tail diverges as one moves away from the planet) is a necessary (but not sufficient) condition for instability of the tail. (2) If $\mathrm{d}a/\mathrm{d}x < 0$ (i.e., the tail converges), then the tail is stable. With $B_{0z}(x, z = 0) > 0$, then $\mathrm{d}a/\mathrm{d}x > 0$ requires that B_{0z} change sign somewhere. If B_{0z} has the same sign everywhere, then the tail equilibrium is stable. For the Earth, it is known that B_{0z} does indeed change sign as one moves into the lobes (e.g., Fairfield, 1979). Thus the flaring of the Earth's lobe field could allow for the possibility of some kind of tearing instability.

The outline of this section is as follows. In Section 3.3.1 we discuss the consequences of the finite normal magnetic field for what is known as the pure ion tearing instability. In Section 3.3.2 we review the stabilizing effects of electron dynamics in the presence of the normal field on the tearing instability. In Section 3.3.3 we consider the implications of the third dimension (out-of-plane coordinate) on the tearing instability. In Section 3.3.4 we describe some recent results on externally driven reconnection. Section 3.3.5 contains a summary and outlook.

3.3.1 The pure ion tearing instability

The tearing hypothesis for the magnetotail was resurrected by Schindler (1974) who suggested that ion Landau damping could drive a pure ion tearing instability in which the electron dynamics was presumed to be unimportant due to the

small value of the electron temperature ($T_e/T_i \ll 1$). He noted that the characteristic scaling of the ion tearing growth rate in the absence of the normal field, valid for $\rho_{i0}/\lambda \ll 1$, would be of the form (Laval *et al.*, 1966)

$$\gamma/\Omega_{i0} \sim (\rho_{i0}/\lambda)^{5/2}, \tag{3.64}$$

where λ is the half-thickness of the current sheet and ρ_{i0} (Ω_{i0}) is the ion gyroradius (cyclotron frequency) in the asymptotic field B_0. During quiet times, the ratio $\rho_{i0}/\lambda \sim 0.03$. Thus the scaling (3.64) would give $\gamma/\Omega_{i0} \sim 2 \times 10^{-4}$ or $1/\gamma \sim 1$ h, which is too long to be relevant to substorm onset times. It was expected, however, that as the current sheet thinned during the growth phase, the growth time for the tearing instability would decrease substantially. This is particularly significant, since it was expected that the condition $\gamma/\Omega_{i0} > B_n/B_0$ would need to be satisfied in order that the free-streaming particle motion which drives the tearing instability would not be destroyed by the gyromotion in the normal field B_n. The scaling (3.64) suggests that for $\rho_{i0}/\lambda \approx 1$, this condition easily would be satisfied for $B_n/B_0 \sim 0.1$.

Subsequent investigations, however, showed that the basic reconnection growth rate increases much less rapidly as $\rho_{i0}/\lambda \to 1$ than suggested by the scaling (3.64). Pritchett *et al.* (1991) and Brittnacher *et al.* (1995) considered the case of pure ion tearing (alternatively, electron–ion tearing with a mass ratio $m_i/m_e = 1$) for the case of very thin current sheets with $\rho_{i0}/\lambda \approx 1$. They obtained a maximum underlying growth rate

$$\gamma_{max}/\Omega_{i0} \approx 0.50(\rho_{i0}/\lambda)^{5/2}/(1 + 2\rho_{i0}^2/\lambda^2). \tag{3.65}$$

The term $1 + 2\rho_{i0}^2/\lambda^2$ in the denominator arises from the inclusion of the particle drift in the cross-tail direction in the particle orbits. For $\rho_{i0}/\lambda \sim 1$, this term clearly differs significantly from unity, and the maximum growth rate for $\rho_{i0}/\lambda = 1$ is only $\gamma_{max}/\Omega_{i0} \approx 0.17$, roughly a factor of 6 smaller than expected from (3.64). Thus even for a sheet as thin as the ion gyroradius ($\sim$400 km), the maximum tearing growth rate is only marginally larger than the typical value of $B_n/B_0 \sim 0.1$. Particle-in-cell (PIC) simulations have confirmed that the stabilization of the pure ion tearing mode in a thin current sheet does indeed occur when $B_n/B_0 \sim \gamma/\Omega_{i0}$ (Pritchett *et al.*, 1991).

The tearing growth rate as a function of m_i/m_e has been calculated by Daughton (1999b) for the case of the Harris neutral sheet. The maximum growth rate decreases slowly with increasing m_i/m_e; for $\rho_{i0}/\lambda = 1$ and $T_i/T_e = 1$, it falls to $\gamma/\Omega_{i0} = 0.07$ at $m_i/m_e = 1836$. It thus seems that it would be very difficult to excite the spontaneous ion tearing instability unless B_n were reduced considerably below its normal value.

3.3.2 Electron stabilization of ion tearing

Traditionally, the analysis of electron stabilization for the ion tearing instability has been carried out using an idealized 2D plasma sheet configuration in the noon–midnight meridional (x, z) plane; no variation in the y direction is considered. In such a configuration and assuming a tearing perturbation $A_{1y} = A_1(x, z)e^{\gamma t}$ and

an electrostatic potential $\Phi_1 = \Phi_1(x,z)\mathrm{e}^{\gamma t}$, the completely general energy principle is (Laval and Pellat, 1964; Schindler, 1966)

$$\delta W = \int \mathrm{d}^3x \Big[|\nabla A_1|^2 - \mu_0 \frac{\mathrm{d}J_0}{\mathrm{d}A_0} |A_1|^2 + \sum_{i,e} 4\pi T \int \mathrm{d}^3v \frac{|\tilde{f}_1|^2}{f_0} \Big]. \tag{3.66}$$

Here, f_0 is the equilibrium distribution function, J_0 is the equilibrium current density, and $\tilde{f}_1 = f_1 - A_1 \partial f_0 / \partial A_0$ is the nonadiabatic part of the perturbed distribution f_1. The first term in (3.66) represents the stabilizing effect of field-line tension, the second term is the destabilizing free energy associated with the adiabatic response to the equilibrium currents, and the last term represents the compressibility effect arising from the perturbed current density due to $\tilde{f}_1$. Various assumptions have been made regarding the nature of the electron dynamics.

Adiabatic electrons

Lembège and Pellat (1982) used a drift-kinetic analysis (which should be valid for time and space scales long compared to the electron cyclotron period and electron Larmor radius) and assumed adiabatic motion for the electrons. They demonstrated that the tearing mode electromagnetic field produces a strong compression of the electron density which is independent of T_e. This perturbation also forces a large electrostatic potential in order to maintain charge neutrality. In the energy principle (3.66), the energy associated with the electron compression exceeds the free energy available from the reversed magnetic field configuration provided that the condition

$$k_x \lambda > (4/\pi) B_\mathrm{n}/B_0 \tag{3.67}$$

is satisfied. In order to violate (3.67) and thus to permit instability, the wavelength of the mode would have to exceed $\sim 60\lambda$. On such a large scale the conditions necessary for the WKB approximation to be valid would be violated, and so Lembège and Pellat concluded that the ion tearing mode was stable.

Effects of turbulence

Several attempts to circumvent this result were made by appealing to the effects of turbulence. Coroniti (1980) argued that, since the plasma sheet contains modest to high levels of electromagnetic turbulence, it is possible that pitch angle scattering by background wave turbulence could invalidate the assumption of adiabatic electron motion. His analysis found an electron tearing mode growth rate proportional to a bounce-averaged pitch angle diffusion coefficient.

Adopting Coroniti's formalism, Büchner and Zelenyi (1987) replaced wave pitch-angle scattering by the stochastic changes in the first adiabatic invariant (μ) which can occur when the plasma sheet thins and the adiabaticity parameter

$$\kappa_\mathrm{e} = (B_\mathrm{n}/B_0)(\lambda/\rho_{\mathrm{e}0})^{1/2} \tag{3.68}$$

becomes less than or of the order of 1. Here $\rho_{\mathrm{e}0}$ is the electron Larmor radius based on B_0. They suggested that the resulting diffusion in μ should permit tearing growth rates comparable to Schindler's estimate (3.64) for the ion tearing mode. With $\kappa_\mathrm{e} \sim 1$, they argued that the electron dynamics would be unimportant.

Canonical momentum conservation

Pellat *et al.* (1991) pointed out that the analysis by Coroniti (1980) contained an error in that it relied on an approximate form of a Green's function solution. The exact solution has the property that the perturbed number of particles on a flux tube is conserved. They showed that this result followed directly from the conservation of the canonical momentum P_y in a 2D system, independent of any assumption of electron adiabaticity. P_y conservation alone was sufficient to constrain the cyclotron excursion in the direction transverse to the magnetic surface. They demonstrated further that neither wave turbulent pitch-angle scattering nor nonadiabatic stochastic first-invariant diffusion would alter the number of particles on a flux tube. They recovered the Lembège–Pellat stability criterion (3.67) under the very mild assumption that $k_x\rho_{\rm en} < 1$, where $\rho_{\rm en}$ is the electron Larmor radius in the $B_{\rm n}$ field. Assuming the proton/electron value for the mass ratio, $T_{\rm i}/T_{\rm e} \approx 7$, $\rho_{\rm i0}/\lambda \sim 1$, and a wavenumber $k_x\lambda \approx 0.5$, one finds that this condition is satisfied for a normal field of only $B_{\rm n}/B_0 \sim 5 \times 10^{-3}$.

2D PIC simulations provided direct confirmation of this electron stabilization effect (Pritchett, 1994). These simulations used a value $B_{\rm n}/B_0 = 0.02$ so that the ion tearing mode was still unstable. With $\rho_{\rm i0}/\lambda$ held fixed at 1, simulations were performed with $m_{\rm i}/m_{\rm e}$ varying from 1 to 64 and $T_{\rm i}/T_{\rm e}$ from 1 to 8. As $k_x\rho_{\rm en}$ approached unity, the tearing mode growth decreased dramatically. Qualitatively similar results were obtained in simulations by Dreher *et al.* (1996) for a mass ratio $m_{\rm i}/m_{\rm e} = 10$ and temperature ratios up to $T_{\rm i}/T_{\rm e} = 20$.

Brittnacher *et al.* (1994) reexamined use of the energy principle as applied to ion tearing. They treated the case of intrinsic pitch-angle diffusion using a Vlasov description and recovered the Lembège–Pellat result (3.67). For the case of external pitch-angle diffusion they employed a drift-kinetic description and found that the energy principle contains an additional term. This new term is stabilizing, however, and thus at best the marginal stability criterion is still the same.

An alternative Vlasov treatment of the onset problem is given in Section 4.3.2. The approach discussed there treats a larger class of distribution functions, avoids the use of inequalities, and introduces the small electron gyroscale regime by considering the formal limit $m_{\rm e} \to 0$. This more refined approach confirms the strong electron stabilization in the appropriate limit.

Fluid treatment

Further insight into the physics of the electron stabilization effect was provided by Quest *et al.* (1996). They employed the standard energy principle formalism given in (3.66). In evaluating the perturbed particle density on a flux tube, they used fluid equations assuming that the electrons were *frozen-in* to the magnetic field. They argued that if the effective gyroradius of the electrons is small compared to both the half-width λ and $1/k_x$ and if spatial diffusion and electron resonance effects are negligible, then it is justifiable to neglect both the inertial term and the off-diagonal pressure tensor elements in the electron momentum equation. There was no requirement that the electron orbits be adiabatic, merely that they were confined to the proximity of a field line, as is required by conservation of P_y (Pellat *et al.*, 1991). This fluid analysis also recovered the Lembège–Pellat result (3.67), and

it further demonstrated that the compressional stabilization is independent of the presence of a (uniform) guide field component B_{0y} in the initial configuration. The electron stabilization is thus a macroscopic fluid effect, independent of the specifics of the electron orbits.

Exact particle orbits

In none of the energy principle analyses described so far was the linear stability problem solved directly. Instead, techniques such as the Schwartz inequality were employed to obtain marginal stability limits; the exact particle orbits were not used. Brittnacher *et al.* (1998) devised a new approach in which the energy equation was solved using a finite element procedure where the quantities that depend on the details of the particle orbits were determined by standard PIC simulation methods. Since the exact orbits were considered, it was possible to take into account the effects of pitch-angle scattering (both intrinsic and induced by an external wave source) and spatial diffusion. They found that none of these effects could destabilize the ion mode. For $k_x\rho_{\rm en} < 1$, the mode was stabilized by the electron compressibility effects. For weaker values of $B_{\rm n}$, finite Larmor radius effects (Galeev and Zelenyi, 1976) were sufficient to stabilize the mode. Thus, the spontaneous ion mode should not occur in the tail current sheet. They found that the electron tearing mode could be reestablished by pitch-angle diffusion, but only for values of $B_{\rm n}/B_0 \approx 10^{-4}$ too small to apply to the near-Earth tail.

Transient electrons

All the previous stability analyses have treated the electron population as basically a single fluid. Sitnov *et al.* (1998) reexamined the tearing stability analysis including the effect of a transient electron population. They stressed that in isotropic self-consistent current sheet models the number density of transient electrons is not a free parameter; its local value depends on basic sheet parameters such as $B_{\rm n}/B_0$ and on the distance z from the neutral plane. Using an energy principle analysis, they found a new version of the stability condition (3.67):

$$k_x\lambda > (4/\pi)(T_{\rm i}/3T_{\rm e})^2 B_{\rm n}/B_0. \tag{3.69}$$

Since $(T_{\rm i}/3T_{\rm e})^2 \sim 5$ in the magnetotail, it is now possible to reach the marginal stability limit for modes that are consistent with the WKB approximation, leaving open the possibility that the tearing mode could be unstable. In a subsequent explicit nonlocal Vlasov linear stability analysis, Sitnov *et al.* (2002) found instability with $T_{\rm e}/T_{\rm i} \ll 1$ when the current sheet was sufficiently long so that the electrons leaving it could be treated as transient particles. The specific dependence of the marginal wavenumber on $T_{\rm i}/T_{\rm e}$ turned out to be less pronounced than given by (3.69). This new result suggests that while the tearing mode is unlikely to be excited in the transition region between the dipole and tail-like magnetic fields, it may very likely be unstable at distances further down the tail where the length of the tail current sheet is much larger than its thickness.

3.3.3 Effects of the third dimension

When the restriction to 2D systems is removed and variations in the cross-tail (y) direction are permitted, the canonical momentum P_y is no longer conserved. It then follows that the particle density along a flux tube need no longer be constant. With the inclusion of the y dependence, a much larger class of instabilities becomes possible, and many of these have been proposed as mechanisms for disrupting the tail current sheet. This subject is treated in detail in Section 3.5 of this work. Here we consider only the rather limited number of investigations that have looked at cross-tail instabilities in the presence of a finite normal field component.

One member of the class of kinetic cross-field instabilities has the character of a kink mode in the y, z plane. This mode was first identified in 2D PIC simulations by Zhu *et al.* (1992), and they found that its growth rate in a thin current sheet could be faster than that of the collisionless tearing instability in the Harris sheet. Pritchett and Coroniti (1996) showed from a two-fluid analysis with finite electron inertia that the long-wavelength kink mode ($k_y\lambda < 1$) is linearly unstable. Since the growth rate is proportional to the magnitude of the relative electron–ion cross-field drift, they referred to the mode as a drift-kink mode. The behavior of this mode in the presence of a normal field component was investigated in 3D PIC simulations by Pritchett *et al.* (1996). They considered the case of a $\rho_{i0}/\lambda = 1$ current sheet with a constant value of $B_n/B_0 = 0.06$ at $z = 0$ and used $m_i/m_e = 16$. In a pure 2D geometry this configuration would be stable to tearing due to the combined effects of electron stabilization and ion gyromotion. In the early stage of the simulation (up to $\Omega_{i0}t \sim 60$), there was clear growth of the drift-kink modes with $k_y\lambda \sim 0.8$–1.2, although their growth rates were reduced compared to the case of $B_n = 0$. There was no indication for any growth of shorter-wavelength lower-hybrid drift modes (Section 3.5.2). Beginning at $\Omega_{i0}t \sim 50$, pure tearing modes began to grow and there was an increase in the B_z^2 field energy, indicating that reconnection was occurring. This initial stage of reconnection led to a further reduction in the local value of B_n. This field finally reached zero in one location by $\Omega_{i0}t \sim 100$, and this event signaled the onset of a highly nonlinear stage which was characterized by the formation of a conventional island configuration. It thus appeared that the kink mode could trigger the onset of reconnection.

It turns out, however, that, unlike the case of the tearing mode, the drift-kink growth rate is extremely sensitive to the value of m_i/m_e. Daughton (1999b) showed that while the growth rate of the kink mode exceeds that of the tearing mode by about a factor of two for $m_i/m_e = 16$, for the realistic proton mass ratio of 1836 the kink growth rate is smaller than the tearing rate by about a factor of 25. Thus low mass ratio simulations probably greatly overestimate the effect of the drift-kink mode. Daughton (1999b) also noted, however, that another type of kink mode could be strongly excited ($\gamma/\Omega_{i0} \sim 0.1$) at realistic mass ratios. This second type of kink mode is driven by the relative drift between two ion species and has been referred to as the ion–ion kink mode (Karimabadi *et al.*, 2003a,b). The maximum growth rate occurs for $k_y\lambda \sim 0.7$, the real frequency is $\omega_r \approx k_y v_d$ (where v_d is the effective single fluid drift velocity at $z = 0$), and the growth rate is always larger than that for the tearing mode. 3D simulations with $m_i/m_e = 100$ (Karimabadi *et al.*, 2003b) showed that the growth of the ion–ion kink mode is not sensitive to the presence of a (weak)

normal field component, unlike the case of the electron–ion kink mode. Thus the ion–ion kink mode is still a possible candidate to reduce or eliminate the effects of electron stabilization.

3.3.4 Externally driven reconnection

Despite its long history, it is by no means clear that the spontaneous tearing instability is the relevant process for explaining substorm onset in the magnetotail. Considerable attention has also been paid to the possibility that substorms could be triggered by external perturbations (Caan *et al.*, 1975; Rostoker *et al.*, 1983; Lyons, 1995, 1996). It appears that a substantial fraction ($\sim$60%) of substorm onsets can be associated with northward turnings of the IMF (Hsu and McPherron, 2003). Prior to onset, a southward IMF imposes an enhanced convection electric field on the magnetotail. A number of MHD and Hall MHD studies (Birn and Hesse, 1996; Rastätter *et al.*, 1999; Birn *et al.*, 1999) have shown that reconnection can be initiated in regions of finite resistivity by such an externally imposed convection electric field. A few studies have considered this possibility in regard to collisionless reconnection.

In a series of 2D and 3D PIC simulations, Horiuchi and collaborators (Horiuchi and Sato, 1994, 1997, 1999; Horiuchi *et al.*, 2001; Pei *et al.*, 2001) considered the effect of applying a very strong driving electric field with $E_y/v_{\rm A}B_0 \sim 0.5$–$1.0$ to a Harris neutral sheet. For the case of open downstream boundary conditions, they found that it was possible to achieve a steady-state reconnection configuration. These studies were not relevant to the onset problem, however. In 2D and 3D studies of the effect of imposing a more realistic ($E_y/v_{\rm A}B_0 \sim 0.1$) convection electric field on a near-Earth plasma sheet equilibrium configuration, Pritchett and Coroniti (1995) and Pritchett *et al.* (1997) found that this process resulted in the formation of a thin current sheet accompanied by the development of a deep minimum in the equatorial B_z field. There was no apparent difficulty in actually driving B_z negative, which then resulted in the tailward expulsion of a plasmoid. Possible limitations of this study were that $m_{\rm i}/m_{\rm e}$ was only 16 and that the reconnection occurred fairly close to the inner (near-Earth) boundary of the simulation.

Here we present some results from a recent 3D PIC simulation (Pritchett, 2005) in which a spatially localized convection electric field is applied to a current sheet equilibrium with $B_{\rm n}/B_0 = 0.04$ at the center of the sheet. The system size is $L_x \times L_y \times L_z = 25.6\,c/\omega_{\rm pi} \times 12.8\,c/\omega_{\rm pi} \times 12.8\,c/\omega_{\rm pi}$, and the driving field is localized near the center of the system in x with a half-width of $3.2\,c/\omega_{\rm pi}$. The field is applied at the z boundaries uniformly in y, and its peak magnitude is $E_y/v_{\rm A}B_0 = 0.2$. The mass ratio is $m_{\rm i}/m_{\rm e} = 100$, $c/v_{\rm A} = 20$, $\omega_{\rm pe}/\Omega_{\rm e} = 2.0$, the temperature ratio is $T_{\rm i}/T_{\rm e} = 5$, and there is a uniform background density $n_{\rm b} = 0.2n_0$. The initial half-thickness of the sheet is moderately large, with $\lambda = 1.6\,c/\omega_{\rm pi}$. The boundary conditions in the x direction are open for particles and magnetic flux. The peak number of particles is 412 million per species, and the maximum particle density per cell is 50 per species. The initial field line configuration is shown in Fig. 3.19a.

It has become traditional to describe the evolution of the reconnection process by the reconnection flux ψ (e.g., Birn *et al.*, 2001, and references therein), which is defined as the difference between the maximum and minimum values of the vector potential $A_y(x,z)$ on the axis $z = 0$. In the presence of the normal field component,

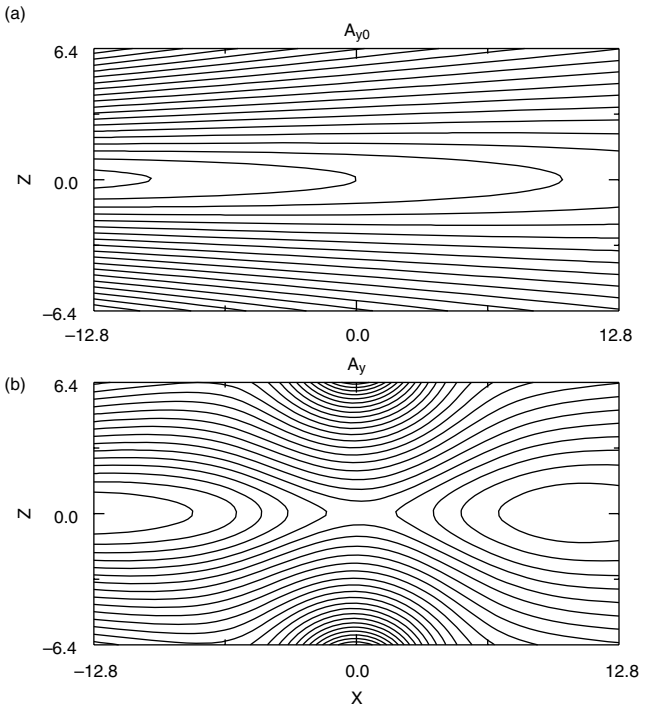

Fig. 3.19. Field line configuration at time (a) $\Omega_{i0}t = 0$ and (b) $\Omega_{i0}t = 36$.

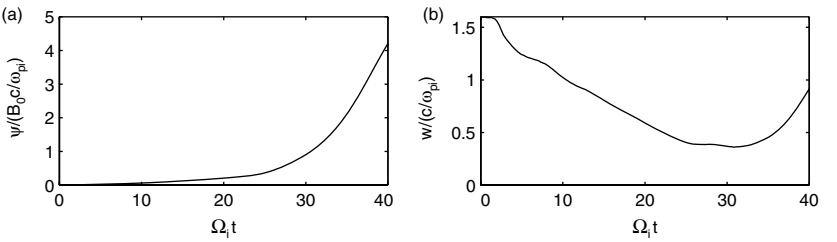

Fig. 3.20. Time histories of (a) the reconnected flux ψ and (b) the current sheet half-thickness w.

the equilibrium function $A_{0y}(x, z = 0)$ itself has a finite ψ value, and so it is necessary to measure ψ in terms of the perturbed $\delta A_y(x, z = 0)$ only. Figure 3.20a shows the development of ψ so defined. The initial noise level in the simulation corresponds to $\psi/(B_0 c/\omega_{\rm pi}) \sim 1 \times 10^{-3}$. There is a relatively long development period of $\Omega_{i0}t \sim 20$ during which ψ grows slowly as the perturbation fields propagate in from the boundary. As shown in Fig. 3.20b, the width of the current layer, defined as the value w_J where $|B_x(0, w_J)| = 0.76 B_0$, decreases during this period from its initial value of $1.6\, c/\omega_{\rm pi}$ to a minimum of $\sim 0.4\, c/\omega_{\rm pi}$. Subsequently, the value of ψ increases much more rapidly, with the peak slope at $\Omega_{i0}t \sim 35$ corresponding

to a reconnection field $E_y/v_{\rm A}B_0 \approx 0.44$. This is more than twice as large as the driving value $E_{0y}/v_{\rm A}B_0 = 0.2$, and it is somewhat larger than the value of ≈ 0.26 which was obtained from the GEM Reconnection Challenge simulations (Birn *et al.*, 2001) where a $\lambda = 0.5\,c/\omega_{\rm pi}$ current sheet was perturbed by an internal flux perturbation.

The thinning of the overall current layer is the result of the formation of an embedded thin electron current layer. Figure 3.21 shows a series of profiles in z at $x = 0$ and averaged over all values of y at various times for (a) the magnetic field B_x and (b) the total current density J_y. The overall thinning is apparent from the increasing magnitude of the slope of B_x through $\Omega_{\rm i0}t = 24$ and from the current density profiles. During this same time interval, the ion profiles $n_{\rm i}$, $v_{y\rm i}$, and $J_{y\rm i}$ (not shown) show relatively little change; there is only a modest steepening of the density profile. In contrast, the electron current density shows a dramatic thinning and increase in magnitude. At $\Omega_{\rm i0}t = 24$, the peak electron current density is about three times as large as that of the ions. This represents an increase by a factor of 15 in the relative electron to ion current value. The half-width at half-maximum of the electron current density at $\Omega_{\rm i0}t = 32$ is only $0.14c/\omega_{\rm pi}$, which is slightly above the local value of the electron inertial length of $\approx 0.12c/\omega_{\rm pi}$.

Figure 3.22a shows the development of the normal field profile $B_z(x,0)$ averaged over all values of y. As noted before, the initial value is $B_z(x,0)/B_0 = 0.04$. During the developmental phase this value is enhanced for negative values of x and reduced for positive values. $B_z(x,0)$ is first driven to zero at $\Omega_{\rm i0}t \approx 21$ at $x \approx 2\,c/\omega_{\rm pi}$. At this time, there is only a weak y dependence in the equatorial B_z field (not shown); the growth rate for mode 1 in y is $\gamma/\Omega_{\rm i0} \sim 0.09$, which is consistent with the linear theory prediction for the ion–ion kink (Karimabadi *et al.*, 2003a). Overall, however, the cross-field modes do not seem to play a major role in the dynamics that force B_z to 0. Shortly after B_z is reversed, there is a significant increase in the reconnection flux ψ (Fig. 3.20a) and hence in the rate of reconnection. At this stage the reconnection proceeds much as for the case of a neutral sheet, and the late nonlinear stage (see Fig. 3.19b for the field lines at $\Omega_{\rm i0}t = 36$) shows little resemblance to the initial normal field configuration.

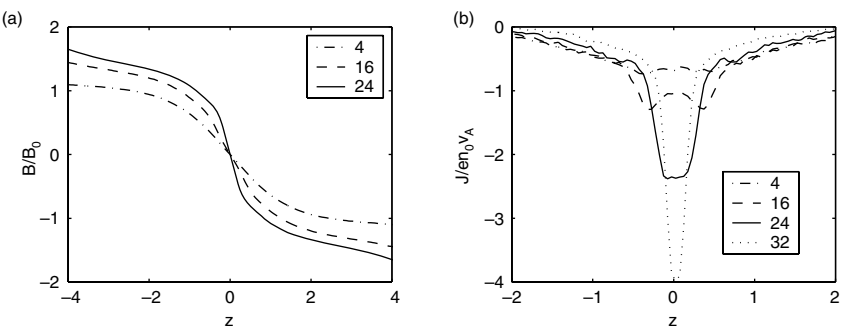

Fig. 3.21. Profiles in z at $x = 0$ and averaged over all values of y at the indicated times $\Omega_{\rm i0}t$ for (a) the magnetic field B_x and (b) the total current density J_y.

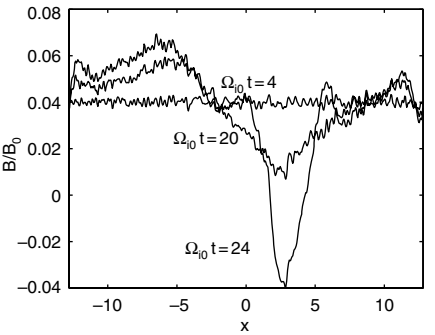

Fig. 3.22. Profiles in x at $z = 0$ and averaged over all values of y at the indicated times $\Omega_{i0}t$ for the magnetic field B_z.

3.3.5 Summary and outlook

Investigations of collisionless magnetic reconnection in the terrestrial magnetotail must, at least for the near-Earth portion of the tail, confront the underlying 2D nature of the tail current sheet. Studies of magnetic reconnection in 1D current sheets do not suffice. This has led to the long history of the onset problem for reconnection in the tail. There are two basic issues associated with the presence of the normal field B_n. The first is that the ion gyromotion in B_n can disrupt the free-streaming motion that provides the collisionless damping to drive the tearing instability. Only if B_n/B_0 is smaller than its typical value of 0.1 and/or the current sheet is unusually thin ($\rho_{i0}/\lambda \approx 1$) can one expect the spontaneous ion tearing instability to survive. Even this limited parameter space is probably excluded by the second effect, namely the electron stabilization. The various kinetic treatments based on the 2D analysis are now in general agreement that the ion tearing mode cannot exist in the transition region between dipole and tail fields where significant disruptions associated with substorm onset occur. The situation further down the tail is less clear.

The linear 2D tearing analysis, however, cannot provide the full story regarding reconnection in the magnetotail. A key feature of magnetospheric reconnection is that it occurs in bounded spatial regions which are, however, topologically open. Particles can ballistically enter the reconnection region, transit through it, and escape, perhaps never to return. The reconnected magnetic flux is also free to flow away from the reconnection region. The initial studies by Sitnov *et al.* (2002) suggest that these effects can alter significantly the previous results. The reconnection community has barely begun to address the consequences of a 3D open topology for reconnection.

A further complication of reconnection in real systems is its bimodal character. Not only does the kinetic physics near the X-line, which breaks the frozen-in condition, lead to large-scale consequences in terms of particle energization and magnetic flux reconfiguration, but the large-scale system reacts back on the local reconnection region in terms of the boundary conditions that are exerted on this region. Thus there is compelling statistical evidence that northward turnings of the IMF are frequently

involved in triggering of substorms. Again, our quantitative understanding of the relevant physical processes is still at an elementary level.

Thus, while at one level the onset problem has been answered – the spontaneous ion tearing instability is unlikely to be operative in the magnetotail – at the more basic level we still do not understand the causal sequences that result in the large-scale reconnection processes associated with a substorm.

3.4 Hall MHD reconnection

A. Bhattacharjee and J. C. Dorelli

As discussed in Section 3.1, the classical models of Sweet–Parker and Petschek leave us with a quandary for low-resistivity plasmas (corresponding to high Lundquist numbers S; Section 2.1). On the one hand, the Sweet–Parker time scale is realizable dynamically in the high-S regime in high-resolution resistive MHD simulations, but it is too slow to explain dynamic processes such as solar flares or magnetospheric substorms. On the other hand, the Petschek model, which yields a faster time scale, appears not to be realizable in the high-S regime.

In addition, steady-state resistive models can provide but one time scale – that of steady reconnection (proportional to $S^{1/2}$ for Sweet–Parker and $\ln S$ for Petschek). However, steady reconnection is not a generic condition. It is a strong theoretical assumption and one that is frequently violated in many dynamical situations of great physical interest. In particular, there are phenomena involving magnetic reconnection in laboratory as well as space plasmas where the dynamics exhibits an impulsiveness, that is, a sudden increase in the time derivative of the growth rate. This is often referred to as the *trigger problem* – the magnetic field configuration evolves slowly for a long period of time, only to undergo a sudden dynamical change over a much shorter period of time. As the classical steady-state reconnection models of Sweet–Parker and Petschek do not include time dependency, they cannot account for the time evolution of the reconnection rate.

In this section, we present recent Hall MHD reconnection models that address the regime of very high Lundquist numbers S. We consider thin current sheets whose width Δ falls into the collisionless range between the electron and ion skin depths, that is, $d_\mathrm{e} \equiv c/\omega_\mathrm{pe} < \Delta \leq c/\omega_\mathrm{pi} \equiv d_\mathrm{i}$ (or $d_\mathrm{e} < \Delta \leq \rho_\mathrm{s}$ in the presence of a guide or toroidal field, where $\rho_\mathrm{s} = \sqrt{\beta} d_\mathrm{i}$). In this regime dissipation is governed by the generalized Ohm's law (3.4)

$$\mathbf{E} + \mathbf{v} \times \mathbf{B} = \eta \mathbf{j} + \frac{m_\mathrm{e}}{ne^2} \frac{\mathrm{d}\mathbf{j}}{\mathrm{d}t} + \frac{\mathbf{j} \times \mathbf{B}}{ne} - \frac{\nabla p_\mathrm{e}}{ne}. \tag{3.70}$$

Here the electron pressure p_e is assumed to be a scalar, and only a portion of the electron inertia term, $\mathrm{d}\mathbf{j}/\mathrm{d}t = \partial \mathbf{j}/\partial t + \mathbf{v} \cdot \nabla \mathbf{j}$, is retained. In contrast to the discussion of Section 3.2, we retain the Ohmic term (first term on the RHS), providing dissipation in competition with the electron inertial term (second term on the RHS). The last two terms on the right-hand side of Eq. (3.70), collectively referred to as the Hall MHD terms, do not contribute to the dissipation in this model. But, as discussed in Section 3.1, they govern whistler and kinetic Alfvén wave dynamics and may thus be responsible not only for fast reconnection but also for a plausible explanation of the trigger problem.

In the following sections we describe some recent analytical and numerical models that focus on the issue of scaling of Hall MHD reconnection in impulsive as well as quasi-steady regimes. It is difficult to determine scaling results by numerical computations alone simply because the range of parameters (such as the electron-to-ion mass ratio and the system size) that can be explored by nonlinear Hall MHD codes is still quite limited. It is therefore useful to consider reduced systems which are amenable to analytic treatment, can be tested and benchmarked numerically, and can be extrapolated to yield scaling results in realistic plasma regimes. In Section 3.4.1, we present results from a reduced collisionless model in which electron inertia provides the dominant mechanism for breaking field lines, and strongly time-dependent current singularities drive impulsive reconnection. In Section 3.4.2, we present results from a semi-collisional 2D Hall MHD model in which resistivity provides the mechanism for breaking field lines.

3.4.1 Impulsive Hall MHD reconnection

Here we present some analytical and numerical results from the so-called two-field model, which is deduced from the primitive Hall MHD equations by means of analytical approximations. The basic assumptions are a large guide field and low beta, so that the compressional wave propagates faster than any other wave in the system and the fluid motion is essentially incompressible. It is assumed that the resistivity is zero, and electron inertia breaks field lines. This model, which is simpler than the full two-fluid or Hall MHD equations, is amenable to analytical treatment in the linear as well as nonlinear regimes, and captures certain essential features of impulsive Hall MHD reconnection dynamics in collisionless plasmas. By a combination of analytical and numerical studies, we are able to obtain scaling results on the reconnection rate that can be compared with results obtained from other computational studies.

The dynamics is two-dimensional, and depends only on the coordinates x and z, with y as an ignorable coordinate. The magnetic field is represented as

$$\mathbf{B}(x,z,t) = B_0\hat{\mathbf{y}} + \nabla\Psi(x,z,t)\times\hat{\mathbf{y}}, \tag{3.71}$$

where B_0 is a constant and large guide field, and $\Psi(x,z,t)$ is a flux function. The velocity is represented as

$$\mathbf{v}(x,z,t) = \hat{\mathbf{y}}\times\nabla\Phi(x,z,t), \tag{3.72}$$

where $\Phi(x,z,t)$ is a stream function. The two-field equations are given by (Grasso *et al.*, 1999)

$$\partial F/\partial t + [\Phi, F] = \rho_{\rm s}^2[U,\Psi], \tag{3.73}$$

$$\partial U/\partial t + [\Phi, U] = [J,\Psi], \tag{3.74}$$

where $J = -\nabla_\perp^2\Psi$, $U = \nabla_\perp^2\Phi$, $F = \Psi + {\rm d}_{\rm e}^2 J$, and the Poisson bracket is defined by $[\Phi, F] \equiv \hat{\mathbf{y}}\cdot\nabla\Phi\times\nabla F$. In Eqs. (3.73) and (3.74), all quantities have been made dimensionless. In particular, distance is normalized by the characteristic equilibrium scale L_z in the z direction, and time is normalized by the Alfvén time scale $\tau_{\rm A} = \sqrt{\mu_0 n_0 m_{\rm i}}L_z/B_{y0}$ based on the magnetic field component B_{y0}. The two dimensionless parameters are the (normalized) electron skin depth $d_{\rm e} = c/(\omega_{\rm pe}L_z)$, where $\omega_{\rm pe}$ is

the electron plasma frequency, and the (normalized) ion sound gyro radius $\rho_s = \sqrt{T_e/m_i}/(\Omega_i L_z) = \rho_i \sqrt{T_e/T_i}$ where T_e and T_i are the electron and ion temperatures, Ω_i is the ion cyclotron frequency, and ρ_i is the ion Larmor radius (also normalized by L_z). The term proportional to ρ_s^2 on the right of Eq. (3.73) is due to finite electron compressibility, and can be traced to the electron pressure gradient term in the generalized Ohm's law (3.70). The linearized versions of Eqs. (3.73) and (3.74) support kinetic Alfvén waves.

For the purpose of the present study, periodic boundary conditions are imposed in both x and z directions, with the domain of a single periodic cell given by $-L_x \le x \le L_x$, and $-L_z \le z \le L_z$. We choose $L_z = \pi$ and $L_x = \pi/\epsilon$, where $\epsilon = L_z/L_x$ is the slab aspect ratio. Due to the symmetry properties of Eqs. (3.73) and (3.74), we can consider $\Psi(\Phi)$ to be an even (odd) function in both x and z for all time, if it is so initially. In the following discussion we consider the linear and nonlinear evolution of the equilibrium given by $J_0 = \Psi_0 = \cos z$, $U_0 = \Phi_0 = 0$. It is doubly periodic, and is unstable with respect to double tearing modes, which grow around resonant surfaces, located at $z = 0$ and $\pm\pi$ in the periodic cell. Despite its apparent simplicity, the two-field model is computationally challenging, because it involves tracking near-singular and dynamic current sheets that grow near-explosively in the nonlinear regime. We use the Magnetic Reconnection Code (MRC) which is a massively parallel code in an Adaptive Mesh Refinement (AMR) framework (Bhattacharjee *et al.*, 2005).

To determine the linear instability of equilibria that depend only on z, we write $\Psi = \psi_0 + \psi_k(z,t)\cos(kx)$, where $k = m\epsilon$, m is an integer and ϵ is the aspect ratio defined earlier. The linear dispersion relation and growth rate of collisionless tearing modes in the two-field model have been obtained analytically using boundary-layer and asymptotic matching techniques (Porcelli, 1991). The analytic theory is mostly based on the large-Δ' approximation, i.e., $\Delta' d_e \gg \min[1, (d_e/\rho_s)^{1/3}]$, where $\Delta' = 2\sigma \tan(\sigma\pi/2)$, $\sigma = \sqrt{1-k^2}$.[2] The parameter Δ' is positive for $0 < k \le 1$, which is necessary for instability. The large Δ' regime generally requires small k because Δ' is proportional to k^{-2} for small k, that is, small $m\epsilon$. When $0.5 \le \epsilon < 1$, only the $m = 1$ mode is linearly unstable. For $\epsilon < 0.5$, a larger range of m-numbers are destabilized, up to a maximum mode number equal to integer (ϵ^{-1}). Bhattacharjee *et al.* (2005) have presented fairly comprehensive results on the linear instability of the system for arbitrary values of the parameters d_e, ρ_s, and k. These results generally confirm the predictions of analytic linear theory in the regime of large Δ' which generally requires small k. In the case $d_e \gg \rho_s$, when Δ' is large, the analytic theory predicts the linear growth rate $\gamma_L \approx k d_e$. For the case $d_e \ll \rho_s$, the analytic theory predicts $\gamma_L \approx k(d_e \rho_s^2)^{1/3}$ in the large-Δ' regime. We note that the linear growth rates depend quite strongly on the aspect ratio (proportional to k), the parameter ρ_s, and even the electron inertia, which enters the parameter d_e, and provides the mechanism for breaking field lines. An important question is how these dependencies are altered in the nonlinear regime.

[2] The parameter Δ' governs the matching of a linear tearing mode between the external, ideal-MHD, solution and the internal solution in the dissipative layer (see, e.g., Biskamp, 2000). $\Delta' > 0$ is a necessary and sufficient condition for linear instability.

It can be shown, under certain strong assumptions (Ottaviani and Porcelli, 1993; Grasso *et al.*, 1999; Bhattacharjee *et al.*, 2005), that when $d_e \neq 0$, $\rho_s \neq 0$ the island half-width w, defined by the relation $\psi(0,0,t) = 1 - w^2(t)/2$, obeys the nonlinear equation

$$\frac{d^2\hat{w}}{d\tilde{t}^2} \approx \frac{1}{4}(\hat{w} + c_J \hat{w}^4), \tag{3.75}$$

where $\tilde{t} = \gamma_L t$ is the time variable normalized by the linear growth rate γ_L, $\hat{w} \equiv w/\delta_L$ where δ_L (equal to $d_e^{1/3}\rho_s^{2/3}$ in the large-Δ' regime) is the linear boundary-layer width, and c_J is a positive quantity, slowly varying in time, of the order of unity. We note that $\psi(0,0,t=0) = 1$ and $w(0) = 0$, and we have included a factor of $1/4$ in the first term of Eq. (3.75) because w grows exponentially with half of the linear growth rate γ_L. Equation (3.75) predicts that the island width grows near-explosively in the nonlinear regime. By the time w becomes of the order of the system size, most of the magnetic flux is reconnected, and the near-explosive growth of the island is quenched. (The quenching process is not described by Eq. (3.75), which breaks down when w becomes of the order of the system size.)

It is worth noting that the tendency for the formation of a current singularity and island blow-up is already inherent in this problem due to the presence of finite electron inertia even when $\rho_s = 0$. It is in this sense that we describe the current singularity as a driver of impulsive reconnection. The analytical model also predicts that the linear as well as the nonlinear reconnection rate does depend on the system size (that is, k). In what follows, we will test the predictions of this analytical model with numerical simulations using the MRC.

Figure 3.23 is a typical image plot of the current density $J(x,z,t) = -\nabla_\perp^2 \psi$ in the nonlinear regime. This picture illustrates the usefulness of AMR grids in resolving intense and thin current sheets produced during collisionless reconnection dynamics. The magnified images in the smaller inserts show clearly the detailed spatial structure

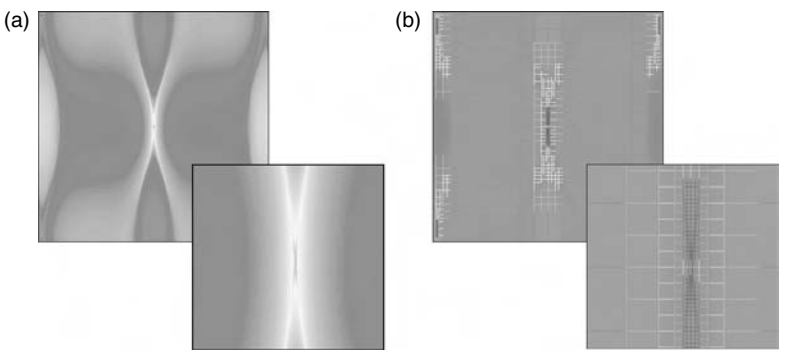

Fig. 3.23. (a) Current density in the nonlinear phase. The smaller inserts are magnified images of the near-singular current sheet at the X-point, showing how AMR enables resolution of the fine structure. (b) We overlay the plot with a visualization of the adaptive grids, as they provide higher resolution near the small-scale structures as needed. See also color plate.

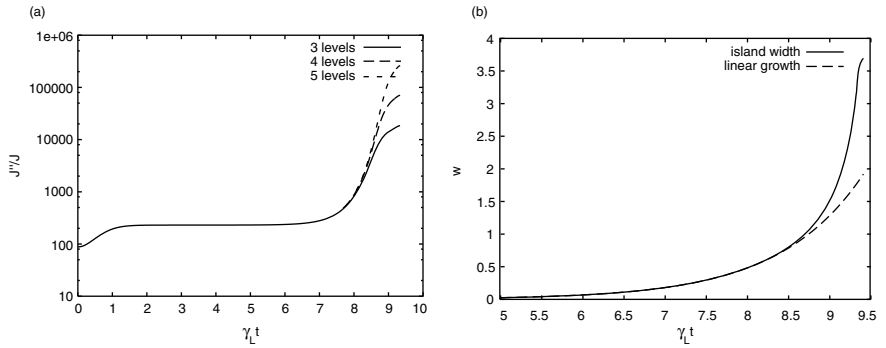

Fig. 3.24. (a) Plot of $J^{-1}(\partial^2 J/\partial x^2)$ at the origin, which is inverse square of the thin current sheet width. Very high resolution is needed to follow the rapidly shrinking current width. (b) Plot of the time evolution of the island width.

in the vicinity of an X-point, which is a signature of collisionless fast reconnection, and the AMR grids used to resolve them.

Figure 3.24a shows a plot of $J^{-1}(\partial^2 J/\partial x^2)$ at the origin, which is essentially the reciprocal of the square of the current sheet width. After a period of exponential growth, this quantity tends to increase very rapidly, consistent with the analytical prediction given by Bhattacharjee *et al.* (2005). We show this plot for three different levels of AMR. It is clear by inspection that the higher the level of AMR, the longer is the blow-up phase, before the process saturates. Figure 3.24b shows a plot of the time evolution of the island width.

In Fig. 3.25, we compare the simulation result from the MRC with the island equation (3.75) for the same parameters as Fig. 3.24. (Note that the ordinate is plotted on a logarithmic scale.) As mentioned above, the constant c_J is not fixed by our analysis. We find that $c_J \approx 0.1$ provides a reasonably good fit for the simulation results.

Shay *et al.* (1999, 2004) have presented extensive numerical results in support of their claim that the reconnection eventually evolves into a late nonlinear phase, which they call the *asymptotic phase*, when the reconnection rate becomes of the order of one-tenth of the Alfvén speed (based on the magnetic field just upstream of the reconnection layer), independent of the electron and the ion skin depth as well as the system size. (See also Section 4.1.) We revisit this question here because the initial condition for the magnetic field used by Shay *et al.* is very similar to the one used here for the field in the x, z plane, perpendicular to the guide field. There are, however, significant differences between our model and theirs. Shay *et al.* use the full Hall MHD equations and take the equilibrium guide field to be zero. We consider an equilibrium with a large and constant guide field, and integrate the reduced two-field equations which are obtained from the full Hall MHD equations in the limit of large toroidal field and low beta. Despite these differences, it is instructive to compare our results with those of Shay *et al.*, because there is no doubt that both simulations exhibit an asymptotic phase. (In these simulations, we explore parameter regimes in which reconnection proceeds nonlinearly to form islands with widths of the order of the system size so that the inequality $z \ll \rho_s, d_e$ is realized.) We suggest that the

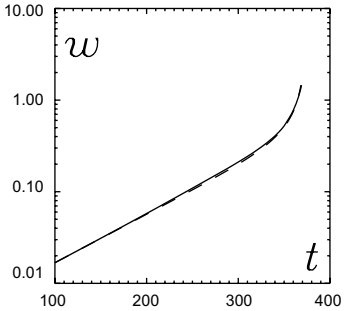

Fig. 3.25. Island half-width $\hat{w}$ as a function of time from numerical simulation (solid curve) and from Eq. (3.75) with $c_J = 0.1$ (dashed curve), for the case with $\rho_s = 0.2$, $d_e = 0.1$, $k = 0.5$, $\gamma_L = 0.0024$.

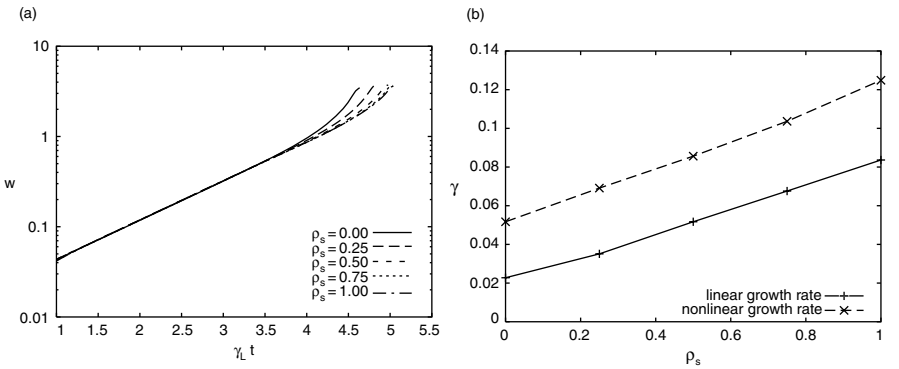

Fig. 3.26. (a) Island width time evolution for different values of ρ_s for $d_e = 0.25$, $\epsilon = 0.5$, in rescaled (with linear growth rate) time. (b) Linear and nonlinear growth rates (at fixed island size) for the runs in Fig. 3.26a.

instantaneous reconnection rate, as measured by the rate of change of the island width (which is proportional to the inflow velocity towards the X-point) is a good diagnostic with which we can test the claim regarding asymptotic reconnection rates.

Figure 3.26a shows five plots of the island width as a function of $\gamma_L t$, where γ_L is the linear growth rate, determined numerically from the MRC for the parameters $d_e = 0.1$ and $\rho_s = 0$, 0.25, 0.5, 0.75, 1.0, holding the aspect ratio ϵ fixed at the value 0.5. We observe that the five plots essentially lie on top of each other for most of the time interval during the evolution of the instability. In other words, the equation $w = w(\gamma_L t)$ is a reasonably good description for the island width evolution for most of the time interval. Had this been the whole story, the issue of scaling of the reconnection rate would be completely settled, and we could claim, following Ottaviani and Porcelli (1993, 1995), that the instantaneous reconnection rate at all times scales as the linear growth rate, which is given by $\gamma_L = k(d_e \rho_s^2)^{1/3}$ in the large-Δ' regime. In turn, this would imply that the reconnection rate is not a "universal constant," and depends on the aspect ratio as well as d_e and ρ_s. Under these conditions, the dependence on the electron mass, which provides the mechanism breaking field lines, is weak

(proportional to $m_e^{-1/6}$) but nonetheless significant because it establishes the point of principle that the reconnection rate is not independent of the parameter that breaks field lines and controls the structure of the current sheet.

We note, however, that the equation $w = w(\gamma_L t)$ is not quite the whole story. The five curves in Fig. 3.26a do not lie on top of each other in the late nonlinear phase, although they tend to be quite close to doing so as the ratio d_e/ρ_s becomes larger. In order to determine numerically the scaling behavior of the time-dependent growth rate in the late nonlinear (or asymptotic) phase, we choose to examine the nonlinear growth rate at a fixed size of the island width ($w = 2$), which falls right in the middle of the late nonlinear phase. (The choice $w = 2$ is admittedly ad hoc, but our qualitative conclusions regarding the late nonlinear phase do not depend on this specific choice.) Figure 3.26b shows the plots of γ_{NL} for the five values of ρ_s given above at fixed island size. For comparison, we also plot γ_L for the same values of ρ_s. From inspection of Fig. 3.26b, we conclude that although the growth rate in the late nonlinear regime shows deviation from the equation $w = w(\gamma_L t)$, this growth rate scales with ρ_s in approximately the same way as γ_L does. A similar conclusion holds for the dependence of the growth rate on d_e in the late nonlinear phase.

We now investigate the dependency of the asymptotic growth rate on the aspect ratio ϵ. Figure 3.27a shows five plots of the island width as a function of $\gamma_L t$, where γ_L is the linear growth rate, determined numerically for fixed $d_e = 0.25$ and $\rho_s = 0.75$, and five different values of the aspect ratio given by $\epsilon = 0.1$, 0.2, 0.3, 0.4, 0.5. Once again, we observe that the five plots essentially lie on top of each other for most of the time interval during the evolution of the instability. In other words, in this case too the equation $w = w(\gamma_L t)$ is a reasonably good description for the island width evolution for most of the time interval. This would imply a strong dependence of the reconnection rate on k, in contrast with the conclusion of Shay and coworkers. However, as in Fig. 3.26a, we note that the five curves in Fig. 3.27a do not lie on top of each other in the late nonlinear phase. So in order to determine numerically the dependence of the time-dependent growth rate on the aspect ratio in the late

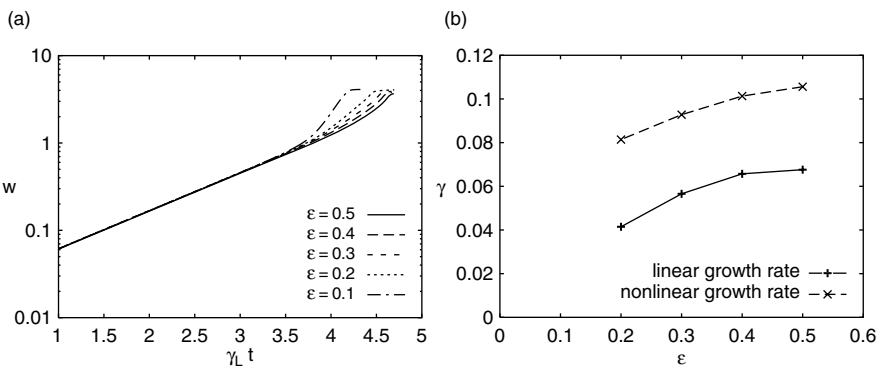

Fig. 3.27. (a) Island width time evolution for different values of ϵ for $\rho_s = 0.75$, $d_e = 0.25$ in rescaled (with linear growth rate) time. (b) Linear and nonlinear growth rates (at fixed island size) for the runs in Fig. 3.27a.

nonlinear phase, we choose to examine the nonlinear growth rate at a fixed size of the island width ($w = 2$).

Figure 3.27b shows the plots of $\gamma_{\rm NL}$ for four values of ϵ at fixed island size. For comparison, we also plot $\gamma_{\rm L}$ for the same values of ϵ. From inspection of Fig. 3.27a, we conclude that although the growth rate in the late nonlinear regime shows deviation from the equation $w = w(\gamma_{\rm L} t)$, this growth rate clearly exhibits a definite dependency on ϵ. However, this dependency of the nonlinear growth rate on ϵ appears to be a little weaker than the dependency of $\gamma_{\rm L}$ on ϵ.

In summary, we have presented linear and nonlinear results on collisionless reconnection in a two-field model, valid in the regime of high guide (or toroidal) field and low plasma beta. In this model, electron inertia breaks field lines, and two-fluid (or Hall MHD) effects enter via the electron pressure gradient term in the generalized Ohm's law. The two parameters representing electron inertia and pressure gradient are $d_{\rm e}$ and $\rho_{\rm s}$, respectively. Even if $\rho_{\rm s} = 0$, the system of equations exhibits near-explosive nonlinear growth of current sheet amplitude and magnetic island width. In the regime $\rho_{\rm s} > d_{\rm e}$ the tendency for near-explosive growth persists, but we repeat for emphasis that this tendency is already inherent in the system without $\rho_{\rm s}$. Thus, in the present model, current singularities drive impulsive reconnection, and it is not surprising that the scaling properties of this system exhibit dependency not only on $\rho_{\rm s}$ but also on $d_{\rm e}$, which breaks field lines and controls the structure of the current sheet. This type of dynamics has been studied by Shay *et al.*, who have suggested that the reconnection rate tends to a "universal" rate of the order of one-tenth of the Alfvén speed (where the Alfvén speed is calculated using the upstream magnetic field strength) in the late nonlinear regime. We have demonstrated that the reconnection rate in the late nonlinear regime of the two-field model attains no such "universal" behavior, but depends on $d_{\rm e}$ and $\rho_{\rm s}$ in approximately the same way as the linear growth rate. We have also demonstrated that this reconnection rate depends on the aspect ratio (or the system size), although this dependency is a little weaker in the late nonlinear regime than it is in linear theory. These dependencies cast some doubt on heuristic analyses which use linear wave dispersion relations to make strong conclusions regarding "universal" reconnection rates in nonlinear regimes.

As discussed above, one of the significant qualitative consequences of the present study is that the dynamics and scaling properties of Hall MHD or two-fluid collisionless reconnection models are not independent of the mechanism that breaks field lines. In the present context, electron inertia is that mechanism, and it introduces filamentary and rapidly time-varying current density structures that persist through the linear as well as nonlinear regimes, and produce dynamics that is quite different than resistive MHD dynamics. That this is so for linear theory has been known for a long time, but the effect persists also in the nonlinear regime of the present model. Thus, in problems of time-dependent collisionless reconnection, current singularities that are dominantly controlled by electron inertia cannot, in general, be assumed to be a sideshow to ion-controlled reconnection. As the nature and dynamics of the current singularities do depend on whether resistivity or electron inertia breaks field lines, the sensitivity of the reconnection rate to these rather different mechanisms can be different.

3.4.2 Resistive Hall MHD reconnection scaling: Role of flux pile-up

We now present analytical and numerical results in a quasi-steady Hall MHD reconnection model where resistivity is the mechanism that breaks field lines. (This complements the study in Section 3.4.1, where electron inertia breaks field lines and the system is strongly time-dependent and impulsive.) While the results of the GEM Reconnection Challenge (Birn *et al.*, 2001) suggest that Hall electric fields can, by themselves, allow magnetic reconnection to occur on time scales which are much shorter than the Sweet–Parker time scale, the question of how this reconnection rate scales with the system size was not addressed by the GEM challenge. Answering this question is particularly important in the context of the solar corona, where the ion inertial length can be smaller than the length of a typical coronal arcade by a factor of ten million. As discussed in Section 3.1.2, Shay *et al.* (1999, 2004) have argued that the *ion inertial region* – the spatial region over which electron and ion bulk velocities decouple – in a 2D reconnection process should have a thickness of the order of an ion inertial length, and a width of the order of ten ion inertial lengths. Thus, they argue that a Sweet–Parker analysis of the ion inertial region implies that the reconnection inflow speed should be about a tenth of an Alfvén speed and insensitive to the system size. In an earlier paper, Biskamp *et al.* (1997) had pointed out that, although the quasi-steady reconnection rate may be insensitive to the mechanism that breaks field lines (consistent with the GEM challenge results), the formation of a macroscopic *ion inertial sheet* (analogous to the Sweet–Parker current sheet in resistive MHD) cannot be ruled out. Subsequent studies (Wang *et al.*, 2001; Dorelli and Birn, 2003; Fitzpatrick, 2004) seem to be consistent with the conjecture advanced by Biskamp *et al.*

In this section, we will approach the problem from a different perspective that draws on an analogy between the current debate about system size scaling and the Petschek versus Sweet–Parker debate of the last several decades. In particular, Biskamp's (Biskamp, 1986) numerical experiments suggested that driven magnetic reconnection occurs, in the context of resistive MHD, via a process of magnetic flux pile-up (see also Parker, 1973b; Sonnerup and Priest, 1975; Priest and Forbes, 1986) rather than in a Petschek configuration. In flux pile-up reconnection, magnetic energy accumulates upstream of a Sweet–Parker current sheet to accommodate a sub-Alfvénic inflow velocity. As the plasma resistivity is decreased, the magnetic pile-up increases, compensating for the resulting decrease in the inflow velocity (which scales like the square root of the resistivity in the Sweet–Parker model); thus, the reconnection rate is insensitive to the plasma resistivity.

However, momentum conservation considerations prevent this resistivity-independent reconnection rate from being realized at arbitrarily small resistivities (Priest, 1996; Litvinenko, 1999). Since the plasma inflow Alfvén Mach number is much less than one, and there is a finite upstream pressure available to drive this sub-Alfvénic inflow, there must be an upper limit to the amount of magnetic energy which can accumulate upstream of the current sheet. Thus, one expects to observe two distinct regimes of flux pile-up reconnection: a presaturation phase, in which the reconnection rate is insensitive to the plasma resistivity; and a postsaturation phase, in which the reconnection rate scales strongly with plasma resistivity.

In principle, one can generalize the above arguments to address the scaling of Hall MHD reconnection with system size. Just as the strong scaling of magnetic pile-up with resistivity in resistive MHD implies that the reconnection rate scales strongly with resistivity in the postsaturation regime, a strong scaling of magnetic flux pile-up with the ion inertial length in Hall MHD implies (by arguments very similar to those made by Litvinenko, 1999) that the reconnection rate scales strongly with the system size (i.e., the ratio of the characteristic system length to the ion inertial length). We illustrate this argument with a simple example (see Dorelli, 2003, for details).

Consider the following incompressible stagnation point flow field:

$$U_x = U_0(x/\lambda), \tag{3.76}$$

$$U_z = -U_0(-z/\lambda), \tag{3.77}$$

where U_0 is a constant with dimensions of speed, and λ is a length scale characterizing the stagnation point flow. If we assume that the magnetic field is unidirectional, $\mathbf{B} = B_x(z)\hat{\mathbf{x}}$, and that $B_x(0) = 0$, then the flow field (3.76) and (3.77) describes the annihilation of antiparallel magnetic fields (in the x, z plane) at a one-dimensional current sheet, with the current flowing in the y direction. One can demonstrate (see, for example, Parker, 1973b; Sonnerup and Priest, 1975) that such a flow field solves the momentum and continuity equations; the magnetic field profile is then determined from Ohm's law, and the thermal pressure, $p(x, z)$, is determined by the conditions of pressure balance:

$$p(x,z) = p_0(x) - \frac{1}{2}\rho U^2 - \frac{B^2}{2\mu_0}, \tag{3.78}$$

where ρ is the plasma density (hereafter assumed to be constant), and p_0 is a constant. As described by Dorelli (2003), one can generalize the analysis of Sonnerup and Priest (1975) to obtain solutions which describe the pile-up of magnetic energy upstream of the current sheet:

$$B_x(\zeta) = E_y\left(\frac{S}{U_0}\right)^{1/2} \exp\Big(-\frac{1}{2}\alpha\zeta^2\Big)\int_0^\zeta \exp\Big(-\frac{1}{2}\alpha u^2\Big)\,\mathrm{d}u \tag{3.79}$$

where $\zeta = (SU_0)^{1/2}z$, $\alpha = 1 + S\delta_\mathrm{i}C$, S is the Lundquist number ($S = \mu_0\lambda v_\mathrm{A}/\eta$), $\delta_\mathrm{i} = d_\mathrm{i}/\lambda$, and C is an arbitrary constant.

Figure 3.28 shows the magnetic field profile given by (3.79) for various values of the ion inertial scale; clearly we can see that, for a fixed Lundquist number, the pile-up scales with δ_i. Thus, if we define "system size" to be the scale of the stagnation point flow, then we see that the flux pile-up required to support a given inflow decreases as the system size decreases. Specifically, if $B_x^{\max}$ is the magnitude of B_x at the location of its local maximum, then:

$$B_x^{\max} = E_y\Big[\frac{2S}{U_0(1+S\delta_\mathrm{i}C)}\Big]^{1/2} D_+(\chi), \tag{3.80}$$

where $D_+(\chi)$ is Dawson's integral (Abramowitz and Stegun, 1964),

$$D_+(u) = \mathrm{e}^{-u^2}\int_0^u \mathrm{e}^{t^2}\,\mathrm{d}t, \tag{3.81}$$

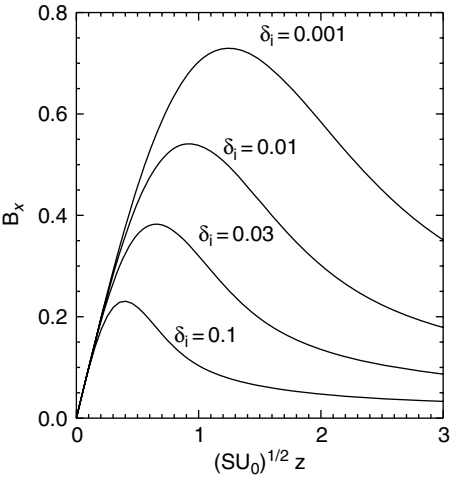

Fig. 3.28. The $(x, z$ plane) magnetic field component (3.79) is shown for several values of δ_i.

and the current sheet thickness χ follows from $1/(2\chi) = D_+(\chi)$. Thus, as the Lundquist number approaches infinity, the magnetic flux pile-up saturates at a level which is independent of the Lundquist number:

$$B_x^{\rm sat} = E_y \Big(\frac{2}{\delta_{\rm i} C}\Big)^{1/2} D_+(\chi). \tag{3.82}$$

Figure 3.29a shows the maximum upstream magnetic field, given by (3.81), as a function of S, where we have set $E_y = 0.009$, $U_0 = 0.1$, and $C = 0.01$. As shown in Fig. 3.29b, a similar pile-up saturation effect, with the saturation level strongly dependent on the ion inertial length (and insensitive to the Lundquist number) in the high-Lundquist number limit, was observed in resistive Hall MHD simulations of magnetic island coalescence (Dorelli and Birn, 2003).

While the observation of flux pile-up in an island coalescence process is not surprising, since such pile-up has been observed previously in the context of resistive MHD (Biskamp, 1986), the δ_i-dependent saturation of the pile-up observed in the Hall MHD runs has implications for the scaling of the reconnection rate with system size. Following Litvinenko (1999), the maximum flux pile-up reconnection rate may be estimated by constraining the upstream plasma pressure to be positive. One obtains (Dorelli, 2003):

$$E_y \approx 1.31(\beta U_0)^{1/2} \Big(\frac{1 + S\delta_{\rm i} C}{S}\Big)^{1/2}. \tag{3.83}$$

When the system size is very large (i.e., when $\delta_{\rm i}$ approaches 0), the maximum reconnection rate decreases as the square root of the Lundquist number; however, for any finite system size, a limit is always reached (for large enough S) in which the reconnection electric field becomes insensitive to S. In this limit, however, the electric field scales strongly with system size ($E_y \propto \delta_{\rm i}^{1/2}$). This dependence of the asymptotic (as

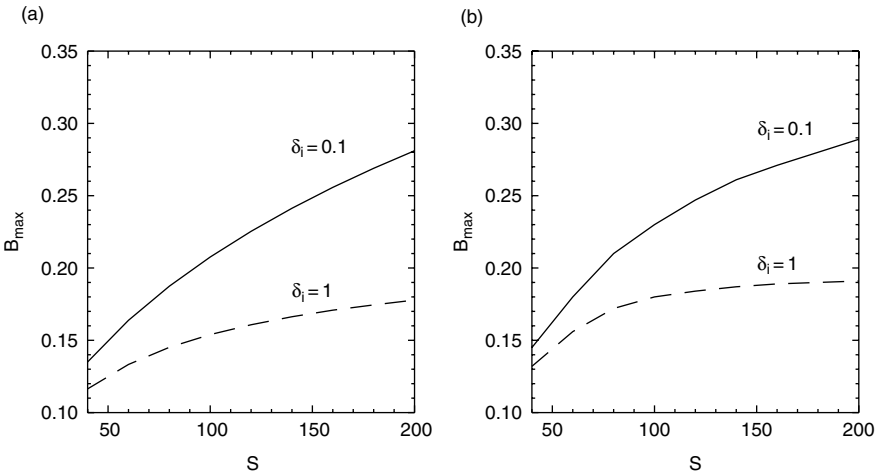

Fig. 3.29. The local maximum of the magnetic field B_x in the pile-up region as a function of the Lundquist number S: (a) from the analytic model given by (3.81); (b) obtained from a simulation of magnetic island coalescence, upstream of the current sheet between the coalescing islands (Dorelli and Birn, 2003).

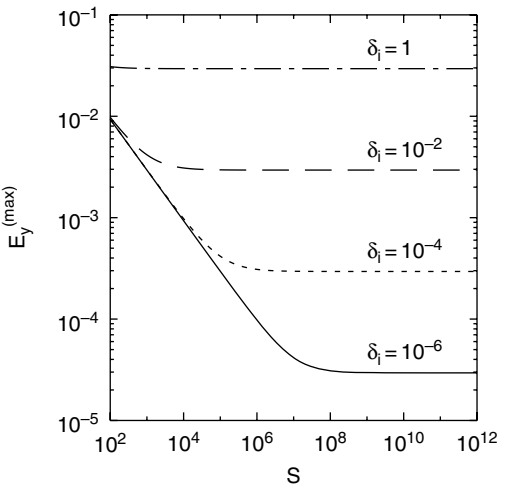

Fig. 3.30. Maximum reconnection electric field (3.83) as a function of S and system size.

S approaches infinity) maximum reconnection electric field on system size is shown in Fig. 3.30.

The physical reason for the reduction in pile-up in Hall MHD flux pile-up reconnection can be understood as a consequence of the spatial structure of the guide field. This field has the form (Dorelli, 2003) $B_y = C\xi\zeta$, where C is an arbitrary constant, $\xi = (SU_0)^{1/2}x$, and $\zeta = (SU_0)^{1/2}z$. From Ampère's law, we can interpret the guide field as a stream function for the current density in the x, z plane. Thus, if the ion

inflow velocity is fixed, then the guide field describes an electron stagnation point flow, the magnitude of which is determined by the first derivatives of B_y near the origin. Thus, if C is independent of the plasma resistivity (i.e., if the first derivatives of the guide field scale inversely with the plasma resistivity), then the magnitude of the electron flow in the x, z plane scales like the square root of S, and less pile-up of magnetic energy is required upstream of the current sheet to support a given reconnection electric field. In other words, fast electron flows may transport magnetic flux into the current sheet without requiring a compensating drop in plasma pressure (so long as the large first derivatives of B_y are spatially localized within the ion inertial layer).

What, then, can we say about the scaling of the Hall MHD reconnection rate with system size? It appears that if Hall MHD reconnection occurs via a magnetic flux pile-up mechanism, where the magnetic pile-up is sensitive to the system size (see for example Wang *et al.*, 2001; Dorelli and Birn, 2003), then one expects to observe, in the large Lundquist number limit, a pile-up saturation effect which renders the reconnection rate sensitive to the system size. To settle this question conclusively, we will have to extend our analytic work to address much more general classes of problems than the one addressed in this section.

3.5 Role of current-aligned instabilities

J. Büchner and W. S. Daughton

In this section we return to the discussion of collisionless mechanisms that might generate nonideal contributions to the electric field $\mathbf{E} + \mathbf{v} \times \mathbf{B} = \mathbf{E}'$, providing dissipation $\mathbf{j} \cdot \mathbf{E}' \neq 0$. Section 3.2 focused on mechanisms that operate even in the absence of modes in the direction of the main current in a reconnecting current sheet. Here we discuss the particular role of current-aligned modes, that is, modes with a wave vector component k_y in the direction of the main current. (Since most of the applications are made to the magnetotail current sheet, we continue to use a magnetospheric coordinate system with x in the direction of the main magnetic field, y in the direction of the current, and z perpendicular to the current sheet.) There are several ways in which such modes might play a role.

Current-aligned modes might directly generate dissipative electric fields. In contrast to the DC electric fields discussed in Section 3.2, this influence involves net effects of alternating or fluctuating electric fields. This represents the classical concept of *anomalous resistivity*, which also entails the idea that the dissipative electric field depends on the local plasma properties, most specifically, the local current density. In the simplest case, this relationship would be governed by Ohm's law, with $\mathbf{E}'$ proportional to $\mathbf{j}$. However, more generally the factor between $\mathbf{E}'$ and $\mathbf{j}$ need not be a constant nor a scalar. Anomalous resistivity due to low-frequency plasma turbulence was considered in numerous papers, based, for instance, on ion-acoustic waves or lower-hybrid drift (LHD) waves (see, e.g., Rowland and Palmadesso, 1983).

But there is also the possibility that unstable current-aligned plasma waves may indirectly and nonlinearly interact with reconnection. Current-aligned modes might alter the structure of the current sheet and thereby change the stability properties and the early (linear) evolution or they might play a role in the nonlinear dynamic

evolution. Modes of particular interest in this kind of interaction are unstable kink- or sausage-type modes of the current sheet and the lower-hybrid drift instability.

In the following we review key theoretical and simulation results and discuss their applicability to experimental and observational findings of current-aligned instabilities as well as their potential importance for reconnection. We focus particularly on lower-hybrid drift modes and kink modes, which are well observed in the magnetosphere. Ballooning modes, driven by pressure gradients in the direction of the magnetic field curvature, will be discussed in Section 4.3. These modes operate also in the ideal MHD limit, although collisionless effects might provide important modifications.

3.5.1 Ion-acoustic instability

A current-driven instability which may cause anomalous resistivity in current sheets is the *ion-acoustic* (also called *ion-sound*) instability (e.g., Manheimer and Flynn, 1971). For space applications it was considered by Kan (1971). Ion-acoustic waves are unstably excited by a resonant interaction of drifting electrons or ions with the electric field oscillations of ion-sound waves (e.g., Krall, 1977), thereby providing momentum exchange between ions and electrons. Ion-sound waves propagate in plasmas with $T_\mathrm{e} \gg T_\mathrm{i}$ but become strongly Landau-damped when $T_\mathrm{e} \approx T_\mathrm{i}$. In the Earth's magnetosphere, the proton temperature is typically about 5 to 10 times larger than the electron temperature, so that ion-acoustic waves are strongly damped. As a result anomalous resistivity due to dissipation of ion-acoustic waves was expected mainly in laboratory plasmas, e.g. theta-pinch experiments (Liewer and Krall, 1973) and solenoidal fusion systems (Davidson *et al.*, 1977). Considering space plasmas, Coroniti (1985) concluded that anomalous resistivity resulting from the quasi-linear saturation of ion-acoustic instability is much too small to account for fast reconnection.

Considerably larger wave amplitudes could, however, be expected for stronger driven currents, for which ion-acoustic instabilities may develop even in plasmas with $T_\mathrm{i} \approx T_\mathrm{e}$. Also, instead of the usually applied one-dimensional quasi-linear theory which leads to plateau formation stopping wave generation, two-dimensional scattering of the electrons at ion fluctuations should be considered. The investigation of such systems can be carried out, however, only by means of numerical simulations, for which Vlasov-code simulations are most appropriate. Even one-dimensional recent Vlasov-code simulations (Watt *et al.*, 2002; Petkaki *et al.*, 2003) claimed a much stronger wave excitation than the one predicted by the one-dimensional quasi-linear theory. These findings revived the interest in the ion-acoustic instability as a possible mechanism for collisionless dissipation in space plasmas. Since these simulations were restricted to low mass ratios, Hellinger *et al.* (2004) and Büchner (2005) repeated the simulations for the same parameters as Watt *et al.* (2002) and Petkaki *et al.* (2003), but for the realistic proton/electron mass ratio $m_\mathrm{i}/m_\mathrm{e} = 1836$, using more accurate Vlasov solvers (see, e.g., Elkina and Büchner, 2005). As a result it appeared that for realistic mass ratios the old quasi-linear estimate can be recovered within an order of magnitude. It has still to be investigated, however, whether dissipation becomes sufficient to support reconnection in more realistic two- and three-dimensional cases,

which permit pitch-angle scattering, or under, quasi-stationary, continuous current flow conditions, driven by external forces.

3.5.2 Lower-hybrid drift instability

Waves in the lower-hybrid frequency range,

$$\Omega_{\rm LH} = \omega_{\rm pi}(1+\omega_{\rm pe}^2/\Omega_{\rm e}^2)^{-1/2}, \tag{3.84}$$

where $\omega_{\rm pi}$ and $\omega_{\rm pe}$ are the ion and electron plasma frequencies, respectively, and $\Omega_{\rm e}$ is the electron cyclotron frequency, are commonly observed in the current sheets at the Earth's magnetopause (e.g., Vaisberg *et al.*, 1983; André *et al.*, 2001; Lucek *et al.*, 2001; Bale *et al.*, 2002; Vaivads *et al.*, 2004a), the magnetotail (e.g., Gurnett *et al.*, 1976; Pu *et al.*, 1981) and in laboratory plasmas (e.g., Takeda and Inuzuka, 2000; Carter *et al.*, 2002b). They arise from the *lower-hybrid drift* (LHD) instability driven by diamagnetic drifts associated with strong pressure gradients, particularly in the boundary regions of the current sheets (Gary and Eastman, 1979; Labelle and Treumann, 1988).

The kinetic LHD instability (LHDI) requires gradients $L/\rho_{\rm i} \lesssim (m_{\rm i}/m_{\rm e})^{1/4}$ where L is the characteristic density scale length. This condition is easily satisfied in magnetospheric plasmas (Huba *et al.*, 1978). For weaker gradients $(m_{\rm i}/m_{\rm e})^{1/4} < L/\rho_{\rm i} < (m_{\rm i}/m_{\rm e})^{1/2}$, the LHDI transforms into the *drift cyclotron* instability (Freidberg and Gerwin, 1977). In the opposite limit of strong plasma pressure gradients $L \lesssim \rho_{\rm i}$, the LHDI becomes a fluid instability, excited through the coupling of a lower-hybrid wave with a drift wave (Huba *et al.*, 1978).

In magnetospheric plasmas, where usually $\omega_{\rm pe}^2 \gg \Omega_{\rm e}^2$, the expression for the lower-hybrid frequency simplifies to $\Omega_{\rm LH} \approx (\Omega_{\rm i}\Omega_{\rm e})^{1/2}$. Simple linear theory predicts that the fastest growing LHD waves are on the electron gyroscale $k_y\rho_{\rm e} \sim 1$, while more generally, due to nonlinear effects, a broad spectrum of wavelengths may be excited, reaching up to $k_y\sqrt{\rho_{\rm e}\rho_{\rm i}} \sim 1$. Unstable LHD waves propagate with diamagnetic drift velocity perpendicular to the local magnetic field (Krall and Liewer, 1971; Liewer and Krall, 1973; Huba *et al.*, 1977).

Perhaps the most attractive feature of LHDI over other current-driven instabilities such as ion-acoustic or Buneman instability, is that it persists for a much broader range of interesting parameters (i.e., weaker drifts and $T_{\rm e} < T_{\rm i}$). The quasi-linear saturation of the LHDI and the corresponding anomalous dissipation is well known (e.g., Davidson and Gladd, 1975). The LHDI therefore has been considered extensively as a possible candidate to enable reconnection through anomalous resistivity generated by wave–particle interactions (Huba *et al.*, 1977, 1980; Winske, 1981; Tanaka and Sato, 1981). However, for a typical current sheet structure, nonlocal kinetic theory predicts that the fastest growing modes are well localized on the edge of the current layer while enhanced fluctuations are required in the central region to produce significant anomalous resistivity (Huba *et al.*, 1980). The effects of finite plasma β and the electron ∇B drift-wave resonance damp the mode in the central region and limit the penetration to distances greater than $\sim L(T_{\rm e}/2T_{\rm i})^{1/2}$, where L is the half-thickness of the sheet. For the fastest growing short-wavelength modes $k_y\rho_{\rm e} \sim 1$, this conclusion is supported by kinetic simulations (Tanaka and Sato, 1981; Winske, 1981; Brackbill *et al.*, 1984),

observations at the magnetopause (Bale *et al.*, 2002), in the magnetotail (Shinohara *et al.*, 1998), and also by laboratory experiments (Carter *et al.*, 2002a,b).

Although the fastest growing linearly unstable LHD modes are on the electron gyroscale $k_y\rho_e \sim 1$, LHD modes are actually unstable over a broad range of wavelengths and frequencies ($\Omega_i < \omega \leq \Omega_{LH}$). Several of the early simulation papers on the LHDI report longer-wavelength electromagnetic instabilities near the center of the sheet after the saturation of the short-wavelength modes (Winske, 1981; Tanaka and Sato, 1981). Two explanations for these waves were recently proposed, one based on a new approach to the nonlocal linear stability (Daughton, 2003) and another based on the nonlinear excitation of a drift resonance between LHD modes generated at the edge of the current sheet and meandering ions at the center of the current sheet (Silin and Büchner, 2003a). Both predict that longer-wavelength LHD modes with wavelengths intermediate between the electron and ion gyroscale $k_y\sqrt{\rho_i\rho_e} \sim 1$ can penetrate into the central region, whereas the fastest growing modes with $k_y\rho_e \sim 1$ are confined to the edge of the current sheet. These new predictions have been confirmed in two dimensions by fully kinetic particle-in-cell (PIC) simulations at high mass ratio (Daughton, 2003).

Figure 3.31 demonstrates these effects, showing the current density $j_y(y, z)$ from a 2D PIC simulation at a realistic mass ratio for a hydrogen plasma, $m_i/m_e = 1836$ (Daughton, unpublished). The initial state is a thin Harris sheet with parameters

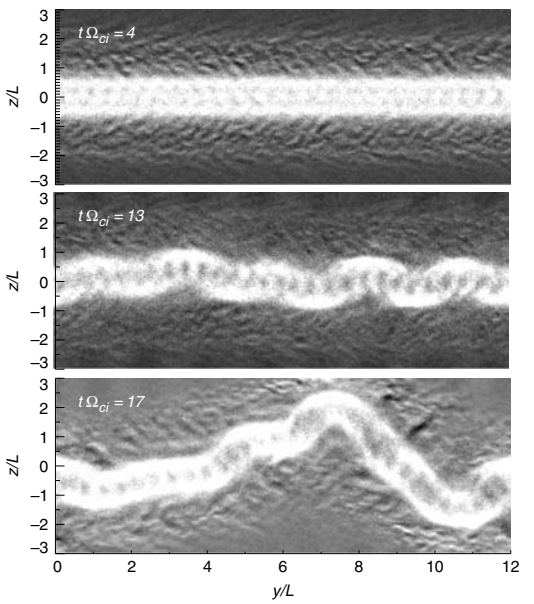

Fig. 3.31. Evolution of the current density $j_y(y, z)$ (grayscale) from a 2D PIC simulation at realistic mass ratio for a hydrogen plasma, $m_i/m_e = 1836$. The three panels demonstrate the transition from the saturation of the fastest growing, short-wavelength, LHD modes with $k_y\rho_e \sim 1$ (top) through intermediate-scale ($k_y(\rho_i\rho_e)^{1/2} \approx 0.8$) modes (center) to long-wavelength ($k_yL \approx 0.5$) ion–ion kink instability (bottom).

$\rho_i/L = 2$, $T_i = T_e$, $\omega_{pe}/\Omega_e = 4$ with a background density of $n_b/n_0 = 0.1$ and box size $12L \times 12L$, where L is the current sheet half-thickness. The grid size is 1024×1024 with 150×10^6 computational particles for each species and a time step of $t\Omega_e = 0.03$. At early time, $t\Omega_i = 4$ (top), the fastest growing, short-wavelength, LHD modes with $k_y\rho_e \sim 1$ have saturated leading to the turbulent fluctuations on the edge of the current layer. At intermediate time, $t\Omega_i = 13$ (middle), growth of the intermediate scale $k_y(\rho_i\rho_e)^{1/2} \approx 0.8$ LHDI is clearly evident in the growing $m = 5$ structure, while at late time, $t\Omega_i = 17$ (bottom), a long-wavelength $k_yL \approx 0.5$ ion–ion kink instability is observed in conjunction with the intermediate LHDI (see also Karimabadi *et al.*, 2003b, and Section 3.5.4).

These simulations have shown that for a current sheet thickness near or less than the ion inertial length, LHD modes may penetrate and modify the central region of the current sheet, initiating long-wavelength modes that saturate at large amplitudes. Similar results have been found by Vlasov-code simulations in three dimensions, but with smaller mass ratio (Silin and Büchner, 2003b). This suggests the possibility that these fluctuations may influence the development of magnetic reconnection. Consistent with these results, Silin and Büchner (2005a) also found that the growth rate increases with the sheet thinning as shown in Fig. 3.32.

It is important to note that the penetration of longer-wavelength LHD modes into the central region appears to require very thin current layers $L \lesssim 0.6\rho_i(\rho_i/L > 1.6$, see Fig. 3.32). Although current sheets in this parameter regime are clearly observed in laboratory plasmas (Yamada *et al.*, 2000; Ji *et al.*, 2004), current layers observed in the magnetosphere are only occasionally that thin (André *et al.*, 2004) but typically somewhat thicker $L \gtrsim \rho_i$. In this parameter regime, the theoretical results consistently predict that the LHDI is confined to the edge region of the current layer, where it is in the wrong location to directly produce the anomalous resistivity needed for reconnection. However, recent explicit 2D kinetic simulations for this parameter regime, using the realistic ion to electron mass ratio $m_i/m_e = 1836$, indicate that the LHDI may, nevertheless, play an important role in the onset of magnetic reconnection (Daughton *et al.*, 2004; Ricci *et al.*, 2004a). Although the unstable LHDI modes

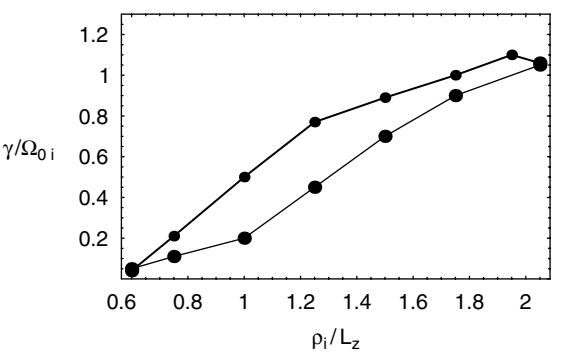

Fig. 3.32. Dependence of the global current-aligned mode (thick line) and tearing-mode instability (thin line) growth rates on the current sheet thickness. After Silin and Büchner (2005a).

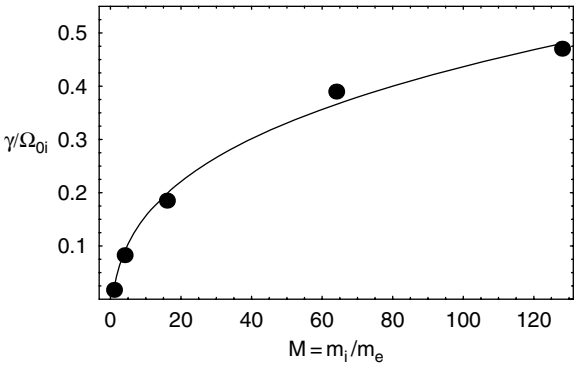

Fig. 3.33. Mass-ratio dependence of the current-aligned mode. Büchner and Kuska (1998a).

are clearly localized on the edge of the layer in these simulations, the nonlinear evolution induces a dramatic bifurcation of the current density and leads to significant anisotropic heating of the electrons in the central region of the sheet. The essential physics involves a resonant scattering of the crossing ion orbits into the noncrossing region of phase space which creates an electrostatic potential structure across the layer. The basic predictions from this model are in good agreement with observations concerning the electron flow velocity, bifurcated current structure and the electron anisotropy.

Since most of the kinetic simulations necessarily still use artificially small ion–electron mass ratios, the mass-ratio dependence of the nonlinear simulation results was investigated by Büchner and Kuska (1998a). Figure 3.33 shows that the growth rate increases mainly for small mass ratios and then saturates towards the realistic mass ratio of 1836.

3.5.3 Lower-hybrid drift instability in non-antiparallel fields

Huba *et al.* (1982) first theoretically considered the lower-hybrid drift instability in non-antiparallel reversed fields. Indeed, while not changing the current sheet equilibrium, a uniform externally imposed current-aligned magnetic guide field introduces a serious change in the current sheet instabilities. While in the generic Harris (1962) sheet with antiparallel magnetic fields the particles crossing the current sheet center may be nongyrotropic and therefore may easily become accelerated by electric fields of unstable modes, in the presence of the guide field this is no longer the case (Büchner and Zelenyi, 1991). Thus, the Hall currents, which play an important role in collisionless reconnection of antiparallel fields, are suppressed in the configurations with sufficiently large guide fields. Also, the structure of the reconnected magnetic field lines changes from closed O-type field lines in the case of antiparallel reconnection to helical (corkscrew) type in the presence of the guide field, i.e., there are no classical X- or O-points as in two-dimensional reconnection (Büchner, 1999).

For the case of finite guide fields Galeev *et al.* (1985) and Kuznetsova and Zelenyi (1985, 1990a) proposed obliquely propagating nonlinearly unstable *drift-tearing*

modes, which could lead to stochastic reconnection. Indeed, in the presence of guide fields, tearing-mode reconnection islands cannot grow coherently to large amplitudes due to the rotation of the wave vector with increasing distance from the central plane. Instead, the authors proposed that small-scale reconnection coupled to a drift mode would lead to *magnetic percolation* (Kuznetsova and Zelenyi, 1990b). These drift-tearing modes, which cause small-scale reconnection, become unstable first near the current sheet center, where they resemble the classical tearing instability. Later, oblique modes arise further away from the current sheet center. The authors speculated that after the magnetic field perturbations exceed a critical level, magnetic islands overlap and the small-scale reconnection might even grow algebraically with time to large amplitudes (Galeev *et al.*, 1985).

Pressure-gradient-driven unstable LHD waves always propagate perpendicular to the local magnetic field (Krall and Liewer, 1971; Liewer and Krall, 1973; Huba *et al.*, 1977). To investigate their possible consequences for reconnection, Silin and Büchner (2003b) recently reconsidered the influence of a guide magnetic field on the resonant LHDI. They found that the unstable LHD waves become decoupled from each other in the presence of the guide field, because they always propagate perpendicular to the local magnetic field. The number of resonant ions becomes smaller as the guide field becomes stronger, and hence the resulting growth rate of the combined mode decreases as well (see Fig. 3.34). Silin and Büchner (2005b) investigated the LHDI in a rotating magnetic field, typical for magnetopause current sheets. They found that in their model the instability saturates at low levels, unable to provide a sufficient amount of anomalous resistivity.

3.5.4 Kink instability

Kink modes are frequently observed in thin current sheets in the magnetotail (e.g., Sergeev *et al.*, 2003, 2004); however, their relation to reconnection remains unclear. They may provide a means to initiate reconnection, they may be excited simultaneously but independently, or they may grow as a consequence of reconnection. Here we discuss particularly their potential role in the initiation of reconnection.

The drift-kink instability is a long wavelength $k_y L \lesssim 1$ electromagnetic mode driven by the relative drift between ions and electrons. It was originally uncovered from fully kinetic simulations of current sheets (Ozaki *et al.*, 1996; Pritchett and

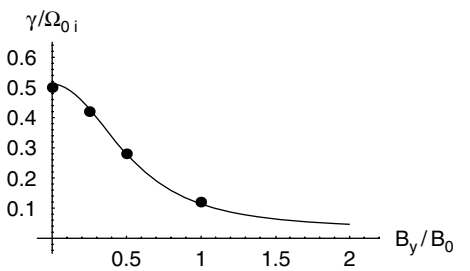

Fig. 3.34. Growth rate of the nonlocal long-wavelength LHDI at the center of the current sheet with a finite guide field B_y for $L = \rho_\mathrm{i}$.

Coroniti, 1996; Pritchett *et al.*, 1996; Zhu and Winglee, 1996; Lapenta and Brackbill, 1997) and gives rise to a large-scale undulation of the layer. Linear Vlasov theory (Daughton, 1999b) predicts substantial growth rates for the artificial mass ratios typically employed in PIC simulations $m_\mathrm{i}/m_\mathrm{e} \lesssim 100$. However, the growth rate is drastically reduced for realistic mass ratio (Daughton, 1999a,b). Comparison between the predicted theoretical scaling and fully kinetic simulations is excellent for relatively modest mass ratio $m_\mathrm{i}/m_\mathrm{e} \lesssim 100$ but deviates significantly at larger mass ratio (Daughton, 2002). The apparent reason for this discrepancy is the presence of the LHDI in these simulations which generates significant ion velocity shear which drives a kinking of the current layer by a Kelvin–Helmholtz type mode (Hesse *et al.*, 1998; Daughton, 2002; Lapenta and Brackbill, 2002; Lapenta *et al.*, 2003).

It is interesting to note that the original linear Vlasov theory of the drift-kink mode also explored the possibility of adding a uniform background plasma to the standard Harris sheet equilibrium (Daughton, 1999b). This introduces a relative drift between the current-carrying and background ion populations and the linear theory predicts large growth rates that are independent of the electron mass. This so-called ion–ion kink instability (Karimabadi *et al.*, 2003a,b) has features which are very similar to the drift-kink mode in terms of wavelength, frequency, and mode structure, but the driving factor is the relative drift between two ion populations. Within a single fluid picture the bulk fluid velocity is sheared, so the mode appears to be closely related to the Kelvin–Helmholtz instability (Hesse *et al.*, 1998) but the typical regime of interest is highly kinetic so there are important modifications. An example of the ion–ion kink mode in a PIC simulation at realistic mass ratio is shown in the bottom panel of Fig. 3.31.

To summarize, the drift-kink mode is very weak in the limit of realistic mass and is not physically interesting. However, the ion–ion kink mode has significant growth rates over a broad range of interesting parameters and is easy to excite with either shear or multiple drifting ion components. The primary stabilizing factor for the mode is the presence of a finite guide field. For the parameter regime relevant to the magnetotail, the properties of the ion–ion kink mode have been systematically examined using a combination of linear Vlasov theory (Karimabadi *et al.*, 2003a) along with full PIC and hybrid simulations (Karimabadi *et al.*, 2003b). Some of the essential properties of the ion–ion kink instability are consistent with recent magnetotail observations (Karimabadi *et al.*, 2003b; Ricci *et al.*, 2004b).

Although it has been suggested that kink instabilities may perhaps play a role in the onset of magnetic reconnection (Lapenta *et al.*, 2003), the precise mechanism by which this would occur has not been identified. To complicate matters, the LHDI is also typically present in 3D kinetic simulations, and there is now fairly convincing evidence that it does play a role in the onset. It is interesting to note that the LHDI modes can be suppressed with the introduction of a sufficient background plasma which increases the plasma β in the edge region. Recent fully kinetic 3D simulations with 20% background density have simulated the simultaneous evolution of an unstable kink mode in conjunction with collisionless tearing (Karimabadi *et al.*, 2003b). Although there are a number of interesting effects observed during the initial phase of these simulations, the final stage of evolution in these 3D simulations is quite similar to the usual 2D tearing scenario.

3.5.5 Drift-sausage instability

Sausage modes in a current sheet are symmetric modes, characterized by periodic thinning and thickening. The localized thinning makes them rather attractive as a means to initiate reconnection. However, results on the existence of such modes are contradictory, so that their importance has not been established.

A threshold of a sausage-type electromagnetic instability of a current sheet was first obtained by Yamanaka (1978), who took into account specifics of the particle motion in antiparallel fields. Neglecting electrostatic effects, Lapenta and Brackbill (1997) solved the linear dispersion relation for a drift-sausage instability based on a straight orbit integration of the linearized Vlasov equation. Their simulation, reported in the same paper, however, revealed only a kink-instability of the sheet. A nonlocal linear theory based on a full orbit integration (Daughton, 1999a, 2003) of the linearized Vlasov equation also did not find evidence for a drift-sausage mode. Likewise, the particle-in-cell simulations of current sheet dynamics listed in Section 3.5.4, which found clear evidence of kink modes, did not observe drift-sausage modes.

In contrast, Büchner and Kuska (1998a,b, 1999) investigating unstable drift-sausage modes also by means of PIC simulations, concluded that drift-sausage modes are nonlinearly unstable, the wavelength of the most unstable mode depending on the mass ratio as $k_y L_z \sim (m_\mathrm{i}/m_\mathrm{e})^{1/4}$. Wiegelmann and Büchner (2000) showed that electrostatic contributions are indeed necessary to cause a nonlinear drift-sausage sheet instability in the current flow direction. Otherwise, if the electrostatic perturbations are artificially suppressed, the tearing-mode instability dominates the current sheet decay. Considering global eigenmodes, Yoon and Lui (2001) found a preference for the sausage mode. According to Yoon *et al.* (2002), for small particle mass ratios $m_\mathrm{i}/m_\mathrm{e}$ asymmetric kink modes should dominate, while for higher mass ratios the sausage mode was more probable. Analytically considering the long-wavelength limit, Silin *et al.* (2002) demonstrated that for the correct consideration of the electrostatic (charge-separation) effects the sausage mode can directly couple into reconnection via the current-aligned longitudinal electric field E_y at the center of the current sheet. The resulting reconnection perturbations have finite wave vectors k_x and k_y. This way, magnetic reconnection in thin current sheets becomes intrinsically three-dimensional, propagating together with the global current sheet instability (*reconnection wave*) as predicted by Büchner and Kuska (1996, 1998b).

Observationally, sausage modes have been identified in the magnetotail current sheet by the Cluster satellite tetrahedron (Volwerk *et al.*, 2004; Fruit *et al.*, 2004). However, the propagation direction of these modes was along the tail, rather than across. Furthermore, they seemed to be a consequence of substorm onset rather than leading into it. Therefore, the role of sausage modes in the onset of reconnection remains unclear, both theoretically and observationally.

3.5.6 Modified two-stream instability

The modified two-stream instability (MTSI) (McBride *et al.*, 1972) and the closely related ion-Weibel instability (IWI), which represents the special case of propagation along the magnetic field (Chang *et al.*, 1990), share many of the features

of the lower-hybrid drift instability, including similar frequencies, growth rates and wavelengths. As discussed in Section 3.5.2, the LHDI is considered as being driven by a density gradient, has maximum growth for $\mathbf{k} \cdot \mathbf{B} = 0$ and operates predominantly in the boundary layers of a current sheet. In contrast, the MTSI/IWI is considered as being driven by the cross-field drift of unmagnetized ions even in the absence of a density gradient. It is predicted to have maximum growth for oblique propagation and to operate predominantly in the region of strongest current, that is, near the center of the current sheet (McBride *et al.*, 1972; Lemons and Gary, 1977; Wu *et al.*, 1983; Chang *et al.*, 1990; Lui *et al.*, 1991; Yoon and Lui, 1993; Lui, 2004).

The distinction between the drivers is somewhat arbitrary, because in self-consistent current sheet models current-associated drifts are typically related to magnetic field and density gradients as well. Using a local approach that includes weak inhomogeneity of both density and magnetic field, Silveira *et al.* (2002) obtained a unified local kinetic treatment of these instabilities, while Yoon and Lui (2004) investigated the transition between LHDI and MTSI on the basis of certain non-Harris type current sheets with signficant $\mathbf{E} \times \mathbf{B}$ drifts, incorporating the spatial variation through varying parameters such as the plasma β and the ion drift speed. In both of these investigations, LHDI and MTSI were distinguished according to the resulting dispersion properties, particularly the wave vector direction of the most unstable modes. Thus, LHDI is predicted to be dominant for Harris-type equilibria, where the relative electron–ion drift is entirely diamagnetic, and for the low-β boundary regions of non-Harris type models (Yoon and Lui, 2004). In contrast, the MTSI is predicted to be dominant in the high-β central region of non-Harris equilibria.

It is important to note that these predictions are based on local kinetic theory which may not be applicable to the central region of a current sheet. Further investigation of these linear predictions requires a nonlocal kinetic treatment in conjunction with 2D and 3D kinetic simulations.

3.5.7 Summary and conclusions

Current investigations have shown that kinetic instabilities in model current sheets might, in principle, provide the plasma nonideality necessary for reconnection in collisionless space plasmas. While the classical one-dimensional $T_e \gg T_i$ ion-acoustic instability does not operate under realistic space plasma conditions, the lower-hybrid drift instability is more likely to operate and play a significant role. While it may be a source of anomalous resistivity under drastic thinning, under less stringent conditions it may alter the current sheet structure and thereby destabilize it and couple to reconnection. Kink instabilities are likely to operate, and are indeed observed in thin magnetotail current sheets (while results on sausage modes are still controversial). However, it is not clear whether and how they might affect reconnection. More realistic 3D model calculations are necessary to further clarify the relationship between current-driven, current-aligned instabilities and fast reconnection in space plasmas.

3.6 Nonthermal particle acceleration

M. Hoshino

Nonthermal particle acceleration in magnetic reconnection is a long-standing problem in cosmic plasmas. In fact, the possibility of accelerating charged particles by an electric field along a magnetic neutral line or, more generally, along a magnetic field line in reconnecting magnetic fields was the reason for introducing the concept of magnetic reconnection, although not the term, by Giovanelli (1946) as a mechanism for particle acceleration in solar flares. The relationship between flares and particle energization by reconnection has been widely recognized after Yohkoh and SOHO observations (e.g., Tsuneta *et al.*, 1992; Sterling *et al.*, 2000). RHESSI observations reported substantial electron acceleration and a double power-law X-ray spectrum in association with flares (Lin *et al.*, 2003).

In the astrophysical context, it is known that almost all young stellar objects emit X-rays with light curves that are quite similar to those of solar flares, characterized by a fast rise and exponential decay, even though the luminosities are very much higher than those of solar flares (Koyama *et al.*, 1996; Montmerle *et al.*, 2000). Furthermore, a good correlation between the emission measure and the plasma temperature can been seen (Feldman *et al.*, 1995; Shibata and Yokoyama, 1999). Therefore, those flares are believed to be related to magnetic reconnection.

Pulsars and their surrounding nebulae are another example of magneto-active objects, and ultra-relativistic particles are known to be generated in the form of synchrotron radiation. The shock acceleration by the interaction of a relativistic pulsar wind with the nebula is the most widely accepted scenario of generation of ultra-high energy particles (Kennel and Coroniti, 1984), but magnetic reconnection is also suggested as another important acceleration process in a *striped magnetic field* in pulsar winds (Coroniti, 1990; Lyubarsky and Kirk, 2001). In fact, on the basis of Chandra X-ray satellite observations, Mori *et al.* (2004) concluded that magnetic energy dissipation is necessary to explain the luminosity of the synchrotron radiation in the Crab nebula. Zenitani and Hoshino (2001, 2005) and Jaroschek *et al.* (2004) suggested that ultra-relativistic particles can be quickly generated by relativistic reconnection.

In most cosmic plasmas, the nonthermal, high-energy spectra are often described by a power-law energy spectrum. Over the last several decades, considerable effort has been devoted toward understanding the formation of such high-energy power laws and the origin of nonthermal particles in reconnection. However, there are many outstanding questions regarding particle acceleration that motivate continuing research in the field. Plasma heating and acceleration in magnetic reconnection is now a frontier subject of plasma astrophysics. In this section, we review the physics of particle acceleration in reconnection by focusing on the Earth's magnetosphere where many key observational data are available. Since the underlying basic physics of reconnection should be universal, it can be expected that properties of reconnection and particle acceleration in the well-studied terrestrial magnetosphere are applicable to other astronomical objects, too.

3.6.1 Basic plasma parameters in the magnetosphere

Before discussing observations of energetic particles, it is useful to discuss typical thermal plasma properties in the terrestrial magnetosphere and specifically

the magnetotail. We focus on the tail region around 20 to 30 R_E distance from Earth where near-Earth reconnection related to substorms is now believed to occur (e.g., Hones, 1979; Nishida *et al.*, 1981; Baumjohann *et al.*, 1991; Nagai *et al.*, 1998).

The ion temperature is always higher than the electron temperature; typical values are a few keV and several hundred eV, respectively. This preferential ion heating is believed to be associated with the primary magnetotail acceleration mechanism at the boundary between the lobe and the plasma sheet.[3] The plasma sheet density is $0.1 \sim 1\,\mathrm{cm}^{-3}$, but during an active reconnection period the density may decrease below $\sim 0.01\,\mathrm{cm}^{-3}$ in the vicinity of an X-type neutral line. The gas pressure of the hot plasma inside the plasma sheet balances the magnetic pressure of the very tenuous lobes with a magnetic field of about 20 nT. The thickness of the electric current sheet which supports the antiparallel lobe magnetic field is usually about $1 \sim 3\,R_E$, but before the onset of substorms the thickness can become as small as the ion inertia length of the order of 1000 km (e.g., Asano *et al.*, 2003).

Based on the above plasma parameters, let us estimate characteristic limits for the electric potential induced in the magnetotail. The Alfvén speed estimated by using the lobe magnetic field and the plasma sheet density is given by

$$v_A = 620 \left(\frac{B_x}{20\ \mathrm{nT}} \right) \left(\frac{0.5\ \mathrm{cm}^{-3}}{n} \right)^{1/2} \ \mathrm{km/s}. \tag{3.85}$$

The reconnecting magnetic field in the plasma sheet may be approximated by

$$B_z = 2 \left(\frac{B_x}{20\ \mathrm{nT}} \right) \left(\frac{M}{0.1} \right) \ \mathrm{nT}, \tag{3.86}$$

where M is the reconnection rate, assumed to be of order 0.1. Therefore, the motional electric field during reconnection in the magnetotail can be estimated as

$$E_y = 1.2 \left(\frac{v_A}{620\ \mathrm{km/s}} \right) \left(\frac{B_x}{20\ \mathrm{nT}} \right) \left(\frac{M}{0.1} \right) \ \mathrm{mV/m}. \tag{3.87}$$

Multiplying Eq. (3.87) by the scale length L of the magnetotail cross-section of about $30\,R_E$, the maximum potential difference induced in the tail in the dawn–dusk direction becomes of the order of

$$e\phi = 240 \left(\frac{v_A}{620\ \mathrm{km/s}} \right) \left(\frac{B_x}{20\ \mathrm{nT}} \right) \left(\frac{M}{0.1} \right) \left(\frac{L}{30\ R_E} \right) \ \mathrm{keV}. \tag{3.88}$$

Thus the plasma in the Earth's magnetotail is characterized by thermal energies well below the available potential energy estimated by Eq. (3.88). On the other hand, there are many observations that show that plasma particles can be effectively accelerated to energies of 1 MeV. These energetic particles are the continuous extension of the thermal population, forming a supra-thermal tail beginning at several multiples of the thermal energy. Most energetic particles seen in the magnetotail seem to be roughly consistent with the available potential energy (see also Section 4.4.4), but the highest energy particles seem to exceed the available potential energy.

[3] However, a similar ratio is also found in the magnetosheath surrounding the magnetosphere (Fig. 1.5), so that an acceleration mechanism that preserves this ratio from this source region is also plausible.

3.6.2 Energetic particle observations and magnetic reconnection

Let us discuss in more detail the energetic particle observations in the Earth's magnetotail. In early satellite observations anisotropic energetic particle bursts have been reported by Sarris *et al.* (1976) and Hones *et al.* (1976). An energetic electron burst with 0.3–1.0 MeV was identified in association with a southward turning of the B_z magnetic field at $x \approx -20$ to $-30\,R_E$ in the magnetotail (Terasawa and Nishida, 1976). The southward turning of B_z suggests that magnetic reconnection is occurring in the magnetotail, because the tail magnetic field during nonreconnection time intervals should have a northward B_z component.

Similar events were also discussed at $x \approx -30\,R_E$ based on a survey of electrons of $\varepsilon \geq 200$ keV by Baker and Stone (1976, 1977), who reported that electron flux enhancements at energies $\varepsilon \geq 1$ MeV are usually associated with neutral sheet crossings. Sarris *et al.* (1981) reported ion distribution over the energy range 100 eV to a few MeV even though the bulk flow speed is not necessarily fast. Möbius *et al.* (1983) analyzed energetic protons of 30–500 keV and energetic electrons of $\varepsilon \geq 75$ keV, and suggested that reconnection near an X-type neutral line is a candidate for the acceleration of the energetic particles.

Although the relationship between the energetic particles and reconnection was plausible, there was no direct evidence of energetic particle production at an X-type neutral line. The spatial extent of the region around the X-line where non-MHD processes take place is of the order of an ion inertia length, so that the observational chance of a satellite traversing this region is very rare. However, Øieroset *et al.* (2002) have recently reported the successful observation of energetic particles in the vicinity of an X-type region. As shown in Fig. 3.35, the fluxes of energetic electrons up to ~300 keV increased approaching the diffusion region, and the energy spectrum has a power-law signature above ~2 keV with the power-law index of −5. Since the single, power-law population is extended up to 300 keV, all energetic particles are

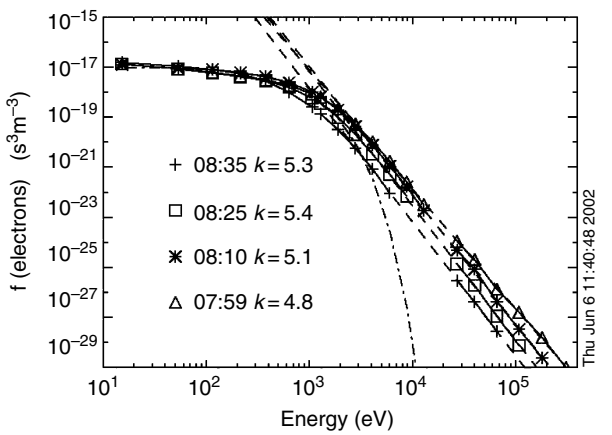

Fig. 3.35. Electron energy spectra observed just on the tailward side of an X-type region. The power-law indexes k of four different time periods are shown in the plot. Adapted from Øieroset *et al.* (2002).

thought to be generated in the same acceleration process. The high-energy electrons of $\sim 300\,\mathrm{keV}$ seem to be consistent with the available potential energy estimated by Eq. (3.88).

The maximum available potential energy, however, may be overestimated, because the reconnection region is believed to be localized within a few Earth radii in the y direction (e.g., Angelopoulos *et al.*, 1994), so that such a large electric potential of $e\phi \sim 240\,\mathrm{keV}$ is not easily induced. The relationship between the observed maximum energy and the available potential energy remains a controversial issue.

Another important issue is the distribution of the energetic particles. In association with magnetic reconnection in the magnetotail, plasma is transported away from the X-type region. During the plasma transport, ions/electrons are drifting toward dusk/dawn and should gain energy. As shown in Fig. 3.36, however, this is not supported by observations. Figure 3.36 shows suprathermal particle observations by the Geotail satellite in the tail (Imada *et al.*, 2002). Electron fluxes of 3.2 keV (right-bottom) and 9.3 keV (left-bottom), the integrated electron flux of energies greater than 38 keV (left-top), and the energetic ion flux of 39.5 keV (right-top) are shown as a function of the dawn–dusk position. The nominal electric field is directed toward the positive y axis, which is the dawn to dusk direction. One can observe asymmetry of the energetic particle distributions, but this asymmetry is not very distinct. We can find the energetic electrons (protons) even in the dusk (dawn) side region. The observed energetic

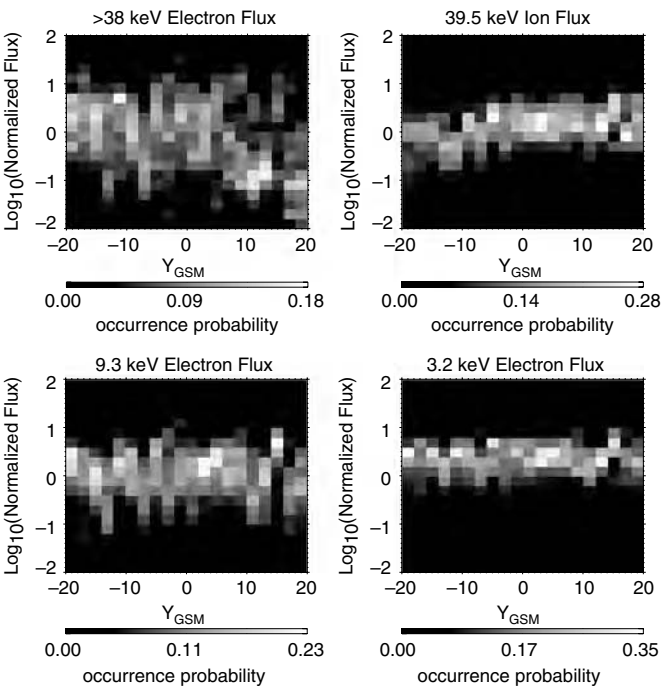

Fig. 3.36. The dawn–dusk distribution of energetic particles. The gray scale shows occurrence probability of particle flux in each $\mathrm{Y_{GSM}}$ bin.

particle distribution is not simply described by a model of the dawn–dusk potential energy gain. A possible explanation is that diffusion processes of particles play an important role in the magnetotail. If the spatial diffusion in the dawn–dusk direction is effectively occurring, the asymmetry of the energetic particle distribution will be smeared out. There is no energy gain during the diffusion process caused by elastic scattering, because the potential energy gain/loss can be compensated by the energy loss/gain from the waves whose scattering centers are embedded in the convecting plasma. In this case, the maximum energy of particles might even exceed the available potential energy under the reconnection acceleration with the diffusion process.

3.6.3 Acceleration of test particles under MHD reconnection fields

The direct energization of charged particles in reconnection is provided by the interaction of the particles with an electric field around the X-type region. In the earliest exploration of particle acceleration during reconnection, people used test particle modeling, where a model of the spatial variation of the time-dependent magnetic and electric fields is given, and they calculated the particle motion and its energization by integrating the Lorentz equation in time. The test particle calculations based on the magnetic and electric field structure obtained by a resistive MHD simulation demonstrated the production of suprathermal particles by moving in the direction of the electric field over a substantial distance (e.g., Sato *et al.*, 1982; Scholer and Jamitzky, 1987; Birn and Hesse, 1994). Time-dependent, strong electric fields generated near the X-type reconnection region in association with a pair of slow shocks are demonstrated as a primary energy source of the reconnection acceleration. In addition to the above acceleration mechanism, Ambrosiano *et al.* (1988) suggested that small-scale MHD turbulence generated in the plasma sheet under a high magnetic Reynolds number enhances the particle acceleration through stochastic scattering.[4]

Frequently, reconnection is considered to evolve in a steady-state manner, with the amplitude of the reconnection electric field more or less constant in time. But it is also postulated that reconnection is nonstationary, and in such a nonsteady reconnection regime the particle acceleration efficiency may be boosted up. Sakai and Ohsawa (1987) discussed a driven reconnection scenario by assuming that the lateral magnetic influx increases in time, and showed the transition to explosive reconnection. Bulanov and Sasorov (1975), Zelenyi *et al.* (1984, 1990), and Deeg *et al.* (1991) have demonstrated the formation of a power-law type energy spectrum from inductive electric fields that grow exponentially in time.

While the above theoretical studies of particle acceleration basically assume that the main acceleration occurs around an X-type region, a more general current sheet may involve multiple X-points in a filamentary current sheet, which also implies intervening magnetic islands with O-points. The magnetic islands might play an important role in trapping particles inside the islands, and if a finite electric field

[4] In Section 4.4 we will discuss test particle simulation results that indicate that, in the geomagnetic tail, betatron or Fermi-type acceleration in the collapsing magnetic field earthward of an X-type neutral line may be more significant than the acceleration in the immediate vicinity of the neutral line.

exists over the plasma sheet, strong particle acceleration can be expected in and around the magnetic islands as well (Kliem, 1994).

3.6.4 Turbulence and wave scattering

Processes responsible for nonthermal high-energy particles are likely to violate adiabatic particle motion, and several waves may contribute to nonadiabatic processes through wave–particle scattering. As noted in Section 3.6.2, the energetic particle distributions do not show clear dawn–dusk asymmetry in the magnetotail, which may be suggestive of a diffusion process across the magnetic field. There has been accumulating evidence that the plasma sheet is in a turbulent state (e.g., Kennel, 1995), and the electric and magnetic field turbulence is believed to be the primary mechanism by which heating and dissipation takes place through scattering of particles.

The frequency band of the turbulence ranges from below the ion cyclotron frequency (of the order of 0.1 Hz in the Earth's magnetotail) to the plasma frequency (of the order of 10 kHz). The observed Fourier power spectral density of the magnetic fields can be approximated by a double power-law spectrum in the MHD range (Hoshino *et al.*, 1994; Bauer *et al.*, 1995). Above MHD frequencies, three different types of wave modes are observed (Gurnett *et al.*, 1976). The most intense waves are broadband electrostatic noise bursts observed in the outer plasma sheet boundary layer (PSBL) in association with large plasma flows, the other two are whistler mode magnetic noise bursts and electrostatic electron cyclotron waves. The whistler waves are also observed in the same region as the broadband electrostatic noise, and are thought to be associated with regions carrying substantial field-aligned currents.

Concerning the large number of waves observed in the Earth's magnetotail, we briefly mention the current understanding of two main generation mechanisms. In the outer plasma sheet boundary regions, an anisotropic ion beam velocity distribution function is often observed during the reconnection phase. The distribution consists of cold incoming ions streaming toward the diffusion region and accelerated outgoing ions. The outgoing ions are thought to be generated in the diffusion region and to be ejected along the reconnecting magnetic field lines (e.g., Hoshino *et al.*, 1998). This outgoing distribution is called the PSBL ion beam. It is expected that the PSBL ion beams can excite Alfvénic/whistler waves propagating along the magnetic field due to the firehose/ion beam cyclotron instability. Arzner and Scholer (2001) performed a large-scale hybrid simulation of reconnection and demonstrated the generation of the PSBL ion beams and the emission of the Alfvénic/whistler waves in the plasma sheet boundary layer, which in turn lead to the evolution of MHD turbulence and the resultant ion thermalization.

Inside the plasma sheet and around the plasma sheet boundary, broadband waves with frequencies from the lower-hybrid frequency to the plasma frequency are also believed to be important for particle scattering (Okada *et al.*, 1994; Cattell *et al.*, 1994). Modern, high-time-resolution satellite measurements show that the broadband electrostatic waves are localized, large-amplitude, electrostatic waves with a series of coherent wave forms, now called *ESW* (Kojima *et al.*, 1994). The scale of ESW is probably tens of electron Debye lengths, but the amplitude is 10 to 100 times that of a large-scale reconnection electric field induced by the global MHD flow (Cattell *et al.*,

1999). Therefore, the small-scale ESW might appear to control the global dynamics including the electron heating and acceleration. The emission mechanism may be attributed to the electron beams generated around the diffusion region in a similar way to the PSBL ion beams, and the waves are excited by either electron bump-in-tail instability (Omura *et al.*, 1994) or Buneman instability (Drake *et al.*, 2003).

3.6.5 Strong acceleration during reconnection

As stated in Section 3.6.3, the earliest particle acceleration studies were done in the framework of prescribed fields or fields computed from resistive MHD reconnection models. It is important to explore the particle acceleration in a self-consistent system of a full particle simulation where the feedback of particle motions via the electric current into the electric and magnetic fields is taken into account. Larger amplitude waves could be generated through kinetic instabilities in the collisionless plasma system. As discussed earlier, the thickness of the plasma sheet is known to become as small as the ion inertia scale before onset of magnetic reconnection, and the plasma sheet that governs the macrodynamics also governs the microscale phenomena. Therefore the microscale plasma dynamics will strongly couple with the macroscale physics. Then we need kinetic modeling of particle acceleration beyond the MHD description. Here we discuss energetic electron acceleration processes obtained by using a full-particle simulation (Hoshino *et al.*, 2001b).

This particle simulation was carried out in two-dimensional (x, z) coordinate space, assuming the Harris solution (Harris, 1962) as the initial condition. In the early phase, a localized external electric field drives the evolution from the outer boundary to initiate reconnection in the center of the simulation box. As time goes on, an X-type neutral line is formed, and in association with the energy conversion from magnetic to kinetic energy, the reconnection outflow in the plasma sheet is ejected from the X-type neutral point. In contrast to resistive MHD models, the energy dissipation around the X-type magnetic diffusion region is provided by particle inertia due to inverse Landau resonance of particles with the reconnection electric field and by the resultant electron pressure anisotropy (Section 3.2).

Figure 3.37 shows a snapshot of the nonlinear evolution of reconnection at $t/\tau_{\rm A} \sim 48.8$, where $\tau_{\rm A}$ is the Alfvén transit time for crossing the plasma sheet. The top panel shows magnetic field lines in the x, z plane (i.e., the reconnection plane), and the bottom panel shows the magnetic field component perpendicular to the reconnection plane B_z, which is generated by Hall electric currents in the thin plasma sheet (Section 3.1).

Figure 3.38 shows energy spectra of electrons integrated over all pitch angles in the whole simulation domain. In the early phase of reconnection before $t/\tau_{\rm A} \sim 41.7$, we find that the electrons are gradually thermalized with time, and the spectra are approximated by a thermal Maxwellian. In the late phase at $t/\tau_{\rm A} \sim 48.8$, the enhancement of suprathermal electrons above the thermal Maxwellian can be clearly seen. By analyzing the positions of those energetic particles, we found that most energetic electrons of $\varepsilon_{\rm ele}/(m_{\rm e}c^2) \geq 0.1$ are situated in the X-type region and around the boundary between the lobe and the plasma sheet, i.e., around the separatrix of reconnecting magnetic field lines.

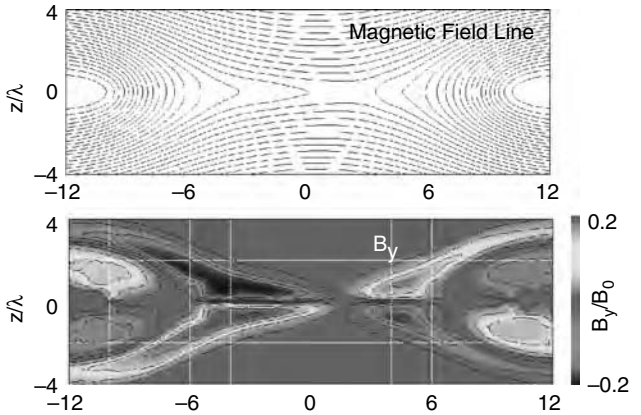

Fig. 3.37. Magnetic field lines in the x, z plane (top) and the contour of the Hall current generated magnetic field B_y (bottom), at $t/\tau_A = 48.8$.

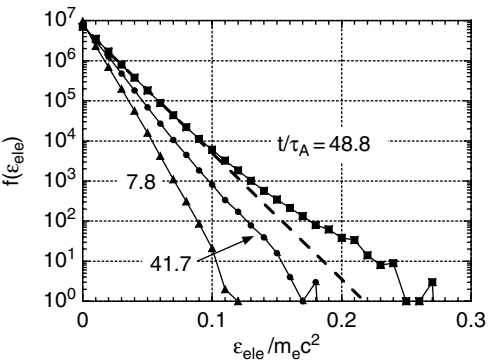

Fig. 3.38. Evolution of electron energy spectra at $t/\tau_A = 7.8, 41.7, 48.8$. The dashed line shows the Maxwellian fit as reference.

In order to understand how and where the electrons get their energies, we have analyzed electron trajectories in the reconnection region. Figure 3.39 shows several typical trajectories. The starting points of the trajectories are denoted S1, S2, etc., while the end points are labeled E1, E2, etc. The S1–E1 curve is one of the most typical orbits showing particle acceleration. The electron is initially accelerated near the X-type region by moving in the negative electric field direction, and is ejected along the magnetic field line at the separatrix boundary. The particle with the S2–E2 trajectory gains much larger energy than the S1–E1 electron does, during several bounce motions in the reconnecting magnetic fields with mirror geometry. The energy gain is provided by the curvature and ∇B drift motions toward the negative y direction. It is important to note that the ratio between the magnetic field curvature radius and the gyroradius, κ, is almost unity in the central plasma sheet, and that a particle with $\kappa \sim 1$ is effectively scattered toward a weak magnetic field region, and has a tendency to stay for a longer time in the plasma sheet (e.g., Delcourt *et al.*, 1996).

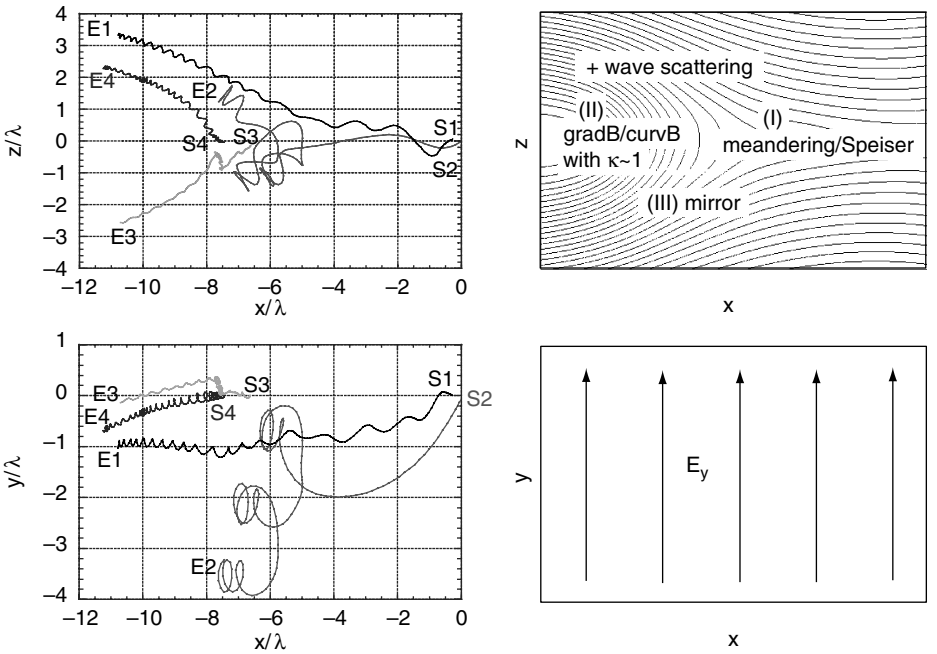

Fig. 3.39. Typical electron trajectories obtained in a particle-in-cell simulation. The left panels show trajectories in the x, z plane (top) and in the x, y plane including the reconnection motional electric fields E_y (bottom). The right-hand panels are a schematic view of the magnetic field lines in the x, z plane and the electric field in the x, y plane.

The S3–E3 trajectory around $x/\lambda = -7.5$ is an example of the cross-field diffusion. The electron is scattered towards the stronger magnetic field region and the positive electric field y direction. The orbit S4–E4 shows pitch-angle scattering, with a change of the pitch of the gyromotion around $x/\lambda = -8$ and -10. We suggest that these trajectories represent the basic scattering processes that play important roles in particle acceleration.

Figure 3.40 shows the wave spectra obtained in the magnetic field pile-up region, where the reconnection outflow plasma collides with the pre-existing plasma. The vertical and horizontal axes are the wave power of $(E_x^2 + E_z^2)$ and the wave frequency, respectively. The wave power is normalized by $(v_{\rm A}B/c)^2$, and the wave frequency is normalized by the electron plasma frequency at the plasma sheet at $t = 0$. The spectrum denoted by the dashed line is taken at the boundary between the lobe and the plasma sheet at $(x/\lambda, z/\lambda) = (-7, 2)$, while the solid line is the spectrum inside the plasma sheet at $(x/\lambda, z/\lambda) = (-7, 0)$. Inside the plasma sheet, we find that the low-frequency waves are strongly enhanced. Around the plasma sheet boundary layer, a broadband spectrum from the low frequency to the plasma frequency can be seen. The spectrum bump around $\omega/\omega_{\rm pe} \sim 0.7$ corresponds to the local plasma frequency, i.e., Langmuir waves. Since we can see the signature of an accelerated electron beam in the distribution function taken around the boundary (Hoshino *et al.*, 2001a), the

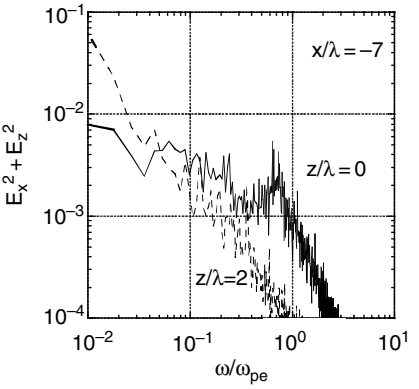

Fig. 3.40. Turbulent wave spectra obtained in the magnetic field pile-up region where the reconnection plasma outflow collides with the O-type magnetic island.

Langmuir waves are thought to be excited by the fast electron beams. The electron beams are generated in and around the X-type region due to the reconnection electric field E_y, and after their energization the accelerated high-speed electrons are ejected along the magnetic field in the boundary between the lobe and the plasma sheet, which in turn excite a strong coherent wave in the plasma frequency band probably through the bump-in-tail instability.

From the above simulation results, we can conclude the following conventional acceleration scenario. The electrons gain their energy around an X-type neutral region during the Speiser/meandering motion (Speiser, 1965; Section 4.4), and those pre-accelerated electrons are transported outward together with the reconnecting magnetic field lines. Around the magnetic field pile-up region formed by the interaction between the fast reconnection outflow and the pre-existing plasma sheet, those unmagnetized particles are further accelerated with the aid of particle scattering which breaks down the adiabatic motion (see Fig. 3.39).

So far we have discussed particle acceleration mainly for (perpendicular) electric fields in the form of the inductive/convection electric field. The electrostatic fields parallel to the magnetic fields may play an important role also, not only for wave–particle scattering but also for strong acceleration. Parallel electrostatic fields have been used to explain particle acceleration in many phenomena such as auroral electron acceleration. They are known to arise from the interruption of the parallel current due to plasma instabilities and from the formation of double layers of electric charge. Recently Drake *et al.* (2003, 2005b) explored the acceleration of particles in a configuration with a guide magnetic field. Magnetized electrons can be efficiently accelerated along the guide field, and those accelerated electrons form an electron beam, which can become faster than the electron thermal speed during reconnection. They showed that the beam electrons can drive strong electrostatic waves in the waveform of ESW in association with electron phase-space holes. The electron hole acceleration may be regarded as one class of field-aligned potential drop acceleration processes. The electron hole acceleration is not static but rather

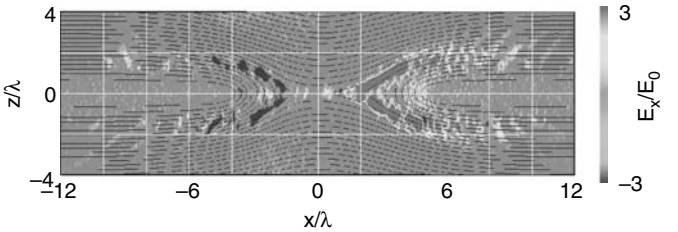

Fig. 3.41. Large-amplitude waves propagating outward from an X-type region along the magnetic field lines. The magnetic field lines and the color contours of E_x are shown, and E_x is normalized by $E_0 = v_A B_0$. See also color plate.

originates in a highly dynamic evolution during the magnetic energy dissipation phase.

A series of large-amplitude electrostatic waves was also found in a reconnection simulation without guide magnetic field. Figure 3.41 shows a snapshot of the electric field E_x obtained in the full particle simulation with a forced boundary condition. The simulation parameters are the same as those discussed in Figs. 3.37 through 3.39, but in addition finite plasma inflow was driven continuously from the top and bottom boundaries. In such a system, one can expect fast and well-developed reconnection with large-amplitude waves. In Fig. 3.41 the amplitudes of the coherent electrostatic waves E_x are found to be several times the magnitude of the inductive electric field E_y, with wavelengths intermediate between electron and ion inertia scales. For spontaneous reconnection in Fig. 3.40, we had already found a signature of Langmuir wave emission, but the amplitudes remained small. The large-amplitude waves in Fig. 3.41 are produced as the result of the nonlinear evolution of the Langmuir waves seen in Fig. 3.40.

In addition to a series of the large-amplitude electrostatic waves propagating along the outer plasma sheet boundary, we also found a pair of polarized V-shape regions near the X-type region. The electric field vectors are directed outward from the X-type region, and ambipolar electric fields are known to be produced in association with Hall electric currents in a thin current sheet (Hoh, 1966; Hoshino, 1987). In the driven system, we find a pair of polarized regions, which has stronger electric field than that seen in spontaneous reconnection, which may play an important role in acceleration. Recently, Hoshino (2005) discussed that some electrons can be trapped by the electrostatic potential well of the polarization field, and during the trapping phase electrons can gain their energies from the convection/inductive reconnection electric field due to the so-called *surfing acceleration* mechanism (e.g., Sagdeev and Shapiro, 1973; Katsouleas and Dawson, 1983). Hoshino (2005) found that relativistic electrons with MeV energies are quickly generated, and the energy spectrum shows a better-developed nonthermal tail than that seen in Fig. 3.38. Although these large-amplitude electrostatic waves are believed to be important for plasma heating and acceleration, there remain many fundamental and theoretical questions to be solved.

3.6.6 Discussions and remaining problems

From the observational and theoretical studies, it is now understood that magnetic reconnection can provide efficient acceleration of particles to suprathermal energies, but in spite of enormous progress many issues still remain unsolved. One of the important issues is whether or not reconnection can generate a power-law energy spectrum. As stated earlier, magnetic energy dissipation is believed to be important for nonthermal particle acceleration in many astrophysical applications. In the terrestrial magnetosphere, the energy spectrum is approximately given by a power law in the high-energy range with a slope of about 3–7 (e.g., Baker and Stone, 1977; Øieroset *et al.*, 2002). In solar flares where reconnection is regarded as one possible acceleration model, the power-law index of suprathermal particles is about 2.5–7 as well. In most space physics and astrophysics contexts, the production of nonthermal particles is more often attributed to the stochastic/diffusive shock acceleration (e.g., Blandford and Ostriker, 1978), because the diffusive shock acceleration can explain the ubiquitous power-law spectrum with an index of 2, which depends weakly on plasma parameters. Contrary to the diffusive shock acceleration, the reconnection acceleration seems to generate softer energy spectra from the observational point of view. Zenitani and Hoshino (2001, 2005) and Jaroschek *et al.* (2004), however, found that reconnection can produce a very hard energy spectrum with a power-law index of unity in the relativistic regime where the Alfvén speed v_A and the thermal velocity are close to the speed of light c. It is still an open question how the nonthermal energy spectrum depends on plasma parameters such as temperature and guide magnetic field, etc.

Another important issue is the spatial energetic particle distribution. The acceleration is basically provided by the inductive/convection electric field in reconnection, and a localization or spatial separation of energetic particles is expected from the fact that ions are accelerated parallel to the electric field and electrons in the antiparallel direction. However, as we stated in Section 3.6.2, dawn–dusk asymmetries of the energetic particles are not clearly seen at least up to several tens of keV. If diffusion due to wave–particle scattering takes effect substantially during acceleration, the asymmetry of the energetic particle distribution in the electric field direction is smeared out, because the potential energy gain/loss is always compensated by the energy loss/gain from the wave during the scattering. Furthermore, for wave–particle interaction, the maximum energy may even exceed the available potential energy. However, it is a controversial issue that the diffusion process plays an important role in plasma transport in the magnetotail. (Another possible explanation, discussed further in Section 4.4, is that betatron and Fermi-type acceleration in the collapsing field earthward of the reconnection site are more important than acceleration near the X-type neutral line.)

Finally we would like to comment on multiscale coupling. It is well known that electric and magnetic field turbulence act to heat the plasma through scattering of particles, but, in addition to this standard paradigm, it has been suggested that coherent, small-scale, large-amplitude electric field waves, often observed in key regions of the terrestrial magnetosphere, are responsible for electron energization. The spatial scale of the small-scale waves is several tens of Debye lengths, but the amplitudes of the waves are 10 to 100 times that of the

motional electric field induced in the MHD scale. Then it is proposed that the microscale processes appear to control the global dynamics. This kind of multiscale coupling process is beginning to shed light not only on space plasma phenomena but also on high-energy astroplasma physics. These observational and theoretical studies are also the key problems of future missions such as MMS/NASA and SCOPE/JAXA that focus on the potentially rich multiscale structuring plasma phenomena that result from the coupling of the MHD scale to the scale of electron kinetics.

4

Reconnection in the magnetosphere

In this chapter we focus particularly on recent advances in observations and simulations of reconnection at the magnetopause and in the near magnetotail, as these are the sites most heavily investigated by observations and simulations. The scenarios at the two sites have characteristic differences. At the magnetopause, reconnection occurs between two topologically distinct regions, the shocked solar wind and the magnetosphere, which also have quite different plasma properties. Reconnection generates a magnetic field component normal to the magnetopause and thereby leads to an interconnection between the two regions. As discussed in Section 1.2 and further in 4.5, magnetopause reconnection may have quasi-stationary features (as indicated in Fig. 1.6) as well as features that indicate localized, temporally limited reconnection (FTEs; Russell and Elphic, 1978; Elphic, 1995; Fig. 1.9). Critical parameters in reconnection at the magnetopause are the magnitude of the magnetic field component in the direction of the magnetopause current (*guide field*), the angle between the magnetic fields on either side of the current sheet, and the plasma properties, all of which may play a role in when and where and how reconnection takes place. Major questions of magnetopause reconnection, to be addressed in Sections 4.1 and 4.2, concern the location of reconnection sites and the temporal variability of the process under different solar wind conditions, both of which may be related to the role of a guide field.

In contrast to magnetopause reconnection, reconnection in the near tail takes place in a current sheet that already contains a magnetic field component normal to the current sheet, and the reconnecting field lines, at least initially, are not topologically distinct. (This changes when reconnection proceeds to lobe field lines.) As discussed in Section 3.3, the critical question here is not the role of a guide field, which tends to be quite small on average, but rather whether and how the normal field component B_z can become reduced to overcome its stabilizing effect. In Section 4.3 we continue the discussion of magnetotail stability, based on recent investigations of ideal MHD stability of 2D equilibria and of the collisionless tearing mode.

The stability discussion is followed by results from large-scale theory and simulations concerning current sheet formation and the consequences of reconnection in the magnetotail (Section 4.4), which also include the effects on currents and particles. Although major features of magnetic reconnection in the magnetotail have been discovered by single satellites or the two International Sun-Earth Explorer (ISEE 1 and 2) spacecraft, particular progress has been made recently by the four-satellite

Cluster mission, which for the first time permitted the calculation of spatial gradients without model assumptions. These observations form the particular focus of Section 4.5. The chapter is completed in Section 4.6 by remote sensing observations, which provide a unique way of determining reconnection rates without *in situ* information.

4.1 Reconnection at the magnetopause: concepts and models

J. C. Dorelli and A. Bhattacharjee

Investigations of magnetic reconnection at the Earth's magnetopause began with Dungey's seminal work on the role of magnetic nulls in the acceleration of auroral particles (Dungey, 1961, 1963). More than 40 years have passed since Dungey's model was published (see Fig. 4.1); nevertheless, as Figs. 1.6 and 1.8 demonstrate, Dungey's two-dimensional cartoons still guide our intuition about the large-scale topology of the magnetospheric magnetic field. However, the two magnetic field topologies envisioned by Dungey in Fig. 4.1 are structurally unstable – that is, generic small perturbations of the magnetic field result in qualitative changes in the field topology (see, for example, the discussion by Lau and Finn, 1990). For pure southward interplanetary magnetic field (IMF) conditions (top panel of Fig. 4.1), the continuum of magnetic nulls in the solar magnetospheric (SM; see Section 1.2) equatorial plane disappears when either the x or y component of the magnetic field is nonvanishing. Similarly, the Dungey topology for pure northward IMF conditions (bottom panel of Fig. 4.1) – in which there is a continuum of magnetic field lines, defining a closed surface (topologically equivalent to a sphere), which originate at the southern cusp null and terminate at the northern cusp null – is destroyed by small perturbations of the SM x or y magnetic field components.

Attempts to extend Dungey's picture to the generic case, in which the IMF orientation is arbitrary, have generally proceeded by treating magnetopause reconnection as a locally two-dimensional process, ignoring effects from the large-scale, three-dimensional magnetic field topology. For example, in the *component reconnection* model (Sonnerup, 1974), results from classical two-dimensional reconnection theory (as described in Section 2.1) are applied to local patches of the magnetopause surface, under the assumption that the direction of the X-line (the ignorable coordinate in the two-dimensional theory) is parallel to both the local magnetopause current density vector and the local magnetic field. A difficulty with this approach (pointed out by Cowley, 1976) is that the local current direction need not be parallel to the X-line in more general geometries. Thus, the component reconnection model fails to uniquely identify an X-line on the magnetopause surface. Instead, it is usually assumed (somewhat arbitrarily) that component reconnection occurs along an X-line which passes through, and extends some distance away from, the subsolar point.

In contrast, the *antiparallel reconnection* hypothesis (Crooker, 1979) predicts the geometry of the X-line as follows: (1) the magnetopause is identified as a two-dimensional surface which perfectly shields the magnetospheric magnetic field from the IMF (see, for example, a tutorial by Stern, 1994, on computing the magnetopause magnetic field in the absence of magnetic merging), treating the magnetopause surface as a tangential discontinuity; (2) the locus of points on the magnetopause surface for which the magnetic field vectors on either side of

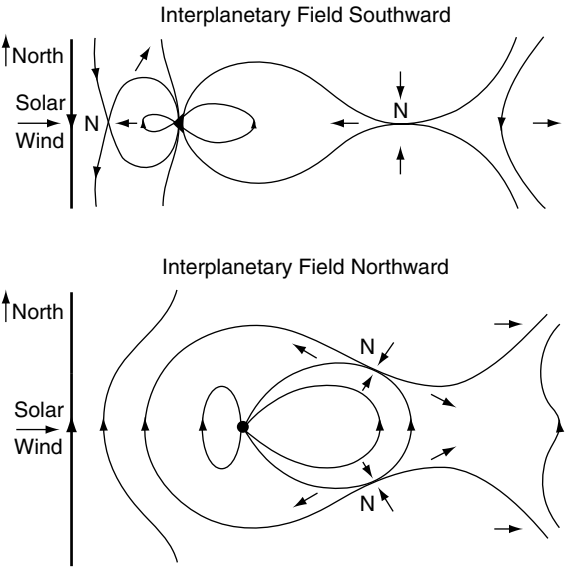

Fig. 4.1. Dungey's original illustrations (Dungey, 1961, 1963) of his reconnecting magnetosphere model.

the surface are antiparallel is constructed (see, for example, Fig. 4.10); (3) results from two-dimensional magnetic reconnection theory are invoked (e.g., Quest and Coroniti, 1981) to argue that the reconnection rate on the magnetopause surface has local maxima at the antiparallel locus. While this procedure predicts a definite merging line geometry, it is not clear that it is appropriate to apply results from two-dimensional tearing mode theory to local patches of the magnetopause surface. For example, recent calculations of tearing mode growth rates in three dimensions, starting with a magnetic field topology which is equivalent to Dungey's closed northward IMF topology (bottom panel of Fig. 4.1) indicate that current density need not be concentrated near the antiparallel loci (Hu *et al.*, 2004) (which necessarily contain the northern and southern magnetic nulls).

It should be noted that the distinction between component reconnection and antiparallel reconnection in space observations is related to, but not necessarily identical to, the distinction between the presence or absence of a guide field, discussed, for instance, in Chapter 3. In observations, as well as in large-scale simulations when the details of the current sheet structure are not resolved, the distinction is based on properties of the magnetic field outside the current sheet, whereas physics investigations of the dissipation mechanism put the emphasis on the presence of the guide field inside the current sheet, and in particular inside the dissipation region. For simple models with a uniform, or nearly uniform, guide field the two classification schemes agree, but in general configurations this need not be the case.

Spacecraft observations have not yet provided us with a convincing global picture of the dayside magnetopause magnetic field topology. As described in Section 4.2, for example, images of the proton aurora obtained by the Far Ultraviolet experiment

(FUV SI-12) on the IMAGE spacecraft have been used to support both the antiparallel (Fig. 4.11) and component (Fig. 4.9) reconnection pictures. Spacecraft observations of accelerated particles and *ion-energy dispersion events* (see Section 4.2) can provide indirect evidence of spatially localized acceleration processes which occur some distance away from the spacecraft. However, associating such particle signatures with distant magnetic reconnection is model dependent: (1) one needs a model of the magnetic field, using Liouville's theorem of the conservation of phase space density along phase space trajectories to map particles from the spacecraft location to the acceleration site; (2) one usually interprets features of the particle distribution functions (e.g., low-energy ion cutoffs) in the context of a model of the local magnetic field geometry at the reconnection site. Further, as is the case with the more recent proton aurora data, such *in situ* observations have also been used to support both the antiparallel (see, for example, Onsager *et al.*, 2001) and component (e.g., Fuselier *et al.*, 1997) reconnection hypotheses.

In this section we address the role of MHD simulations in computing the structure and dynamics of Earth's dayside magnetopause. Solving this problem involves attacking two of the fundamental problems in the MHD theory of magnetic reconnection: (1) What is the geometry and topology of magnetic reconnection in three-dimensional space and astrophysical systems (in which one cannot associate magnetic reconnection with the break-up of rational magnetic surfaces, as one typically does in systems with toroidal topology)? (2) How is fast magnetic reconnection (proceeding on Alfvénic time scales) possible when the classical collisional resistivity (Spitzer and Härm, 1953) is negligible? Addressing these two questions goes beyond the classical, two-dimensional MHD theory of magnetic reconnection described in Section 2.1 and requires non-MHD effects (discussed in Chapter 3). In addition, new three-dimensional concepts such as *separator reconnection* (treated, in the solar physics context, in Section 5.2) have to be considered.

4.1.1 Three-dimensional reconnection at the dayside magnetopause

Vacuum superposition models, in which a uniform IMF, aligned with the Earth's dipole axis, is superimposed on Earth's dipole field, were among the earliest models of the magnetospheric magnetic field topology (Dungey, 1961, 1963; Forbes and Speiser, 1971; Cowley, 1973). As we have noted, this topology is structurally unstable, that is, it is no longer applicable when the IMF is not exactly southward or exactly northward (with respect to the dipole axis). For generic IMF conditions, the magnetic field topology of the vacuum superposition model is characterized by two isolated magnetic nulls (where the field vanishes) joined by a separator loop which marks the intersection of two separatrix surfaces. This topology is shown in Fig. 4.2 for a generic northward IMF case (the generic southward case has the same topology; for the sake of brevity, we will consider only the northward case). The notations of Fig. 4.2 are those of Lau and Finn (1990), given in brackets in the following discussion (see also Section 2.4).

The local structure of a *negative* null (type A null), determined from the eigenvalues of the $\nabla \mathbf{B}$ matrix of magnetic field partial derivatives, is such that a single field line, the *spine* (γ_A *line*), diverges away from the null, while an infinite number of field lines converge toward the null, forming the *fan* (Σ_A *surface*). Similarly, near a

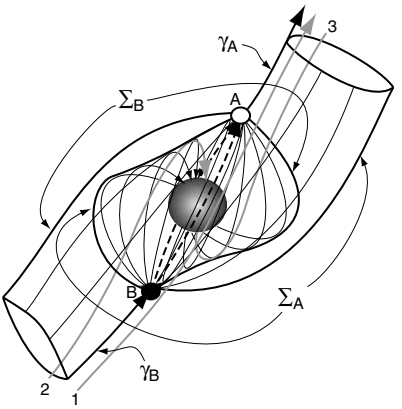

Fig. 4.2. Vacuum superposition model of Earth's magnetosphere under generic northward IMF conditions. The notations follow Lau and Finn (1990) with γ lines corresponding to spines (Section 2.4) and Σ surfaces corresponding to fans. There are several distinct topological classes of field lines: (1) Solar wind field lines, located outside both Σ surfaces; (2) open field lines, located within one Σ surface but external to the other Σ surface (under northward IMF conditions, such field lines, marked 2 and 3 in the figure, are said to "overdrape" the dayside magnetopause as they penetrate into the magnetosphere to intersect Earth's surface); (3) closed field lines, which are contained within both Σ surfaces. The two Σ surfaces intersect to form a single *separator line* which joins the A and B nulls to form a null–null loop.

positive null (type B null), a single spine $\gamma_{\rm B}$ *line* converges toward the null, while an infinite number of field lines diverge away from the null to form the fan $\Sigma_{\rm B}$ *surface*. The two fan surfaces intersect to form a closed field line, the *separator*, consisting of two parts which diverge away from the positive (type B) null and converge toward the negative (type A) null.

Let us now consider the steady-state case, in which the electric and magnetic fields are independent of time. The electric field $\mathbf{E}$ can be written in terms of a potential, Φ: $\mathbf{E} = -\nabla\Phi$. Further, in the ideal MHD limit, Ohm's law takes the form $\mathbf{E} = -\mathbf{v} \times \mathbf{B}$, so that the electrostatic potential is constant along magnetic field lines:

$$\mathbf{B} \cdot \nabla\Phi = 0. \tag{4.1}$$

We are now in a position – following Stern (1973), Greene (1988) and Lau and Finn (1990) – to investigate how the magnetic field topology of Fig. 4.2 influences the dayside magnetopause reconnection process. First, we define our volume of interest to be the region between two spherical surfaces, S_1 and S_2, where S_1 is the Earth's surface, and S_2 is centered on Earth with a radius $R \gg 1\ R_{\rm E}$ (such that S_2 is in the solar wind). Given values of Φ on S_2, we use Eq. (4.1) to determine Φ on S_1. Now, consider the class of field lines which lie on the $\Sigma_{\rm A}$ surface. By definition, all such field lines converge toward the A null before merging into a single field line, the $\gamma_{\rm A}$ line, which diverges away from A. Since the $\gamma_{\rm A}$ line intersects S_1, all of the field lines on the $\Sigma_{\rm A}$ surface map different locations on S_2 to the same point, P_1, on S_1. Therefore, since there is a finite solar wind electric field in the Earth's rest frame,

($\mathbf{E}_{SW} = -\mathbf{v}_{SW} \times \mathbf{B}_{SW}$, where $\mathbf{E}_{SW}$, $\mathbf{v}_{SW}$, and $\mathbf{B}_{SW}$ are the solar wind electric, bulk velocity, and magnetic fields, respectively) the electrostatic potential at P_1 is singular in the ideal MHD limit. This singularity is often referred to as the *Stern singularity*, after Stern (1973), who identified it as a signature of magnetic reconnection at the dayside magnetopause.

The Stern singularity is a symptom of the breakdown of the ideal MHD description of field line motion on the magnetic separatrix surfaces of Fig. 4.2. If one follows a solar wind field line (line 1 in Fig. 4.2) as it approaches the dayside magnetopause segment of the separator line (line segment BA in Fig. 4.2), then the field line velocity, $\mathbf{v}_{FL} = -\mathbf{E} \times \mathbf{B}/B^2$, becomes infinite at the A and B nulls, as field line 1 splits into lines 2 and 3 (each of which has one end intersecting S_1 and the other intersecting S_2). If, on the other hand, there is a finite volume of nonvanishing parallel electric field through which the separator passes, then the Stern singularity can be removed, and the field line velocity is no longer infinite (see, for example, Fig. 15 of the review by Siscoe, 1988).

Thus, we see that simple potential mapping, using Eq. (4.1), in a vacuum superposition magnetic field topology allows us to deduce that the breakdown of ideal MHD – necessary for magnetic merging to occur at the dayside magnetopause – manifests itself as a volume of nonvanishing parallel electric field, $E_{\|}$ which contains one or more segments of the separator line. However, without moving beyond kinematics (in which the magnetic field topology is given and the resulting ideal MHD flow field is derived) to consider self-consistent dynamics (in which the influence of the plasma flow on the magnetic field topology is considered), we cannot make any conclusions about the spatial distribution of the parallel electric field on the magnetopause surface. For example, the antiparallel hypothesis predicts that the volume of nonvanishing $E_{\|}$ consists of two separate, disconnected regions which contain A and B. The component reconnection hypothesis, on the other hand, predicts that the volume of nonvanishing $E_{\|}$ consists of a single region which contains the subsolar point. Of course, in the context of the vacuum superposition model, there are many other possibilities. One interesting possibility, referred to as *separator reconnection* (see Section 5.2), involves the formation of a thin current ribbon along the separator line (analogous to thin current sheets which form by deformation of X-type nulls in two dimensions; see Fig. 2.3). Such a current ribbon would be the three-dimensional analogue of the two-dimensional Sweet–Parker current sheet, converting magnetic energy into plasma energy by a combination of Ohmic dissipation within the sheet and bulk acceleration by $\mathbf{j} \times \mathbf{B}$ and pressure gradient forces at the edges of the sheet. Such a ribbon (and its associated parallel electric field) might extend all the way from A to B, in which case the reconnection geometry would display geometric features of both antiparallel (near the nulls) and component (near the subsolar point) reconnection.

4.1.2 The Sweet–Parker time scale problem

Let us assume that the Stern singularity at the magnetopause is eliminated via the formation of thin current sheets which contain one or more segments of the dayside separator line. Such current sheets are expected to undergo reconnection, associated with $E_{\|}$ and Joule dissipation. This allows changes in the magnetic flux

contained within the distinct flux volumes defined by the fan (Σ_A and Σ_B) separatrix surfaces. As discussed in Section 4.6, one can estimate the reconnection rate by remote sensing of ionospheric convection across Earth's polar cap boundaries. In the vacuum superposition model, the polar cap boundaries correspond to the intersections of the Σ_A and Σ_B surfaces with the surface S_1 (i.e., Earth's surface). Referring again to Fig. 4.2, the northern polar cap boundary corresponds to the intersection of Σ_B with Earth's surface, while the southern polar cap boundary corresponds to the intersection of Σ_A with Earth's surface. Thus, any ionospheric convection across the northern (southern) polar cap boundary corresponds to flow of plasma across the Σ_B (Σ_A) surface. The rate at which polar cap flux changes is given by the line integral, taken around the separator, of the parallel electric field. Magnetopause reconnection electric fields inferred from radar observations of ionospheric convection (see Fig. 4.25 and accompanying text) are typically a few tenths of a mV/m. If we assume that this parallel electric field is associated with a thin current sheet at the magnetopause and apply the classical two-dimensional reconnection theory (Section 2.1) to compute the inflow speed v_e (the speed at which magnetic flux is transported into the current sheet), we get $v_e \approx E_\parallel / B_e$, where B_e is now the projection of the upstream magnetic field in the plane perpendicular to $E_\parallel$. Using $B_e \approx 20\,\mathrm{nT}$, we get $v_e \approx 0.15\, v_A$, where v_A is the upstream Alfvén speed ($v_A \approx 100\,\mathrm{km/s}$ if the plasma density upstream of the current sheet is taken to be $20\,\mathrm{cm}^{-3}$.

Is it possible to explain observed parallel electric fields by invoking the resistive MHD theory of reconnection in thin current sheets (Parker, 1957; Sweet, 1958a; Section 2.1)? Referring to Fig. 2.1 and Section 2.1, we note that the Sweet–Parker theory predicts that v_e scales like the square root of the plasma resistivity. Thus, the Sweet–Parker theory predicts that thin current sheets which form on the nearly collisionless magnetopause are essentially tangential discontinuities (i.e., the component of the magnetic field normal to the sheet is much smaller than the component parallel to the sheet), with negligible parallel electric fields and negligible plasma flow across the magnetic separatrices. We will refer to this disparity between observed reconnection time scales and that predicted by the Sweet–Parker theory as the *Sweet–Parker time scale problem.*

As discussed in Section 2.1, Petschek (1964) suggested a solution to the Sweet–Parker time scale problem, in which the thin current sheet bifurcates into two pairs of slow-mode shock waves, resulting in a microscopic diffusion region the dimensions of which scale like the plasma resistivity (Fig. 2.2). However, in resistive MHD simulations, one generally observes long, thin Sweet–Parker sheets unless a localized resistivity model is imposed (Biskamp, 1986; Biskamp and Schwarz, 2001). However, Biskamp's numerical experiments revealed another possible solution of the Sweet–Parker time scale problem. Recall that the Sweet–Parker theory assumes that the upstream magnetic field (B_e) is insensitive to the Lundquist number, S. In simulations, however, one often observes that B_e increases as the plasma resistivity decreases (see, for example, Biskamp, 1986). The physical reason for this effect is easy to understand. As the resistivity decreases, the rate at which magnetic flux can be transported into the current sheet drops. If the rate at which magnetic flux is added to the upstream region is larger than the rate at which it is transported into the sheet, then the magnetic field strength increases and magnetic energy

accumulates just upstream of the current sheet (*magnetic pile-up*), thereby also enhancing the reconnection electric field.

While such magnetic pile-up can render the reconnection rate insensitive to the Lundquist number, this insensitivity cannot hold for arbitrarily small plasma resistivity. As pointed out by Priest (1996) and Litvinenko (1999), momentum conservation in steady state requires that the plasma pressure upstream of the current sheet decreases to balance the increase in the upstream magnetic pressure. Since the upstream pressure must be positive, there must be a limit to the amount of magnetic energy which can accumulate upstream of the current sheet. It turns out (see Litvinenko, 1999, for details) that the maximum flux pile-up reconnection rate consistent with positive upstream plasma pressure again scales like the square root of the plasma resistivity. Thus, whether the Sweet–Parker time scale problem is relevant in a driven, steady reconnection context depends on whether one is in the *presaturation* Lundquist number regime (in which magnetic pile-up renders the reconnection rate insensitive to the Lundquist number) or the *postsaturation* regime (in which the pile-up has saturated and the reconnection rate begins to scale strongly with the Lundquist number). However, the classical plasma resistivity is so low at the dayside magnetopause that invoking magnetic pile-up to explain observed reconnection electric fields would require much larger magnetosheath magnetic fields than are observed. Chapter 3 presents possible solutions of this problem, in which Hall electric fields can allow the flux pile-up to saturate well before the reconnection rate begins to stall due to the finite upstream plasma pressure (see also Dorelli, 2003; Dorelli and Birn, 2003).

4.1.3 Global MHD simulations of magnetopause reconnection

There have been numerous attempts to apply resistive MHD simulations of Earth's magnetosphere (often referred to in the literature simply as *global MHD simulations*) to the problem of determining the magnetic field topology of the magnetosphere under various IMF conditions (see, for example, Fedder *et al.*, 1995; Raeder *et al.*, 1995; Crooker *et al.*, 1998; Siscoe *et al.*, 2001). However, none of these previous studies has quantitatively addressed the role of magnetic nulls and their associated separatrix surfaces in constraining the dynamics of magnetic reconnection at Earth's dayside magnetopause. Furthermore, previous global MHD studies have not systematically addressed the scaling of the magnetopause reconnection rate with plasma resistivity. In this section, we describe recent results from the University of New Hampshire Geospace General Circulation Model (GGCM) simulation code (Raeder, 1999) which quantitatively address the following two questions: (1) What is the topology of the dayside magnetopause magnetic field under generic northward IMF conditions (i.e., when the SM B_y and B_z components have comparable magnitudes)? (2) How does the magnetopause reconnection rate scale with plasma resistivity under pure southward IMF conditions?

Figure 4.3 shows a close-up view of the dayside magnetopause computed by the GGCM code under pure southward IMF conditions (using GSE, Geocentric Solar Ecliptic, coordinates defined in Section 1.2). The left panel is a three-dimensional view of the magnetosheath stagnation point flow (3D arrows), showing how magnetic field lines are convected toward the magnetopause current sheet (located

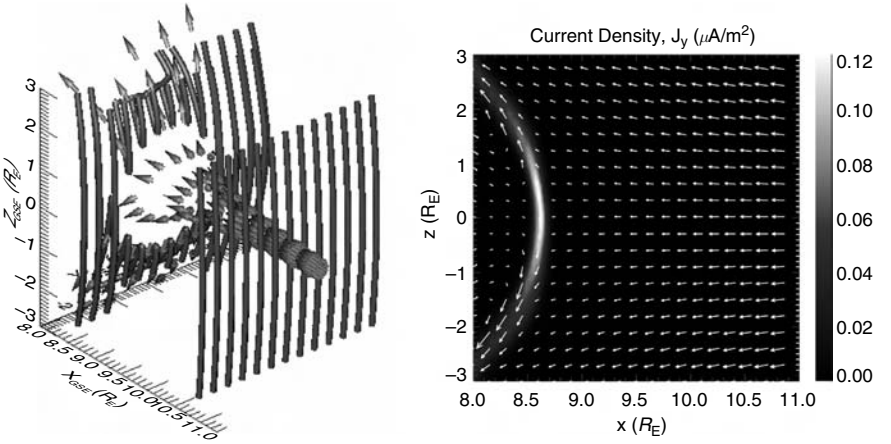

Fig. 4.3. GGCM simulation of a thin current sheet which forms at the dayside magnetopause under pure southward IMF conditions. The left panel shows the three-dimensional structure of the stagnation point flow (arrow glyphs) near the subsolar point (the magnetic field is represented by streamtubes); the right panel shows the y component of the current density in the noon–midnight meridian plane (white arrows in the right panel show the bulk velocity field projected onto the plane).

at $x_{\mathrm{GSE}} \approx 8.7\,R_{\mathrm{E}}$ on the x_{GSE} axis), where they undergo magnetic reconnection as the flow field diverges away from the stagnation point. The right panel shows the y_{GSE} component of the current density in the noon–midnight meridian plane. The white arrows show the bulk velocity field. Two important conclusions about the reconnection physics can be drawn by inspection of the right panel of Fig. 4.3. First, the aspect ratio of the current sheet is large: the width of the sheet is several Earth radii, while the thickness is less than a tenth of an Earth radius. Further, the bulk velocity field diverges away from the stagnation point (indicating decelerating inflow) rather than converging toward it (which would indicate accelerating inflow). The structure of the flow field and the geometry of the current sheet suggest that the Sweet–Parker, rather than the Petschek model, is the relevant model, of reconnection at the dayside magnetopause.

Figure 4.4 confirms this suggestion. The left panel of Fig. 4.4 shows the plasma density in the noon–midnight meridian plane. Note that the density decreases (by roughly ten percent) from its value of about $28\,\mathrm{cm}^{-3}$ just downstream of the bow shock (located at $x_{\mathrm{GSE}} \approx 12\,R_{\mathrm{E}}$) to about $25\,\mathrm{cm}^{-3}$ just upstream of the current sheet. This density increase is a consequence of the decrease in plasma pressure (see the curve marked P in the right panel) which accompanies the pile-up of magnetic energy in the magnetosheath (see the B_z curve in the right panel). As discussed in Section 2.1, one can interpret the magnetic pile-up, and the associated decrease in plasma pressure upstream of the current sheet, as a slow-mode expansion which is characteristic of flux pile-up reconnection. In contrast, the Petschek configuration is characterized by a slow-mode compression, in which the pressure increases (and the magnetic field decreases) as one approaches the current sheet.

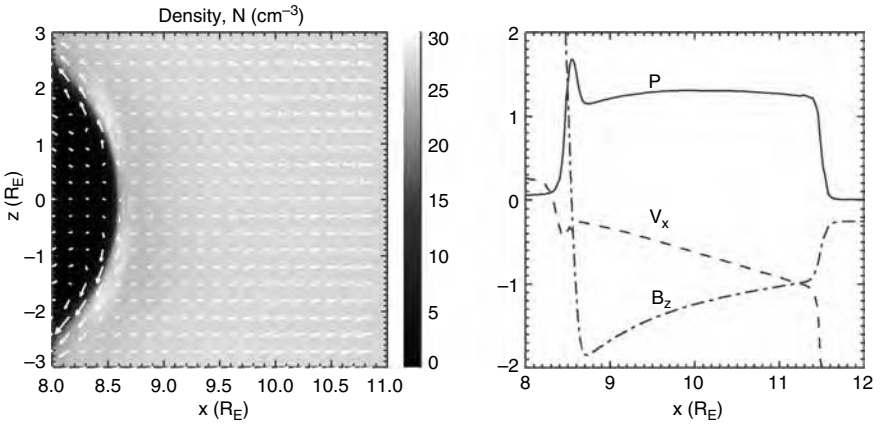

Fig. 4.4. Magnetic pile-up and associated plasma depletion upstream of the current sheet, corresponding to Fig. 4.3. The left panel shows the plasma density in the noon–midnight meridian plane; the right panel shows the plasma pressure (P), the x component of the bulk velocity (v_x), and the z component of the magnetic field (B_z) along the Sun–Earth line. The magnetopause current sheet is located at $x \approx 8.7\,R_{\rm E}$.

These arguments are qualitative, however, being based on a two-dimensional, approximate theory (e.g., Priest and Forbes, 1986) which is valid when the pile-up is not too large. As Fig. 4.3 demonstrates, the subsolar magnetopause stagnation point flow is three-dimensional. That is, the streamlines diverge nearly uniformly away from the subsolar point (which is located at roughly $x_{\rm GSE} = 8.7\,R_{\rm E},\ y_{\rm GSE} = z_{\rm GSE} = 0$). It turns out that the three-dimensional flow can be accurately modeled near the $x_{\rm GSE}$ axis in the magnetosheath (see Dorelli *et al.*, 2004, for details), using an analytical solution of the resistive MHD equations first obtained by Sonnerup and Priest (1975):

$$v_x = -v_0 x, \quad v_y = v_0 y(1-\kappa), \quad v_z = v_0 z\kappa, \tag{4.2}$$

$$B_x = 0, \quad B_y = 0, B_z = f(x), \tag{4.3}$$

where v_0 is a constant which determines the strength of the driving flow, κ is a parameter controlling the anisotropy of the flow in the GSE y,z plane, and $f(x)$ gives the z component of the magnetic field as a function of x (i.e., normal to the one-dimensional current sheet in the y,z plane at $x = 0$), which satisfies the following equation:

$$\frac{1}{S}\frac{{\rm d}^2 f}{{\rm d}x^2} + v_0 x \frac{{\rm d}f}{{\rm d}x} + v_0 \kappa f = 0. \tag{4.4}$$

Craig *et al.* (1997) note that the general solution of Eq. (4.4) can be written as follows:

$$f(x) = C_1 x (S v_0)^{1/2} M\left(\frac{\kappa+2}{2}, \frac{3}{2}, -S v_0 \frac{x^2}{2}\right) + C_2 M\left(\frac{\kappa}{2}, \frac{1}{2}, -S v_0 \frac{x^2}{2}\right). \tag{4.5}$$

Setting $C_2 = 0$ in Eq. (4.5) (i.e., imposing the boundary condition that the magnetic field vanishes at the stagnation point), one obtains pile-up scaling laws: $B_e \propto S^{\kappa/2}$ and $E_y \propto S^{-\kappa/2}$, where B_e is the magnitude of B_z at its local maximum (just upstream of the current sheet), and E_y is the electric field at the local maximum of B_z (the reconnection electric field). Figure 4.5 shows a comparison between the scalings predicted by the Sonnerup and Priest (1975) theory (solid lines, with $\kappa = 0.4$) and those computed from the GGCM simulations (squares). While the amount of pile-up observed in the simulations is less than that predicted by the Sonnerup and Priest (1975) theory for the highest two Lundquist numbers (this can be explained by a combination of compressibility and numerical resistivity effects, as discussed by Dorelli *et al.*, 2004), the scaling of the upstream flow seems to compensate for this to some extent. The reconnection electric field in the simulations scales approximately like $S^{-0.2}$, which is consistent with the prediction of the Sonnerup and Priest (1975) theory.

We turn now to the question of the topology of the magnetopause magnetic field under generic northward IMF conditions. To address this question, we have tracked the magnetic nulls in the GGCM simulation, using a bisection technique developed by Greene (1992). Figure 4.6 shows the *magnetic skeleton* computed from the GGCM model under steady northward IMF conditions in which the y and z components of the IMF are equal. The magnetic skeleton is computed as follows: (1) magnetic nulls within the simulation domain are located, (2) starting from a spherical-polar grid of seed points centered on each null, magnetic field streamlines are computed. The two panels of Fig. 4.6 show two views of the magnetic skeleton: the left panel shows a view from the Sun; the right panel shows a view from the northern dusk octant. To guide the eye, black lines indicate the direction of the IMF, the direction of the first closed magnetospheric field line passing through the Sun–Earth line, the direction of the separator line (predicted by the vacuum superposition model), and the direction of the subsolar reconnection outflow predicted by the separator reconnection model.

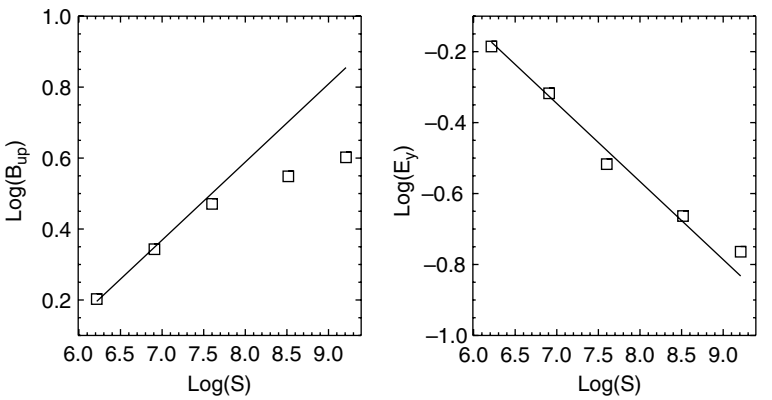

Fig. 4.5. Upstream magnetic field (left panel) and reconnection electric field (right panel) as functions of the Lundquist number. The solid lines show the prediction of the Sonnerup and Priest (1975) theory; the squares show the results of the GGCM simulation.

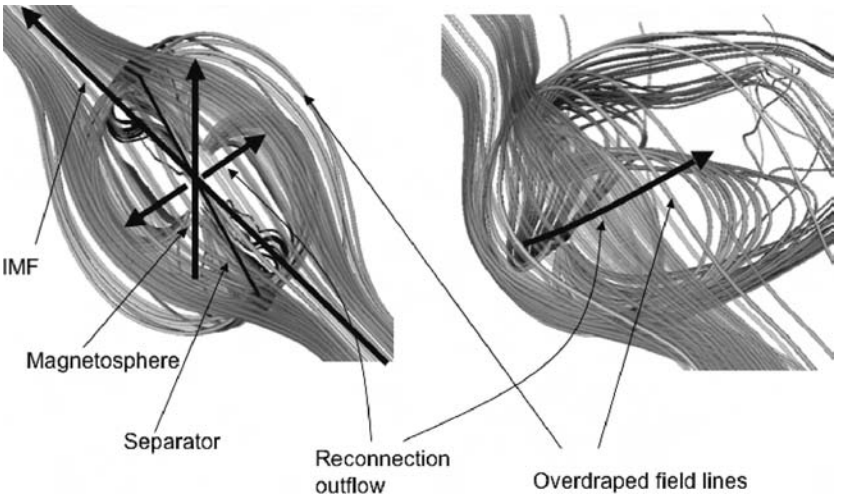

Fig. 4.6. Two views of the magnetic skeleton computed from a GGCM simulation of magnetopause reconnection under generic northward IMF conditions. The left figure shows a view from the Sun; the right panel shows a view from the northern dusk octant.

It is clear from comparing Fig. 4.2 with 4.6 that the magnetopause magnetic field topology observed in the GGCM simulations is similar to the vacuum superposition topology in the following respects: (1) There are two cusp magnetic nulls – a type A null in the northern hemisphere, and a type B null in the southern hemisphere; (2) Open, *overdraped* field lines originating near the magnetic nulls seem to lie on surfaces (similar to the Σ surfaces in Fig. 4.2) which extend from the dayside around the magnetopause surface to the nightside; (3) the orientations of IMF field lines near the subsolar point are within a few degrees of the line (marked "Separator" in Fig. 4.6) joining the two cusp nulls.

Further evidence that the magnetopause magnetic field topology is similar to that of the vacuum superposition model is shown in Fig. 4.7. The left panel shows the surface which separates IMF field lines from open, overdraped field lines (which have one end in the solar wind and the other end intersecting Earth's surface). The right panel shows the open–closed separatrix surface, which separates open field lines from closed field lines (both ends of which intersect Earth's surface). Note that the open–closed separatrix surface is distorted into a local *cusp* shape near the magnetic nulls (the red and blue spheres), resulting in north–south and east–west asymmetries of the separatrix surface which are similar to those predicted by the vacuum superposition model shown in Fig. 4.2. Current density on both separatrix surfaces is distributed in *ribbons* which are approximately spatially coincident, suggesting that the current sheet is spatially organized along regions, extending from one cusp null to the other, where the two separatrices intersect. Further, the magnitude of the current density does not have local maxima at either of the two cusp nulls. Instead, it has a local maximum near the subsolar point. The geometry of the stagnation point outflow is not isotropic; rather, it is similar to that of the current sheet, with

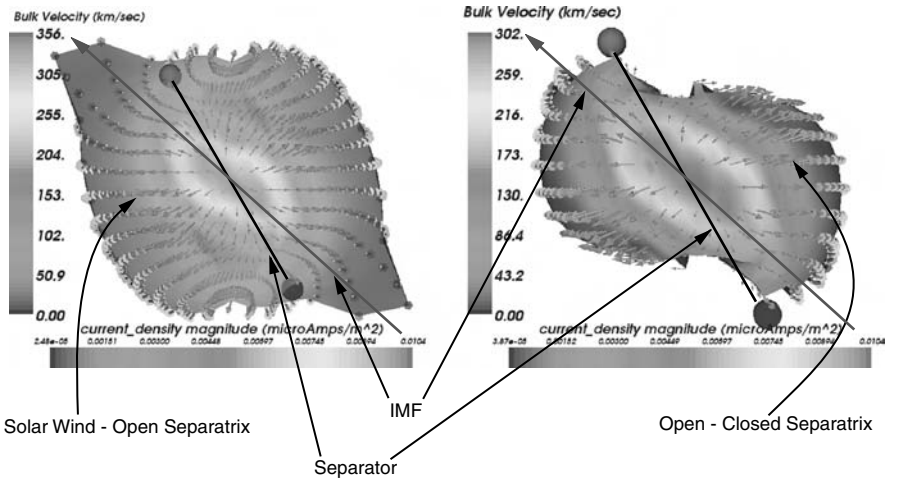

Fig. 4.7. Magnetic separatrices computed from a GGCM simulation of magnetopause reconnection under generic northward IMF conditions. The left panel shows the surface separating solar wind field lines from *overdraped* open field lines; the right panel shows the surface separating open field lines from closed field lines. Arrow glyphs show the bulk velocity field on the separatrix surfaces. Each surface is color coded according to the magnitude of the current density on the surface. See also color plate.

approximately Alfvénic outflow at the edges of the sheet (based on the magnetic field magnitude just upstream of the sheet, $v_A \approx 160\,\mathrm{km/s}$). Thus, there is compelling evidence from the GGCM simulations that, under generic northward IMF conditions, magnetic reconnection occurs at the dayside magnetopause via the formation of a thin Sweet–Parker current ribbon which extends from one cusp null to the other across the dayside magnetopause surface. The topology is reminiscent of a separator reconnection topology (Fig. 4.2), in which solar wind field lines reconnect with magnetospheric field lines along the current ribbon to form new overdraped open field lines.

4.1.4 Summary

As we have seen, resistive magnetohydrodynamics can be a useful tool in addressing some of the fundamental questions surrounding the theory of magnetic reconnection at Earth's dayside magnetopause. Such simulations have elucidated the nature of the Sweet–Parker time scale problem by making connections with the classical two-dimensional resistive MHD theories (Section 2.1). In addition to highlighting deficiencies in the resistive MHD model, these connections to simple analytic theories suggest solutions to the time scale problem (Section 3.4) which invoke non-MHD effects such as Hall electric fields. Further, global MHD simulations allow us to explore the large-scale topology of the dayside magnetopause in a way which is not yet possible with *in situ* spacecraft or remote sensing observations, suggesting that the apparent conflict between the antiparallel and component reconnection hypotheses might be resolved in the context of the global separator reconnection model.

High-resolution global MHD simulations (Raeder, 2005) have also begun to shed light on the formation of flux transfer events (FTEs; see Section 1.2 and Fig. 1.9) as a consequence of intermittent, spatially and temporally localized reconnection. These simulations reproduce major observed features, such as bipolar magnetic field signatures, enhanced core pressure, and intermittent finite-duration events. The major factor in obtaining these signatures was the breaking of the symmetry between the flow and the magnetic field and sufficient spatial resolution, whereas the dissipation mechanism apparently had no significant effect on the FTE features, as long as it did not cause spatially extended diffusion.

4.2 Observations of magnetopause reconnection

K. J. Trattner, S. A. Fuselier, and S. M. Petrinec

As indicated by Figs. 1.6, 1.8, and 4.1, field lines that have recently been reconnected at the magnetopause map to the vicinity or inside of the Earth's magnetospheric cusp regions. That is a reason why this region forms a particular focus in this section. Early observations at the magnetopause and in the cusps which indicated plasma and magnetic flux transfer from the solar wind into the magnetosphere gave the first, indirect, evidence for magnetic reconnection at the magnetopause (e.g., Aubry *et al.*, 1970; Burch, 1974; Rosenbauer *et al.*, 1975). Direct and incontrovertible evidence for reconnection at the magnetopause was provided by the high time resolution plasma and field observations from the International Sun-Earth Explorer (ISEE) spacecraft (e.g., Paschmann *et al.*, 1979; Sonnerup *et al.*, 1981; Gosling *et al.*, 1982), which demonstrated that local flow and field properties were indeed consistent with transport across the magnetopause resulting from reconnection.

Most of these observations addressed kinetic and plasma fluid features of narrow *jets* of plasma observed outside the diffusion region (i.e., outside the region where the ions and electrons become demagnetized and the magnetic field reconnects). An important analysis tool is the *Walén test* (Sonnerup *et al.*, 1987), which checks the plasma flow and magnetic field for consistency with transport across the magnetopause boundary. While these observations are consistent with quasi-steady, persistent reconnection, other signatures, specifically those of flux transfer events (FTEs, see Fig. 1.9) are interpreted as the consequences of temporally and spatially localized reconnection (e.g., Russell and Elphic, 1978; Elphic, 1995). These features consist particularly of characteristic bipolar magnetic field perturbations, indicating traveling flux rope structures in the vicinity of the magnetopause. They were found to be accompanied by plasma signatures that confirm that these flux ropes connect magnetosheath and magnetospheric plasmas (Thomsen *et al.*, 1987). Four-satellite Cluster observations have now provided further details about the structure of FTEs (Sonnerup *et al.*, 2004).

With the launch of the Polar spacecraft in 1996 and, subsequently, the IMAGE and Cluster spacecraft, attention was focused again on the magnetospheric cusps and their role in understanding magnetic reconnection. Polar and Cluster spacecraft have also established features of the ion diffusion region and its associated magnetic and electric field perturbations and turbulence and have provided possible glimpses into the tiny electron diffusion region (e.g., Mozer *et al.*, 2002) and electron current layers, presumably connected to the diffusion region (André *et al.*, 2004).

Recent observations have solidified several issues about reconnection and provided answers to questions raised by previous observations: (1) How continuous and stable is the process, and (2) where are the reconnection sites at the magnetopause and what controls their location? Observations pertaining to these two questions are presented in this section. The focus is on recent observations from a variety of spacecraft. These observations establish that reconnection is a persistent process at the magnetopause, which rarely ceases. Changes in the upstream conditions, in particular changes in the orientation of the Interplanetary Magnetic Field (IMF), cause reconnection sites to shift but do not cause reconnection to stop, even at high latitudes, where reconnection sites were once thought to move tailward in a super-Alfvénic flow. Multi-spacecraft observations in the Earth's magnetospheric cusps show that the reconnection rate may change at the magnetopause, but this rate is much less variable than originally thought. Many of the features observed in the cusp that were attributed to a variable reconnection rate are actually evidence of spatial structures, which move in response to the changing solar wind conditions.

Lacking direct identification of reconnection sites at the magnetopause, two basic models of reconnection emerged in the 1970s. These models are the *antiparallel reconnection model* and the *component reconnection model* (Section 4.1). In the antiparallel reconnection model, magnetic reconnection proceeds at the magnetopause only at locations where the IMF and the magnetospheric magnetic fields are very close to antiparallel (Crooker, 1979; Luhmann *et al.*, 1984). In the component model, reconnection can occur anywhere on the magnetopause (e.g., Cowley and Owen, 1989), but the usual assumption is that it occurs along a neutral line that is hinged at the subsolar point and tilted depending on the IMF B_y component (Moore *et al.*, 2002). The newer observations discussed here show that both models have merit. New results that paint the location of the reconnection site on the magnetopause demonstrate evidence for both antiparallel and component, or tilted neutral line, reconnection. The section concludes with open questions and a discussion of the direction of future observations at the magnetopause and their contribution to understanding this important process.

4.2.1 When does magnetopause reconnection occur?

Reconnection at the magnetopause has been observed to persist over long periods of time. This is clearly demonstrated by recent observations from the Imager for Magnetopause-to-Aurora Global Exploration (IMAGE) spacecraft and the Cluster suite (Fig. 4.8). During an extended interval (~ 4 hours) of northward IMF, the Cluster spacecraft observed accelerated flows associated with reconnection jets, poleward and tailward of the northern cusp. These jets appear in the x component of the ion velocity moment as measured by one of the spacecraft, displayed in the left panel of Fig. 4.8. At this time, the Cluster spacecraft were on an outbound pass through the magnetopause. Simultaneously, far ultraviolet emissions from the dayside ionosphere were observed remotely by one of the Spectrographic Imagers comprising the Far Ultraviolet experiment (FUV SI-12) onboard the IMAGE spacecraft. These are Doppler-shifted Lyman-α (121.8 nm) emissions, caused primarily by charge exchange due to the precipitation of energetic protons into the ionosphere. The imager does not allow for the determination of the exact Doppler shift or

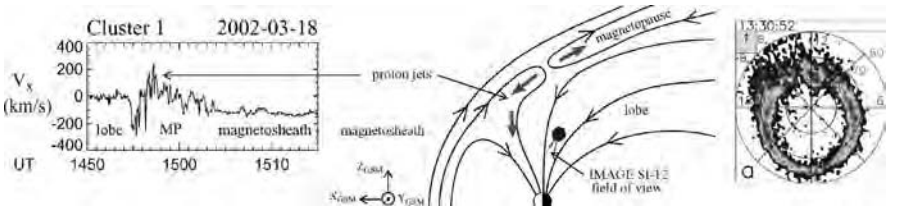

Fig. 4.8. IMAGE and Cluster observations of continuous reconnection at the magnetopause, poleward of the cusp during an extended interval of northward IMF. The observations of reconnection jets at the high-latitude magnetopause on March 18, 2002 by Cluster (left panel) and a proton auroral spot by IMAGE on the same field lines (right panel) provide evidence that the proton spot represents the remote signatures of reconnection. Cluster sampled the magnetopause for just 5 minutes, but IMAGE tracked the proton spot for ~ 4 hours (not shown), implying continuous reconnection. Adapted from Phan *et al.* (2003); Frey *et al.* (2003).

energy of the emitting hydrogen atom. However, as confirmed by modeling of the instrument response function, it is most sensitive to proton precipitation in the energy range from 2 to 8 keV (Frey *et al.*, 2002). These emissions were found to lie within an isolated region of the dayside ionosphere, on the same field lines as those sampled by Cluster. (Field line tracking was accomplished with the Tsyganenko T89, T96 and T01 magnetospheric magnetic field models (Tsyganenko, 2002, and references therein).) These ionospheric emissions persisted without interruption over the entire time period, as shown in the sample image displayed in the right panel of Fig 4.8, adapted from Phan *et al.* (2003) and Frey *et al.* (2003). However, the emissions did move in local time, as the reconnection site at the magnetopause changed its location in response to variations of the y component of the IMF.

4.2.2 Where does magnetopause reconnection occur?

Another major question about magnetic reconnection is where reconnection occurs at the magnetopause. As mentioned above, there are two scenarios: (a) antiparallel reconnection, where shear angles between the magnetospheric field and the IMF are near 180° (e.g., Crooker, 1979; Luhmann *et al.*, 1984; Gosling *et al.*, 1991), and (b) component reconnection, where magnetic shear angles are significantly different from 180° (Gosling *et al.*, 1982; Onsager and Fuselier, 1994; Fuselier *et al.*, 1997, 2000b), and have even been observed to be as low as 50° (Gosling *et al.*, 1990).

For northward IMF conditions, only recently has there been a direct observation of reconnection poleward of the cusp (Kessel *et al.*, 1996). Even more recently, Trattner *et al.* (2004) concluded that for northward IMF both reconnection scenarios occur simultaneously. The reconnection line located poleward of the cusp extends from the rather small antiparallel reconnection site into regions where the magnetic fields are no longer strictly antiparallel. This result is also in agreement with conclusions by Onsager *et al.* (2001) who reported the existence of very long reconnection lines during northward IMF conditions.

The antiparallel reconnection site for strictly southward IMF conditions covers the entire dayside magnetosphere along the magnetic equator. When a strong B_y component is present, the antiparallel reconnection sites split up, causing two

separated reconnection locations in different hemispheres (e.g., Crooker, 1979). In contrast, the component reconnection tilted neutral line model (e.g., Sonnerup, 1974; Cowley, 1976; Sonnerup *et al.*, 1981; Cowley and Owen, 1989; Fuselier *et al.*, 2002) for southward IMF conditions predicts that a neutral line runs across the dayside magnetosphere through the subsolar point regardless of the magnitude of the B_y component. The magnitude of the B_y component would only determine the tilt of the neutral line relative to the equatorial plane.

The newest observational tool to distinguish between antiparallel reconnection sites and a tilted X-line is the proton aurora imaging FUV SI-12 instrument onboard the IMAGE spacecraft. While ionospheric emissions caused by precipitating ions originating from reconnection regions located at the antiparallel sites would result in discontinuous emission intensities across local noon, tilted X-line reconnection would result in a single uninterrupted emission line that smoothly crosses local noon (Fuselier *et al.*, 2002). Figure 4.9 shows the y, z projections of magnetic field lines from the T96 magnetic field model that originate at the equatorward edge of a continuous ionospheric emission line observed by IMAGE/FUV on June 8, 2000 at 9:44 UT during southward IMF conditions. Also indicated with thick gray lines are the antiparallel reconnection sites at the magnetopause for the solar wind conditions observed at that time. The magnetic field lines originating from the ionospheric emissions do not coincide with the regions where antiparallel reconnection is expected to occur. However, the field lines are consistent with a tilted neutral line that passes through the subsolar region as predicted by the component reconnection model.

An example of antiparallel reconnection sites is shown in Fig. 4.10. Plotted is the magnetic field shear angle at the magnetopause for the July 25, 2001 Cluster cusp crossing, as seen from the Sun. The magnetopause shear angle is calculated from the magnetospheric field directions using the T96 field model at the Sibeck *et al.* (1991)

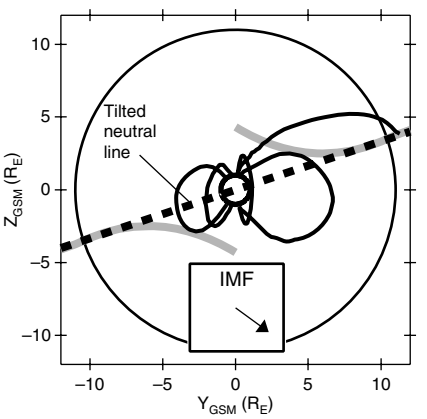

Fig. 4.9. Projections of magnetic field lines originating at the equatorward edge of ionospheric emissions caused by precipitating cusp ions; based on the Tsyganenko T96 magnetic field model. Also shown are the antiparallel reconnection regions (gray lines). The magnetic field lines do not connect to antiparallel reconnection regions but are consistent with a tilted reconnection line model (dashed line); after Fuselier *et al.* (2002).

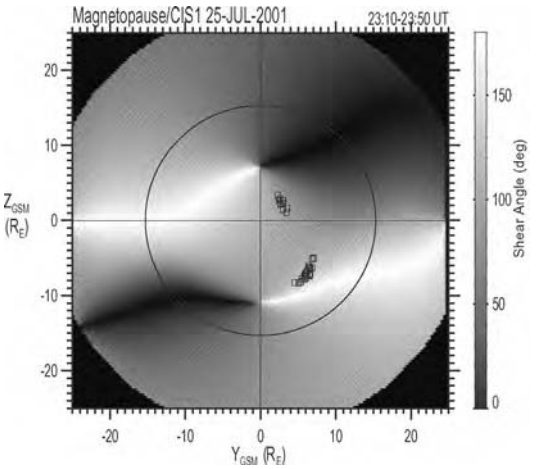

Fig. 4.10. The magnetic field shear angle at the magnetopause as seen from the Sun, calculated from the magnetic field direction of the T96 (Tsyganenko, 1995) model and the draped IMF conditions (Cooling *et al.*, 2001) at the magnetopause for the July 25, 2001, Cluster cusp crossing. White areas show the antiparallel reconnection regions. Square symbols represent the locations of the reconnection line at the magnetopause for the SC4 cusp crossing. The locations were determined by tracing the calculated distances to the reconnection line back along the geomagnetic field line in the T96 model, starting at the position of the Cluster SC4 satellite in the magnetosphere.

magnetopause location and the IMF conditions during the Cluster cusp crossing, by considering draping of the IMF around the magnetopause (Kobel and Flückiger, 1994; Cooling *et al.*, 2001). White regions represent antiparallel magnetic field regions at the magnetopause while black regions represent parallel magnetic field conditions. The circle in Fig. 4.10 represents the location of the terminator plane.

The nature of the July 25 Cluster cusp event is discussed in more detail below and was characterized as a so called *double cusp* event, featuring two ion-energy dispersion events which were subsequently identified as spatial cusp features (Trattner *et al.*, 2003). The square symbols overlaid in the shear angle plot show the location of the reconnection lines at the magnetopause. Both locations are on the dayside magnetopause. These locations were derived based on distances calculated by using the low-velocity cutoffs of the precipitating and mirrored magnetosheath populations observed by the time-of-flight Composition and Distribution Function Analyzer (CODIF) onboard the Cluster SC4 satellite located in the cusp (Trattner *et al.*, 2005). These distances were traced back from the satellite position to the magnetopause along magnetospheric field lines using the T96 field model.

The reconnection line for the first dispersion event of the Cluster cusp crossing on July 25, 2001 is located close to the antiparallel reconnection region in the dusk sector of the southern hemisphere, which is within the error derived for these distance calculations. The antiparallel reconnection region for the second dispersion event is located in the dawn sector of the northern hemisphere with a significant section of the region close to the equator. However, while the location of the reconnection

line for the second cusp dispersion event traced from Cluster observations is in the northern hemisphere, it is also in the dusk sector. This section of the reconnection line is close to local noon and the shear angle at that location is only about 120°, classifying this as a component reconnection event.

More insight into the nature and differences of the two reconnection lines for this Cluster cusp event were provided by observations from IMAGE/FUV. Figure 4.11 shows the SI12 image observed on July 25, 2001, at 23:17:40 UT and mapped into invariant latitude/magnetic local time. There is a distinct band of dayside emissions along the auroral oval in the dawn sector at about 77° invariant latitude (S) but much weaker emissions on the duskside. Figure 4.10 showed that the dusk reconnection line is located in the southern hemisphere. To observe the ionospheric signature from this southern hemisphere reconnection line in the northern cusp, magnetospheric field lines opened in the southern hemisphere must convect northward and tailward. However, they first need to make their way north to the equator against the magnetosheath bulk flow. This will result in small convection velocities such that ions injected onto these field lines will have a slower velocity compared to ions injected on the dawnside northern hemisphere reconnection line where newly opened magnetic field lines convect with the magnetosheath bulk flow. SI12 images are sensitive to a specific velocity range of precipitating ions. While the Cluster observations showed that there were downward precipitating ions in the dusk sector (the first ion-energy

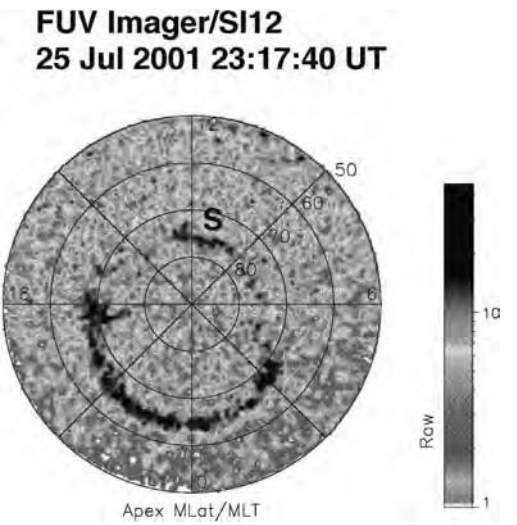

Fig. 4.11. Image/FUV observations of the northern polar region during the Cluster cusp crossing on July 25, 2001. Only the second ion-energy dispersion event (S) observed by SC1 and SC4 produces detectable emissions in the SI12 sensor. The second dispersion event was traced to a magnetopause location in the northern hemisphere while the first dispersion was traced to the southern hemisphere. While precipitating ions from the first dispersion were observed by the CIS instruments on Cluster, these precipitations were not strong enough to produce FUV emissions to be detected by Image.

dispersion event, see below), those ions did not have the necessary velocity to produce large enough photon flux to be observed by the SI12 sensor.

This was not the case for the second dispersion event observed by the Cluster satellites. The dawn emission band observed by IMAGE is caused by the high energy ions at the open–closed field line boundary of the dawn convection cell. The emission band in the dawn sector shows the extent of the reconnection line in the ionosphere for these second Cluster dispersion events and the SI12 image reveals that the continuous emission band on the dawnside of the magnetosphere crosses local noon into the dusk sector. The observation by the IMAGE/FUV instrument is in agreement with the result of the location of the reconnection line calculated from Cluster 3D measurements shown in Fig 4.10.

This Cluster cusp crossing on July 25, 2001 was interpreted as an antiparallel reconnection event. The IMAGE/FUV observations support the antiparallel reconnection scenario. The emissions show that the second dawnside reconnection line (S) in the northern hemisphere originated most probably in the antiparallel reconnection region but subsequently crossed local noon and extended into a region where the model magnetic fields are no longer strictly antiparallel. An alternative would be that the model magnetic fields do not represent the true field orientation near noon.

4.2.3 The stability of high-latitude reconnection

When the IMF is northward, magnetic reconnection is believed to occur at the magnetopause poleward (tailward) of the cusps (Fig 1.8). This was deduced initially from topological considerations (Dungey, 1963), and later from observational evidence (Omel'chenko *et al.*, 1983; Gosling *et al.*, 1991, 1996; Kessel *et al.*, 1996; Matsuoka *et al.*, 1996; Fuselier *et al.*, 2000b,a; Avanov *et al.*, 2001; Onsager *et al.*, 2001). Understanding of the presence of stable high-latitude reconnection, however, has been complicated by the fact that the magnetosheath on the flanks of the magnetosphere is close to the unshocked solar wind speed; i.e., super-Alfvénic. The complication stems from the fact that if the reconnected magnetic field lines are dragged tailward instead of earthward, and if the reconnected plasma population cannot overcome the tailward flow, then plasma cannot reach the dayside magnetosphere, and the reconnection site itself will not remain stationary. However, it is often observed that high-latitude reconnection can be quite stable, in spite of the fact that the neighboring magnetosheath flow is often super-Alfvénic. It has been suggested (Fuselier *et al.*, 2000a) that this is accomplished by the presence of a depletion layer at the magnetopause boundary, which reduces the magnetosheath plasma density while increasing the magnetic field. This increases the effective magnetosheath Alfvén velocity, thus allowing steady reconnection to occur at high latitudes. One recent statistical study (Petrukovich *et al.*, 2003) has examined, using spacecraft observations and models, the location of high-latitude reconnection and, indirectly, the strength of the plasma depletion layer. Particle distributions from the Toroidal Imaging Mass-Angle Spectrometer (TIMAS) instrument onboard the Polar spacecraft sampled near the magnetospheric cusp were analyzed using time-of-flight calculations (Onsager *et al.*, 1990), and the T96 magnetic field model (Tsyganenko, 1995) was used to estimate for each interval the location of the high-latitude magnetopause reconnection site. Analytic models of the magnetosheath conditions (Spreiter

et al., 1966; Kobel and Flückiger, 1994; Petrinec and Russell, 1997; Petrinec *et al.*, 1997) were used to determine the Alfvén speed and Mach number at the location site. All mapped sites were found to lie in super-Alfvénic regions, which suggests that steady reconnection could not occur. However, since the velocity-dispersed ion signatures associated with reconnection were observed near the cusp, it was realized that reconnection was indeed occurring for extended periods. This paradox could only be resolved with the inclusion of a plasma depletion layer, which acts to stabilize the reconnection site. Estimates of the strength of the plasma depletion layer (Petrukovich *et al.*, 2003) were found to be consistent with that determined from theoretical considerations by Zwan and Wolf (1976).

4.2.4 The variability of reconnection

Over the last two decades there has been a debate as to whether dayside reconnection is quasi-steady or transient (e.g., Newell and Sibeck, 1993; Lockwood *et al.*, 1994, and references therein). A smooth and continuous latitude dispersion in the cusp should be expected for a steady rate of reconnection at the magnetopause. However, satellite observations from this region show that the energy of precipitating ions is rarely smooth and continuous with increasing latitude. Rather, these observations show complicated structures with variations in flux levels and sudden changes in the energy of the precipitating ions (e.g., Newell *et al.*, 1991; Escoubet et al., 1992).

The existence of these steps in the ion-energy dispersion, also known as *stepped* or *staircase* cusp ion signatures, has been predicted by Cowley *et al.* (1991) and Smith *et al.* (1992), based on a model by Cowley and Lockwood (1992) of how ionospheric convection is excited. In this pulsating cusp model (see also Lockwood and Smith, 1989a,b), the cusp steps are the result of pulses of enhanced magnetopause reconnection (changes in the reconnection rate at the magnetopause) that creates neighboring flux tubes in the cusp with different time histories since reconnection. A significant characteristic of temporal steps is their convection with the open magnetic field lines under the joint action of magnetic tension and shocked solar wind flow. This creates an ever-changing structural profile of precipitating cusp ions.

The pulsating cusp model was further supported by combining satellite observations with ground-based observations from the EISCAT radar (Lockwood *et al.*, 1995; Neudegg *et al.*, 1999; Milan *et al.*, 2000; McWilliams *et al.*, 2001). Convecting flux tubes caused by reconnection pulses would move along the convection flow. Therefore, the observation of flow across a step in the cusp ion-energy dispersion revealed the temporal nature of cusp structures.

Flux tubes on open field lines with precipitating magnetosheath ions could also be spatially separated, emanating from multiple X-lines. Crossing the boundary into such a spatially separated different flux tube would also appear as a step in the ion-energy dispersion due to the different time history since reconnection for field lines within the two flux tubes (Lockwood *et al.*, 1995). However, this step would not be convected with the solar wind but would appear as a standing feature in the cusp (e.g., Newell *et al.*, 1991; Lockwood and Davis, 1996). Independent of the time delay between the cusp crossings or the satellite velocities, the satellites should encounter unchanged cusp structures at about the same latitude, observing a spatial feature.

Such an observation would indicate that the reconnection rate at the magnetopause is rather stable and not highly variable or even stops entirely for a limited period of time.

To avoid the ambiguity of single satellite observations in distinguishing between spatial and temporal effects, several event studies using multi-spacecraft observations documented the existence of such spatial cusp structures, sometimes also referred to as double cusps. Particularly important were investigations where satellite missions or combinations of satellites cross the cusp almost simultaneously at different altitudes, e.g., Dynamics Explorer DE-1 and -2 (Onsager *et al.*, 1995), Interball and Polar (Trattner *et al.*, 1999), Defense Meteorological Satellite Program (DMSP) (Wing *et al.*, 2001), and Fast Auroral Snapshot (FAST) and Polar (Trattner *et al.*, 2002a,b). They found that stepped ion distributions during stable solar wind and IMF conditions are not consistent with the pulsed reconnection model. While individual cusp crossings for different solar wind conditions are very different, cusp crossings by two satellites during stable solar wind conditions are remarkably similar for several hours.

While the Cluster satellites do not cross the cusp at different altitudes, the four satellites with identical instrumentation together with simultaneous ground observations by the SuperDARN radar array have demonstrated the importance of multi-spacecraft/multi-instrument studies to understand and separate the temporal from the spatial scale. Figure 4.12 shows two composite plots that combine the temporal and spatial separations of the Cluster spacecraft in the cusp into one panel. The top panel shows an example for a spatial cusp structure that is the result of multiple reconnection lines at the magnetopause (see Figs. 4.10 and 4.11). The bottom panel shows an example for a temporal cusp structure that is most likely the result of variations of the reconnection rate at the magnetopause.

For both panels, the blue and red lines show the magnetic footpoints of Cluster satellites SC1 and SC4 in the ionosphere, respectively. The footpoints are plotted on top of geographical maps of the northern polar regions. Overlaid along the magnetic footpoints are omnidirectional H+ differential flux measurements ($1/(\mathrm{cm}^2\ \mathrm{s\ sr\ keV/e)}$) observed by the CODIF instrument that is part of the Cluster Ion Spectrometers (CIS) (Rème *et al.*, 2001) onboard the Cluster satellites. Measurements from the low-energy cutoff of the Cluster/CIS instruments are plotted at the magnetic footpoints with higher energies extending away from the footpoints. Red and white regions in the color spectrograms represent high flux levels while blue and black colors represent low flux values. White solid lines in Fig. 4.12 represent the average location of the auroral oval while the dashed white line represents the terminator. Also shown is the ionospheric convection path (gray lines) derived from SuperDARN radar observations, where solid and dashed gray lines represent the dusk and dawn convection cells, respectively.

The top panel of Fig. 4.12 shows the Cluster cusp crossing on July 25, 2001, which was also discussed above. Only two spacecraft, SC1 and SC4, are shown because the CODIF instrument on SC2 was not operational while SC3 was still on closed field lines for the time of interest. Both satellites were moving poleward over northern Canada close to the Alaska territory. Two black lines in the color spectrogram mark the location where the satellites crossed the open–closed field line boundary and entered the cusp region. Both spacecraft subsequently observed the typical cusp

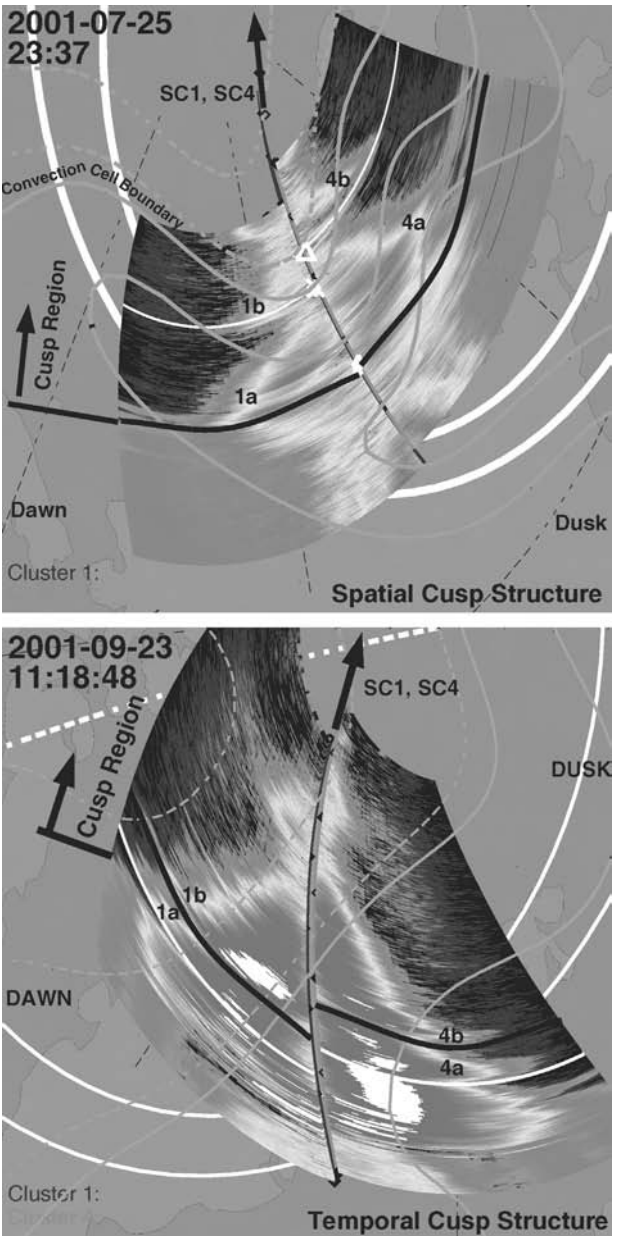

Fig. 4.12. Composite plot of Cluster magnetic footpoints and ionospheric convection streamlines for a spatial and temporal cusp event. Overlaid on the magnetic footpoints are Cluster/CIS flux measurements. White lines represent the average location of the auroral oval while the dashed line represents the terminator. White lines in the color spectrogram show the position of the satellites for the time indicated on the panels. See also color plate.

ion-energy dispersion events for southward IMF conditions (1a and 4a in the top panel of Fig. 4.12), with lower energy ions arriving at higher latitudes (e.g., Reiff *et al.*, 1977; Smith and Lockwood, 1996). The ion-energy distribution decreased smoothly, indicating a constant magnetospheric reconnection rate at the magnetopause. At 23:37 UT the Cluster satellites were deep inside the cusp. Their positions are marked with star (SC1) and triangle (SC4) symbols along the path of the magnetic footpoints. Originating at these symbols are white lines, marking the time index in the color spectrograms.

At 23:37 UT, SC4 was slightly ahead of SC1 at higher latitudes. Also shown for that time index are the ionospheric convection cells (solid and dashed gray lines) derived from the SuperDARN radar data. At that time, both spacecraft encountered a sudden increase in the ion energy of precipitating cusp ions (1b and 4b), consistent with a typical step-up ion signature that can occur if the satellite crossed onto magnetic field lines that were reconnected more recently. Following the sudden step-up signature, the ion energy of the precipitating cusp ions decreased again with increasing latitude showing the typical ion-energy dispersion events observed earlier.

A detailed analysis of this event (Trattner *et al.*, 2003) revealed that the convection cells changed positions at 23:37 UT. Both satellites moved poleward into the direction of an equatorward directed bulge in the ionospheric convection path which effectively brings the boundary between the dawn and dusk convection cells to lower latitudes, into the path of the cluster satellites. At 23:37 UT the convection cell boundary moved rapidly equatorward while the Cluster satellites SC1 and SC4 have progressed far enough poleward to be overtaken by the equatorward moving dawn convection cell. The transition from one convection cell to another resulted in an almost simultaneous sudden increase of the ion-energy dispersion (structures 1b and 4b) on both satellites, indicating that the ion open–closed field line boundary in the dawn convection cell is much closer to the SC1 and SC4 magnetic footpoints than in the dusk convection cell (see also Fig. 4.10). The fact that the sudden increase in the energy of the precipitating cusp ions coincided with the satellites moving into a neighboring and spatially separated flux tube (or convection cell) demonstrates the existence of spatially separated flux tubes as discussed by, e.g., Trattner *et al.* (2002a). Subsequently, the two ion-energy dispersion events for the July 25, 2001, Cluster cusp crossing have been traced to spatially separated reconnection lines located in different hemispheres (see Fig. 4.10).

The bottom panel of Fig. 4.12 shows the Cluster cusp crossing on September 23, 2001. The magnetic footpoints of Cluster SC1 and SC4 are located over Greenland with the satellites moving poleward. After crossing the open–closed field line boundary and entering the cusp, both satellites observed the typical ion-energy dispersion events for southward IMF conditions with lower energy ions arriving at higher latitudes. The bottom panel of Fig. 4.12 also shows the ionospheric convection cells at about 11:18 UT with the Cluster satellites moving oblique to the ionospheric convection direction. For that time index, the Cluster satellites SC1 and SC4 were inside the cusp and their position is marked with white lines in the color spectrograms.

At about 11:18 UT, SC1 encountered the first step-up cusp structure (1a) for this Cluster cusp crossing. SC4, positioned just downstream and poleward of SC1 along

the convection path, encountered a similar step marked (4a) about one minute later. Observing a similar step feature about 1° higher in latitude and about 1 minute later than the low latitude satellite is consistent with a convecting temporal cusp structure as predicted by the pulsed reconnection model (see also Lockwood and Smith, 1989a,b).

The same scenario repeats itself for the second cusp step-up structure. The black lines in the bottom panel of Fig. 4.12 mark the position of the Cluster satellites at 11:25 UT when SC1 encountered a second cusp step-up feature (1b). SC4, positioned again just downstream and poleward of SC1, encountered a similar step marked (4b) about one minute and 1° higher in latitude. Both step structures observed by one spacecraft seem to have convected 1° poleward in the direction of the convection path within about 1 minute, which represents a convection velocity of about 1.5 km/s, in agreement with observed convection speed in the ionosphere of about 1.2 km/s, as measured by the SuperDARN radars (see also Lockwood *et al.*, 1990; Pinnock *et al.*, 1993).

In summary, cusp structures are the result of temporal and spatial effects. The mechanisms to create temporal and spatial structures are:

(1) Cusp structures are the result of temporal changes in the location of convection patterns that either drastically shorten or lengthen the convection length of magnetic field lines from the ion open–closed field line boundary to the position where they are intercepted by the satellites. The change can be a smooth reversal of a previous ion-energy dispersion or a sudden step (e.g., Trattner *et al.*, 2003).

(2) Cusp structures are caused by the entry into a different convection cell or flux tube where the location of the ion open–closed field line boundary was significantly different from the old cell. This can result in a step-up or step-down ion-energy dispersion event. The observed cusp structure is a spatial structure and will appear unchanged for satellites at every altitude (Trattner *et al.*, 2002a,b).

(3) Cusp structures are caused by variation of the reconnection rate at the reconnection location. This temporal cusp structure will be convected with the open geomagnetic field lines and travel along the ionospheric convection direction. In agreement with the pulsating cusp model (e.g., Lockwood and Smith, 1989a) fast low-altitude satellites overtaking the convecting structure encounter a step-down ion-energy dispersion event while slow high-altitude satellites are overtaken by the convecting cusp structure and encounter a step-up dispersion profile.

4.2.5 Conclusions and discussion

Magnetic reconnection between the IMF and the geomagnetic field is believed to be the dominant process whereby mass and energy are transferred from the solar wind into the magnetosphere. While there have been many observations of the consequences of magnetic reconnections at the magnetopause (e.g., jets of plasma), to date, there are only a small number of *in situ* measurements at the center of the diffusion region directly at the magnetopause (e.g., Mozer *et al.*, 2002; Phan *et al.*, 2004; Vaivads *et al.*, 2004b). These studies confirm the important role of Hall electric fields in the vicinity of the reconnection site, consistent with computer simulations of collisionless reconnection (Chapter 3). Coverage of these magnetopause observations, however, has been too limited to support meaningful

statistical studies of the global distribution and the morphology of merging sites on the magnetopause or to assess the validity of various proposed models for the initiation of magnetopause reconnection.

In contrast, a region extensively covered by satellite observations is the magnetospheric cusp, which can be used to estimate the variability of the reconnection process and remotely trace the location of the reconnection sites (e.g., Lockwood *et al.*, 1995; Onsager *et al.*, 1995; Trattner *et al.*, 2002a, 2005). Of particular importance for the location of the reconnection site is the orientation of the IMF. With changing IMF orientation the location of the reconnection site shifts, moving from lower latitudes for a more southward field to higher latitude for more northward fields. In case of directly northward IMF conditions, reconnection is expected to occur poleward of the cusps (e.g., Fuselier *et al.*, 2002).

Cusp observations indicate the existence of long reconnection lines in the northern and southern hemispheres where shear angles between the magnetospheric field and the IMF are near 180° (antiparallel reconnection) as well as tilted reconnection lines across the subsolar point where magnetic shear angles have been found to be significantly different from 180° (component reconnection) (e.g., Fuselier *et al.*, 2002). Long reconnection lines poleward of the cusps that combine antiparallel and component reconnection sites have also been reported (e.g., Trattner *et al.*, 2004).

One of the fundamental properties of reconnection is its variability. Reconnection is a time-varying process causing convecting step-like discontinuities in the ion dispersion signatures of precipitating solar wind ions in the cusp. These convecting structures have been interpreted as evidence for reconnection pulses (e.g., Lockwood and Smith, 1989a), resulting from short-term enhancements of the reconnection rate at the magnetopause, followed by intervals of slower or no reconnection.

Cusp observations also revealed that structures in the ion dispersion signatures in the cusp can be the result of spatially separated flux tubes caused by multiple reconnection lines at the magnetopause (e.g., Trattner *et al.*, 2005). The occurrence of such structures, especially during stable solar wind conditions indicates that the reconnection process can be very stable and persistent. Cusp structures can also be the result of a change in the convection path of newly opened field lines and therefore the location of the satellite within the flux tube.

4.3 Stability of the magnetotail

K. Schindler

As pointed out in Chapter 1, an understanding of the role of magnetic reconnection in magnetospheric and other activity also involves investigating the conditions that prevail before reconnection starts. With sufficient knowledge about these conditions one would be able to predict when and where reconnection occurs. The present state of the art is far from that ideal situation. In the cases that are discussed here, the preonset phase is considered to consist of a slow evolution generated by external forces. In the context of magnetospheric substorms, this phase might be identified as the substorm growth phase (McPherron, 1970; Baker *et al.*, 1981; Section 1.2). During that phase energy is supplied to the system, largely in the form of magnetic energy, leading to stretching of the tail and a thinning of the tail current sheet. After the onset of reconnection the system shows a fast evolution, associated with

a change of magnetic topology and a release of magnetic energy (Baker *et al.*, 1985). A theoretical approach to the slow evolution and current sheet formation, as well as simulations of the dynamic evolution will be discussed in the following section.

In this section we address two particular problems that pertain to the substorm growth phase or, more generally, to the context of current sheet formation or intensification prior to the onset of reconnection. The first question is whether ideal MHD instabilities, such as the ballooning mode, can arise prior to, or during, current sheet formation and perhaps act as a trigger for reconnection. This question is considered for two-dimensional equilibria subject to three-dimensional perturbations. The use of ideal MHD limits the results to rather broad sheets such as observed in the early stages of the growth phase of magnetospheric substorms. The second problem relates to the onset of collisionless tearing and supplements the discussion in Section 3.3.

4.3.1 MHD stability of magnetotail-like configurations

The MHD ballooning mode has been suggested to occur as a consequence of the strong field line curvature in the center of the plasma sheet (Roux *et al.*, 1991; Bhattacharjee *et al.*, 1998; Miura, 2001; Cheng and Zaharia, 2004), although other authors obtained evidence for ballooning stability (e.g., Lee and Wolf, 1992). The contrasting results on ballooning stability motivated a recent study (Schindler and Birn, 2004) of stretched magnetotail equilibria with the aim to clarify the parameter regimes of MHD stability and instability. Here is a summary of that work. This investigation does not address the nonlinear development of ballooning and whether it could lead to a (further) concentration of the cross-tail current and thereby initiate reconnection.

Equilibrium

The equilibrium configurations are two-dimensional with $\partial/\partial y = 0$ and the magnetic field $\mathbf{B}$ lying in the x, z plane. The x axis points tailward. $\mathbf{B}$ is derived from a flux function $A(x, z)$, such that $\mathbf{B} = \nabla A \times \nabla y$. The equilibrium is stretched in the sense that the aspect ratio $\epsilon = L_z/L_x \ll 1$, where L_x and L_z are characteristic lengths associated with the x- and z-dependence of $\mathbf{B}$ and the plasma pressure p. The pressure and the current density j_y are functions of A alone and are related by $j_y = \mathrm{d}p/\mathrm{d}A$. The flux function $A(x, z)$ satisfies the Grad–Shafranov equation

$$-\frac{1}{\mu_0}\Delta A = \frac{\mathrm{d}p(A)}{\mathrm{d}A}. \tag{4.6}$$

One of the main points of interest is the effect of the large field line curvature occurring at the vertex of closed field lines with $\kappa \cdot \nabla p > 0$, which in principle favors the ballooning instability.

Another important point is to clarify the role of a background pressure. Often, an increase of $\beta = 2\mu_0 p/B^2$ destabilizes, which here raises the question of how stability is affected by the superposition of a constant background pressure.

Stability criterion

The basic stability criterion can be understood in the following way. By specializing the MHD variational principle (Bernstein *et al.*, 1958) for the present equilibrium conditions one obtains the functional

$$\delta W = \frac{1}{2\mu_0}\int\left\{\left|\frac{\mathbf{B}\cdot\nabla A_1}{B}\right|^2 + V_c|A_1|^2 + |\mathbf{B}\cdot\nabla\xi_y|^2 + \left|\frac{\nabla A\cdot\nabla A_1 + JA_1}{B} - B\frac{\partial\xi_y}{\partial y}\right|^2 + \mu_0\gamma p|\nabla\cdot\xi|^2\right\}\mathrm{d}^3r, \tag{4.7}$$

where γ is the adiabatic index, $J=\mu_0 j_y$, and ξ is the displacement vector. Further,

$$A_1 = -\xi\cdot\nabla\mathbf{A} \tag{4.8}$$

is the perturbation of the flux function and

$$V_c = \nabla\cdot\frac{J\nabla A}{B^2} - \frac{J^2}{B^2} - \frac{\mathrm{d}J}{\mathrm{d}A}. \tag{4.9}$$

The quantity V_c is directly related to the field line curvature vector $\kappa=\mathbf{b}\cdot\nabla\mathbf{b}$, where $\mathbf{b}=\mathbf{B}/B$, as V_c can be written as

$$V_c = -\frac{2\mu_0}{B^2}\kappa\cdot\nabla\mathbf{p}. \tag{4.10}$$

V_c assumes large negative values at the field line vertex where B becomes small.

Positive-definiteness of δW is necessary and sufficient for stability with respect to ideal MHD. The displacement vector is chosen to vanish on the boundary. For a derivation of (4.7) see Schindler *et al.* (1983).

Let us concentrate on the third term of the integrand of (4.7). If we simply drop it, we obtain a functional, positive-definiteness which is still sufficient for stability. Interestingly, the third term also vanishes in the ballooning limit, which provides necessity (de Bruyne and Hood, 1989). Thus, positive-definiteness of the functional

$$\delta W' = \frac{1}{2\mu_0}\int\left\{\left|\frac{\mathbf{B}\cdot\nabla\mathbf{A_1}}{\mathbf{B}}\right|^2 + V_c|A_1|^2 + \left|\frac{\nabla A\cdot\nabla A_1 + JA_1}{B} - B\frac{\partial\xi_y}{\partial y}\right|^2 + \mu_0\gamma p|\nabla\cdot\xi|^2\right\}\mathrm{d}^3r \tag{4.11}$$

is necessary and sufficient for ideal-MHD stability.

Minimization with respect to $\partial\xi_y/\partial y$ and $\mathbf{b}\cdot\xi$ reduces (4.11) to the functional

$$\delta w = \frac{1}{2\mu_0}\int\left(\left|\frac{\partial A_1}{\partial s}\right|^2 + V_c|A_1|^2 + \frac{1}{J^2\,\overline{q}}\left|\overline{V_c A_1}\right|^2\right)\frac{\mathrm{d}s}{B}, \tag{4.12}$$

where

$$q = \frac{1}{\mu_0\gamma p} + \frac{1}{B^2} \tag{4.13}$$

and the bar denotes the average

$$\overline{(\cdots)} = \frac{\int(\cdots)\mathrm{d}s/B}{\int \mathrm{d}s/B}. \tag{4.14}$$

In (4.12) and (4.14) the s-integration is understood as arc-length integration along a selected field line. By (4.8) $A_1(s)$ is subject to the line-tying boundary condition ($A_1 = 0$).

It is well known that the functional (4.12) provides a useful criterion for the ballooning instability (e.g., Lee and Wolf, 1992). The sufficiency property for arbitrary modes has been introduced into magnetospheric stability in the recent work that is summarized here.

Results and interpretation

Stability investigations were carried out by numerical minimization of (4.12). Here the main results obtained with three different equilibrium models are summarized, concentrating on closed field lines and symmetric modes, the preferred situation for ballooning. For more general results and details see Schindler and Birn (2004). The study was limited to the regime of small values of the aspect ratio ϵ. For most purposes it was found convenient to replace the x coordinate by $x_1 = \epsilon x$ in equilibrium quantities. The main results can be summarized as follows.

(1) Unstable field regions were found only for cases with strong tailward pressure decay, specifically for $p \propto \exp(-x_1)$ and $p \propto 1/x_1^n,\ n > 10$. Configurations with more moderate pressure variation were found stable.

(2) In all cases of instability the superposition of a moderate background pressure was sufficient for complete stabilization.

(3) The results were found to be in good agreement with the formal entropy criterion, stating that $\mathrm{d}S/\mathrm{d}p < 0$ is necessary and sufficient for stability, where $S = \ln(pW^\gamma)$ with W being the differential flux tube volume $W = \int \mathrm{d}s/B$. (The entropy criterion is known from the study of the interchange mode.)

Figure 4.13 illustrates the accuracy to which the entropy criterion describes the minimization results. In this case the equilibrium was presented by the Voigt model (Voigt, 1986), where the magnetic flux function and the pressure are given by

$$A = -\frac{2}{\pi}\cos\left(\frac{\pi}{2}z\right)\mathrm{e}^{-x_1}, \tag{4.15}$$

$$p = \frac{A^2}{2}\left(\frac{\pi^2}{4} - \epsilon^2\right) + p_0. \tag{4.16}$$

The z coordinate is subject to the condition $0 \le |z| \le 1$, which confines the model to closed field lines; the constant background pressure p_0 was added in view of present purposes.

For two further models it was found that equilibria with moderate tailward pressure variation are stable. In one of the two models the asymptotic solution of (4.6) for small ϵ and exponential $p(A)$ was used, which in a suitable dimensionless form is given by

$$A(x_1, z) = \ln\left[\frac{\cosh\left(\sqrt{2\hat{p}(x_1)}\,z\right)}{\sqrt{2\hat{p}(x_1)}}\right], \tag{4.17}$$

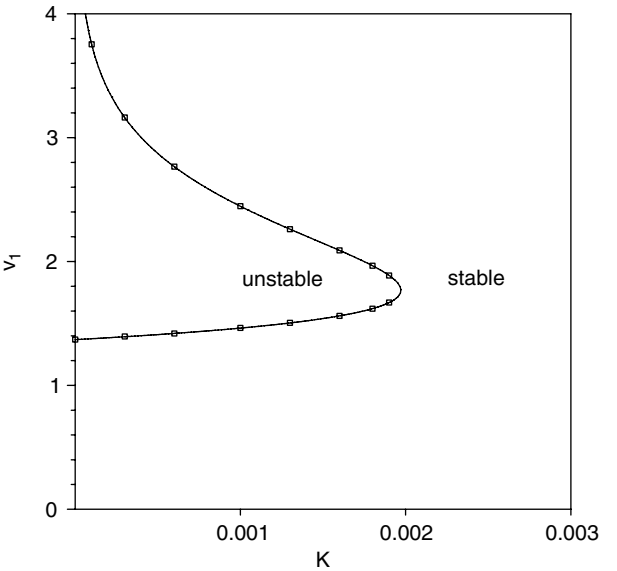

Fig. 4.13. Stability diagram of the Voigt model computed for $\epsilon = 0.01$. The plot shows the K, v_1 plane, where K denotes the background pressure normalized by the maximum pressure (at the earthward boundary), and v_1 is the x_1 coordinate of the field line vertex. The square symbols mark the boundary of the unstable region obtained by numerical minimization, the full curve corresponds to the marginal entropy criterion $\mathrm{d}S/\mathrm{d}p = 0$.

where $\hat{p}(x_1)$ is the pressure on the x axis, understood as a function of x_1. This function can be chosen arbitrarily. The stability of the model (4.17) was investigated for the power law

$$\hat{p} = \frac{1}{x_1^n}, \quad n > 0. \tag{4.18}$$

All cases with $n < 10$ were found stable in the numerical minimizations, while choices with $n > 10$ gave unstable field regions. Again, this result was consistent with the entropy criterion, as Fig. 4.14 illustrates; note that p decreases with v_1, such that $\mathrm{d}S/\mathrm{d}v_1 > 0$ means stability. The stability transition at $n = 10$ is clearly visible. The necessity of the entropy criterion could have been expected from earlier results (Lee and Wolf, 1992), but the sufficiency came as a surprise.

Antisymmetric modes were found stable for moderate pressure variation (the power-law cases were found stable for $n < 6$). Open field lines were stable in all cases studied.

The results listed above raise two main questions:

(1) Addressing the realistic cases of moderate decrease of $\hat{p}$ with x_1: Why does the strong curvature at the vertex (with V_c of order $1/\epsilon^2$) not cause instability?
(2) Why does the background pressure stabilize, although increasing pressure is known to destabilize in other cases?

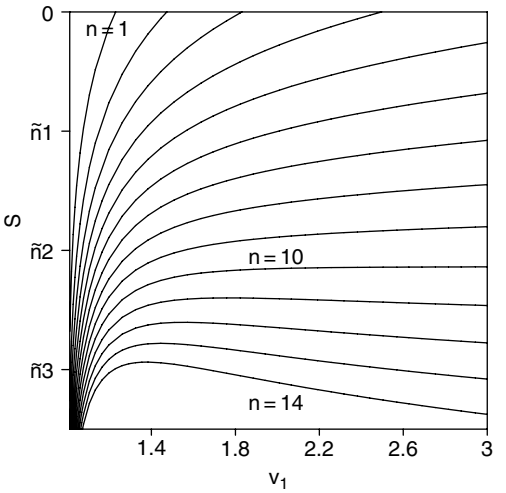

Fig. 4.14. Entropy S as a function of the vertex position v_1 on the x_1 axis.

Regarding the first question, it is true that for small ϵ the curvature term (second term in the integrand of (4.12)) becomes strongly negative, i.e., destabilizing. However, the positive compressibility term (third term) becomes large also and, as was shown analytically, for the minimizing mode the leading terms of an asymptotic expansion for small ϵ exactly cancel. In the remaining expression the sign of the minimum of δw is given by the sign of $-\mathrm{d}S/\mathrm{d}p$. (There is a formal alternative, which, however, did not become effective in any of the cases of the three models treated numerically.)

The following plausibility argument should help to understand the central role of entropy without going into the formal details of the rigorous derivation. Entropy enters the stability problem through a relationship that for small ϵ assumes the form

$$J^2\overline{q}+\overline{V_\mathrm{c}}=\frac{J^2}{\mu_0\gamma}\frac{\mathrm{d}S}{\mathrm{d}p}. \tag{4.19}$$

This result can be obtained by applying Gauss's theorem to (4.9).

The relevance of the relationship (4.19) is readily illustrated by considering the Euler–Lagrange equation associated with variation of (4.12),

$$-B\frac{\partial}{\partial s}\left(\frac{1}{B}\frac{\partial A_1}{\partial s}\right)+V_\mathrm{c}A_1+\frac{V_\mathrm{c}}{J^2\overline{q}}\overline{V_\mathrm{c}A_1}=\lambda A_1, \tag{4.20}$$

where λ is the eigenvalue resulting from the normalizing constraint on A_1, fixing the integral $\int A_1^2/(2B)\,\mathrm{d}s$. The sign of the minimum eigenvalue determines stability. Averaging (4.20), using (4.19) and considering symmetric modes gives

$$\lambda=\frac{1}{\mu_0\gamma\overline{q}}\frac{\mathrm{d}S}{\mathrm{d}p}\frac{\overline{V_\mathrm{c}A_1}}{\overline{A_1}}-\frac{1}{W\overline{A_1}}\left[\frac{1}{B}\frac{\partial A_1}{\partial s}\right]_\mathrm{b}, \tag{4.21}$$

where the subscript b refers to the boundary. Anticipating that typically the minimizing eigenfunction A_1 has its maximum at the vertex and from there smoothly

decays toward the boundary without changing its sign one finds that for small ϵ the second term of the right-hand side of (4.21) is negligible and that $\overline{V_c A_1}/\overline{A_1}$ has the sign of V_c which is negative for the models considered here. So the sign of λ is given by the sign of $-\mathrm{d}S/\mathrm{d}p$, such that $\mathrm{d}S/\mathrm{d}p < 0$ is necessary and sufficient for stability.

The stabilizing effect of the background pressure, addressed by the second question, has the following reason. Generally, pressure enters the functional (4.12) in two ways. The curvature term depends on the pressure gradient (see (4.10)) and the compressibility term on the pressure itself (via q, see (4.13)). Increasing the pressure in an arbitrary way will result in a complicated interplay between stabilization and destabilization, and experience indicates that destabilization can well dominate under suitable circumstances. However, in the present case of imposing a constant background pressure, the pressure gradient remains unchanged so that we are left with the stabilizing effect of the compressibility term.

4.3.2 Collisionless tearing

The treatment of the collisionless tearing instability in the framework of the Vlasov theory has a long and complicated history (see Section 3.3). In view of the complex structure of the problem several authors have applied different assumptions or ad-hoc simplifications and have obtained conflicting results. A clarifying breakthrough was achieved (Lembège and Pellat, 1982; Pellat *et al.*, 1991; Brittnacher *et al.*, 1995; Quest *et al.*, 1996) by showing that for a sufficiently small electron gyroscale a magnetic field component B_n normal to the sheet has a strong stabilizing effect. This effect had been excluded by an ad-hoc assumption in earlier work (Schindler, 1974). As shown by Pellat *et al.* (1991), the B_n-stabilization is valid in the regime where $\zeta = k\rho_n \ll 1$, k being the wavenumber of the perturbation along the sheet (x-direction) and ρ_n the electron gyroradius in the center where the magnetic field magnitude is B_n. For a more detailed discussion see Section 3.3.

In spite of this breakthrough, several details remained unclear. The analysis was based on Schwarz's inequality (Morse and Feshbach, 1953), so that the actual strength of the stabilization was unknown. Also, the distribution functions were limited to drifting Maxwellians, where the electric potential can be ignored. In the following a refined approach is sketched, which removes those shortcomings by avoiding inequalities and by admitting a large class of distribution functions. We consider the formal limit $m_e \to 0$ and then discuss the conditions under which this limit is a valid approximation.

The equilibrium distribution functions have the standard form $F(H, P)$ with

$$F' = \partial F(H, P)/\partial H < 0, \tag{4.22}$$

where H is the Hamiltonian and P the canonical momentum with respect to the invariant direction, here chosen as the y direction.

The approach starts out from an exact form of the variational principle for two-dimensional plasmas based on the Vlasov theory (Schindler *et al.*, 1973; Schindler, 1974). In addition to Liouville's theorem and quasi-neutrality, that approach uses constant P as the only further constraint on the particle orbits. (Any additional constraint, such as the conservation of the magnetic moment would lead to additional

stabilization; see also Pellat *et al.* (1991).) One finds a variational expression of the form

$$\mathcal{V}_2 = \frac{1}{2}\int \Big(\frac{(\nabla A_1)^2}{\mu_0} - \frac{\mathrm{d}j_y}{\mathrm{d}A} A_1^2 + a\varphi_1^2 - a[\![(\langle \Psi_{s1}\rangle_s)^2]\!] \Big)\, \mathrm{d}x\ \mathrm{d}z \tag{4.23}$$

and the quasi-neutrality condition

$$\varphi_1 = [\![\langle \Psi_{s1}\rangle_s]\!]. \tag{4.24}$$

In (4.23) and (4.24) the following notation is used:

$$\langle \ldots \rangle_s = \frac{\int_{\psi_{s0}\le H_{s0}} \ldots \,\mathrm{d}x\ \mathrm{d}z}{\int_{\psi_{s0}\le H_{s0}} \mathrm{d}x\ \mathrm{d}z}, \tag{4.25}$$

$$[\![\ldots]\!] = \frac{\sum_s \int \ldots q_s^2 F_s'\ \mathrm{d}\tau}{\sum_s \int q_s^2 F_s'\ \mathrm{d}\tau}, \tag{4.26}$$

where $\psi_{s0} = (P - q_s A)^2/(2m_s) + q_s\phi$, $\Psi_{s1} = \psi_{s1}/q_s$, $\varphi_1 = \phi_1 - \frac{\mathrm{d}\phi}{\mathrm{d}A} A_1$ and

$$a = \sum_s a_s, \qquad a_s = \int q_s^2 F_s'\ \mathrm{d}\tau \tag{4.27}$$

with the τ-integration extending over velocity space. The subscript s refers to the particle species, q_s and m_s are particle mass and charge, respectively. By quasi-neutrality, the current density j_y and the electric potential ϕ of the equilibrium become functions of the equilibrium flux variable A alone.

The physical regime of small electron gyroscale is appropriately realized by the formal limit of vanishing electron mass m_e with the equilibrium electron temperature T_e kept fixed. Here T_e is not a thermodynamic temperature, it is defined kinetically, i.e., in terms of the energy associated with random motion.

For a single ion species with charge e one finds that for $m_\mathrm{e} \to 0$ (4.23) assumes the form

$$\mathcal{V}_2 = \frac{1}{2}\int \Bigg[\frac{(\nabla A_1)^2}{\mu_0} - \frac{\mathrm{d}j_y}{\mathrm{d}A} A_1^2 + |a_\mathrm{i}| \big[\big[\big(\langle \Psi_{\mathrm{i}1}\rangle_i - [\![\langle \Psi_{s1}\rangle_i]\!]_i \big)^2 \big]\big]_i + n_0 Q^2 \left(\frac{5}{3} k_\mathrm{B} T_\mathrm{e} + \frac{e^2 n_0}{|a_\mathrm{i}|} \right) \Bigg]\, \mathrm{d}x\ \mathrm{d}z, \tag{4.28}$$

where

$$Q(A) = \frac{1}{W(A)} \frac{\mathrm{d}}{\mathrm{d}A} \int_A A_1 \frac{\mathrm{d}s}{B}, \qquad W(A) = \int_A \frac{\mathrm{d}s}{B}, \tag{4.29}$$

and n_0 is the equilibrium electron (or ion) number density.

If for the ion distribution function one chooses a drifting Maxwellian, $e^2 n/|a_\mathrm{i}|$ becomes $k_\mathrm{B} T_\mathrm{i}$. Then (4.29) implies the inequality

$$\mathcal{V}_2 > \mathcal{V}_2^* \tag{4.30}$$

with

$$\mathcal{V}_2^* = \frac{1}{2}\int \Big(\frac{(\nabla A_1)^2}{\mu_0} - \frac{\mathrm{d}j_y}{\mathrm{d}A} A_1^2 + Q^2 n_0 k_\mathrm{B} T \Big)\, \mathrm{d}x\ \mathrm{d}z, \tag{4.31}$$

where $T = T_e + T_i$. The expression (4.31) is consistent with the result of Lembège and Pellat (1982), and Pellat *et al.* (1991). As shown there for the WKB-regime, the term involving Q scales as kLB_0/B_n, causing strong stabilization for small B_n (see also Section 3.3). The same conclusion applies to (4.28). So the present more refined approach confirms strong electron stabilization in the appropriate limit.

To investigate the range of validity of this approach, the leading correction terms for small but nonvanishing m_e were included. One finds that they can be neglected if ρ_n is much smaller than the shortest length scale of the electromagnetic field with respect to the x-variation. For $kL_x > 1$ this reduces to the condition $k\rho_n \ll 1$ of Pellat *et al.* (1991).

4.3.3 Discussion

Under the model conditions that were specified in Section 4.3.1, in all cases that were studied strongly stretched magnetotail configurations with moderate decrease of $\hat{p}(x_1)$ were found to be stable with respect to arbitrary ideal MHD modes. This means that under those circumstances an ideal MHD instability is not available as a pre-TCS process. This supports a scenario in which a thin current sheet is formed in a quasi-steady fashion as a consequence of the external forces.

The stability of the magnetotail under the present conditions is consistent with 2D and 3D MHD simulations (Birn, 1980; Birn *et al.*, 1996) of stretched magnetotail configurations, which did not produce any evidence for an instability in the ideal MHD regime. Within the present framework, the entropy criterion implies that an initially stable configuration cannot become unstable during an adiabatic evolution. Notably, this applies to a class of adiabatic sequences that lead to loss of equilibrium (Birn and Schindler, 2002).

This scenario also covers a situation where the thinning of the current sheet proceeds until the electrons become sufficiently nongyrotropic (ζ about 1 or larger) for a collisionless tearing mode to start. This also would mean the onset of reconnection, if one defines reconnection appropriately, that is, by the new connection of field lines without the necessity of the presence or formation of neutral points (Section 2.3). This onset scheme was confirmed by two-dimensional kinetic simulation studies (Hesse and Schindler, 2001; see Section 3.3). These simulations used the tail-asymptotic model (4.17) with (4.18) for $n = 1.2$, which lies in the range of observed values. Reconnection started when, by external driving, a local decrease of the normal magnetic field component B_n developed, which led to nongyrotropic electrons. The ion/electron mass ratio was 100. At the minimum of B_n the (formal) electron gyroscale exceeded the x-dimension of the system.

In the same work the variational expression (4.31) was investigated with the help of simplified test functions. In particular, the decay of the stabilizing electron term with a progressive thinning of the current sheet was studied by considering the quantity

$$Y = \frac{\int Q^2 n_0 k_B T \, \mathrm{d}x \, \mathrm{d}z}{|\int \mathrm{d}j/\mathrm{d}A A_1^2 \, \mathrm{d}x \, \mathrm{d}z|} \tag{4.32}$$

as a function of ζ. Roughly, Y reduces to 1 at values of ζ near 1. This requires rather thin sheets. However, it is worthwhile noting that the sheet thickness does not necessarily have to be reduced to the electron gyroscale ρ_0 evaluated outside the

sheet. Setting $\zeta = k\rho_n = 1$ gives $L = kL\rho_n = \rho_0 B_0/(cB_n)$, where we have set $kL = 1/c$. To make sure that the first term in (4.31) is not dominating, typically $c \approx 3$ is sufficient. So, at onset, L scales as $\rho_0 B_0/B_n$ rather than as ρ_0. The physical reason is that, for achieving a substantial reduction of Q, the length scale of the mode with respect to x has to become comparable with the width of the particle orbit in the center of the sheet, which scales as $\rho_n = \rho_0 B_0/B_n$. The precise onset conditions are not yet known. Note that the present orbit dynamics can only provide sufficient stability criteria. Choosing exact orbits can lead to additional stabilization, even for $\zeta > 1$ (Brittnacher *et al.*, 1998).

In a three-dimensional picture current-aligned microinstabilities (Section 3.5) may occur before collisionless tearing starts. Examples of relevant instabilities are the lower-hybrid (Drake *et al.*, 1984; Daughton *et al.*, 2004) or the kinetic kink mode (Lapenta and Brackbill, 1997), discussed in Section 3.5. However, the mere presence of a microinstability does not imply the onset of reconnection. A final evaluation of the reconnection scenarios for magnetospheric and solar activity requires considerably more effort in the investigation of the preonset conditions, both from fluid and kinetic points of view.

4.4 Simulations of reconnection in the magnetotail

J. Birn

Only very recently have the magnetospheric reconnection sites themselves been subjected to direct probing (Sections 4.2 and 4.5). The dominant identification of reconnection thus has been made by its consequences. In this section we further discuss causes and consequences of magnetotail reconnection based on MHD approaches, particularly numerical simulations, in which reconnection is enabled by ad-hoc resistivity or even by numerical dissipation in the codes. The underlying assumption is that the large-scale structure and dynamic behavior of the magnetotail are governed by conservation laws that are well included in the MHD approach, so that the detailed knowledge (and modeling) of the processes in the vicinity of the reconnection site, as discussed in Chapter 3, is not necessary. This is analogous to the treatment of jump conditions across shocks, which are independent of the detailed shock physics.

Our discussion focuses on several particular aspects: The conditions that enable the onset of reconnection, particularly, the formation of thin current sheets in the near tail; the formation and structure of plasmoids; the generation of fast plasma bulk flows; the formation of the substorm current wedge; and the role of reconnection and of the dynamic evolution of the tail in the acceleration of charged particles and the resulting increases of energetic particle fluxes in the inner tail.

4.4.1 Thin current sheet formation

As mentioned in Sections 1.2 and 4.3, the formation of a thin current sheet in the near-Earth tail region, late in the growth phase of substorms, appears to be a crucial element in the initiation of a substorm and is well established observationally (e.g., McPherron *et al.*, 1987; Baker and McPherron, 1990; Mitchell *et al.*, 1990; Sergeev *et al.*, 1993; Pulkkinen *et al.*, 1994; Sanny *et al.*, 1994). Here we are interested in the relation between the formation of a thin current sheet and external, that is,

solar wind conditions that cause the structural changes of the substorm growth phase and might act as a trigger of substorm onset. Both MHD and particle simulations have consistently demonstrated that a thin current sheet can form as a consequence of the addition of magnetic flux to the lobes (e.g., Schindler and Birn, 1993; Pritchett, 1994; Hesse *et al.*, 1996; Birn *et al.*, 1998a), which is a consequence of frontside reconnection. Recently, Birn and Schindler (2002) demonstrated that the formation of a thin current sheet may be the final phase leading to a loss of equilibrium, when the magnetotail changes adiabatically (i.e., entropy conserving) in response to magnetic flux transfer and deformations imposed by the solar wind. These results, obtained by two-dimensional quasi-equilibrium theory, were confirmed by two- and three-dimensional numerical MHD simulations (Birn *et al.*, 2003, 2004c).

The characteristic structure of such a thin current sheet near the critical limit is illustrated by Fig. 4.15, showing magnetic field lines and the cross-tail current density (gray scale). Since this current sheet forms within the plasma sheet region, where field lines are connected to Earth at both ends, the thin sheet assumes a cusplike structure where the intensified current region extends from the equatorial plane along two *horns* toward the Earth. This may be a reason for the frequently observed bifurcated structure of thin current sheets (Section 4.5.4). Other causes may lie in the self-consistent collisionless structure itself involving, for instance, deviations from pressure isotropy (Sitnov *et al.*, 2003; Birn *et al.*, 2004b).

In the theoretical investigations and MHD simulations, the formation of such a thin current sheet in the *near* tail is closely related to the fact that the boundary deformation is characterized by a steepening of the flaring angle of field lines in the x, z plane particularly in the near-tail region. Such an increase of flaring is expected from the erosion of dayside magnetic flux (Maezawa, 1974) resulting in a tailward transport and an observed increase in tail radius on the nightside (Maezawa, 1975). These features, as well as the corresponding formation of a thin current sheet embedded in the near-tail plasma sheet, were indeed also confirmed by global MHD simulations of the substorm growth phase (Kuznetsova *et al.*, 2005, private communication).

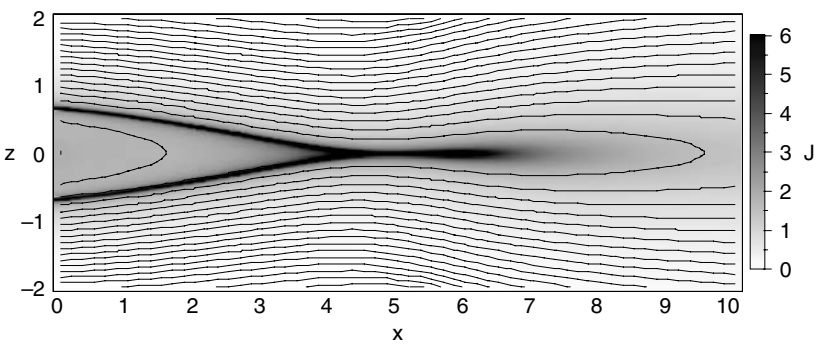

Fig. 4.15. Structure of a thin embedded current sheet, formed as a consequence of boundary deformations (Birn and Schindler, 2002) near the critical limit to a loss of equilibrium. Solid lines are magnetic field lines and the gray scale indicates the current density in arbitrary units.

4.4.2 Plasmoid formation and structure

Whereas the close relation between magnetotail boundary deformations and thin current sheet formation as a means toward tail instability is well established, the actual onset mechanism of tail instability and its possible relation to an external trigger (such as a northward excursion of a pre-existing southward IMF; see Section 3.3) are not yet identified. In contrast, the macroscopic consequences of reconnection are better understood, although some controversy still exists. After the current intensification and thinning has reached a stage where ideal MHD breaks down and reconnection is enabled, the tail evolution in MHD models follows the qualitative picture shown in Fig. 1.6. Stretching and compression in the inner magnetotail leads to the pinching and reconnection of closed field lines into new shorter closed ones and closed loops that comprise part of the plasmoid. In a two-dimensional picture this process involves two magnetic neutral points, one of X-type and one of O-type (in the center of the plasmoid). When this picture is extended into the third dimension, the X-point becomes an X-line and the O-point an O-line. Furthermore, due to the finite extent of magnetic reconnection in the cross-tail dimension, the X-line and O-line cannot extend to infinity but become connected at some distance away from the midnight meridian plane ($y = 0$), forming a closed loop. This fact was first pointed out by Vasyliunas (1976) and confirmed through numerical simulations by Birn and Hones (1981).

However, exact north–south symmetry, where B_x and B_y vanish together in the neutral sheet, represents a highly singular case, and more commonly the tail includes an, albeit small, net cross-tail magnetic field component, which does not vanish where $B_x = 0$. In that case, field lines do not reconnect with themselves but rather with some neighboring field line. The three-dimensional structure of a generalized plasmoid in such a case is illustrated in Fig. 4.16, obtained from an MHD simulation (Birn and Hesse, 1990). The field lines identified as plasmoid field lines are defined by the property that they cross the x, y plane (equatorial plane) more than once. This is equivalent to a definition in terms of closed loops in the symmetric case. In the nonsymmetric case this definition is no longer invariant, because it depends on the choice of the plane at which intersections are investigated. In this particular case, it gives a reasonable representation of the plasmoid/flux rope, because the deviation from the symmetric case is small. It is interesting to note that, despite the smallness of the net cross-tail magnetic field component B_y of only a small percentage of the main component B_x, the plasmoid field lines exhibit only a few windings around the plasmoid axis.

Initially, the reconnected field lines remain connected to the Earth at both ends (top panel of Fig. 4.16). There are no uniquely identifiable separatrices or separators; the conditions of no-null reconnection (Section 2.3) apply. Later, when closed field lines reconnect with lobe field lines, or field lines from opposite lobes with each other, one might distinguish different topologies and separatrices between regions of different topology with possible intersections at separators. However, as indicated by the bottom panel of Fig. 4.16, flux bundles with different connections are interwoven and wrapped around each other, so that the magnetic topology becomes rather complicated in the region identified as plasmoid. This fine structure becomes more pronounced when the net cross-tail magnetic field gets smaller. Certainly, the local

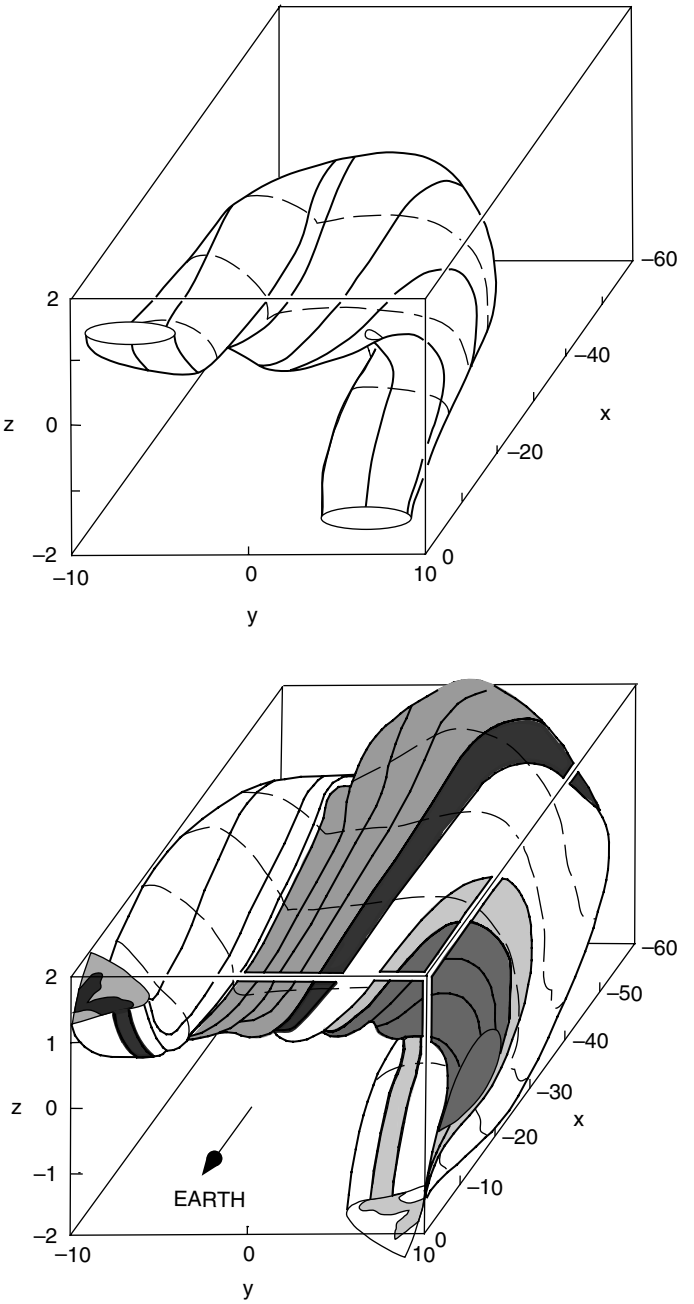

Fig. 4.16. Three-dimensional structure of a departing plasmoid/flux rope in a simulation of magnetotail reconnection including a net cross-tail magnetic field component (after Birn and Hesse, 1990). The top panel shows an early stage when all field lines are still connected to the Earth, the bottom panel shows a more advanced stage when the plasmoid consists of helical field lines that are connected to the Earth at both ends (white), interwoven with partially and fully separated field lines (shades of gray).

distinction of magnetic connectivity becomes meaningless when the fine scale reaches the scale of the particle gyroradius.

It is noteworthy that in the picture illustrated by Fig. 4.16 plasmoid severance is not an instantaneous process but is characterized by a continuous increase of magnetic flux bundles that first become partially and then fully separated from Earth. This process is topologically equivalent to the outward propagation of a CME (Chapter 5; Gosling *et al.*, 1995), although there is no evidence that a CME becomes fully disconnected within the distances explored by satellites.

North–south symmetry, as well as dawn–dusk symmetry, are generally violated in global simulations that use actual solar wind properties and Earth's dipole orientation as input (e.g., Pulkkinen *et al.*, 1998; Wiltberger *et al.*, 2000; Raeder *et al.*, 2001). Although substorm effects in such simulations are still basically consistent with the neutral line, plasmoid picture, they also show not only more complicated magnetic structures (such as the plasmoids pictured in Fig. 4.16), but also plasma flow features more akin to localized flow bursts (Section 4.5.7) than to organized tailward and earthward flows (Wiltberger *et al.*, 2000; Raeder *et al.*, 2001). Global simulations also differ from local simulations by their boundary conditions. Specifically, the tail connects on the earthward side to an ionosphere model that closes the field-aligned currents generated by the tail processes. Raeder *et al.* (2001) found that there is a significant feedback from the ionosphere that in part controls the reconnection onset in the tail. Systematic variations of the ionosphere conductance show that the ionosphere can in principle even inhibit near-Earth reconnection completely by tying field lines in the ionosphere (Raeder *et al.*, 1996). Thus, understanding the boundary conditions of the tail may be just as important as understanding the local processes.

4.4.3 Plasma flow and the substorm current wedge

Before the advent of numerical simulations, it was expected that the anomalous dissipation that enables reconnection would also be the cause of the current disruption and deviation into the substorm current wedge. However, this was not confirmed by MHD simulations, which found that the features of the substorm current wedge are more closely related to the dynamic evolution and the plasma flow initiated by reconnection than to the dissipation at the reconnection site (Birn and Hesse, 1991; Hesse and Birn, 1991; Scholer and Otto, 1991; Birn *et al.*, 1999). This mechanism is illustrated by Fig. 4.17. When the earthward flow from the reconnection site slows down and is diverted azimuthally away from midnight, it causes a twist or shear of the magnetic field and builds up field-aligned currents. It is easy to see that the twist illustrated in Fig. 4.17 corresponds to field-aligned currents into the ionosphere on the dawn side with an opposite twist and current out of the ionosphere on the dusk side (not shown), consistent with the substorm current wedge (Fig. 1.7).

We note that the current wedge mechanism illustrated in Fig. 4.17 is not universally accepted and that an alternative view exists, which is based on a more turbulent current disruption mechanism in the inner tail (Lui, 1996). Also, the braking of the earthward flow is not necessary to generate the twist or shear of the magnetic field. This was demonstrated by Birn *et al.* (2004a) through simulations of the dynamics of

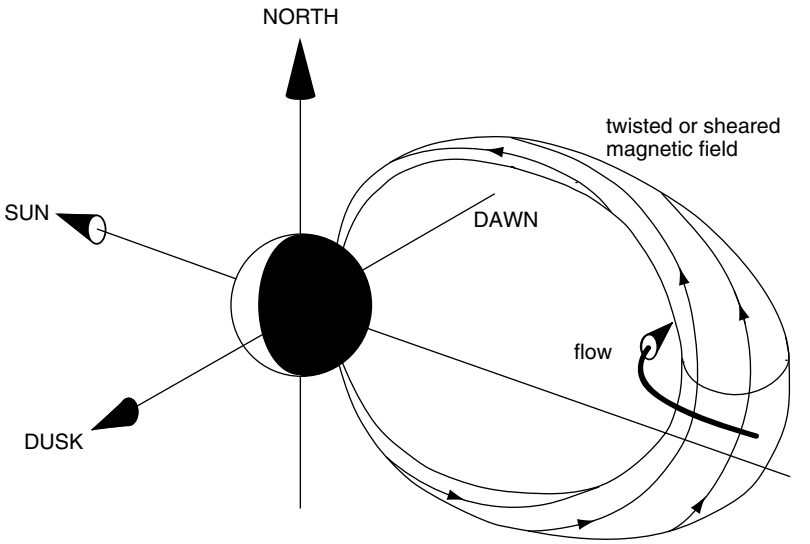

Fig. 4.17. Build-up of field-aligned currents, as found in MHD simulations of tail dynamics. The diversion of earthward flow away from midnight causes a twist of magnetic flux tubes and a shear between the affected field lines and unaffected field lines at larger distance from the neutral sheet. This shear or twist corresponds to field-aligned currents toward the Earth on the dawnside and away from the Earth on the duskside, which are part of the substorm current wedge (Fig. 1.7).

earthward moving entropy-depleted magnetic flux tubes (*bubbles*, Pontius and Wolf, 1990), which are the expected result of localized reconnection. The depletion of the entropy content was suggested earlier as an important mechanism in the earthward transport of flux tubes, associated with bursty bulk flows (Pontius and Wolf, 1990; Chen and Wolf, 1993, 1999; see also Section 4.5.7). The bubble simulations confirmed that the depletion was indeed an important factor in permitting the flux tubes to penetrate closer to the Earth. They also showed that earthward moving bubbles were associated with field-aligned current systems, directed earthward on the dawnward edge and tailward on the duskward edge, as in the substorm current wedge. This is consistent with current systems attributed to observed bursty bulk flows and their connection with auroral features (Sergeev *et al.*, 1996; Kauristie *et al.*, 2000; Nakamura *et al.*, 2001b; Sergeev *et al.*, 2004). In the bubble simulations, the field-aligned currents are generated by the twist of magnetic flux tubes through vortical plasma motion outside the bubble near its earthward front, similar to the mechanism depicted in Fig. 4.17. This may also be visualized as a bubble plowing its way through surrounding field lines and pushing them to the side, while becoming more dipolar itself.

4.4.4 Particle acceleration

Particle acceleration processes that operate in the vicinity of the reconnection site have already been discussed in Section 3.6. For these processes the detailed structure and dynamics of the collisionless plasma are very important and

a self-consistent description appears necessary. Earlier, the acceleration of ions and electrons in the vicinity of the neutral line provided an attractive explanation for increases in energetic particle fluxes (*injections*) in the range of tens to hundreds of keV in the near-tail region, observed particularly by geosynchronous satellites. However, the fact that more refined satellite observations indicate that the near-Earth neutral line predominantly forms tailward of $\sim$20 R_E (e.g., Nagai *et al.*, 1998) provides an inconsistency of this model with the fact that energetic particle injections at geosynchronous orbit are typically dispersionless near midnight (e.g., Baker, 1984; Birn *et al.*, 1997a), indicating an acceleration site close by.

This discrepancy was solved by test particle calculations using the time dependent fields of an MHD simulation of tail dynamics (Birn *et al.*, 1997b, 1998b) or assumed electric and magnetic fields, capturing the main elements of the dynamic evolution (Li *et al.*, 1998; Zaharia *et al.*, 2000): a spatial localization and an earthward propagation of a region of enhanced cross-tail electric field. In the MHD simulation, these properties followed self-consistently from the dipolarization of the magnetic field associated with localized earthward plasma flow from the reconnection site. It is consistent with the *convection surge* mechanism proposed by Quinn and Southwood (1982) and Mauk (1986); however, the spatial localization in the cross-tail direction provides an important additional element.

The characteristic acceleration mechanism is illustrated in Fig. 4.18. It shows a typical orbit of an accelerated test ion (proton) integrated in the time dependent electric and magnetic fields of an MHD simulation (Birn and Hesse, 1996; Birn *et al.*, 1997b). The electric field is characterized by a strong enhancement in the central region, which is associated with the earthward collapse (dipolarization) of reconnected field lines. The magnitude of this $(-\mathbf{v}\times\mathbf{B})$ field may even exceed the magnitude of the electric field at the reconnection site. The proton starts near the dawn flank of the tail and at first exibits a so-called *Speiser orbit* (Speiser, 1965), characterized by one-half of a gyration around the weak equatorial field B_z, followed by a gyromotion along a field line toward the Earth. After mirroring closer to the Earth, the ion gyrates back into the neutral sheet, does another half gyration around B_z and another gyro-orbit toward the Earth and back into the tail. When the ion encounters the region of enhanced cross-tail electric field it becomes accelerated and its gyroradius increases even outside the neutral sheet. The kinetic energy of this particular ion increases from $\sim$60 keV to $\sim$180 keV.

The electron acceleration is basically similar to the ion acceleration, except that the electron orbits are mainly adiabatic, that is, conserving the magnetic moment (Birn *et al.*, 1998b, 2004c). Accelerated electrons typically originate from the duskward boundary. Depending on their pitch angle, they may bounce many times between their mirror points, while drifting towards the center tail. When they reach the central region of earthward collapse they participate in the earthward $\mathbf{E}\times\mathbf{B}$ drift and become accelerated through a betatron or Fermi mechanism, depending on the pitch angle. Except for the bounce motion, this is similar to the history of typical 90° pitch angle accelerated electrons.

Although, in contrast to the electrons, the acceleration of ions is largely nonadiabatic, the net acceleration found in these test particle investigations was similar for both species at energies above several tens of keV, which explains the similarities of

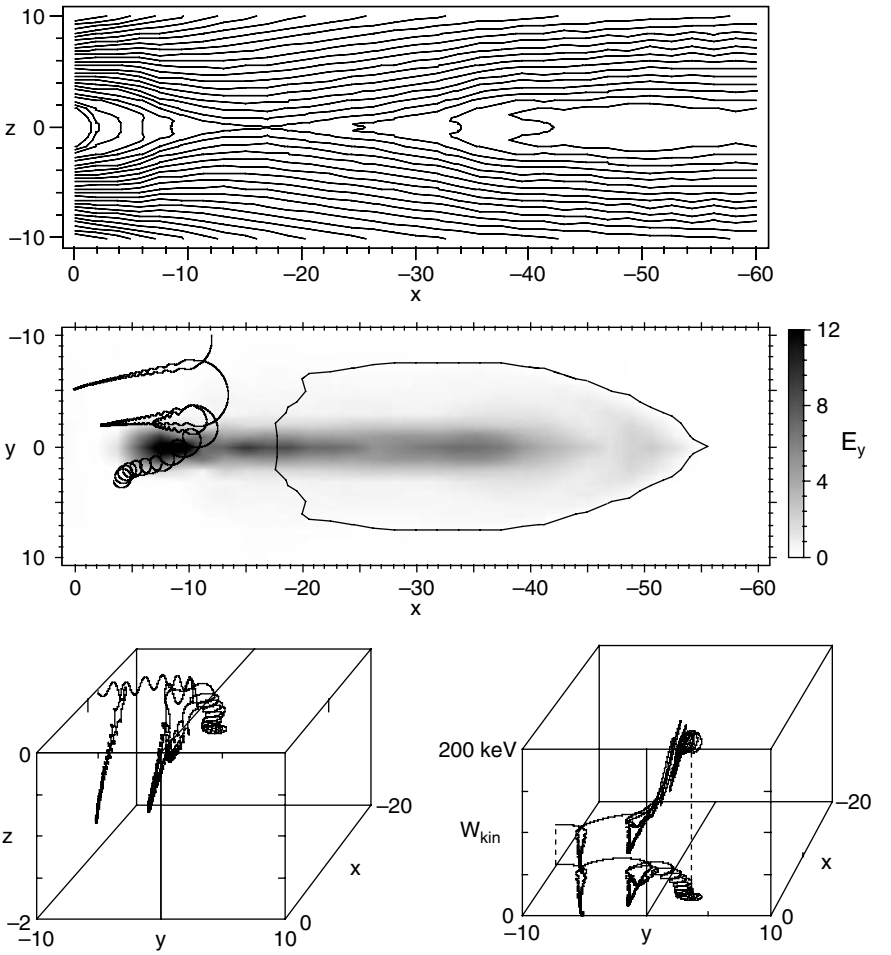

Fig. 4.18. Characteristic particle acceleration in the dynamic magnetotail based on test particle tracing in the electromagnetic field of an MHD simulation (Birn and Hesse, 1996). The center panel shows the projection of an ion orbit in the equatorial plane overlaid on a snapshot of the cross-tail electric field (gray scale) and the magnetic neutral line (thin solid line). The corresponding instantaneous magnetic field structure is shown in the top panel. The bottom panels shows perspective views of the ion orbit (left) and of the ion energy above the equatorial projection of the orbit (right). The proton starts near the dawn flank at an energy of ∼60 keV and becomes energized to 180 keV when it crosses the region of enhanced electric field.

ion and electron injections at such energies. At lower energies (less than a few tens of keV) both ions and electrons found in the near tail in the simulations mostly originate from the more distant tail along the plasma sheet boundaries. A major difference, however, stems from the difference in the bounce periods of ions and electrons. The ions entering the near tail from the more distant tail on not yet reconnected field lines have bounce periods comparable to or larger than the characteristic time of the field collapse. As a consequence, after mirroring closer to the Earth, the ions may

be on field lines that are already collapsed and connect to the near tail earthward of the region of strong E_y. Because of the localization of the induced electric field, these ions therefore circumvent the region of strong E_y and do not get accelerated. This explains why the lower-energy limit of enhanced particle fluxes is significantly higher for ions than for electrons (Birn *et al.*, 1997a).

We note that this is just one of the reasons why the low-energy limit of flux enhancements is different for ions and electrons. The history of particles may vary significantly depending on time, location, and pitch angle of particles. Additional effects are primarily related to differences in source regions. In this context the neutral line might play a role in diverting particles and thereby affecting fluxes even at locations far away. The test particle simulations clearly show that the electric field in the collapsing magnetic field region plays the dominant role in the particle acceleration, rather than the field at the reconnection site itself. This resolves the above mentioned apparent inconsistency of the neutral line model of substorms with the fact that observed dispersionless injections imply an acceleration site much closer than the inferred site of reconnection. The important role of localized, earthward propagating, electric field pulses was further supported by the excellent agreement between observed particle injections and models based on energetic particle orbit calculations that included the drift around the Earth (Li *et al.*, 1998), leading to so-called *drift echos* (Lanzerotti *et al.*, 1967, 1971; Belian *et al.*, 1978).

4.5 Observations of tail reconnection

W. Baumjohann and R. Nakamura

Because of the difficulty of separating temporal variations and spatial structure in a highly dynamic system, measurements with a single spacecraft have always been problematic and led to debate. This was especially true when trying to explore the site of reconnection in the near-Earth magnetotail. While sophisticated and detailed studies of this region using data from the Geotail spacecraft (e.g., Nagai *et al.*, 1998, 2001, 2003) revealed some of its internal structure, some ambiguity still prevailed.

In this section we report on the present state of investigating reconnection in the vicinity of the near-Earth neutral line based on recent Cluster measurements. Being a constellation of four identical spacecraft, Cluster allows discrimination of spatial and temporal variations in magnetic field and plasma parameters. Thus it is ideal to study the structure and dynamics of plasma and fields relevant to reconnection. In this section we first present an example of multipoint observation of current sheet crossings near the X-line and discuss the effects of unmagnetized ions including the Hall current. We then discuss the closure of the Hall current, followed by a brief discussion of new results on the consequences of reconnection such as bursty bulk flows, plasmoids, and slow-mode shocks.

4.5.1 Cluster tetrahedron

The Cluster spacecraft were launched in summer 2000 and put into a polar orbit with an apogee of about 19 R_E. Cluster traverses the magnetotail from mid July to end October, crossing the plasma sheet in a nearly regular tetrahedron form. The typical configuration of the Cluster tetrahedron during the 2001 tail season is shown in Fig. 4.19. Most of the Cluster data discussed here were obtained by the Flux-Gate

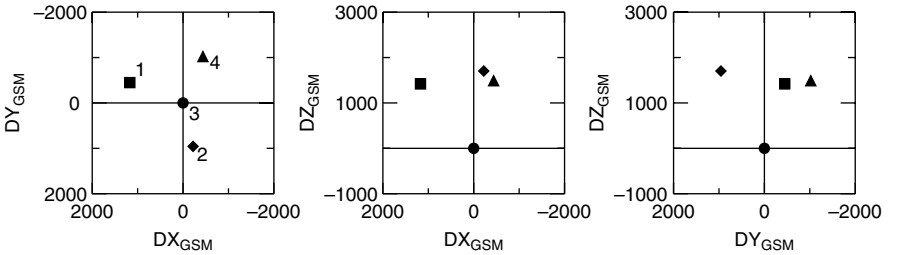

Fig. 4.19. Typical Cluster tetrahedron configuration during the 2001 tail season.

Magnetometer (FGM; Balogh *et al.*, 2001) and by the Cluster Ion Spectrometry (CIS; Rème *et al.*, 2001) unless noted otherwise.

4.5.2 Current sheet structure

Spacecraft traveling in the plasma sheet often observe rapid large amplitude variations of the magnetic field, sometimes with a change of polarity (a change in the sign of the prevailing B_x component). Such variations indicate rapid up–down oscillations of the current sheet known as *flapping* (Zhang *et al.*, 2002; Runov *et al.*, 2003b; Sergeev *et al.*, 2003, 2004). Being an interesting phenomenon in itself, flapping provides a possibility to probe the internal structure of the current sheet.

Figure 4.20 shows an example of current sheet crossings during an episode of intensive flapping. The top two panels on the left-hand side show the x component of the magnetic field at all four spacecraft (upper panel) and the proton bulk velocity (data from Cluster 1, 3, and 4 only) observed during a large storm-time substorm on October 1, 2001. A set of rapid current sheet crossings during intervals A–D were used to reconstruct the structure of magnetic field and electric current inside the current sheet. The resulting current density $\mathbf{j} = \nabla \times \mathbf{B}/\mu_0$ and the magnetic field curvature vector $\mathbf{C} = (\mathbf{b}\cdot\nabla)\mathbf{b}$, where $\mathbf{b} = \mathbf{B}/B$, are shown in the two mid panels. The calculations show that the electric current was very strong (about $30\,\mathrm{nA/m^2}$) during intervals A, B, and C and less intense during interval D. The x component of the magnetic field curvature vector was dominant during all the crossings and reversals from negative to positive and vice versa indicate a complex magnetic field topology and the close encounter of a magnetic neutral line.

The panels on the right-hand side of Fig. 4.20 show the reconstructed spatial profiles of current density and magnetic field. The method of reconstruction is based on linear gradient estimation (Chanteur, 1998). It is supposed that during the flapping the current sheet is simply translated without any change of its structure and the streamline derivative $\mathrm{d}\mathbf{B}/\mathrm{d}t = \partial\mathbf{B}/\partial t + (\mathbf{U}\cdot\nabla)\mathbf{B} = 0$. Then integration of the translation velocity projected onto the local current sheet normal $U_\mathrm{n} = \partial B_x/\partial t/\nabla_\mathrm{n} B_x$ during the crossing gives an estimate for the vertical scale Z^* (see Runov *et al.*, 2005). The current density profiles have very similar shapes and show that during intervals A, B, and C Cluster crosses a single-peaked thin current sheet with a half-thickness of about one ion gyroradius. The profile during interval D shows a change in the

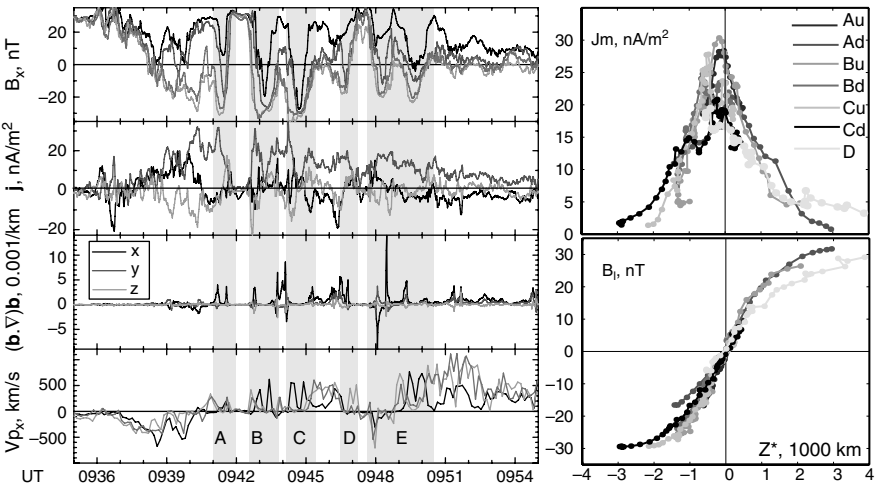

Fig. 4.20. Cluster observations during a flapping event on October 1, 2001 (left-hand panel): B_x from Cluster/FGM, components of the current density $\mathbf{j} = \nabla \times \mathbf{B}/\mu_0$, and the magnetic curvature vector $\mathbf{C} = (\mathbf{b} \cdot \nabla)\mathbf{b}$, and x component of the proton bulk velocity from Cluster/CIS. Reconstructed profiles of current density (cross-tail component) and maximum variance component of the magnetic field for current sheet crossing A–D (right-hand panel). Index u denotes upward motion of the sheet, B_x changes from positive to negative, and d indicates downward motion (Runov *et al.*, 2005). See also color plate.

current sheet structure. Interval E, with reversals of the magnetic field curvature vector and ion bulk flow direction, will be discussed below.

4.5.3 X-line encounter and Hall currents

During the repeated current sheet crossings in interval E in Fig. 4.20, Cluster observed a fast flow reversal from tailward, with a maximum speed of 800 km/s, to earthward, with maximum value of 700 km/s. The magnetic field curvature vector, calculated from four-point magnetic field observations (see also Shen *et al.*, 2003), also reversed, first pointing tailward during the tailward flow, then earthward during the earthward flow. The corresponding reversals of the magnetic field curvature and proton bulk velocity indicate that Cluster crossed a tailward traveling magnetic X-line (Runov *et al.*, 2003a).

Figure 4.21 illustrates the situation. The three bottom rows show snapshots of the magnetic field and proton bulk velocity measured by Cluster at three consecutive instances, during which the X-line passes over the spacecraft. Two upper rows present a schematic view of the Cluster tetrahedron position fitted to a simulated magnetic field and ion flow around an X-line (adapted from Hoshino *et al.*, 2001b). Note that Cluster observations of the earliest times are plotted at the right, since the X-line moved tailward, or the location of Cluster relative to the X-line moved earthward.

At 09:48:02 UT (right column) Cluster 1, 3, and 4 detected tailward flow. Cluster 1 and 2 detected earthward and dawnward ($B_y < 0$) magnetic field, while the magnetic field detected by Cluster 3 was tailward and duskward ($B_y > 0$). Cluster 4, staying

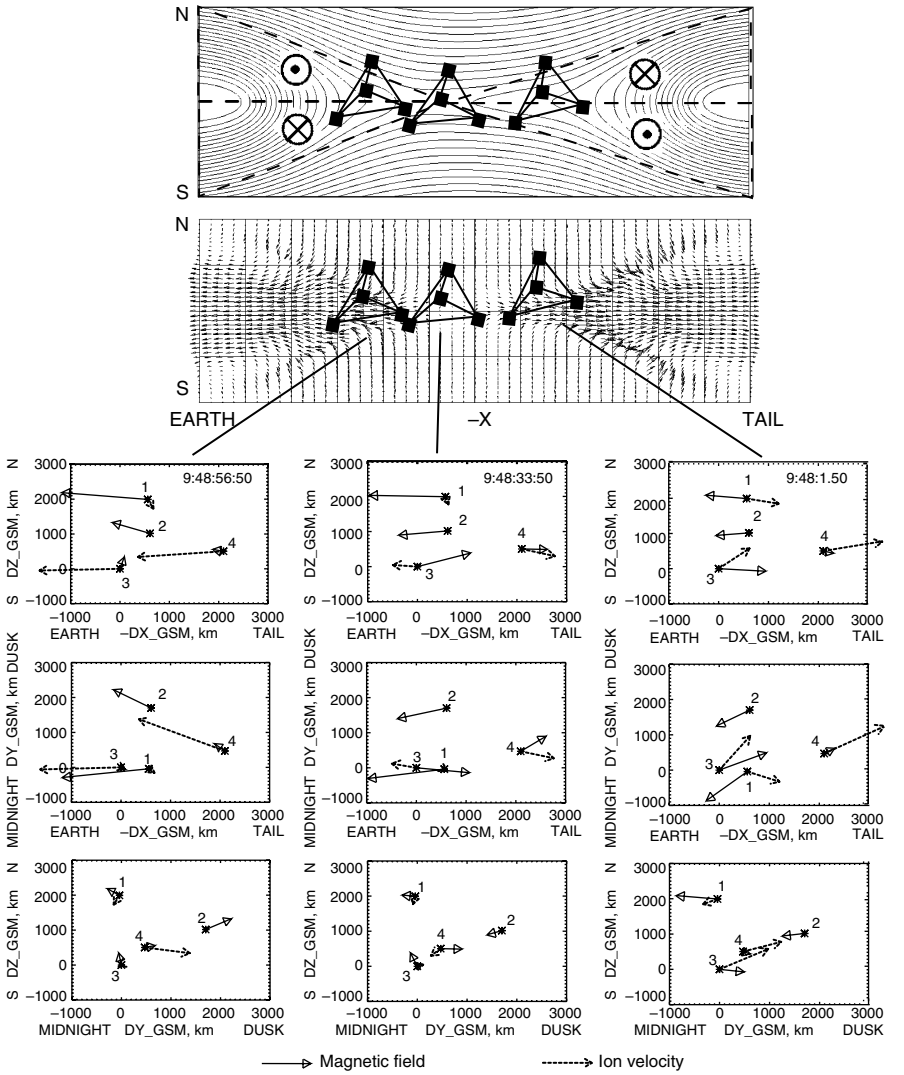

Fig. 4.21. Cluster observations of the magnetic X-line. Bottom panels: Snapshots of magnetic field and ion bulk velocity vectors in three GSM projections. The two upper figures are sketches of spacecraft positions with respect to the X-line, using magnetic field lines and ion velocity vectors from a simulation by Hoshino *et al.* (2001b). The symbols $\odot$ and $\otimes$ give the direction of the B_y component.

closest to the neutral sheet, saw a very weak magnetic field, directed tailward and duskward. Cluster 2, 3, and 4 found a weakly negative B_z. Since the weakly positive B_z at Cluster 1 seems to be a short-lived (5 s) fluctuation (the average value during the tailward flow (09:47–09:49 UT) is -2 nT), these data show that Cluster was located tailward of the X-line.

At 09:48:34 UT (mid column) the pair of spacecraft most separated along x (Cluster 3 and 4) detected oppositely directed ion flow: Cluster 4 saw tailward and

Cluster 3, earthward flow. Cluster 1, staying in a stronger magnetic field, observed slower ion flow directed mostly southward. The magnetic field topology also changed drastically: Cluster 1, 2, and 3 observed a magnetic field directed dawnward in the y, z plane (bottom row), while Cluster 4 saw the field directed duskward. Thus, the separatrix apparently was located in between Cluster 4 and the other three: Cluster probed the close vicinity of the X-line. Since B_z at Cluster 1 and 3 was positive, while Cluster 2, separated along the y direction, showed a small negative B_z, the magnetic field around the X-line was highly nonuniform in all three directions and the typical scales were comparable to the Cluster separation. Cluster 2 and 3, separated by 1000 km along z, detected almost equal magnitude but oppositely directed B_x, which roughly yields a current sheet half-thickness of about 500 km near the X-line.

At 09:48:57 UT Cluster 3 and 4 observed strong earthward flow, while the flow detected by Cluster 1 was southward and much weaker. All four spacecraft detected a positive z component of the magnetic field. At the same time, the magnetic field observed by Cluster 1 had a dawnward component, while observations by Cluster 2 and 4 showed a duskward magnetic field component. The magnetic field from Cluster 3 was slightly dawnward and tailward.

The B_y observations can be interpreted as the observation of the Hall quadrupolar magnetic field structure (Section 3.1), first observed by Nagai *et al.* (1998) and schematically shown in the upper row of Fig. 4.21 and the sketch in Fig. 4.22 (after Runov *et al.*, 2003a). Indeed, at 09:48:02 UT, when Cluster was located tailward of the X-line, the two spacecraft (Cluster 1 and 2) staying in the northern hemisphere observed dawnward ($B_y < 0$) magnetic field, while the other two, situated in the southern hemisphere, detected $B_y > 0$. At 09:48:34 the situation was more complex: Cluster 3 and 4, located in the southern hemisphere at opposite sides of the X-line detected oppositely directed out-of-plane magnetic fields (negative at Cluster 3 and positive at Cluster 4), which is consistent with the theoretical picture. Cluster 1, detecting the ion inflow, was likely located outside of the Hall zone. Cluster 2 was probably situated very close to the separatrix, where the Hall effect is negligible.

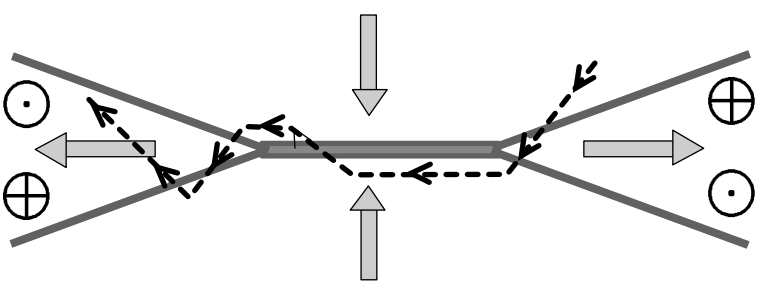

Fig. 4.22. Sketch of Cluster observations of Hall magnetic fields and current sheet structure around the reconnection region, the dashed line indicates the trajectory of Cluster, the symbols $\odot$ and $\otimes$ indicate the direction of the Hall magnetic fields, and the wide arrows show the main plasma flow direction. After Runov *et al.* (2003a).

During the earthward flow interval (09:48:57 UT) Cluster 2 and 4, staying in the northern hemisphere, showed $B_z > 0$, while Cluster 3 in the southern hemisphere detected $B_y < 0$, which is again consistent with the Hall reconnection model. Cluster 1, detecting ion inflow, was again located outside of the Hall current system region.

The quadrupolar out-of-plane magnetic field component is a manifestation of the Hall current system which has a direction opposite to the main flow direction indicated by the wide arrows in Fig. 4.22. The Hall currents result from ion–electron decoupling within the ion diffusion region with a characteristic scale of the ion inertial length (Sections 3.1 and 3.2). These signatures were previously detected by Geotail (Nagai *et al.*, 2001; Asano *et al.*, 2004) and Wind (Øieroset *et al.*, 2001) spacecraft, however, simultaneous multipoint observations by Cluster show, for the first time, the spatial structure of the Hall region.

4.5.4 Bifurcated current sheets

Nakamura *et al.* (2002b), using Cluster four-point measurements, found that the magnetotail current sheet sometimes exhibits a double-peaked profile of the electric current density. Such bifurcated current sheets may exist during intervals of high-speed ion flow (Runov *et al.*, 2003a) as well as during intervals with $|V_x| \leq 100\,\mathrm{km/s}$ (Sergeev *et al.*, 2003; Asano *et al.*, 2005). Their thickness varies from about $1\,R_\mathrm{E}$ (Runov *et al.*, 2004) down to less than 1500 km (Asano *et al.*, 2005).

The existence of thin bifurcated sheets may be closely associated with the formation of thin embedded current sheets at small scales (see also Section 4.4.1) prior to or during reconnection. Indeed, Runov *et al.* (2003a), analyzing the current sheet structure around the X-line encounter in interval E in Fig. 4.20, showed that during the tailward and earthward flow intervals the current sheet was bifurcated, with broad *valleys* between peaks of the current. The scale of the valleys was approximately 3000–4000 km. In between the oppositely directed flows the current sheet was very thin, with a half-thickness of 500 km, and had a flat profile near the maximum of the current ($\sim 20\,\mathrm{nA/m^2}$). This is depicted schematically in Fig. 4.22.

4.5.5 Hall current closure

The Hall currents generated in the ion diffusion require continuation currents outside the ion diffusion region. At the lobe side, the closure of the Hall currents takes place via cold electrons flowing into the ion diffusion region. At the outflow region, on the other hand, accelerated electrons exiting along the magnetic field provide currents into the ion diffusion region. Such behavior of the electrons has been observed previously by Geotail (Fujimoto *et al.*, 2001; Nagai *et al.*, 2001) and by Wind spacecraft (Øieroset *et al.*, 2001). These field-aligned currents can be observed also well outside the reconnection region. In particular, at the earthward side of the reconnection region, they may even extend to the auroral acceleration region. Cluster also observed such downward–upward field-aligned current pairs associated with a transient encounter of energetic ion beams, which suggests a connection to the ion diffusion region as illustrated in Fig. 4.23 (adapted from Nakamura *et al.*, 2004b). Multipoint observations suggested that the scale size of the downward current was at maximum comparable to the ion inertia length so that it plausibly connects to the

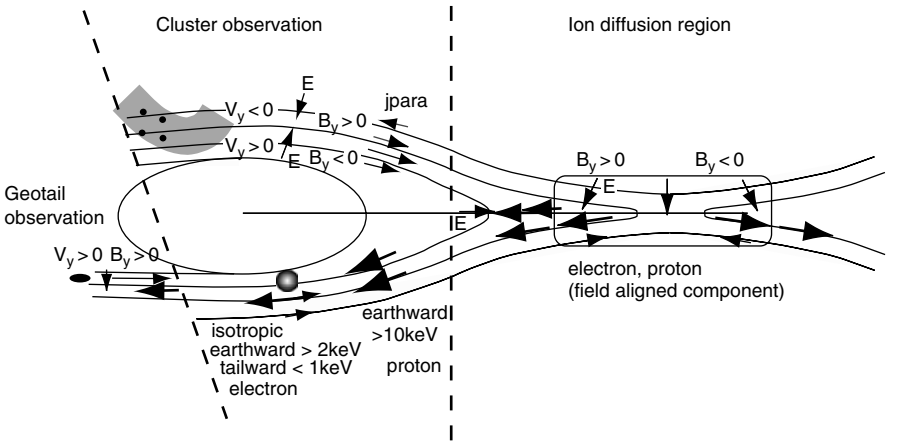

Fig. 4.23. Summary of observations by Cluster during a transient entry into the plasma sheet between 12:40 and 12:41 UT on October 10, 2001 substorm event (left-hand side) and illustration of possible relationship to the reconnection region. For Cluster observations field signatures are showing in the northern hemisphere, while particle signatures are illustrated in the southern hemisphere assuming they are symmetric in hemisphere. (adapted from Nakamura *et al.*, 2004b).

near-Earth X-line and is driven by Hall effects in the reconnection region as proposed by Fujimoto *et al.* (2001). Consistent with the electric field found in the vicinity of the ion diffusion region (Nagai *et al.*, 2003), a southward electric field ($-\mathbf{V} \times \mathbf{B}$ field from the drift of cold ions) was observed at Cluster.

The field-aligned current system closing the Hall current near the reconnection region has also been inferred using the electron moments from Geotail observations (Asano *et al.*, 2004). The Plasma Electron And Current Experiment (PEACE; Johnstone *et al.*, 1997) onboard Cluster also succeeded in measuring the field-aligned electron currents at the earthward side of the reconnection region (Alexeev *et al.*, 2005). In addition to confirming the downward (towards the X-line) and upward (away from the X-line) field-aligned currents near the plasma sheet boundary and the plasma sheet side, respectively, as predicted from the closure of the Hall currents, their observations showed a layer of stronger downward currents at the interface between the downward and upward currents. These different layers of field-aligned currents could be due to two nested diffusion regions possibly related to the effect of the heavy ions (Alexeev *et al.*, 2005). For the same event, even finer structures with temporal scales less than 1 s were observed to be embedded in the inflowing field-aligned beams (Asano *et al.*, 2005) based on the high-temporal resolution measurement of the 500 eV field-aligned electrons with the Electron Drift Instrument (EDI; Paschmann *et al.*, 2001) onboard Cluster.

4.5.6 Other features

An excitation of electrostatic waves with amplitudes $\leq 400\,\mathrm{mV/m}$ and frequencies varying from ion cyclotron to lower hybrid, and electrostatic solitary waves with amplitudes of 25 mV/m and much higher frequencies were observed

during the reconnection event discussed in Section 4.5.3 (Fig. 4.21) between 09:47 and 09:51 UT (Cattell *et al.*, 2002b) by the Electric Field and Wave (EFW) instrument (Gustafsson *et al.*, 2001). These waves may provide the dissipation needed for reconnection in an advanced stage.

Another important new observation for this reconnection event is the ion composition. During the thin current sheet interval, 09:45–09:55 UT, pressure as well as density was dominated by O^+ rather than H^+ (Kistler *et al.*, 2005), which was interpreted as being due to storm-time ion outflow from the ionosphere. In the O^+ ion dominated thin current sheet, the O^+ ions were found to carry about 5–10% of the cross-tail current (Kistler *et al.*, 2005). Detailed analysis of the distribution function showed separate O^+ layers above and below the thin current sheet (Wilber *et al.*, 2004). It was suggested that the O^+ in the reconnection region experienced a ballistic acceleration (Wygant *et al.*, 2005), based on the observation of a large-amplitude bipolar electric field (± 60 mV/m) observed by EFW directed normal to the current sheets for the same event. Cluster therefore opened up a new interesting topic to investigate from the observational point of view: the effect of the multicomponent plasma in the reconnection.

4.5.7 Consequences of tail reconnection

One of the major consequences of reconnection is the generation of fast plasma flows, which for a long time have been used as the major indicator of the occurrence of reconnection and for the identification of the location of the reconnection site. Statistical analyses of Geotail ion flow measurements thus concluded, from a distinction between the substorm-related onset of tailward and earthward flows, that usually near-Earth reconnection starts in the tail region between $20\,R_E$ and $30\,R_E$ distance from the Earth (Nagai *et al.*, 1998).

Plasma bulk acceleration might take place not only in the immediate vicinity of the reconnection site but also at slow shocks, which in the Petschek model (Section 2.1) extend outward from the diffusion region. Slow-mode shocks connected to the ion diffusion region have been identified in the tail by previous studies (e.g., Feldman *et al.*, 1987; Øieroset *et al.*, 2000) based on Walén analysis (e.g., Sonnerup *et al.*, 1987) and checking Rankine–Hugoniot shock jump conditions. Using multi-composition plasma observation by Cluster, Eriksson *et al.* (2004) performed a similar analysis by taking into account also the contributions from oxygen ions during a substorm X-line event when Cluster observed fast tailward and earthward flows. The successful joint Walén and slow shock analysis of the tailward flows within the plasma sheet presented further evidence in favor of Petschek-type reconnection at distances $X_{GSM} > -19\,R_E$ of the near-Earth magnetotail. The failure of both the Walén test and the Rankine–Hugoniot analysis of the earthward flow portion of the plasma flow reversal event were interpreted to be associated with the strong earthward gradient of the magnetic field in the inner magnetosphere.

Due to its apogee Cluster observes many more earthward high-speed flows than tailward flows. This enabled new results to be obtained on consequences of reconnection at the earthward side of the X-line(s), namely earthward propagating southward then northward magnetic field disturbances related to plasmoids/flux rope (Slavin *et al.*, 2003a; Zong *et al.*, 2004), traveling compression regions (Slavin *et al.*, 2003b)

and nightside flux transfer events (Penz *et al.*, 2004; Sergeev *et al.*, 2004), analogous to features more commonly observed tailward of the reconnection site. Multipoint analyses by Cluster were used to measure the current density and check a force-free model (Slavin *et al.*, 2003b) and energetic particle boundaries (Zong *et al.*, 2004) to show the structures of the plasmoid/flux rope. Yet, since the plasma flows jetting toward the Earth are significantly influenced by the strong dipolar field and pressure gradient, it still remains unknown to what extent these structures can be treated as motion of a stable structure in the analyses. Similar magnetic features were interpreted as transient profiles associated with a change in the reconnection rate at a remote X-line, allowing a determination of the location of the X-line (Penz *et al.*, 2004; Sergeev *et al.*, 2004). Determination of the field topology would be a key to differentiating whether these structure are coming from a single X-line or signature of multiple X-lines.

The bursty bulk flows (BBFs) and related phenomena, which are attributed to local reconnection that is not necessarily substorm related (Section 1.2), were also intensively studied by Cluster spacecraft using multipoint observations. A statistical analysis was performed by Nakamura *et al.* (2004a) to estimate the typical scale size of BBFs. It was suggested that the full width of the flow channel is on average 2–3 R_E in the dawn–dusk direction and 1.5–2 R_E in the north–south direction. Furthermore, BBFs were found to be accompanied by different types of magnetic field disturbances such as dipolarization (Nakamura *et al.*, 2002a), low-frequency wave activity (Volwerk *et al.*, 2003, 2004), and turbulence (Vörös *et al.*, 2003, 2004).

The role of reconnection and fast flows in substorms has been one of the key topics in the magnetosphere. Using Cluster, together with the other spacecraft and ground-based observations, several case studies determined reconnection to be the key process leading to a major substorm onset (Baker *et al.*, 2002; Sergeev *et al.*, 2005), although multiple pseudo-break-ups preceding the major onsets complicate the determination of the cause and effect arguments of the initial disturbance. During a more simple isolated earthward flow burst event, magnetosphere–ionosphere coupling processes were studied by conjugate dense ionospheric observations showing BBF-associated field-aligned and ionospheric current systems (Grocott *et al.*, 2004; Nakamura *et al.*, 2005).

4.6 Remote sensing of reconnection

M. P. Freeman, G. Chisham, and I. J. Coleman

Remote sensing – the acquisition of information about an object without being in physical contact with it – has been the basis for our understanding of magnetic reconnection in the Universe. Telescope observations have revealed a solar magnetic field and related it through magnetic reconnection to the structure and dynamics of solar plasma (Giovanelli, 1948; Kopp and Pneuman, 1976). Remote sensing of electrical currents in space from magnetic fluctuations on the ground inspired the magnetic reconnection model of plasma convection within the magnetosphere (Dungey, 1961). In recent years, amazing movies of dynamical reconfigurations of solar prominences and arcades by the SOHO and TRACE spacecraft and of Earth's aurora by the Polar and IMAGE spacecraft have emphasized the spatial and temporal complexity and motivated new magnetic reconnection models (Aulanier *et al.*, 2000; Fletcher *et al.*,

2001; Freeman and Watkins, 2002). Remote sensing of planetary aurorae (Grodent *et al.*, 2003; Cowley *et al.*, 2005) and other astronomical objects such as collapsing black holes (Igumenshchev *et al.*, 2003) have suggested magnetic reconnection to be a universal phenomenon.

Whilst remote sensing is a powerful tool in the study of magnetic reconnection, it is necessarily an indirect measurement, and typically only on magnetohydrodynamic (MHD) scales. Thus it is also desirable to have *in situ* measurements localized within the broader time and space range of indirect remote sensing. *In situ* observations have greatly enhanced our understanding of the plasma and magnetic field environment within the reconnecting current sheet down to electron scales (Øieroset *et al.*, 2001; Mozer *et al.*, 2002). They have also provided some measurements of the reconnection rate at the magnetopause (Sonnerup *et al.*, 1981; Lindqvist and Mozer, 1990) that can be a valuable point of comparison with remote sensing measurements (Pinnock *et al.*, 2003). Importantly, the Earth's magnetosphere occupies a privileged position in being the only natural environment in which reconnection can be sensed both remotely and *in situ*. In this section we shall present a method of remotely sensing magnetic reconnection in the magnetosphere from the ionosphere (Vasyliunas, 1984) and discuss examples of its use in advancing reconnection knowledge.

4.6.1 Method

Magnetic reconnection can be defined as the breaking and reconnecting of magnetic field lines to connect them in a different way (Schindler *et al.*, 1988, Chapter 2). Thus, magnetic reconnection can be remotely measured by: (a) detecting regions of different magnetic connectivity and (b) measuring the rate of change of their magnetic flux or, more generally, the transport of magnetic flux across the separatrices dividing the regions of different connectivity.

Figures 1.6a and 4.1a show examples of this for the classical open magnetosphere model (Dungey, 1961) appropriate for southward interplanetary magnetic field (IMF) with one magnetic reconnection X-line site at the low-latitude magnetopause and one in the Earth's magnetic tail. Separatrices emanating from each X-line divide the magnetic field into four regions with three distinct magnetic topologies: (1) *Closed* magnetic field lines with both ends on the Earth. (2) *Open* magnetic field lines with one end on the Earth and one end in the solar wind. (3) *Free* magnetic field lines with neither end attached to the Earth. The different topologies give rise to different plasma properties in each region that can be detected at their footpoints, as discussed below. In this way, the reconnection separatrices are mapped to the ionosphere without an explicit magnetic field model. Out of the noon–midnight plane (neglecting distortion by azimuthal fields), the closed field lines form a torus around the Earth such that the dayside and nightside closed field line regions are joined (Fig. 1.5). Consequently, the boundary between closed and open magnetic field lines in the ionosphere is approximately a circle of constant geomagnetic latitude in each polar hemisphere. As discussed in Section 4.1, this simple topology becomes structurally unstable when the 2D symmetry in Figs. 1.6a and 4.1a is broken, for instance, by the presence of a y component of the magnetic field. Nevertheless, one can still identify surfaces that separate regions of different magnetic topology.

Assuming this, the total net reconnection rate is given by the rate of change of magnetic flux F in any of these regions. Measuring reconnection from the ionosphere offers the advantages that the measurement area A enclosing this flux is minimized, and that the magnetic field in the ionosphere $\mathbf{B_i}$ is approximately incompressible and thus can be described by a static empirical model, such as the *International Geomagnetic Reference Field*. Consequently, the rate of change of magnetic flux is given by

$$\dot{F} = \dot{F}_\mathrm{p} - \dot{F}_\mathrm{t} = B_\mathrm{i}\dot{A}, \tag{4.33}$$

where $\dot{X}$ denotes the time derivative of X and the middle expression is appropriate for the case shown in Fig. 1.6a where $\dot{F}_\mathrm{p}$ and $\dot{F}_\mathrm{t}$ are the total reconnection rates along the magnetopause and magnetotail X-lines, respectively.

Complications arise from scenarios in which the topology of the magnetic field lines with footpoints on the Earth is not changed by reconnection. For magnetopause reconnection during dominantly northward IMF (Figs. 1.8 and 4.1b), reconnection X-lines are expected at high northern and southern latitudes (Dungey, 1963). Asymmetry between the northern and southern hemispheres (e.g., due to magnetic dipole tilt or a component of the IMF in addition to the north–south component) may mean that reconnection involving an open magnetic field line with its footpoint on the Earth changes its connectivity but not its topology (Reiff and Burch, 1985). For magnetotail reconnection, Figs. 1.6b–d show an example within the neutral line model of substorms (Baker *et al.*, 1996) that might occur immediately after the onset of a substorm (see Section 1.2). The formation of a near-Earth X-line simultaneously with a distant X-line means that a closed field line previously reconnected at the distant X-line is reconnected again but remains closed, while a severed part forms free *plasmoid* (O-type) magnetic field lines. However, this scenario is transient because the plasmoid is being ejected downtail out of the system. In the presence of a net cross-tail magnetic field component the symmetry of Fig. 1.6 is broken, and plasmoid field lines no longer form closed loops but rather helically wound lines, which initially are still connected to Earth (illustrated by Fig. 4.16, top panel). Although the connections have changed, no topology change takes place at this stage.

In any event, assuming that the plasma properties on each side of the ionospheric footpoint of the reconnection separatrix are sufficiently different to identify it, the local reconnection rate can be remotely sensed in the ionosphere by measuring the rate of transport of magnetic flux across unit length of the ionospheric separatrix, such as between closed and open magnetic field line regions:

$$E = v'_\mathrm{n} B_\mathrm{i}, \tag{4.34}$$

where v'_n is the field line velocity normal to the separatrix measured in the rest frame of the separatrix. In the F-region ionosphere, electrons are frozen into the magnetic field (i.e., ideal electron MHD) such that the field line velocity equals the electron velocity and thus E is the electric field component tangential to the separatrix. Moving into a general measurement frame in which the separatrix moves with velocity $\mathbf{u}$, we get

$$E = (v_\mathrm{n} - u_\mathrm{n})B_\mathrm{i}, \tag{4.35}$$

where v_n and u_n are the field line velocity and separatrix velocity, respectively, normal to the separatrix in the measurement frame. In contrast to the total reconnection rate, a magnetospheric magnetic field model is required to relate the local ionospheric reconnection rate to the local reconnection rate at the X-line in the magnetosphere (i.e., to relate the unit length in the ionosphere to the corresponding length along the X-line).

Thus, ionospheric remote sensing of magnetic reconnection requires the following measurements: (1) $\mathbf{E} \times \mathbf{B}$ drift velocity normal to the reconnection separatrix, (2) position and velocity of the reconnection separatrix. Let us now consider the methods used to measure these.

$\mathbf{E} \times \mathbf{B}$ drift velocity normal to the reconnection separatrix

Measurements of the $\mathbf{E} \times \mathbf{B}$ drift velocity in the ionosphere have been made for many years by spacecraft and ground-based radars. More indirect estimates have also been made using ground-based magnetometers to infer currents within the ionosphere, which can be related to the electric field via Ohm's law. Such observations have provided average convection patterns for given solar wind and magnetospheric conditions that have clearly shown them to be driven by magnetic reconnection, and also provided evidence suggesting transient and localized reconnection. However, to measure convection structure unambiguously from local to global scales in time and space requires networks of spacecraft, radars, or magnetometers. Such measurements have become possible from the *Super Dual Auroral Radar Network* (SuperDARN, Greenwald *et al.*, 1995). The radars measure the line-of-sight component of the $\mathbf{E} \times \mathbf{B}$ drift velocity of ionospheric plasma from the Doppler shift of coherently reflected echoes from naturally occurring irregularities in electron density. Estimates of the 2D $\mathbf{E} \times \mathbf{B}$ drift velocity vector in the ionospheric plane can be derived either by combining measured velocity components at the same ionospheric location from two or more radars looking from different directions or by using the line-of-sight measurements to fit a global solution for the velocity stream function (electrostatic potential) expressed as a series expansion in spherical harmonics and constraining the solution using limited information from a statistical convection model parametrized by the IMF orientation (Ruohoniemi and Baker, 1998; Chisham *et al.*, 2002; Provan *et al.*, 2002). Figure 4.24 shows an example of a SuperDARN convection map derived from measurements from six radars in a 2-min interval. The 2D velocity can then be resolved normal to a reconnection separatrix identified from a number of observational methods as follows.

Position and velocity of the reconnection separatrix

Particle precipitation The most direct and reliable method for locating the reconnection separatrix uses measurements by polar-orbiting spacecraft of the energy spectrum of approximately magnetic field-aligned electrons and ions that precipitate to ionospheric altitude without being mirrored by the magnetic field. From numerous observations made by the DMSP satellites, the energy spectra have been categorized into different types corresponding to different plasma regions in the Earth's magnetosphere (Newell *et al.*, 1991, 1996), some of which are on open magnetic field lines

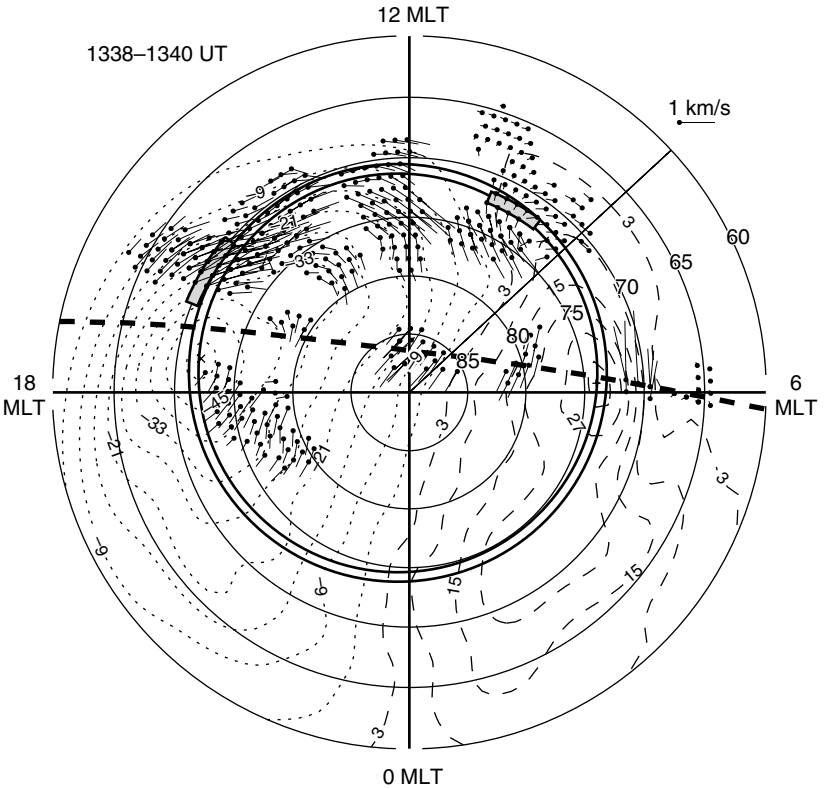

Fig. 4.24. A map of ionospheric convection in the northern polar ionosphere measured by SuperDARN. Geomagnetic latitude contours are shown by the thin black circles, magnetic local times are indicated around the lowest latitude circle. Short lines indicate 2D velocity vectors estimated from a spherical harmonic fit to available line-of-sight velocity measurements. Dots indicate the origin of the vectors. The dotted and dashed curves show the flow streamlines. Other features are explained in the main text.

and others on closed (Sotirelis and Newell, 2000). Thus one can identify the open–closed field line boundary (OCB), on which the reconnection separatrices lie in the most common reconnection scenario of Fig. 1.6a. More generally, the magnetopause reconnection separatrix can be identified for any IMF orientation from a dispersed ion signature (Burch *et al.*, 1980). A similar signature of the near-Earth reconnection separatrix in the magnetotail (Fig. 1.6b–d) may also exist (Sotirelis *et al.*, 1999).

Thus, the reconnection separatrix can be identified from its associated particle precipitation boundary (PPB) in most cases when it is crossed by a DMSP satellite or other polar-orbiting spacecraft with similar particle instrumentation. However, information on the separatrix position and velocity is limited by the long orbital period of about 100 min during which no more than two OCB crossings are made in each polar hemisphere, requiring considerable extrapolation in time and space. This can be improved by using data from more than one polar-orbiting spacecraft when available (Sotirelis *et al.*, 1998), but coverage is still a significant limitation.

Optical emissions When particles precipitate into the denser ionosphere they collide with other particles to give off light, causing the aurorae. The intensity and wavelength of the emission depends on the flux and energy of the precipitating particles and the particle composition of the ionosphere (Rees, 1963). Thus there is reason to believe that auroral observations at certain wavelengths should be able to identify the PPBs associated with reconnection. Most ground-based optical measurements are made in the red (630 nm) and green (557 nm) spectral lines. On the nightside, both of these lines correspond to precipitation energies associated with closed field lines and thus the OCB is identified with the poleward boundary of either red or green line emission, although the red line is thought to be the best indicator (Blanchard *et al.*, 1995). On the dayside, the reconnection separatrix is identified with the poleward edge of dominantly green-line emissions but the *equatorward* edge of dominantly red-line emissions, because high fluxes of low-energy electrons excite red aurorae on newly reconnected field lines in the cusp region (Lockwood *et al.*, 1993). Spacecraft imagers measure in other wavelengths besides the visible. In a large statistical study, the poleward boundary of UV emissions in the Lyman–Birge–Hopfield *Long* (LBHL) range (164–178 nm) measured by the Ultraviolet Imager (UVI) instrument on board the NASA Polar satellite (Torr *et al.*, 1995) has been shown to match closely the PPB proxy of the OCB measured by DMSP particle instruments, except in the early morning magnetic local time (MLT) sector (0–9 MLT) (Carbary *et al.*, 2003). Here, UV emissions in the 130–140 nm range appear to provide a more reliable proxy for the OCB (Wild *et al.*, 2004).

In contrast to the particle detectors on polar-orbiting spacecraft, ground-based optical imagers, such as those in the MIRACLE network (Syrjäsuo *et al.*, 1998), can sample a fixed latitude every 20 s continuously throughout the night, which may last for 3 months in the winter at polar latitudes, although observations are interrupted by clouds and the full Moon. Each image covers a circular area of ∼600 km diameter at ∼ 1 km resolution. Satellite-based optical imagers, such as Polar UVI, can image the aurora over an entire polar ionosphere at lower spatial resolution (∼30 km square at orbit apogee) every 37 s for prolonged periods of ∼9 hours per orbit. UV imagers are able to make observations in sunlight, although dayglow can dominate over the auroral emission at times.

Ionospheric electron density Particle precipitation also affects electron number density in the ionosphere through enhanced ionization. Thus, another OCB proxy has been identified with a latitudinal transition in ionospheric electron density, measured by the Sondrestrom incoherent scatter radar. On the nightside, the proxy is a sharp latitudinal cutoff of electron density in the E-region ionosphere, that is correlated with the 630 nm optical proxy of the nightside OCB (de la Beaujardière *et al.*, 1991; Blanchard *et al.*, 1996, 1997). On the dayside, the proxy is a latitudinal transition from high peak ionization rate or low peak altitude to low peak ionization rate or high peak altitude, derived from the electron density measurements (Blanchard *et al.*, 2001). This is correlated with the DMSP particle proxy of the dayside OCB.

HF radar spectral width Although designed to measure the $\mathbf{E} \times \mathbf{B}$ drift velocity of ionospheric plasma, a number of other diagnostics from the SuperDARN radars have been found to be useful. One of these is the width of the backscattered power spectrum (derived from the decorrelation time of the autocorrelation function of the backscattered radar signal), which is a measure of nonstationarity in the ionospheric medium on scales smaller than the radar sampling scales (i.e., 7 s and 45 km) (Villain *et al.*, 1996). Individual comparisons between a high spectral width region near noon MLT and particle signatures of newly reconnected magnetic field lines in the cusp region showed the sharp equatorward boundary of high spectral width to coincide with the OCB (Baker *et al.*, 1995). Similar latitudinal transitions from low to high spectral width are also apparent at other MLTs (Chisham and Freeman, 2004). Statistical studies have shown that such spectral width boundaries (SWBs) are a good proxy for the OCB in the 8–14 and 18–2 MLT sectors, but are displaced equatorward of the OCB in the 2–8 MLT sector (Chisham *et al.*, 2004b, 2005a). This MLT variation in the SWB latitude matches that of the poleward boundary of UV emissions in the LBH band referred to above. In the 14–18 MLT sector, the probability distribution of SWBs has two peaks in latitude with the more poleward SWBs ($>74^\circ$ latitude) being a good proxy for the OCB (Chisham *et al.*, 2005b).

Convection reversal From the open magnetosphere model for southward IMF (Fig. 1.6a), the OCB can also be expected to coincide with the convection reversal boundary between anti-sunward flow on high-latitude open magnetic field lines and sunward flow on lower-latitude closed field lines. Observationally, the convection reversal boundary proxy is found to be statistically co-located with the DMSP particle proxy of the OCB near noon MLT, but is progressively equatorward of it towards dawn and dusk (Sotirelis *et al.*, 2005), due to plasma circulation from viscous (nonreconnection) processes.

4.6.2 Examples

Pioneering studies

Remote sensing of magnetic reconnection in the magnetotail using the above method was pioneered by de la Beaujardière *et al.* (1991) and Blanchard *et al.* (1996, 1997) using the Sondrestrom incoherent scatter radar. They investigated how the magnetotail reconnection rate varied with magnetic local time, IMF variations, and substorm activity. The technique was later developed to remotely sense the reconnection rate at the magnetopause and its response to variations in the IMF (Blanchard *et al.*, 2001). However, these studies were limited to measurements along a magnetic meridian, such that the orientation of the separatrix had to be assumed and the reconnection rate was determined only at one point.

Remote sensing of spatially extended reconnection (at the magnetopause) began with the studies of Baker *et al.* (1997) and Pinnock *et al.* (1999) using the *Polar Anglo-American Conjugate Experiment* (PACE), comprising one HF radar in each polar hemisphere. These studies revealed the orientation of the reconnection separatrix to be variable in time and space and tilted by up to 40–50° with respect to a

contour of constant geomagnetic latitude, such that the assumptions in the earlier single-point studies were not always valid. Also, by comparing the reconnection rate integrated over the radar field of view with the global reconnection rate inferred from other measurements, the studies suggested that the reconnection separatrix was rarely contained within the radar field of view, highlighting the need for networks of radars to image the entire reconnection separatrix.

State of the art studies

A few studies have begun to do this using SuperDARN, supplemented by other instruments. Milan *et al.* (2003) studied the variation of the total net reconnection rate and the relationship between magnetopause and magnetotail reconnection during two substorm cycles. Using Eq. (4.33), the total net reconnection rate was calculated from the rate of change of the area of the open field line region. The OCB was monitored almost continuously in time and space using a combination of the poleward boundary of UV emissions determined from the Polar UVI, the equatorward boundary of high spectral width determined from six SuperDARN radars, and the poleward boundary of high-energy precipitation determined from three polar-orbiting spacecraft. The polar cap area was found to increase and decrease by a factor of three during the interval of study in a manner consistent with the near-Earth neutral line model (Section 1.2, Baker *et al.*, 1996). Separating the contributions from magnetopause and magnetotail reconnection, Milan *et al.* (2003) showed that nightside reconnection from the first substorm lasted less than 200 min, and likely only 100 min – the duration of the recovery phase of the first substorm.

Pinnock *et al.* (2003) studied the extent, and spatial and temporal variation of magnetopause reconnection during due southward IMF, addressing the scenario shown in Figure 1.6a. Figure 4.24 shows a snapshot of ionospheric convection at the time of one spacecraft encounter with the magnetopause when bidirectional plasma jets associated with reconnection were observed (Phan *et al.*, 2000). The bold circular annulus bounds the expected location of the OCB based on a lowest order extrapolation in space and time of observed OCB proxies from a DMSP F-13 satellite pass (bold dashed line) and from the Goose Bay radar. SWBs identified at this time from the Goose Bay and Finland radars are shown by the gray shaded regions. From a sequence of such snapshots, Pinnock *et al.* (2003) derived the ionospheric projection of the magnetopause reconnection rate wherever radar data existed, as summarized in the upper panel of Fig. 4.25. Overall, reconnection occurred over the entire MLT extent of radar observations from 8 to 16 MLT. Mapping this to the equatorial magnetopause using an empirical magnetic field model with a magnetopause position calibrated using the actual spacecraft encounters, suggests the reconnection separatrix length to be at least 38 R_E, extending beyond both the dawn and dusk flanks of the magnetopause.

The spatial distribution of the reconnection rate is relatively stable in time. The reconnection rate is relatively uniform in space over the morning sector, but appears to be more spatially structured in the afternoon sector. This structuring could be due to a genuine spatial variation in the reconnection rate or could arise from mesoscale structure of the OCB which is not captured by the lowest order approximation used (note the difference between the SWB and the fitted OCB in this sector in Fig. 4.24).

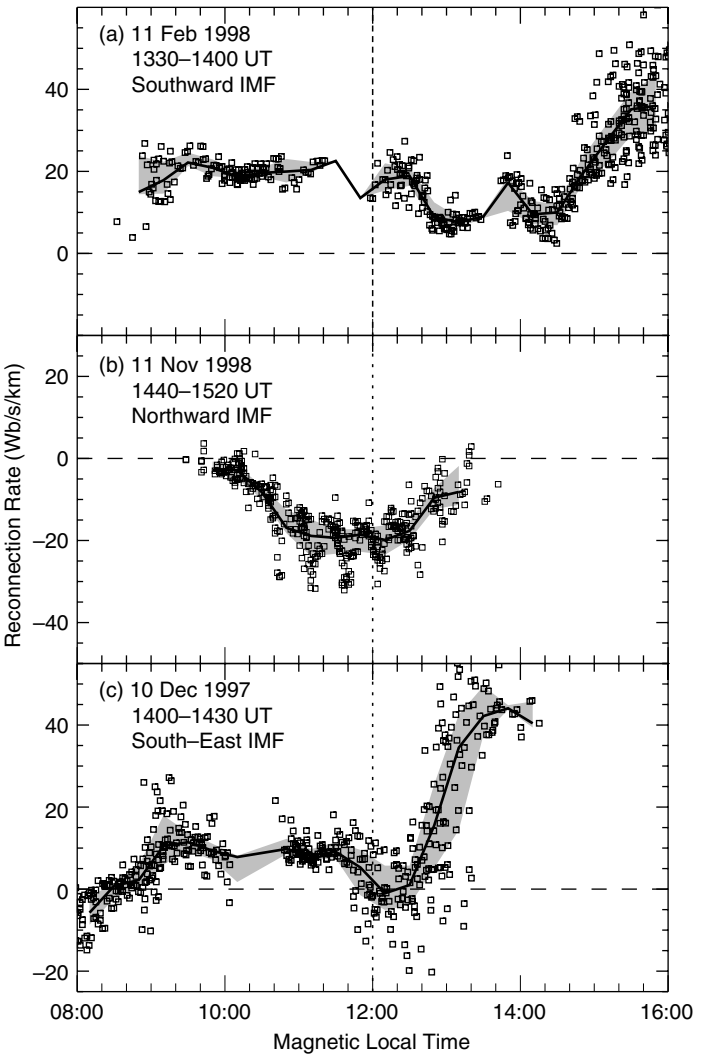

Fig. 4.25. The reconnection rate along the ionospheric projection of the magnetopause separatrix for (a) southward IMF, (b) northward IMF, and (c) intermediate IMF. Squares indicate individual measurements. The median and inter-quartile ranges of these in 20-min MLT bins are shown by the bold solid lines and gray shaded regions, respectively.

In either case, a physical explanation for this structure is unknown. The typical rate of magnetic flux reconnection per unit length of the separatrix in the ionosphere is $\sim 20\,\mathrm{Wb\ s^{-1}\ km^{-1}}$. Integrating this over the entire separatrix in its rest frame gives a minimum global reconnection rate of $\sim 150\,\mathrm{kWb/s}$ and dividing by the separatrix length at the magnetopause gives an average reconnection rate there of $\sim 0.6\,\mathrm{Wb\ s^{-1}\ km^{-1}}$, comparable with independent *in situ* spacecraft estimates under

similar conditions. To within the 2-min resolution of the observations, the results show that reconnection was continuous but probably variable in time.

This study has been complemented by a similar analysis of reconnection during an interval of steady, northward IMF (Chisham *et al.*, 2004a). The ionospheric projection of the magnetopause reconnection rate is summarized in the middle panel of Fig. 4.25. In this case, the reconnection separatrix was largely contained within the MLT extent of radar observations from 10 to 13 MLT, as can be seen by the drop to small reconnection electric fields at the MLT limits. The reconnection separatrix was found to map to the high-latitude magnetopause, anti-sunward of the cusp, with a length of $\leq 11\ R_{\rm E}$. The global reconnection rate of 10–16 kWb/s is an order of magnitude smaller than for the southward IMF case, whereas the average reconnection rate of $\sim 0.2\,{\rm Wb\ s^{-1}\ km^{-1}}$ at the magnetopause is only a factor of three lower. The spatial structure of the reconnection rate is again relatively stable in time and uniform in space over the central region between 10 and 12:30 MLT. Again, reconnection was continuous but probably variable in time.

The bottom panel shows the ionospheric projection of the magnetopause reconnection rate during steady southward IMF but with an eastward component of comparable magnitude, derived here from another study of reconnection (Coleman *et al.*, 2001). For this intermediate IMF case, the reconnection separatrix appears to be split into two parts with an area of negligible reconnection in between around noon MLT. When mapped to the magnetopause, the reconnection separatrix was found to lie close to the equator in the morning sector but at high latitude close to the cusp in the afternoon sector. The length of the reconnection separatrix was not fully imaged by the available radar data. The reconnection rate at the separatrix in the ionosphere is $\sim 10\,{\rm Wb\ s^{-1}\ km^{-1}}$ in the morning sector but $\sim 40\,{\rm Wb\ s^{-1}\ km^{-1}}$ in the afternoon. However, when mapped to the magnetopause this disparity is less and the average reconnection rate there is ~ 0.5–$1\,{\rm Wb\ s^{-1}\ km^{-1}}$, comparable with that derived for the southward IMF case.

4.6.3 Discussion

The examples in Section 4.6.2 illustrate how outstanding questions of magnetic reconnection that were difficult or inaccessible to study by localized ground-based or *in situ* observations can now be addressed. Since remote sensing provides a more continuous, larger-scale view of reconnection, it now seems easier to address the three general questions: (1) Where does reconnection occur? (2) What is the reconnection rate? (3) When does reconnection occur?

The location of magnetic reconnection on the Earth's magnetopause provides a strong constraint for magnetic reconnection theories and models. Plasma and magnetic field conditions vary widely over the magnetopause surface, such that the reconnection location can be used to identify the most favorable conditions for reconnection. In the three magnetopause examples summarized above, the location, stability, and rate of reconnection were remotely sensed for steady southward, northward, and intermediate IMF orientations. The measurement of reconnection around the entire equatorial magnetopause for due southward IMF and at high latitude anti-sunward of the cusp for northward IMF indicates that reconnection is not inhibited by high (probably super-Alfvénic) background flow speed and furthermore occurs

only in regions of maximal magnetic shear (i.e., antiparallel magnetosheath and magnetospheric magnetic fields). The intermediate IMF example was presented by Coleman *et al.* (2001) as a specific test of this antiparallel hypothesis, being under the conditions for which the ionospheric remote sensing signatures of antiparallel reconnection would be most different from low-latitude component reconnection (i.e., confined to the equatorial plane). Recognizing that antiparallel reconnection gives rise to bifurcated reconnection sites on the magnetopause whose positions depend on the IMF orientation and on the Earth's magnetic dipole tilt, the ionospheric projection of these sites is most separated in the winter polar hemisphere when the IMF is in this intermediate orientation, although the gap between them in the ionosphere is only 1–2 h of MLT. Although this separation is not clearly resolved in the bottom panel of Fig. 4.25, the reconnection rate does clearly drop to zero near noon as predicted by the antiparallel reconnection hypothesis. More convincingly, Coleman *et al.* (2001) predicted the split reconnection sites to elicit a particularly unusual and distinct convection signature, which is observed in the SuperDARN data. Furthermore, a double cusp signature was observed in a simultaneous overflight of the DMSP spacecraft, providing independent evidence of a bifurcated reconnection separatrix. Further events have been studied which show the characteristic convection signature, except in one case (Chisham *et al.*, 2002). Additional evidence has also come from ground-based optical observations of a bifurcated cusp under similar IMF and seasonal conditions (Sandholt and Farrugia, 2003). An alternative method to remotely sense the location of reconnection using particle observations from a polar-orbiting spacecraft has concluded that component and antiparallel reconnection may occur simultaneously on the magnetopause (Trattner *et al.*, 2004; Section 4.2) although the statistical basis for this has recently been contested (Abel *et al.*, 2005).

If the antiparallel reconnection hypothesis is borne out by further observation then this provides an interesting challenge to 3D global MHD reconnection theory and models. These predict that 3D MHD reconnection is more component-like than antiparallel-like, especially for IMF with a southward component (Siscoe *et al.*, 2001, see also Section 4.1). Reconnection is found to generally occur along the separator line connecting two magnetic null points near the cusp and passing through the subsolar region, and is mainly concentrated at low and middle latitudes around the subsolar region. This appears to contradict the observation of a gap with negligible reconnection rate near noon MLT in the Coleman *et al.* (2001) study. However, it has been suggested that optical observations under similar conditions could be explained within the 3D MHD framework (Sandholt and Farrugia, 2003). Further research is required, preferably combining optical and radar ionospheric remote sensing and *in situ* spacecraft observations at the magnetopause with 3D MHD models.

Accepting the mapping of ionospheric reconnection separatrices to antiparallel magnetic field regions on the magnetopause, the difference in the total magnetopause reconnection rate for the northward and southward IMF examples is primarily attributable to the length of the locus or loci where magnetospheric and magnetosheath field lines are antiparallel, which is necessarily shorter for due northward IMF. The average reconnection rate per unit length of the magnetopause for the northward IMF case is relatively similar to that for southward IMF (and

for intermediate IMF). Local MHD reconnection models suggest that the reconnection rate for antiparallel magnetic fields is proportional to the local Alfvén speed and it would be interesting to compare the remote sensing results with *in situ* measurements of the Alfvén speed in the predicted magnetopause reconnection regions.

To date, no equivalent ionospheric remote sensing studies of the location, structure, and rate of nightside reconnection have been published, although studies are underway (Mai-Mai Lam, private communication). Whilst the nightside reconnection rate can certainly be measured at the OCB, corresponding to a single and/or distant X-line in the magnetotail, ionospheric remote sensing of the reconnection rate at the near-Earth neutral line requires research to identify a suitable ionospheric proxy for this separatrix (Sotirelis *et al.*, 1999). The Milan *et al.* (2003) study showed that nightside reconnection was variable through the substorm and even ceased totally, but it is unclear how the relative contributions of these two magnetotail reconnection sites vary. Besides this, ionospheric remote sensing of the location of the reconnection sites in the magnetotail is very uncertain due to the greater uncertainties in mapping from the ionosphere to the magnetotail compared with mapping to the magnetopause.

Finally, the examples presented above concentrated on the properties of reconnection for a steady-state IMF or on long substorm time scales, and on spatial scales comparable with the global scale. There is considerable evidence that flows, magnetic fields, currents, aurora, and other phenomena associated with reconnection fluctuate on all scales in time and space (Freeman and Watkins, 2002). This would not be unexpected given the turbulent nature of the IMF and the nonlinear nature of solar wind/magnetosphere coupling. It would be interesting to use the remote sensing method to measure the inferred fluctuations in the reconnection rate but more work needs to be done to improve the analysis methods and the resolution and continuity of the observations.

5

Reconnection in the Sun's atmosphere

5.1 Coronal heating

E. R. Priest

Understanding how the Sun's outer atmosphere, or *corona*, is heated to a few million degrees by comparison with the temperature of its surface (or *photosphere*), namely only 6000 K, is one of the major challenges in astronomy or plasma physics. Until thirty years ago the main way of glimpsing the corona was during a solar eclipse (Fig. 1.1a), when the Moon cuts out the glare of the photosphere in white light and the much fainter corona comes into view with beautiful structures that are dominated for the most part by the magnetic field.

The corona has a threefold structure of *coronal holes, coronal loops,* and *X-ray bright points*, which was revealed by soft X-ray images from early rockets and Skylab. The Yohkoh satellite, in particular, has shown the corona to be an MHD world (Fig. 1.1b), with myriads of coronal loops continually interacting with one another. In the magnetically open regions (coronal holes) the plasma is streaming rapidly outwards as the fast solar wind, but in magnetically closed regions the magnetic field is able to contain the plasma at a higher density. Active regions lying above sunspot groups show up as a collection of loops in soft X-rays or EUV: images from the TRACE instrument reveal the highly complex nature of these loop systems (Fig. 5.1).

The energy required to heat the corona is typically $300\,\mathrm{Wm}^{-2}$ ($3\times10^5\,\mathrm{erg\ cm\ s}^{-1}$) in a quiet region or coronal hole and $5000\,\mathrm{Wm}^{-2}$ in an active region. The energy flux from the solar surface due to photospheric motions moving the footpoints of coronal magnetic fields is plentiful: since $\mathbf{E}=-\mathbf{v}\times\mathbf{B}$, the Poynting flux is

$$\frac{\mathbf{E}\times\mathbf{B}}{\mu_0}\approx\frac{v_\mathrm{h}B_\mathrm{h}B_\mathrm{v}}{\mu_0},$$

where v_h is the horizontal velocity and $B_\mathrm{h}, B_\mathrm{v}$ are the horizontal and vertical components of the magnetic field. Thus, in order of magnitude, a typical v_h of $0.1\,\mathrm{km\ s}^{-1}$, B_v of 200 G and B_h of 100 G would give a Poynting flux of $10^4\,\mathrm{Wm}^{-2}$. However, although B_v is measured well, the value of B_h is highly uncertain and depends on the nature of the coronal interactions, and therefore on the heating mechanism itself. Also, the details of how the energy flux is converted into heat and the efficiency of the various proposed heating mechanisms have not yet been determined.

In the corona the plasma velocity is generally much smaller than the Alfvén speed ($v_\mathrm{A}=B/\sqrt{\mu_0\rho}$), which is typically $1000\,\mathrm{km\ s}^{-1}$ (e.g., for a coronal magnetic field

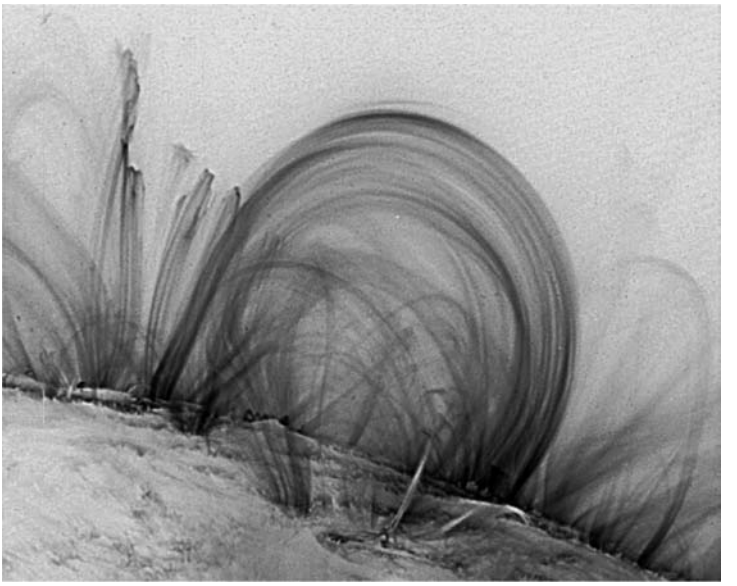

Fig. 5.1. An active region imaged by the Transition Region and Coronal Explorer (TRACE) (courtesy A. Title).

(B) of 10 G and a density (n) of $10^{15}\,\mathrm{m}^{-3}$). We therefore have a force balance, in which the ratio of the pressure gradient to the magnetic force is the plasma beta

$$\beta \approx \frac{3.5\,nT}{10^{21}B^2},$$

which is of order unity in strongly magnetic parts of the photosphere (where $n = 10^{23}\,\mathrm{m}^{-3}$, $B = 1500\,\mathrm{G}$, $T = 6000\,\mathrm{K}$) and also in the high corona (where $n = 10^{14}\,\mathrm{m}^{-3}$, $B = 2\,\mathrm{G}$, $T = 10^6\,\mathrm{K}$). However, in the low corona or in active regions (where $n = 10^{15}\,\mathrm{m}^{-3}$, $B = 200\,\mathrm{G}$, $T = 2 \times 10^6\,\mathrm{K}$, say), $\beta << 1$ and so we have a force-free equilibrium

$$\mathbf{j} \times \mathbf{B} = 0,$$

in which the magnetic pressure dominates over the thermal plasma pressure.

The coronal magnetic field is incredibly complex and such complexity may be described in terms of the magnetic *skeleton* (Priest *et al.*, 1996), which consists of a series of null points, *separatrices* (surfaces of field lines that generally originate from the fans of nulls and separate topologically distinct regions of space), and *separators* (field lines which join one 3D null point to another and represent the intersection of two separatrices – see Sections 5.1.4 and 5.2). Current sheets tend to form and dissipate at separatrices and separators, where the magnetic connectivity of coronal footpoints is discontinuous, but they can also do so at quasi-separatrices where the magnetic connectivity has steep gradients (Priest and Démoulin, 1995; Titov *et al.*, 2002), as described in Section 5.3.

Two classes of models for heating the corona have been proposed, namely reconnection and magnetic waves (e.g., Roberts, 1991; Goossens, 1991). However,

observational searches have shown that, at low frequencies (30–1000 s), waves do not appear to be present at high enough amplitude for coronal heating, although they are seen to be initiated by flares (e.g., Nakariakov *et al.*, 1999). Thus, reconnection is now seen as the most likely mechanism for coronal heating in most of the corona, although high-frequency ion-cyclotron waves may be important in the high corona, as evidenced by the surprisingly high line widths observed with the UVCS instrument on SOHO (Kohl *et al.*, 1997). Furthermore, Yohkoh and SOHO observations have given a wide range of evidence in favor of reconnection at work in the corona, notably the presence of cusps and interacting loops (Yoshida and Tsuneta, 1996), X-ray jets (Shibata *et al.*, 1992), explosive events (Dere *et al.*, 1989; Innes *et al.*, 1997), EIT brightenings (Bergmans and Clette, 1999), and rotating macrospicules (Pike and Mason, 1998).

Several ways have been proposed in which the corona may be heated by magnetic reconnection, namely: driven reconnection (Section 5.1.1), turbulent relaxation (Section 5.1.2), binary reconnection (Section 5.1.3), separator reconnection (Section 5.1.4), braiding and coronal tectonics (Section 5.1.5). As well as describing these, we also compare separator and separatrix heating (Section 5.1.4) and describe a recent estimate of the coronal recycling time (Section 5.1.6).

5.1.1 X-ray bright points: driven reconnection

X-ray bright points were first seen on rocket images and studied with Skylab by Golub *et al.* (1974, 1976). They are typically 20 Mm across and are uniformly distributed over the solar surface, with about 200 being present at one time and 1500 being born each day. Their mean lifetime is 8 hours and they are situated above pairs of opposite polarity magnetic fragments in the photosphere. One third of the bright points lie above emerging flux regions and so can be explained by the *emerging flux model* (Heyvaerts *et al.*, 1977), whereas the remainder lie above cancelling magnetic flux regions (Harvey, 1985; Martin *et al.*, 1985) and may be accounted for by the *converging flux model* (Priest *et al.*, 1994; Parnell *et al.*, 1994), in which the convergence of photospheric magnetic fragments drives reconnection in the overlying corona. The basic idea, illustrated in Fig. 5.2, is that magnetic flux emerges in a supergranule cell and then moves to the boundary, where one polarity tends to

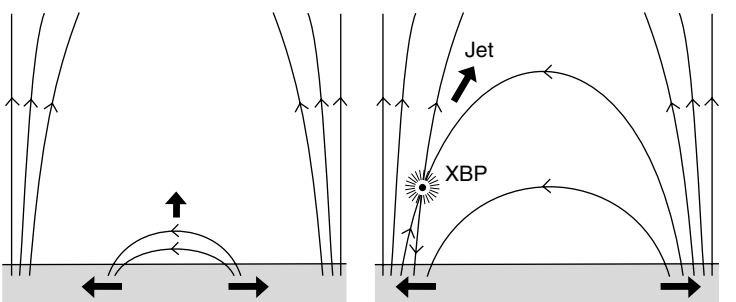

Fig. 5.2. The converging flux model for X-ray bright points.

accumulate while the other reconnects with opposite-polarity network. The model has been confirmed by a comparison with high-resolution X-ray (NIXT) observations.

5.1.2 Magnetic relaxation

At the same time as coronal structures are trying to evolve through nonlinear force-free equilibria in response to footpoint motions, they also tend to relax by 3D reconnection towards linear force-free states that conserve global magnetic helicity. Relaxation tends not to destroy magnetic helicity when the magnetic Reynolds number is very large, but it can convert it from one kind to another, such as from mutual to self helicity.

Heyvaerts and Priest (1984) suggested that the corona may be heated by relaxation as it evolves through a series of linear force-free states with the footpoint connections not preserved but the force-free constant (α) determined from the evolution of relative magnetic helicity (Berger and Field, 1984)

$$H_{\mathrm{m}} = \int (\mathbf{A} + \mathbf{A}_0)(\mathbf{B} - \mathbf{B}_0)\ \mathrm{d}V,$$

where $\mathbf{A}$ is the vector potential and $\mathbf{A}_0$, $\mathbf{B}_0$ refer to corresponding potential values with the same normal field at the boundary. Boundary motions cause the magnetic helicity to change in time according to

$$\frac{\mathrm{d}H_{\mathrm{m}}}{\mathrm{d}t} = 2 \int (\mathbf{B} \cdot \mathbf{A}_0)(\mathbf{v} \cdot \mathbf{n}) - (\mathbf{v} \cdot \mathbf{A}_0)(\mathbf{B} \cdot \mathbf{n})\ \mathrm{d}S.$$

Conceptually, photospheric motions tend to build up energy in a nonlinear force-free field, which then goes unstable and relaxes to a linear force-free field by reconnection.

Several extensions of the basic theory have been constructed. Vekstein *et al.* (1991) suggested intermediate relaxation to a state between the nonlinear and linear fields, while Vekstein *et al.* (1993) suggested that the corona is in a state of partial relaxation with the closed fields being relaxed linear force-free states and the open fields being potential. Furthermore, Heyvaerts and Priest (1992) realized that their earlier theory was incomplete, since it depends on an unknown relaxation time, so they proposed a more self-consistent approach assuming that photospheric motions maintain the corona in a state with a turbulent viscosity (ν^*) and diffusivity (η^*). First of all, they calculated the global resistive MHD state driven by boundary motions and deduced the heat flux ($F_{\mathrm{H}}(\nu^*, \eta^*)$). Secondly, they used cascade theories of turbulence to determine the values of ν^* and η^* which result from that F_{H}. This approach was applied to an arcade, a flux tube and to heating by wave motions. It was found to give reasonable heating and turbulence levels.

5.1.3 Binary reconnection

The surface of the Sun is covered with a multitude of magnetic sources which are continually moving around and which produce a highly complex magnetic field in the overlying corona, known as the *magnetic carpet* (Schrijver *et al.*, 1997). A key question is: what is the effect of the relative motions of photospheric sources in driving reconnection, and therefore heating, in the overlying corona? One possibility is *separator heating* due to the high-order interactions of several sources (see Sections 5.1.4

and 5.2), but a more fundamental process considered by Priest *et al.* (2003b) is the binary interaction due to pairs of sources.

The skeleton of the field due to two unbalanced sources (stars) in the photosphere is shown in Fig. 5.3, where a null point (filled circle) closest to the smaller source possesses a spine (thick line) that joins the null point to the weaker source and to infinity. It also possesses a fan surface of field lines that arch over the weaker source in the form of a dome and intersect the photosphere in a dashed curve. Part of the magnetic flux from the stronger source lies below the separatrix dome, while the remaining flux lies above it and links out to distant sources.

The suggestion is that the fundamental heating mechanism is one of so-called *binary reconnection* due to the motion of a given magnetic source relative to its nearest neighbor. The heating is due to several effects: (i) the 3D reconnection of field lines that start up joining the sources and end up joining the largest source to other more distant sources; (ii) the viscous or resistive damping of the waves that are emitted by the sources as their relative orientation rotates; and (iii) the relaxation of the nonlinear force-free fields that join the two sources and that are built up by the relative motion of the two sources.

5.1.4 Separator reconnection

Several distinct types of reconnection are associated with null points, namely, spine, fan, and separator reconnection (Priest and Titov, 1996) and, in particular, separator reconnection is a prime candidate for coronal heating. Numerical experiments have been conducted on this possibility (Galsgaard and Nordlund, 1997; Parnell and Galsgaard, 2004) and the way in which it operates in detail has been studied by Longcope and coworkers, as follows.

Having shown how a current sheet may form along a separator (Longcope and Cowley, 1996), a stick–slip model for reconnection was developed together with the

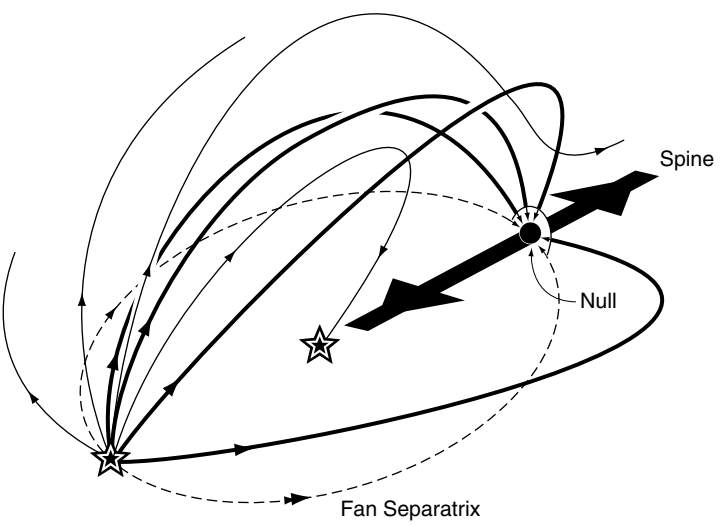

Fig. 5.3. Skeleton of the field due to two unbalanced sources (stars).

concept of a "minimum-current corona" (Longcope, 1996). The assumption is that, due to slow motions of the photospheric footpoints, the corona continually relaxes to a flux-constrained equilibrium in which the magnetic fluxes within each domain are conserved but the field lines within each domain can slip through the plasma or move their footpoints (Longcope, 2001). Such equilibria have potential magnetic fields in each domain and current sheets along the separators. The theory has been applied to X-ray bright points (Longcope, 1998).

Priest *et al.* (2005) stress that in general the effect of slow photospheric motions on complex coronal magnetic configurations will be to generate three forms of current, namely, distributed currents throughout the volume, current sheets on separators, and current sheets on separatrices. They compare energy storage and heating at separators and separatrices by using reduced MHD to model coronal loops that are much longer than they are wide.

For example, Fig. 5.4 schematically shows a section across a cylindrical loop. Figures 5.4a and 5.4b show the initial states at the two ends when there are two discrete sources (large dots) of magnetic flux at each end, with a separatrix separating the field lines from the two sources, and a separator that is the intersection of the two separatrices. After spinning and rotating all four sources, current sheets will be created along the separatrices and separator (Fig. 5.4c), and after reconnection the sheets dissipate and the configuration reduces to a relaxed state (Fig. 5.4d) that conserves magnetic helicity. They deduce that separatrices are twice as effective for coronal heating as separators, for observed footpoint motions.

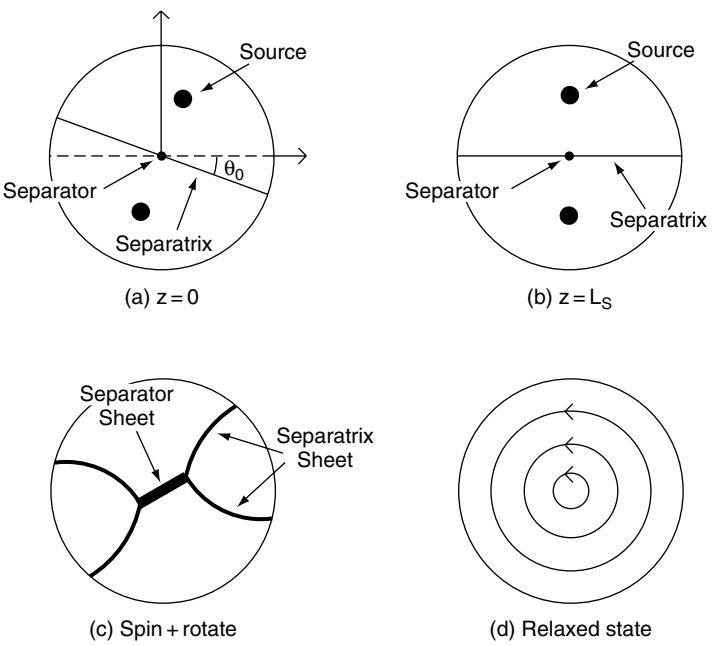

Fig. 5.4. Projection of magnetic field lines in a section across the coronal part of a flux tube for (a) initial state at $z = 0$, (b) initial state at $z = L_s$, (c) configuration after spinning and rotating sources, (d) relaxed state.

5.1.5 Coronal tectonics

In determining the effect of the magnetic carpet on coronal heating, three factors are important: the concentration of flux in the photosphere into discrete intense flux tubes; their continual motion; and the fact that the global topology of the complex coronal field consists of a collection of topologically separate volumes divided from one another by *separatrix* surfaces.

A *coronal tectonics model* for coronal heating (Priest *et al.*, 2002) takes account of these three factors. Each coronal loop has a magnetic field that links the solar surface in many sources. The flux from each source is topologically distinct and is separated from each other by separatrix surfaces (Fig. 5.5). As the sources move, the coronal magnetic field slips and forms current sheets along the separatrices, which then reconnect and heat. Thus, in our view, the corona is filled with myriads of separatrix current sheets continually forming and dissipating.

But the fundamental flux units in the photosphere are likely to be intense flux tubes with fields of 1200 G, diameters of 100 km (or less) and fluxes of 3×10^{17} Mx (or less). A simple X-ray bright point thus links to a hundred sources and each TRACE loop probably consists of at least ten finer, as yet unresolved, loops.

Whereas Parker's braiding model assumes complex footpoint motions acting on a uniform field, Priest *et al.* (2002) consider the effect of simple motions on an array of flux tubes that is anchored in small discrete sources. For a simple model consisting of an array of flux tubes anchored in two parallel planes, they have demonstrated the formation of current sheets and have estimated the heating. A more realistic model would have the sources asymmetrically placed so as to create many more separatrices, or, more realistic still, it would place all the sources on one plane and have mixed polarity. The basic principles would, however, be unchanged.

The results give a uniform heating along each separatrix, so that each (sub-telescopic) coronal flux tube would be heated uniformly. But at least 50% of the photospheric flux closes low down in the magnetic carpet (Close *et al.*, 2004b), so the remaining 50% forms large-scale connections. Thus, the magnetic carpet would be heated more effectively than the large-scale corona. Unresolved observations of coronal loops would give enhanced heating near the loop feet in the carpet, while the upper parts of coronal loops would be heated uniformly but less strongly.

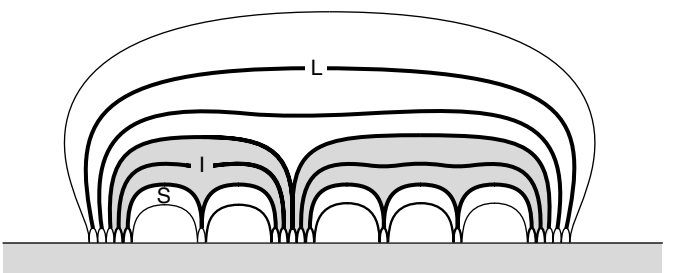

Fig. 5.5. A schematic of a coronal loop consisting of many sub-volumes, each linked to a separate source and divided from one another by *separatrix* surfaces.

5.1.6 Coronal reconnection time

Photospheric sources of the coronal magnetic field are highly fragmentary and concentrated into intense flux tubes threading the solar surface. They are also highly dynamic, with magnetic flux emerging continually in the quiet Sun and then undergoing processes of fragmentation, merging, and cancellation, in such a way that the quiet Sun photospheric flux is reprocessed very quickly, in only 14 hours (Hagenaar, 2001).

Recently, Close *et al.* (2004b) have wondered what the corresponding coronal reprocessing time is, and have used observed quiet-Sun magnetograms from the MDI instrument on SOHO to construct the coronal magnetic field lines and study their statistical properties. For the region they considered, 50% of the flux closed down within 2.5 Mm of the photosphere and 95% within 25 Mm, the remaining 5% extending to larger distances or being open (Fig. 5.6). They then tracked the motion of individual magnetic fragments in the magnetogram and recalculated the coronal field lines and their connectivity. In so doing, they discovered the startling fact that the time for all the field lines in the quiet Sun to change their connections is only 1.5 hours. In other words, an incredible amount of reconnection is continually taking place – indeed, enough to provide the required heating of the corona.

5.1.7 Conclusion

Coronal heating is likely to be produced by a variety of mechanisms. Several of those that have been proposed over the past ten years are apparently viable and so more detailed modeling and observations are required in order to distinguish between them. Magnetic reconnection has emerged as the most likely process, especially in view of the extremely short coronal recycling time that has been deduced by Close *et al.* (2004b), but the mechanism in which it operates is as yet unknown.

Likely mechanisms include the following. For X-ray bright points, driven reconnection in the converging flux model is probable. For coronal loops, the recent realization of the extreme complexity of the coronal field with myriads of separatrix and separator current sheets forming and dissipating in the coronal tectonics scenario (Priest *et al.*, 2002) is highly appealing. However, within that scenario, several mechanisms or ways of describing the heating process are possible, such as: turbulent magnetic relaxation, binary reconnection, and separator reconnection.

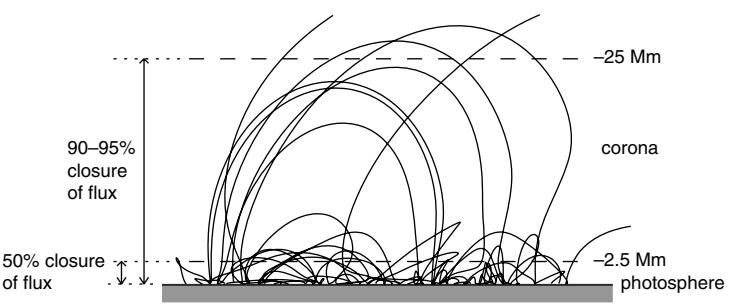

Fig. 5.6. Magnetic field lines in the quiet Sun (Close *et al.*, 2004b).

In future, there is a need to develop collisionless versions of the above mechanisms, since the coronal mean free path is typically 10 km, much larger than the widths of the reconnecting current sheets. Furthermore, a series of planned space missions (Solar B, 2006; Solar Dynamics Observatory, 2008; Solar Orbiter, 2017) will certainly produce surprises and provide further observational details of coronal heating processes.

5.2 Separator reconnection

D. W. Longcope

As discussed in Section 5.1, separators (i.e., lines where topological boundaries, separatrices, intersect) are preferred sites for current intensification and reconnection. In this section we therefore focus on reconnection at a separator (Priest and Titov, 1996). Models of quasi-static evolution show that current tends to accumulate at topological boundaries, making it possible for a localized reconnection electric field to liberate magnetic energy stored throughout the coronal field by separator reconnection. We first present a simple example of a two-dimensional, quadrupolar coronal field model (Section 5.2.1), followed by a three-dimensional generalization (Section 5.2.2). Section 5.2.3 addresses specifics of reconnection in this context and Section 5.2.4 presents observational evidence for separator reconnection.

5.2.1 X-point current in two dimensions

The simplest example of quasi-static energy storage punctuated by rapid reconnection is found in a two-dimensional, quadrupolar coronal field. Four sunspots, denoted P1, N2, P3, and N4 are distributed along the photospheric surface, $z = 0$, in a sequence of alternating sign (see Fig. 5.7a). The two-dimensional coronal field created by these sources is written $\mathbf{B} = \nabla A \times \hat{\mathbf{x}}$, so that field lines can be visualized by contouring the flux function $A(y, z)$. We take the field initially to be current-free, $\nabla \times \mathbf{B} = -\hat{\mathbf{x}}\nabla^2 A = 0$, so that it has the minimum energy possible subject to the photospheric field distribution. This field contains a single X-point, $\mathbf{x}_\mathrm{o}$, above the photosphere. The contour at the saddle point, $A(y, z) = A(\mathbf{x}_\mathrm{o})$, defines four separatrix field lines shown as dark curves in Fig. 5.7a, originating at the X-point and terminating in each of the four photospheric sources. These curves divide the coronal half-space into four topologically distinct classes of field lines, called *flux domains*.

The domain consisting of field lines connecting sources P3 and N2 lies directly under the X-point. For the potential field shown in Fig. 5.7a domain P3–N2 accounts for 30% of the flux leaving P3; the remaining flux connects P3 to N4. The photospheric sources then move slowly due to forces originating below the surface, leading to a new potential coronal field with a different apportionment of domain fluxes. In Fig. 5.7b sources P3 and N2 have approached one another to create a potential field with more flux in domains P1–N4 and P3–N2 (the shaded contours) and less in domains P1–N2 and P3–N4. In order to achieve this new potential field (the new minimum energy state) it would be necessary to reconnect field lines from the latter two domains to create new field lines for the shaded portions of the former domains. The extent of the reconnection required is quantified by ΔA, the difference in $A(\mathbf{x}_\mathrm{o})$ before and after the photospheric motion.

A perfectly conducting corona is incapable of supporting the electric field to reconnect field lines. In this case the field will not be able to relax to the potential

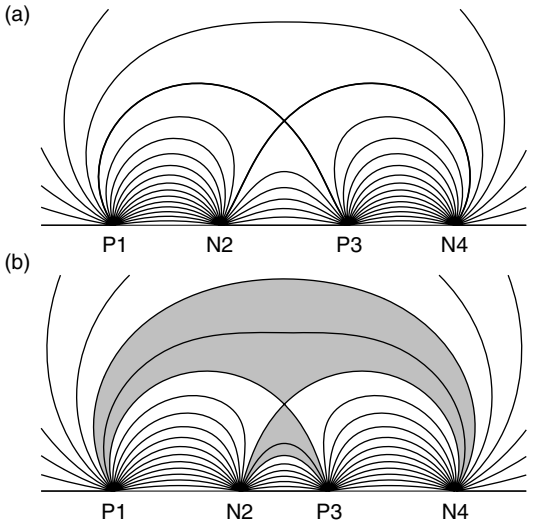

Fig. 5.7. Two-dimensional potential fields from four photospheric sources. Solid lines are contours of $A(y, z)$ which are field lines. (a) The initial field showing separatrices as dark curves meeting at the X-point. (b) The potential field after sources P3 and N2 have moved toward the center. The shaded region shows the flux which must be transfered through the X-point to produce this field from field (a).

field which is its state of minimum energy. A class of equilibrium coronal fields maintaining the original apportionment of domain fluxes, which is therefore consistent with ideal coronal evolution, was first proposed by Priest and Raadu (1975), refined by Hu and Low (1982), and generalized by subsequent authors (Aly and Amari, 1989; Titov, 1992). This field is current-free except for a current sheet (a discontinuity in $\mathbf{B}$) where the X-point formerly was (see Fig. 5.8). It can be shown (Longcope, 2001) that this field has the minimum energy possible subject to the constraint on the flux in domain P3–N2: it is the *flux-constrained equilibrium* (FCE). The size and net current in the sheet depend on ΔA, shown shaded in Fig. 5.8. Figure 5.8b shows the effect of a smaller ΔA: a shorter current sheet carrying less current.

The singularity in the flux-constrained equilibrium is related to the equilibrium current sheet first described by Green (1965) and later by Syrovatskii (1971), an example of which is shown in Fig. 5.9a. Far from the sheet this field approaches an X-point structure, $\mathbf{B} = B'(y\hat{\mathbf{z}} + z\hat{\mathbf{y}})$, set by the boundary conditions. A sheet carrying current I will have an extent (width)

$$\Delta = \sqrt{\frac{4\mu_0 |I|}{\pi B'}}. \tag{5.1}$$

The field adjacent to the sheet vanishes at each tip and increases to a maximum $B_\mathrm{o} = B'\Delta/\sqrt{2}$ at the middle. The direction of the field is discontinuous across the sheet, but its magnitude is not.

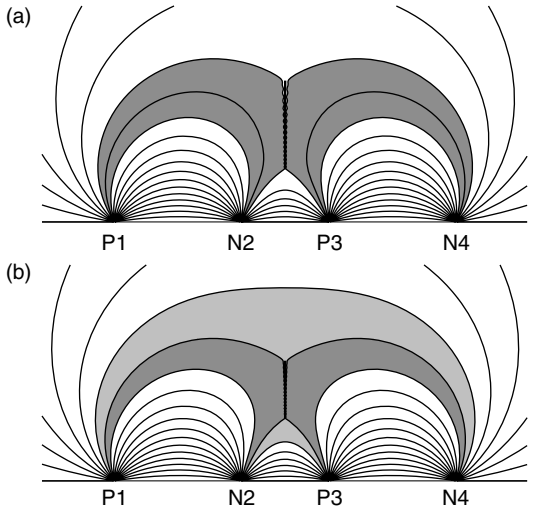

Fig. 5.8. Flux-constrained Priest–Raadu equilibria for photospheric source locations matching Fig. 5.7b. (a) The equilibrium whose flux apportionment matches the initial field from Fig. 5.7a. The current sheet is shown as a dark vertical line, and the shaded regions are those field lines which would have been reconnected had the field relaxed to its potential state. (b) The case where ΔA is half as large. The lighter shading shows reconnected flux and the darker shows unreconnected flux. The current sheet is shorter and carries less current than that in (a).

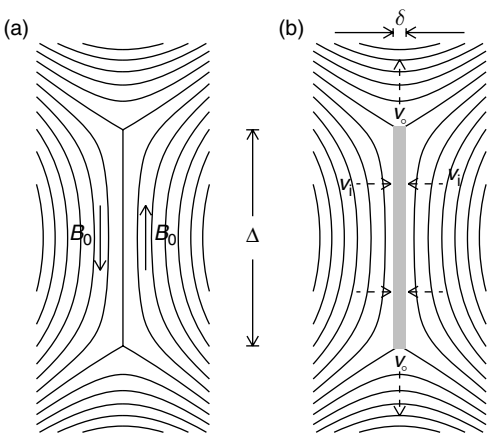

Fig. 5.9. Two-dimensional current sheets. (a) A singular equilibrium sheet of the Green–Syrovatskii type. The width Δ and field strength B_o are fixed by the total current I and asymptotic magnetic shear B'. The sheet occurs at the vertical discontinuity across which the field direction changes from downward (left) to upward (right). (b) The corresponding Sweet–Parker sheet of thickness δ, is shown as a shaded layer. The slow inflows, v_i, and Alfvénic outflows, v_o, are shown as dashed arrows.

Placing the Green–Syrovatskii current sheet at the X-point of the potential coronal field changes the flux function of the separatrices by (Longcope and Cowley, 1996; Longcope, 2001)

$$\Delta A = \frac{\mu_0 I}{4\pi} \ln\left(\frac{16\pi \mathrm{e} B' z_\mathrm{o}^2}{\mu_0 |I|}\right), \tag{5.2}$$

where $\mathrm{e} = 2.7128$ is the base of the natural logarithm and B' is the magnetic shear at the potential X-point located at $\mathbf{x}_\mathrm{o} = (0, z_\mathrm{o})$. For a specified flux constraint, ΔA, this equation may be inverted to find the current $I(\Delta A)$, and from that the width $\Delta(\Delta A)$. The energy per unit length by which the current sheet raises the field's energy is (Syrovatskii, 1981; Longcope, 2001)

$$\Delta W(\Delta A) = \int_0^{\Delta A} I(\Delta A')\, \Delta A' = \frac{\mu_0 I^2}{32\pi^2} \ln\left(\frac{16\pi\sqrt{\mathrm{e}} B' z_\mathrm{o}^2}{\mu_0 |I|}\right). \tag{5.3}$$

This is the free magnetic energy stored throughout the field as a result of the flux constraint. By eliminating the flux constraint magnetic reconnection can liberate at least this much energy. (For a derivation of the basic properties of a separator current sheet, see Priest *et al.* (2005).)

The flux constrained equilibrium described above is the minimum energy state for the field under perfectly conducting evolution. It will therefore be an attractor for nonlinear dynamical evolution with some form of energy dissipation. Studies indicate that such a singular field can be approached only asymptotically from a continuous initial condition (Wang and Bhattacharjee, 1994; Klapper, 1998), so the FCE may never be achieved. The evolution will, however, seek to concentrate a net current of approximately $I(\Delta A)$ into a vertical layer of width $\Delta(\Delta A)$, even if its thickness can never decrease to zero.

Small nonideal effects, such as the presence of magnetic resistivity η, will not affect the global dynamics which establishes the current sheet with global parameters, I, Δ, and B_o, but will dictate the inner structure of the sheet, including its thickness δ. The effect of resistivity can be characterized in terms of the Lundquist number of the current sheet

$$S_\Delta \equiv \frac{B_\mathrm{o}\Delta}{\eta\sqrt{\mu_0\rho}} \simeq \frac{1}{\eta\sqrt{\mu_0\rho}} \left|\oint \mathbf{B}\cdot \mathrm{d}\mathbf{l}\right| = \frac{|I|}{\eta\sqrt{\rho/\mu_0}}. \tag{5.4}$$

The denominator of the right-most expression is a current $I_\mathrm{sp} \equiv \eta\sqrt{\rho/\mu_0}$, depending only on the local properties of the plasma. Classical, collisional resistivity (*Spitzer resistivity* (Spitzer, 1962)) in a fully ionized hydrogen plasma of temperature T_6 Mk and electron density $n_\mathrm{e} = n_9 \times 10^9\,\mathrm{cm}^{-3}$ leads to current parameter $\mathrm{i}_\mathrm{sp} \simeq 2.3 \times 10^{-3}\, T_6^{-3/2} n_9^{1/2}$ A. Thus any foreseeable current concentration in the solar corona ($|I| \gg 10^6$ A) will have an extremely large Lundquist number, $S_\Delta = |I|/I_\mathrm{sp}$.

Sweet–Parker theory (Section 2.1) provides a self-consistent model for the properties of a quasi-steady-state current sheet in the presence of uniform magnetic resistivity η. Due to the slowness of Sweet–Parker reconnection the ideal evolution outside the sheet will tend toward equilibrium, establishing the global current sheet with parameters Δ, I, and B_o as described above. These parameters, as well as the

Lundquist number of the sheet, are all set by the external evolution and thus by the photospheric boundary condition. The thickness of the Sweet–Parker current sheet,

$$\delta = S_\Delta^{-1/2}\Delta = \sqrt{\frac{4\mu_0 I_{\rm sp}}{\pi B'}}, \tag{5.5}$$

depends on the plasma and on B', the magnetic shear of the external field. The reconnection electric field within the current sheet drives an inflow velocity

$$v_{\rm i} \sim S_\Delta^{-1/2}\frac{B_{\rm o}}{\sqrt{\mu_0\rho}} = \sqrt{\frac{2I_{\rm sp}B'}{\pi\rho}}. \tag{5.6}$$

In notable contrast to cases of driven magnetic reconnection, this inflow does not depend on the rate at which the photospheric sources move. This velocity is in fact so small ($\sim$0.3 m/s) that it appears to the external dynamics that the current sheet is an equilibrium with no flow at all.

The Sweet–Parker reconnection transfers flux across the X-point, thereby somewhat mollifying the flux deficit ΔA: $\mathrm{d}(\Delta A)/\mathrm{d}t = B_{\rm o}v_{\rm i}$. At this rate the potential field can be reestablished after a time

$$\tau_{\rm sp} \equiv \frac{\Delta A}{B_{\rm o}v_{\rm i}} \sim S_\Delta^{1/2}\frac{\sqrt{\mu_0\rho}}{B'}. \tag{5.7}$$

The factor on the right is the Alfvén time, $\tau_{\rm A} = \sqrt{\mu_0\rho}/B'$ over which a disturbance will propagate into the X-point of the potential field (Craig and Watson, 1992; Hassam, 1992). Since $S_\Delta \gg 1$ the reconnection time is extremely long compared with the ideal dynamics of the external field. This is effectively equivalent to the assumed absence of reconnection during which the quasi-steady current sheet is established. Finally, we note that the Ohmic power dissipation at the sheet, $P_{\rm sp} \sim \Delta W/\tau_{\rm sp}$, is so small that it can be entirely neglected.

In spite of the current sheet and resistive electric field, the scenario described above is one of quasi-static current accumulation and energy storage if fast reconnection (Section 2.1) does not occur. Slow motion of the photospheric sources demanded a readjustment of the coronal equilibrium. Under the assumption that reconnection was even slower than the photospheric motion, the new equilibrium could not be a potential field. Even if the field within each domain could fully relax, the lack of fast reconnection would prevent the transfer of flux between domains and thereby demands current accumulation at domain interfaces; specifically at the X-point. Due to the quasi-static nature of the model, the current accumulated depends on the photospheric displacement, quantified by ΔA, but not the velocity. If the current accumulation is structured according to Sweet–Parker theory, then the resistive electric field it creates will accomplish negligible reconnection or energy dissipation, consistent with the assumption of quasi-static external evolution.

The current sheet is not, therefore, an engine of reconnection in this scenario but is rather one of energy storage. If substantial reconnection is to occur, as observations suggest it does, the Sweet–Parker current sheet must be somehow disrupted in order to substantially enhance its electric field. Once this happens, the magnetic energy, $\Delta W(\Delta A)$, stored in the equilibrium current sheet may be converted into other forms. We return to consider actual reconnection within a three-dimensional geometry.

5.2.2 Separator current in three dimensions

A three-dimensional generalization of the quadrupolar geometry above was first outlined by Sweet (1958b), and later studied by numerous others (Baum and Bratenahl, 1980; Syrovatskii, 1981; Hénoux and Somov, 1987; Gorbachev and Somov, 1988; Priest and Forbes, 1989). The same four sunspots (flux sources) are arranged on the photospheric plane, $z = 0$, but no longer in a straight line (see Fig. 5.10). As in the two-dimensional case, the potential field anchored to these sources consists of four classes of field lines which define four flux domains. In the potential field these four domains meet not at a point, as they did in two dimensions, but rather along a single field line called the *separator* (the dark curve in Fig. 5.10). This separator field line plays the same topological role in this three-dimensional field as the X-point did in the two-dimensional field of Fig. 5.7a. Reapportionment of flux between domains requires an electric field along the separator (Sweet, 1958b); the absence of such an electric field will lead to the accumulation of current in a thin current ribbon there.

With the exception of the four sources, P1, N2, P3, and N4, the photosphere is assumed to have no vertical field, but will in general have horizontal field throughout. This horizontal photospheric field spreads outward and inward from positive and negative sources respectively. According to the Poincaré index theorem (Molodenskii and Syrovatskii, 1977) it must vanish at exactly two points when the field is continuous; these points are denoted by triangles in Fig. 5.10 and labeled B1 and A2. Each has the structure of a three-dimensional null point: two spine field lines and a surface of fan field lines all terminating at the null point (Cowley, 1973; Lau and Finn, 1990; Parnell *et al.*, 1996). The fan surface of the negative null, A2, consists of field lines which almost all originate in one of the positive sources, P1 or P3 as shown in Fig. 5.11a. The surface forms a dome separating the field lines ending at N2 (beneath the dome) from those ending at N4, outside it. The fan surface of the positive null, B1 (not shown), forms a similar dome over P3 separating its flux from that of P1.

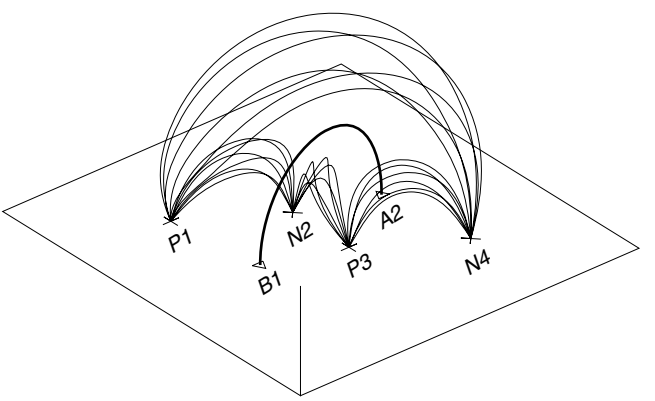

Fig. 5.10. Sweet's configuration illustrating the interaction of four flux sources in a three-dimensional potential corona. The sources are marked with + and × and null points with △ (negative) and ▽ (positive). Thin solid lines are representative field lines from each of the four flux domains. The dark solid line is the separator field line at which all four domains meet.

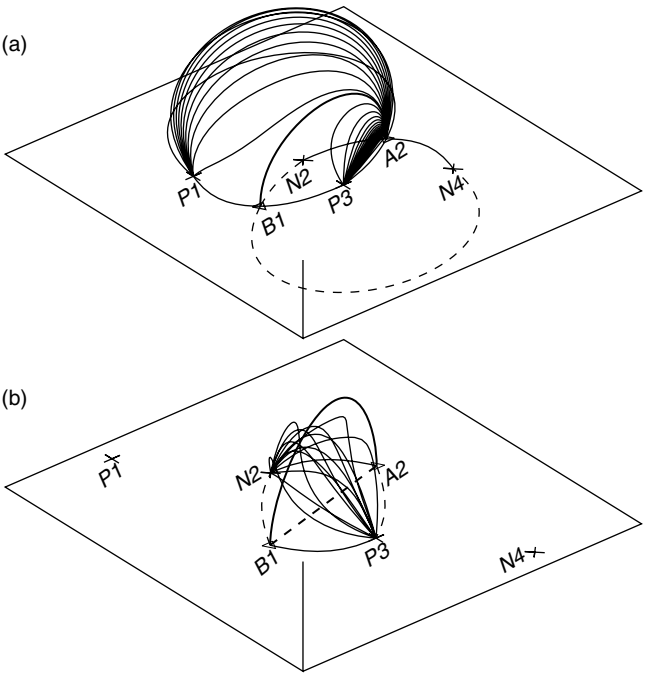

Fig. 5.11. One separatrix and the only separator in Sweet's configuration. (a) Fan field lines from the negative null point A2 shown as solid curves extending into the corona, $z > 0$, to form a dome over the negative sources N2. The dashed and solid lines within the photospheric plane are the footprint of the other fan (not shown). The thick solid line is the separator; it is that part of the fan surface separating field lines ending in P3 from those ending in P1. (b) The isolating loop $\mathcal{Q}$ consisting of the separator (dark solid line) and a photospheric return path (dark dashed line). Thin solid lines in the corona are representatives of flux domain P3–N2, each passing through $\mathcal{Q}$. Dashed and solid curves within the photospheric plane are the fan traces and spines of the null points.

Together the two separatrices partition the coronal volume into its four flux domains. The separatrices intersect along a single field line, the separator, which begins at B1 and ends at A2. All field lines in domain P3–N2 must pass under this curve since they must lie beneath both of the separatrix domes at once. Adding a curve connecting the null points along the photosphere (the thick dashed curve in Fig. 5.11b) creates a closed loop $\mathcal{Q}$ through which every P3–N2 field line must pass. The net flux in that domain may thus be expressed as the integral

$$\psi_{32} = \oint_{\mathcal{Q}} \mathbf{A} \cdot \mathrm{d}\mathbf{l}, \tag{5.8}$$

where $\mathbf{A}$ is the vector potential. Any change in the flux of domain P3–N2 requires a loop voltage around $\mathcal{Q}$. Except for transport across the photosphere, corresponding to flux emergence or submergence, such a loop voltage must result from a parallel electric field along the separator: *separator reconnection* (Priest and Titov, 1996).

As the flux sources move slowly across the photosphere the potential field above will evolve. As it does so, the potential flux in domain P3–N2, denoted $\psi_{32}^{(\mathrm{v})}$, will change by an amount $\Delta\psi$. Without a parallel electric field along the separator such a flux transfer would be impossible and the coronal field could not relax to its potential state. Once again we can adopt the flux-constrained equilibrium as a field consistent with nonresistive coronal evolution. This is the state of minimum magnetic energy for a specified flux ψ_{32}. It is current-free except for a ribbon flowing along the separator (Longcope, 2001, see Fig. 5.12). The width of this ribbon and the current it carries are determined by the discrepancy $\Delta\psi_{32} = \psi_{32} - \psi_{32}^{(\mathrm{v})}$ between actual flux and potential flux.

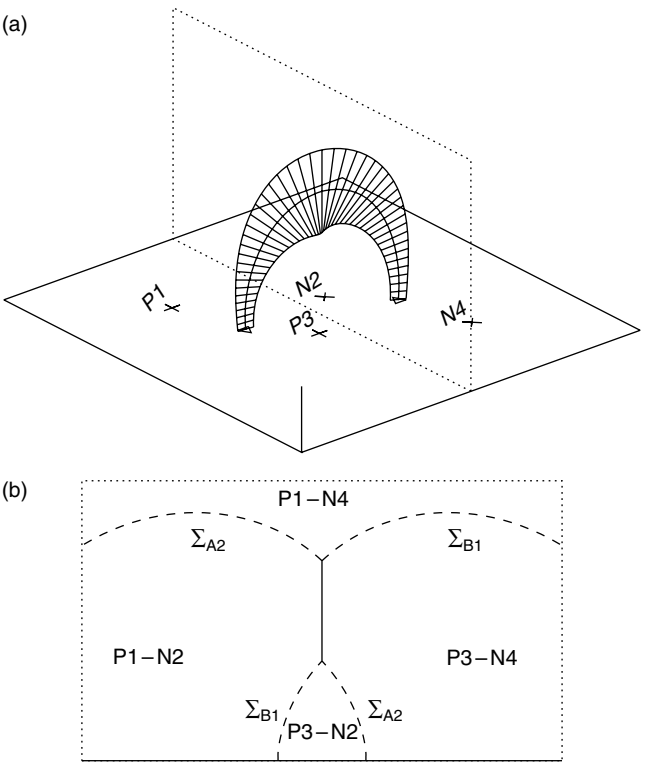

Fig. 5.12. The flux-constrained equilibrium resulting from a rotation of sources P3 and N2 about the central point. (a) The shape of the current ribbon is indicated by a series of span-wise ribs crossing the potential separator. The photospheric null points of the potential field are once again shown as a $\triangle$ and a $\triangledown$. The current flows from $\triangle$ to $\triangledown$ (roughly from the right to the left of the picture). The dotted rectangle is a surface used to illustrate the structure of the field. (b) The separatrices crossing the surface (dashed curves). Separatrix Σ_{A2} originates in A2, similar to the one shown in Fig. 5.11a. It separates field lines ending in N2 from those ending in N4. The two separatrices partition the plane into the four labeled domains: P1–N2 etc. The dark vertical line is the current sheet occurring at the intersection of the two separatrices; the current flows out of the page.

As in the two-dimensional case, the FCE may be constructed by adding a current sheet to the potential magnetic field. The potential field in the neighborhood of the separator will have a local shear perpendicular to its axis denoted $B'(\ell)$, where ℓ is the length coordinate along the separator (Longcope and Silva, 1998; Longcope and Magara, 2004). A current sheet carrying current I will have a width, $\Delta(\ell) = \sqrt{4\mu_0|I|/\pi B'(\ell)}$, in direct analogy with the Green–Syrovatskii sheet of two-dimensional theory. This will vary, as it does in Fig. 5.12, due to variation in the shear along the separator.

The addition of this current ribbon contributes a self-flux (Longcope and Silva, 1998; Longcope and Magara, 2004)

$$\Psi^{(\mathrm{cr})} = \frac{\mu_0 I L}{4\pi} \ln\left(\frac{\mathrm{e} I^\star}{|I|}\right), \tag{5.9}$$

where L is the length of the potential field's separator and $I^\star$ characterizes its local magnetic shear (it is proportional to L^2 times the shear parameter $B'(\ell)$ averaged over its length, using the geometric mean). This expression is the analogue of (5.2) with the X-point's height, z_o, replaced by L times a factor from the separator's geometry. The flux constraint requires that $\Psi^{(\mathrm{cr})} = \Delta\psi$, thereby fixing the current I in terms of the boundary conditions. The additional magnetic energy demanded by the flux constraint is found by integrating the work required to build the current

$$\Delta W(\Delta\psi) = \int_0^{\Delta\psi} I(\Delta\psi')\,\Delta\psi' = \frac{\mu_0 I^2 L}{32\pi^2} \ln\left(\frac{\sqrt{\mathrm{e}} I^\star}{|I|}\right). \tag{5.10}$$

5.2.3 Initiation of reconnection

Solar flare observations suggest that coronal magnetic energy accumulates slowly (quasi-statically) in the corona before being rapidly converted into other forms such as thermal energy, bulk kinetic energy, and nonthermal particles. The leading hypothesis has long been that magnetic reconnection is responsible for this rapid energy conversion. One possibility is that fast reconnection continually takes place and prevents the build-up of substantial current sheets. In this case a solar flare could occur after build-up of energy in a force-free field (rather than a current sheet) when an ideal eruptive instability or nonequilibrium onset drives the formation of a current sheet and fast reconnection below the erupting flux tube (e.g., Priest and Forbes, 1990; Forbes and Priest, 1995; Section 5.5). Another possible scenario that is being described in this section is that fast reconnection does not occur and that energy may be stored globally in a configuration containing a substantial current sheet, from which a parallel electric field, localized to the magnetic separator, may quickly release it. As we have seen, though, Spitzer resistivity with slow Sweet–Parker reconnection within a steady-state current sheet is not capable of producing a significant electric field. In this second scenario, there must therefore be some other mechanism responsible for producing a reconnection electric field to transfer flux between coronal domains. Such a mechanism, whatever it might be, appears to remain inactive for long periods during the quasi-static energy accumulation, and then abruptly switches on to release the stored energy. The electric field will transfer flux between coronal domains and thereby lower the energy of the magnetic

field. What form the magnetic energy is converted to will depend on the detailed mechanism producing the electric field.

The large spatial scales and the nature of the observed reconnection seem to make it unlikely that collisionless mechanisms, such as whistler mediated reconnection (Chapter 3), are involved. The width of a Sweet–Parker current sheet given by Eq. (5.5) is $\delta \sim 6\,\mathrm{m}$, for a typical shear value $B' \sim 10^{-10}\,\mathrm{T/m}$ (field strength $B \sim 100\,\mathrm{G}$ structured on scales $\sim 100\,\mathrm{Mm}$). This is substantially larger than the collisionless skin depth, $c/\omega_{\mathrm{pe}} \simeq 0.15\,\mathrm{m}$, but comparable to $c/\omega_{\mathrm{pi}} = 6\,\mathrm{m}$. On the other hand, the separator current sheet is dominated by a strong magnetic field component parallel to the current (*guide field*) which might reduce the effectiveness of whistler mediated reconnection (Biskamp *et al.*, 1997, see also Sections 3.1 and 3.2).

Current sheets are known to be susceptible to several types of instability (see Syrovatskii, 1981; Priest and Forbes, 2000, for an extensive discussion), any of which might conceivably enhance the effective resistivity or disrupt the sheet altogether. Two-dimensional models show that the resistive tearing mode (Furth *et al.*, 1963) can become unstable in current sheets whose aspect ratio, $r = \Delta/\delta \sim S_\Delta^{1/2}$ exceeds a critical value r_{cr} (Bulanov *et al.*, 1979; Somov and Titov, 1985; Forbes and Priest, 1987). Unless the critical aspect ratio is well in excess of $r_{\mathrm{cr}} \sim 10^5$ (two-dimensional studies suggest it is closer to $r_{\mathrm{cr}} \sim 10^2$), or the resistivity is already considerably enhanced, the threshold of this instability, $|I| > r_{\mathrm{cr}}^2 I_{\mathrm{sp}}$, would be negligibly small in typical coronal fields.

Another example of an instability which might initiate separator reconnection is the ion-acoustic instability (Somov and Titov, 1985) which is triggered when the electron drift speed, J/en_{e}, exceeds the ion sound speed, c_{s}. The ratio of these speeds within the Sweet–Parker current sheet is

$$\frac{J}{en_{\mathrm{e}}c_{\mathrm{s}}} = \frac{|I|}{\delta\Delta}\frac{\sqrt{m_{\mathrm{p}}/k_{\mathrm{B}}}}{en_{\mathrm{e}}T^{1/2}} = S_\Delta^{1/2}\frac{\pi B'\sqrt{m_{\mathrm{p}}/k_{\mathrm{B}}}}{4\mu_0 en_{\mathrm{e}}T^{1/2}} = \sqrt{\frac{|I|}{I_{\mathrm{ia}}}}. \tag{5.11}$$

For the Spitzer resistivity this ratio exceeds unity when the sheet current exceeds $I_{\mathrm{ia}} \simeq 10^8\,T_6^{-1/2} n_9^{5/2} (B'_{-8})^{-2}\,\mathrm{A}$, where B'_{-8} is the magnetic shear parameter in units of G/Mm (i.e., $10^{-10}\,\mathrm{T/m}$). If the resistivity is enhanced above the Spitzer value the ion-acoustic threshold I_{ia} would increase by the same factor.

5.2.4 Observation of separator reconnection

Observations of a reconnection episode resembling the scenario above were made by the TRACE, SOHO, Yohkoh, and GOES satellites over the period August 10–11, 2001 (Longcope *et al.*, 2005). At approximately 7:30 UT on August 10 a bipolar active region (9574) began to emerge just north of an existing active region (9570). Magnetograms made by SOI/MDI on SOHO (Scherrer *et al.*, 1995) were used to construct a model of the evolution of the magnetic sources (see Fig. 5.13). Modeling the two active regions as four magnetic sources (actually as four collections of sources) there is a single magnetic separator overlying the domain interconnecting the emerging positive source (P051) to the pre-existing negative source (N01). The flux of each emerging source grows steadily for the next 30 hours, at $\dot{\Phi} \simeq 1.22 \times 10^{17}\,\mathrm{Mx/s}$. This causes the interconnecting flux in the potential field, $\psi^{(\mathrm{v})}(t)$, to increase as well, at approximately one-third that rate.

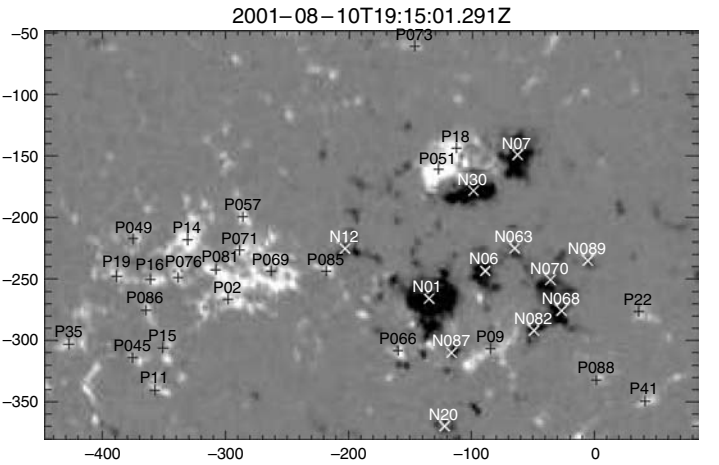

Fig. 5.13. The photospheric magnetic field at 19:15 UT August 10, 2001 is shown as a grayscale. The emerging active region (9574) is the concentrated bipole to the north; the pre-existing active region (9570) in the south contains a concentrated leading (negative) sunspot and more disperse following (positive) plage to the east (left). The positive and negative sources used to model this field are shown as + and × along with their labels. Axes are in seconds of arc from disk center.

Theories and observations imply that the two poles of an active region are completely coupled when they first emerge. EUV images (171 $\mathring{A}$) made at high time cadence by TRACE reveal numerous coronal loops interconnecting the two active regions (see Fig. 5.14). These must be the result of magnetic reconnection at the separator, since no other process could forge field lines of this novel connectivity.

Longcope *et al.* (2005) measured the diameter of each interconnecting EUV loop over the course of the 41-hour observation. Multiplying by a coronal field strength and correcting for loops too faint or too hot to see in the 171 $\mathring{A}$ passband gives the interconnecting flux $\psi(t)$ shown in Fig. 5.15. This remains initially small (very few interconnecting loops are seen) even as the potential flux, $\psi^{(\mathrm{v})}(t)$, rises steadily. At approximately 6:00 UT on August 11 (22.5 hours after emergence) there is a sudden burst of reconnection and ψ rises to meet the potential value $\psi^{(\mathrm{v})}$ (see Fig. 5.15). This transfer of $\Delta\psi = 1.1 \times 10^{21}\,\mathrm{Mx}$ within 3 hours demands a separator loop voltage of $\mathrm{d}\psi/\mathrm{d}t \simeq 10^9\,\mathrm{V}$. Coincident with this reconnection there is a sudden elevation in the soft X-ray flux observed by GOES and Yohkoh (not shown). The net power radiated over this interval is estimated to be $E \simeq 2.4 \times 10^{30}\,\mathrm{erg}$ (Longcope *et al.*, 2005).

According to the model of Section 5.2.2, the $L \simeq 200\,\mathrm{Mm}$ long separator between the active regions should have accumulated current during the first 22.5 hours during which reconnection was inoperative. A flux discrepancy $\Delta\psi = 1.1 \times 10^{21}\,\mathrm{Mx}$ generates, according to Eq. (5.9), a current of $1.34 \times 10^{11}\,\mathrm{A}$ and thereby stores $\Delta W = 1.4 \times 10^{31}\,\mathrm{erg}$ of magnetic energy (Longcope *et al.*, 2005). The radiation observed during the reconnection episode accounts for one-sixth of this energy. This much of the separator reconnection scenario appears borne out by the observations.

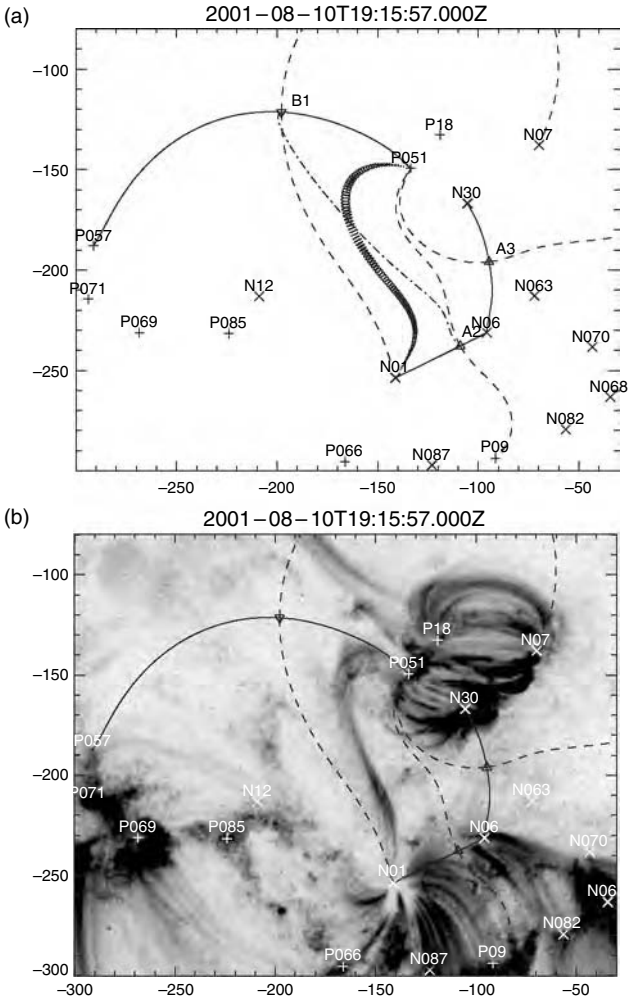

Fig. 5.14. Field lines in the domain interconnecting AR9570 (N01) and AR9574 (P051). (a) The magnetic model extrapolated from sources found in the MDI magnetogram. Positive and negative sources are denoted by + and ×; positive and negative nulls by ▽ and △. Dashed and solid lines are the fan traces and spines from the three null points shown. The dash-dotted line is a projection of the magnetic separator linking B1 to A2. A set of circles outlines a bundle of field lines ($\Phi = 2 \times 10^{18}$ Mx) from the interconnecting domain under the separator. (b) An image in 171 Å shown in reverse grayscale. The sources, nulls and footprints from (a) are superimposed for reference.

The structure of a Sweet–Parker current sheet is determined primarily by the magnetic shear B' of the potential separator. In this configuration B' tends to decrease with height roughly as B/z. For the field at 6:23 UT August 11, when the reconnection occurs, it is $B' \simeq 3\,\mathrm{G/Mm}$ low in the corona, and reaches a minimum of $B' = 0.2\,\mathrm{G/Mm}$ at the $z = 72\,\mathrm{Mm}$ apex (where $B = 17\,\mathrm{G}$). This decrease in B'

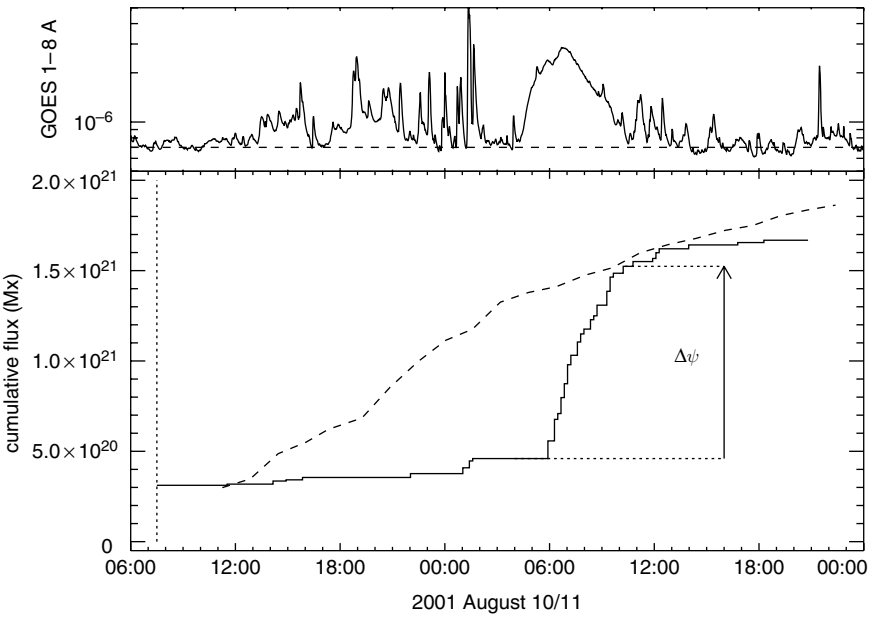

Fig. 5.15. The bottom panel shows interconnecting flux inferred from EUV loops (ψ, solid) and in the potential field ($\psi^{(\mathrm{v})}$, dashed). The dotted vertical line shows the time at which AR9574 began to emerge. The top panel is the 1–8 Å flux from GOES.

with height makes the current ribbon wider at the top, as in Fig. 5.12. Adopting plasma parameters $n_\mathrm{e} = 10^9\,\mathrm{cm}^{-3}$ and $T = 10^6\,\mathrm{K}$, the sheet's thickness would grow from $\delta = 3.5\,\mathrm{m}$ to $13\,\mathrm{m}$ at the apex. Were the current sheet $\Delta = 30\,\mathrm{Mm}$ wide at the apex it would have a field $B_\mathrm{o} \simeq 4\,\mathrm{G}$ perpendicular to the current, reversing across the sheet. The component parallel to the current, $B \simeq 17\,\mathrm{G}$, is considerably larger than this.

5.2.5 Summary

The foregoing reviewed simple two- and three-dimensional models of energy storage in quadrupolar coronal fields. A photospheric field consisting of discrete flux sources, such as sunspots or active region concentrations, gives rise to a coronal field with a set of distinct flux domains. These domains are bounded by separatrices which intersect at separators. Slow motion at the photosphere will cause the coronal field to change quasi-statically through magnetic equilibria. Applying constraints only on the fluxes in each domain, the equilibrium will have current concentrated at its separator. If a reconnection electric field develops along this current sheet it will transfer flux between domains thereby liberating stored energy. Classical resistivity at a current sheet will not produce such an energy release. Observations suggest that current accumulates for some time in spite of its resistivity, before reconnection suddenly occurs.

5.3 Pinching of coronal fields

V. S. Titov

Section 5.2 addressed the formation of current sheets, as a means leading to reconnection, at topological magnetic features such as null points, separator lines, and separatrix surfaces (Priest and Forbes, 2000), focusing specifically on separators. An alternative way to achieve a similar result is to form current sheets by complex photospheric motions in coronal magnetic fields with an initially simple topology (Parker, 1994). Since the topological structure of the magnetic field is preserved by ideal MHD flows, these two approaches look rather different at first sight.

The difference between them becomes less dramatic if one remembers that the magnetic field itself is generated by complicated plasma motions below the photosphere. Thus the complexity of observed coronal magnetic structures (and so their topological features) ultimately originates from the complexity of the plasma motions. In fact, such a difference becomes even less significant if one considers the concept of quasi-separatrix layers (QSLs). First introduced by Priest and Démoulin (1995) and their relation to the process of current sheet formation. This process will here be referred to as *magnetic pinching* – a term used in laboratory plasma physics which seems to be rather precise, at least for configurations with a hyperbolic field structure.

Contrary to genuine separatrix surfaces, QSLs are not topological but geometrical features, which can be formed, for example, in a simple arcade-like coronal field by continuous large-scale MHD flows of ideal plasma if they include a stagnation point for a sufficiently long period of time. The significance of stagnation-type flows for building up small-scale structures in a large-scale magnetic field has been clearly emphasized by Cowley *et al.* (1997) and previously demonstrated analytically and numerically in the context of the coronal heating problem by many authors (van Ballegooijen, 1985; Mikić *et al.*, 1989; Longcope and Strauss, 1994; Galsgaard and Nordlund, 1996). The purpose of this section is to review some new results on the properties of QSLs and their relationship to the pinching of coronal magnetic fields, in particular, in large-scale solar flares.

5.3.1 Definition of QSL

Consider a generic set of field lines connecting photospheric domains of positive and negative polarity in a solar active region (Fig. 5.16). In Cartesian coordinates with the photosphere given by $z=0$, the locations of field line footpoints may be written in terms of coordinates (x_+, y_+) and (x_-, y_-) in the $z=0$ plane. The connections of the footpoints by field lines then define two mutually inverse mappings, which can be represented by vector functions $(X_-(x_+, y_+), Y_-(x_+, y_+))$ and $(X_+(x_-, y_-), Y_+(x_-, y_-))$. These functions describe the field line connectivity globally, while the corresponding Jacobian matrices describe it locally.

In order to determine the location of the QSLs, Priest and Démoulin (1995) proposed using the norm of these matrices

$$N_\pm \equiv N(x_\pm, y_\pm) = \left[\left(\frac{\partial X_\mp}{\partial x_\pm} \right)^2 + \left(\frac{\partial X_\mp}{\partial y_\pm} \right)^2 + \left(\frac{\partial Y_\mp}{\partial x_\pm} \right)^2 + \left(\frac{\partial Y_\mp}{\partial y_\pm} \right)^2 \right]^{1/2}, \tag{5.12}$$

by requiring that $N_\pm \gg 1$ for the field lines belonging to QSLs.

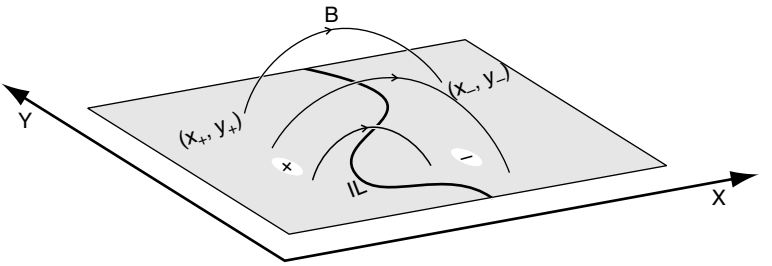

Fig. 5.16. The photospheric plane and magnetic field lines connecting positive and negative polarities, which are separated by the inversion line IL.

Applications of this measure for structural analysis of magnetic fields in real events justified the usefulness of this definition (Démoulin *et al.*, 1997; Démoulin, 2005), especially in identifying regions with a strong variation of magnetic connectivity. Nevertheless, N can be replaced by something more self-consistent for characterizing the connectivity, because it suffers from the following two shortcomings. Firstly, N is not discriminating enough to differentiate between QSLs and flux tubes connecting small and large polarities, where $N \gg 1$ in the polarity with the smaller size. Secondly, contrary to what one would expect, the norm gives generally different values for N_+ and N_- for the footpoints of the same field line.

Both these shortcomings may be overcome by adopting instead the following value Q (Titov *et al.*, 2002):

$$Q_+ = \frac{-N_+^2}{B_{z+}/B_{z-}^*} \equiv Q_-^* = \frac{-N_-^{*2}}{B_{z-}^*/B_{z+}}, \tag{5.13}$$

or equivalently

$$Q_- = \frac{-N_-^2}{B_{z-}/B_{z+}^*} \equiv Q_+^* = \frac{-N_+^{*2}}{B_{z+}^*/B_{z-}}. \tag{5.14}$$

Here the minus sign is introduced to compensate for the negativeness of the normal magnetic component B_{z-}, while asterisking some of the functions indicates that their arguments $x_\mp$ and $y_\mp$ are substituted by $X_\mp(x_\pm, y_\pm)$ and $Y_\mp(x_\pm, y_\pm)$, respectively. This means that (x_+, y_+) and (x_-, y_-) are not arbitrary points on the photosphere but the footpoints of a particular field line. Because of the conservation of magnetic flux, the ratios B_{z+}/B_{z-}^* and B_{z-}/B_{z+}^* coincide with the determinants of the corresponding Jacobian matrices, so they determine the expansion–contraction factors along such a field line. In practice, these ratios are easier to compute, so it is better to use them in (5.13) and (5.14) rather than the Jacobian determinants, which enter into the original expression of Q (Titov *et al.*, 2002). Since in real computations the numerical grid on the photosphere is fixed, it is convenient to use only the left-hand sides of (5.13) or (5.14) for positive or negative polarities, respectively.

The value Q has a clear geometrical meaning, which is revealed by noticing that an infinitesimal circle maps along a given field line into an infinitesimal ellipse. The

calculations show that its aspect ratio equals $Q/2+\sqrt{Q^2/4-1}$, so that, when it is large, it tends to Q. Thus, Q characterizes the degree of squashing of the corresponding infinitesimal flux tube. It is natural then to postulate that *the QSL is a layer-like flux tube consisting of magnetic field lines with* $Q \gg 2$. Here $Q=2$ is the lowest bound that corresponds to the field line along which an infinitesimal circle maps into a circle. This definition of QSLs is justified by existing sequences of configurations where QSLs turn into genuine separatrix surfaces in the limit of $Q \to \infty$ (Titov *et al.*, 2002).

Another independent measure of the field line connectivity is the degree of expansion or contraction

$$K_+ = \log|B_{z+}/B^*_{z-}| \equiv -K^*_- = -\log|B^*_{z-}/B_{z+}|, \tag{5.15}$$

or equivalently

$$K_- = \log|B_{z-}/B^*_{z+}| \equiv -K^*_+ = -\log|B^*_{z+}/B_{z-}|. \tag{5.16}$$

This measure determines how much the cross-sections of infinitesimal flux tubes expand or contract from one photospheric polarity to the other. In real configurations with nonuniform photospheric distributions of the normal magnetic field B_z, the distribution of K also reveals the footprints of QSLs and helps us to understand their elastic properties. The latter is very important for understanding the mechanism of magnetic pinching (Section 5.3.3).

Since the Jacobian matrix, in general, has four independent elements, there must be two additional characteristics of field line connectivity, which are independent of the direction of mapping. These characteristics are related to the orientation of the major axes of the infinitesimal ellipses discussed above and are not as visual as Q- and K-distributions. In spite of that, it is possible to visualize elegantly all the information contained in the Jacobian matrices by constructing the so-called *orthogonal parquet* (Titov *et al.*, 2002), which is a network formed by the integral lines of the field of major axes of the above ellipses. The parametrization of the integral lines may be chosen so that the sizes of the parquet tiles depict the local squashing and expansion or contraction of the elemental flux tubes. This geometrical construction is rather appealing for a structural analysis of magnetic configurations and so it deserves further investigation.

5.3.2 Examples of QSLs

Here we illustrate the above theory by considering two examples of configurations which have been used for modeling solar flares. The simplest example is a quadrupole potential configuration proposed first by Sweet (1969) and then studied in more detail by Baum and Bratenahl (1980) and Gorbachev and Somov (1988). It considered a topological approach, where the preferred place for magnetic reconnection is associated with a separator field line. Since the separator is determined as a special field line connecting two magnetic null points, its existence is inseparably related to the presence of the nulls. Both nulls in such a configuration are present, however, only if the photospheric magnetic flux is concentrated in finite areas. Thus the concept of a separator is applicable to realistic configurations only if it is a good approximation to regard the photospheric flux as being concentrated in

discrete patches. On the other hand, a separator together with its associated nulls tends to disappear when the magnetic flux is distributed smoothly over the whole photosphere.

Such a difficulty may be resolved by generalizing the concept of separator to the concept of a *hyperbolic flux tube* (HFT), which is simply a union of two intersecting QSLs (Titov *et al.*, 2002). It is bounded by the magnetic flux surface $Q = \text{const.} \gg 1$ having a nontrivial shape such that the cross-sections of the HFT continuously transform along it as follows

$$\diagup \rightarrow \times \rightarrow \times \rightarrow \diagdown. \tag{5.17}$$

Thus, starting from a narrow strip at one polarity, the cross-section branches out with a second strip in the form of a cross up in the corona and then the first strip shrinks subsequently toward the other polarity to leave the second strip there as a footprint of the HFT (see Figs. 5.17 and 5.18).

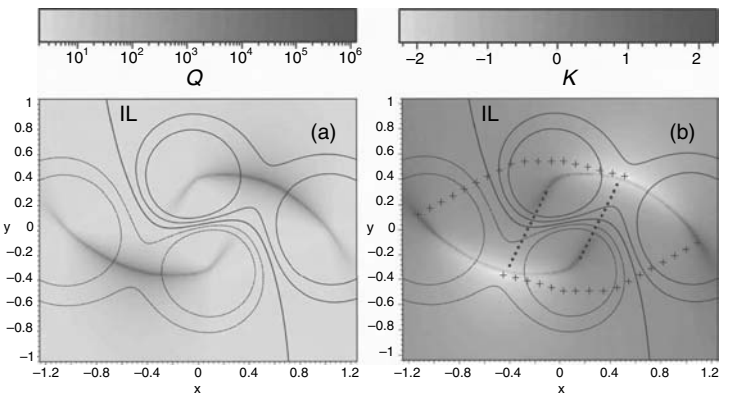

Fig. 5.17. Photospheric distributions of (a) the squashing degree Q and (b) the expansion–contraction degree K, superimposed on a few iso-contours of the corresponding magnetogram for a potential quadrupole configuration (see the details in Titov *et al.* (2002)); the dots and pluses trace four HFT ribs projected vertically onto the photosphere (see Fig. 5.18).

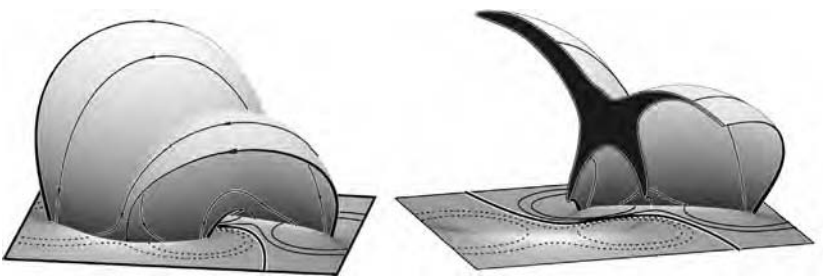

Fig. 5.18. The magnetic flux surface $Q = 100$ enclosing an HFT (left) and half of the same surface (right) demonstrating the shape of the mid cross-section of the HFT. In both panels the photospheric distribution of K is shown together with the magnetogram iso-contours, as in Fig. 5.17.

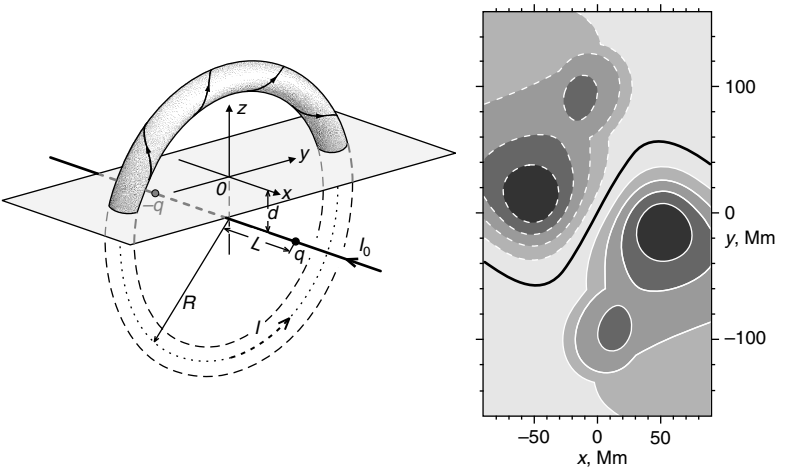

Fig. 5.19. The model of a twisted magnetic field of Titov and Démoulin (1999): a force-free circular flux rope (left) with a net current I is embedded in a potential background field produced by fictitious subphotospheric magnetic charges $-q$, q and a line current I_0 to generate in the corona a field whose photospheric magnetogram (right) resembles a typical solar active region. The solid and dashed lines represent iso-contours of B_z in positive and negative polarities, respectively.

A similar combination of QSLs exists in the model of a divergence-free twisted configuration (Démoulin *et al.*, 1996). Below we consider its force-free analogue proposed by Titov and Démoulin (1999) (see Fig. 5.19), which provides an approximate, cylindrically symmetric equilibrium consisting of a thin force-free toroidal flux rope with a net current I, major radius R, and minor radius a. The radial outward-directed Lorenz self-force is balanced with the help of a field by two fictitious magnetic charges of opposite sign which are placed at the symmetry axis of the torus at distances $\pm L$ from the torus plane. That axis lies below the photospheric plane $z = 0$ at a depth d. The resulting field outside the torus is current-free and contains a concentric magnetic X-line between the torus and its center. A toroidal field component created by a fictitious line current I_0 running along the axis of symmetry is also added. The presence of this component turns the neighborhood of the X-line into an HFT, which is revealed in the corresponding photospheric distributions of both Q and K (Titov *et al.* (2003a); Fig. 5.20).

One can see that the major squashing of elemental flux tubes occurs in very thin layers (QSLs) such that their footprints are narrow fishhook-like strips. The magnetic flux surface $Q = 100$ rooted at the contours of these strips encloses the HFT (Fig. 5.21) with the variation of its cross-section being similar to that of the above potential quadrupole field (5.17), except that the whole structure is also twisted. This fact directly demonstrates the structural stability of HFTs – the configurations containing HFTs might be significantly different but their HFTs are rather similar. It should be noted also that such a similarity does not depend on the value of $Q = \text{const.} \gg 1$ which is used to define the boundary of the HFT.

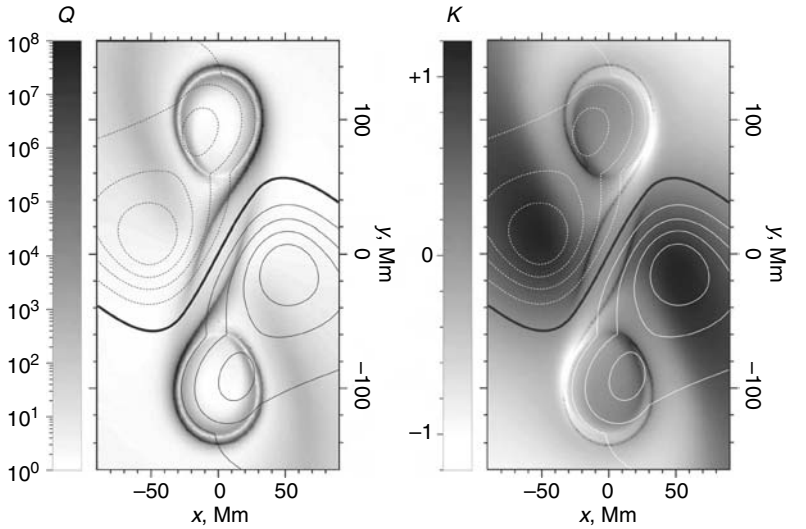

Fig. 5.20. The photospheric distribution of squashing degree Q (left) and expansion–contraction degree K (right) for the twisted configuration shown in Fig. 5.19. The magnetogram iso-contours are superimposed on both distributions.

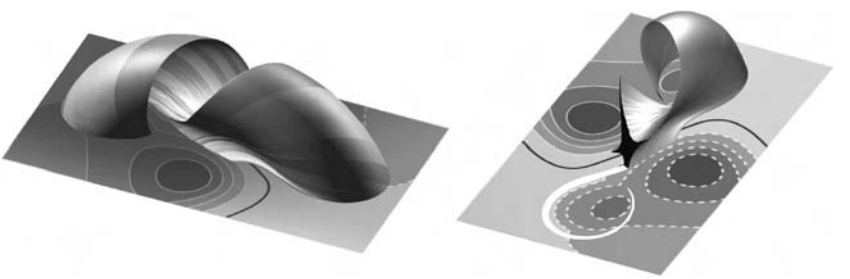

Fig. 5.21. An HFT (left) in the twisted configuration (see Fig. 5.19) with its field line structure depicted by strips shaded differently and a cut (right) through the HFT by a midplane with its cross-section and footprint shown in black and white, respectively.

5.3.3 Implications for the process of current layer formation

QSLs are of great importance for understanding 3D magnetic reconnection on the Sun, since the conditions for their appearance in the solar corona are less restrictive than for the genuine separatrix surfaces. Of special interest is their realization in the form of HFTs considered above, because HFTs play the role of separators in situations where the latter do not exist. In fact, two separatrix fan surfaces intersecting along a separator is a degenerate case of an HFT.

Similar to separators, HFTs are favorable sites for the formation of strong current layers. Physically, this seems to be due to the special elastic properties of HFTs. Indeed, as mentioned above, HFTs are a natural part of quadrupolar potential or twisted configurations. It is characteristic of the field lines belonging to such HFTs that they connect regions of strong and weak magnetic fields on the photosphere.

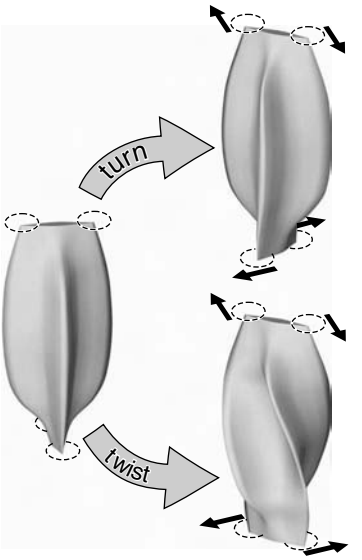

Fig. 5.22. Simplified HFT in a Parker-type model of the coronal magnetic field and two basic types of HFT deformation due to shears driven by sunspot motions. Sunspots are shown by circles at the top and bottom planes representing opposite photospheric polarities.

Therefore, they are *stiff* at one footpoint and *flexible* at the other, which in combination with their arrangement in the HFT provides favorable conditions for its pinching by stagnation-type flows. The latter can be naturally driven, for example, by shearing flows between moving sunspots adjacent to the tips of HFT footprints.

To demonstrate this, consider a straightened-out HFT which can be obtained in a Parker-type model by smoothly concentrating the magnetic flux in two sunspots at both polarity planes as shown in Fig. 5.22. Taking into account the above-mentioned properties of HFTs, it is natural to assume that the shearing displacements between sunspots can easily propagate into the coronal volume by vanishing in amplitude towards the opposite polarity. One can imagine then two extreme cases of the antiparallel displacements of the sunspots. They may cross the footprints of the HFT as if trying to either turn or twist it by producing two qualitatively different deformations of its coronal midpart. The superposition of the displacements propagating from both polarities yields at the midplane in these cases either rotation- or stagnation-type flows. It will then result in two different patterns of deformation for the Lagrangian grid.

One can see from Fig. 5.23, obtained in a kinematic approach by Titov *et al.* (2003b), that in the case of twist the grid is mostly distorted in a narrow region. Thus, in this case the midpart of the HFT must be pinching to a strong current layer. From the superposition of the photospheric shear velocities interpolated linearly between the polarity planes, it is possible to derive the current density at the most-distorted midpoint

$$j_z^* = \frac{2}{\mu_0}\left(h + \frac{B_\parallel}{2L}\right)\sinh\xi. \tag{5.18}$$

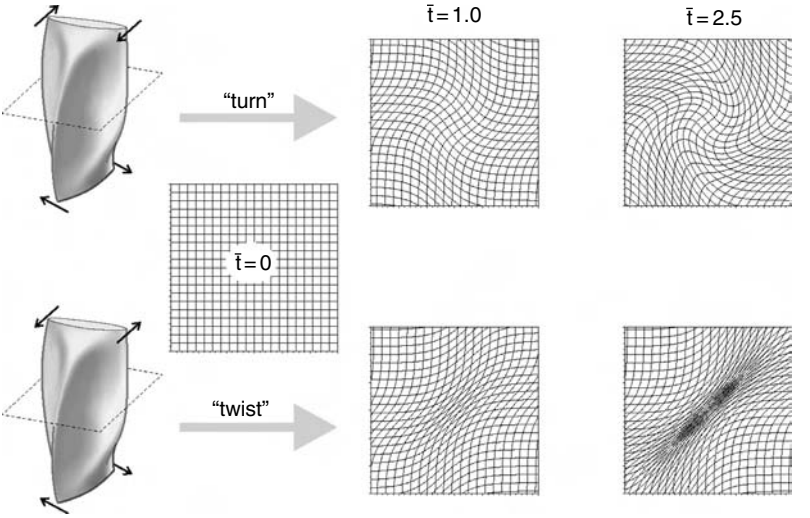

Fig. 5.23. Nonpinching (top) and pinching (bottom) deformations of a HFT in the (dashed outlined) plane $z = 0$ due to turning and twisting shearing motions, respectively, applied to the HFT footprints.

Here $2L$ is the distance between polarity planes, h and $B_\parallel$ are the initial values, respectively, of the transverse field gradient and longitudinal field at the midpoint, and

$$\xi = \frac{v_\mathrm{s} t}{l_\mathrm{sh}} \tag{5.19}$$

is the dimensionless displacement of each sunspot moving with a velocity v_s over time t and creating together with its neighboring spot a shear region of a half-width l_sh. It shows that for $\xi > 1$ the pinching of the midpart of the HFT causes the respective current density to grow exponentially with the displacement of the spots. Such an exponential dependence is due to stagnation-type flows appearing in the middle of the HFT. This was also shown previously by Longcope and Strauss (1994) for a multiple flux tube system, where a similar process developed because of coalescence instability.

The kinematic estimation can be improved at large ξ if one relaxes the major unbalanced stress in the forming current layer by allowing it to compress in the transverse direction until it becomes approximately force free. The resulting equilibrium current density at the midpoint is given by (Titov *et al.*, 2003b)

$$j^*_{z\,\mathrm{eq}} \simeq j^*_z \left[1 + \mathrm{e}^{\xi} \left(0.91 \frac{h l_\mathrm{sh}}{B_\parallel} + 0.57 \frac{l_\mathrm{sh}}{L} \right)^2 \right], \tag{5.20}$$

which, compared to its kinematic analogue j^*_z, has an additional factor growing exponentially with the displacement ξ and increasing with decreasing $B_\parallel$. In particular, in the limit $B_\parallel \to 0$ we would formally obtain that $j^*_{z\mathrm{eq}} \to \infty$, which is in agreement

with the analysis of current accumulation at null points (Bulanov and Olshanetskii, 1984; Priest and Titov, 1996; Rickard and Titov, 1996).

As is seen from both estimates (5.18) and (5.20), the current layer should be formed even if $h = 0$ or, in other words, if the initial field is uniform. This is not surprising, because the twisting pair of photospheric shearing motions interlocks the field lines in the coronal volume by forming an HFT and pinching it to a thin current layer. Such a result is in agreement with the earlier numerical simulations motivated by the so-called Parker problem, where this process has been studied for more complicated interlocking photospheric motions (Mikić *et al.*, 1989; Longcope and Strauss, 1994; Galsgaard and Nordlund, 1996). It is also evident from the above estimates that the additional presence of the transverse hyperbolic field ($h \neq 0$) only enhances the pinching effect.

The numerical MHD simulations of Galsgaard *et al.* (2003) confirmed that a twisting (but not turning) pair of shearing motions across the HFT footprints yields this effect. It implies that in reality current layers are formed in HFTs if the twisting component of such motions dominates over the turning one. Unfortunately, this conclusion cannot be considered as final, because the simulations have been performed only for an HFT whose initial squashing degree was not large enough ($\sim$40). Therefore, the observed pinching effect could be, in principle, attributed to the imposed boundary motions rather than to the structural properties of the HFT (Démoulin, 2005). Therefore, further investigations are required to resolve this uncertainty.

Driving the system by suitable horizontal motions is not the only way to cause HFT pinching. What is required is a suitable stagnation-type flow, which can be driven in several other ways. For example, a kink instability or other type of instability of a flux rope can drive such flows and pinch the HFT in the above way (Kliem *et al.*, 2004; Török *et al.*, 2004). Alternatively, the emergence of magnetic flux from below the photosphere may cause a similar effect.

5.4 Numerical experiments on coronal heating

K. Galsgaard

5.4.1 The photospheric–coronal connection

The energy required to maintain the corona at its very high temperature is indirectly supplied by the kinetic energy in the underlying convection zone, where the plasma β is larger than unity and the local dynamics is determined by the pressure gradient; this implies that the magnetic field is advected almost passively with the convective flows. Moving into the corona the situation changes, since the plasma β becomes less than unity and so the magnetic Lorentz force determines the dynamics. Convective motions in and below the photosphere advect the magnetic field around. The effects of these motions propagate, using the magnetic field, into the corona in the form of a Poynting flux, providing an energy flux into the corona that can be used to maintain the high coronal temperature.

Historically, two main theoretical classes of model have competed in explaining how this energy is liberated in the corona. The discrimination between them relates to the ratio between the characteristic driving time of the photospheric perturbation and

the Alfvén crossing time along a magnetic field line. When this ratio is less than unity, the perturbation behaves like a wave on a string. In the opposite case, where the ratio is larger than unity, the loop is exposed to a systematic perturbation and large-scale current sheets are expected to form and dissipate. In this chapter the emphasis is on current sheet heating mechanisms (see also Section 5.1).

The photosphere provides us with the best possibility for measuring the magnetic field vector, while coronal measurements are almost nonexistent. We are therefore not able to determine directly the structure of the coronal field. On the other hand, it is often suggested that the bright strand-like structures seen in high-resolution EUV and X-ray observations represent the structure of the magnetic field lines. This argument is based on the assumption that the coronal plasma is frozen to the magnetic field and the heat conduction along the field is much more efficient than conduction across the field, which tends to make local excess heating spread only along the magnetic field.

To make realistic models of coronal heating mechanisms one needs to have an idealized picture of the structure of the coronal magnetic field and the photospheric driving. The magnetic structure can, to a first approximation, be found using various field extrapolation techniques using the magnetic field distribution in the photosphere. For example, Close *et al.* (2004b) showed that even a potential mapping of the photospheric field into the corona produces very complex structures, where a single photospheric flux patch connects to many neighboring flux patches of opposite polarity. The boundaries between regions of different connectivity (separatrices) are especially susceptible for accumulating the stress imposed by continuous advection of the photospheric flux sources and significant current accumulations are expected to concentrate here.

Another interesting result by Close *et al.* (2004b) is the complicated magnetic field structure that results from the extrapolation, which allows for the presence of magnetic null points in the corona. These are the natural extension of 2D X-points where reconnection takes place and so are expected to be locations where magnetic energy release may also take place through 3D reconnection processes (see, e.g., Priest and Forbes, 2000). Observations (Filippov, 1999) have previously suggested that 3D nulls exist in the coronal magnetic field. These suggestions are based on large-scale structures of the inferred magnetic field and require that the structure is maintained down to very short length scales.

In the following, three different experiments and their relation to fast energy release in the solar corona are discussed. Section 5.4.2 focuses on experiments where magnetic null points provide the location for strong current accumulation and subsequent magnetic reconnection. Section 5.4.3 represents a simple interaction between two flux sources embedded in a large-scale background magnetic field – a representation of the small-scale development of the flux in the magnetic carpet. Finally, in Section 5.4.4 the concept of magnetic flux braiding is discussed.

5.4.2 Magnetic nulls and separators

In 2D, magnetic reconnection can only take place at some form of X-point, a location in space where the magnetic field vector vanishes. When investigating reconnection in 3D, it is natural to start looking at 3D null points. They provide a more

complicated magnetic structure defined by a spine axis and a fan plane (Priest and Titov, 1996). In the simplest case where the spine axis is perpendicular to the fan plane and the fan plane is rotationally symmetric around the spine, then a 2D plane through the fan plane and including the spine axis resembles a stretched 2D X-point, where the flux domains are separated from each other by the spine axis and the fan plane. Rickard and Titov (1996) showed that only two primary kinds of current structure tend to accumulate at the null; namely, a current cylinder along the spine axis and current sheet that is confined to the fan plane. The two perturbation modes resemble either a twist of the field around the spine axis or a tilt of the spine axis relative to the fan plane. Some investigations of single null points have been conducted numerically, showing that they can be perturbed in different ways to attract current and be local hosts for reconnection (Craig *et al.*, 1995, 1999; Craig and Fabling, 1996). This is the case both for systematic stresses and also for waves (Galsgaard *et al.*, 2002; McLaughlin and Hood, 2004, 2005), where it is found that the fast mode wave converges on the null and dissipates all its energy in its vicinity.

If a magnetic configuration does not contain a singularity, then nulls can only appear in pairs of two. In the most common case they will be created through a bifurcation process (Priest *et al.*, 1996) where two fan planes intersect in a single field line that connects the two nulls. This field line, the separator line, is the center of a hyperbolic field line structure (e.g., Priest and Titov, 1996). This structure is unstable to perturbations that make the X-point collapse to form a current concentration.

Galsgaard and Nordlund (1997) investigated a 3D magnetic field configuration containing eight null points. The initial magnetic field was defined to be 3D periodic using the ABC flow definition known from dynamo flows,

$$\mathbf{B} = B_0 \left(\cos y - \sin z, \cos z - \sin x, \cos x - \sin y\right). \tag{5.21}$$

Here B_0 is a scaling factor and x, y, z are coordinates in the interval 0 to 2π. This is a constant-α force-free magnetic field. It has a complex structure with each null point connecting to eight neighboring nulls. Two of these connections are by spine–spine connections, while the remaining six connections are defined by intersections of two fan planes. The fan–fan connections can further be divided into two subclasses. Half of these connect two nulls that are close to each other – about half of the box dimensions, while the other half connect nulls that are separated by more than twice this distance. The nulls are of the simple type (rotationally symmetric) locally, but with clear nonlinear effects appearing at just a short distance from the nulls. In the left panel of Fig. 5.24 the initial configuration is shown. The isosurfaces show the locations of the nulls, while field lines that are traced from the vicinity of the nulls indicate the magnetic topology. From this it can be seen that the three connections between close neighbors all connect through the locations with a low concentration of magnetic field lines. Using isosurfaces of weak magnetic field magnitude, these connections are seen as tunnels connecting the nulls (right panel of Fig. 5.24). These tunnels turn out to be the dynamically important locations when the magnetic field is stressed.

The magnetic field is enclosed in a 3D domain that is 2D periodic and satisfies frozen-in conditions on the boundaries in the third direction. A large-scale sinusoidal shear velocity perturbation is imposed on the boundaries in such a way that the

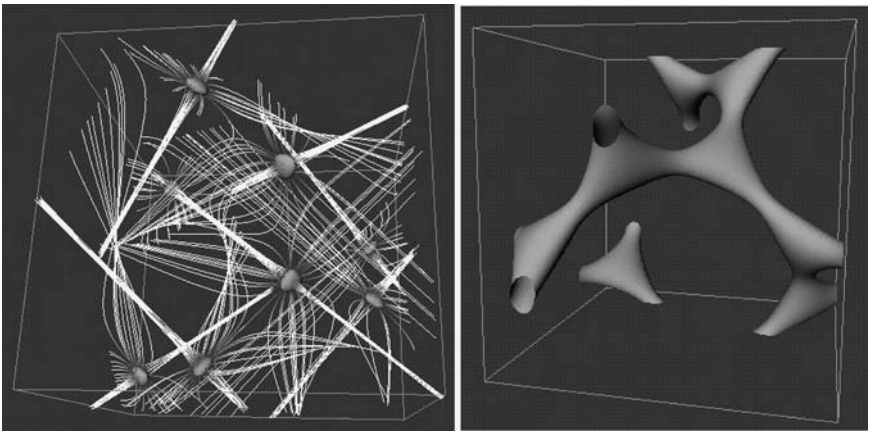

Fig. 5.24. Left, the initial setup for the eight null point experiment. The isosurfaces indicate the location of the nulls, while the field lines show the topology of the magnetic field. Right panel shows an isosurface of low magnetic field magnitude, showing the weak field tunnels connecting the nulls. Notice that the two 3D domains are not seen at the same viewing angle (Galsgaard and Nordlund, 1997).

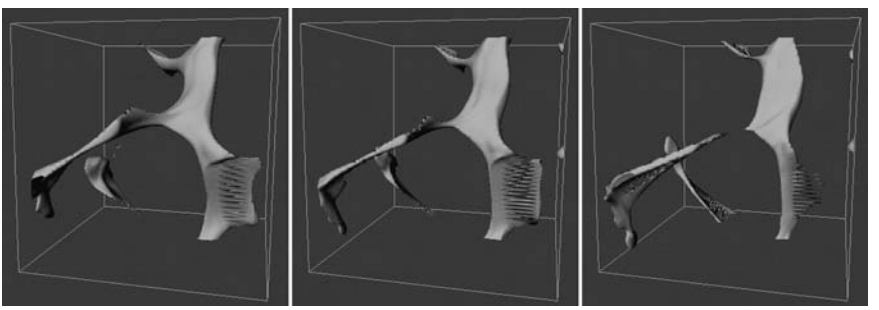

Fig. 5.25. The panels show the time evolution of weak-field tunnels. The locations with a ribbon-like isosurface correspond to the locations of strong current concentrations (Galsgaard and Nordlund, 1997).

amplitudes have opposite signs on the two boundaries. Independent of the direction and phase of the imposed boundary driving, the perturbations propagate into the domain and the stress accumulates at the same spatial locations, namely, at the weak-field tunnels hosting the separators that connect the neighboring nulls in the domain. The order in which the separators collapse depends on the actual boundary stress, but as time progresses all of these connections accumulate strong currents (Fig. 5.25).

By taking a closer look at the development of one of these separator connections, Galsgaard *et al.* (2000) showed how the stress propagates from the driving boundary and perturbs the structure around the separator line. The initial orthogonal X-type structure experiences a stress that initiates a collapse of the region about halfway between the two nulls. From here it spreads along the separator towards the nulls. As it reaches the nulls, they start to degenerate and within a short time

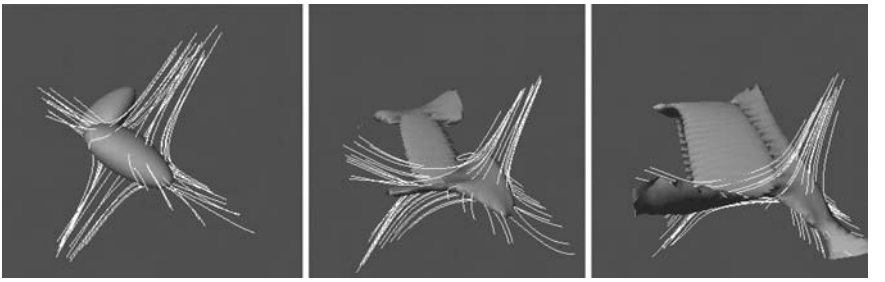

Fig. 5.26. The panels show the time evolution of the locations of weak magnetic field (red isosurfaces) and current (green isosurfaces). This shows how the accumulation of strong current along the separator lines is associated with changes in the local field line topology (Galsgaard *et al.*, 2000). See also color plate.

the characteristic 3D null point structure is perturbed in a way that resembles a collapsed 2D X-point (Fig. 5.26). The main difference here is that the magnetic component along the separator dominates the magnetic field and represents a pressure that is not present in the pure 2D situation. This additional pressure slows the advection of flux into the current sheet, but also increases the local Alfvén velocity.

From the structure of the X-type field along the separator line it is clear that the collapse of the X-point can only take place in two orthogonal directions, such that the separator lines in both cases maintain their identity, with the induced current sheet connecting two Y-points. Expanding this collapse structure to the 3D nulls, it is clear that the structure of the field in the vicinity of the null becomes almost two-dimensional within roughly an Alfvén crossing time of the region.

This indicates that if new magnetic nulls are formed through bifurcation processes (Brown and Priest, 1999), for instance, when new magnetic flux emerges into the corona, the time it takes before the nulls become involved in reconnection is likely to be very short and the identification of a clear 3D null structure more difficult.

The effect of the reconnection is to launch jets that eject plasma from the diffusion region with Alfvénic velocities. In this case, jet sheets extending all the way along the edges of the current sheets are formed and slow-mode shocks are found to develop along the extensions of the fan surfaces, giving about a 90-degree opening angle for the outflow region. In this manner the reconnection process resembles that of 2D reconnection.

This investigation shows that the magnetic field tends to collapse along the separator connecting two nulls. In no case has current started to accumulate at a single null in the domain. This stresses the importance of the separator over a single null point as a location for current accumulation and subsequent magnetic reconnection. This is further stressed by the experiment discussed in the following section.

5.4.3 Flybys

From an analysis of the magnetic connectivity of a potential field extrapolation of a photospheric magnetogram, Close *et al.* (2004b) showed that most of the magnetic flux only reaches a relatively low height and that the field line mapping

has a complicated connectivity pattern. They found that a single flux concentration connects to many opposite flux elements. Such a mapping provides the basis for the presence of many separatrix surfaces that may attract current as the sources are advected randomly around by the convective motions. The flux interaction between different flux sources therefore becomes vital for understanding the dynamical evolution of the magnetic field structure, as stressed in the *coronal tectonics* scenario (Priest *et al.*, 2002; Section 5.1). Longcope (1998), for example, investigated this situation in a simplified setup. He used the *minimum-current corona* (MCC) approximation where free magnetic energy in a sheared system is concentrated in a separator current sheet, while the rest of the domain remains in a potential state. The simple model consists of two localized sources, of equal but opposite flux, embedded in a constant background magnetic field. Starting from an initial potential magnetic field configuration, the structure of the magnetic field can have three different topologies: namely, when the sources are unconnected, when they are partially connected, and when they are fully connected. In each case two 3D null points will exist on the photospheric boundary, with their fan surfaces defining the separatrix surfaces that mark the boundary between the source and the background flux. Starting from totally unconnected sources, the MCC approach shows how current builds up along the separator as the fan planes start to touch and the sources are advected past one another. Different assumptions regarding the energy release provide different evolution scenarios with, in general, bursty energy releases.

Galsgaard *et al.* (2000) investigated this scenario numerically. The setup differed slightly from the one used by Longcope (1998), in that they for simplicity used 2D periodic boundary conditions. The initial field contained two unconnected magnetic sources that were advected past one another by imposed motions on the photospheric boundary. Figure 5.27 shows the initial conditions of the experiment and the location of the imposed boundary motions. The dynamical evolution passed through a series of phases. Firstly, the two sources are unconnected and their flux systems are forced to interact by the imposed boundary motion. The advection forces the source flux to move into the tail of the other flux source. This flux is not locally rooted in

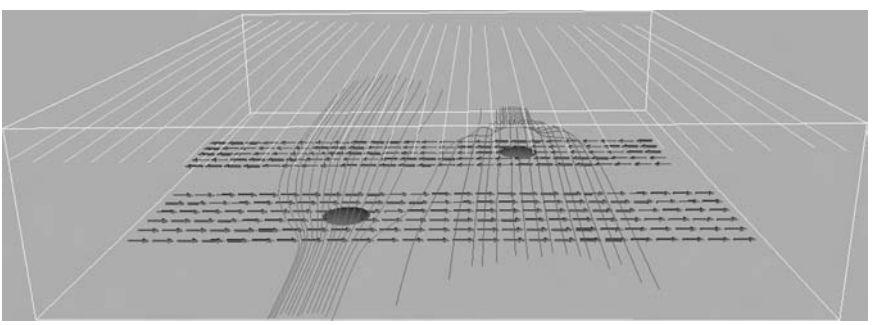

Fig. 5.27. The isosurfaces mark the locations of the two flux sources. The field lines outline the separatrix surfaces dividing space into three independent flux regions and the overlying magnetic field. The vectors on the base represent the direction and relative strength of the imposed driving profile (Galsgaard *et al.*, 2000).

the boundary and is simply lifted up over the approaching source. As this process is continued the fluxes from the two sources become entwined and form a twisted configuration. This builds up a highly twisted current concentration that eventually reaches all the way along the separator connecting the two nulls. The magnetic field reconnects and the two sources become partially connected. As the sources pass the point of closest approach, a potential extrapolation of the field would give a fully connected configuration. In the numerical experiment this is not the case, since the amount of flux connecting the two sources continues to increase after this point. While flux is still being connected between the two sources, new current structures start to form between the connected flux and the external flux. This separator current concentration is formed as a response to the rapid change in orientation between the closed flux connecting the sources and the fully open flux above it (Fig. 5.28).

Neither the potential field approach adopted by Close *et al.* (2004b) nor the MCC approach used by Longcope (1998) allow for detailed investigations of the way the reconnection process changes the connectivity between different flux patches. To investigate this Parnell and Galsgaard (2004) defined a large number of starting points for tracing magnetic field lines from one source. As the sources were advected with a known flow that maintained the spatial structure of the sources, it was possible to associate an amount of flux to each starting point and to follow the evolution of the field line connectivity with time. This showed that the source connectivity changes in a complicated way, with both the processes of connecting and reopening the source connectivity taking place simultaneously over a period of time. Figure 5.29 shows the changing connectivity at three different times. Counting up the flux in the three connectivity groups as a function of time one clearly sees the overlap between the processes of connecting and reopening the magnetic flux (top panel of Fig. 5.30). The deviation is very apparent when comparing this evolution with that obtained when assuming the reconnection is instantaneous and the magnetic field is at all times maintained potential (bottom left panel of Fig. 5.30).

From the change in connectivity one can derive a normalized reconnection rate. By doing a number of experiments with different parameters it was possible to derive the dependence of the reconnection rates on the driving velocity and the orientation of

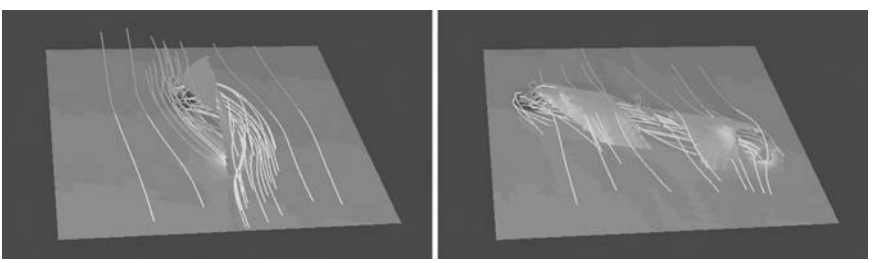

Fig. 5.28. Left panel shows the large separator current sheet, green, created by the first interaction between the flux from the two flux sources. Right panel represents a later time where the sources have passed the point of closest approach. The current isosurface now represents the separatrix surface where the reopening of the magnetic field takes place. The field lines indicate the structure of the magnetic field in the two situations (Galsgaard *et al.*, 2000). See also color plate.

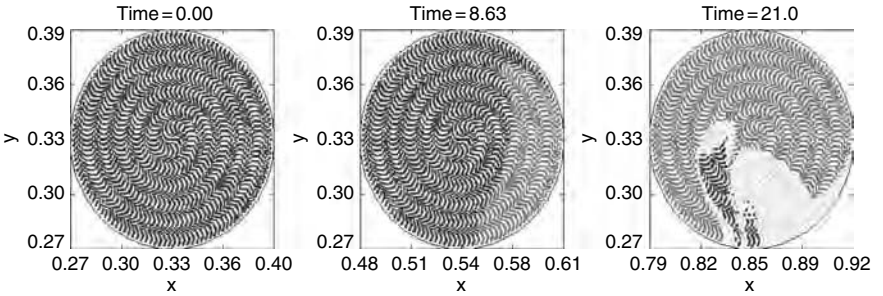

Fig. 5.29. The panels visualize the change in connectivity of one source as a function of time. The blue color represents the initially open flux, the red color the flux connected between the two sources, and finally the green represents the flux that has reopened again (Galsgaard and Parnell, 2004). See also color plate.

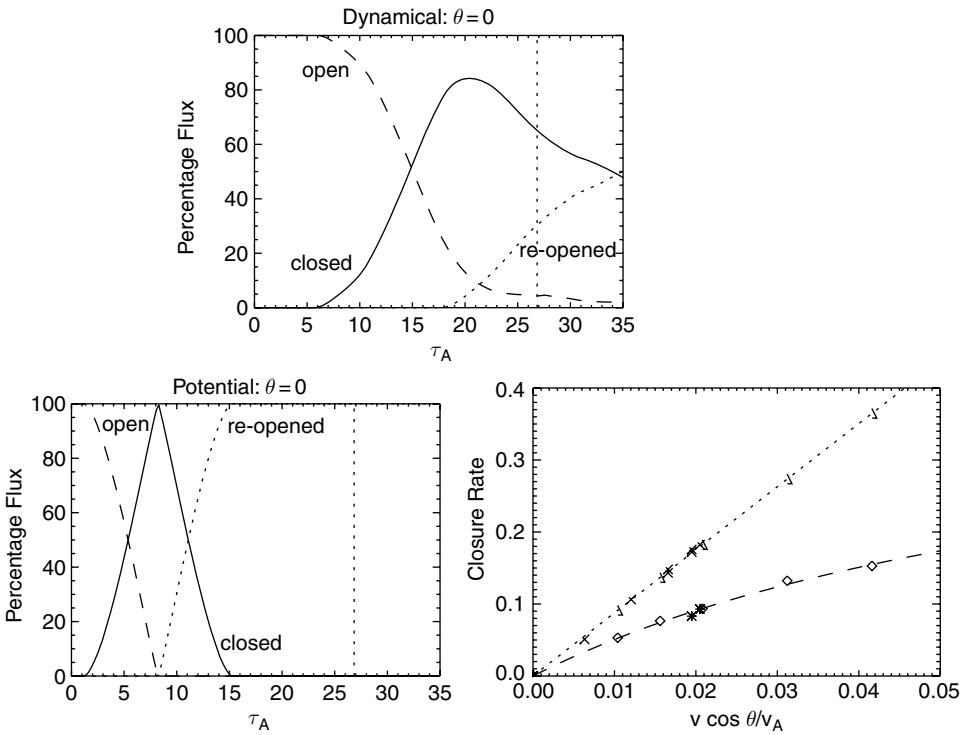

Fig. 5.30. The top panel shows the change in normalized flux in the three types of connectivity; open, closed, and reopened for one of the MHD experiments. The bottom left panel represents the same three graphs for a potential evolution. The bottom right panel gives the reconnection rates as functions of the driving velocity. The dashed line represents the MHD experiments, while the dotted line is for the potential model (Parnell and Galsgaard, 2004; Galsgaard and Parnell, 2004).

the overlying magnetic field (bottom right panel of Fig. 5.30). From these experiments an expression for the mean dynamical reconnection rate for the closing of the field is derived. For a comparison the same is done for the potential model:

$$R_{\mathrm{MHD}} = \frac{0.60 v_{\mathrm{d}} \cos\theta}{v_{\mathrm{d}} \cos\theta + 0.11}, \tag{5.22}$$

$$R_{\mathrm{pot}} = 8.8 v_{\mathrm{d}} \cos\theta. \tag{5.23}$$

Here v_{d} is the driving velocity measured in terms of the peak Alfvén velocity in the sources and θ the angle of the overlying magnetic field with respect to the direction of the line connecting the sources at their minimum distance. Only the reconnection rate for closing the field is given here, for, as can be seen in Fig. 5.30, the field has not reopened again when the driving is stopped. This influences the determination of the value in a way that is not simple to estimate. For the cases where it was possible, the reopening process proceeds at about half the speed of the closing. The main reason for this difference relates to the fact that the closing is a strongly forced process where the two flux systems can only pass through each other by reconnecting. The opening on the other hand takes place in a more relaxed environment, where the driving arises due to a force balance between the connected field and the fully open magnetic field. In this case the fields can slowly slip past one another and the force pushing the two flux regions together is smaller. For photospheric driving velocities, the dynamical reconnection rate is about half the rate found from the potential model.

When the dynamical evolution is compared with the potential or MCC model, two differences become clear. In the MCC the current is accumulating in a nontwisted separator current sheet connecting the two photospheric null points and both the closing and reopening processes occur through separator reconnection. Also due to the potential nature of the magnetic field in those models, there are no twisted magnetic field lines. From the discussion above and from Fig. 5.28 it is seen that both of these conditions are changed in the MHD experiment. Twisted field lines are a natural consequence of the shearing of the field lines that form the initial current sheet. This introduces magnetic helicity and the field lines that connect the two sources contain a significant twist. Further, the opening does not take place through the separator current sheet, but through separatrix surfaces. Only in the case where the opening process is started from a potential partly connected setup will the opening of the field happen by separator reconnection. In this case the current sheet is not twisted, but instead forms a bridge-like structure along the separator with the reconnection jets being in the horizontal plane. In the previous section, Section 5.4.2, it is mentioned that a separator line can collapse along two different orientations relative to the two intersecting fan planes. This experiment shows exactly this, and how which of these orientations is chosen depends on which way the flux flows along the separator structure.

When the evolution starts from a potential model, the energy input can be roughly estimated using a simple expression for the Poynting flux (Galsgaard and

Parnell, 2004, 2005). In the main phase of the experiment the Poynting flux is given by

$$P_{\mathrm{f}} \approx \frac{1}{\mu_0} \frac{B_{\mathrm{n}}^2 v_{\mathrm{d}}^2 t_{\mathrm{d}}}{L}, \tag{5.24}$$

where B_{n} is the normal component of the magnetic field, v_{d} the driving velocity, t_{d} the time since start of driving, and L the distance to the opposite anchored footpoint of the field line. Equation (5.24) shows that, when changing the driving velocity, the Poynting flux scales linearly with the imposed driving velocity for a given advection distance ($v_{\mathrm{d}} t_{\mathrm{d}}$). The time it takes to reach the same advection distance scales with $1/v_{\mathrm{s}}$, and so to a first approximation the total energy input is independent of the driving velocity. Comparing experiments with different driving velocity and taking into account the velocity scaling, one finds that the evolution of the experiments shows the same behavior (left panel of Fig. 5.31). Differences can be seen and these depend on the driving velocity. The differences are mostly related to the initial phase where the Poynting flux can be shown to be proportional to the ratio between the driving velocity and the local Alfvén velocity. In the main phase that follows, the Poynting flux increases nearly linearly with time until the boundary driving is stopped. The bumps are due to wave propagation through the domain that perturbs the sources.

The right panel of Fig. 5.31 shows the corresponding Joule dissipation as a function of advection distance. Integrating the dissipation over time for the same advection distance, the experiments release approximately the same amount of energy. This correspondence between the energy input and the output is not surprising, as the response in all cases depends strongly on the same basic evolution of the magnetic field. The important factor from an observational point of view is therefore directly

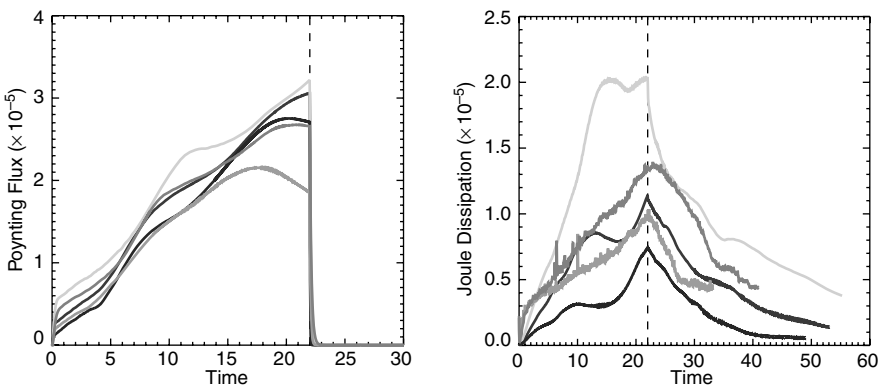

Fig. 5.31. The left panel shows the scaled development of the Poynting flux for five different experiments as a function of the advection distance. The difference at the start is due to the initial phase where P_{f} has a different dependence on v_{d}. The right panel shows the Joule dissipation for the same events scaled as a function of the advection distance (Parnell and Galsgaard, 2004). See also color plate.

related to the time scale of the event. The shorter it is, the more dramatic is the energy release and therefore also the impact on the plasma parameters, such as temperature.

These arguments are true only for the initial phase where the structure of the magnetic field is still dominated by the initial potential magnetic field configuration. If the driving is continued for a long time, then the sources pass around the periodic domain several times and the rise speed of the Poynting flux is found to decrease significantly shortly after the experiments were generally stopped. At the same time the Joule dissipation continues to rise, but is maintained at a level smaller than the Poynting flux. The free energy in the domain therefore continues to increase and a final statistical equilibrium is not reached for the present experiments.

The present investigations do not include a proper treatment of the energy equation and the atmospheric profile is not appropriate for detailed derivations of observational properties. One can make simple predictions as to where the energy release will increase the plasma temperature. Using the knowledge of which field lines reconnect as a function of time, their path through space can be used to localize regions where the effect of reconnection would be felt. By making the assumption that all plasma along these field lines is heated by an amount that scales linearly with the amount of reconnected flux and inversely with the length of the loop, the structure of the heated area may be derived. Doing this shows that the structure of the event, for the closing phase, is very compact, outlining a region that is larger and more structured than the separator current sheet. In the later phase where the opening of the flux dominates, the structure becomes much more fragmented in both space and time (Fig. 5.32). One possible reason for this difference between closing and reopening phases relates to the fact that this approach only identifies half of the reconnected field lines, namely the ones that connect to the sources, while the reconnected field lines that enter the coronal field cannot be identified. To make a more realistic assessment of the observational appearance of this type of reconnection, one has to include a realistic

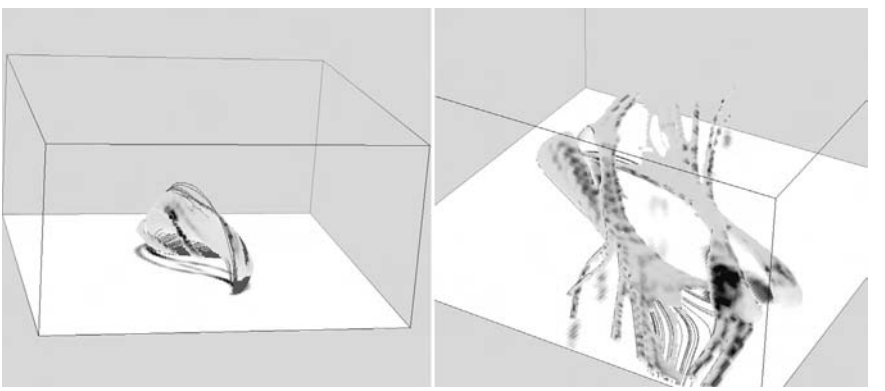

Fig. 5.32. The panels show the structure of the plasma heated by the reconnection event. The left panel represents the separator reconnection phase connecting the two sources, while the right panel shows the structure of the heated field lines during separatrix reconnection when the field is reopened. In the right panel the isosurface structure is rotated 180 degrees to represent the effect of reconnection from both sources (after Galsgaard and Parnell, 2005).

treatment of the energy equation and atmospheric stratification. Also, calculating the skeleton (Priest *et al.*, 1997) will prove invaluable in understanding the details of the reconnection process.

5.4.4 Flux braiding

One of the most widely discussed methods for coronal heating is magnetic flux braiding. The idea was first described by Parker (1972) and has been developed further in the coronal tectonics model (Priest *et al.*, 2002). The concept is based on a systematic braiding of magnetic flux. When this is continued for long enough, Parker argues that localized tangential discontinuities will develop at various locations inside the loop. In the presence of magnetic diffusivity, the free magnetic energy can be released by reconnection. To simplify the analysis Parker assumed a model where a curved solar loop is stretched out to fit into a Cartesian domain. The magnetic flux would be frozen on the two end boundaries and the assumed convective motions would slowly stress the system. From simple arguments Parker (1988) shows how an initially straight magnetic field that is braided by footpoint motions will reach a state where the Poynting flux input equals the requirement for a nano-flare energy release. This exercise shows that the magnetic field needs to be stressed until the field lines reach a given angle with the vertical. Using Eq. (5.24), one can estimate this angle assuming an equipartition between the energy input and energy loss. The important consequences of this are two-fold; firstly, if the magnetic diffusivity decreases, then the total energy input to the corona increases, as the angle of the field line increases before it starts reconnecting. Secondly, the method is self-adjusting to a level that suits exactly the physical parameters in the corona.

The braiding idea was investigated analytically by van Ballegooijen (1986), who looked at the mapping of the field between two boundaries in a Cartesian domain. On one boundary a series of random sinusoidal shear motions were imposed for a period of time, while the velocity on the opposite boundary was maintained zero. He found the peak current magnitude inside the domain to increase exponentially with the number of independent shear motions, the reason being that the shear motions decrease the characteristic length scale of magnetic structures inside the domain. This investigation was followed by Mikić *et al.* (1989), who numerically confirmed the trend for an exponential growth of the current magnitude. A problem with this approach is the fact that boundary motions were imposed only on one boundary, while the magnetic structure was maintained fixed on the opposite boundary. This imposes a limitation on the "freedom" of the magnetic field lines and therefore restricts the growth of the current with time, as seen in the experiments that followed. These allowed imposed boundary motions on both boundaries, so that the current was able to build up much faster. In fact only two independent orthogonal shear events (Galsgaard and Nordlund, 1996) or two nonaligned vortex flows (Hendrix and Van Hoven, 1996) are required to obtain an exponential growth of the current. These flows allow the field inside the domain to braid more easily. The stress from the boundaries cannot be released as the field lines cannot propagate through each other and a large current sheet is formed between two sets of converging field lines. This situation is illustrated in Fig. 5.33, which schematically shows the effect of the imposed boundary motions. This particular structure of the magnetic field initiates a local stagnation flow close to the center of the nonmoving central magnetic field lines.

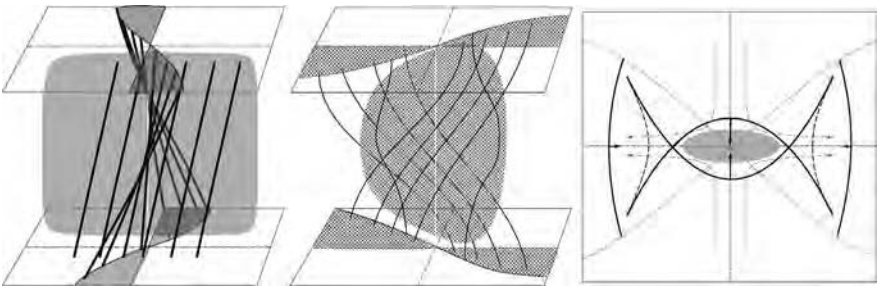

Fig. 5.33. The three panels illustrate how the field line structure changes as the braiding is continued. First a simple shear is formed. The following orthogonal shear motion creates locations around which the field lines lock into each other. As the shear motion is continued the current increases exponentially (Galsgaard and Nordlund, 1996).

As long as the flow is ideal, then a field line with a given tangential component will approach the center on an exponential time scale. The distance between field lines of opposite, but equal, tangential components decreases exponentially with time due to the stagnation flow. In the ideal limit, this results in an exponential growth of the current with time. Independent of the value of the magnetic diffusivity, after a finite time, the current will reach a magnitude where a balance between advection and diffusion will be reached in the current sheet. From a simple analysis of the induction equation, using the assumption of the stagnation flow, it can be shown that this time depends logarithmically on the value of the magnetic diffusivity. Therefore, even in a plasma with a very low value of the diffusivity, this balance is reached within a finite time.

A concern from 2D reconnection investigations has been to find ways in which the reconnection process could proceed fast, releasing sufficient energy in a short enough time to account for dynamical events like solar flares. The situation seen at the beginning of all of these experiments consists of a large-scale current sheet that extends almost all the way between the two driving boundaries. Following most 2D predictions, the time scale for diffusing the magnetic energy will be long due to the large length scales involved in this structure. The numerical experiments show that for small driving velocities, dissipation takes place in large monolithic current sheets even after many random driving periods. As the driving velocity increases, the structure of the magnetic field changes. The outflow velocity of the initial reconnection event becomes large enough to change significantly the ambient magnetic field and initiate the formation of secondary current concentrations. This process is continued as a cascade process that continues all the way down to the resolution limit. This is also a way to bypass the problem with the reconnection speed of large monolithic current sheets, simply by decreasing the length scale of the sheets until the dissipation matches the requirement. Figure 5.34 shows a snapshot late in the experiments where several strong current sheets have developed. The field reaches a state where MHD turbulence becomes responsible for the energy release. As in hydrodynamic turbulence the dissipation becomes independent of the viscosity, the magnetic dissipation also becomes independent of the value of the magnetic diffusivity.

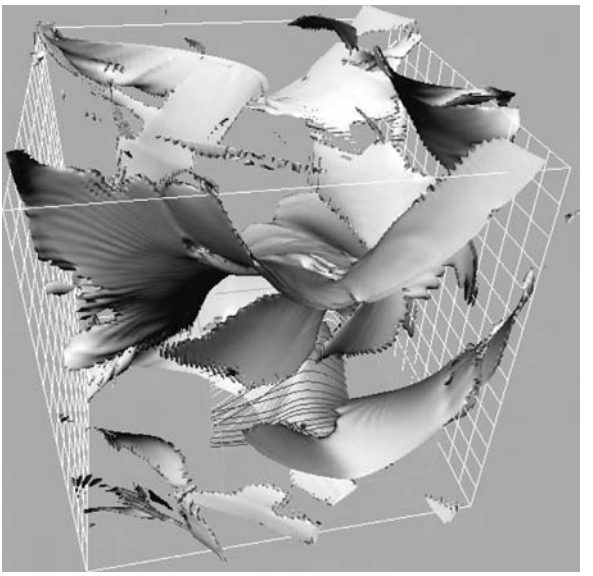

Fig. 5.34. The isosurfaces show the locations of strong current (Galsgaard and Nordlund, 1996).

Equation (5.24) shows how the Poynting flux depends on characteristic values for the magnetic field, driving velocity, and time scales. Galsgaard and Nordlund (1997) made a comparison between a Poynting flux defined by initial experiment parameters and the average dissipation in the experiments. This showed a linear relation between the expression for the energy input estimated from initial characteristics of the magnetic field and the actual dissipation over more than four orders in magnitude (Fig. 5.35). This could not have been expected a priori. The dynamical evolution in the experiments depends on the driving velocity, changing from the large-scale structures into smaller scales. If the dissipation depends on magnetic diffusivity, it would have been expected that there should be significant deviations from this relation as the characteristic parameters going into the expression of the real Poynting flux change with time. As this is not the case it indirectly implies the dynamical evolution is independent of the value of the magnetic diffusivity. This conclusion is supported by Hendrix and Van Hoven (1996), who show that the energy dissipation has a dependence on the magnetic diffusivity that is close to zero, or if at all an inverse dependence on the diffusivity.

From Parker's cartoons of the braiding process one has the impression that the magnetic field reaches a very complicated state with many twists and turns. Investigations of the numerical experiments show a different picture. Here a winding number can be derived using a number of field line traces started from points close together. Doing this, it is found that the distribution function of the winding number has most of its weight within $\pm$ unity of a turn, and only a small tail has values above this, Fig. 5.36. This may be explained by the fact that the time scale for braiding the field lines to a large winding number is significantly longer than the reconnection

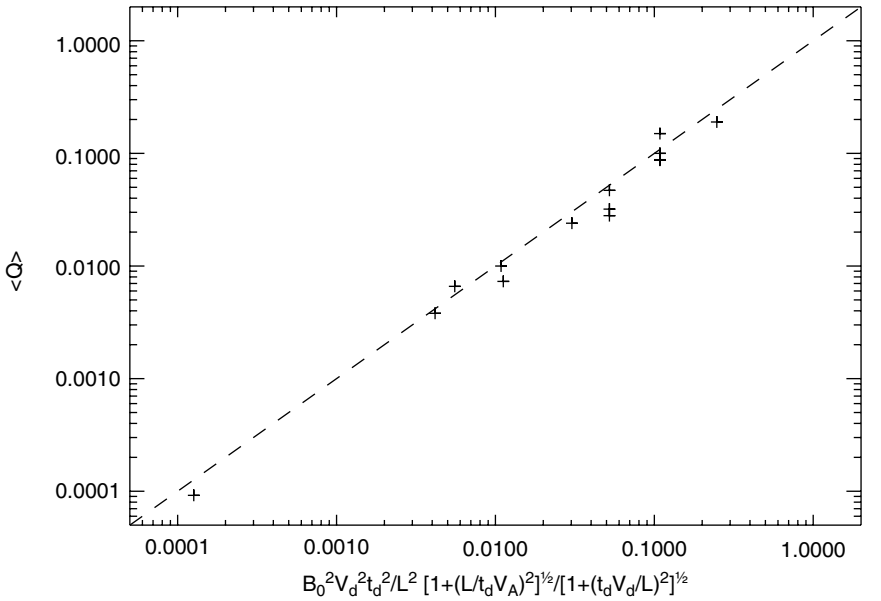

Fig. 5.35. The average Joule dissipation, Q, versus the Poynting flux, Eq. (5.24), determined from characteristic values of the initial conditions for the numerical experiments (Galsgaard and Nordlund, 1996).

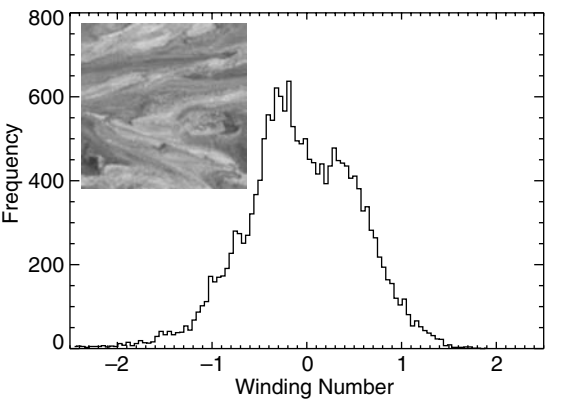

Fig. 5.36. The frequency distribution of the winding number determined for a uniform sample of field lines with start points on one of the driving boundaries. The image indicates how the winding numbers are distributed seen from the bottom boundary (Galsgaard and Nordlund, 1996).

time for removing the windings. It can therefore be stated that the fraction of field lines with a larger than unity winding must be located within a region where the diffusive process dominates the dynamical evolution, rapidly bringing the winding number below unity again.

An important problem in investigating the appearance of the corona has been to determine the distribution of the energy release along a loop. One way to approach this is to use observational data from a region where the structure of the magnetic field is well defined. By assuming the structure to be one-dimensional, the energy deposition profile can be found by optimizing the temperature profile obtained from the 1D energy equation to the observations. Priest *et al.* (1998) used this approach for a large Yohkoh loop, and suggested that the energy deposition along the high-temperature upper coronal part of the loop may be uniform (see also Mackay *et al.*, 2000; Aschwanden, 2001; Reale, 2002). It is, however, difficult to interpret the observations, so what do the numerical simulations say about this issue? The experiments discussed above do not include a realistic atmospheric model and also, for simplicity, ignore the effects of optically thin radiation and anisotropic heat conduction. Despite this, an analysis of the distribution of Joule dissipation in a braiding experiment was done by Galsgaard *et al.* (1999). The special and temporal 3D dissipation profile was averaged into a 1D array along the loop. The result is a dissipation profile with a nearly uniform distribution along the loop. The numerical model can be said to represent only the coronal part of the loop. Galsgaard (2002) investigated the implications of including a stratified atmosphere, radiation, and anisotropic heat conduction on the energy deposition profile. Repeating the analysis shows that a large amount of energy is deposited below the transition zone, followed by a rapid decrease before a near-uniform distribution is reached for the coronal part of the domain. Despite the smaller amount of energy released in the corona, the effect on the temperature is much larger here due to the significantly lower plasma temperature. It should be mentioned that the dynamical solution is highly complex in both time and space. The actual variations along individual field lines are therefore significant, implying that the above average values hide significant localized variations, which have a large impact on the appearance of individual field lines in the model. Similar conclusions follow from the coronal tectonics model (Priest *et al.*, 2002).

One limitation of these experiments is that they do not take properly into account the large-scale curvature of the closed magnetic field and the variations in length scale of a complicated coronal magnetic field structure. This is included in the experiments by Gudiksen and Nordlund (2004, 2005a,b), in which they make a big effort to make the whole scenario as realistic as possible. The initial magnetic field configuration is determined as a potential extrapolation of a smoothed active region magnetogram. They impose a "photospheric" boundary driving that resembles the convection motions in both structure and power distribution. They include a highly stratified atmosphere going from the lower transition region into the corona. Finally, they include all the relevant terms in the energy equation. After an initial phase the evolution reaches a steady state where many localized energy release events are initiated throughout the domain. Scaling the parameters they confirm that the convective motions are capable of supplying the energy needed for maintaining a hot corona. These experiments confirm the scenario of heating in many small current sheets (e.g., Priest *et al.*, 2002), and that the locations where energy dissipation takes place have similar characteristics to those discussed above. By passing the data through a "TRACE" filter, virtual images of the model corona are obtained. This provides

images that look very much like TRACE images, with localized loop structures that exist for as long as they are being heated.

They conclude that the results of the simulations put important question marks against most of the simple assumptions regarding 1D loop approximations, at least for the smaller EUV loops that are often taken for granted. These points concern hydrostatic equilibrium, time independence, symmetric heating profiles, and constant cross-section.

5.4.5 Summary

Over the last 10–15 years many numerical experiments have tried to understand the processes responsible for the energy release in the solar corona. We have come a long way, in terms of understanding which different mechanisms are likely to release magnetic energy. Driven magnetic reconnection is a good candidate for many energy release events, but what is the most important magnetic topology hosting these events? The various 3D reconnection processes that are possible are known, but we still have to learn how they behave in more detail.

Magnetic null points are fascinating in many ways. If the magnetic structure contains a single null then it will be involved in the process. If several exist and they are connected by separator lines, then it seems that only separator reconnection contributes significantly to the process. In this case, as the separator collapses, the structure becomes locally almost two-dimensional.

Potential models of the magnetic carpet (Close *et al.*, 2004a) show that the coronal magnetic field must be structurally complicated with lots of structure at low heights. Understanding the processes that change the connectivity of this field is important for predicting its dynamical evolution. The experiments discussed above show that driven reconnection includes the possibility of having a complicated mapping of the flux while it reconnects. It also shows that the rate of reconnection depends on how strong the forcing is and how easily the field can avoid the stress from building up. It is found that the average dynamical reconnection rate is always less than the comparable rate for a potential evolution. The energy input depends on the prehistory of the field. The more stressed the situation is, the more likely it is that simple models will not predict the correct input or the energy deposition available for heating the plasma.

The effects of boundary motions provide insight to the reconnection process in cases where no magnetic singularity exists. These experiments suggest that the energy dissipation becomes independent of the magnetic resistivity when the system is randomly stressed for a longer time. This is possible as the magnetic structure evolves from a large-scale structured situation into an MHD turbulence regime. The newest experiments prove that it is possible at present to conduct fairly realistic simulations of smaller active regions on the Sun. The results confirm that photospheric motions are capable of maintaining a hot corona. They also show that most of the previous simplifications used for modeling simple 1D coronal loops are not true and that it is not possible to model these using well-defined distribution functions.

We are at a transition point in time. We can choose to work with simplified models where the physical consequences are easy to interpret, or to leap into the difficult art of large-scale computing of close to realistic simulations with more difficulties in

understanding the detailed processes at work. The simplified models can be of great help in increasing understanding provided they are closely motivated by complex observations and numerical experiments.

5.5 Solar flares

K. Kusano and T. Sakurai

Solar flares are the biggest explosions in our solar system, and they are now widely believed to be caused by the sudden liberation of free energy stored in the solar coronal magnetic field. Multiple wavelength observations by modern satellites strongly suggest that magnetic reconnection is the principal process for the energy conversion in solar flares. In particular, a typical cusp-like feature of post-flare loops observed in soft X-rays is a strong piece of evidence in favor of the reconnection model (Tsuneta, 1996).

The so-called CSHKP model (Carmichael, 1964; Sturrock, 1966; Hirayama, 1974; Kopp and Pneuman, 1976) has been established as a standard model, which explains post-flare loops as a consequence of magnetic reconnection across the thin current sheet located above the magnetic neutral line. However, the fundamental question of what triggers solar flares still remains to be solved. The trigger problem of solar flares is related to asking where, when, how, and why magnetic reconnection can be initiated explosively in the solar corona. These questions are closely related to the attempt to forecast space weather. Since the trigger of solar flares is intrinsically a transition process from a quiescent state to a dynamical state, it is not necessarily the same as the fast reconnection problem, which has been mainly investigated in a steady reconnection framework.

Since any free energy in the solar corona should be supplied from the lower layers of the Sun, one of the major concerns in the trigger problem is how a thin current sheet, which should form the diffusion region, can be formed in a time scale much shorter than that of the photospheric motion. In order to give an answer, we have to understand the causal relationship between photospheric activity and coronal dynamics.

Related to this problem, it is also important to understand the physical processes working prior to flare onset. For instance, the characteristic structure called a *sigmoid* (Rust and Kumar, 1996), which is a forward-S or inverse-S shaped loop, has often been observed by the Yohkoh soft-X ray telescope (Tsuneta *et al.*, 1991) in association with eruptive phenomena, such as flares (Canfield *et al.*, 1999), coronal dimmings (Sterling and Hudson, 1997), and coronal mass ejections (CME) (Leamon *et al.*, 2002). A sigmoidal structure is widely believed to be a precursor of eruptive events.

A sigmoid could be a manifestation of the sheared and twisted nature of the coronal magnetic field. Therefore, magnetic shear and/or twist, which are often proportional to the magnetic component parallel to the magnetic polarity inversion line, are thought to be crucial ingredients in the trigger of flares. In fact, the largest flares tend to occur in delta spot groups with a polarity configuration inverted from Hale's law (Fisher *et al.*, 2000). One possible explanation for this is that such inverted delta-type spots might be formed through the emergence of a magnetic knot caused by a helical kink instability, which can grow in a strongly twisted flux tube (Linton *et al.*,

1999). It also suggests that magnetic helicity is relevant for the trigger mechanism of solar flares.

The object of this section is to review briefly several models for trigger mechanisms of solar flares, which have been proposed mainly in the last decade. Afterwards, we discuss the role of magnetic helicity in the solar corona, and also describe a new model for a trigger mechanism that the author has proposed recently.

5.5.1 Ideal MHD processes

There are several time scales involved in solar coronal dynamics: the magnetohydrodynamic (MHD) time scale $\tau_{\rm mhd} = L/v_{\rm A}$, the time scale of photospheric motion $\tau_{\rm p} = L/v_{\rm p}$, the resistive tearing time scale $\tau_{\rm tear} = S^{1/2}\tau_{\rm A}$ and the resistive diffusion time scale $\tau_{\rm res} = S\tau_{\rm mhd}$, where L is the spatial scale, $v_{\rm p}$ the photospheric motion speed, $v_{\rm A}$ the Alfvén speed, and S the magnetic Reynolds number. For the characteristic parameters of the solar corona (Priest and Forbes, 2000), we can estimate

$$\tau_{\rm mhd} : \tau_{\rm p} : \tau_{\rm tear} : \tau_{\rm res} = 1 : 10^6 : 10^7 : 10^{14} \quad \text{(s)}.$$

The large gap between the time scales suggests that only the ideal MHD process may be able to provide a consistent explanation for the sudden onset of flares, because the impulsive phase of a flare lasts typically only a couple of minutes.

Thus, an ideal MHD instability, particularly the kink mode, has been the focus of many studies (Hood and Priest, 1979; Gerrard *et al.*, 2002; Fan and Gibson, 2004; Kliem *et al.*, 2004; Török *et al.*, 2004, Inoue and Kusano, 2006). For instance, recently, Török and Kliem (2004) successfully developed a simulation model, in which morphological structures observed by TRACE (Handy *et al.*, 1999) can be well reproduced in terms of a kink mode instability, as shown in Fig. 5.37. The structural

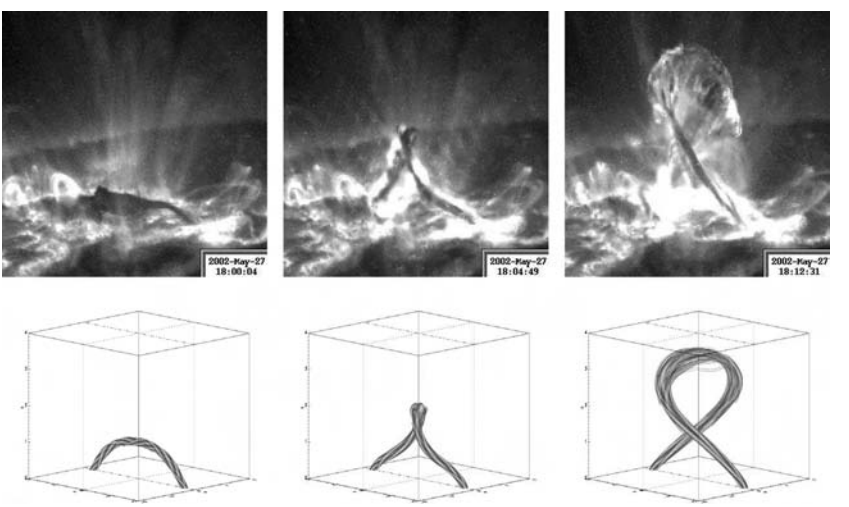

Fig. 5.37. Top: TRACE 195 Å image of the confined eruption event observed on May 27, 2002. Bottom: Magnetic field lines calculated from a 3D simulation of a kink-unstable flux tube (Török and Kliem, 2004).

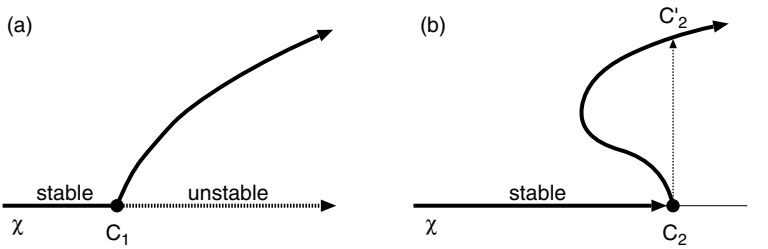

Fig. 5.38. Illustration of the equilibrium branches in (a) supercritical bifurcation and (b) subcritical bifurcation.

resemblance between the observations and the numerical model suggests that the kink instability may well be involved in the flaring process, at least in some events.

However, in spite of these successes, the role of the kink instability in the flare trigger process is not yet completely understood. In most simulation models, the instability is set up in the initial state, but it is not yet clear how the solar corona is destabilized. In general, when the instability arises through a supercritical bifurcation, the growth rate of the instability changes continuously from negative to positive with the change of a control parameter χ (see Fig. 5.38). In the solar corona, the stability should be affected by photospheric conditions, which evolve much more slowly than the characteristic MHD time scale. Thus, it is likely that the coronal configuration slowly evolves, tracing the saturated state of the instability, when the system exceeds the stability threshold (C_1). In such a case, the sensitivity of the instability saturation level to the boundary conditions (rather than the instability growth rate) is a concern. Otherwise, some nonlinear processes have to help increase the growth rate (e.g., Wilson and Cowley, 2004).

Recently, several new simulations have been developed to study the whole process of flux emergence of a twisted magnetic flux tube out of the subphotospheric region (Fan and Gibson, 2004; Magara, 2004; Manchester *et al.*, 2004; Galsgaard *et al.*, 2005). These models have revealed that the electric current channel of a sigmoid-like structure can be created through the interaction between the kinking flux tube and the pre-existing coronal magnetic field after the flux emergence. Although all these simulation models are still highly simplified, one of the possible scenarios is that the current sheet structure generated by the ideal MHD mode leads to the onset of resistive instability.

Another possible scenario is provided by subcritical bifurcation theory, in which a stable equilibrium disappears when the relevant parameter (χ) slowly exceeds a threshold (C_2), and thus a transition to another state may result (see Fig. 5.38b). A series of studies by Forbes *et al.* (1994) and Forbes and Priest (1995) proposed a theoretical model, in which the onset of flares and filament eruptions occurs as a result of a loss of equilibrium. In their theory, the relevant parameter is given by the ratio between the tension force sustaining the flux rope and the repulsive force acting on it. 2D and 3D numerical simulations by Forbes (1990) and Roussev *et al.* (2003) have demonstrated that this scenario can work as the loop feet separation is slowly reduced by a converging motion towards the magnetic neutral line.

5.5.2 Morphological models

In the CSHKP model, magnetic reconnection occurs at a vertical current sheet above a polarity inversion line. If an open field line configuration, in which only one end of the field lines is tied to the solar surface, is formed first, reconnection simply occurs between the fields from opposite polarity regions. However, Aly's conjecture (Aly, 1984) suggests that open field configurations may not be accessible, since they would have a higher energy than any closed configuration. Thus initiation of reconnection from a completely open field is unlikely.

As a result, several morphological models have been proposed in order to explain how to form the CSHKP model configuration. One is the so-called *tether cutting model* (Sturrock, 1989; Moore and Roumeliotis, 1992), in which reconnection first proceeds beneath the magnetic rope or in the lower part of the arcade. Then, the tension force of the field lines, which ties the magnetic rope onto the solar surface, is decreased, and the eruption of the flux rope can be initiated. The physical mechanism underlying the eruptive process in this scenario is probably related to the loss-of-equilibrium theory described in the previous section.

Although the tether cutting model is one of the most popular models for the onset of flares as well as CMEs, it does not specify the detailed mechanism whereby reconnection is initiated. One possible explanation is that reconnection takes place when the magnetic shear exceeds a threshold (Mikić *et al.*, 1988; Mikić and Linker, 1994; Kusano, 2002). This magnetic shear model can be understood as a process in which an overaccumulation of magnetic helicity leads to a loss of stability and/or the loss of equilibrium (Kusano *et al.*, 1995; Kusano and Nishikawa, 1996). The other scenario (Inhester *et al.*, 1992; Amari *et al.*, 2003) proposes that the converging motion toward the magnetic neutral line leads to reconnection at the center of the sheared arcade. Also, emergence of magnetic flux with a polarity opposite to the pre-existing arcade may trigger tether-cutting reconnection. For instance, Chen and Shibata (2000) and Amari *et al.* (2000) demonstrated this scenario in terms of 2D and 3D numerical models, respectively.

Another morphological argument was provided by the *breakout model*, which was originally investigated by Antiochos *et al.* (1999). The following conditions have to be satisfied for this model to trigger the eruption. One is a multipole topology, which has a magnetic null point above the top of an arcade field. Another is magnetic shear imposed near the magnetic neutral line. Then, the breakout model predicts that magnetic reconnection should occur first at the null point above the central arcade, because the sheared field pushes up the central arcade. The rising of the magnetic arcade begins by decreasing the unsheared overlying flux. As a result, a vertical current sheet is thought to be generated at the center of the arcade field underneath the flux rope. Several numerical simulations have been undertaken based on the breakout scenario (MacNeice *et al.*, 2004), and the changes of topology have been studied (Maclean *et al.*, 2005).

Many attempts have been made to examine these two morphological models by comparing with the observed data (e.g., Sterling and Moore, 2004). However, the observations are still not good enough to reject either of the models. One reason is that they all were developed basically as 2D models, with translational symmetry along the arcade axis, although flaring occurs in practice in highly complicated 3D fields.

5.5.3 Relation to magnetic helicity injection

Recently, several new methods have been developed to measure the magnetic helicity flux out of the photosphere into the solar corona using magnetograph observations (Chae, 2001; Kusano *et al.*, 2002; Démoulin and Berger, 2003; Kusano *et al.*, 2004a; Longcope, 2004; Welsch *et al.*, 2004). They all adopt the principle that magnetic evolution should be governed by the ideal induction equation,

$$\frac{\partial \boldsymbol{B}}{\partial t} = -\nabla \times \boldsymbol{E}, \qquad \text{and} \qquad \boldsymbol{E} + \mathbf{v} \times \boldsymbol{B} = \mathbf{0}. \tag{5.25}$$

Then, the relative magnetic helicity flux (Berger and Field, 1984),

$$\dot{H} = \int_S \boldsymbol{E} \times \boldsymbol{A}_\mathrm{P} \cdot \mathrm{d}\boldsymbol{S},$$

across the photosphere S can be derived applying an inversion technique to Eq. (5.25) and using the data for $\boldsymbol{B}$ and $\partial \boldsymbol{B}/\partial t$, where $\boldsymbol{A}_\mathrm{P}$ is the vector potential of the corresponding potential magnetic field.

Based on this method, Kusano *et al.* (2002) and Yokoyama *et al.* (2003) revealed that helicity injection in flare-productive active regions is highly complicated both in time and space. Furthermore, Maeshiro *et al.* (2005) clarified through the analysis of several active regions that the soft X-ray radiation from active regions is almost proportional both to the intensity of the magnetic helicity injection and the probability of the reversal of magnetic shear. These results imply that solar coronal activity is sensitive not only to the intensity of the magnetic helicity injection but also to the complexity of the magnetic shear structure, particularly to the reversal of magnetic shear.

Measurements of the magnetic helicity flux (Kusano *et al.*, 2002; Yamamoto *et al.*, 2005) suggested also that, even in flare-productive active regions, the magnetic helicity supplied to an active region, when normalized by the square of the total magnetic flux in each region, is of the order of 10^{-2}. This result indicates that the averaged helicity injection activity is usually too weak to make a twist of more than one turn in the magnetic flux of an entire active region. It contradicts the idea that an overaccumulation of magnetic helicity causes solar flares.

Recently, Wang *et al.* (2004) studied the typical helicity pattern which is associated with CMEs, using vector magnetograms of several active regions, and found evidence that newly emerging flux often brings up magnetic shear with a sign opposite to the dominant helicity of the active region. Moreover, the flare/CME initiation site is characterized by a close contact with magnetic flux of opposite helicity. This new revelation suggests that the interaction and reconnection of flux systems with opposite shear is a key element in the mechanism of flare/CME initiation, as predicted by the new model explained in the following section.

5.5.4 Reversed-shear flare model

Although magnetic shear is a characteristic feature of a flare-productive active region, recent observations (Kusano *et al.*, 2002; Yokoyama *et al.*, 2003) suggest that not only the magnitude of magnetic helicity but also the spatial structure of magnetic shear should be important for the triggering of solar flares. Kusano *et al.* (2003, 2004a) proposed that a solar flare could be triggered by magnetic reconnection between oppositely sheared magnetic fields near a polarity inversion

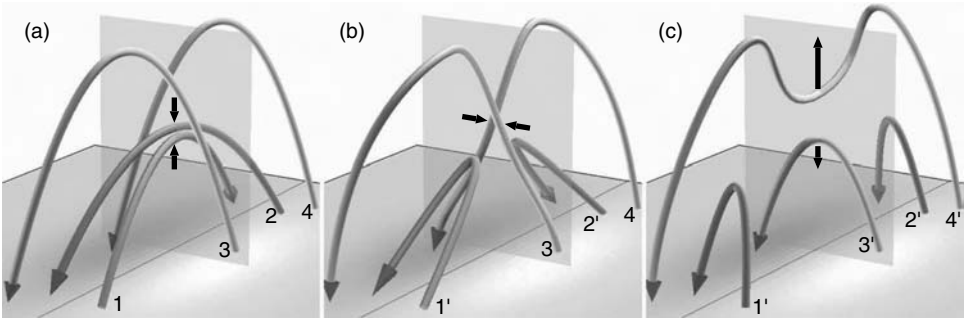

Fig. 5.39. Illustration of the three-dimensional field line structure in the reversed-shear flare model. Panels a, b, and c represent the tearing instability phase, the collapsing phase, and the erupting phase, respectively.

line (see Fig. 5.39). This *reversed-shear flare model* predicts that, if tearing mode instability grows enough at a shear inversion layer between field lines as illustrated by 1 and 2 in Fig. 5.39a, the magnetic arcade should collapse into the reconnection point because the axial magnetic flux is annihilated, as shown in Fig. 5.39b, and the result is that a vertical current sheet is generated.

After that, reconnection at the vertical current sheet ejects more sheared field lines (4' in Fig. 5.39c) upward like the tether cutting model. On the other hand, the downflow from the vertical current sheet strongly drives the tearing mode reconnection at the shear inversion layer between line 3' and reversed-shear field existing in the lower part (not shown in the figure). A mutual excitation of two magnetic reconnection processes, in which one reconnection drives another in the 3D configuration, is able to accelerate the process, even though it is originally initiated by the tearing mode instability. The reversed-shear flare model may provide a scenario in which a shear-free field is efficiently reconstructed on the solar surface through the annihilation and ejection of magnetic helicity due to the double reconnection.

Kusano *et al.* (2004a) and Kusano (2005) demonstrated by three-dimensional magnetohydrodynamic simulations that a large-scale eruption of a magnetic arcade is indeed caused by a magnetic shear reversal at the center of the magnetic arcade. This simulation also accounts for the formation of a sigmoidal field (S+ to S− in Fig. 5.40a) prior to the onset of the eruption (Kusano, 2005). It was suggested that the formation of the sigmoid results from the relaxation toward a force-free minimum energy state (Taylor, 1986), since the shearing structure inside the sigmoidal flux is well approximated by a linear force-free field.

When the calculation was continued for a much longer period after the formation of the sigmoid, the magnetic arcade collapsed and a magnetic cusp structure was created above the sigmoidal region (Fig. 5.40b), as predicted by the model. The cusp structure is well consistent with the standard CSHKP model, but the weak sigmoidal field can survive near the photospheric boundary because the sigmoidal flux is subject only to the tearing mode reconnection rather than that at the vertical current sheet. The result contrasts to some previous models of sigmoids based on the

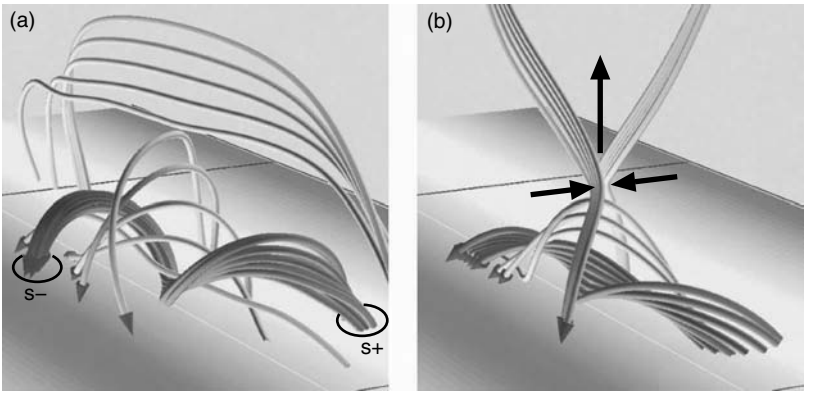

Fig. 5.40. Three-dimensional dynamic simulation of a reversed-shear arcade (Kusano 2005). Panels a and b represent the structure of magnetic field lines before and after the onset of eruption, respectively. Solid arrows indicate typical plasma flow.

kink instability, which predicted that the kinking deformation of a sigmoid should lead to the ejection of the sigmoid itself.

5.5.5 Summary

For the last decade, several models have been proposed to explain the trigger mechanism of solar flares. Although most of the models are consistent with the standard CSHKP model, at least as far as morphological features are concerned, it is still an open question as to which model is most likely to explain the trigger process of flares.

Even though simulation studies have greatly contributed to our understanding of nonlinear solar flare processes, there is a serious limitation in current numerical models. In most of the previous simulations, the resistive time scale and the time scale of the photospheric motion are artificially shortened in order to make the calculation more tractable. However, the main concern of the trigger problem is how to explain the causal relationship between processes having very different time scales. Therefore, more advanced simulation models, with more realistic boundary conditions and a more sophisticated diffusion process, should be developed in future. They may help us to understand the complicated nonlinear mechanism in the solar flare trigger process and to solve this long-standing puzzle.

5.6 Particle acceleration in flares: theory

T. Neukirch, P. Giuliani, and P. D. Wood

It is generally accepted that the energy released during solar eruptions (flares, coronal mass ejections, prominence eruptions) is stored in the magnetic field before the eruption. Theoretical models of solar eruptions invariably include magnetic reconnection as a physical process for the release of magnetic energy and its conversion into other forms of energy such as bulk flow energy, thermal energy, and nonthermal energy. Whereas the phenomena observed to occur on large (MHD) scales are generally well explained by the so-called standard model, this is not the case for the small-scale (kinetic) aspects of flares. In particular it is not clear how the large numbers of

energetic particles observed in flares are generated over very short time scales. Also, the total energy of the accelerated particle population is estimated to be as large as 50% of the total energy released in some flares. Therefore the problem of solar flare particle acceleration is one of the most important and interesting problems in solar physics. Since similar phenomena are believed to occur in many other astrophysical objects throughout the Universe, advancing our understanding of solar particle acceleration will also have implications for astrophysics in general.

Magnetic reconnection is regarded as particularly important for the generation of nonthermal particles, but a detailed understanding of the relevant physical processes is not yet available. Since magnetic reconnection in its generic form is associated with magnetic field-aligned (parallel) electric fields (e.g., Hesse and Schindler, 1988; Schindler *et al.*, 1988), the most obvious possibility of energizing charged particles is by direct acceleration through the parallel electric field. A large amount of work has therefore been done on this problem, almost exclusively using the test particle approach. We will give an overview of this work in Section 5.6.1, with emphasis on some recent studies. Another class of acceleration mechanisms is directly associated with the reconnection process, but does not rely on the parallel electric field generated by reconnection. Examples are acceleration at a fast standing shock supposed to form where the reconnection outflow encounters stronger magnetic field regions beneath the reconnection site, or acceleration by the Fermi or betatron mechanism in the collapsing magnetic trap formed by the magnetic field lines transported out of the reconnection region. Mechanisms of this type will be discussed in Section 5.6.2. Last, but not least, we will discuss in Section 5.6.3 acceleration mechanisms which (so far) have no direct relation to magnetic reconnection. In particular, these are stochastic acceleration mechanisms based on second-order Fermi acceleration by turbulence or resonant wave–particle interaction. We will focus on mechanisms for impulsive solar flares and omit the discussion of interplanetary particle acceleration associated with coronal mass ejections. Due to the limited space available we do not make any claim regarding completeness of this review, but refer the reader to the excellent reviews by Miller *et al.* (1997) and Aschwanden (2002).

5.6.1 Direct acceleration by the reconnection electric field

In its generic form (Section 2.3; Hesse and Schindler, 1988; Schindler *et al.*, 1988) magnetic reconnection is associated with parallel electric fields. These parallel fields have been connected with particle acceleration for a number of space and astrophysical phenomena, including solar flares (e.g., Giovanelli, 1946; Schindler *et al.*, 1991; Hesse, 1995), since charged particles can be directly accelerated by the parallel electric field (DC acceleration).

DC acceleration models can be divided into sub-Dreicer and super-Dreicer models according to the strength of the parallel electric field as compared to the Dreicer field[1] (Dreicer, 1959)

$$E_{\mathrm{D}} \approx 6 \cdot 10^{-3} \left[\frac{n}{10^{15}\ \mathrm{m}^{-3}}\right] \left[\frac{T}{10^{6}\ \mathrm{K}}\right] \frac{\mathrm{V}}{\mathrm{m}}. \tag{5.26}$$

[1] The actual value of the critical electric field above which particles are accelerated indefinitely is actually $0.214\,E_{\mathrm{D}}$ (e.g., Benz, 2002, p. 217)

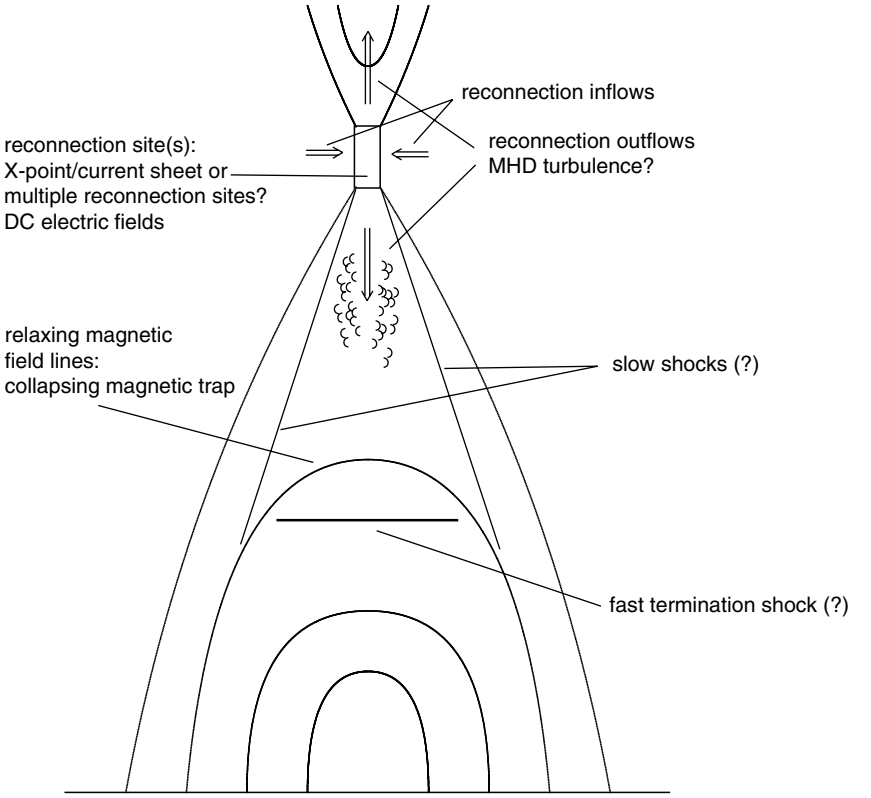

Fig. 5.41. Schematic sketch of the general MHD flare scenario. Possible acceleration sites and mechanisms are indicated. For further discussion see the main text.

In sub-Dreicer field models (e.g., Holman, 1985; Tsuneta, 1985; Benka and Holman, 1994) thermal electrons are accelerated up to a certain maximum (runaway) speed at which a stable balance between the acceleration by the electric field and the deceleration by Coulomb collisions is reached. Since the sub-Dreicer fields are quite weak they have to exist over length scales ($\approx$30 000 km) which are comparable to the length of the loops involved in a flare. Sub-Dreicer field models are able to explain some of the characterics of high-energy flare emission, but it is, for example, not at all clear which physical mechanism could generate the large-scale electric fields which are assumed in these models.

Observational and theoretical estimates of the parallel electric field strength associated with reconnection in flares give values of the order $10^2 - 10^3$ V/m (e.g., Poletto and Kopp, 1986; Schindler *et al.*, 1991; Forbes, 1997) which is substantially super-Dreicer. Therefore, the models of flare particle acceleration in reconnection generated DC fields are super-Dreicer models.

Usually, the reconnection magnetic field models used to study flare particle acceleration are stationary two-dimensional X-point or current sheet fields with or without a guide field component in the invariant direction. A lot of this work is directly related to similar studies of particle acceleration in the magnetotail. As the solar corona is

usually believed to be a low-β plasma, the coronal magnetic fields are assumed to be force free. In most models this is achieved by adding a strong magnetic field component in the invariant direction (guide field) to a 2D X-point or current sheet field.

Studies of test particle orbits with X-point topologies without a guide field have been presented by, e.g., Bulanov and Sasorov (1976), Vekstein and Browning (1997) and Heerikhuisen *et al.* (2002), whereas similar investigations including a guide field have been described by, e.g., Bulanov (1980), Bruhwiler and Zweibel (1992), Mori *et al.* (1998), and Browning and Vekstein (2001). For laboratory applications, investigations of test particle orbits in an X-point plus guide magnetic field were also carried out by Egedal and coworkers (Egedal and Fasoli, 2001a,b; Egedal *et al.*, 2001; Egedal, 2002).

Flare particle acceleration in current sheets without a guide field has been investigated by, e.g., Martens (1988) and Martens and Young (1990). The influence of a guide field on the acceleration process in current sheets has been investigated by Zhu and Parks (1993), Litvinenko (1996) (see also, e.g., Litvinenko and Somov, 1993), and by Zharkova and Gordovskyy (2004b). Acceleration in magnetic fields with combined current sheet and X-point topology has been studied, for example, by Heerikhuisen *et al.* (2002), Craig and Litvinenko (2002), Zharkova and Gordovskyy (2004a), and Wood and Neukirch (2005).

Except for Heerikhuisen *et al.* (2002) (see also Craig and Litvinenko, 2002) who use an exact stationary reconnective annihilation solution (with vanishing guide field) of the MHD equations found by Craig and Henton (1995), all these studies choose their magnetic field ad hoc or from purely kinematic considerations, i.e., no attempts are made to solve the MHD equations fully or approximately. This is usually justified as representing the magnetic field structure correctly in the vicinity of the nonideal region. Also, with the exception of Wood and Neukirch (2005), all authors use a spatially constant electric field in the invariant direction. This is consistent with the assumptions of stationarity and spatial invariance.

The typical procedure is then to integrate the equation of motion for charged particles in the given fields, either (semi-)analytically or numerically, and to construct the distribution function of particle energies as the particles leave the acceleration region (i.e., the vicinity of the X-point or the current sheet). This is usually done by following the method introduced by Bulanov and Sasorov (1976), who calculate the outgoing energy distribution function under the assumption of an initially uniform particle flux into the reconnection region. The resulting energy distributions usually have a power-law behavior ($f(E) \sim E^{-\gamma}$) for the energy range relevant for flares. For values of the parallel electric field in the range quoted above, charged particles are relatively easily accelerated to energies observed in flares.

Typically, particles drift into the region close to the X-point or the center of the current sheet where they experience acceleration by the electric field in the invariant direction until they eventually leave the region of (relatively) weak magnetic field. A (strong) guide field has the effect that the particles stay longer in the region of weaker magnetic field and are thus accelerated to higher energies (see, e.g., Litvinenko (1996) for an investigation of this effect for the case of a current sheet model).

One feature of most of the above models is that they take the electric field to be constant. Although this is consistent with the kinematic MHD equations, it is also unrealistic for a reconnection region since the parallel electric field associated

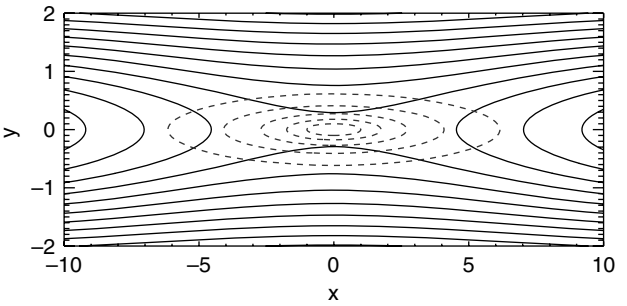

Fig. 5.42. Magnetic field used in the study by Wood and Neukirch (2005). Shown is the projection of field lines onto the x, y plane in the region of the X-point. The dashed lines are contour lines of the parallel electric field, which has a maximum at the X-point.

reconnection should be strongly localized (Hesse and Schindler, 1988; Schindler *et al.*, 1988). Therefore, Wood and Neukirch (2005) have undertaken a study in which the parallel electric field is localized. The magnetic field used in this paper is a modified Harris sheet field (Harris, 1962) including an X-point (see Fig. 5.42) and a strong guide field. The electric field is determined from Ohm's law using a stagnation point flow for the perpendicular component and a resistive term for the parallel component. The parallel electric field is strongly localized (see Fig. 5.42) using a localized resistivity. The motion of electrons in these fields is calculated numerically using the guiding center approximation (justified by the strong guide field) with initial positions in the reconnection inflow region where the parallel electric field is negligible. Orbits are calculated for a range of initial velocities. Using Liouville's theorem, any given initial distribution function in the inflow region can then in principle be calculated in the outflow region using the particle orbits.

For typical solar parameter values Wood and Neukirch (2005) find that for a Maxwellian velocity distribution and uniform spatial density in the inflow region, the particles with energies above a couple of keV have a power-law energy distribution with a power-law index of $\approx$1.5 (see Fig. 5.43). A detailed investigation (Wood, 2004) shows furthermore that the high-energy particles ($E_{\rm kin} \geq 5\,{\rm keV}$) are concentrated in narrow beams around the separatrix field lines (see Fig. 5.44).

Figure 5.44 also shows that the electrons are only accelerated along two of the four separatrix field lines. The figure shows only electrons which drift into the acceleration region from above, but their counterparts drifting in from below would be accelerated along the same two separatrix field lines. For protons the guiding center approximation is not generally valid in this configuration, but a few calculations with a full orbit code show that for the case here protons would be accelerated along the two separatrices along which no high-energy electrons are found. This asymmetry of proton and electron acceleration has been investigated in detail by Zharkova and Gordovskyy (2004a,b), but with a different magnetic field configuration and a spatially constant electric field.

A general problem of this type of acceleration mechanism is that for a realistic size of the accelerating domain (i.e., the domain with nonvanishing $E_\parallel$) the number of

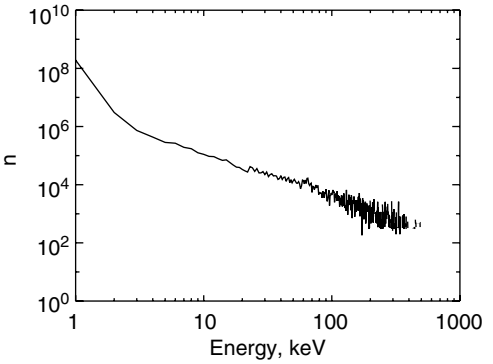

Fig. 5.43. Energy spectrum of particles in the outflow region ($x = 30$ current sheet widths) for the model of Wood and Neukirch (2005). The inflow distribution function is uniform in space and Maxwellian in velocity. The high-energy part of the distribution is a power law with index $\gamma \approx 1.5$.

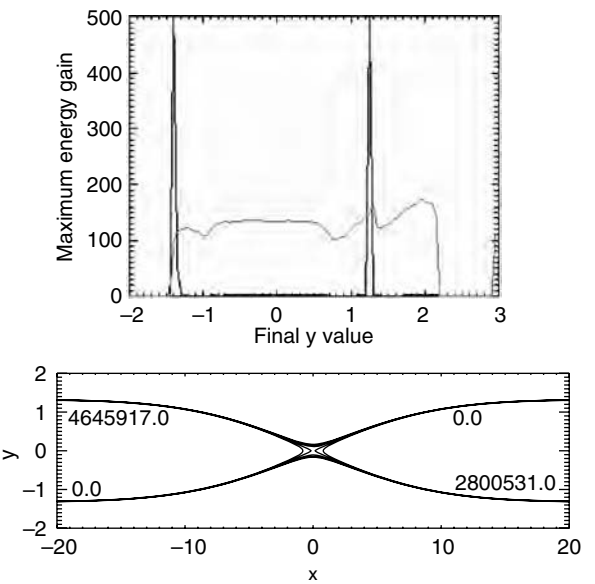

Fig. 5.44. The upper panel shows the total energy gain for each particle orbit as a function of y at $|x| = 30L_{\rm cs}$ in the outflow region. The sharp maxima coincide with the positions of the separatrix field lines for this $|x|$. The weaker line shows that the y distribution of particles of all energies is roughly uniform. This indicates that only particles gaining large amounts of energy are concentrated along the separatrices. The lower panel shows the number of particles above 5 keV which leave the acceleration region along one of the separatrix field lines. Only orbits of electrons drifting into the reconnection region from above have been taken into account (Wood, 2004).

particles accelerated falls way short (by several orders of magnitude) of the numbers required to explain the observed nonthermal emission (see, e.g., Wood and Neukirch, 2005). To solve this problem one would either have to make the acceleration region unrealistically large, for example by assuming a very extended reconnecting current sheet (Litvinenko (1996) assumes a current sheet length of 10^4 km with a width of 500 km), or to assume that a large number of small reconnection sites exists in the acceleration region which could compensate the shortage of particles from a single site.

The models discussed so far all use electromagnetic fields which do not change with time. Time-dependent fields could potentially be used to explain time variations of flare emission or the observed spectra. Particle acceleration in time-dependent analytical fields has been studied, e.g., by Fletcher and Petkaki (1997), Petkaki and MacKinnon (1997), and Hamilton *et al.* (2003). Fields taken from MHD simulations of a reconnecting current sheet have been used, e.g., by Kliem (1994) and Kliem *et al.* (2000). More recently Turkmani *et al.* (2005) have used the fields from MHD braiding experiments for test particle calculations. In this study the particles can be accelerated in a number of acceleration sites which are distributed stochastically throughout the simulation domain. It is, however, not entirely clear how this numerical experiment is related to the general MHD picture of solar flares and more work in this direction needs to be done.

A general problem of test particle calculations is that they do not provide a self-consistent picture of the acceleration process. This can be justified if the generated high-energy particle population is only a small fraction of the thermal background population. Due to the large number of high-energy particles generated this is not necessarily the case for solar flares. It would therefore be highly desirable that the test particle calculations are supplemented by self-consistent kinetic calculations. The largest problem will be to overcome the huge gap between the kinetic scales (a few meters to kilometers) and MHD scales (order 10^4 km).

5.6.2 Acceleration mechanisms associated with reconnection

The mechanisms discussed so far all rely on direct acceleration by the reconnection electric field. There are, however, other possibilities to transfer the released magnetic energy into particle energy. These possibilities are indirect because they involve the transformation of the magnetic energy into another form of energy (usually bulk flow energy) which is then tapped for the acceleration process.

One such possibility has been suggested by Moore *et al.* (1995) and Larosa *et al.* (1996). These authors use simple physical arguments to describe how particles might be energized by a turbulent reconnection outflow via diffusive second-order Fermi acceleration. The theory has not, however, been developed beyond the point of general estimates. More recently, Selkowitz and Blackman (2004) investigated stochastic Fermi acceleration in the low-energy regime including both steady and diffusive acceleration in their model. They also propose that very high-energy electrons ($E > 100$ keV) could be generated by a loop-top fast-mode shock (see below).

It has also been suggested that a fast MHD shock could develop at the point where the reconnection outflow encounters the stronger magnetic field regions of the magnetic loops beneath the reconnection region (e.g., Forbes, 1986). Tsuneta

and Naito (1998) have discussed the possible role of such a fast shock for particle acceleration. Somov and Kosugi (1997) have included a fast shock as an intrinsic feature of one of their collapsing magnetic trap models. In their model the shock does not directly accelerate particles but scatters particles back into the magnetic trap (see below). Observational evidence for the existence of fast shocks is, at least at the moment, sparse, but some radio observations of flares have been interpreted as signatures for a fast termination shock (Aurass and Mann, 2004).

Tsuneta and Naito (1998) suggest that first-order Fermi acceleration at the fast shock could be responsible for the large number of high-energy electrons in solar flares (see Fig. 5.41). A general problem for electron Fermi acceleration by shocks is that injection energies higher than the typical thermal energy at coronal temperatures are needed to explain the generation of the bulk of the nonthermal population with energies of 20–100 keV. Tsuneta and Naito (1998) argue that a combination of preheating of the particles by the slow shocks associated with flare reconnection and the shock being oblique can overcome this difficulty, and make a direct connection between the fast shock and the existence of hard X-ray loop-top sources observed in some flares (e.g., Masuda *et al.*, 1994). However, detailed self-consistent calculations of the formation of a fast shock under flare conditions and demonstrations that it provides a viable acceleration mechanism for solar flare particles have yet to be undertaken.

Selkowitz and Blackman (2004) investigate the consequences of a combination of second-order (stochastic) Fermi acceleration in the low-energy regime (10–100 keV) with a loop-top fast shock producing particles with energies above 100 keV by first-order Fermi acceleration. In this scenario the necessary injection energies would be provided by the second-order Fermi process in the turbulent reconnection outflow region.

The outflow from the reconnection region will generally be associated with a relaxation of the stressed pre-flare magnetic field into a lower energy state by a shrinkage of magnetic field lines (e.g., Forbes and Acton, 1996). Charged particles would become trapped either between the legs of the relaxing loops or alternatively between the points where the relaxing field lines cross a loop-top fast-mode shock. Somov and Kosugi (1997) have suggested that this *collapsing magnetic trap* should lead to an increase in the energy of the trapped particle population by the betatron effect and by first-order Fermi acceleration. Since the magnetic moment of the trapped particles, $\mu = mv_\perp^2/2B$, is approximately conserved, an increase in the magnetic field magnitude B has to be accompanied by the same increase in the perpendicular particle energy, $mv_\perp^2/2$ (betatron acceleration). The trapped particles also carry out a (quasi-)periodic motion between mirror points which are located either in the loop legs or at a fast-mode loop-top shock (see Fig. 5.41). The approximate conservation of the second adiabatic invariant, $J = \oint p_\parallel \mathrm{d}l$, leads to an increase in the parallel momentum, $p_\parallel$, because the distance between the mirror points decreases as the length of the field lines decreases (first-order Fermi acceleration). A similar particle energization process during substorms in the Earth's magnetotail has been suggested by Birn *et al.* (1997b, 1998b) to explain dispersionless particle injections observed frequently by geosynchronous satellites. General theoretical investigations regarding the role of the two processes in collapsing magnetic traps and their relevance for solar flares have been carried out by, e.g., Somov and Bogachev (2003). The effect

of Coulomb collisions of the accelerated particle population with the background corona has been studied by Kovalev and Somov (2003). Whereas these studies only use general properties of collapsing magnetic traps, Karlicky and Kosugi (2004) have used a specific simple model for a collapsing magnetic trap to study the acceleration occurring in their model, including the effects of Coulomb collisions. They also discuss the possibility of explaining loop-top hard X-ray sources and radio emission observed in flares within the framework of the model. In general, the work on collapsing traps carried out so far is promising, but more detailed studies are necessary to be able to make a final judgement about the effectiveness of this mechanism for flare particle acceleration.

5.6.3 Other acceleration mechanisms

We have so far discussed flare acceleration mechanisms which have an obvious direct or indirect association with magnetic reconnection. For the mechanisms we will discuss now this association is at least unclear. In particular these are the so-called stochastic acceleration mechanisms.

In general, in stochastic acceleration mechanisms particles gain or lose energy over short time intervals, but on the average gain energy over longer times. Examples are second-order Fermi acceleration caused by random scattering/mirroring of particles in (strongly) turbulent magnetic fields or resonant wave–particle interaction in weakly turbulent plasmas. Apart from solar flares, stochastic acceleration mechanisms have been studied in astrophysics in general for a long time, in particular in connection with the acceleration and transport of cosmic rays.

In the context of solar flares, a general assumption made either explicitly or implicitly by stochastic acceleration models is that a substantial amount of energy released on large (MHD) scales is transferred into a turbulent cascade. This energy is then in turn used to generate the high-energy particle population by stochastic acceleration. How and where the energy released on large scales is converted into plasma turbulence is at present unclear. As already discussed in Section 5.6.2, one possibility is that the high-speed flows in the reconnection outflow regions become turbulently unstable (e.g., Moore *et al.*, 1995; Larosa *et al.*, 1996; Selkowitz and Blackman, 2004). Another possibility would be that the time evolution of the flare magnetic field causes oscillations in the relaxing and shrinking magnetic loops which could then cascade to smaller scales. It is worth pointing out, however, that if the fraction of the total flare energy ending up in high-energy particles is really as high as 50% the energy transfer processes involved in these scenarios have to be extremely efficient.

Stochastic acceleration is usually investigated using quasi-linear kinetic theory, in which the time evolution of the particle distribution functions is determined by a Fokker–Planck equation in momentum space:

$$\frac{\partial f}{\partial t} = \frac{1}{p^2} \nabla_{\mathbf{p}} \cdot \left(p^2 \mathbf{D} \cdot \nabla_{\mathbf{p}} f \right) + S(\mathbf{p}, t).$$

Here $\mathbf{p}$ is particle momentum, $\mathbf{D}$ is the matrix of Fokker–Planck coefficients (here only including the momentum space variables) and $S(\mathbf{p}, t)$ summarizes possible source or sink terms. In addition there can be terms describing systematic energy losses or gains (as opposed to diffusive processes) which we have omitted here. None of the present models includes any spatial information which would allow a coupling to

MHD flare models. The coefficients of the Fokker–Planck equation are determined by the interaction of the particles with the turbulent magnetic field which is normally regarded as a (random) superposition of wave modes. In many cases the Fokker–Planck equation is simplified further by assuming gyrotropic or isotropic distribution functions. For a detailed treatment of the derivation of the Fokker–Planck equation and its coefficients based on the various plasma wave modes we refer the reader to Schlickeiser (2002).

The physical mechanism behind the net acceleration of particles by small amplitude wave modes is the resonance between the cyclotron frequency of the particles (or integer multiples of it) and the frequencies of the waves present in the turbulent spectrum, taking into account the Doppler shift caused by motion of the particle (for a detailed discussion see, e.g., Miller *et al.*, 1997). Obviously if a particle gains energy its resonance condition will change, and for particles to be accelerated from thermal energies to the energies observed in solar flares a spectrum of waves with the right distribution of frequencies has to be present in the acceleration region.

A number of acceleration models based on wave–particle resonances have been suggested to operate for electrons and protons/ions during solar flares. We will here only discuss a few recent suggestions. For a more detailed account we refer the reader to Miller *et al.* (1997). Miller and Roberts (1995) have investigated how protons could be accelerated from thermal to relativistic energies by gyroresonant interaction with a turbulent cascade of Alfvén waves, presenting numerical solutions of the Fokker–Planck equation coupled with an equation for the evolution of the turbulent wave energy density. Their calculations indicate that even for very low levels of turbulent magnetic energy (compared to the energy density of the ambient magnetic field) a sufficient number of protons can be accelerated to energies required to produce γ-ray lines observed in flares on the observed time scales ($\leq$a few seconds).

Electrons could be accelerated by a similar cascade for fast-mode waves, but the level of turbulence needed is very high (Steinacker and Miller, 1992). Instead the electrons could be accelerated by the fast-mode waves through transit time damping, which can be regarded as the magnetic equivalent of Landau damping (see, e.g., Stix, 1992). Using an approach similar to the one for protons used by Miller and Roberts (1995), Miller *et al.* (1996) show that transit time damping in combination with a turbulent fast-mode cascade can accelerate a sufficient number of electrons to hard X-ray producing energies on the observed time scales. Again, the level of turbulence needed is comparatively small. Since transit time damping affects only the parallel velocity components of the electrons, Miller *et al.* (1996) had to postulate the presence of a mechanism which isotropizes the electron distribution function. Lenters and Miller (1998) improved the model by including Coulomb collisions and pitch-angle scattering.

In these and other studies (e.g., Ramaty, 1979; Park and Petrosian, 1995, 1996; Park *et al.*, 1997) the stochastic acceleration of electrons and protons/ions is treated separately, making an ad hoc choice of the wave mode necessary for acceleration of the particle species studied. In a recent paper Petrosian and Liu (2004) have investigated the acceleration of electrons and protons in an integrated model, yielding promising results. The model has also been used to study the acceleration of ^{3}He and ^{4}He and

seems to be able to explain the observed large enrichment of ^{3}He in impulsive solar energetic particle events (Liu *et al.*, 2004b).

In summary, stochastic acceleration models can explain many of the observational features of flares. Since they can in principle operate within large volumes, the number problem is not as severe as for other acceleration mechanisms and they can explain the acceleration of electrons and protons to the observed energies. One particular advantage of stochastic acceleration based on wave–particle resonance is that it can explain the preferential acceleration of particular ions. This is difficult to achieve with other acceleration mechanisms.

5.6.4 Summary

Understanding the physical mechanisms leading to the generation of high-energy particles in solar flares is one of the outstanding problems in solar physics. Since similar processes are probably operating in other astrophysical objects as well, progress made for solar flares will be important for astrophysics in general. Over the past decade the observations of solar flares have been considerably improved and we are reaching a position where the theories of particle acceleration in flares are strongly constrained by observations. On the other hand there is still a considerable gap between between the macroscopic (MHD) theory of flares and the microscopic (kinetic) theory of particle acceleration. Closing this gap is a formidable task, but it is this challenge that makes the problem of particle acceleration in solar flares one of the most interesting problems in solar physics.

5.7 Fast particles in flares: observations

L. Fletcher

The link between the reconfiguration of coronal magnetic fields and fast particles was established quite early on in flare physics. Giovanelli (1948) suggested that H_α chromospheric flare brightenings were due to electrons *energized* in inductive electric fields set up in the neighborhood of a sunspot. He was envisaging a relatively low level of energization, but the *sudden ionospheric disturbances* (SID) (e.g., Ellison, 1950) caused by ionization of the D-region by an enhanced flux in the ultraviolet, extreme UV, and X-ray, suggested the presence of much higher energy flare particles. Observations of the ionizing flux itself had to wait until the era of balloon and space-borne instrumentation; for example, Arnoldy *et al.* (1967) established the correlation of SIDs with flare X-ray bursts observed with the OGO-I and III satellites.

At present, the primary diagnostic for flare-accelerated electrons is X-ray emission, interpreted as electron–ion bremsstrahlung. Brown (1971) showed that the observed spectrum of X-rays can be inverted, i.e., deconvolved with the photon production cross-section, to deduce the source-averaged spectrum of accelerated electrons producing it. The diagnostic is quite well-understood for bremsstrahlung produced by a hot thermal plasma (thermal bremsstrahlung), or by nonthermal electrons in a relatively cold plasma background *target* (collisional bremsstrahlung). For the latter, with the assumption of a collisionally thick target (i.e., beam electrons lose energy via Coulomb collisions as they radiate) properties of the *primary* accelerated electron spectrum can also be deduced. The *hard* or *nonthermal* component of the

X-ray spectrum has generally attracted the most interest from the point of view of acceleration, with the lower energy X-ray radiation assumed to be a response to the primary energy input. However, coronal flare sources observed at a few tens of keV probably reveal another facet of electron acceleration (though they are as yet little explored, either observationally or theoretically).

The radio domain is also rich in electron diagnostics. Both coherent and incoherent mechanisms operate. During the impulsive phase, incoherent gyrosynchrotron emission dominates at centimetric sometimes and millimetric wavelengths. Several different signatures of beam-generated coherent plasma emission are also observed, such as decimetric spikes and Type III bursts. Flare electrons can also continue into space producing interplanetary Type IIIs, detected as waves and particles *in situ*. The infrared to EUV regime offers only model-dependent particle diagnostics, but high spatial and temporal resolution data mean that locations of emission sources and their relationship to the magnetic configuration can be investigated in great detail. Solar flares also accelerate copious quantities of ions, which are detected both *in situ*, at >0.3 AU, and remotely via the γ-ray lines they produce at the Sun. This chapter discusses in greater detail the remotely sensed diagnostics for accelerated particles in flares.

5.7.1 Hard X-ray emission

The definition of *hard* X-ray (HXR) is somewhat fluid, but let us settle on a photon energy range from 20 keV to 500 keV. HXR spectroscopy was first carried out inadvertently by balloon-borne scintillation counters (Peterson and Winckler, 1959), and thereafter in the sixties and seventies with balloon, rocket, and satellite experiments, including the OSO/OGO series. In the 1980s the Hard X-ray Imaging Spectrometer HXIS (van Beek *et al.*, 1980) on the Solar Maximum Mission added imaging. HXIS showed intense, discrete HXR sources at energies up to 30 keV, and joint observations with ultraviolet confirmed that these were formed in the chromosphere (e.g., Hoyng *et al.*, 1981). Now known as *HXR footpoints*, they are interpreted as bremsstrahlung radiation produced when fast electrons encounter the dense chromosphere. However, it was demonstrated that only $\sim$20% of the hard X-ray emission at energies between 16 and 30 keV came from resolved sources: the remainder presumably appearing as diffuse emission (MacKinnon *et al.*, 1985). In some events, coronal emission was also seen (e.g., Hoyng *et al.*, 1981). Subsequent HXR imaging instruments, Hinotori (e.g., Ohki *et al.*, 1982) and the Yohkoh Hard X-ray Telescope (Kosugi *et al.*, 1991), confirmed HXR footpoints and made several well-resolved observations of coronal HXR sources (e.g., Masuda *et al.*, 1994) with photon energies up to at least 50 keV. Coronal sources are amply confirmed by RHESSI.

Based on the collisional thick-target interpretation, properties of the flare electron population can be summarized as follows (see review by Miller *et al.*, 1997). For a large flare, 10^{36}–10^{37} electrons s^{-1} must be accelerated to above 20 keV for several tens of seconds, giving a total energy above 20 keV of 10^{31} erg. Acceleration takes place on time scales of a second or so, and is fragmented into sub-second bursts. At typical coronal densities of 10^9 cm^{-3}, a coronal volume of $(10^9\,\mathrm{cm})^3$ would be depleted of electrons within a second, therefore any acceleration mechanism must

provide for a continuous supply of electrons to the corona, and the geometry must be such as to be able to process a huge number of electrons per second.

RHESSI

The Ramaty High-Energy Solar Spectroscopic Imager (Lin *et al.*, 2002), launched in February 2002, merits a brief description since its combination of spatial, spectral, and temporal resolution is historically unique and has provided many challenges for flare physics. Onboard the RHESSI spacecraft are nine identical detectors, each a single germanium crystal. The arrival of an X-ray photon in a detector generates an energy-dependent number of electron–hole pairs. The electrons are drawn to a central anode and register as a pulse. The theoretical energy resolution is about 1 keV at energies up to 100 keV, and about 5 keV in the γ-ray range (MeV).

Imaging is achieved by rotating modulating collimators. In front of each detector is a pair of grids, aligned so that the slits and slats in the rear and front grids are exactly parallel. Each of the nine detectors has a different slit–slat spacing. As the whole assembly rotates with the spacecraft (at $\sim$14 rpm) around an axis joining the front and rear grids, photons from the Sun are either blocked or can reach the detector, depending on their angle of incidence. The photon flux is thus modulated, with the modulation pattern at each detector depending on the slit–slat spacing and source position. Combining modulation patterns from several detectors yields the source surface brightness distribution. Modulation of the lower energy photons (a few tens of keV) by the finest grids gives an angular resolution of around 2 arcseconds, or 1500 km on the Sun. Higher energy photons are only modulated by the thicker grids, so the angular information is not so detailed.

5.7.2 HXR spectroscopy

Early HXR spectroscopic data broadly speaking supported a model of a hot (quasi-)thermal source dominating at electron energies below $\sim$20 keV, with a (sometimes broken) power law, or exponential electron distribution above. These spectra were not very detailed, but the high spectral resolution RHESSI spectroscopic observations now provide strong motivation for detailed modeling, including processes such as electron–electron bremsstrahlung, noncollisional particle losses and photospheric albedo. Theoretically these effects were always part of the picture – observationally we can now hope to disentangle them, an integral part of getting at the underlying accelerated electron spectrum.

Spectroscopy proceeds in two complementary strands. In forward fitting, a trial electron spectrum is folded through the HXR cross-section, the result compared with the observed HXR spectrum, and the electron parameters adjusted until an acceptable fit is obtained. This method is fast and transparent, but presumes an electron spectral model (usually a single or broken power law in energy, with a thermal component at low energies). Grigis and Benz (2004) find electron spectral indices ranging from 3 to 9, and typical temperatures of the thermal component of 20–40 MK. The spectral index is strongly correlated with the nonthermal flux, and varies throughout the flare, over subpeaks with durations of much less than a minute in a *soft–hard–soft* manner (e.g., Fletcher and Hudson, 2002; Grigis and Benz, 2004). This appears to be an elementary property of the acceleration process.

The second approach to deriving electron spectra is via numerical inversion of the photon spectrum. With some prior assumption about the bremsstrahlung cross-section, the electron spectrum can be obtained by differentiating the photon spectrum under some constraints of smoothness or regularization (e.g., Piana, 1994). This is a more data-driven approach (subject to its own problems) and the subtleties of the electron spectra have come to light primarily via inversion. Using early balloon-flight data, Johns and Lin (1992) recovered impulsive phase electron spectra consistent with a broken power law above 20 keV and a hot (∼30 MK) thermal component. Piana *et al.* (2003) analyzed the July 23, 2002 RHESSI flare, and confirmed the basic broken power law (found also using forward-fitting by Holman *et al.*, 2003), and a low-energy spectrum consistent with a multithermal plasma with a broad temperature distribution. However, a significant new feature is a dip in the source-averaged electron spectrum at 25–45 keV (Fig. 5.45), which has many possible interpretations.

Perhaps the simplest interpretation is a low-energy cutoff at 30–50 keV, or shallowing in the slope of the accelerated electron spectrum. In this case, the spectral slope below this energy is also of importance in characterizing the transport and energy-loss mechanisms. However, the dip at 25–45 keV can also be seen as a bump at around 55 keV. This could be caused by backscatter of HXR photons from electrons in the dense chromosphere (e.g., Bai and Ramaty, 1978; Johns and Lin, 1992; Kontar *et al.*, 2003), giving a contribution in an energy range dependent on the spectral slope of the primary photon spectrum and the source position. Correcting for photospheric albedo reduces the size of the dip but it is not yet known whether it can be removed altogether. It could be X-rays from the charge- and current-neutralizing return current that, theoretically, flows co-spatially with the beam. Zharkova and Gordovskyy (2005) have performed numerical simulations of this, finding a bump, but at lower energies than observed.

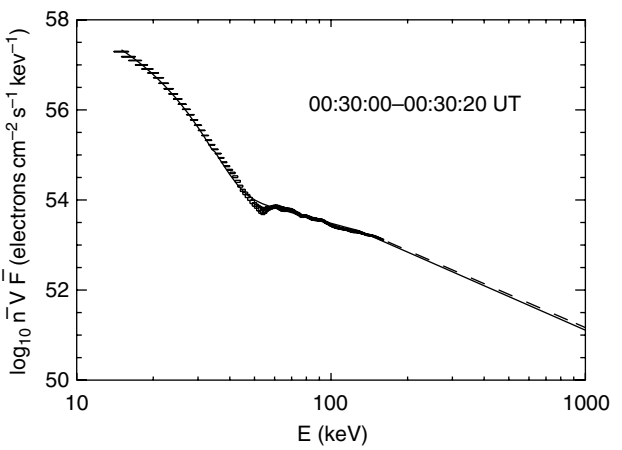

Fig. 5.45. Source-averaged electron spectrum obtained by inversion of the RHESSI bremsstrahlung spectrum in the July 23, 2002 flare. Note the *dip* at energies of around 25–45 keV. Figure from Piana *et al.* (2003).

Forward-fitting is also carried out in small *microflare* events. These have temperatures around 10–15 MK and steep power-law photon spectra above about 10 keV (e.g., Krucker *et al.*, 2002; Hannah *et al.*, 2004). Collisional thick-target analysis of a single GOES B-class event (i.e., four orders of magnitude less thermal energy than a large flare) by Hannah *et al.* (2004) implies a total energy in nonthermal electrons of around 10^{29} erg (for a low-energy cutoff of 20 keV). The thermal energy in the same event derived from the EUV by Liu *et al.* (2004a) is around 10^{28} erg. The thick-target interpretation might be incorrect, but we do know that microflares also show microwave signatures (e.g., Gary *et al.*, 1997; Qiu *et al.*, 2004) and Type III bursts, providing further evidence for substantial nonthermal electron components even in these tiny events.

5.7.3 Flare imaging: HXR to infrared

The first recorded observation of a solar flare was in white light (Carrington, 1859) and showed bright footpoints. However, white-light enhancements are hard to detect, and occur mainly in the largest flares, so in the decades before space-based observations, flare footpoints were observed primarily in H_α. From this time the term *two-ribbon* flare originates: two bright (and often very convoluted) ribbons of H_α emission were seen, often separating rapidly and followed by an arcade of loops joining the locations where the ribbons had been. Ribbons emit also in the IR, UV, and EUV. HXR and radio sources are found at two or three footpoints in the ribbon, and are at or near the ends of bright soft X-ray (SXR, ∼1–2 keV) loops, often with strong, impulsive SXR footpoints suggestive of strong heating (e.g., Hudson *et al.*, 1994; Mrozek and Tomczak, 2004). Figure 5.46 shows an example of a two-ribbon flare observed in EUV, low- and high-energy HXR, and γ-rays.

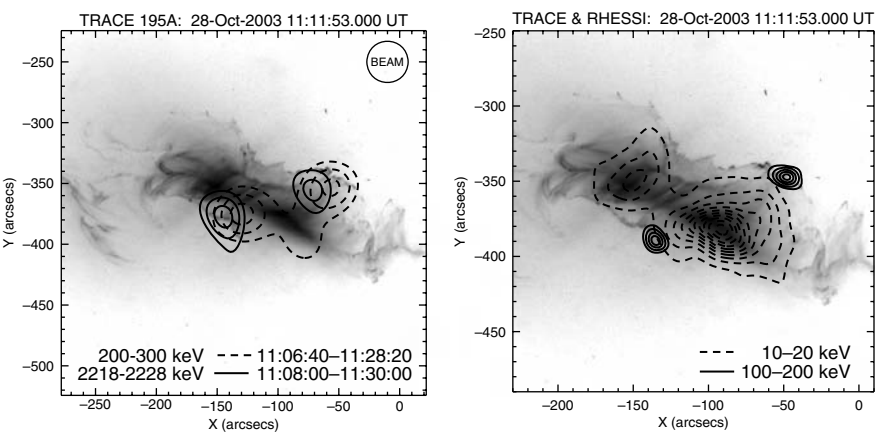

Fig. 5.46. Multiwavelength observations of the October 28, 2004 flare. In both panels, the background image is TRACE 195 Å emission. Left: the dashed contours are HXR emission in the 200–300 keV range, and the solid contours are γ-ray centroids at 2.2 MeV. Image from Hurford *et al.* (2005). Right: the dashed (extended) contours are HXR emission between 10 and 20 keV and the solid between 100 and 200 keV. Image courtesy of Säm Krucker, UC Berkeley.

HXR footpoint sources

Yohkoh/HXT showed predominantly double or multiple footpoint flares, (Sakao *et al.*, 1996). Single footpoints could have been unresolved multiple footpoints, or with a conjugate footpoint below the dynamic range (around 5 to 10) of Yohkoh/HXT. The predominance of double footpoints suggests that conjugate footpoints are usually of approximately equal brightness. Footpoints were observed to move; for instance, Sakao *et al.* (2000) demonstrated a tendency for rapidly separating footpoints to be associated with flares with a photon spectrum breaking upwards at high energy. Although Yohkoh/HXT observed thousands of HXR flares, only one was reported as a two-ribbon HXR flare (Masuda *et al.*, 2001). This was during the well-observed July 14, 2000 event, remarkable for the symmetry with respect to the magnetic neutral line of its EUV flare arcade. Its magnetic configuration may in fact have been quasi-2D, especially in its late phase. Even with RHESSI imaging, which has a better dynamic range (of about 20), we still find that HXR sources of a few tens of keV and above tend to be concentrated into two or three footpoints, rather than distributed along a whole ribbon. This implies that, apart from a few exceptional cases, the high fluxes of very energetic electrons are preferentially accelerated in certain parts of the inherently 3D reconnecting structure.

Other wavelengths – IR to EUV – are not generally used as electron flux/spectral diagnostics, although the wings of the H_α line can be used in principle to diagnose total electron flux (Canfield *et al.*, 1984). However, UV and optical footpoints are better resolved in space and time than HXR sources, so can be used to track the evolution of electron energy deposition sites. White-light flare emission is thought to be due to an increase in the free–free and free–bound emission in the chromosphere (Hudson, 1972; Aboudarham and Henoux, 1986). Radiative backwarming of the chromosphere is predicted to lead to observable increases in the infrared (Hudson, 1972). This has recently been observed by Xu *et al.* (2004) to occur in the same spatial locations as RHESSI HXR footpoints.

Footpoint motions

Footpoints are assumed to map the ends of field lines which at any instant are involved in reconnection, so the rate at which flux is advected into the coronal reconnection region can be deduced from the product of the footpoint speed and the photospheric magnetic field strength (Forbes and Priest, 1984). In a strictly 2D configuration this is equal to the reconnection electric field. Using H_α flare ribbons, Poletto and Kopp (1986) first deduced a reconnection electric field on the order of $100\,\mathrm{Vm}^{-1}$ during the gradual phase of a large flare. Subsequently, Qiu *et al.* (2002), Asai *et al.* (2004) and others have carried out similar analyses, finding electric field strengths on the order of a few kV m^{-1} during the flare impulsive phase. These latter authors also identified correlations between the footpoint separation rate and the HXR flux.

Attempts to understand the 3D configuration from footpoint excitation use multi-wavelength observations and theoretical magnetic field extrapolations. Both Aulanier *et al.* (2000) and Fletcher *et al.* (2001) deduced the presence of a coronal spine-fan configuration (using magnetograms, UV/EUV and X-ray observations), while Metcalf *et al.* (2003) found evidence for quasi-separatrix layers, by showing

that the path of a rapidly moving Yohkoh/HXT source and a white-light source followed the theoretical location of the intersection of magnetic quasi-separatrix layers with the photosphere. RHESSI shows many examples of moving HXR footpoints. For example, Fletcher and Hudson (2002) found systematic footpoint separations, with a rough correlation between the separation rate and the HXR spectral index. Footpoints were observed to separate along, rather than perpendicular to, the moving flare ribbons observed in EUV – a behavior inconsistent with simple 2D reconnection models. This was also seen in the two-ribbon X-class flare that occurred on July 23, 2003. Krucker *et al.* (2003) tracked three HXR footpoints for 10–15 minutes, with periods of rapid movement corresponding to high HXR fluxes. The presence of more than two moving footpoints suggests at least three flux domains involved in the reconnection process.

TRACE flare footpoints are typically on the order of an arcsecond across or less, and follow meandering trajectories. However, the collective motion of many UV sources forms a narrow *excitation front* sweeping across the lower atmosphere. Fletcher *et al.* (2004) tracked the individual TRACE UV footpoints that comprise a flare ribbon as it swept across the chromosphere. At the level of individual UV sources within the ribbon, a good correlation was found between the UV intensity and the product of footpoint speed and line-of-sight magnetic field strength. However, uncorrelated intensity in adjacent groups of footpoints indicates a spatially fragmented, rather than continuous, coronal reconnection rate.

Coronal HXR sources

With SMM/HXIS, van Beek *et al.* (1981) found coronal sources at 3.5–16 keV. Observations of an occulted flare (i.e., with footpoints beyond the solar limb) with the Solar X-ray Telescope on Hinotori extended this to at least 25 keV (Takakura *et al.*, 1983). These sources were generally interpreted as thermal bremsstrahlung from a hot target. The claim of an impulsive, and by implication, nonthermal coronal component was first made by Masuda *et al.* (1994) using Yohkoh/HXT, but this observation suffered from the dynamic range and source confusion limitations encountered when imaging usually diffuse coronal HXR sources together with intense chromospheric ones. In a study of 14 occulted Yohkoh/HXT flares, Tomczak (2001) put this claim on a stronger footing, demonstrating that coronal sources exhibit both gradual and impulsive HXR emission (apparently originating in the same source, with the impulsive spikes being more energetic). Hudson *et al.* (2001) observed a moving Yohkoh/HXT coronal HXR source, interpreted as fast electrons trapped in the expanding field of a coronal mass ejection (also showing slowly drifting decimetric emission).

RHESSI coronal sources occur at energies from a few to several tens of keV, and are frequently moving. Coronal HXR spectra are usually softer than those of their footpoints (though Hudson (1978) observed an extremely hard coronal source via limb occultation). They often appear prior to the footpoint sources (as for example in the July 23, 2003 flare where Lin *et al.* (2003) report a rise-phase coronal source with a wholly nonthermal spectrum) and are maintained long after the impulsive phase has passed. Emslie *et al.* (2003) fit the coronal source in the main phase of the July 23, 2002 flare by an isothermal Maxwellian, but the variation of coronal source

centroid position as a function of energy in the April 21, 2002 event (Gallagher *et al.*, 2003) shows that sources need not be isothermal. Karlický *et al.* (2004) require also a thin-target nonthermal bremsstrahlung component to explain their moving coronal sources (also radio emitters) and in a small number of events the majority of HXR photons up to 50 keV are generated in the corona (Veronig and Brown, 2004) and are interpreted as collisional thick target emission in a dense coronal loop (on the order of $10^{11}\,\mathrm{cm}^{-3}$).

Plausible explanations for coronal sources include: (i) emission from a fast-mode shock, occurring where the outflow jet from a coronal reconnection region impacts on a dense, static loop system below (Tsuneta and Naito, 1998); (ii) signatures of the current sheet itself or its heated outflow regions (e.g., Sui and Holman, 2003); (iii) particles trapped and possibly further accelerated in the field below a current sheet (e.g., Somov and Kosugi, 1997; Fletcher and Martens, 1998). All of the above predict that coronal sources will rise as time progresses, which is observed. Ji *et al.* (2003) have also found a RHESSI coronal source coincident with an erupting filament (which eventually fails to leave the Sun), suggesting extreme heating, possibly of the filament material, as a flux rope rises and interacts with the surrounding field.

5.7.4 Nonthermal radio emissions

During the impulsive phase both coherent and incoherent radio emission is observed. In the centimeter range, gyrosynchrotron emission dominates, produced primarily by electrons trapped in the strong magnetic field of flare loops. HXR and microwave emission are often described as coming from *the same* population of accelerated electrons, meaning electrons accelerated in the same event with comparable energies. Kosugi *et al.* (1988) found the best correlation to exist between $\leq$80 keV HXR and 17 GHz Nobeyama data in impulsive events, suggesting that the cm-wavelength emission is generated by electrons with $E \leq 200$ keV. White *et al.* (2003) have provided the first simultaneous observations of coronal HXR and microwave emission during the pre- and impulsive phase of a solar flare, which suggest an extended coronal population of density $10^{10}\,\mathrm{cm}^{-3}$ above 20 keV. Gyrosynchrotron emission is beamed along the direction of travel of the electrons and is sensitive to local field strength, so it can be used, together with HXRs, to constrain the electron angular distribution. For example, Melnikov *et al.* (2002) and Lee and Gary (2000) find evidence for perpendicular anisotropies in the injected electron distributions.

Type III bursts are high brightness temperature radio sources drifting rapidly in frequency. They occur predominantly at decimeter wavelengths and are a plasma collective effect, resulting from mode-conversion of Langmuir waves generated by a beam of electrons. The burst frequency is the local plasma frequency or its second harmonic, and from the drift rate we deduce that the beams are traveling at around one-third of the speed of light, usually moving outwards from the Sun. In some strong flares Aschwanden *et al.* (1995) found correlated sequences of outward-propagating bursts, typically delayed by several tenths of a second with respect to HXR bursts. The size of the delays implies that the upward-propagating beams start to produce radio emission at a height of $\sim$50 000 km. However, not every HXR event is accompanied by a Type III signature. Type IIIs require a beam instability (a positive slope in velocity space) to develop at an appropriate electron energy for exciting radio

frequencies, and the magnetic geometry might not always permit this. There is also the possibility of wave absorption or suppression. Conversely, Type III events are frequently observed in the absence of an X-ray flare. However, it requires a far smaller flux of electrons to make an observable Type III than to make an observable HXR event, so this is not surprising. The spatial association between Type III bursts and plasma structures in the corona can be probed: for example, Raulin *et al.* (1996) find that the centroids of Type III sources are aligned along Yohkoh soft-X-ray jets, suggesting that the electrons propagate along the jets, in relatively dense material. Radio emission from slowly drifting plasmoids during the flare impulsive phase (Khan *et al.*, 2002; Karlický *et al.*, 2004) are interpreted as plasma emission generated by electron beams penetrating into the plasmoid magnetic field structure.

Type II radio bursts during the gradual phase are slowly drifting, broadband radio signals. Their detailed time and frequency structure is consistent with fast electrons accelerated in short bursts at the head of a slowly drifting shock, usually interpreted as a CME bow shock. Recently Aurass *et al.* (2002) have reported a stationary Type II burst, which does not drift in frequency and is therefore consistent with a standing shock, possibly that produced when a downward-directed outflow jet from a coronal reconnection region impacts the top of post-reconnection coronal loops.

5.7.5 Ions

Narrow γ-ray lines originate from ambient heavy ions raised to excited nuclear states by collisions with accelerated protons or α-particles. Broad lines arise from excited states of heavy ions which are themselves accelerated. Nuclear states de-excite rapidly, so prompt lines reflect the instantaneous fast ion population. Line emission occurs primarily in the 4–7 MeV range and requires excitation energies of 10–30 MeV per nucleon of the exciting particles (Ramaty *et al.*, 1979). Chupp *et al.* (1975) using OSO-7 made the first detection of de-excitation lines from carbon and oxygen at 4.4 and 6.1 MeV, respectively, as well as the neutron capture line at 2.22 MeV. Flare γ-rays have also been observed by the SMM Gamma-Ray Spectrometer, the Compton Gamma-Ray Observatory (CGRO), the Yohkoh Gamma-Ray Spectrometer, GRANAT/PHEBUS, and latterly by RHESSI.

Miller *et al.* (1997) summarize the ion properties as follows. Ions are accelerated up to energies of $\sim$100 MeV on time scales of a second, and to a GeV on time scales of a few seconds. Proton acceleration continues for several tens of seconds at $\sim 10^{35}\,\mathrm{s}^{-1}$. The total energy content in protons above 1 MeV is $\sim 10^{31}$ erg. The characteristic abundances of ion species vary, depending on the type of flare. The most significant variation is in the ^{3}He/^{4}He ratio. Impulsive flare *in situ* measurements give a ratio up to about 1, compared to a typical coronal value of 5×10^{-4}. In gradual long-duration flares the ratio is compatible with the coronal value. Similarly, both *in situ* and spectroscopic measurements in impulsive flares show abundances of neon, magnesium, silicon, and iron to oxygen enhanced by a factor between two and eight over coronal values. Gradual flare *in situ* observations usually show ratios consistent with coronal values (however, see Murphy *et al.*, 1991, for a counter-example).

The neutron capture line arises when a neutron, produced in a nuclear reaction (between protons above 30–100 MeV and ambient ions), is captured by a proton to form deuterium. The capture produces a line at 2.223 MeV. Neutrons take a long

time to slow down to the energy at which they can be captured, and can penetrate deep in the solar atmosphere where the radiation is formed. The neutron capture line is thus delayed by $\sim$100 s compared to other γ-radiation. The line shape can be used to constrain the angular distribution of the primary flare protons. Murphy *et al.* (2003) have found evidence for pitch-angle scattering of these particles. This line was the first γ-ray line to be imaged by RHESSI; an example is shown in Fig. 5.46. Curiously, in the first image of its kind (Hurford *et al.*, 2003), the 2.22 MeV source was substantially offset from the hard X-ray sources, suggesting protons and electrons were accelerated in different parts of the magnetic structure.

Ratios of the fluences in strong de-excitation lines to that in the neutron capture line can, when combined with numerical simulation of ion propagation and interaction, constrain the spectral index and angular distribution of accelerated ions (e.g., Hua and Lingenfelter, 1987). The Doppler shifts due to recoil of excited ions affect γ-ray line shapes and allow further constraints to be placed on the directionality and angular distribution of accelerated protons and α-particles (Ramaty and Crannell, 1976). Share *et al.* (2002) have determined that the most likely proton/alpha distribution generating γ-ray lines is a broad *forward isotropic* distribution, perhaps due to strong pitch-angle scattering by MHD turbulence. However, RHESSI de-excitation line spectra reported by Smith *et al.* (2003), with higher energy resolution than previous experiments, are consistent with a forward isotropic distribution only if the particles are traveling along field lines highly inclined to the local vertical (giving an increased Doppler shift, in line with the observations). Otherwise, a directly beamed distribution is needed.

Flare-excited nuclei also emit positrons which slow down before directly annihilating on electrons, or forming positronium. Both of these processes will produce a line at 511 keV (from the singlet state of positronium in the latter case). The line was first seen in 1972 (Chupp *et al.*, 1975) and is also a delayed line, due to the time taken for the positrons to slow down and annihilate. A further 511 keV channel involving the interaction of α-particles with ^{3}He can be used to constrain the accelerated α angular distribution, which is again found to be forward isotropic or isotropic (Share *et al.*, 2004).

The continuum above $\sim$50 MeV is pion-decay emission, the pions originating from protons or ions with energies $\geq$ 300 MeV/nucleon scattering from ambient nuclei. CGRO detected $E > 50$ MeV continuum emission persisting for several hours, produced in the high corona (e.g., Kanbach *et al.*, 1993). Rank *et al.* (2001) demonstrated that the flux decay times are inconsistent with what would be expected if the radiation came from fast particles trapped in a coronal magnetic bottle, and argued that particle acceleration is ongoing during the several hours over which they radiate.

5.7.6 Conclusions

This review attempts to summarize the observations of signatures of accelerated electrons and ions in solar flares. Despite more than forty years of detailed and dedicated observations, our knowledge of the spectral and spatial distribution of these particles, which carry a significant fraction of the total flare energy, is rather meager. We have a broad-brush picture of the numbers of particles involved, general

spectral shapes and time evolution, and radiation signatures produced, but no clear observational picture of how they are accelerated and how they are related to the evolving solar magnetic field. Moreover, the intermediate step between particle acceleration and particle radiation – i.e., particle transport – tends to neglect collective effects in the solar plasma (with the exception of studies of Type III radio emission). However, it seems likely to the author that a full exploitation of – in particular – RHESSI and radio spectral observations is directing us to a reexamination of the theory of particle transport and radiation in flares, while the spatial information from the IR to γ-rays points to a three-dimensional complexity that our magnetic field and acceleration models must ultimately grow to encompass.

Definition of specific notations

International System (SI) units are used throughout this book with the following common notations:

$\mathbf{A}$	vector potential
$\mathbf{B}$	magnetic induction
c	speed of light in vacuum
e	elementary charge
$\mathbf{E}$	electric field
η	electrical resistivity
ϵ_0	permittivity of free space
γ	ratio of specific heats; adiabatic constant
$\mathbf{j}$	electric current density
$m_\mathrm{e},\ m_\mathrm{i}$	electron, ion mass
M_A	Alfvén Mach number
μ_0	permeability of free space
n	number density
ν_ei	electron/ion collision frequency
$\Omega_\mathrm{e},\ \Omega_\mathrm{i}$	electron, ion gyrofrequency
$\omega_\mathrm{pe},\ \omega_\mathrm{pi}$	electron, ion plasma frequency
$\mathbf{P}$	pressure tensor
p	pressure
ρ	mass density
S	Lundquist number
t	time
T	temperature
$\mathbf{v}$	flow velocity
v_A	Alfvén speed

References

Abel, G. A., Freeman, M. P., and Chisham, G. (2005). Comment on "Location of the reconnection line for northward interplanetary magnetic field" by K. J. Trattner, S. A. Fuselier, and S. M. Petrinec. *J. Geophys. Res.* **110**, doi:10.1029/2004JA010973.

Aboudarham, J. and Henoux, J. C. (1986). Energy deposition at temperature minimum level and white light flares. *Astron. Astrophys.* **156**, 73–78.

Abraham, R., Marsden, J. E., and Ratiu, T. (1983). *Manifolds, Tensor Analysis and Applications*. Applied Mathematical Sciences, vol. 75. (Berlin: Springer).

Abramowitz, M. and Stegun, I. A. (1964). *Handbook of Mathematical Functions*. Applied Mathematics Series, vol. 55. (Washington, DC: National Bureau of Standards).

Akasofu, S.-I. (1968). *Polar Magnetospheric Substorms*. (Dordrecht: D. Reidel).

Alexeev, I. V., Owen, C. J., Fazakerley, A. N., *et al.* (2005). Cluster observations of currents in the plasma sheet during reconnection. *Geophys. Res. Lett.* **32**, doi:10.1029/2004GL021420.

Aly, J. J. (1984). On some properties of force-free magnetic fields in infinite regions of space. *Astrophys. J.* **283**, 349–362.

Aly, J. J. and Amari, T. (1989). Current sheets in two-dimensional potential magnetic fields. I. General properties. *Astron. Astrophys.* **221**, 287–294.

Amari, T., Luciani, J. F., Mikić, Z., and Linker, J. (2000). A twisted flux rope model for coronal mass ejections and two-ribbon flares. *Astrophys. J.* **529**, L49–L52.

Amari, T., Luciani, J. F., Aly, J. J., Mikić, Z., and Linker, J. (2003). Coronal mass ejection: Initiation, magnetic helicity, and flux ropes. I. Boundary motion-driven evolution. *Astrophys. J.* **585**, 1073–1086.

Ambrosiano, J., Matthaeus, W. H., Goldstein, M. L., and Plante, D. (1988). Test particle-acceleration in turbulent reconnecting magnetic fields. *J. Geophys. Res.* **93**, 14383–14400.

André, M., Behlke, R., Wahlund, J.-E., *et al.* (2001). Multi-spacecraft observations of broadband waves near the lower hybrid frequency at the earthward edge of the magnetopause. *Ann. Geophys.* **19**, 1471–1481.

André, M., Vaivads, A., Buchert, S. C., Fazakerley, A. N., and Lahiff, A. (2004). Thin electron-scale layers at the magnetopause. *Geophys. Res. Lett.* **31**, L03803, doi:10.1029/2003GL018137.

Angelopoulos, V., Baumjohann, W., Kennel, C. F., *et al.* (1992). Bursty bulk flows in the inner central plasma sheet. *J. Geophys. Res.* **97**, 4027.

Angelopoulos, V., Kennel, C. F., Coroniti, F. V., *et al.* (1994). Statistical characteristics of bursty bulk flow events. *J. Geophys. Res.* **99**, 21257–21280.

Antiochos, S. K., DeVore, C. R., and Klimchuk, J. A. (1999). A model for solar coronal mass ejections. *Astrophys. J.* **510**, 485–493.

Antiochos, S. K., Karpen, J. T., and DeVore, C. R. (2002). Coronal magnetic field relaxation by null-point reconnection. *Astrophys. J.* **575**, 578–584.

Arnoldy, R. L., Kane, S. R., and Winckler, J. R. (1967). A study of energetic solar flare x-rays. *Solar Phys.* **2**, 171–178.

Arzner, K. and Scholer, M. (2001). Magnetotail reconnection: Simulation predictions on magnetic time series. *Earth Planets Space* **53**, 653–661.

Asai, A., Yokoyama, T., Shimojo, M., *et al.* (2004). Flare ribbon expansion and energy release rate. *Astrophys. J.* **611**, 557–567.

Asano, Y., Mukai, T., Hoshino, M., *et al.* (2003). Evolution of the thin current sheet in a substorm observed by Geotail. *J. Geophys. Res.* **108**, 1189, doi:1029/2002JA009785.

Asano, Y., Mukai, T., Hoshino, M., *et al.* (2004). Current sheet structure around the near-Earth neutral line observed by Geotail. *J. Geophys. Res.* **109**, A02212, doi:10.1029/2003JA010114.

Asano, Y., Nakamura, R., Baumjohann, W., *et al.* (2005). How typical are atypical current sheets? *Geophys. Res. Lett.* **32**, doi:10.1029/2004GL021834.

Aschwanden, M. J. (2001). Revisiting the determination of the coronal heating function from Yohkoh data. *Astrophys. J.* **559**, L171.

Aschwanden, M. J. (2002). *Particle Acceleration and Kinematics in Solar Flares.* (Dordrecht: Kluwer Academic Publishers).

Aschwanden, M. J., Benz, A. O., Dennis, B. R., and Schwartz, R. A. (1995). Solar electron beams detected in hard x-rays and radio waves. *Astrophys. J.* **455**, 347.

Atkinson, G. (1966). A theory of polar substorms. *J. Geophys. Res.* **71**, 5157.

Aubry, M. P., Russell, C. T., and Kivelson, M. G. (1970). Inward motion of the magnetopause before a substorm. *J. Geophys. Res.* **75**, 7019.

Aulanier, G., Deluca, E. E., Antiochos, S. K., McMullen, R. A., and Golub, L. (2000). The topology and evolution of the Bastille Day flare. *Astrophys. J.* **540**, 1126–1142.

Aurass, H. and Mann, G. (2004). Radio observation of electron acceleration at solar flare reconnection outflow termination shocks. *Astrophys. J.* **615**, 526–530.

Aurass, H., Vršnak, B., and Mann, G. (2002). Shock-excited radio burst from reconnection outflow jet? *Astron. Astrophys.* **384**, 273–281.

Avanov, L. A., Smirnov, V. N., Waite, Jr., J. H., Fuselier, S. A., and Vaisberg, O. L. (2001). High-latitude magnetic reconnection in sub-Alfvénic flow: Interball tail observations on May 29, 1996. *J. Geophys. Res.* **106**, 29491.

Aydemir, A. Y. (1992). Nonlinear studies of m = 1 modes in high-temperature plasmas. *Phys. Fluids B* **4**, 3469.

Bai, T. and Ramaty, R. (1978). Backscatter, anisotropy, and polarization of solar hard X-rays. *Astrophys. J.* **219**, 705–726.

Baker, D. N. (1984). Particle and field signatures of substorms in the near tail. In *Magnetic Reconnection in Space and Laboratory Plasmas*, Geophysical Monograph Series, E. W. Hones, Jr., ed. (Washington, DC: American Geophysical Union), 193.

Baker, D. N. and McPherron, R. L. (1990). Extreme energetic particle decreases near geostationary orbit: A manifestation of current diversion within the inner plasma sheet. *J. Geophys. Res.* **95**, 6591–6599.

Baker, D. N. and Stone, E. C. (1976). Energetic electron anisotropies in the magnetotail: Identification of open and closed field lines. *Geophys. Res. Lett.* **3**, 557–560.

Baker, D. N. and Stone, E. C. (1977). Observations of energetic electrons ($E \geq 200\,\mathrm{keV}$) in the Earth's magnetotail: Plasma sheet and fireball observations. *J. Geophys. Res.* **82**, 1532–1546.

Baker, D. N., Hones, Jr., E. W., Higbie, P. R., Belian, R. D., and Stauning, P. (1981). Global properties of the magnetosphere during a substorm growth phase: A case study. *J. Geophys. Res.* **86**, 8941.

Baker, D. N., Bame, S. J., Birn, J., *et al.* (1984). Direct observations of passages of the distant neutral line (80–140 R_E) following substorm onsets: ISEE-3. *Geophys. Res. Lett.* **11**, 1042.

Baker, D. N., Fritz, T. A., McPherron, R. L., *et al.* (1985). Magnetotail energy storage and release during the CDAW 6 substorm analysis intervals. *J. Geophys. Res.* **90**, 1205–1216.

Baker, D. N., Pulkkinen, T. I., Angelopoulos, V., Baumjohann, W., and McPherron, R. L. (1996). Neutral line model of substorms: Past results and present view. *J. Geophys. Res.* **101**, 12975.

Baker, D. N., Peterson, W. K., Eriksson, S., *et al.* (2002). Timing of magnetic reconnection initiation during a global magnetospheric substorm onset. *Geophys. Res. Lett.* **29**, 2190, doi:10.1029/2002GL015539.

Baker, K. B., Dudeney, J. R., Greenwald, R. A., *et al.* (1995). HF radar signatures of the cusp and low-latitude boundary layer. *J. Geophys. Res.* **100**, 7671–7695.

Baker, K. B., Rodger, A. S., and Lu, G. (1997). HF-radar observations of the dayside magnetic merging rate: A Geospace Environment Modeling boundary layer campaign study. *J. Geophys. Res.* **102**, 9603–9617.

Bale, S. D., Mozer, F. S., and Phan, T. (2002). Observation of lower hybrid drift instability in the diffusion region at a reconnecting magnetopause. *Geophys. Res. Lett.* **29**, 2180.

Balogh, A., Carr, C. M., Acuña, M. H., *et al.* (2001). The Cluster magnetic field investigation: Overview of inflight perfomance and initial results. *Ann. Geophys.* **19**, 1207–1217.

Bauer, T., Baumjohann, W., Treumann, R. A., Sckopke, N., and Lühr, H. (1995). Low-frequency waves in the near-Earth plasma sheet. *J. Geophys. Res.* **100**, 9605–9617.

Baum, P. J. and Bratenahl, A. (1980). Flux linkages of bipolar sunspot groups: A computer study. *Solar Phys.* **67**, 245–258.

Baumjohann, W., Paschmann, G., and Lühr, H. (1990). Characteristics of high-speed ion flows in the plasma sheet. *J. Geophys. Res.* **95**, 3801.

Baumjohann, W., Paschmann, G., Nagai, T., and Lühr, H. (1991). Superposed epoch analysis of the substorm plasma sheet. *J. Geophys. Res.* **96**, 11605–11608.

Belian, R. D., Baker, D. N., Higbie, P. R., and Hones, Jr., E. W. (1978). High-resolution energetic particle measurements at 6.6 R_E, 3. High-energy proton drift echos. *J. Geophys. Res.* **83**, 4857–4862.

Benka, S. G. and Holman, G. D. (1994). A thermal/nonthermal model for solar hard X-ray bursts. *Astrophys. J.* **435**, 469–481.

Benz, A. O. (2002). *Plasma Astrophysics*, second edition (Dordrecht: Kluwer Academic Publishers).

Berger, M. A. (1984). Rigorous new limits on magnetic helicity dissipation in the solar corona. *Geophys. Astrophys. Fluid Dynamics* **30**, 79.

Berger, M. A. (1986). Topological invariants of field lines rooted in planes. *Geophys. Astrophys. Fluid Dynamics* **34**, 265.

Berger, M. A. and Field, G. B. (1984). The topological properties of magnetic helicity. *J. Fluid Mech.* **147**, 133–148.

Bergmans, D. and Clette, F. (1999). Active-region EUV transient brightenings. *Solar Phys.* **186**, 207–229.

Bernstein, I. B., Freeman, E. A., Kruskal, M. D., and Kulsrud, R. M. (1958). An energy principle for hydromagnetic stability problems. *Proc. Roy. Soc., Ser. A* **244**, 17.

Bhattacharjee, A., Ma, Z. W., and Wang, X. (1998). Ballooning instability of a thin current sheet in the high-Lundquist-number magnetotail. *Geophys. Res. Lett.* **25**, 861–864.

Bhattacharjee, A., Germaschewski, K., and Ng, C. S. (2005). Current singularities: Drivers of impulsive reconnection. *Phys. Plasmas* **12**, 042305.

Birn, J. (1980). Computer studies of the dynamic evolution of the geomagnetic tail. *J. Geophys. Res.* **85**, 1214.

Birn, J. and Hesse, M. (1990). The magnetic topology of the plasmoid flux rope in a MHD simulation of magnetotail reconnection. In *Physics of Magnetic Flux Ropes*, Geophysical Monograph Series, vol. 58, C. T. Russell, E. R. Priest, and L. C. Lee, eds. (Washington, DC: American Geophysical Union), 655.

Birn, J. and Hesse, M. (1991). The substorm current wedge and field-aligned currents in MHD simulations of magnetotail reconnection. *J. Geophys. Res.* **96**, 1611.

Birn, J. and Hesse, M. (1994). Particle acceleration in the dynamic magnetotail: Orbits in self-consistent three-dimensional MHD fields. *J. Geophys. Res.* **99**, 109–119.

Birn, J. and Hesse, M. (1996). Details of current disruption and diversion in simulations of magnetotail dynamics. *J. Geophys. Res.* **101**, 15345.

Birn, J. and Hones, Jr., E. W. (1981). Three-dimensional computer modelling of dynamic reconnection in the geomagnetic tail. *J. Geophys. Res.* **86**, 6802.

Birn, J. and Schindler, K. (2002). Thin current sheets in the magnetotail and the loss of equilibrium. *J. Geophys. Res.* **107**, SMP18, doi:10.1029/2001JA0291.

Birn, J., Sommer, R. R., and Schindler, K. (1975). Open and closed magnetospheric tail configurations and their stability. *Astrophys. Space Sci.* **35**, 389.

Birn, J., Hesse, M., and Schindler, K. (1996). MHD simulations of magnetotail dynamics. *J. Geophys. Res.* **101**, 12939.

Birn, J., Thomsen, M. F., Borovsky, J. E., *et al.* (1997a). Characteristic plasma properties of dispersionless substorm injections at geosynchronous orbit. *J. Geophys. Res.* **102**, 2309.

Birn, J., Thomsen, M. F., Borovsky, J. E., *et al.* (1997b). Substorm ion injections: Geosynchronous observations and test particle orbits in three-dimensional dynamic MHD fields. *J. Geophys. Res.* **102**, 2325–2342.

Birn, J., Hesse, M., and Schindler, K. (1998a). Formation of thin current sheets in space plasmas. *J. Geophys. Res.* **103**, 6843.

Birn, J., Thomsen, M. F., Borovsky, J. E., *et al.* (1998b). Substorm electron injections: Geosynchronous observations and test particle simulations. *J. Geophys. Res.* **103**, 9235–9248.

Birn, J., Hesse, M., Haerendel, G., Baumjohann, W., and Shiokawa, K. (1999). Flow braking and the substorm current wedge. *J. Geophys. Res.* **104**, 19895.

Birn, J., Drake, J. F., Shay, M. A., *et al.* (2001). Geospace environmental modeling (GEM) magnetic reconnection challenge. *J. Geophys. Res.* **106**, 3715–3719.

Birn, J., Schindler, K., and Hesse, M. (2003). Formation of thin current sheets in the magnetotail: Effects of propagating boundary deformations. *J. Geophys. Res.* **108**, 1337, doi:10.1029/2002JA009641.

Birn, J., Hesse, M., and Schindler, K. (2004a). On the propagation of bubbles in the geomagnetic tail. *Ann. Geophys.* **22**, 1773.

Birn, J., Hesse, M., Schindler, K., and Hesse, M. (2004b). Thin electron current sheets and their relation to auroral potentials. *J. Geophys. Res.* **109**, A02217, doi:10.1029/2003JA010303.

Birn, J., Thomsen, M. F., and Hesse, M. (2004c). Electron acceleration in the dynamic magnetotail: Test particle orbits in three-dimensional MHD simulation fields. *Phys. Plasmas* **11**, 1825.

Birn, J., Galsgaard, K., Hesse, M., *et al.* (2005). Forced magnetic reconnection. *Geophys. Res. Lett.* **32**, L06105, doi:10.1029/2004GL022058.

Biskamp, D. (1986). Magnetic reconnection via current sheets. *Phys. Fluids* **29**, 1520–1531.

Biskamp, D. (2000). *Magnetic Reconnection in Plasmas.* (Cambridge: Cambridge University Press).

Biskamp, D. and Schindler, K. (1971). Instability of two-dimensional collisionless plasmas with neutral points. *Plasma Phys.* **13**, 1013–1026.

Biskamp, D. and Schwarz, E. (2001). Localization, the key to fast magnetic reconnection. *Phys. Plasmas* **8**, 4729–4731.

Biskamp, D., Schwarz, E., and Drake, J. F. (1997). Two-fluid theory of collisionless magnetic reconnection. *Phys. Plasmas* **4**, 1002–1009.

Blanchard, G. T., Lyons, L. R., Samson, J. C., and Rich, F. J. (1995). Locating the polar-cap boundary from observations of 6300 Å auroral emission. *J. Geophys. Res.* **100**, 7855–7862.

Blanchard, G. T., Lyons, L. R., de la Beaujardière, O., Doe, R. A., and Mendillo, M. (1996). Measurement of the magnetotail reconnection rate. *J. Geophys. Res.* **101**, 15265–15276.

Blanchard, G. T., Lyons, L. R., and de la Beaujardière, O. (1997). Magnetotail reconnection rate during magnetospheric substorms. *J. Geophys. Res.* **102**, 24303–24312.

Blanchard, G. T., Ellington, C. L., Lyons, L. R., and Rich, F. J. (2001). Incoherent scatter radar identification of the dayside magnetic separatrix and measurement of magnetic reconnection. *J. Geophys. Res.* **106**, 8185–8195.

Blandford, R. D. and Ostriker, J. P. (1978). Particle acceleration by astrophysical shocks. *Astrophys. J.* **221**, L29–L32.

Brackbill, J. U., Forslund, D. W., Quest, K. B., and Winske, D. (1984). Nonlinear evolution of the lower-hybrid drift instability. *Phys. Fluids* **27**, 2682.

Brittnacher, M., Quest, K. B., and Karimabadi, H. (1994). On the energy principle and ion tearing in the magnetotail. *Geophys. Res. Lett.* **21**, 1591.

Brittnacher, M., Quest, K. B., and Karimabadi, H. (1995). A new approach to the linear theory of single-species tearing in two-dimensional quasi-neutral sheets. *J. Geophys. Res.* **100**, 3551.

Brittnacher, M., Quest, K. B., and Karimabadi, H. (1998). A study of the effect of pitch angle and spatial diffusion on tearing instability using a new finite element based linear code. *J. Geophys. Res.* **103**, 4587.

Brown, D. S. and Priest, E. R. (1999). Topological bifurcations in 3D magnetic fields. *Proc. Roy. Soc.* **455**, 3931–3951.

Brown, D. S. and Priest, E. R. (2001). The topological behaviour of 3D null points in the sun's corona. *Astron. Astrophys.* **367**, 339–346.

Brown, J. C. (1971). The deduction of energy spectra of non-thermal electrons in flares from the observed dynamic spectra of hard x-ray bursts. *Solar Phys.* **18**, 489.

Browning, P. K. and Vekstein, G. E. (2001). Particle acceleration at an X-type reconnection site with a parallel magnetic field. *J. Geophys. Res.* **106**, 18677–18692.

Bruhwiler, D. L. and Zweibel, E. G. (1992). Energy spectrum of particles accelerated near a magnetic x line. *J. Geophys. Res.* **97**, 10825–10830.

Büchner, J. (1999). Three-dimensional magnetic reconnection in astrophysical plasmas – kinetic aproach. *Astrophys. Space Sci.* **264**, 25.

Büchner, J. and Elkina, N. (2006). Vlasov code simulation of anomalous resistivity. *Space Sci. Rev* **121**, 237–252.

Büchner, J. and Kuska, J.-P. (1996). Three-dimensional collisionless reconnection through thin current sheets: Theory and selfconsistent simulations. In *Proceedings of the IIIrd International Conference on Substorms (ICS-3)*, E. J. Rolfe and B. Kaldeich, eds. (Noordwijk: ESA Publications Division), 373.

Büchner, J. and Kuska, J.-P. (1998a). Kinetic effects controlling the onset of 3-D tail reconnection large scale coherent reconnection. In *SUBSTORMS-4*, S. Kokubun and Y. Kamide, eds. (Tokyo/ Amsterdam: Terra Scientific Publishing Company/Kluwer Academic Publishers), 461–466.

Büchner, J. and Kuska, J.-P. (1998b). Magnetospheric research with advanced techniques. In *Proceedings of the 9th Committee on Space Research Colloquium*, R. L. Xu and A. T. Y. Lui, eds. (Amsterdam: Elsevier Science), 179.

Büchner, J. and Kuska, J.-P. (1999). Sausage mode instability of thin current sheets as a cause of magnetospheric substorms. *Ann. Geophys.* **17**, 604.

Büchner, J. and Zelenyi, L. M. (1987). Chaotization of the electron motion as the cause of an internal magnetotail instability and substorm onset. *J. Geophys. Res.* **92**, 13456.

Büchner, J. and Zelenyi, L. M. (1991). Regular and chaotic particle motion in sheared magnetic field reversals. *Adv. Space Res.* **11**, 177.

Bulanov, S. V. (1980). The energy spectrum of particles accelerated near a singular magnetic field line. *Soviet Astronomy Letters* **6**, 206.

Bulanov, S. V. and Olshanetskii, M. A. (1984). Magnetic collapse near zero points of the magnetic field. *Phys. Lett.* **100A**, 35–38.

Bulanov, S. V. and Sasorov, P. V. (1975). Energetic spectrum of particles accelerated in the vicinity of the magnetic field zero line. *Astron. Zh.* **52**, 767–771.

Bulanov, S. V. and Sasorov, P. V. (1976). Energy spectrum of particles accelerated in the neighborhood of a line of zero magnetic field. *Soviet Astronomy* **52**, 763–771.

Bulanov, S. V., Sakai, J., and Syrovatskii, S. I. (1979). Disruptive instability in a quasi-stationary MHD configuration. *Sov. J. Plasma Phys.* **5**, 157–163.

Burch, J. L. (1974). Observations of interaction between interplanetary and geomagnetic fields. *Rev. Geophys. Space Phys.* **12**, 363.

Burch, J. L., Reiff, P. H., Spiro, R. W., Heelis, R. A., and Fields, S. A. (1980). Cusp region particle precipitation and ion convection for northward interplanetary magnetic field. *Geophys. Res. Lett.* **7**, 393–396.

Caan, M. N., McPherron, R. L., and Russell, C. T. (1973). Solar wind and substorm related changes in the lobes of the geomagnetic tail. *J. Geophys. Res.* **78**, 8087–8096.

Caan, M. N., McPherron, R. L., and Russell, C. T. (1975). Substorm and interplanetary magnetic field effects on the geomagnetic tail lobes. *J. Geophys. Res.* **80**, 191.

Cafaro, E., Grasso, D., Pegorano, F., Porcelli, F., and Saluzzi, A. (1998). Invariants and geometric structures in nonlinear hamiltonian magnetic reconnection. *Phys. Rev. Lett.* **80(20)**, 4430–4433.

Cai, H. J. and Lee, L. C. (1997). The generalized ohm's law in collisionless magnetic reconnection. *Phys. Plasmas* **4**, 509.

Canfield, R. C., Gunkler, T. A., and Ricchiazzi, P. J. (1984). The H-alpha spectral signatures of solar flare nonthermal electrons, conductive flux, and coronal pressure. *Astrophys. J.* **282**, 296–307.

Canfield, R. C., Hudson, H. S., and McKenzie, D. E. (1999). Sigmoidal morphology and eruptive solar activity. *Geophys. Res. Lett.* **26**, 627–630.

Carbary, J. F., Sotirelis, T., Newell, P. T., and Meng, C.-I. (2003). Auroral boundary correlations between UVI and DMSP. *J. Geophys. Res.* **108**, 1018, doi:10.1029/2002JA009378.

Carmichael, H. (1964). A process for flares. In *AAS/NASA Symposium on the Physics of Solar Flares*, W. N. Hess, ed. (Washington, DC: NASA), 451.

Carrington, R. C. (1859). Description of a singular appearance seen in the Sun on September 1, 1859. *Mon. Not. R. Astron. Soc.* **20**, 13–15.

Carter, T. A., Ji, H., Trintchouk, F., Yamada, M., and Kulsrud, R. M. (2002a). Measurement of lower-hybrid drift turbulence in a reconnecting current sheet. *Phys. Rev. Lett.* **88**, 5001.

Carter, T. A., Yamada, M., Ji, H., Kulsrud, R. M., and Trintchouk, F. (2002b). Experimental study of lower-hybrid drift turbulence in a reconnecting current sheet. *Phys. Plasmas* **9**, 3272.

Cassak, P. A., Shay, M. A., and Drake, J. F. (2005). Catastrophe model for fast magnetic reconnection onset. *Phys. Rev. Lett.* **95**, 235002/1–4.

Cattell, C., Mozer, F., Tsuruda, K., *et al.* (1994). Geotail observations of spiky electric fields and low-frequency waves in the plasma sheet and plasma sheet boundary. *Geophys. Res. Lett.* **21**, 2987.

Cattell, C. A., Dombeck, J., Wygant, J. R., *et al.* (1999). Comparisons of polar satellite observations of solitary wave velocities in the plasma sheet boundary and the high altitude cusp to those in the auroral zone. *Geophys. Res. Lett.* **26**, 425–428.

Cattell, C., Crumley, J., Dombeck, J., Wygant, J., and Mozer, F. S. (2002a). Polar observations of solitary waves at the Earth's magnetopause. *Geophys. Res. Lett.* **29**, 1065.

Cattell, C., Dombeck, J., Wygant, J., Mozer, F. S., and André, M. (2002b). The role of waves in magnetotail dynamics. In *Proceedings of the Sixth International Conference on Substorms*, R. M. Winglee, ed. (University of Washington, Seattle), 443–449.

Cattell, C., Dombeck, J., Wygant, J., *et al.* (2005). Cluster observations of electron holes in association with magnetotail reconnection and comparison to simulations. *J. Geophys. Res.* **110**, A01211, doi:10.1029/2004JA010519.

Chae, J. (2001). Observational determination of the rate of magnetic helicity transport through the solar surface via the horizontal motion of field line footpoints. *Astrophys. J.* **560**, L95–L98.

Chang, C. L., Wong, H. K., and Wu, C. S. (1990). Electromagnetic instabilities attributed to a cross-field ion drift. *Phys. Rev. Lett.* **65**, 1104.

Chanteur, G. (1998). Spatial interpolation for four spacecraft: Theory. In *Analysis Methods for Multi-Spacecraft Data*, G. Paschmann and P. Daly, eds. (Noordwijk: ESA), 349–369.

Chen, C. X. and Wolf, R. A. (1993). Interpretation of high-speed flows in the plasma sheet. *J. Geophys. Res.* **98**, 21409.

Chen, C. X. and Wolf, R. A. (1999). Theory of thin-filament motion in Earth's magnetotail and its application to bursty bulk flows. *J. Geophys. Res.* **104**, 14613.

Chen, P. F. and Shibata, K. (2000). An emerging flux trigger mechanism for coronal mass ejections. *Astrophys. J.* **545**, 524–531.

Cheng, C. Z. and Lui, A. T. Y. (1998). Kinetic ballooning instability for substorm onset and current disruption observed by AMPTE/CCE. *Geophys. Res. Lett.* **25**, 4019.

Cheng, C. Z. and Zaharia, S. (2004). MHD ballooning instability in the plasma sheet. *Geophys. Res. Lett.* **31**, L06809.

Chisham, G. and Freeman, M. P. (2004). An investigation of latitudinal transitions in the SuperDARN Doppler spectral width parameter at different magnetic local times. *Ann. Geophys.* **22**, 1187–1202.

Chisham, G., Coleman, I. J., Freeman, M. P., and Pinnock, M. (2002). Ionospheric signatures of split reconnection X-lines during conditions of IMF $B_z < 0$ and $|B_y| \sim |B_z|$: Evidence for the antiparallel merging hypothesis. *J. Geophys. Res.* **107**, 1323, doi:10.1029/2001JA009124.

Chisham, G., Freeman, M. P., Coleman, I. J., *et al.* (2004a). Measuring the dayside reconnection rate during an interval of due northward interplanetary magnetic field. *Ann. Geophys.* **22**, 4243–4258.

Chisham, G., Freeman, M. P., and Sotirelis, T. (2004b). A statistical comparison of SuperDARN spectral width boundaries and DMSP particle precipitation boundaries in the nightside ionosphere. *Geophys. Res. Lett.* **31**, L02804, doi:10.1029/2003GL019074.

Chisham, G., Freeman, M. P., Sotirelis, T., *et al.* (2005a). A statistical comparison of SuperDARN spectral width boundaries and DMSP particle precipitation boundaries in the morning sector ionosphere. *Ann. Geophys.* **23**, 733–743.

Chisham, G., Freeman, M. P., Lam, M. M., *et al.* (2005b). A statistical comparison of SuperDARN spectral width boundaries and DMSP particle precipitation boundaries in the afternoon sector ionosphere. *Ann. Geophys.* **23**, 3645–3654.

Chuang, I., Durrer, R., Turok, N., and Yurke, B. (1991). Cosmology in the laboratory: Defect dynamics in liquid crystals. *Science* **251**, 1336.

Chupp, E. L., Forrest, D. J., and Suri, A. N. (1975). High energy gamma-ray radiation above 300 keV associated with solar activity. In *IAU Symposium 68: Solar Gamma-, X-, and EUV Radiation.* (Dordrecht: Reidel), 341–359.

Close, R., Parnell, C. E., Mackay, D. H., and Priest, E. R. (2004a). Statistical flux tube properties of 3D magnetic carpet fields. *Solar Phys.* **212**, 251.

Close, R., Parnell, C. E., and Priest, E. R. (2004b). Recycling of the solar corona's magnetic field. *Astrophys. J.* **612**, L81–L84.

Coleman, I. J., Chisham, G., Pinnock, M., and Freeman, M. P. (2001). An ionospheric convection signature of antiparallel reconnection. *J. Geophys. Res.* **106**, 28995–29008.

Cooling, B. M. A., Owen, C. J., and Schwartz, S. J. (2001). Role of the magnetosheath flow in determining the motion of open flux tubes. *J. Geophys. Res.* **106**, 18763.

Coppi, B., Laval, G., and Pellat, R. (1966). Dynamics of the geomagnetic tail. *Phys. Rev. Lett.* **16**, 1207.

Coroniti, F. V. (1980). On the tearing mode in quasi-neutral sheets. *J. Geophys. Res.* **85**, 6719.

Coroniti, F. V. (1985). Space plasma turbulent dissipation – reality or myth? *Space Sci. Rev.* **42**, 399–410.

Coroniti, F. V. (1990). Magnetically striped relativistic magnetohydrodynamic winds: The Crab-nebula revisited. *Astrophys. J.* **349**, 538–545.

Cowley, S. C., Longcope, D. W., and Sudan, R. N. (1997). Current sheets in MHD turbulence. *Phys. Rep.* **283**, 227–251.

Cowley, S. W. H. (1973). A qualitative study of the reconnection between the Earth's magnetic field and an interplanetary field of arbitrary orientation. *Radio Sci.* **8**, 903–913.

Cowley, S. W. H. (1976). Comments on the merging of non-antiparallel magnetic fields. *J. Geophys. Res.* **81**, 3455.

Cowley, S. W. H. and Lockwood, M. (1992). Excitation and decay of solar driven flows in the magnetosphere-ionosphere system. *Ann. Geophys.* **10**, 103.

Cowley, S. W. H. and Owen, C. J. (1989). A simple illustrative model of open flux tube motion over the dayside magnetopause. *Planet. Space Sci.* **37**, 1461.

Cowley, S. W. H., Freeman, M. P., Lockwood, M., and Smith, M. F. (1991). The ionospheric signatures of flux transfer events. In *CLUSTER: Dayside Polar Cusp*, C. I. Barron, ed. (European Space Agency Special Publication, ESA SP-330, ESTEC, Noordwijk, Netherlands), 105.

Cowley, S. W. H., Badman, S. V., Bunce, E. J., *et al.* (2005). Reconnection in a rotation-dominated magnetosphere and its relation to Saturn's auroral dynamics. *J. Geophys. Res.* **110**, A02201, doi:10.1029/2004JA010796.

Cowling, T. G. (1953). Solar electrodynamics. In *The Sun*, G. P. Kuiper, ed. (Chicago: University of Chicago Press), 532–591.

Craig, I. J. D. and Fabling, R. B. (1996). Exact solutions for steady state, spine, and fan magnetic reconnection. *Astrophys. J.* **462**, 969–976.

Craig, I. J. D. and Henton, S. M. (1995). Exact solutions for steady state incompressible magnetic reconnection. *Astrophys. J.* **450**, 280–288.

Craig, I. J. D. and Litvinenko, Y. E. (2002). Particle acceleration scalings based on exact analytic models for magnetic reconnection. *Astrophys. J.* **570**, 387–394.

Craig, I. J. D. and Watson, P. G. (1992). Fast dynamic reconnection at an x-type neutral point. *Astrophys. J.* **393**, 385–395.

Craig, I. J. D., Fabling, R. B., Henton, S. M., and Rickard, G. J. (1995). An exact solution for steady state magnetic reconnection in three dimensions. *Astrophys. J. Lett.* **455**, L197–L199.

Craig, I. J. D., Fabling, R. B., and Watson, P. G. (1997). The power output of spine and fan magnetic reconnection solutions. *Astrophys. J.* **485**, 383–388.

Craig, I. J. D., Fabling, R. B., Heerikhuisen, J., and Watson, P. G. (1999). Magnetic reconnection solutions in the presence of multiple nulls. *Astrophys. J.* **523**, 838–848.

Crooker, N. U. (1979). Dayside merging and cusp geometry. *J. Geophys. Res.* **10**, 951.

Crooker, N. U., Lyon, J. G., and Fedder, J. A. (1998). MHD model merging with IMF B_Y: Lobe cells, sunward polar cap convection, and overdraped lobes. *J. Geophys. Res.* **103**, 9143–9151.

Dahlburg, R. B. and Antiochos, S. K. (1995). Reconnection of antiparallel magnetic flux tubes. *J. Geophys. Res.* **100**, 16991.

Dahlburg, R. B., Antiochos, S. K., and Norton, D. (1997). Magnetic flux tube tunneling. *Phys. Rev. E* **56**, 2094.

Daughton, W. (1999a). Two-fluid theory of the drift-kink instability. *J. Geophys. Res.* **104**, 28701.

Daughton, W. (1999b). The unstable eigenmodes of a neutral sheet. *Phys. Plasmas* **6**, 1329.

Daughton, W. (2002). Nonlinear dynamics of thin current sheets. *Phys. Plasmas* **9**, 3668.

Daughton, W. (2003). Electromagnetic properties of the lower-hybrid drift instability in a thin current sheet. *Phys. Plasmas* **10**, 3103–3119.

Daughton, W., Lapenta, G., and Ricci, P. (2004). Nonlinear evolution of the lower-hybrid drift instability in a current sheet. *Phys. Rev. Lett.* **93**, 105004.

Davidson, R. C. and Gladd, N. T. (1975). Anomalous transport properties associated with the lower-hybrid-drift instability. *Phys. Fluids* **18**, 1327.

Davidson, R. C., Gladd, N. T., Wu, C. S., and Huba, J. D. (1977). Effects of finite plasma beta on the lower-hybrid-drift instability. *Phys. Fluids* **20**, 301.

de Bruyne, P. and Hood, A. W. (1989). Bounds on the ideal MHD stability of line-tied 2-D coronal magnetic fields. *Solar Phys.* **123**, 241–269.

de la Beaujardière, O., Lyons, L. R., and Friis-Christensen, E. (1991). Sondrestrom radar measurements of the reconnection electric field. *J. Geophys. Res.* **96**, 13907–13912.

Deeg, H.-J., Borovsky, J. E., and Duric, N. (1991). Particle acceleration near X-type magnetic neutral lines. *Phys. Fluids B* **9**, 2660–2674.

Delcourt, D., Sauvard, J. A., Martin, Jr., R. F., and Moore, T. E. (1996). On the nonadiabatic precipitation of ions from the near-Earth plasma sheet. *J. Geophys. Res.* **101**, 17409–17418.

Démoulin, P. (2006). Extending the concept of separatrices to QSLs for magnetic reconnection. *Adv. Space Res.* **37**, 1269–1282.

Démoulin, P. and Berger, M. A. (2003). Magnetic energy and helicity fluxes at the photospheric level. *Solar Phys.* **215**, 203–215.

Démoulin, P., Priest, E. R., and Lonie, D. P. (1996). 3D magnetic reconnection without null points, 2. Application to twisted flux tubes. *J. Geophys. Res.* **101**, 7631–7646.

Démoulin, P., Bagala, L. G., Mandrini, C. H., Hénoux, J. C., and Rovira, M. G. (1997). Quasi-separatrix layers in solar flares. II. Observed magnetic configurations. *Astron. Astrophys.* **325**, 305–317.

Dere, K. P., Barto, J.-D. F., and Brueckner, G. E. (1989). Explosive events in the solar transition zone. *Solar Phys.* **123**, 41–68.

Dorelli, J. (2003). Effects of Hall electric fields on the saturation of forced antiparallel magnetic field merging. *Phys. Plasmas* **10**, 3309–3314.

Dorelli, J. and Birn, J. (2003). Whistler-mediated magnetic reconnection in large systems: Flux pile-up and the formation of thin current sheets. *J. Geophys. Res.* **108**, 1133.

Dorelli, J. C., Hesse, M., Kuznetsova, M., Rastaetter, L., and Raeder, J. (2004). A new look at driven magnetic reconnection at the terrestrial dayside magnetopause. *J. Geophys. Res.* **109**, A12216, doi:10.1029/2004JA010458.

Drake, J. F. and Lee, Y. C. (1977). Kinetic theory of tearing instabilities. *Phys. Fluids* **20**, 1341.

Drake, J. F., Guzdar, P. N., Hassam, A. B., and Huba, J. D. (1984). Nonlinear mode coupling theory of the lower-hybrid-drift instability. *Phys. Fluids* **27**, 1148–1159.

Drake, J. F., Swisdak, M., Cattell, C., *et al.* (2003). Formation of electron holes and particle energization during magnetic reconnection. *Science* **299**, 873–877.

Drake, J. F., Shay, M. A., Thongthai, W., and Swisdak, M. (2005). Production of energetic electrons during magnetic reconnection. *Phys. Rev. Lett.* **94**, 095001.

Dreher, J., Arendt, U., and Schindler, K. (1996). Particle simulations of collisionless reconnection in magnetotail configuration including electron dynamics. *J. Geophys. Res.* **101**, 27375.

Dreicer, H. (1959). Electron and ion runaway in a fully ionized gas. I. *Phys. Rev.* **115**, 238–249.

Dungey, J. W. (1953). Conditions for the occurrence of electrical discharges in astrophysical systems. *Phil. Mag.* **44**, 725–738.

Dungey, J. W. (1958). *Electrodynamical Phenomena in Cosmical Physics*. (London: Cambridge University Press).

Dungey, J. W. (1961). Interplanetary magnetic field and auroral zones. *Phys. Rev. Lett.* **6**, 47.

Dungey, J. W. (1963). The structure of the exosphere or adventures in velocity space. In *Geophysics, The Earth's Environment*, C. DeWitt, J. Hieblot, and L. LeBeau, eds. (New York: Gordon and Breach), 503.

Egedal, J. (2002). A drift kinetic approach to stationary collisionless magnetic reconnection in an open cusp plasma. *Phys. Plasmas* **9**, 1095.

Egedal, J. and Fasoli, A. (2001a). Single-particle dynamics in collisionless magnetic reconnection. *Phys. Rev. Lett.* **86**, 5047–5050.

Egedal, J. and Fasoli, A. (2001b). The topology of guiding center orbits in a linear magnetic cusp. *Phys. Plasmas* **8**, 4042–4052.

Egedal, J., Fasoli, A., Tarkowski, D., and Scarabosio, A. (2001). Collisionless magnetic reconnection in a toroidal cusp. *Phys. Plasmas* **8**, 1935–1943.

Elkina, N. and Büchner, J. (2005). A new conservative unsplit method for the solution of the Vlasov equation. *J. Comp. Phys.* **213**, 862–875.

Ellison, M. A. (1950). Ionospheric effects of solar flares. *Mon. Not. R. Astron. Soc.* **110**, 626.

Elphic, R. C. (1995). Observations of flux transfer events: A review. In *Physics of the Magnetopause*, P. Song, B. U. Ö. Sonnerup, and M. F. Thomsen, eds. (Washington, DC: American Geophysical Union), 225.

Emslie, A. G., Kontar, E. P., Krucker, S., and Lin, R. P. (2003). RHESSI hard x-ray imaging spectroscopy of the large gamma-ray flare of 2002 July 23. *Astrophys. J.* **595**, L107–L110.

Erickson, G. M. and Wolf, R. A. (1980). Is steady convection possible in the Earth's magnetotail? *Geophys. Res. Lett.* **7**, 897.

Eriksson, S., Øieroset, M., Baker, D. N., *et al.* (2004). Walén and slow mode shock analyses in the near-Earth magnetotail in connection with a substorm onset on 27 August 2001. *J. Geophys. Res.* **109**, A05212, doi:10.1029/2003JA010534.

Escoubet, C. P. *et al.* (1992). Staircase ion signature in the polar cusp: A case study. *Geophys. Res. Lett.* **19**, 1735.

Fairfield, D. H. (1979). On the average configuration of the geomagnetic tail. *J. Geophys. Res.* **84**, 1950–1958.

Fairfield, D. H. (1985). Solar wind control of magnetospheric pressure (CDAW 6). *J. Geophys. Res.* **90**, 1201–1204.

Fairfield, D. H. and Ness, N. F. (1970). Configuration of the geomagnetic tail during substorms. *J. Geophys. Res.* **75**, 7032.

Fan, Y. and Gibson, S. E. (2004). Numerical simulations of three-dimensional coronal magnetic fields resulting from the emergence of twisted magnetic flux tubes. *Astrophys. J.* **609**, 1123–1133.

Fedder, J. A., Lyon, J. G., Slinker, S. P., and Mobarry, C. M. (1995). Topological structure of the magnetotail as a function of interplanetary magnetic field direction. *J. Geophys. Res.* **100**, 3613–3621.

Feldman, U., Laming, J. M., and Doschek, G. A. (1995). The correlation of solar-flare temperature and emission measure extrapolated to the case of stellar flares. *Astrophys. J.* **451**, L79–L81.

Feldman, W. C., Tokar, R. L., Birn, J., *et al.* (1987). Structure of a slow mode shock observed in the plasma sheet boundary layer. *J. Geophys. Res.* **92**, 83.

Filippov, B. (1999). Observation of a 3D magnetic null point in the solar corona. *Solar Phys.* **185**, 297–309.

Fisher, G. H., Fan, Y., Longcope, D. W., Linton, M. G., and Pevtsov, A. A. (2000). The solar dynamo and emerging flux. *Solar Phys.* **192**, 119–139.

Fitzpatrick, R. (2004). Scaling of forced magnetic reconnection in the Hall-magnetohydrodynamic Taylor problem. *Phys. Plasmas* **11**, 937–946.

Fletcher, L. and Hudson, H. S. (2002). Spectral and spatial variations of flare hard X-ray footpoints. *Solar Phys.* **210**, 307–321.

Fletcher, L. and Martens, P. C. H. (1998). A model for hard X-ray emission from the top of flaring loops. *Astrophys. J.* **505**, 418–431.

Fletcher, L. and Petkaki, P. (1997). Particle acceleration and transport in reconnecting plasmas. *Solar Phys.* **172**, 267–270.

Fletcher, L., Metcalf, T. R., Alexander, D., Brown, D. S., and Ryder, L. A. (2001). Evidence for the flare trigger site and three-dimensional reconnection in multiwavelength observations of a solar flare. *Astrophys. J.* **554**, 451–463.

Fletcher, L., Pollock, J. A., and Potts, H. E. (2004). Tracking of trace ultraviolet flare footpoints. *Solar Phys.* **222**, 279–298.

Forbes, T. G. (1986). Fast-shock formation in line-tied magnetic reconnection models of solar flares. *Astrophys. J.* **305**, 553–563.

Forbes, T. G. (1990). Numerical simulation of a catastrophe model for coronal mass ejections. *J. Geophys. Res.* **95**, 11919–11931.

Forbes, T. G. (1997). Reconnection theory for flares (invited). In *Observations in Magnetic Reconnection in the Solar Atmosphere*, Astronomical Society of the Pacific Conference Series. (ASP Conference Series), 259–267.

Forbes, T. G. (2000). Solar and stellar flares. *Phil. Trans. R. Soc.* **358**, 711–727.

Forbes, T. G. (2001). The nature of Petschek-type reconnection. In *Magnetic Reconnection in Space and Laboratory Plasmas*, M. Hoshino, R. L. Stenzel, and K. Shibata, eds. (Tokyo: Terra Scientific Publishing Co.), 423–429.

Forbes, T. G. and Acton, L. W. (1996). Reconnection and field line shrinkage in solar flares. *Astrophys. J.* **459**, 330.

Forbes, T. G. and Priest, E. R. (1984). Reconnection in solar flares. In *Solar Terrestrial Physics: Present and Future*, D. Butler and K. Papadopoulos, eds. (Washington, DC: NASA RP-1120), 1–35.

Forbes, T. G. and Priest, E. R. (1987). A comparison of analytical and numerical models for steadily driven reconnection. *Rev. Geophys.* **25**, 1583–1607.

Forbes, T. G. and Priest, E. R. (1995). Photospheric magnetic field evolution and eruptive flares. *Astrophys. J.* **446**, 377–389.

Forbes, T. G. and Speiser, T. W. (1971). Mathematical models of the open magnetosphere: applications to dayside aurora. *J. Geophys. Res.* **76**, 7542–7551.

Forbes, T. G., Priest, E. R., and Isenberg, P. A. (1994). On the maximum energy release in flux-rope models of eruptive flares. *Solar Phys.* **150**, 245–266.

Frankel, T. (1997). *The Geometry of Physics. An Introduction.* (Cambridge: Cambridge University Press).

Freeman, M. P. and Watkins, N. W. (2002). The heavens in a pile of sand. *Science* **298**, 979–980.

Freidberg, J. P. and Gerwin, R. A. (1977). Lower hybrid drift instability at low drift velocities. *Phys. Fluids* **20**, 1311.

Frey, H. U., Mende, S. B., Immel, T. J., *et al.* (2002). Proton aurora in the cusp. *J. Geophys. Res.* **107**, doi:10.1029/2001JA900161.

Frey, H. U., Phan, T. D., Fuselier, S. A., and Mende, S. B. (2003). Continuous magnetic reconnection at Earth's magnetopause. *Nature* **426**, 533, doi:10.1038/nature02084.

Fruit, G., Louarn, P., Budnik, E., *et al.* (2004). On the propagation of low-frequency fluctuations in the plasma sheet: 2. Characterization of the MHD eigenmodes and physical implications. *J. Geophys. Res.* **109**, A03217, doi:10.1029/2003JA010229.

Fujimoto, M., Nagai, T., Yokokawa, N., *et al.* (2001). Tailward electrons at the lobe-plasma sheet interface detected upon dipolarizations. *J. Geophys. Res.* **106**, 21255.

Furth, H. P., Killeen, J., and Rosenbluth, M. N. (1963). Finite-resistivity instabilities of a sheet pinch. *Phys. Fluids* **6**, 459–484.

Fuselier, S. A., Anderson, B. J., and Onsager, T. G. (1997). Electron and ion signatures of field line topology at the low-shear magnetopause. *J. Geophys. Res.* **102**, 4847.

Fuselier, S. A., Petrinec, S. M., and Trattner, K. J. (2000a). Stability of the high-latitude reconnection site for steady northward IMF. *Geophys. Res. Lett.* **27**, 473.

Fuselier, S. A., Trattner, K. J., and Petrinec, S. M. (2000b). Cusp observations of high- and low-latitude reconnection for northward interplanetary magnetic field. *J. Geophys. Res.* **105**, 253.

Fuselier, S. A., Frey, H. U., Trattner, K. J., Mende, S. B., and Burch, J. L. (2002). Cusp aurora dependence on interplanetary magnetic field Bz. *J. Geophys. Res.* **107**, doi:10.1029/2001JA900165.

Galeev, A. A. (1979). Reconnection in the magnetotail. *Space Sci. Rev.* **23**, 411–425.

Galeev, A. A. and Sagdeev, R. Z. (1984). *Current Instabilities and Anomalous Resistivity of Plasma*. (Amsterdam: North-Holland), 270–303.

Galeev, A. A. and Zelenyi, L. M. (1976). Tearing instability in plasma configurations. *Sov. Phys. JETP (Engl. Transl.)* **43**, 1113.

Galeev, A. A., Zelenyi, L. M., and Kuznetsova, M. M. (1985). Nonlinear drift tearing mode: Hard onset and stabilization mechanisms. *JETP Lett.* **41**, 387.

Gallagher, P. T., Lawrence, G. R., and Dennis, B. R. (2003). Rapid acceleration of a coronal mass ejection in the low corona and implications for propagation. *Astrophys. J.* **588**, L53–L56.

Galsgaard, K. (2002). Flux braiding in a stratified atmosphere. In *ESA SP-505: SOLMAG 2002. Proceedings of the Magnetic Coupling of the Solar Atmosphere Euroconference*. (Norwijk: ESA), 269–271.

Galsgaard, K. and Nordlund, A. (1996). Heating and activity of the solar corona: 1. Boundary shearing of an initially homogeneous magnetic field. *J. Geophys. Res.* **101**, 13445–13460.

Galsgaard, K. and Nordlund, A. (1997). Heating and activity of the solar corona: 3. Dynamics of a low-beta plasma with 3D null points. *J. Geophys. Res.* **102**, 231–248.

Galsgaard, K. and Parnell, C. (2004). Fragment driven magnetic reconnection. In *ESA SP-575: SOHO 15. Proceedings of the Coronal Heating SOHO conference*, R. W. Walsh, J. Ireland, D. Danesy, and B. Fleck, eds. (Norwijk: ESA), 351–356.

Galsgaard, K. and Parnell, C. E. (2005). Elementary heating events – Magnetic interactions between two flux sources. iii Energy considerations. *Astron. Astrophys.* **439**, 335–349.

Galsgaard, K., Mackay, D., Priest, E. R., and Nordlund, A. (1999). On the location of energy release and temperature profiles along coronal loops. *Solar Phys.* **189**, 95–108.

Galsgaard, K., Parnell, C., and Blaizot, J. (2000). Elementary heating events – magnetic interactions between two flux sources. *Astron. Astrophys.* **362**, 383.

Galsgaard, K., Priest, E. R., and Titov, V. S. (2002). Numerical experiments on wave propagation towards a 3D null point due to rotational motions. *J. Geophys. Res.* **108**, 1042.

Galsgaard, K., Titov, V. S., and Neukirch, T. (2003). Magnetic pinching of hyperbolic flux tubes. II. Dynamic numerical model. *Astrophys. J.* **595**, 506–516.

Galsgaard, K., Moreno-Insertis, F., Archontis, V., and Hood, A. (2005). A three-dimensional study of reconnection, current sheets, and jets resulting from magnetic flux emergence in the sun. *Astrophys. J.* **618**, L153–L156.

Gary, D. E., Hartl, M. D., and Shimizu, T. (1997). Nonthermal radio emission from solar soft x-ray transient brightenings. *Astrophys. J.* **477**, 958.

Gary, S. P. and Eastman, T. E. (1979). The lower hybrid drift instability at the magnetopause. *J. Geophys. Res.* **84**, 7378.

Gerrard, C. L., Arber, T. D., and Hood, A. W. (2002). The triggering of MHD instabilities through photospheric footpoint motions. *Astron. Astrophys.* **387**, 687–699.

Giovanelli, R. G. (1946). A theory of chromospheric flares. *Nature* **158**, 81–82.

Giovanelli, R. G. (1948). Chromospheric flares. *Mon. Not. R. Astron. Soc.* **108**, 163–176.

Gold, T. and Hoyle, F. (1960). On the origin of solar flares. *Mon. Not. R. Astron. Soc.* **120**, 89–105.

Golub, L., Krieger, A. S., Silk, J., Timothy, A., and Vaiana, G. S. (1974). Solar X-ray bright points. *Astrophys. J.* **189**, L93–L97.

Golub, L., Krieger, A. S., and Vaiana, G. S. (1976). Distribution of lifetimes for coronal soft X-ray bright points. *Solar Phys.* **49**, 79–90.

Goossens, M. (1991). MHD waves and wave heating in non-uniform plasmas. In *Advances in Solar System MHD*, E. R. Priest and A. W. Hood, eds. (Cambridge: Cambridge University Press), 137–172.

Gorbachev, V. S. and Somov, B. V. (1988). Photospheric vortex flows as a cause for two-ribbon flares: A topological model. *Solar Phys.* **117**, 77–88.

Gosling, J. T., Asbridge, J. R., Bame, S. J., *et al.* (1982). Evidence for quasi-stationary reconnection at the dayside magnetopause. *J. Geophys. Res.* **87**, 2147.

Gosling, J. T., Thomsen, M. F., Bame, S. J., Elphic, R. C., and Russell, C. T. (1990). Plasma flow reversal at the dayside magnetopause and the origin of asymmetric polar cusp convection. *J. Geophys. Res.* **95**, 8073.

Gosling, J. T., Thomsen, M. F., Bame, S. J., Elphic, R. C., and Russell, C. T. (1991). Observations of reconnection of interplanetary and lobe magnetic field lines at the high-latitude magnetopause. *J. Geophys. Res.* **96**, 14097.

Gosling, J. T., Birn, J., and Hesse, M. (1995). Three-dimensional magnetic reconnection and the magnetic topology of coronal mass ejection events. *Geophys. Res. Lett.* **22**, 869.

Gosling, J. T., Thomsen, M. F., Bame, S. J., Le, G., and Russell, C. T. (1996). Observations of magnetic reconnection at the lobe magnetopause. *J. Geophys. Res.* **101**, 24765.

Grasso, D., Pegoraro, F., Porcelli, F., and Califano, F. (1999). Hamiltonian magnetic reconnection. *Plasma Phys. Contr. Fusion* **41**, 1497.

Green, R. M. (1965). Modes of annihilation and reconnection in magnetic fields. In *Stellar and Solar Magnetic Fields*, R. Lust, ed. IAU Symposium 22. (Amsterdam: North-Holland), 398–404.

Greene, J. (1988). Geometric properties of three-dimensional reconnecting fields with magnetic nulls. *J. Geophys. Res.* **93**, 8583–8590.

Greene, J. (1992). Locating three-dimensional roots by a bisection method. *J. Comp. Phys.* **98**, 194–198.

Greenwald, R. A., Baker, K. B., Dudeney, J. R., *et al.* (1995). DARN/SUPERDARN, a global view of the dynamics of high-latitude convection. *Space Sci. Rev.* **71**, 761–796.

Grigis, P. C. and Benz, A. O. (2004). The spectral evolution of impulsive solar X-ray flares. *Astron. Astrophys.* **426**, 1093–1101.

Grocott, A., Yeoman, T. K., Nakamura, R., *et al.* (2004). Multi-instrument observations of the ionospheric counterpart of a bursty bulk flow in the near-Earth plasma sheet. *Ann. Geophys.* **22**, 1061–1075.

Grodent, D., Clarke, J. T., Waite, Jr., J. H., *et al.* (2003). Jupiter's polar auroral emissions. *J. Geophys. Res.* **108**, 1366, doi:10.1029/2003JA010017.

Gudiksen, B. V. and Nordlund, Å. (2004). Bulk heating and slender magnetic loops in the solar corona. *Astrophys. J.* **572**, L113–L116.

Gudiksen, B. V. and Nordlund, Å. (2005a). An ab initio approach to solar coronal loops. *Astrophys. J.* **618**, 1031–1038.

Gudiksen, B. V. and Nordlund, Å. (2005b). An ab initio approach to the solar coronal heating problem. *Astrophys. J.* **618**, 1020–1030.

Gurnett, D. A., Frank, L. A., and Lepping, R. P. (1976). Plasma-waves in distant magnetotail. *J. Geophys. Res.* **81**, 6059–6071.

Gustafsson, G., André, M., Carozzi, T., *et al.* (2001). First results of electric field and density observations by CLUSTER EFW based on initial months of operation. *Ann. Geophys.* **19**, 1219.

Hagenaar, H. J. (2001). Ephemeral regions on a sequence of full-disk Michelson Doppler Imager magnetograms. *Astrophys. J.* **555**, 448–461.

Hagenaar, H. J., Schrijver, C. J., and Title, A. M. (2003). The properties of small magnetic regions on the solar surface and the implications for the solar dynamo(s). *Astrophys. J.* **584**, 1107–1119.

Hamilton, B., McClements, K. G., Fletcher, L., and Thyagaraja, A. (2003). Field-guided proton acceleration at reconnecting x-points in flares. *Solar Phys.* **214**, 339–352.

Handy, B. N., Acton, L. W., Kankelborg, C. C., *et al.* (1999). The Transition Region And Coronal Explorer. *Solar Phys.* **187**, 229–260.

Hannah, I. G., Christe, S., Krucker, S., *et al.* (2004). RHESSI microflare statistics. In *ESA SP-575: SOHO 15 Coronal Heating.* (Noordwijk: ESA), 259.

Harris, E. G. (1962). On a plasma sheath separating regions of oppositely directed magnetic field. *Nuovo Cimento* **23**, 115.

Harvey, K. L. (1985). The relationship between coronal bright points as seen in He I 10830 and the evolution of the photospheric network magnetic fields. *Astrophys. J.* **38**, 875–883.

Hassam, A. B. (1984). Collisional tearing in field-reversed configurations. *Phys. Fluids* **27**, 2877–2880.

Hassam, A. B. (1992). Reconnection of stressed magnetic fields. *Astrophys. J.* **399**, 159–163.

Heerikhuisen, J., Litvinenko, Y. E., and Craig, I. J. D. (2002). Proton acceleration in analytic reconnecting current sheets. *Astrophys. J.* **566**, 512–520.

Hellinger, P., Travnicek, P., and Menietti, J. D. (2004). Effective collsion frequency due to ion-acoustic instability: Theory and simulation. *Geophys. Res. Lett.* **31**, L10806, doi:10.1029/2004GL020028.

Hendrix, D. L. and Van Hoven, G. (1996). Magnetohydrodynamic turbulence and implications for solar coronal heating. *Astrophys. J.* **467**, 887–893.

Hénoux, J. C. and Somov, B. V. (1987). Generation and structure of the electric currents in a flaring activity complex. *Astron. Astrophys.* **185**, 306–314.

Hesse, M. (1995). Three-dimensional magnetic reconnection in space- and astrophysical plasmas and its consequences for particle acceleration. In *Reviews of Modern Astronomy*, vol. 8, G. Klare, ed. (Hamburg: Astronomische Gesellschaft), 323–348.

Hesse, M. and Birn, J. (1991). On dipolarization and its relation to the substorm current wedge. *J. Geophys. Res.* **96**, 19417.

Hesse, M. and Birn, J. (1993). Parallel electric fields as acceleration mechanisms in three-dimensional magnetic reconnnection. *Adv. Space Res.* **13**, 249.

Hesse, M. and Schindler, K. (1988). A theoretical foundation of general magnetic reconnection. *J. Geophys. Res.* **93**, 5559–5567.

Hesse, M. and Schindler, K. (2001). The onset of magnetic reconnection in the magnetotail. *Earth Planets Space* **53**, 645–653.

Hesse, M. and Winske, D. (1993). Hybrid simulations of collisionless ion tearing. *Geophys. Res. Lett.* **20**, 1207.

Hesse, M. and Winske, D. (1998). Electron dissipation in collisionless magnetic reconnection. *J. Geophys. Res.* **103**, 26479.

Hesse, M., Winske, D., Kuznetsova, M., Birn, J., and Schindler, K. (1995). Hybrid simulations of collisionless ion tearing. *Geophys. Res. Lett.* **20**, 1207.

Hesse, M., Winske, D., and Kuznetsova, M. (1996). Hybrid modeling of the formation of thin current sheets in magnetotail configurations. *J. Geomagn. Geoelec.* **48**, 749.

Hesse, M., Winske, D., Birn, J., and Kuznetsova, M. (1998). Predictions and explanations of plasma sheet dissipation processes: Current sheet kinking. In *Substorms-4: International Conference on Substorms-4*, S. Kokubun and Y. Kamide, eds. (Terra Scientific Publishing Company/Kluwer Academic Publishers, Tokyo/Amsterdam), 437.

Hesse, M., Schindler, K., Birn, J., and Kuznetsova, M. (1999). The diffusion region in collisionless magnetic reconnection. *Phys. Plasmas* **6**, 1781–1795.

Hesse, M., Birn, J., and Kuznetsova, M. (2001a). Collisionless magnetic reconnection: Electron processes and transport modeling. *J. Geophys. Res.* **106**, 3721.

Hesse, M., Kuznetsova, M., and Birn, J. (2001b). Particle-in-cell simulations of three-dimensional collisionless magnetic reconnection. *J. Geophys. Res.* **106**, 29831–29841.

Hesse, M., Kuznetsova, M., and Hoshino, M. (2002). The structure of the dissipation region for component reconnection: Particle simulations. *Geophys. Res. Lett.* **29**, 1563, doi:10.1029/2001GL014714.

Hesse, M., Kuznetsova, M., and Birn, J. (2004). The role of electron heat flux in guide-field magnetic reconnection. *Phys. Plasmas* **11**, 5387.

Hewett, D. W., Frances, G. E., and Max, C. E. (1988). New regimes of magnetic reconnection in collisionless plasma. *Phys. Rev. Lett.* **61**, 893.

Heyvaerts, J. and Priest, E. R. (1984). Coronal heating by reconnection in DC current systems – A theory based on Taylor's hypothesis. *Astron. Astrophys.* **137**, 63–78.

Heyvaerts, J. and Priest, E. R. (1992). A self-consistent model for solar coronal heating. *Astrophys. J.* **390**, 297–308.

Heyvaerts, J., Priest, E. R., and Rust, D. M. (1977). An Emerging Flux Model for the solar flare phenomenon. *Astrophys. J.* **216**, 123–137.

Hirayama, T. (1974). Theoretical model of flares and prominences. I: Evaporating flare model. *Solar Phys.* **34**, 323–338.

Hoh, F. C. (1966). Stability of sheet pinch. *Phys. Fluids* **9**, 227.

Holman, G. D. (1985). Acceleration of runaway electrons and Joule heating in solar flares. *Astrophys. J.* **293**, 584–594.

Holman, G. D., Sui, L., Schwartz, R. A., and Emslie, A. G. (2003). Electron bremsstrahlung hard x-ray spectra, electron distributions, and energetics in the 2002 July 23 solar flare. *Astrophys. J.* **595**, L97–L101.

Holzer, R. E. and Slavin, J. A. (1979). A correlative study of magnetic flux transfer in the magnetosphere. *J. Geophys. Res.* **84**, 2573–2578.

Hones, Jr., E. W. (1977). Substorm processes in the magnetotail: Comments on "On hot tenuous plasma fireballs and boundary layers in the Earth's magnetotail" by L. A. Frank, L. L. Ackerson, and R. P. Lepping. *J. Geophys. Res.* **82**, 5633.

Hones, Jr., E. W. (1979). Transient phenomena in the magnetotail and their relation to substorms. *Space Sci. Rev.* **23**, 393–410.

Hones, Jr., E. W. (1984). Structure of the magnetotail at 220 R_E and its response to geomagnetic activity. *Geophys. Res. Lett.* **11**, 5.

Hones, Jr., E. W., Palmer, I. D., and Higbie, P. R. (1976). Energetic protons of magnetospheric origin in the plasma sheet associated with substorms. *J. Geophys. Res.* **81**, 3866–3874.

Hood, A. W. and Priest, E. R. (1979). Kink instability of solar coronal loops as the cause of solar flares. *Solar Phys.* **64**, 303–321.

Horiuchi, R. and Sato, T. (1994). Particle simulation study of driven magnetic reconnection in a collisionless plasma. *Phys. Plasmas* **1**, 3587.

Horiuchi, R. and Sato, T. (1997). Particle simulation study of collisionless driven reconnection in a sheared magnetic field. *Phys. Plasmas* **4**, 277.

Horiuchi, R. and Sato, T. (1999). Three-dimensional particle simulation of plasma instabilities and collisionless reconnection in a current sheet. *Phys. Plasmas* **6**, 4565.

Horiuchi, R., Pei, W., and Sato, T. (2001). Collisionless driven reconnection in an open system. *Earth Planets Space* **53**, 439.

Hornig, G. (1997). The covariant transport of electromagnetic fields and its relation to magnetohydrodynamics. *Phys. Plasmas* **4**, 646.

Hornig, G. (2001). *An Introduction to the Geometry and Topology of Fluid Flows*. (Dordrecht: Kluwer), 295–313.

Hornig, G. and Priest, E. R. (2003). Evolution of magnetic flux in an isolated reconnection process. *Phys. Plasmas* **10**, 2712–2721.

Hornig, G. and Schindler, K. (1996). Magnetic topology and the problem of its invariant definition. *Phys. Plasmas* **3**, 781–791.

Hoshino, M. (1987). The electrostatic effect for the collisionless tearing mode. *J. Geophys. Res.* **92**, 7368–7380.

Hoshino, M. (2005). Electron surfing acceleration in magnetic reconnection. *J. Geophys. Res.* **110**, doi:10.1029/2005JA011220.

Hoshino, M., Nishida, A., Yamamoto, T., and Kokubun, S. (1994). Turbulent magnetic field in the distant magnetotail: Bottom-up process of plasmoid formation? *Geophys. Res. Lett.* **21**, 2935–2938.

Hoshino, M., Mukai, T., Yamamoto, T., and Kokubun, S. (1998). Ion dynamics in magnetic reconnection: Comparisons between numerical simulations and Geotail observations. *J. Geophys. Res.* **103**, 4509–4530.

Hoshino, M., Hiraide, K., and Mukai, T. (2001a). Strong electron heating and non-Maxwellian behavior in magnetic reconnection. *Earth Planets Space* **53**, 627–634.

Hoshino, M., Mukai, T., Terasawa, T., and Shinohara, I. (2001b). Suprathermal electron acceleration in magnetic reconnection. *J. Geophys. Res.* **106**, 25979–25997.

Hoyle, F. (1949). *Some Recent Researches in Solar Physics*. (London: Cambridge University Press).

Hoyng, P., Duijveman, A., Boelee, A., *et al.* (1981). Hard X-ray imaging of two flares in active region 2372. *Astrophys. J.* **244**, L153–L156.

Hsu, T.-S. and McPherron, R. L. (2003). Occurrence frequencies of IMF triggered and nontriggered substorms. *J. Geophys. Res.* **108**, 1307, doi:10.1029/2002JA009442.

Hu, S., Bhattacharjee, A., Dorelli, J., and Greene, J. M. (2004). The spherical tearing mode. *Geophys. Res. Lett.* **31**, L19806, doi:10.1029/2004GL020977.

Hu, Y. Q. and Low, B. C. (1982). The energy of electric current sheets. I. Models with moving magnetic dipoles. *Solar Phys.* **81**, 107–119.

Hua, X.-M. and Lingenfelter, R. E. (1987). Solar flare neutron production and the angular dependence of the capture gamma-ray emission. *Solar Phys.* **107**, 351–383.

Huba, J. D. (2004). *NRL Plasma Formulary, Revised 2004.* (Washington, DC: Naval Research Laboratory).

Huba, J. D. and Rudakov, L. I. (2004). Hall magnetic reconnection rate. *Phys. Rev. Lett.* **93**, 175003.

Huba, J. D., Gladd, N. T., and Papadopoulos, K. (1977). The lower-hybrid-drift instability as a source of anomalous resistivity for magnetic field line reconnection. *Geophys. Res. Lett.* **4**, 125.

Huba, J. D., Gladd, N. T., and Papadopoulos, K. (1978). Lower-hybrid-drift wave turbulence in the distant magnetotail. *J. Geophys. Res.* **83**, 5217.

Huba, J. D., Drake, J. F., and Gladd, N. T. (1980). Lower-hybrid-drift instability in field reversed plasmas. *Phys. Fluids* **23**(3), 552.

Huba, J. D., Gladd, N. T., and Drake, J. F. (1982). The lower hybrid drift instability in non-antiparallel reversed field plasmas. *J. Geophys. Res.* **87**, 1697.

Hudson, H. S. (1972). Thick-target processes and white-light flares. *Solar Phys.* **24**, 414.

Hudson, H. S. (1978). A purely coronal hard X-ray event. *Astrophys. J.* **224**, 235–240.

Hudson, H. S., Strong, K. T., Dennis, B. R., *et al.* (1994). Impulsive behavior in solar soft X-radiation. *Astrophys. J.* **422**, L25–L27.

Hudson, H. S., Kosugi, T., Nitta, N. V., and Shimojo, M. (2001). Hard X-radiation from a fast coronal ejection. *Astrophys. J.* **561**, L211–L214.

Hurford, G. J., Schwartz, R. A., Krucker, S., *et al.* (2003). First gamma-ray images of a solar flare. *Astrophys. J.* **595**, L77–L80.

Hurford, G. J., Krucker, S., Lin, R. P., *et al.* (2006). Gamma-ray imaging of the 2003 October/November solar flares. *Astrophys. J.* **644**, L93–L96.

Hurricane, O., Fong, B. H., and Cowley, S. C. (1997). Nonlinear magnetohydrodynamic detonation, Part I. *Phys. Plasmas* **4**, 3565.

Igumenshchev, I. V., Narayan, R., and Abramowicz, M. A. (2003). Three-dimensional magnetohydrodynamic simulations of radiatively inefficient accretion flows. *Astrophys. J.* **592**, 1042–1059.

Imada, S., Hoshino, M., and Mukai, T. (2002). The dawn–dusk asymmetry of energetic and thermal electrons: The Geotail observations. In *Substorms-5*, R. M. Winglee, ed. (Seattle: University of Washington), 388–393.

Imshennik, V. S. and Syrovatskii, S. I. (1967). Two-dimensional flow of an ideally conducting gas in the vicinity of the zero line of a magnetic field. *Sov. Phys. JETP Lett. (Engl. Transl.)* **15**, 656–664.

Inhester, B., Birn, J., and Hesse, M. (1992). The evolution of line-tied coronal arcades including a converging footpoint motion. *Solar Phys.* **138**, 257–281.

Innes, D. E., Inhester, B., Axford, W. I., and Wilhelm, K. (1997). Bi-directional plasma jets produced by magnetic reconnection on the Sun. *Nature* **386**, 811–813.

Inoue, S. and Kusano, K. (2006). Three-dimensional Simulation Study of Flux Rope Dynamics in the Solar Corona. *apj.* Jul. **645**, 742–756, doi: 10.1086/503153.

Jaroschek, C. H., Lesch, H., and Treumann, R. A. (2004). Relativistic kinetic reconnection as the possible source mechanism for high variability and flat spectra in extragalactic radio sources. *Astrophys. J.* **605**, L9–L12.

Jemella, B. D., Shay, M. A., Drake, J. F., and Rogers, B. N. (2003). Impact of frustrated singularities on magnetic island evolution. *Phys. Rev. Lett.* **91**, 125002.

Jemella, B. D., Drake, J. F., and Shay, M. A. (2004). Singular structure of magnetic islands resulting from reconnection. *Phys. Plasmas* **11**, 5668–5672.

Ji, H., Wang, H., Schmahl, E. J., Moon, Y.-J., and Jiang, Y. (2003). Observations of the failed eruption of a filament. *Astrophys. J.* **595**, L135–L138.

Ji, H., Terry, S., Yamada, M., *et al.* (2004). Electromagnetic fluctuations during fast reconnection in a laboratory plasma. *Phys. Rev. Lett.* **92**, 115001.

Johns, C. M. and Lin, R. P. (1992). The derivation of parent electron spectra from bremsstrahlung hard X-ray spectra. *Solar Phys.* **137**, 121–140.

Johnstone, A. D., Alsop, C., Burge, S., *et al.* (1997). PEACE: A plasma electron and current experiment. *Space Sci. Rev.* **79**, 351–398.

Kan, J. R. (1971). Ion-wave current instabilities and anomalous resistivity. *Phys. Fluids* **14**, 2740–2747.

Kanbach, G., Bertsch, D. L., Fichtel, C. E., *et al.* (1993). Detection of a long-duration solar gamma-ray flare on June 11, 1991 with EGRET on COMPTON-GRO. *Astron. Astrophys. Suppl.* **97**, 349–353.

Karimabadi, H., Daughton, W., Pritchett, P. L., and Krauss-Varban, D. (2003a). Ion-ion kink instability in the magnetotail: 1. Linear theory. *J. Geophys. Res.* **108**, 1400, doi:10.1029/2003JA010026.

Karimabadi, H., Pritchett, P. L., Daughton, W., and Krauss-Varban, D. (2003b). Ion-ion kink instability in the magnetotail: 2. Three-dimensional full particle and hybrid simulations and comparison with observations. *J. Geophys. Res.* **108**, 1401, doi:10.1029/2003JA010109.

Karlicky, M. and Kosugi, T. (2004). Acceleration and heating processes in a collapsing magnetic trap. *Astron. Astrophys.* **419**, 1159–1168.

Karlický, M., Fárník, F., and Krucker, S. (2004). High-frequency slowly drifting structures and X-ray sources observed by RHESSI. *Astron. Astrophys.* **419**, 365–373.

Katsouleas, T. and Dawson, J. M. (1983). Unlimited electron acceleration in laser-driven plasma waves. *Phys. Rev. Lett.* **51**, 392–395.

Kauffman, L. (1991). *Knots and Physics.* Series on Knots and Everything, vol. 1. (London: World Scientific).

Kaufmann, R. L. (1987). Substorm currents: Growth phase and onset. *J. Geophys. Res.* **92**, 7471.

Kauristie, K., Sergeev, V. A., Kubyshkina, M. V., *et al.* (2000). A conjugate study of wind and ground-based observations during transient plasma sheet flows. *J. Geophys. Res.* **105**, 10667.

Kennel, C. F. (1995). *Convection and Substorms: Paradigms of Magnetospheric Phenomenology.* (Dordrecht, Netherlands: Oxford University Press).

Kennel, C. F. and Coroniti, F. V. (1984). Confinement of the Crab pulsar's wind by its supernova remnant. *Astrophys. J.* **283**, 694–709.

Kessel, R. L., Chen, S.-H., Green, J. L., *et al.* (1996). Evidence of high-latitude reconnection during northward IMF: Hawkeye observations. *Geophys. Res. Lett.* **23**, 583.

Khan, J. I., Vilmer, N., Saint-Hilaire, P., and Benz, A. O. (2002). The solar coronal origin of a slowly drifting decimetric-metric pulsation structure. *Astron. Astrophys.* **388**, 363–372.

Kida, S. and Takaoka, M. (1994). Reconnection of vorticity. *Ann. Rev. Fluid Mech.* **26**, 169.

Kistler, L., Mouikis, C., Möbius, E., *et al.* (2005). The contribution of non-adiabatic ions to the crosstail current and O^+ dominated thin plasma sheet. *J. Geophys. Res.* **110**, A06213, doi:10.1029/2004JA010653.

Kivelson, M. G. and Spence, H. E. (1988). On the possibility of quasi-static convection in the quiet magnetotail. *Geophys. Res. Lett.* **15**, 1541.

Klapper, I. (1998). Constraints on finite-time current sheet formation at null points in two-dimensional ideal incompressible magnetohydrodynamics. *Phys. Plasmas* **5**, 910–914.

Kleva, R. G., Drake, J. F., and Waelbroeck, F. (1995). Fast reconnection in high-temperature plasmas. *Phys. Plasmas* **2**, 23.

Kliem, B. (1994). Particle orbits, trapping, and acceleration in a filamentary current sheet model. *Astrophys. J. Suppl. Ser.* **90**, 719–728.

Kliem, B., Karlický, M. and Benz, A. O. (2000). Solar flare radio pulsations as a signature of dynamic magnetic reconnection. *Astron. Astrophys.* **360**, 715–728.

Kliem, B., Titov, V. S., and Török, T. (2004). Formation of current sheets and sigmoidal structure by the kink instability of a magnetic loop. *Astron. Astrophys.* **413**, L23–L26.

Kobel, E. and Flückiger, E. O. (1994). A model of the steady state magnetic field in the magnetosheath. *J. Geophys. Res.* **99**, 23617.

Kohl, J. L., Noci, G., Antonucci, E., *et al.* (1997). Thickness variations along coronal loops observed by the Soft X-ray Telescope on Yohkoh. *Solar Phys.* **175**, 613–644.

Kojima, H., Matsumoto, H., Miyatake, T., *et al.* (1994). Relation between electrostatic solitary waves and hot plasma flow in the plasma sheet boundary layer: GEOTAIL observation. *Geophys. Res. Lett.* **21**, 2919–2922.

Kondrashov, D., Feynman, J., Liewer, P. C., and Ruzmaikin, A. (1999). Three-dimensional magnetohydrodynamic simulations of the interaction of magnetic flux tubes. *Astrophys. J.* **519**, 884.

Kontar, E. P., Brown, J. C., Emslie, A. G., *et al.* (2003). An explanation for non-power-law behavior in the hard x-ray spectrum of the 2002 July 23 solar flare. *Astrophys. J.* **595**, L123–L126.

Koplik, J. and Levine, H. (1993). Vortex reconnection in superfluid helium. *Phys. Rev. Lett.* **71**, 1375.

Kopp, R. A. and Pneuman, G. W. (1976). Magnetic reconnection in the corona and the loop prominence phenomenon. *Solar. Phys.* **50**, 85–98.

Kosugi, T., Dennis, B. R., and Kai, K. (1988). Energetic electrons in impulsive and extended solar flares as deduced from flux correlations between hard X-rays and microwaves. *Astrophys. J.* **324**, 1118–1131.

Kosugi, T., Masuda, S., Makishima, K., *et al.* (1991). The hard X-ray telescope (HXT) for the Solar-A mission. *Solar Phys.* **136**, 17–36.

Kovalev, V. A. and Somov, B. V. (2003). The role of collisions in the particle acceleration in solar-flare magnetic traps. *Astron. Lett.* **29**, 409–415.

Koyama, K., Hamaguchi, K., Ueno, S., Kobayashi, N., and Feigeloson, E. D. (1996). Discovery of hard X-rays from a cluster of protostars. *Publ. Astron. Soc. Japan* **48**, L87–L92.

Krall, N. A. (1977). Shear stabilization of lower hybrid drift instabilities. *Phys. Fluids* **20**, 311.

Krall, N. A. and Liewer, P. C. (1971). Low-frequency instabilities in magnetic pulses. *Phys. Rev.* **4**, 2094.

Krucker, S., Christe, S., Lin, R. P., Hurford, G. J., and Schwartz, R. A. (2002). Hard X-ray microflares down to 3 keV. *Solar Phys.* **210**, 445–456.

Krucker, S., Hurford, G. J., and Lin, R. P. (2003). Hard x-ray source motions in the 2002 July 23 gamma-ray flare. *Astrophys. J.* **595**, L103–L106.

Kulsrud, R. M. (2001). Magnetic reconnection: Sweet–Parker versus Petschek. In *Magnetic Reconnection in Space and Laboratory Plasmas*, M. Hoshino, R. L. Stenzel, and K. Shibata, eds. (Tokyo: Terra Scientific Publishing Co.), 417–419.

Kusano, K. (2002). Numerical study of three-dimensional magnetohydrodynamic instability in the solar coronal magnetic arcades. *Astrophys. J.* **571**, 532–539.

Kusano, K. and Nishikawa, K. (1996). Bifurcation and stability of coronal magnetic arcades in a linear force-free field. *Astrophys. J.* **461**, 415–423.

Kusano, K., Suzuki, Y., and Nishikawa, K. (1995). A solar flare triggering mechanism based on the Woltjer-Taylor minimum energy principle. *Astrophys. J.* **441**, 942–951.

Kusano, K., Maeshiro, T., Yokoyama, T., and Sakurai, T. (2002). Measurement of magnetic helicity injection and free energy loading into the solar corona. *Astrophys. J.* **577**, 501–512.

Kusano, K., Yokoyama, T., Maeshiro, T., and Sakurai, T. (2003). Annihilation of magnetic helicity: A new model for solar flare onset. *Adv. Space Res.* **32**, 1931–1936.

Kusano, K., Maeshiro, T., Yokoyama, T., and Sakurai, T. (2004). Study of Magnetic Helicity in the Solar Corona. In *Proc. of The Fifth Solar-B Science Meeting*, The Astronomical Society of the Pacific, ASP Conference Series, Sakurai, T. and Sekii, T. Dec. 175–184.

Kusano, K., Maeshiro, T., Yokoyama, T., and Sakurai, T. (2004a). The trigger mechanism of solar flares in a coronal arcade with reversed magnetic shear. *Astrophys. J.* **610**, 537–549.

Kusano, K., Maeshiro, T., Yokoyama, T., and Sakurai, T. (2004b). Study of magnetic helicity in the solar corona. In *Proc. of The Fifth Solar-B Science Meeting*, T. A. S. of the Pacific, ed. Vol. 325. (ASP Conference Series, San Francisco, California), 175–184.

Kusano, K. (2005). Simulation Study of the Formation Mechanism of Sigmoidal Structure in the Solar Corona. *apj.* Oct. **631**, 1260–1269, doi: 10.1086/432570.

Kuznetsova, M. M. and Zelenyi, L. M. (1985). Stability and structure of the perturbations of the magnetic surfaces in the magnetic transitional layer. *Plasma Phys. Controlled Fusion* **27**, 363.

Kuznetsova, M. M. and Zelenyi, L. M. (1990a). Nonlinear evolution of magnetic island in a sheared magnetic field with uniform plasma background. *Plasma Phys. Controlled Fusion* **32**, 1183.

Kuznetsova, M. M. and Zelenyi, L. M. (1990b). The theory of FTE stochastic percolation model. *Geophys. Monograph* **58**, 473.

Kuznetsova, M., Hesse, M., and Winske, D. (1998). Kinetic quasi-viscous and bulk flow inertia effects in collisionless magnetotail reconnection. *J. Geophys. Res.* **103**, 199.

Kuznetsova, M. M., Hesse, M., and Winske, D. (2001). Collisionless reconnection supported by nongyrotropic pressure effects in hybrid and particle simulations. *J. Geophys. Res.* **106**, 3799–3810.

Labelle, J. and Treumann, R. A. (1988). Plasma waves at the dayside magnetopause. *Space Sci. Rev.* **47**, 175–202.

Landau, L. D. and Lifshitz, E. M. (1987). *Fluid Mechanics*. (Oxford: Butterworth-Heinemann).

Lanzerotti, L. J., Roberts, C. S., and Brown, W. L. (1967). Temporal variations in the electron flux at synchronous altitudes. *J. Geophys. Res.* **72**, 5893.

Lanzerotti, L. J., Maclennan, C. G., and Robbins, M. F. (1971). Proton drift echos in the magnetosphere. *J. Geophys. Res.* **76**, 259.

Lapenta, G. and Brackbill, J. U. (1997). A kinetic theory for the drift-kink instability. *J. Geophys. Res.* **102**, 27099.

Lapenta, G. and Brackbill, J. U. (2002). Nonlinear evolution of the lower hybrid drift instability: Current sheet thinning and kinking. *Phys. Plasmas* **9**, 1544.

Lapenta, G., Brackbill, J. U., and Daughton, W. S. (2003). The unexpected role of the lower-hybrid drift instability in magnetic reconnection in three dimensions. *Phys. Plasmas* **10**, 1577–1587.

Larosa, T. N., Moore, R. L., Miller, J. A., and Shore, S. N. (1996). New promise for electron bulk energization in solar flares: Preferential Fermi acceleration of electrons over protons in reconnection-driven magnetohydrodynamic turbulence. *Astrophys. J.* **467**, 454.

Lau, Y. T. and Finn, J. M. (1990). Three dimensional kinematic reconnection in the presence of field nulls and closed field lines. *Astrophys. J.* **350**, 672–691.

Lau, Y.-T. and Finn, J. M. (1996). Magnetic reconnection and the topology of interacting twisted flux tubes. *Phys. Plasmas* **3**, 3983.

Laval, G. and Pellat, R. (1964). Methode d'etude de la stabilité de certaines solutions de l'equation Vlasov. *Comptes Rendus Acad. Sci.* **259**, 1706.

Laval, G., Pellat, R., and Vuillemin, M. (1966). Instabilités electromagnétiques des plasmas sans collisions. In *Plasma Physics and Controlled Fusion Research*, vol. II. (Vienna: International Atomic Energy Agency), 259.

Leamon, R. J., Canfield, R. C., and Pevtsov, A. A. (2002). Properties of magnetic clouds and geomagnetic storms associated with eruption of coronal sigmoids. *J. Geophys. Res.* **107**, 1234.

Lee, D. Y. and Wolf, R. A. (1992). Is the Earth's magnetotail balloon unstable? *J. Geophys. Res.* **97**, 19251–19257.

Lee, J. and Gary, D. E. (2000). Solar microwave bursts and injection pitch-angle distribution of flare electrons. *Astrophys. J.* **543**, 457–471.

Lembège, B. and Pellat, R. (1982). Stability of a thick two-dimensional quasineutral sheet. *Phys. Fluids (B)* **25**, 1995–2004.

Lemons, D. S. and Gary, S. P. (1977). Electromagnetic effects on the modified two-stream instability. *J. Geophys. Res.* **82**, 2337.

Lenters, G. T. and Miller, J. A. (1998). Electron acceleration in solar flares by fast-mode waves: Coulomb collisions. *Astrophys. J.* **493**, 451.

Li, X., Baker, D. N., Temerin, M., and Reeves, G. D. (1998). Simulation of dispersionless injections and subsequent drift echoes of energetic electrons associated with substorms. *Geophys. Res. Lett.* **25**, 3763.

Liewer, P. C. and Krall, N. A. (1973). Self-consistent approach to anomalous resistivity applied to theta-pinch experiments. *Phys. Fluids* **16**, 1953.

Lin, J. and Forbes, T. G. (2000). Effects of reconnection on the coronal mass ejection process. *J. Geophys. Res.* **105**, 2375–2392.

Lin, R. P. and Hudson, H. S. (1971). 10-100 kev electron acceleration and emission from solar flares. *Solar Phys.* **17**, 412–435.

Lin, R. P., *et al.* (2002). The Reuven Ramaty High-Energy Solar Spectroscopic Imager (RHESSI). *Solar Phys.* **210**, 3–32.

Lin, R. P., Krucker, S., Hurford, G. J., *et al.* (2003). RHESSI observations of particle acceleration and energy release in an intense solar gamma-ray line flare. *Astrophys. J.* **595**, L69–L76.

Lindqvist, P.-A. and Mozer, F. S. (1990). The average tangential electric field at the noon magnetopause. *J. Geophys. Res.* **95**, 17137–17144.

Linton, M. G. and Antiochos, S. K. (2002). Theoretical energy analysis of reconnecting twisted magnetic flux tubes. *Astrophys. J.* **581**, 703–717.

Linton, M. G. and Antiochos, S. K. (2005). Magnetic flux tube tunneling versus slingshot. *Astrophys. J.* **625**, 506–521.

Linton, M. G. and Priest, E. R. (2003). Three-dimensional reconnection of untwisted magnetic flux tubes. *Astrophys. J.* **595**, 1259–1276.

Linton, M. G., Fisher, G. H., Dahlburg, R. B., and Fan, Y. (1999). Relationship of the multimode kink instability to delta-spot formation. *Astrophys. J.* **522**, 1190–1205.

Linton, M. G., Dahlburg, R. B., and Antiochos, S. K. (2001). Reconnection of twisted flux tubes as a function of contact angle. *Astrophys. J.* **553**, 905–921.

Litvinenko, Y. E. (1996). Particle acceleration in reconnecting current sheets with a nonzero magnetic field. *Astrophys. J.* **462**, 997–1004.

Litvinenko, Y. E. (1999). The pressure limitations on flux pile-up reconnection. *Solar Phys.* **186**, 291–300.

Litvinenko, Y. E. and Craig, I. J. D. (1999). Magnetic energy release in flux pile-up merging. *Solar Phys.* **189**, 315–329.

Litvinenko, Y. E. and Somov, B. V. (1993). Particle acceleration in reconnecting current sheets. *Solar Phys.* **146**, 127–133.

Litvinenko, Y. E., Forbes, T. G., and Priest, E. R. (1996). A strong limitation on the rapidity of flux-pile-up reconnection. *Solar Phys.* **167**, 445–448.

Liu, C., Qiu, J., Gary, D. E., Krucker, S., and Wang, H. (2004a). Studies of microflares in RHESSI hard x-ray, Big Bear solar observatory Hα, and Michelson Doppler Imager magnetograms. *Astrophys. J.* **604**, 442–448.

Liu, S., Petrosian, V., and Mason, G. M. (2004b). Stochastic acceleration of ^{3}He and ^{4}He by parallel propagating plasma waves. *Astrophys. J.* **613**, L81–L84.

Lockwood, M. and Davis, C. J. (1996). On the longitudinal extent of magnetopause reconnection pulses. *Ann. Geophys.* **14**, 865.

Lockwood, M. and Smith, M. F. (1989a). Low-altitude signatures of the cusp and flux transfer events. *Geophys. Res. Lett.* **16**, 879.

Lockwood, M. and Smith, M. F. (1989b). Reply to comment by P. T. Newell on "Low-altitude signatures of the cusp and flux transfer events" by M. Lockwood and M. F. Smith. *Geophys. Res. Lett.* **17**, 305.

Lockwood, M., Cowley, S. W. H., Sandholt, P. E., and Lepping, R. P. (1990). The ionospheric signatures of flux transfer events and solar wind dynamic pressure changes. *J. Geophys. Res.* **95**, 17113.

Lockwood, M., Carlson, Jr., H. C., and Sandholt, P. E. (1993). Implications of the altitude of transient 630-nm dayside auroral emission. *J. Geophys. Res.* **98**, 15571–15587.

Lockwood, M., Cowley, S. W. H., and Smith, M. F. (1994). Comment on: "B_y fluctuations in the magnetosheath and azimuthal flow velocity transient in the dayside ionosphere" by P. T. Newell and D. G. Sibeck. *Geophys. Res. Lett.* **21**, 1819.

Lockwood, M., Davis, C. J., Smith, M. F., Onsager, T. G., and Denig, W. F. (1995). Location and characteristics of the reconnection X-line deduced from low-altitude satellite and ground-based observations, Defense Meteorological Satellite Program and European Incoherent Scatter data. *J. Geophys. Res.* **100**, 21803.

Longcope, D. W. (1996). Topology and current ribbons: A model for current, reconnection and flaring in a complex, evolving corona. *Solar Phys.* **169**, 91–121.

Longcope, D. W. (1998). A model for current sheets and reconnection in X-ray bright points. *Astrophys. J.* **507**, 433–442.

Longcope, D. W. (2001). Separator current sheets: Generic features in minimum-energy magnetic fields subject to flux constraints. *Phys. Plasmas* **8**, 5277–5290.

Longcope, D. W. (2004). Inferring a photospheric velocity field from a sequence of vector magnetograms: The minimum energy fit. *Astrophys. J.* **612**, 1181–1192.

Longcope, D. W. and Cowley, S. C. (1996). Current sheet formation along three-dimensional magnetic separators. *Phys. Plasmas* **3**, 2885–2897.

Longcope, D. W. and Magara, T. (2004). A comparison of the minimum current corona to a magnetohydrodynamic simulation of quasi-static coronal evolution. *Astrophys. J.* **608**, 1106–1123.

Longcope, D. W. and Silva, A. V. R. (1998). A current ribbon model for energy storage and release with application to the flare 1992 Jan. 7. *Solar Phys.* **179**, 349–377.

Longcope, D. W. and Strauss, H. R. (1994). The form of ideal current layers in line-tied magnetic fields. *Astrophys. J.* **437**, 851–859.

Longcope, D. W., Brown, D. S., and Priest, E. R. (2003). On the distribution of magnetic null points above the solar photosphere. *Phys. Plasmas* **10**, 3321–3334.

Longcope, D. W., McKenzie, D., Cirtain, J., and Scott, J. (2005). Observations of separator reconnection to an emerging active region. *Astrophys. J.* **630**, 596–614.

Lucek, E. A., Cargill, P., Dunlop, M. W., *et al.* (2001). The magnetopause at high time resolution: Structure and lower-hybrid waves. *Geophys. Res. Lett.* **28**, 681–684.

Luhmann, J. R., Walker, R. J., Russell, C. T., *et al.* (1984). Patterns of potential magnetic field merging sites on the dayside magnetopause. *J. Geophys. Res.* **89**, 1739.

Lui, A. T. Y. (1996). Current disruption in the Earth's magnetosphere: Observations and models. *J. Geophys. Res.* **101**, 13067.

Lui, A. T. Y. (2004). Potential plasma instabilities for substorm expansion onsets. *Space Sci. Rev.* **113**, 127–206.

Lui, A. T. Y., Chang, C.-L., Mankofsky, A., Wong, H.-K., and Winske, D. (1991). A cross-field current instability for substorm expansions. *J. Geophys. Res.* **96**, 11389.

Lyons, L. R. (1995). A new theory for magnetospheric substorms. *J. Geophys. Res.* **100**, 19069.

Lyons, L. R. (1996). Substorms: Fundamental observational features, distinction from other disturbances, and external triggering. *J. Geophys. Res.* **101**, 13011.

Lyons, L. R. and Pridmore-Brown, D. C. (1990). Force balance near an X-line in a collisionless plasma. *J. Geophys. Res.* **95**, 20903.

Lyubarsky, Y. and Kirk, J. G. (2001). Reconnection in a striped pulsar wind. *Astrophys. J.* **547**, 437–448.

Mackay, D., Galsgaard, K., and Priest, E. R. (2000). How accurately can we determine the coronal heating mechanism in the large-scale solar corona? *Solar Phys.* **193**, 93.

MacKinnon, A. L., Brown, J. C., and Hayward, J. (1985). Quantitative analysis of hard X-ray 'footpoint' flares observed by the Solar Maximum Mission. *Solar Phys.* **99**, 231–262.

Maclean, R., Beveridge, C., Longcope, D. W., Brown, D. S., and Priest, E. R. (2004). A topological analysis of the magnetic breakout model for an eruptive solar flare. *ESA SP-575: SOHO 15 Coronal Heating*, Walsh, R.∼W., Ireland, J., Danesy, D., and Fleck, B. Dec. 485–490.

Maclean, R., Beveridge, C., Longcope, D. W., Brown, D. S., and Priest, E. R. (2005). A topological analysis of the magnetic breakout model for an eruptive solar flare. *Proc. R. Soc. Lond. A* **461**, 2099–2120.

MacNeice, P., Antiochos, S. K., Phillips, A., *et al.* (2004). A numerical study of the breakout model for coronal mass ejection initiation. *Astrophys. J.* **614**, 1028–1041.

Maeshiro, T., Kusano, K., Yokoyama, T., and Sakurai, T. (2005). A statistical study of the correlation between magnetic helicity injection and soft X-rays. *Astrophys. J.* **624**, 1069–1084.

Maezawa, K. (1974). Dependence of the magnetopause position on the southward interplanetary magnetic field. *Planet. Space Sci.* **22**, 1443.

Maezawa, K. (1975). Magnetotail boundary motion associated with geomagnetic substorms. *J. Geophys. Res.* **80**, 3543.

Magara, T. (2004). A model for dynamic evolution of emerging magnetic fields in the sun. *Astrophys. J.* **605**, 480–492.

Manchester, W., Gombosi, T., DeZeeuw, D., and Fan, Y. (2004). Eruption of a buoyantly emerging magnetic flux rope. *Astrophys. J.* **610**, 588–596.

Mandt, M. E., Denton, R. E., and Drake, J. F. (1994). Transition to whistler mediated magnetic reconnection. *Geophys. Res. Lett.* **21**, 73–76.

Manheimer, W. M. and Flynn, R. (1971). Anomalous resistivity and ion-acoustic turbulence. *Phys. Rev. Lett.* **27**, 1175–1179.

Martens, P. C. H. (1988). The generation of proton beams in two-ribbon flares. *Astrophys. J.* **330**, L131–L133.

Martens, P. C. H. and Young, A. (1990). Neutral beams in two-ribbon flares and in the geomagnetic tail. *Astrophys. J. Suppl.* **73**, 333–342.

Martin, S. F., Livi, S. H. B., and Wang, J. (1985). The cancellation of magnetic flux. II. In a decaying active region. *Astrophys. J.* **38**, 929–959.

Masuda, S., Kosugi, T., Hara, H., Tsuneta, S., and Ogawara, Y. (1994). A loop-top hard X-ray source in a compact solar flare as evidence for magnetic reconnection. *Nature* **371**, 495.

Masuda, S., Kosugi, T., and Hudson, H. S. (2001). A hard X-ray two-ribbon flare observed with Yohkoh/HXT. *Solar Phys.* **204**, 55–67.

Matsuoka, A., Tsuruda, K., Hayakawa, H., Mukai, T., and Nishida, A. (1996). Electric field structure and ion precipitation in the polar region associated with northward interplanetary magnetic field. *J. Geophys. Res.* **101**, 10711.

Mauk, B. H. (1986). Quantitative modeling of the "convection surge" mechanism of ion acceleration. *J. Geophys. Res.* **91**, 13423.

McBride, J. B., Ott, E., Boris, J. P., and Orens, J. H. (1972). Theory and simulation of turbulent heating by the modified two-stream instability. *Phys. Fluids* **15**, 2367.

McLaughlin, J. A. and Hood, A. W. (2004). MHD wave propagation in the neighbourhood of a two-dimensional null point. *Astron. Astrophys.* **420**, 1129–1140.

McLaughlin, J. A. and Hood, A. W. (2005). MHD wave propagation in the neighbourhood of two null points. *Astron. Astrophys.* **435**, 315–325.

McPherron, R. L. (1970). Growth phase of magnetospheric substorms. *J. Geophys. Res.* **75**, 5592.

McPherron, R. L. and Manka, R. H. (1985). Dynamics of the 1054 UT March 22, 1979 substorm event: CDAW 6. *J. Geophys. Res.* **90**, 1175–1190.

McPherron, R. L., Russell, C. T., and Aubry, M. P. (1973). Phenomenological model of substorms. *J. Geophys. Res.* **78**, 3131.

McPherron, R. L., Nishida, A., and Russell, C. T. (1987). Is near-Earth current sheet thinning the cause of auroral substorm onset? In *Quantitative Modeling of Magnetosphere-Ionosphere Coupling Processes*, Y. Kamide and R. A. Wolf, eds. (Kyoto, Japan: Kyoto Sangyo University), 252.

McWilliams, K. A., Yeoman, T. K., and Cowley, S. W. H. (2001). Two-dimensional electric field measurements in the ionospheric footprint of a flux transfer event. *Ann. Geophys.* **18**, 1584.

Melnikov, V. F., Shibasaki, K., and Reznikova, V. E. (2002). Loop-top nonthermal microwave source in extended solar flaring loops. *Astrophys. J.* **580**, L185–L188.

Metcalf, T. R., Alexander, D., Hudson, H. S., and Longcope, D. W. (2003). TRACE and Yohkoh observations of a white-light flare. *Astrophys. J.* **595**, 483–492.

Mikić, Z. and Linker, J. A. (1994). Disruption of coronal magnetic field arcades. *Astrophys. J.* **430**, 898–912.

Mikić, Z., Barnes, D. C., and Schnack, D. D. (1988). Dynamical evolution of a solar coronal magnetic field arcade. *Astrophys. J.* **328**, 830–847.

Mikić, Z., Schnack, D. D., and Van Hoven, G. (1989). Creation of current filaments in the solar corona. *Astrophys. J.* **338**, 1148–1157.

Milan, S. E., Lester, M., Cowley, S. W. H., and Brittnacher, M. (2000). Convection and auroral response to a southward turning of the IMF: Polar UVI, CUTLASS and IMAGE signatures of transient magnetic flux transfer at the magnetopause. *J. Geophys. Res.* **105**, 15741.

Milan, S. E., Lester, M., Cowley, S. W. H., *et al.* (2003). Variations in the polar cap area during two substorm cycles. *Ann. Geophys.* **21**, 1121–1140.

Miller, J. A. and Roberts, D. A. (1995). Stochastic proton acceleration by cascading Alfven waves in impulsive solar flares. *Astrophys. J.* **452**, 912–932.

Miller, J. A., LaRosa, T. N., and Moore, R. L. (1996). Stochastic electron acceleration by cascading fast mode waves in impulsive solar flares. *Astrophys. J.* **461**, 445–464.

Miller, J. A., Cargill, P. J., Emslie, A. G., *et al.* (1997). Critical issues for understanding particle acceleration in impulsive solar flares. *J. Geophys. Res.* **102**, 14631–14659.

Mitchell, D. G., Williams, D. J., Huang, C. Y., Frank, L. A., and Russell, C. T. (1990). Current carriers in the near-Earth cross-tail current sheet during substorm growth phase. *Geophys. Res. Lett.* **17**, 583.

Miura, A. (2001). Ballooning instability as a mechanism of the near-Earth onset of substorms. *Space Sci. Rev.* **95**, 1387–1398.

Möbius, E., Scholer, M., Hovestadt, D., and Paschmann, G. (1983). Energetic particles in the vicinity of a possible neutral line in the plasma sheet. *J. Geophys. Res.* **88**, 7742–7752.

Moffatt, H. (1978). *Magnetic Field Generation in Electrically Conducting Fluids.* (Cambridge: Cambridge University Press).

Molodenskii, M. M. and Syrovatskii, S. I. (1977). Magnetic fields of active regions and their zero points. *Sov. Astron.* **21**, 734–741.

Montmerle, T., Grosso, N., Tsuboi, Y., and Koyama, K. (2000). Rotation and X-ray emission from protostars. *Astrophys. J.* **532**, 1097.

Moore, R. L. and Roumeliotis, G. (1992). Triggering of eruptive flares – destabilization of the preflare magnetic field configuration. *Lecture Notes in Physics* **399**, 69.

Moore, R. L., Larosa, T. N., and Orwig, L. E. (1995). The wall of reconnection-driven magnetohydrodynamic turbulence in a large solar flare. *Astrophys. J.* **438**, 985.

Moore, T. E., Fok, M.-C., and Chandler, M. O. (2002). The dayside reconnection (x) line, *J. Geophys. Res.* **107**, doi:10.1029/2002JA009381.

Mori, K., Sakai, J., and Zhao, J. (1998). Proton acceleration near an X-type magnetic reconnection region. *Astrophys. J.* **494**, 430.

Mori, K., Burrows, D. N., Hester, J. J., *et al.* (2004). Spatial variation of X-ray spectrum of the Crab nebula. *Astrophys. J.* **609**, 186–193.

Morse, P. M. and Feshbach, H. (1953). *Methods of Theoretical Physics.* (New York: McGraw-Hill).

Mozer, F. S., Bale, S. D., and Phan, T. D. (2002). Evidence of diffusion regions at a subsolar magnetopause crossing. *Phys. Rev. Lett.* **89**, 015002.

Mrozek, T. and Tomczak, M. (2004). Solar impulsive soft X-ray brightenings and their connection with footpoint hard X-ray emission sources. *Astron. Astrophys.* **415**, 377–389.

Murphy, R. J., Ramaty, R., Reames, D. V., and Kozlovsky, B. (1991). Solar abundances from gamma-ray spectroscopy – comparisons with energetic particle, photospheric, and coronal abundances. *Astrophys. J.* **371**, 793–803.

Murphy, R. J., Share, G. H., Hua, X.-M., *et al.* (2003). Physical implications of RHESSI neutron-capture line measurements. *Astrophys. J.* **595**, L93–L96.

Nagai, T., Fujimoto, M., Saito, Y., *et al.* (1998). Structure and dynamics of magnetic reconnection for substorm onsets with Geotail observations. *J. Geophys. Res.* **103**, 4419–4440.

Nagai, T., Shinohara, I., Fujimoto, M., *et al.* (2001). Geotail observations of the Hall current system: Evidence of magnetic reconnection in the magnetotail. *J. Geophys. Res.* **106**, 25929–25950.

Nagai, T., Shinohara, I., Fujimoto, M., *et al.* (2003). Structure of the Hall current system in the vicinity of the magnetic reconnection site. *J. Geophys. Res.* **108**, 1357, doi:10.1029/2003JA009900.

Nakamura, R., Baumjohann, W., Brittnacher, M., *et al.* (2001a). Flow bursts and auroral activations: Onset timing and footpoint location. *J. Geophys. Res.* **106**, 10777–10789.

Nakamura, R., Baumjohann, W., Schödel, R., *et al.* (2001b). Earthward flow bursts, auroral streamers, and small expansions. *J. Geophys. Res.* **106**, 10791–10802.

Nakamura, R., Baumjohann, W., Klecker, B., *et al.* (2002a). Motion of the dipolarization front during a flow burst event observed by Cluster. *Geophys. Res. Lett.* **29**, 1942, doi:10.1029/2002GL015763.

Nakamura, R., Baumjohann, W., Runov, A., *et al.* (2002b). Fast flow during current sheet thinning. *Geophys. Res. Lett.* **29**, 2140, doi:10.1029/2002GL016200.

Nakamura, R., Baumjohann, W., Mouikis, C., *et al.* (2004a). Spatial scale of high-speed flows in the plasma sheet observed by Cluster. *Geophys. Res. Lett.* **31**, L09894, doi:10.1029/2004GL019558.

Nakamura, R., Baumjohann, W., Nagai, T., *et al.* (2004b). Flow shear near the boundary of the plasma sheet observed by Cluster and Geotail. *J. Geophys. Res.* **109**, A05204, doi:10.1029/2003JA010174.

Nakamura, R., Amm, O., Laakso, H., *et al.* (2005). Localized fast flow disturbance observed in the plasma sheet and in the ionosphere. *Ann. Geophys.* **23**, 553–566.

Nakariakov, V., Ofman, L., DeLuca, E., Roberts, B., and Davila, J. (1999). TRACE observations of damped coronal loop oscillations: implications for coronal heating. *Science* **285**, 862–864.

Neudegg, D. A., Yeoman, T. K., Cowley, S. W. H., *et al.* (1999). A flux transfer event observed at the magnetopause by the Equator-S spacecraft and in the ionosphere by the CUTLASS HF radar. *Ann. Geophys.* **17**, 707.

Newell, P. T. and Sibeck, D. G. (1993). Upper limits on the contribution of FTE's to ionospheric convection. *Geophys. Res. Lett.* **20**, 2829.

Newell, P. T., Burke, W. J., Sanchez, E. R., *et al.* (1991). The low-latitude boundary layer and the boundary plasma sheet at low altitude: Prenoon precipitation regions and convection reversal boundaries. *J. Geophys. Res.* **96**, 21013–21023.

Newell, P. T., Feldstein, Y. I., Galperin, Y. I., and Meng, C.-I. (1996). Morphology of nightside precipitation. *J. Geophys. Res.* **101**, 10737–10748.

Nishida, A., Hayakawa, H., and Hones, Jr., E. W. (1981). Observed signatures of reconnection in the magnetotail. *J. Geophys. Res.* **86**, 1422–1436.

Nishida, A., Mukai, T., Yamamoto, T., and Saito, Y. (1995). GEOTAIL observations on the reconnection process in the distant tail in geomagnetic active times. *Geophys. Res. Lett.* **22**, 2453.

Ohki, K., Tsuneta, S., Takakura, T., *et al.* (1982). Hard x-ray imaging by SXT – comparisons with Hα data. In *Solar Flares.* (Woodbury, NY: American Institute of Physics), 102.

Øieroset, M., Phan, T. D., Lin, R. P., and Sonnerup, B. U. Ö. (2000). Walén and variance analyses of high-speed flows observed by wind in the midtail plasma sheet: Evidence for reconnection. *J. Geophys. Res.* **105**, 25247.

Øieroset, M., Phan, T. D., Fujimoto, M., Lin, R. P., and Lepping, R. P. (2001). In situ detection of collisionless reconnection in the Earth's magnetotail. *Nature* **412**, 414–417.

Øieroset, M., Lin, R. P., Phan, T. D., Larson, D. E., and Bale, S. D. (2002). Evidence for electron acceleration up to $\sim 300\,\mathrm{keV}$ in the magnetic reconnection diffusion region of Earth's magnetotail. *Phys. Rev. Lett.* **89**, 195001.

Okada, T., Tsuruda, K., Hayakawa, H., *et al.* (1994). GEOTAIL observations of electrostatic waves in the lower hybrid frequency range in the plasma sheet boundary layer. *Geophys. Res. Lett.* **21**, 2931.

Omel'chenko, A. N., Vaisberg, O. L., and Russell, C. T. (1983). Further analysis of plasma bursts in Earth's boundary layer at high latitudes. *Cosmic Res.* **21**, 687.

Omura, Y., Kojima, H., and Matsumoto, H. (1994). Computer simulation of electrostatic solitary waves – a nonlinear model of broad-band electrostatic noise. *Geophys. Res. Lett.* **21**, 2923–2936.

Onsager, T. G. and Fuselier, S. A. (1994). The location of magnetic reconnection for northward and southward interplanetary magnetic field. In *Solar System Plasmas in Space and Time*, Geophysical Monograph Series, J. L. Burch and J. H. Waite, Jr., eds. vol. 84. (Washington, DC: American Geophysical Union), 183.

Onsager, T. G., Thomsen, M. F., Gosling, J. T., and Bame, S. J. (1990). Electron distributions in the plasma sheet boundary layer: Time-of-flight effects. *Geophys. Res. Lett.* **17**, 1837.

Onsager, T. G., Chang, S.-W., Perez, J. D., Austin, J. B., and Jano, L. X. (1995). Low-altitude observations and modeling of quasi-steady magnetopause reconnection. *J. Geophys. Res.* **100**, 11831.

Onsager, T. G., Scudder, J. D., Lockwood, M., and Russell, C. T. (2001). Reconnection at the high-latitude magnetopause during northward interplanetary magnetic field conditions. *J. Geophys. Res.* **106**, 25467.

Ottaviani, M. and Porcelli, F. (1993). Nonlinear collisionless magnetic reconnection. *Phys. Rev. Lett.* **71**, 3802.

Ottaviani, M. and Porcelli, F. (1995). Fast nonlinear magnetic reconnection. *Phys. Plasmas* **11**, 4104.

Ozaki, M. and Sato, T. (1997). Interactions of convecting magnetic loops and arcades. *Astrophys. J.* **481**, 524.

Ozaki, M., Sato, T., Horiuchi, R., and Group, C. S. (1996). Electromagnetic instability and anomalous resistivity in a magnetic neutral sheet. *Phys. Plasmas* **3**, 2265.

Papadopoulos, K. (1977). Review of anomalous resistivity for the ionosphere. *Rev. Geophys. Space Phys.* **15**, 113–127.

Park, B. T. and Petrosian, V. (1995). Fokker-Planck equations of stochastic acceleration: Green's functions and boundary conditions. *Astrophys. J.* **446**, 699.

Park, B. T. and Petrosian, V. (1996). Fokker-Planck equations of stochastic acceleration: A study of numerical methods. *Astrophys. J. Suppl.* **103**, 255.

Park, B. T., Petrosian, V., and Schwartz, R. A. (1997). Stochastic acceleration and photon emission in electron-dominated solar flares. *Astrophys. J.* **489**, 358.

Parker, E. N. (1957). Sweet's mechanism for merging magnetic fields in conducting fluids. *J. Geophys. Res.* **62**, 509–520.

Parker, E. N. (1972). Topological dissipation and the small-scale fields in turbulent gases. *Astrophys. J.* **174**, 499–510.

Parker, E. N. (1973a). Comments on the reconnexion rate of magnetic fields. *J. Plasma Phys.* **9**, 49–63.

Parker, E. N. (1973b). The reconnection rate of magnetic fields. *Astrophys. J.* **180**, 247–252.

Parker, E. N. (1988). Nanoflares and the solar X-ray corona. *Astrophys. J.* **330**, 474–479.

Parker, E. N. (1994). *Spontaneous Current Sheets in Magnetic Fields: With Applications to Stellar X-Rays*. (New York: Oxford University Press).

Parnell, C. E. and Galsgaard, K. (2004). Elementary heating events – magnetic interactions between two flux sources. II Rates of flux reconnection. *Astron. Astrophys.* **428**, 595–612.

Parnell, C. E. and Priest, E. R. (1995). A converging flux model for the formation of an X-ray bright point above a supergranule cell. *Geophys. Astrophys. Fluid Dynamics* **80**, 255–276.

Parnell, C. E., Priest, E. R., and Golub, L. (1994). The three-dimensional structures of X-ray bright points. *Solar Phys.* **151**, 57–74.

Parnell, C. E., Smith, J. M., Neukirch, T., and Priest, E. R. (1996). The structure of three-dimensional magnetic neutral points. *Phys. Plasmas* **3**, 759–770.

Parnell, C. E., Neukirch, T., Smith, J. M., and Priest, E. R. (1997). Structure and collapse of three-dimensional magnetic neutral points. *Geophys. Astrophys. Fluid Dynamics* **84**, 245–271.

Paschmann, G., Sonnerup, B. U. Ö., Papamastorakis, I., *et al.* (1979). Plasma acceleration at the Earth's magnetopause: Evidence for reconnection. *Nature* **282**, 243–282.

Paschmann, G., Quinn, J. M., Torbert, R. B., *et al.* (2001). The electron drift instrument on Cluster: Overview of first results. *Ann. Geophys.* **19**, 1273–1288.

Pei, W., Horiuchi, R., and Sato, T. (2001). Long time scale evolution of collisionless driven reconnection in two-dimensional open system. *Phys. Plasmas* **8**, 3251.

Pellat, R., Coroniti, F. V., and Pritchett, P. L. (1991). Does ion tearing exist? *Geophys. Res. Lett.* **18**, 143.

Penz, T., Semenov, V. S., Ivanova, V. V., *et al.* (2004). Application of a reconstruction method for the reconnection rate applied to Cluster. In *Proc. 5th Intl. Conf. on Problems of Geocosmos*. (St. Petersburg: University of St. Petersburg), 109–111.

Peterson, L. E. and Winckler, J. R. (1959). Gamma-ray burst from a solar flare. *J. Geophys. Res.* **64**, 697.

Petkaki, P. and MacKinnon, A. L. (1997). Particle acceleration in dynamical collisionless reconnection. *Solar Phys.* **172**, 279–286.

Petkaki, P., Watt, C. E. J., Home, R. B., and Freeman, M. P. (2003). Anomalous resistivity in non-maxwellian plasmas. *J. Geophys. Res.* **108**, SMP 14; doi:10.1029/2003JA010092.

Petrinec, S. M. and Russell, C. T. (1997). Hydrodynamic and MHD equations across the bow shock and along the surfaces of planetary obstacles. *Space Sci. Rev.* **79**, 757.

Petrinec, S. M., Mukai, T., Nishida, A., Yamamoto, T., and Nakamura, T. K. (1997). Geotail observations of magnetosheath flow near the magnetopause, using Wind as a solar wind monitor. *J. Geophys. Res.* **102**, 26943.

Petrosian, V. and Liu, S. (2004). Stochastic acceleration of electrons and protons. I. Acceleration by parallel-propagating waves. *Astrophys. J.* **610**, 550–571.

Petrukovich, A. A., Baumjohann, W., Nakamura, R., *et al.* (2003). Plasma sheet structure during strongly northward IMF. *J. Geophys. Res.* **108**, 1258, doi:10.1029/2002JA009738.

Petschek, H. E. (1964). Magnetic field annihilation. In *AAS/NASA Symposium on the Physics of Solar Flares*, W. N. Hess, ed. (Washington, DC: NASA SP-50), 425–439.

Phan, T. D., Kistler, L. M., Klecker, B., *et al.* (2000). Extended magnetic reconnection at the Earth's magnetopause from detection of bi-directional jets. *Nature* **404**, 848–850.

Phan, T. D., Frey, H., Frey, S., *et al.* (2003). Simultaneous Cluster and IMAGE observations of cusp reconnection and auroral proton spot for northward IMF. *Geophys. Res. Lett.* **30**, 1509, doi:10.1029/2003GL016885.

Phan, T. D., *et al.* (2004). Cluster observations of continuous reconnection at the magnetopause under steady interplanetary magnetic field conditions. *Ann. Geophys.* **22**, 2355.

Piana, M. (1994). Inversion of bremsstrahlung spectra emitted by solar plasma. *Astron. Astrophys.* **288**, 949–959.

Piana, M., Massone, A. M., Kontar, E. P., *et al.* (2003). Regularized electron flux spectra in the 2002 July 23 solar flare. *Astrophys. J.* **595**, L127–L130.

Pike, C. D. and Mason, H. E. (1998). Rotating features observed with the SOHO Coronal Diagnostic Spectrometer. *Solar Phys.* **182**, 333–348.

Pinnock, M., Rodger, A. S., Dudeney, J. R., *et al.* (1993). Observations of an enhanced convection channel in the cusp ionosphere. *J. Geophys. Res.* **98**, 3767.

Pinnock, M., Rodger, A. S., Baker, K. B., Lu, G., and Hairston, M. (1999). Conjugate observations of the day-side reconnection electric field: A GEM boundary layer campaign. *Ann. Geophys.* **17**, 443–454.

Pinnock, M., Chisham, G., Coleman, I. J., *et al.* (2003). The location and rate of dayside reconnection during an interval of southward interplanetary magnetic field. *Ann. Geophys.* **21**, 1467–1482.

Poletto, G. and Kopp, R. A. (1986). Macroscopic electric fields during two-ribbon flares. In *The Lower Atmosphere of Solar Flares; Proceedings of the Solar Maximum Mission Symposium.* (Sunspot, NM: National Solar Observatory/Sacramento Peak), 453–465.

Pontin, D. I., Hornig, G., and Priest, E. R. (2004). Kinematic reconnection at a magnetic null point: Spine-aligned current. *Geophys. Astrophys. Fluid Dynamics* **98**, 407–428.

Pontin, D. I., Galsgaard, K., Hornig, G., and Priest, E. R. (2005a). A fully magnetohydrodynamic simulation of 3D non-null reconnection. *Phys. Plasmas* **12**, 052307.

Pontin, D. I., Hornig, G., and Priest, E. R. (2005b). Kinematic reconnection at a magnetic null point: Fan-aligned current. *Geophys. Astrophys. Fluid Dynamics* **99**, 77–93.

Pontius, Jr., D. H. and Wolf, R. A. (1990). Transient flux tubes in the terrestrial magnetosphere. *Geophys. Res. Lett.* **17**, 49.

Porcelli, F. (1991). Collisionless $m = 1$ tearing mode. *Phys. Rev. Lett.* **66**, 425.

Porcelli, F., Borgogno, D., Califano, F., Ottaviani, M., Grasso, D., and Pegoraro, F. (2002). Recent advances in collisionless magnetic reconnection. *Plasma Phys. Controlled Fusion* **44**, B389–405.

Priest, E. R. (1981). Current sheets. In *Solar Flare Magnetohydrodynamics*, E. R. Priest, ed. (Newark, NJ: Gordon and Breach), 139.

Priest, E. R. (1996). Reconnection of magnetic lines of force. In *Solar and Astrophysical MHD Flows*, K. Tsinganos, ed. (Dordrecht: Kluwer), 151–170.

Priest, E. R. and Démoulin, P. (1995). Three-dimensional magnetic reconnection without null points. 1. Basic theory of magnetic flipping. *J. Geophys. Res.* **100**, 23443–23463.

Priest, E. R. and Forbes, T. G. (1986). New models for fast steady-state magnetic reconnection. *J. Geophys. Res.* **91**, 5579–5588.

Priest, E. R. and Forbes, T. G. (1989). Steady magnetic reconnection in three dimensions. *Solar Phys.* **119**, 211–214.

Priest, E. R. and Forbes, T. G. (1990). Magnetic field evolution during prominence eruptions and two-ribbon flares. *Solar Phys.* **126**, 319–350.

Priest, E. R. and Forbes, T. G. (1992). Magnetic flipping – reconnection in three dimensions without nulls. *J. Geophys. Res.* **97**, 1521–1531.

Priest, E. R. and Forbes, T. G. (2000). *Magnetic Reconnection: MHD Theory and Applications.* (Cambridge: Cambridge University Press).

Priest, E. R. and Raadu, M. A. (1975). Preflare current sheets in the solar atmosphere. *Solar Phys.* **43**, 177–188.

Priest, E. R. and Titov, V. S. (1996). Magnetic reconnection at three-dimensional null points. *Phil. Trans. R. Soc.* **354**, 2951–2992.

Priest, E. R., Parnell, C. E., and Martin, S. F. (1994). A converging flux model of an X-ray bright point and an associated canceling magnetic feature. *Astrophys. J.* **427**, 459–474.

Priest, E. R., Lonie, D. P., and Titov, V. S. (1996). Bifurcations of magnetic topology by the creation or annihilation of null points. *J. Plasma Phys.* **56**, 507–530.

Priest, E. R., Foley, C. R., Heyvaerts, J., *et al.* (1998). The nature of the heating mechanism for the diffuse solar corona. *Nature* **393**, 545.

Priest, E. R., Heyvaerts, J. F., and Title, A. M. (2002). A Flux Tube Tectonics model for solar coronal heating driven by the magnetic carpet. *Astrophys. J.* **576**, 533–551.

Priest, E. R., Hornig, G., and Pontin, D. I. (2003a). On the nature of three-dimensional magnetic reconnection. *J. Geophys. Res.* **108**, 1285, doi:10.1029/2002JA009812.

Priest, E. R., Longcope, D. W., and Titov, V. S. (2003b). Binary reconnection and the heating of the solar corona. *Astrophys. J.* **598**, 667–677.

Priest, E. R., Longcope, D. W., and Heyvaerts, J. (2005). Coronal heating at separators and separatrices. *Astrophys. J.* **624**, 1057–1071.

Pritchett, P. L. (1994). Effect of electron dynamics on collisionless reconnection in two-dimensional magnetotail equilibria. *J. Geophys. Res.* **99**, 5935.

Pritchett, P. L. (2001a). Collisionless magnetic reconnection in a three-dimensional open system. *J. Geophys. Res.* **106**, 25961.

Pritchett, P. L. (2001b). Geospace Environment Modeling magnetic reconnection challenge: Simulations with a full particle electromagnetic code. *J. Geophys. Res.* **106**, 3783.

Pritchett, P. L. (2005). Externally driven magnetic reconnection in the presence of a normal magnetic field. *J. Geophys. Res.* **110**, A05209, doi:10.1029/2004JA010948.

Pritchett, P. L. and Coroniti, F. V. (1995). Formation of thin current sheets during plasma sheet convection. *J. Geophys. Res.* **100**, 23551.

Pritchett, P. L. and Coroniti, F. V. (1996). The role of the drift kink mode in destabilizing thin current sheets. *J. Geomagn. Geoelectr.* **48**, 833.

Pritchett, P. L. and Coroniti, F. V. (2004). Three-dimensional collisionless magnetic reconnection in the presence of a guide field. *J. Geophys. Res.* **109**, A01220.

Pritchett, P. L., Coroniti, F. V., Pellat, R., and Karimabadi, H. (1991). Collisionless reconnection in two-dimensional magnetotail equilibria. *J. Geophys. Res.* **96**, 11523.

Pritchett, P. L., Coroniti, F. V., and Decyk, V. K. (1996). Three-dimensional stability of thin quasi-neutral current sheets. *J. Geophys. Res.* **101**, 27413.

Pritchett, P. L., Coroniti, F. V., and Pellat, R. (1997). Convection-driven reconnection and the stability of the near-Earth plasma sheet. *Geophys. Res. Lett.* **24**, 873.

Provan, G., Yeoman, T. K., Milan, S. E., Ruohoniemi, J. M., and Barnes, R. (2002). An assessment of the "map-potential" and "beam-swinging" techniques for measuring the ionospheric convection pattern using data from the SuperDARN radars. *Ann. Geophys.* **20**, 191–202.

Pu, Z.-Y., Quest, K. B., Kivelson, M. G., and Tu, C. Y. (1981). Lower-hybrid-drift instability and its associated anomalous resistivity in the neutral sheet of Earth's magnetotail. *J. Geophys. Res.* **86**, 8919–8928.

Pu, Z. Y., Korth, A., Chen, Z. X., *et al.* (1997). MHD drift ballooning instability near the inner edge of the near-Earth plasma sheet and its application to substorm onset. *J. Geophys. Res.* **102**, 14397.

Pulkkinen, T. I., Baker, D. N., Mitchell, D. G., *et al.* (1994). Thin current sheets in the magnetotail during substorms: CDAW 6 revisited. *J. Geophys. Res.* **99**, 5793–5803.

Pulkkinen, T. I., Baker, D. N., Wiltberger, M., *et al.* (1998). Pseudobreakup and substorm onset: Observations and MHD simulations compared. *J. Geophys. Res.* **103**, 14847.

Qiu, J., Lee, J., Gary, D. E., and Wang, H. (2002). Motion of flare footpoint emission and inferred electric field in reconnecting current sheets. *Astrophys. J.* **565**, 1335–1347.

Qiu, J., Liu, C., Gary, D. E., Nita, G. M., and Wang, H. (2004). Hard x-ray and microwave observations of microflares. *Astrophys. J.* **612**, 530–545.

Quest, K. B. and Coroniti, F. V. (1981). Tearing at the dayside magnetopause. *J. Geophys. Res.* **86**, 3289–3298.

Quest, K. B., Karimabadi, H., and Brittnacher, M. (1996). Consequences of particle conservation along a flux surface for magnetotail tearing. *J. Geophys. Res.* **101**, 179–183.

Quinn, J. M. and Southwood, D. J. (1982). Observations of parallel ion energization in the equatorial region. *J. Geophys. Res.* **87**, 10536.

Raeder, J. (1999). Modeling the magnetosphere for northward interplanetary magnetic field: Effects of electrical resistivity. *J. Geophys. Res.* **104**, 17357–17367.

Raeder, J. (2006). Flux transfer events: 1. Generation mechanism for nearly southward IMF. *Ann. Geophys.* **24**, 381–392.

Raeder, J., Walker, R. J., and Ashour-Abdalla, M. (1995). The structure of the distant geomagnetic tail during long periods of northward IMF. *Geophys. Res. Lett.* **22**, 349–352.

Raeder, J., Berchem, J., and Ashour-Abdalla, M. (1996). The importance of small scale processes in global MHD simulations: Some numerical experiments. In *The Physics of Space Plasmas*,

vol. 14, T. Chang and J. R. Jasperse, eds. (Cambridge, MA: MIT Center for Theoretical Geo/Cosmo Plasma Physics), 403.

Raeder, J., McPherron, R. L., Frank, L. A., *et al.* (2001). Global simulation of the geospace environment modeling substorm challenge event. *J. Geophys. Res.* **106**, 381.

Ramaty, R. (1979). Energetic particles in solar flares. In *AIP Conf. Proc. 56: Particle Acceleration Mechanisms in Astrophysics*. (Woodbury, NY: American Institute of Physics), 135–154.

Ramaty, R. and Crannell, C. J. (1976). Solar gamma-ray lines as probes of accelerated particle directionalities in flares. *Astrophys. J.* **203**, 766–768.

Ramaty, R., Kozlovsky, B., and Lingenfelter, R. E. (1979). Nuclear gamma-rays from energetic particle interactions. *Astrophys. J. Suppl.* **40**, 487–526.

Rank, G., Ryan, J., Debrunner, H., McConnell, M., and Schönfelder, V. (2001). Extended gamma-ray emission of the solar flares in June 1991. *Astron. Astrophys.* **378**, 1046–1066.

Rastätter, L., Hesse, M., and Schindler, K. (1999). Hall-MHD modeling of near-Earth magnetotail current sheet thinning and evolution. *J. Geophys. Res.* **104**, 12301.

Raulin, J. P., Kundu, M. R., Nitta, N., and Raoult, A. (1996). Radio continuum and type III bursts associated with coronal x-ray structures. *Astrophys. J.* **472**, 874.

Reale, F. (2002). More on the determination of the coronal heating function from Yohkoh data. *Astrophys. J.* **580**, 566–573.

Rees, M. H. (1963). Auroral ionization and excitation by incident energetic electrons. *Planet. Space Sci.* **11**, 1209–1218.

Reiff, P. H. and Burch, J. L. (1985). IMF By-dependent plasma flow and Birkeland currents in the dayside magnetosphere, 2, A global model for northward and southward IMF. *J. Geophys. Res.* **90**, 1595–1609.

Reiff, P. H., Hill, T. W., and Burch, J. L. (1977). Solar wind plasma injections at the dayside magnetospheric cusp. *J. Geophys. Res.* **82**, 479.

Rème, H., *et al.* (2001). First multispacecraft ion measurements in and near the Earth's magnetosphere with the identical Cluster ion spectrometry (CIS) experiment. *Ann. Geophys.* **19**, 1303–1354.

Ricci, P., Lapenta, G., and Brackbill, J. U. (2002). GEM reconnection challenge: Implicit kinetic simulations with the physical mass ratio. *Geophys. Res. Lett.* **29**, doi:10.1029/2002GL015314.

Ricci, P., Brackbill, J. U., Daughton, W., and Lapenta, G. (2004a). Influence of the lower hybrid drift instability on the onset of magnetic reconnection. *Phys. Plasmas* **11**, 4489.

Ricci, P., Lapenta, G., and Brackbill, J. U. (2004b). Structure of the magnetotail current: Kinetic simulation and comparison with satellite observations. *Geophys. Res. Lett.* **31**, L06801.

Rickard, G. J. and Titov, V. S. (1996). Current accumulation at a three dimensional magnetic null. *Astrophys. J.* **472**, 840–852.

Roberts, B. (1991). Magnetohydrodynamic waves in the Sun. In *Advances in Solar System Magnetohydrodynamics*, E. R. Priest and A. W. Hood, eds. (Cambridge: Cambridge University Press), 105–136.

Rogers, B. N., Denton, R. E., Drake, J. F., and Shay, M. A. (2001). Role of dispersive waves in collisionless magnetic reconnection. *Phys. Rev. Lett.* **87**, 195004.

Rosenbauer, H., Grünwaldt, H., Montgomery, M. D., Paschmann, G., and Sckopke, N. (1975). HEOS 2 plasma observations in the distant polar magnetosphere: The plasma mantle. *J. Geophys. Res.* **80**, 2723.

Rostoker, G., Baumjohann, W., and Russell, C. T. (1983). A case study of the response of the magnetosphere to changes in the interplanetary medium. *J. Geophys. Res.* **88**, 170.

Roussev, I. I., Forbes, T. G., Gombosi, T. I., *et al.* (2003). A three-dimensional flux rope model for coronal mass ejections based on a loss of equilibrium. *Astrophys. J.* **588**, L45–L48.

Roux, A., Perraut, S., Robert, P., *et al.* (1991). Plasma sheet instability related to the westward traveling surge. *J. Geophys. Res.* **96**, 17697.

Rowland, H. L. and Palmadesso, P. J. (1983). Anomalous resistivity due to low-frequency turbulence. *J. Geophys. Res.* **88**, 7997–8002.

Runov, A., Nakamura, R., Baumjohann, W., *et al.* (2003a). Current sheet structure near magnetic X-line observed by Cluster. *Geophys. Res. Lett.* **30**, 1579, doi:10.1029/2002GL016730.

Runov, A., Nakamura, R., Baumjohann, W., *et al.* (2003b). Cluster observation of a bifurcated current sheet. *Geophys. Res. Lett.* **30**, 1036, doi:10.1029/2002GL016136.

Runov, A., Sergeev, V., Nakamura, R., *et al.* (2004). Properties of a bifurcated current sheet observed on August 29, 2001. *Ann. Geophys.* **22**, 25352540.

Runov, A., Sergeev, V. A., Nakamura, R., *et al.* (2005). Reconstruction of the magnetotail current sheet structure using multi-point Cluster measurements. *Planet. Space Sci.* **53**, 237–243.

Ruohoniemi, J. M. and Baker, K. B. (1998). Large-scale imaging of high-latitude convection with Super Dual Auroral Radar Network HF radar observations. *J. Geophys. Res.* **103**, 20797–20811.

Russell, C. T. and Elphic, R. C. (1978). Initial ISEE magnetometer results: Magnetopause observations. *Space Sci. Rev.* **22**, 681.

Rust, D. M. and Kumar, A. (1996). Evidence for helically kinked magnetic flux ropes in solar eruptions. *Astrophys. J.* **464**, L199–L202.

Sagdeev, R. A. and Shapiro, V. D. (1973). Influence of transverse magnetic-field on Landau damping. *JETP Lett. (Engl. Transl.)* **17**, 279–282.

Sakai, J.-I. and Ohsawa, Y. (1987). Particle-acceleration by magnetic reconnection and shocks during current loop coalescence in solar-flares. *Space Sci. Rev.* **46**, 113–198.

Sakao, T., Kosugi, T., Masuda, S., *et al.* (1996). Characteristics of hard X-ray double sources in impulsive solar flares. *Adv. Space Res.* **17**, 67.

Sakao, T., Kosugi, T., Masuda, S., and Sato, J. (2000). Evolution of magnetic field structure and particle acceleration in solar flares. *Adv. Space Res.* **26**, 497–500.

Sandholt, P. E. and Farrugia, C. J. (2003). Does the aurora provide evidence for the occurrence of antiparallel magnetopause reconnection? *J. Geophys. Res.* **108**, 1466, doi:10.1029/2003JA010066.

Sanny, J., McPherron, R. L., Russell, C. T., *et al.* (1994). Growth-phase thinning of the near-Earth current sheet during the CDAW 6 substorm. *J. Geophys. Res.* **99**, 5805–5816.

Sarris, E. T., Krimigis, S. M., and Armstrong, T. P. (1976). Observation of magnetospheric bursts of high-energy protons and electrons at 35 $R_{\rm E}$ with IMP-7. *J. Geophys. Res.* **81**, 2342–2355.

Sarris, E. T., Krimigis, S. M., Lui, A. T. Y., *et al.* (1981). Relationship between energetic particles and plasmas in the distant plasma sheet. *Geophys. Res. Lett.* **8**, 349–352.

Sato, T. and Hayashi, T. (1979). Externally driven magnetic reconnection and a powerful magnetic energy converter. *Phys. Fluids* **22**, 1189–1202.

Sato, T., Matsumoto, H., and Nagai, K. (1982). Particle acceleration in time-developing magnetic reconnection process. *J. Geophys. Res.* **87**, 6089–6097.

Savrukhin, P. V. (2001). Generation of suprathermal electrons during magnetic reconnection at the sawtooth crash and disruption instability in the t-10 tokamak. *Phys. Rev. Lett.* **86**, 3036–3039.

Scherrer, P. H., Bogart, R. S., Bush, R. I., *et al.* (1995). The solar oscillations investigation – Michelson Doppler Imager. *Solar Phys.* **162**, 129–188.

Schindler, K. (1966). A variational principle for one-dimensional plasmas. In *Proceedings of the Seventh International Conference on Phenomena in Ionized Gases, vol. II.* (Grodevinska Knjiga, Beograd, Yugoslavia), 736.

Schindler, K. (1972). A self-consistent theory of the tail of the magnetosphere. In *Earth's Magnetospheric Processes*, B. M. McCormac, ed. (Norwell, MA: D. Reidel), 200.

Schindler, K. (1974). A theory of the substorm mechanism. *J. Geophys. Res.* **79**, 2803.

Schindler, K. (1995). Kinematics of magnetic reconnection in three dimensions. In *Physics of the Magnetopause*, P. Song, B. U. Ö. Sonnerup, and M. F. Thomsen, eds. Geophysical Monograph. (Washington, DC: American Geophysical Union), 197.

Schindler, K. and Birn, J. (1993). On the cause of thin current sheets in the near-Earth magnetotail and their possible significance for magnetospheric substorms. *J. Geophys. Res.* **98**, 15477.

Schindler, K. and Birn, J. (2004). MHD-stability of magnetotail equilibria including a background pressure. *J. Geophys. Res.* **109**, doi:10.1029/2004JA010537, A10208.

Schindler, K., Pfirsch, D., and Wobig, H. (1973). Stability of two-dimensional collison-free plasmas. *Plasma Phys.* **15**, 1165.

Schindler, K., Birn, J., and Janicke, L. (1983). Stability of two-dimensional pre-flare structures. *Solar Phys.* **87**, 103.

Schindler, K., Hesse, M., and Birn, J. (1988). General magnetic reconnection, parallel electric fields, and helicity. *J. Geophys. Res.* **93**, 5547–5557.

Schindler, K., Baker, D. N., Birn, J., *et al.* (1989). Analysis of an extended period of earthward plasma flow at ∼220 R_E: CDAW-8. *J. Geophys. Res.* **94**, 15177.

Schindler, K., Hesse, M., and Birn, J. (1991). Magnetic field-aligned electric potentials in nonideal plasma flows. *Astrophys. J.* **380**, 293–301.

Schlickeiser, R. (2002). *Cosmic Ray Astrophysics*. (Berlin: Springer).

Scholer, M. (1989). Undriven magnetic reconnection in an isolated current sheet. *J. Geophys. Res.* **94**, 8805–8812.

Scholer, M. and Jamitzky, F. (1987). Particle orbits during the development of plasmoids. *J. Geophys. Res.* **92**, 12181–12186.

Scholer, M. and Otto, A. (1991). Magnetotail reconnection: Current diversion and field-aligned currents. *Geophys. Res. Lett.* **18**, 733.

Scholer, M., Sidorenko, I., Jaroscheck, C. H., Treumann, R. A., and Zeiler, A. (2003). Onset of collisionless magnetic reconnection in thin current sheets: Three-dimensional particle simulations. *Phys. Plasmas* **10**, 3521.

Schrijver, C. J., Title, A. M., Ballegooijen, A. A., Hagenaar, H. J., and Shine, R. A. (1997). Sustaining the quiet photospheric network: the balance of flux emergence, fragmentation, merging and cancellation. *Astrophys. J.* **487**, 424–436.

Schrijver, C. J., Title, A. M., Harvey, K. L., *et al.* (1998). Large-scale coronal heating by the small-scale magnetic field of the sun. *Nature* **394**, 152–154.

Selkowitz, R. and Blackman, E. G. (2004). Stochastic Fermi acceleration of subrelativistic electrons and its role in impulsive solar flares. *Mon. Not. R. Astron. Soc.* **354**, 870–882.

Sergeev, V. A., Tanskanen, P., Mursula, K., Korth, A., and Elphic, R. C. (1990). Current sheet thickness in the near-Earth plasma sheet during substorm growth phase. *J. Geophys. Res.* **95**, 3819.

Sergeev, V. A., Mitchell, D. G., Russell, C. T., and Williams, D. J. (1993). Structure of the tail plasma/current sheet at ∼11 R_E and its changes in the course of a substorm. *J. Geophys. Res.* **98**, 17345.

Sergeev, V. A., Angelopoulos, V., Gosling, J. T., Cattell, C. A., and Russell, C. T. (1996). Detection of localized, plasma-depleted flux tubes or bubbles in the midtail plasma sheet. *J. Geophys. Res.* **101**, 10817.

Sergeev, V., Runov, A., Baumjohann, W., *et al.* (2003). Current sheet flapping motion and structure observed by Cluster. *Geophys. Res. Lett.* **30**, 1327, doi:10.1029/2002GL016500.

Sergeev, V., Runov, A., Baumjohann, W., *et al.* (2004). Orientation and propagation of current sheet oscillations. *Geophys. Res. Lett.* **31**, L05807, doi:10.1029/2003GL019346.

Sergeev, V. A., Kubyshkina, M. V., Baumjohann, W., *et al.* (2005). Transition from substorm growth to substorm expansion phase as observed with a radial configuration of ISTP and Cluster spacecraft. *Ann. Geophys.* **23**, 2183–2198.

Share, G. H., Murphy, R. J., Kiener, J., and de Séréville, N. (2002). Directionality of solar flare-accelerated protons and α-particles from γ-ray line measurements. *Astrophys. J.* **573**, 464–470.

Share, G. H., Murphy, R. J., Smith, D. M., Schwartz, R. A., and Lin, R. P. (2004). RHESSI $e^+ - e^-$ annihilation radiation observations: Implications for conditions in the flaring solar chromosphere. *Astrophys. J.* **615**, L169–L172.

Shay, M. A. and Drake, J. F. (1998). The role of electron dissipation on the rate of collisionless magnetic reconnection. *Geophys. Res. Lett.* **25**, 3759–3762.

Shay, M. A., Drake, J. F., and Rogers, B. N. (1999). The scaling of collisionless, magnetic reconnection for large systems. *Geophys. Res. Lett.* **26**, 2163–2166.

Shay, M. A., Drake, J. F., Rogers, B. N., and Denton, R. E. (2001). Alfvenic collisionless magnetic reconnection and the Hall term. *J. Geophys. Res.* **106**, 3759–3772.

Shay, M. A., Drake, J. F., Swisdak, M., and Rogers, B. N. (2004). The scaling of embedded collisionless magnetic reconnection. *Phys. Plasmas* **11**, 2199.

Shellard, E. (1987). Reconnection of topological defects. *Nucl. Phys. B* **282**, 624.

Shen, C., Li, X., Dunlop, M., *et al.* (2003). Analysis on the geometrical structure of magnetic field in the current sheet based on Cluster measurements. *J. Geophys. Res.* **108**, 1168, doi:10.1029/2002JA009612.

Shibata, K. and Yokoyama, T. (1999). Origin of the universal correlation between the flare temperature and the emission measure for solar and stellar flares. *Astrophys. J.* **526**, L49–L52.

Shibata, K., Ishido, Y., Acton, L. W., *et al.* (1992). Observations of X-ray jets with the Yohkoh Soft X-ray Telescope. *Publ. Astron. Soc. Japan* **44**, L173–L179.

Shinohara, I., Nagai, T., Fujimoto, M., *et al.* (1998). Low-frequency electromagnetic turbulence observed near the substorm onset site. *J. Geophys. Res.* **103**, 20365.

Sibeck, D. G., Lopez, R. E., and Roelof, E. C. (1991). Solar wind control of the magnetopause shape, location, and motion. *J. Geophys. Res.* **96**, 5489.

Silin, I. and Büchner, J. (2003a). Kinetic instabilities of thin current sheets. Results of $2^1/_2$D Vlasov code simulations. *Phys. Plasmas* **10**, 1299–1307.

Silin, I. and Büchner, J. (2003b). Nonlinear instability of thin current sheets in antiparallel and guided magnetic fields. *Phys. Plasmas* **10**, 3561–3570.

Silin, I. and Büchner, J. (2005a). Small-scale reconnection due to lower-hybrid drift instability in current sheets with sheared fields. *Phys. Plasmas* **12**, 35–50.

Silin, I. and Büchner, J. (2005b). Three-dimensional Vlasov-code simulations of magnetopause-like current sheets. *Adv. Space Res.* **37**, 1354–1362.

Silin, I., Büchner, J., and Zelenyi, L. M. (2002). Instabilities of collisionless current sheets: Theory and simulations. *Phys. Plasmas* **9**, 1104.

Silveira, O. J. G., Ziebell, L. F., Gaelzer, R., and Yoon, P. H. (2002). Unified formulation for inhomogeneity-driven instabilities in the lower-hybrid range. *Phys. Rev. E* **65**, 036407.

Siscoe, G. L. (1988). The magnetospheric boundary. In *Physics of Space Plasmas*, T. Chang, G. B. Crew, and J. R. Jasperse, eds. (Cambridge, MA: Scientific), 3–78.

Siscoe, G. L., Erickson, G. M., Sonnerup, B. U. Ö., *et al.* (2001). Global role of $E_{\|}$ in magnetopause reconnection: An explicit demonstration. *J. Geophys. Res.* **106**, 13015–13022.

Sitnov, M. I., Malova, H. V., and Sharma, A. S. (1998). Role of the temperature ratio in the linear stability of the quasi-neutral sheet tearing mode. *Geophys. Res. Lett.* **25**, 269.

Sitnov, M. I., Sharma, A. S., Guzdar, P. N., and Yoon, P. H. (2002). Reconnection onset in the tail of Earth's magnetosphere. *J. Geophys. Res.* **107**, 1256, doi:10.1029/2001JA009148.

Sitnov, M. I., Guzdar, P. N., and Swisdak, M. (2003). A model of the bifurcated current sheet. *Geophys. Res. Lett.* **30**, 1712, doi:10.1029/2003GL017218.

Slavin, J. A., Smith, E. J., Tsurutani, B. T., *et al.* (1984). Substorm associated traveling compression regions in the distant tail: ISEE 3 geotail observations. *Geophys. Res. Lett.* **11**, 657.

Slavin, J. A., Smith, E. J., Sibeck, D. G., *et al.* (1985). An ISEE 3 study of average and substorm conditions in the distant magnetotail. *J. Geophys. Res.* **90**, 10875.

Slavin, J. A., Lepping, R. P., Gjerloev, J., *et al.* (2003a). Cluster measurements of electric current density within a flux rope in the plasma sheet. *Geophys. Res. Lett.* **30**, 1362, doi:10.1029/2003GL016411.

Slavin, J. A., Owen, C. J., Dunlop, M. W., *et al.* (2003b). Cluster four spacecraft measurements of small traveling compression regions in the near tail. *Geophys. Res. Lett.* **30**, 2208, doi:10.1029/2003GL018438.

Smith, D. M., Share, G. H., Murphy, R. J., *et al.* (2003). High-resolution spectroscopy of gamma-ray lines from the X-class solar flare of 2002 July 23. *Astrophys. J.* **595**, L81–L84.

Smith, E. J., Lockwood, M., and Cowley, S. W. H. (1992). The statistical cusp: The flux transfer event model. *Planet. Space Sci.* **40**, 1251.

Smith, M. F. and Lockwood, M. (1996). Earth's magnetospheric cusp. *Rev. Geophys.* **34**, 233.

Somov, B. (1992). *Physical Processes in Solar Flares.* (Dordrecht: Kluwer).

Somov, B. and Titov, V. S. (1985). Magnetic reconnection in high-temperature plasma solar flares. *Solar Phys.* **102**, 79–96.

Somov, B. V. and Bogachev, S. A. (2003). The betatron effect in collapsing magnetic traps. *Astron. Lett.* **29**, 621–628.

Somov, B. V. and Kosugi, T. (1997). Collisionless reconnection and high-energy particle acceleration in solar flares. *Astrophys. J.* **485**, 859–868.

Sonnerup, B. U. Ö. (1970). Magnetic-field reconnection in a highly conducting incompressible fluid. *J. Plasma Phys.* **4**, 161–174.

Sonnerup, B. U. Ö. (1974). Magnetopause reconnection rate. *J. Geophys. Res.* **79**, 1546.

Sonnerup, B. U. Ö. and Ledley, B. G. (1979). Ogo-5 magnetopause structure and classical reconnection. *J. Geophys. Res.* **84**, 399–405.

Sonnerup, B. U. Ö. and Priest, E. R. (1975). Resistive MHD stagnation-point flows at a current sheet. *J. Plasma Phys.* **14**, 283–294.

Sonnerup, B. U. Ö., Paschmann, G., Papamastorakis, I., *et al.* (1981). Evidence for magnetic field reconnection at the Earth's magnetopause. *J. Geophys. Res.* **86**, 10049–10067.

Sonnerup, B. U. Ö., *et al.* (1984). Reconnection of magnetic fields. In *Solar Terrestrial Physics: Present and Future, NASA Ref. Pub. 1120*, D. M. Butler and K. Papadapolous, eds. (Washington, DC: NASA), Chapter 1.

Sonnerup, B. U. Ö., Papamastorakis, I., Paschmann, G., and Lühr, H. (1987). Magnetopause properties from AMPTE/IRM observations of the convection electric field: Method development. *J. Geophys. Res.* **92**, 12137–12159.

Sonnerup, B. U. Ö., Hasegawa, H., and Paschmann, G. (2004). Anatomy of a flux transfer event seen by Cluster. *Geophys. Res. Lett.* **31**, L11803, doi:10.1029/2004GL020134.

Sotirelis, T. and Newell, P. T. (2000). Boundary-oriented electron precipitation model. *J. Geophys. Res.* **105**, 18655–18673.

Sotirelis, T., Newell, P. T., and Meng, C.-I. (1998). Shape of the open-closed boundary of the polar cap as determined from observations of precipitating particles by up to four DMSP satellites. *J. Geophys. Res.* **103**, 399–406.

Sotirelis, T., Newell, P. T., Meng, C.-I., and Hairston, M. (1999). Low-altitude signatures of magnetotail reconnection. *J. Geophys. Res.* **104**, 17311–17321.

Sotirelis, T., Ruohoniemi, J. M., Barnes, R. J., *et al.* (2005). Comparison of SuperDARN radar boundaries with DMSP particle precipitation boundaries. *J. Geophys. Res.* **110**, A06302, doi:10.1029/2004JA010732.

Soward, A. M. and Priest, E. R. (1977). Fast magnetic reconnection. *Phil. Trans. R. Soc. Lond. A* **284**, 369–417.

Speiser, T. W. (1965). Particle trajectories in model current sheets. 1. Analytical solutions. *J. Geophys. Res.* **70**, 4219–4226.

Spitzer, L. (1962). *Physics of Fully Ionized Gases.* (New York: Interscience).

Spitzer, L. and Härm, R. (1953). Transport phenomena in a completely ionized gas. *Phys. Rev.* **89**, 977–981.

Spreiter, J. R., Summers, A. L., and Alksne, A. Y. (1966). Hydromagnetic flow around the magnetosphere. *Planet. Space Sci.* **14**, 223.

Steinacker, J. and Miller, J. A. (1992). Stochastic gyroresonant electron acceleration in a low-beta plasma. I. Interaction with parallel transverse cold plasma waves. *Astrophys. J.* **393**, 764–781.

Steinolfson, R. S. and Van Hoven, G. (1984). Nonlinear evolution of the resistive tearing mode. *Phys. Fluids* **27**, 1207–1214.

Sterling, A. C. and Hudson, H. S. (1997). Yohkoh SXT observations of x-ray "dimming" associated with a halo coronal mass ejection. *Astrophys. J.* **491**, L55–L58.

Sterling, A. C. and Moore, R. L. (2004). External and internal reconnection in two filament-carrying magnetic cavity solar eruptions. *Astrophys. J.* **613**, 1221–1232.

Sterling, A. C., Hudson, H. S., Thompson, B. J., and Zarro, D. M. (2000). Yohkoh SXT and SOHO EIT observations of sigmoid-to-arcade evolution of structures associated with halo coronal mass ejections. *Astrophys. J.* **532**, 628–647.

Stern, D. P. (1973). A study of the electric field in an open magnetospheric model. *J. Geophys. Res.* **78**, 7292–7305.

Stern, D. P. (1994). The art of mapping the magnetosphere. *J. Geophys. Res.* **99**, 17169–17198.

Stix, T. H. (1992). *Waves in Plasmas.* (New York: American Institute of Physics).

Strachan, N. and Priest, E. R. (1994). A general family of nonuniform reconnection models with separatrix jets. *Geophys. Astrophys. Fluid Dynamics* **74**, 245–274.

Sturrock, P. A. (1966). Model of the high-energy phase of solar flares. *Nature* **211**, 695.

Sturrock, P. A. (1989). The role of eruption in solar flares. *Solar Phys.* **121**, 387–397.

Sui, L. and Holman, G. D. (2003). Evidence for the formation of a large-scale current sheet in a solar flare. *Astrophys. J.* **596**, L251–L254.

Sumners, D. (1990). Untangling DNA. *Math. Intell.* **12**, 71–80.

Sweet, P. A. (1958a). The neutral point theory of solar flares. In *Electromagnetic Phenomena in Cosmical Physics*, B. Lehnert, ed. (Cambridge: Cambridge University Press), 123–134.

Sweet, P. A. (1958b). The production of high energy particles in solar flares. *Nuovo Cimento* **8**, 188–196.

Sweet, P. A. (1969). Mechanisms of solar flares. *Ann. Rev. Astron. Astrophys.* **7**, 149–177.

Swisdak, M., Rogers, B. N., Drake, J. F., and Shay, M. A. (2003). Diamagnetic suppression of component magnetic reconnection at the magnetopause. *J. Geophys. Res.* **108**, 1218.

Swisdak, M., Drake, J. F., Shay, M. A., and McIlhargey, J. G. (2005). Transition from antiparallel to component magnetic reconnection. *J. Geophys. Res.* **110**, A05210.

Syrjäsuo, M. T., Pulkkinen, T. I., Janhunen, P., *et al.* (1998). Observations of substorm dynamics using the MIRACLE network. In *Int. Conf. Substorms-4*, S. Kokubun and Y. Kamide, eds. (Tokyo: Terra Scientific Publishing Company), 111–114.

Syrovatskii, S. I. (1971). Formation of current sheets in a plasma with a frozen-in strong magnetic field. *Sov. Phys. JETP (Engl. Transl.)* **33**, 933–940.

Syrovatskii, S. I. (1981). Pinch sheets and reconnection in astrophysics. *Ann. Rev. Astron. Astrophys.* **19**, 163–229.

Takakura, T., Tsuneta, S., Nitta, N., *et al.* (1983). Hard X-ray imaging of a solar limb flare with the X-ray telescope aboard the HINOTORI satellite. *Astrophys. J.* **270**, L83–L87.

Takeda, Y. and Inuzuka, H. (2000). Anomalous resistivity caused by nonlinear lower hybrid waves in a high-voltage linear plasma discharge. *Phys. Lett. A* **265**, 282–287.

Tanaka, M. (1995a). The macro-em particle simulation method and a study of collisionless magnetic reconnection. *Comp. Phys. Comm.* **87**, 117.

Tanaka, M. (1995b). Macro-particle simulations of collisionless magnetic reconnection. *Phys. Plasmas* **2**, 2920.

Tanaka, M. (1996). Asymmetry and thermal effects due to parallel motion of electrons in collisionless magnetic reconnection. *Phys. Plasmas* **3**, 3998–4009.

Tanaka, M. (2001). The origins of electrical resistivity in magnetic reconnection: studies by 2D and 3D macro particle simulations. *Earth Planets Space* **53**, 463–472.

Tanaka, M. and Sato, T. (1981). Simulations on lower hybrid drift instability and anomalous resistivity in the magnetic neutral sheet. *J. Geophys. Res.* **86**, 5541.

Tandberg-Hanssen, E. (1994). *The Nature of Solar Prominences.* (Dordrecht: Kluwer Academic Publishers).

Tandberg-Hanssen, E. and Emslie, A. G. (1988). *The Physics of Solar Flares.* (New York: Cambridge University Press).

Terasawa, T. (1983). Hall current effect on tearing mode instability. *Geophys. Res. Lett.* **10**, 475–478.

Terasawa, T. and Nishida, A. (1976). Simultaneous observations of relativistic electron bursts and neutral-line signatures in the magnetotail. *Planet. Space Sci.* **24**, 855–866.

Thomsen, M. F., Stansberry, J. A., Barne, S. J., Fuselier, S. A., and Gosling, J. T. (1987). Ion and electron velocity distributions within flux transfer events. *J. Geophys. Res.* **92**, 12127.

Titov, V. S. (1992). On the method of calculating two-dimensional potential magnetic fields with current sheets. *Solar Phys.* **139**, 401–404.

Titov, V. S. and Démoulin, P. (1999). Basic topology of twisted magnetic configurations in solar flares. *Astron. Astrophys.* **351**, 707–720.

Titov, V. S., Hornig, G., and Démoulin, P. (2002). Theory of magnetic connectivity in the solar corona. *J. Geophys. Res.* **7**, doi:10.1029/2001JA000278.

Titov, V. S., Démoulin, P., and Hornig, G. (2003a). Hyperbolic flux tubes in flaring magnetic configurations. *Astron. Nachrichten* **3**, 17–18.

Titov, V. S., Galsgaard, K., and Neukirch, T. (2003b). Magnetic pinching of hyperbolic flux tubes. I. Basic estimations. *Astrophys. J.* **582**, 1172–1189.

Tomczak, M. (2001). The analysis of hard X-ray radiation of flares with occulted footpoints. *Astron. Astrophys.* **366**, 294–305.

Török, T. and Kliem, B. (2004). The kink instability in solar eruptions. *Proc. SOHO-15 Conference (ESA SP-575)* **575**, 56–61.

Török, T., Kliem, B., and Titov, V. S. (2004). Ideal kink instability of a magnetic loop equilibrium. *Astron. Astrophys.* **413**, L27–L30.

Torr, M. R., Torr, D. G., Zukic, M., *et al.* (1995). A Far Ultraviolet Imager for the International Solar-Terrestrial Physics Mission. *Space Sci. Rev.* **71**, 329–383.

Trattner, K. J., Fuselier, S. A., Peterson, W. K., *et al.* (1999). On spatial and temporal structures in the cusp. *J. Geophys. Res.* **104**, 28411.

Trattner, K. J., Fuselier, S. A., Peterson, W. K., *et al.* (2002a). Temporal versus spatial interpretation of cusp ion structures observed by two spacecraft. *J. Geophys. Res.* **107**, 1287, doi:10.1029/2001JA000181.

Trattner, K. J., Fuselier, S. A., Peterson, W. K., and Carlson, C. W. (2002b). Spatial features observed in the cusp under steady solar wind conditions. *J. Geophys. Res.* **107**, 1288, doi:10.1029/2001JA000262.

Trattner, K. J., Fuselier, S. A., Yeoman, T. K., *et al.* (2003). Cusp structures: Combining multi-spacecraft observations with ground based observations. *Ann. Geophys.* **21**, 2031.

Trattner, K. J., Fuselier, S. A., and Petrinec, S. M. (2004). Location of the reconnection line for northward interplanetary magnetic field. *J. Geophys. Res.* **109**, A03219, doi:10.1029/2003JA009975.

Trattner, K. J., Fuselier, S. A., Petrinec, S. M., *et al.* (2005). The reconnection sites of spatial cusp structures. *J. Geophys. Res.* **110**, A04207, doi:10.1029/2004JA010722.

Tsuneta, S. (1985). Heating and acceleration processes in hot thermal and impulsive solar flares. *Astrophys. J.* **290**, 353–358.

Tsuneta, S. (1996). Structure and dynamics of magnetic reconnection in a solar flare. *Astrophys. J.* **456**, 840–849.

Tsuneta, S. and Naito, T. (1998). Fermi acceleration at the fast shock in a solar flare and the impulsive loop-top hard X-ray source. *Astrophys. J.* **495**, L67–L70.

Tsuneta, S., Acton, L., Bruner, M., *et al.* (1991). The soft X-ray telescope for the SOLAR-A mission. *Solar Phys.* **136**, 37–67.

Tsuneta, S., Hara, H., Shimizu, T., *et al.* (1992). Observation of a solar flare at the limb with the Yohkoh soft X-ray telescope. *Publ. Astron. Soc. Japan* **44**, 63–69.

Tsyganenko, N. A. (1995). Modeling the Earth's magnetospheric magnetic field confined within a realistic magnetopause. *J. Geophys. Res.* **100**, 5599.

Tsyganenko, N. A. (2002). A model of the near magnetosphere with a dawn–dusk asymmetry: 2. Parameterization and fitting to observations. *J. Geophys. Res.* **107**, 1176, doi:10.1029/2001JA000220.

Turkmani, R., Vlahos, L., Galsgaard, K., Cargill, P. J., and Isliker, H. (2005). Particle acceleration in stressed coronal magnetic fields. *Astrophys. J.* **620**, L59–L62.

Ugai, M. (1988). MHD simulations of fast reconnection spontaneously developing in a current sheet. *Comp. Phys. Comm.* **49**, 185–192.

Uzdensky, D. A. and Kulsrud, R. M. (2000). Two-dimensional numerical simulation of the resistive reconnection layer. *Phys. Plasmas* **7**, 4018–4030.

Vaisberg, O. L., Galeev, A. A., Zelenyi, L. M., *et al.* (1983). Fine structure of the magnetopause based on measurements on the Prognoz-7 and Prognoz-8 satellites. *Kosmich. Issled.* **21**, 57–63.

Vaivads, A., André, M., Buchert, S. C., *et al.* (2004a). Cluster observations of lower-hybrid turbulence within thin layers at the magnetopause. *Geophys. Res. Lett.* **31**, L03804.

Vaivads, A., Khotyaintsev, Y., André, M., *et al.* (2004b). Structure of the magnetic reconnection diffusion region from four-spacecraft observations. *Geophys. Res. Lett.* **31**, L03804.

van Ballegooijen, A. A. (1985). Electric currents in the solar corona and the existence of magnetostatic equilibrium. *Astrophys. J.* **298**, 421–430.

van Ballegooijen, A. A. (1986). Cascade of magnetic energy as a mechanism of coronal heating. *Astrophys. J.* **311**, 1001–1014.

van Beek, H. F., Hoyng, P., Lafleur, B., and Simnett, G. M. (1980). The hard X-ray imaging spectrometer HXIS. *Solar Phys.* **65**, 39–52.

van Beek, H. F., de Jager, C., Schadee, A., *et al.* (1981). The limb flare of 1980 April 30 as seen by the hard X-ray imaging spectrometer. *Astrophys. J.* **244**, L157–L162.

Vasyliūnas, V. M. (1975). Theoretical models of magnetic field line merging, 1. *Rev. Geophys. Space Phys.* **13**, 303–336.

Vasyliunas, V. (1976). An overview of magnetospheric dynamics. In *Magnetospheric Particles and Fields*, B. M. McCormac, ed. (Dordrecht: D. Reidel), 99.

Vasyliunas, V. M. (1984). Steady state aspects of magnetic field line merging. In *Magnetic Reconnection in Space and Laboratory Plasmas*, Geophysical Monograph Series, E. W. Hones, Jr., ed. (Washington, DC: American Geophysical Union), 25.

Vekstein, G. and Browning, P. K. (1997). Electric-drift generated trajectories and particle acceleration in collisionless magnetic reconnection. *Phys. Plasmas* **4**, 2261–2268.

Vekstein, G. E., Priest, E. R., and Steele, C. D. C. (1991). Magnetic reconnection and energy release in the solar corona by Taylor relaxation. *Solar Phys.* **131**, 297–318.

Vekstein, G. E., Priest, E. R., and Steele, C. D. C. (1993). On the problem of magnetic coronal heating by turbulent relaxation. *Astrophys. J.* **417**, 781–789.

Veronig, A. M. and Brown, J. C. (2004). A coronal thick-target interpretation of two hard x-ray loop events. *Astrophys. J.* **603**, L117–L120.

Villain, J. P., André, R., Hanuise, C., and Grésillon, D. (1996). Observation of the high latitude ionosphere by HF radars: Interpretation in terms of collective wave scattering and characterization of turbulence. *J. Atmos. Terr. Phys.* **58**, 943–958.

Voigt, G. (1986). Magnetospheric equilibrium and slow adiabatic convection. In *Solar Wind and Magnetosphere Coupling*, Y. Kamide and J. A. Slavin, eds. (Tokyo: Terra Scientific), 233.

Volwerk, M., Glassmeier, K.-H., Runov, A., *et al.* (2003). Kink mode oscillation of the current sheet. *Geophys. Res. Lett.* **30**, 1320, doi:10.1029/2002GL016467.

Volwerk, M., Baumjohann, W., Glassmeier, K.-H., *et al.* (2004). Compressional waves in the Earth's neutral sheet. *Ann. Geophys.* **22**, 303–315.

Vörös, Z., Baumjohann, W., Nakamura, R., *et al.* (2003). Multi-scale magnetic field intermittence in the plasma sheet. *Ann. Geophys.* **21**, 1955–1964.

Vörös, Z., Baumjohann, W., Nakamura, R., *et al.* (2004). Magnetic turbulence in the plasma sheet. *J. Geophys. Res.* **109**, A11215, doi:10.1029/2004JA010404.

Waelbroeck, F. W. (1989). Current sheets and nonlinear growth of the m = 1 kink-tearing mode. *Phys. Plasmas* **1**, 2372–2380.

Wang, J., Zhou, G., and Zhang, J. (2004). Helicity patterns of coronal mass ejection-associated active regions. *Astrophys. J.* **615**, 1021–1028.

Wang, X. and Bhattacharjee, A. (1994). Current sheets and reconnection driven by footpoint motion in two-dimensional coronal loops with x-type neutral lines. *Astrophys. J.* **420**, 415–421.

Wang, X., Bhattacharjee, A., and Ma, Z. W. (2001). Scaling of collisionless forced reconnection. *Phys. Rev. Lett.* **87**, 1–4.

Watt, C. E. J., Horne, J. B., and Freeman, M. P. (2002). Ion-acoustic resistivity in plasmas with similar ion and electron temperatures. *Geophys. Res. Lett.* **29**, 1004.

Webb, D. F. (2000). Understanding CMEs and their source region. *J. Atmos. Sol. Terr. Phys.* **62**, 1415–1426.

Welsch, B. T., Fisher, G. H., Abbett, W. P., and Regnier, S. (2004). ILCT: Recovering photospheric velocities from magnetograms by combining the induction equation with local correlation tracking. *Astrophys. J.* **610**, 1148–1156.

Wesson, J. A. (1987). *Tokamaks.* (Oxford: Oxford University Press).

White, S. M., Krucker, S., Shibasaki, K., *et al.* (2003). Radio and hard x-ray images of high-energy electrons in an X-class solar flare. *Astrophys. J.* **595**, L111–L114.

Wiegelmann, T. and Büchner, J. (2000). Kinetic simulations of the coupling between current instabilities and reconnection in thin current sheets. *Nonlinear Proc. Geophys.* **7**, 141.

Wilber, M., Lee, E., Parks, G. K., *et al.* (2004). Cluster observations of velocity space-restricted ion distributions near the plasma sheet. *Geophys. Res. Lett.* **31**, L24802, doi:10.1029/2004GL020265.

Wild, J. A., Milan, S. E., Owen, C. J., *et al.* (2004). The location of the open-closed magnetic field line boundary in the dawn sector auroral ionosphere. *Ann. Geophys.* **22**, 3625–3639.

Wilson, H. R. and Cowley, S. C. (2004). Theory for explosive ideal magnetohydrodynamic instabilities in plasmas. *Phys. Rev. Lett.* **92**, 175006.

Wiltberger, M., Pulkkinen, T. I., Lyon, J. G., and Goodrich, C. C. (2000). MHD simulation of the magnetotail during the December 10, 1996, substorm. *J. Geophys. Res.* **105**, 27649.

Wing, S., Newell, P. T., and Rouhoniemi, J. M. (2001). Double cusp: Model prediction and observational verification. *J. Geophys. Res.* **106**, 25571.

Winske, D. (1981). Current-driven microinstabilities in a neutral sheet. *Phys. Fluids* **24**, 1069.

Wood, P. D. (2004). Elements of solar activity – particle acceleration and filament formation. Ph.D. thesis, University of St. Andrews.

Wood, P. D. and Neukirch, T. (2005). Electron acceleration in reconnecting current sheets. *Solar Phys.* **226**, 73–95.

Wu, C. S., Zhou, Y. M., Tsai, S. T., *et al.* (1983). A kinetic cross-field streaming instability. *Phys. Fluids* **26**, 1259.

Wygant, J. R., Cattell, C. A., Lysak, R., *et al.* (2005). Cluster observations of an intense normal component of the electric field at a then reconnecting current sheet in the tail and its role in the shock-like acceleration of the ion fluid into the separatrix region. *J. Geophys. Res.* **110**, A09206.

Xu, Y., Cao, W., Liu, C., *et al.* (2004). Near-infrared observations at 1.56 microns of the 2003 October 29 X10 white-light flare. *Astrophys. J.* **607**, L131–L134.

Yamada, M., Ono, Y., Hayakawa, A., and Katsurai, M. (1990). Magnetic reconnection of plasma toroids with cohelicity and counterhelicity. *Phys. Rev. Lett.* **65**, 721.

Yamada, M., Ji, H., Hsu, S., *et al.* (2000). Experimental investigation of the neutral sheet profile during magnetic reconnection. *Phys. Plasmas* **7**, 1781.

Yamamoto, T. T., Kusano, K., Maeshiro, T., and Sakurai, T. (2005). Magnetic helicity injection and sigmoidal coronal loops. *Astrophys. J.* **624**, 1072–1079.

Yamanaka, K. (1978). Threshold of electromagnetic instability in a magnetic neutral sheet. *Physica Scripta* **17**, 15.

Yan, M., Lee, L. C., and Priest, E. R. (1992). Fast magnetic reconnection with small shock angles. *J. Geophys. Res.* **97**, 8277–8293.

Yokoyama, T., Kusano, K., Maeshiro, T., and Sakurai, T. (2003). Relation between magnetic helicity injection and flare activities in active region NOAA 8100. *Adv. Space Res.* **32**, 1949–1952.

Yoon, P. H. and Lui, A. T. Y. (1993). Nonlinear analysis of generalized cross-field current instability. *Phys. Fluids B* **5**, 836.

Yoon, P. H. and Lui, A. T. Y. (2001). On the drift-sausage mode in one-dimensional current sheet. *J. Geophys. Res.* **106**, 1939.

Yoon, P. H. and Lui, A. T. Y. (2004). Lower-hybrid drift and modified two-stream instabilities in current sheet equilibrium. *J. Geophys. Res.* **109**, A02210.

Yoon, P. H., Lui, A. T. Y., and Sitnov, M. I. (2002). Generalized lower-hybrid drift instabilities in current-sheet equilibrium. *Phys. Plasmas* **9**, 1526.

Yoshida, T. and Tsuneta, S. (1996). Temperature structure of solar active regions. *Astrophys. J.* **459**, 342–346.

Zaharia, S., Cheng, C. Z., and Johnson, J. R. (2000). Particle transport and energization associated with substorms. *J. Geophys. Res.* **105**, 18741.

Zeiler, A., Biskamp, D., Drake, J. F., *et al.* (2002). Three-dimensional particle simulations of collisionless magnetic reconnection. *J. Geophys. Res.* **107**, 1230, doi:10.1029/2001JA000287.

Zelenyi, L. M., Lipatov, A. S., Lominadze, J. G., and Taktakishvili, A. T. (1984). The dynamics of the energetic proton bursts in the course of the magnetic field topology reconstruction. *Planet Space Sci.* **32**, 312–324.

Zelenyi, L. M., Lominadze, J. G., and Taktakishvili, A. L. (1990). Generation of the energetic proton and electron bursts in planetary magnetotails. *J. Geophys. Res.* **95**, 3883–3891.

Zenitani, S. and Hoshino, M. (2001). Generation of non-thermal particles in relativistic magnetic reconnection of pair plasmas. *Astrophys. J.* **562**, L63–L66.

Zenitani, S. and Hoshino, M. (2005). Three-dimensional evolution of a relativistic current sheet: Triggering of magnetic reconnection by the guide field. *Phys. Rev. Lett.* **95**, doi:10.1103PRL95.095001.

Zhang, T. L., Baumjohann, W., Nakamura, R., Balogh, A., and Glassmeier, K.-H. (2002). A wavy twisted neutral sheet observed by Cluster. *Geophys. Res. Lett.* **29**, 1899, doi:10.1029/2002GL015544.

Zharkova, V. V. and Gordovskyy, M. (2004a). Energy spectra of particles accelerated in a reconnecting current sheet with the guiding magnetic field. *Mon. Not. R. Astron. Soc.* **356**, 1107–1116.

Zharkova, V. V. and Gordovskyy, M. (2004b). Particle acceleration asymmetry in a reconnecting nonneutral current sheet. *Astrophys. J.* **604**, 884–891.

Zharkova, V. and Gordovskyy, M. (2005). The kinetic effects of electron beam precipitation and resulting hard X-ray intensity in solar flares. *Astron. Astrophys.* **432**, 1033–1047.

Zhu, Z. and Parks, G. (1993). Particle orbits in model current sheet with a nonzero B_y component. *J. Geophys. Res.* **98**, 7603–7608.

Zhu, Z. and Winglee, R. M. (1996). Tearing instability, flux ropes, and the kinetic current sheet kink instability in the Earth's magnetotail: A three dimensional perspective from particle simulations. *J. Geophys. Res.* **101**, 4885.

Zhu, Z., Winglee, R. M., and Parks, G. K. (1992). The importance of cross-tail dynamics: A comparative study of kink and tearing instabilities in the tail (abstract). *Eos, Trans. AGU* **73**, 461.

Zong, Q.-G., Fritz, T. A., Pu, Z. Y., *et al.* (2004). Cluster observations of earthward flowing plasmoid in the tail. *Geophys. Res. Lett.* **31**, L18803, doi:10.1029/2004GL020692.

Zwan, B. J. and Wolf, R. A. (1976). Depletion of solar wind plasma near a planetary boundary. *J. Geophys. Res.* **81**, 1636.

Index